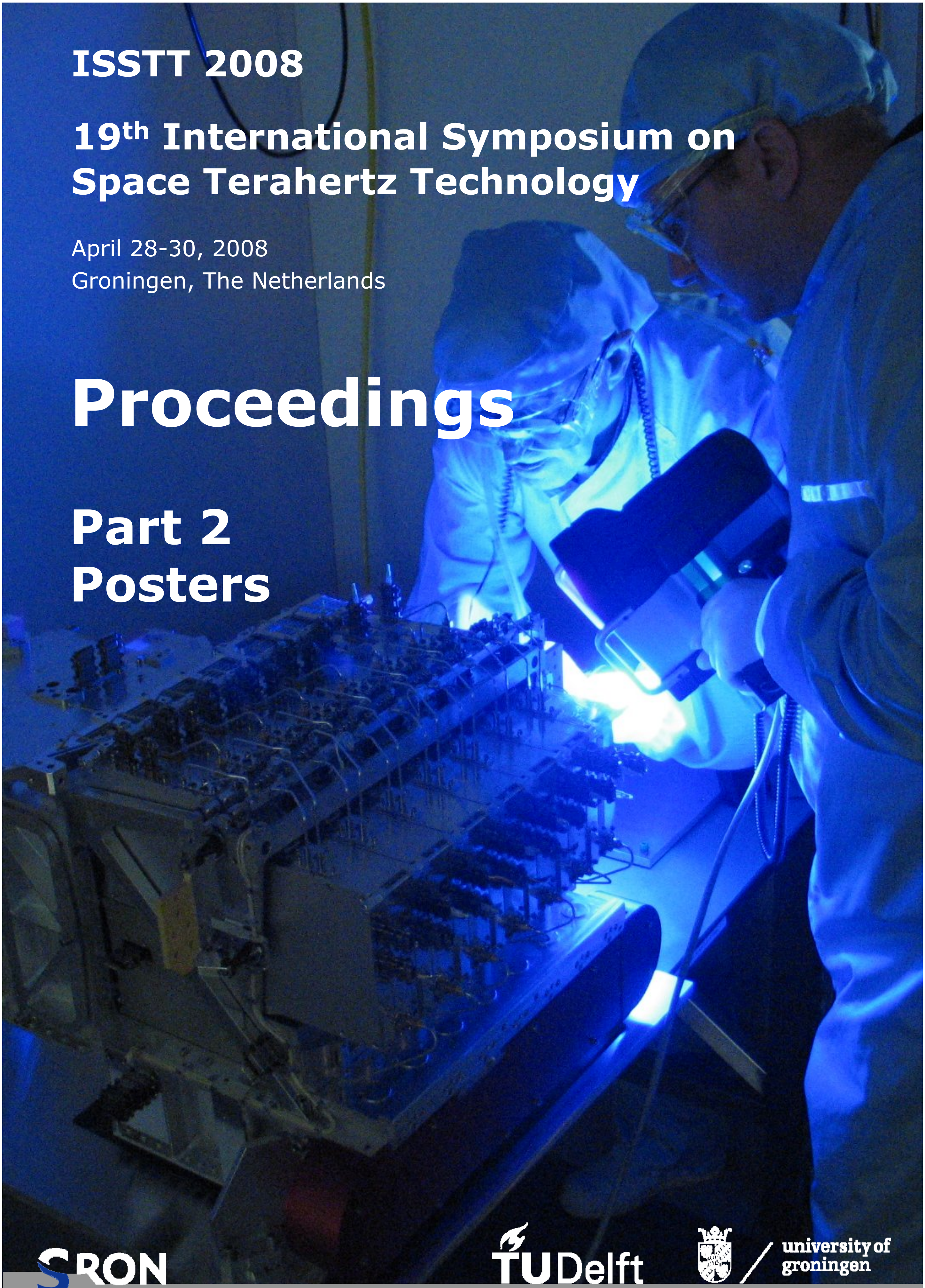

ISSTT 2008

19th International Symposium on Space Terahertz Technology

April 28-30, 2008
Groningen, The Netherlands

Proceedings

Part 2
Posters

SRON
Netherlands Institute for Space Research
Netherlands Organisation for Scientific Research

TU Delft

university of groningen

Table of Contents

Posters 2 **HEB Mixers**

Posters 3 **SIS Mixers**

Posters 4 **Herschel-HIFI**

Posters 5 **Direct Detectors**

Posters 6 **THz Receivers & Backends**

Posters 7 **Local Oscillators**

Posters 7 **Local Oscillators**

Posters 8 **Schottky Mixers**

Posters 9 **ALMA**

Posters 11 **Novel Devices and Measurements**

Posters 12 **Optics and Components**

Dome A, Antarctica: Prospectives for Terahertz Astronomy from the Ground

C.A. Kulesa[1], C.K. Walker[1], M. Schein[1], D. Golish[1], N. Tothill[2], P. Siegel[3], S. Weinreb[3], G. Jones[3], J. Bardin[3], K. Jacobs[4], C.L. Martin[5], J. Storey[6], M. Ashley[6], J. Lawrence[6], D. Luong-Van[6], J. Everett[6], L. Wang[7], L. Feng[8], Z. Zhu[8], J. Yan[8], J. Yang[8], X-G. Zhang[8], X. Cui[9], X. Yuan[9], J. Hu[10], Z. Xu[10], Z. Jiang[11], H. Yang[11], Y. Li[11], B. Sun[11], W. Qin[11], Z. Shang[12]

[1]*Steward Observatory, University of Arizona, Tucson, AZ 85721, USA*
[2]*University of Exeter, Exeter, UK*
[3]*California Institute of Technology, Pasadena, CA 91125, USA*
[4]*University of Cologne, Cologne, Germany*
[5]*Oberlin College, USA*
[6]*University of New South Wales, Australia*
[7]*Texas A&M University, USA*
[8]*Purple Mountain Observatory, China*
[9]*Nanjing Institute of Astronomical Optics Technology, China*
[10]*National Astronomical Observatory of China, China*
[11]*Polar Research Institute of China, China*
[12]*Tianjin Normal University, China*
* Contact: ckulesa@as.arizona.edu, phone +1-520-621-6540

***Abstract*— Over a decade of site testing and operation of submillimeter telescopes has shown that the high Antarctic Plateau (South Pole) and Chilean Atacama desert (Chajnantor) are exceptional ground-based sites for submillimeter and terahertz astronomy. The highest sites at both locations (Dome A and the Chajnantor and Sairecabur summits) show great promise in yielding even more favorable conditions. To test the conditions at Dome A, we have deployed Pre-HEAT, a 20 cm aperture submillimeter-wave telescope with a 660 GHz (450 micron) Schottky diode heterodyne receiver and digital FFT spectrometer for the Plateau Observatory (PLATO) developed by the University of New South Wales. In January 2008 it was deployed to Dome A, the summit of the Antarctic plateau, as part of a scientific traverse led by the Polar Research Institute of China. Dome A may be one of the best sites in the world for ground based Terahertz astronomy, based on the exceptionally cold, dry and stable conditions which prevail there. Pre-HEAT is measuring the 450 micron sky opacity at Dome A and mapping the Galactic Plane in the ^{13}CO J=6-5 line, constituting the first submillimeter measurements from Dome A. It is field-testing many of the key technologies for its name sake, a successor mission called HEAT: the High Elevation Antarctic Terahertz telescope. Exciting prospects for submillimeter astronomy from Dome A and the status of Pre-HEAT will be presented.**

I. INTRODUCTION

It has long been recognized that astronomical observations in the far-infrared (i.e. terahertz and submillimeter) are strongly attenuated by the opacity of atmospheric water vapor, nitrogen, ozone and oxygen. The most appropriate sites for long-wavelength astronomical telescopes have therefore been high, dry mountain sites. Among these, the most prominent are the summit of Mauna Kea in Hawaii, the Chajnantor plain and summit in the high Atacama desert of northern Chile, and the high Antarctic plateau. With the large-scale development of the Chajnantor plain for the Atacama Large Millimeter Array (ALMA), numerous new submillimeter-wave telescopes have arrived in Chile, ranging from small, dedicated telescopes (e.g. the 0.5-meter RLT[1] and 4-meter NANTEN2[2] telescopes) to large-scale observatories (10-meter ASTE[3], 12-meter APEX[4], and the planned 25-meter CCAT[5] reflector).

With significantly colder and drier conditions than both Mauna Kea and the Chilean Atacama desert[6], the high ice plateau of the Antarctic continent offers tantalizing prospects for astronomical observations at submillimeter wavelengths. With the advent of the 1.7-meter AST/RO telescope at the geographic South Pole, these prospects were quantified[7]. The South Pole site offers very low water vapor content in winter (~0.25 mm precipitable water vapor) superlative atmospheric stability and generally comparable transparency to the ALMA site at Chajnantor below a frequency of 1 THz. At higher frequencies, the significant dry air opacity of the South Pole owing to its comparatively low elevation (2.8 km versus 5.1 km at Chajnantor) was likely to limit the atmospheric transparency, though observations at 1.5 THz were made from the AST/RO telescope[8] before it was decommissioned to make way for the 10-meter South Pole Telescope (SPT).

The excellent submillimeter conditions obtainable from the South Pole has led to renewed interest in sites higher up on the Antarctic plateau. In 2003, the University of New South Wales installed the Automated Astrophysical Site Testing International Observatory[9] (AASTINO) at the 3.2 km elevation summit of Dome C with a 350 micron tipping radiometer among its complement of instruments. In its first season of observing, it was clearly demonstrated that conditions were both more stable and transparent than at South Pole[10]. Subsequently, expectations for the 4.1 km high summit of the Antarctic plateau (Dome A) were high[11].

It was not until 2005, when the first inland traverse to Dome A was achieved by the Polar Research Institute of China (PRIC), that an automated weather station (AWS) was installed at the site. The AWS measurements have shown that the site is colder, drier, calmer, and exhibits much lower atmospheric pressure than the South Pole (e.g. 570 versus 680 mbar)[12], indicating favorable conditions for observations at terahertz frequencies.

As a part of a 2008 International Polar Year PANDA expedition to Dome A conducted by PRIC and the Chinese Academy of Sciences (CAS), an international team set out to construct a series of experiments to quantify the site conditions at Dome A and perform initial astronomical observations. The resulting PLATeau Observatory (PLATO)[13] was designed and constructed at the University of New South Wales in Sydney, Australia in 2006-7, culminating in the integration and testing of the science experiments starting in September 2007, the delivery of the observatory to the Chinese expedition in November 2007, and the successful installation of PLATO at Dome A in January 2008. After a 4000 km oceanic voyage, a 1300 km overland traverse, and over 120 days of completely unattended operation, PLATO and its subsystems are still operational as of late May 2008.

The submillimeter component of the PLATeau Observatory is called "Pre-HEAT". It is a technological

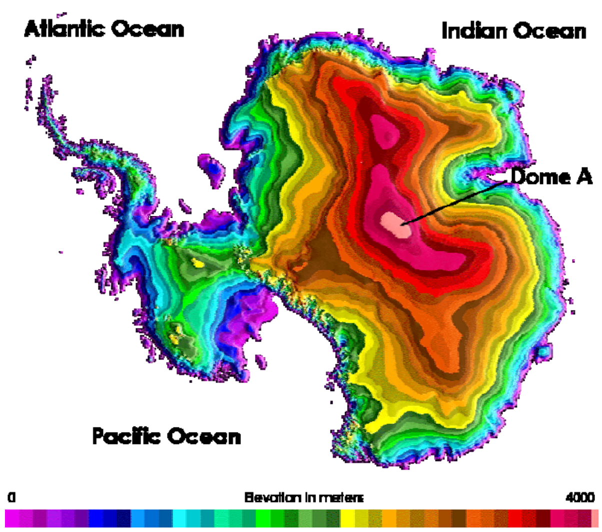

Figure 1: Topographic relief map of the Antarctic plateau; Dome A represents the summit, near the geographic center of the continent.

prototype for the High Elevation Antarctic Terahertz telescope (HEAT), and is comprised of a Schottky-diode heterodyne receiver operating at a frequency of 660 GHz (450 microns wavelength) coupled to a 20 cm aperture single-axis telescope and a digital Fast-Fourier-Transform (FFT) spectrometer.

II. Design Considerations

Pre-HEAT is designed with two principal scientific goals: to measure the 450 micron sky opacity over Dome A, and to perform spectral line observations of the Galactic Plane in the ^{13}CO J=6-5 line at 661 GHz. To achieve the same (10 arcminute) angular resolution of the landmark Columbia/CfA Galactic Plane CO J=1-0 surveys[14], a 20 cm aperture is required at 660 GHz. While pyroelectric detectors are most commonly deployed on submillimeter tipping radiometers, the requirement of sensitive, high-resolution spectroscopy suggests instead the use of an uncooled heterodyne receiver. A Schottky-diode mixer receiver, coupled with commercially-available IF amplifiers and filters[15], was provided by P. Siegel at JPL/Caltech for the experiment.

PLATO was designed around an average power budget of ~800 watts during winter, stemming exclusively from a redundant series of six diesel engines in a secondary module separated from the main instrument module by a span of 50 meters. The power specification for Pre-HEAT is therefore <200 watts at peak. Since a standard rack-mounted computer alone can absorb this entire power allotment, an embedded systems model permeates the entire design of Pre-HEAT.

The harshest environmental concern for the design and construction of Pre-HEAT is naturally the extreme cold, from the brightly-lit summers reaching a balmy -30° C (-20° F) to dark winter nights as low as -90° C (-130° F). While resistive heaters are available inside the highly insulated PLATO instrument module to provide some temperature stabilization, efficient reuse of instrument waste heat is critical to maintaining the operation of the most sensitive electronics and especially (moving) telescopic components.

Corollary to thermal control is the prevention of frost. Although the cold Antarctic air is only capable of supporting a small burden of water vapor, it is still supersaturated with respect to the frost point of ice. Thus, exposed metal surfaces which couple well to the cold infrared sky will cool radiatively below the frost- and dew-point temperatures, and accumulate ice. Judicious resistive heating of optical surfaces, mechanical deicing measures, and passive insulation and baffling to minimize radiative cooling, are all design requirements for astronomical instrumentation in Antarctica. The additional need for completely autonomous operation for up to a year at a time underlines the overarching need for a modular approach, using simple, robust components with streamlined interfaces.

Although the operation of PLATO and Pre-HEAT is unmanned, their installation would not be! With 50% less oxygen content in the air than at sea level, human physical and mental strength deteriorates greatly. Thus, a simple installation procedure with components that can be readily carried by no more than 2-3 people at altitude is necessary.

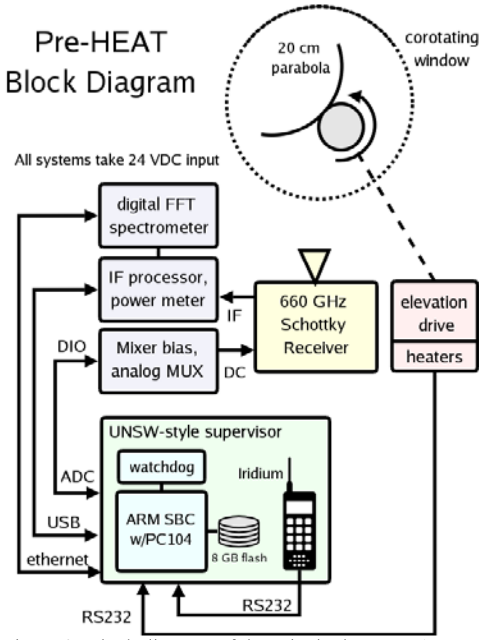

Figure 2: Block diagram of the principal Pre-HEAT subsystems

III. Pre-HEAT Subsystems

A block diagram depicting the overall system architecture of the Pre-HEAT experiment is shown in Figure 2.

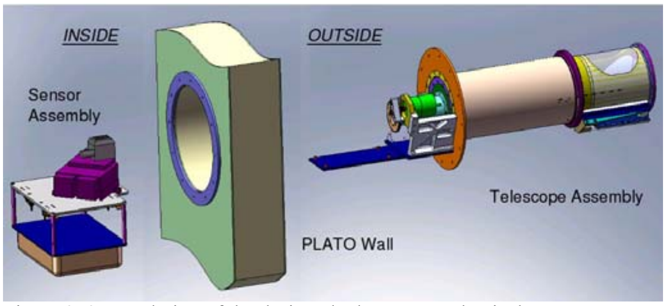

Figure 3: 3D rendering of the designed telescope mechanical structures, demonstrating the ease of assembly on-site. The masses of the inside and outside components are 10 kg and 35 kg, respectively.

A. Optical and Mechanical Assembly

The two-piece telescope assembly was designed for ease of installation (Figure 3) and machined at Larson Engineering in Boulder, CO. Two nested aluminum cylinders are spaced by a pair of low-temperature ring bearings. The outer cylinder is fitted with a radial mount to match the bolt pattern of the PLATO instrument module, and the rotating inner cylinder houses the telescope. A 1/64” thick sheet of HDPE serves as the entrance window, and a 20x28 cm 90^{o} off-axis f/5 parabola mounted at one end of the cylinder serves as the primary mirror. The focal length was set by the the Gaussian beam propagating from the feed-horn of the heterodyne receiver, and provided an edge-taper of 10 dB. Standing waves in the tube are reduced by multiple layers of silicon carbide grit embedded in layers of Stycast epoxy, providing an absorptive layer atop the otherwise reflective aluminum surface. Thin aluminum plates baffle the telescope optical beam, reducing the solid angle of cold sky seen by both the primary mirror and window. Constructed at the University of Exeter, these baffles minimize radiative cooling while allowing convective “heating” from ambient airflow. On the fixed outer tube lies a reference load which the telescope can reference by pointing down toward the ground. This absorptive cell can be heated to two different temperatures to measure the receiver noise temperature and gain for calibration. The fixed reference load is flanked by soft nylon brushes that articulate against the moving cylinder of the telescope structure, removing frost accumulation during inclement weather. Such conditions can be detected by careful monitoring of the structure temperature compared to the ambient air temperature. Thermal sensing of Pre-HEAT is performed by a series of eight AD590 two-terminal IC temperature transducers located throughout the mechanical structure.

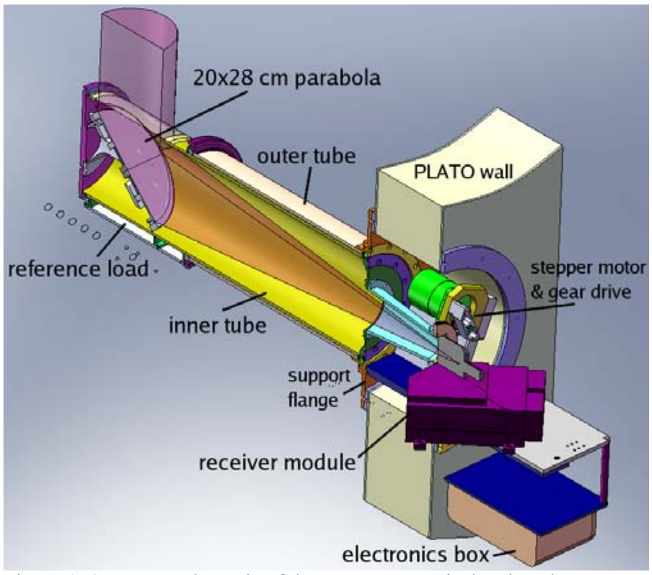

Figure 4: Cut-away schematic of the Pre-HEAT optical path and mechanical subassemblies.

Motor control of the telescope is provided by a low-temperature NEMA-34 sized stepper motor from Empire Magnetics, driven by a OEM750X stepper controller from Parker/Compumotor, which is in turn controlled via RS-232 from the Pre-HEAT computer. A cut-away cross section of the telescope assembly is shown in Figure 4, and a photo of the installed telescope at the summit of Dome A, Antarctica is shown in Figure 5.

Figure 5: The Pre-HEAT telescope installed onto the PLATO instrument module at Dome A. Photo from January 2008, courtesy Z. Zhu and Z. Xu.

A. Power Distribution and Conditioning

The PLATO-supplied bus voltage is 24-30 VDC, depending on the temperature and charge state of PLATO's 24V, 320 A-hr battery bank. The charge of the 6-gel-cell bank is maintained by diesel generators in winter, and augmented by solar panels in summer. Owing to the diverse needs of the Pre-HEAT electronics, a power conditioning module is needed to distribute proper voltages to the different components of the experiment.

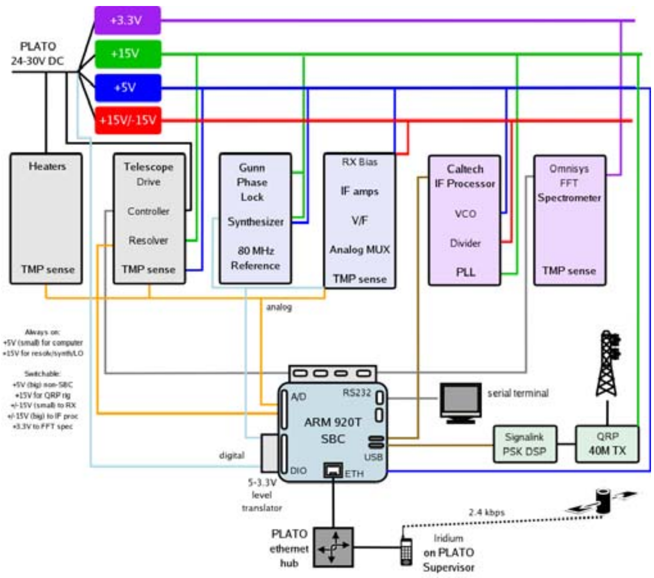

Figure 6: Block diagram of the power distribution module, showing the interrelation of the power buses, the electronics subsystems, and the digital control buses.

A series of efficient (>82%) switching DC/DC converters are employed to provide separate digital and analog 5V, +/- 15V and +3.3V power buses, as shown in Figure 6. Each DC/DC converter can be remotely controlled using TTL-level logic inputs to fine-tune the power consumption of the instrument, and is bypassed with an appropriate LC "pi" filter for the elimination of switching noise and other transients. Waste heat from the DC/DC converters is heatsunk to the electronics box chassis, coupled to the more sensitive electronics components and thermally strapped to the receiver module to provide sufficient heat to eliminate frost accumulation.

The all-up power consumption of the Pre-HEAT instrument in normal operation is 40 watts, peaking to 90 watts during a telescope slew. External resistive heaters that ward off frost accumulation add an additional 80 watts. Thus, the normal average load presented to PLATO by Pre-HEAT during winter operation is 125-150 watts.

B. Receiver Module

The Pre-HEAT receiver module is derived from the fundamental planar-Schottky-diode mixer receiver provided by P. Siegel at Caltech/JPL, and is shown in Figure 7. The 656 GHz local oscillator (LO) from Radiometer Physics uses an InP Gunn diode oscillator followed by a whisker-contacted Schottky-varactor-diode sextupler multiplier. A folded Fabry-Perot diplexer is used to inject the LO and sky signals into the 660 GHz receiver feed-horn. The measured room-temperature double-sideband (DSB) noise temperature was 3500K at a 5 GHz Intermediate Frequency (IF). At a reduced LO power of 250 microwatts (as delivered to Dome A), the noise temperature increased to ~5000K DSB.

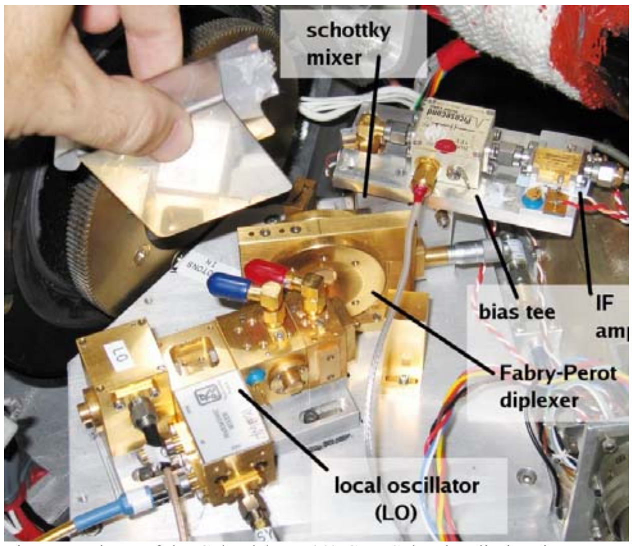

Figure 7: Photo of the Caltech/JPL 660 GHz Schottky-diode mixer receiver as installed onto the Pre-HEAT telescope during integration

C. IF Processor and digital FFT spectrometer

The 1-12 GHz wide IF signal from the Schottky mixer is amplified, low-pass filtered, diplexed, and passed to a HP 10 MHz-18 GHz total power detector, whose analog output is amplified and sent to the Pre-HEAT computer for digitization. The diplexed IF signal is also sent to the spectroscopic IF chain, principally comprised of an IF downconverter and a digital FFT spectrometer. The IF downconverter was built at Caltech as a prototype for the Supercam 64-beam 345 GHz heterodyne array being built at the SORAL lab at the University of Arizona[16]. It mixes the 4.75-5.25 GHz portion of the IF with a phase-locked 4.75 GHz Hittite local oscillator to provide a 0-500 MHz baseband signal for the FFT spectrometer, after sufficient amplification and analog bandpass filtering to eliminate aliasing from out of band signals. Total power detection is provided by a V/F converter followed by a fast counter. Command and control of the IF processor is via a USB interface to an RS232-to-fiber optic transceiver. The FFT spectrometer board (Figure 8) was designed and constructed by Omnisys AB in Sweden and also served as a prototype for the Supercam array. For a total of 10 watts of input DC power, a total of 1 GHz of bandwidth (2 IF inputs) is digitized using two dual-1Gsps Atmel 8-bit ADCs and FFT'd into a power spectrum using an on-board Xilinx Virtex-4 FPGA. For this particular prototype, the output is sent over a serial RS-232 interface to the Pre-HEAT control computer for subsequent processing and storage.

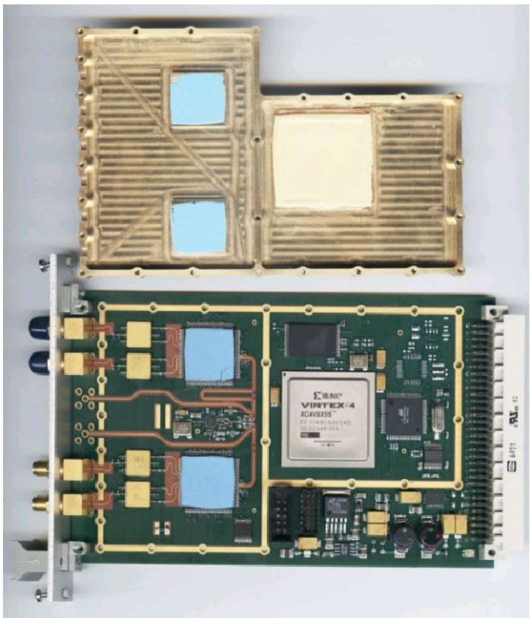

Figure 8: Prototype digital FFT spectrometer board (and machined heatsink) from Omnisys AB provides 1000 MHz of spectrometer bandwidth shared across 2 IF inputs for 10 watts of input DC power.

D. Computer Control and Software

Robustness of the command and control system for Pre-HEAT is paramount to its success. Based on cost, simplicity of design, cold component testing at -30^{o} to -80^{o}C, and generality of software design and interface, a TS-7200 single board computer from Technologic Systems was selected for control of Pre-HEAT (Figure 8). A power consumption of 2 watts operates a 200 MHz ARM9 RISC processor with 32 MB of SRAM, PC-104 bus architecture, 100 Mbit ethernet interface, digital I/O, an 8-channel ADC, two USB and two serial (RS-232) interfaces. Mass storage is provided by an industrial-rated CompactFlash card with 8 GB capacity, rated and tested for operation below -40^{o}C. A multi-port serial board and a battery-backed real time clock (RTC) board are added onto the TS-7200's PC-104 bus to augment its capabilities. The NetBSD 4.0 operating system, an open-source derivative of 4.4BSD UNIX, is adopted to operate the TS-7200, owing to the OS's frugal use of resources, rich cross-platform development environment, and simple, robust architecture. The digital I/O lines on the TS-7200 are used to generate the digital (I2C, SPI and synthesizer) buses that course through the electronics box, providing remote control of the receiver and LO bias voltages, phase lock settings, and synthesizer frequency. The many monitored analog signals in Pre-HEAT are routed to an analog multiplexer (MUX) board, which selects one of 32 analog inputs to a single ADC channel on the TS-7200.

Software control of the various Pre-HEAT hardware components (receiver, IF processor, telescope, spectrometer) is modularized into several TCP/IP socket servers, which each listen for ASCII text commands to perform. Observing sequences are scheduled by the UNIX cron daemon and are reconfigured remotely using PLATO's Iridium PPP modem connection using the short burst data (SBD) protocol. Before an observation is carried out, basic environmental and instrument configuration checks are performed; if these checks do not pass, an error is reported and the telescope will park at the "stow" position (primary mirror pointed downwards, HDPE window facing the heated reference load) until the next scheduled observation. When "safed", the telescope will still perform periodic short slews to assure that it doesn't freeze in place. This "safe" mode can be overridden by remote software commands.

IV. PRE-HEAT STATUS

Pre-HEAT was first turned on at the summit of Dome A, Antarctica on 14 January 2008, and achieved first light on 19 January. Manual operation of the instrument proceeded from 24 January until the end of February. Autonomous operation followed in early March and continues to this day (late May, 2008). The performance of the instrument is sufficient to measure the sky opacity at 660 GHz, and excellent opacity data has been measured and collected. The total power measurement of the Sun was measured in February, validating the optical performance of the telescope and, together with the Moon, providing pointing calibration sources. It is expected that the first Galactic Plane maps of ^{13}CO J=6-5 are imminent and will be achieved by the end of May. In addition to astronomical detection of ^{13}CO, it is also possible to make measurements of atmospheric ozone and other atmospheric trace species, by altering the LO frequency and/or adjusting the 4-5 GHz LO frequency of the Caltech IF downconverter. Such measurements are also imminent, pending minor adjustments to the current suite of software.

Not all has been flawless; after a sequence of accidental power failures during the installation of the instruments, the receiver suffered a 4-fold drop in performance. This degradation is consistent with a loss of about half of the local oscillator (LO) power, and is likely at the whisker-contacted schottky-varactor multiplier stages (particularly the final frequency tripler from 219 GHz to 656 GHz). The receiver has worked stably since, and with the reduced operating temperature (-40^{o}C) as of the time of this writing, the DSB receiver temperature has improved from its January value of ~16,000K to a May value of ~14,000K. The performance hit has only impacted the rate at which meaningful astronomical spectra can be accumulated, and reduces the mapping coverage of the ^{13}CO survey accordingly.

The (Pre-)HEAT web page can be used to learn more about Pre-HEAT, explore the data taken so far and view graphical displays of preliminary scientific results. The permanent URL is: http://soral.as.arizona.edu/heat/

V. Future Prospects

The success of Pre-HEAT and the spectacular conditions at Dome A make the prospects for submillimeter and terahertz observations from the Antarctic plateau very enticing. Indeed, Figure 9 shows the terahertz atmospheric transmission modeled[17] from Dome A based on the 661 GHz opacity already measured from Dome A, *and the conditions are still improving* as the Antarctic plateau continues to plunge toward midwinter.

A natural upgrade path from Pre-HEAT, using the same PLATO module, would be the 50 cm HEAT telescope. Coupled with 800, 1460, and 1900 GHz subharmonically-pumped, planar-Schottky-diode receivers, HEAT would provide 1-3 arcminute resolution spectral line maps of the Milky Way in the light of the three major forms of carbon in the Galaxy: the CO molecule in its J=7-6 transition at 806.5 GHz, the J=2-1 transition of the fine structure line of atomic carbon, C^0, at 809.3 GHz, and the ionized carbon (C^+) fine structure line at 1900.5 GHz. In addition, the 1461.3 GHz line of ionized nitrogen (N^+) would provide an extinction-free measure of the low-density warm ionized interstellar medium in the Galaxy, a measure of the star formation rate. In combination with existing CO, HI and recombination line maps of the Galaxy, *the survey performed by HEAT would help illuminate the complete life cycle of interstellar gas that governs the evolution of galaxies and the formation of star and planet systems.* For example, the HEAT surveys should reveal giant molecular clouds forming from diffuse atomic gas for the first time, and determine how much interstellar molecular hydrogen (H_2) is invisible to conventional millimeter-wave CO surveys. Such surveys highlight the large-scale ecology of the Galaxy that provides context to the detailed studies of the interstellar medium and star formation that larger facilities like the Stratospheric Observatory for Infrared Astronomy (SOFIA) and the Herschel Space Observatory will provide in the near future.

It would be possible to deploy the HEAT telescope in place of the Pre-HEAT telescope as early as the 2009-10 Austral summer. With the more established logistical presence at Dome A that PRIC/CAS intend to create in future years, a cryogenic instrument package for HEAT could be deployed, and naturally, larger submillimeter telescopes could eventually be constructed to take the Galactic science learned from (Pre-)HEAT and apply it as a template for deriving star forming and interstellar properties of distant galaxies. Dome A would also serve as an excellent technological testbed for the development of next-generation (esp. heterodyne) detector arrays before their application to airborne and orbital platforms.

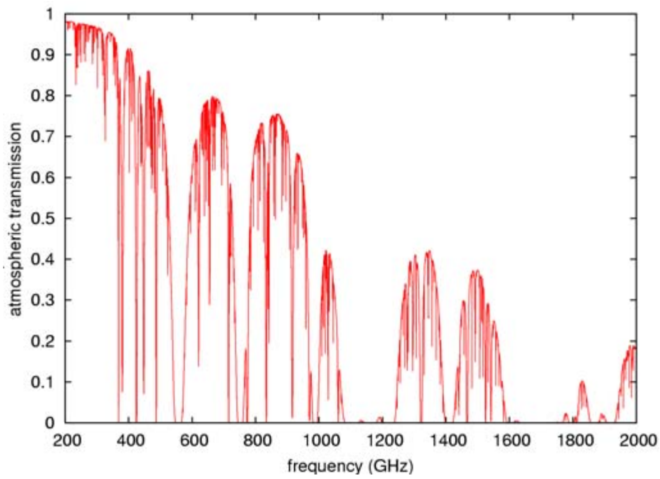

Figure 9: Preliminary model of 0.2 to 2 THz atmospheric transmission over Dome A based on the current measurements at 660 GHz from Pre-HEAT (through April 2008). Winter has only started: atmospheric transmission is expected to peak in the June-September timeframe!

The exceptional submillimeter capabilities of sites like Dome A and its counterpart in the highest peaks above the ALMA site in Chile represent great promise for enabling new science at submillimeter and terahertz frequencies for many years to come.

ACKNOWLEDGEMENTS

The authors wish to thank all members of the Polar Research Institute of China's 2008 Dome A expedition for their heroic effort in reaching the summit and for providing invaluable assistance to the expedition astronomers in setting up the PLATO observatory and its attendant instruments. Construction of Pre-HEAT was financially supported from the US National Science Foundation under the auspices of Small Grants for Exploratory Research (ANT-0735854).

REFERENCES

[1] Marrone, D. P., Blundell, R., Tong, E., Paine, S. N., Loudkov, D., Kawamura, J. H., Luhr, D., Barrientos, C., "Observations in the 1.3 and 1.5 THz Atmospheric Windows with the Receiver Lab Telescope", 16th International Symposium on Space Terahertz Technology (2005).

[2] Kawamura, A., Mizuno, N., Yonekura, Y., Onishi, T., Mizuno, A., Fukui, Y., "NANTEN2: A Submillimeter Telescope for Large Scale Surveys at Atacama", Astrochemistry: Recent Successes and Current Challenges, Proceedings of the 231st Symposium of the International Astronomical Union, p 275 (2005).

[3] Ezawa, H., Kawabe, R., Kohno, K., Yamamoto, S., "The Atacama Submillimeter Telescope Experiment (ASTE)", Proc. SPIE, 5489, 763-772 (2004).

[4] Güsten, R., et al., "APEX: the Atacama Pathfinder EXperiment", Proc. SPIE, 6267, 37 (2006).

[5] Sebring, T.A., Giovanelli, R., Radford, S., Zmuidzinas, J., "Cornell Caltech Atacama Telescope (CCAT): a 25-m aperture telescope above 5000-m altitude", Proc. SPIE, 6267, 75 (2006).

[6] Chamberlin, R., "Comparisons of saturated water vapor column from radiosonde, and mm and submm radiometric opacities at the South Pole", ASP Conference Proceedings, 266, 172 (2002).

[7] Chamberlin, R.A., Martin, R.N., Martin, C.L., Stark, A.A., "Submillimeter atmospheric FTS at the geographic South Pole", Proc. SPIE, 4855, 609-620 (2003).

[8] Oberst, T. E., Parshley, S. C., Stacey, G. J., Nikola, T., Löhr, A., Harnett, J. I., Tothill, N. F. H., Lane, A. P., Stark, A. A., Tucker, C. E., "Detection of the 205 um [N II] Line from the Carina Nebula", ApJ, 652, L125-L128, (2006).

[9] Lawrence, J. S., Ashley, M. C. B., Burton, M. G., Calisse, P. G., Dempsey, J. T., Everett, J. R., Mather, O., Storey, J. W. V., Travouillon, T., "The AASTINO: Automated Astrophysical Site Testing International Observatory", Proceedings of the Conference on Towards Other Earths: DARWIN/TPF and the Search for Extrasolar Terrestrial Planets, ESASP 539, 497-501 (2003).

[10] Calisse, P.G., Ashley, M.C. B., Burton, M.G., Phillips, M.A., Storey, J.W.V., Radford, S.J. E., Peterson, J.B., "Submillimeter Site Testing at Dome C, Antarctica", PASA, 21, 256-263 (2004).

[11] Lawrence, J. S., "Infrared and Submillimeter Atmospheric Characteristics of High Antarctic Plateau Sites", PASP, 116, 482-492, (2004).

[12] Australian Antarctic Division, Australian Antarctic Data Centre website: http://www.aad.gov.au/weather/aws/dome-a/ , (2008).

[13] Lawrence, J.S. et al., "The PLATO Antarctic site testing observatory", Proc. SPIE, 7012, (2008).

[14] Dame, T. M., Hartmann, Dap, Thaddeus, P., "The Milky Way in Molecular Clouds: A New Complete CO Survey", ApJ, 547, 792-813 (2001).

[15] Siegel, P.H., Mehdi, I., Dengler, R.J., Lee, T.H., Humphrey, D.A., Pease, A., Zimmermann, R., Zimmermann, P., "A 640 GHz planar-diode fundamental mixer/receiver", Microwave Symposium Digest, 2, 407-410 (1998).

[16] Groppi, C. et al. "SuperCam: a 64 pixel heterodyne imaging spectrometer", Proc. SPIE, 7020, (2008).

[17] Paine, S., "am atmospheric model", SMA memo #152, (2004).

Progress of Space Terahertz Technology in China*

Cunlin Zhang and Guozhong Zhao

Department of Physics, Capital Normal University, Beijing 100037, China

Contact: Cunlin_zhang@mail.cnu.edu.cn

Terahertz science and technology attract more and more attentions of scientists and techniques in the recent years. The space terahertz technology is becoming into a hot spot in the field of the space research and the space application. We present the progress of space terahertz technology in china in this paper. Except for the exploring the application of terahertz technology on the space positioning, the remote sensing, and the monitoring of cosmic rays, and so on, we are focusing on the application of the new technologies of terahertz imaging on the space technology. Instead of the point-by-point scanning of terahertz imaging, we have developed the two-demission quasi-real time of terahertz imaging technology. The infrared CCD with the operating wavelength of around 800 nm is used for the imaging of terahertz field by the electro-optic sampling. The scope of imaging depends on the size of the electro-optic crystal. The corresponding software is explored based on the LabVIEW programming. The stand-off terahertz imaging by the CCD detection is going on the development based on the cooperation between the Institute of Space Technology of China and the key lab of Terahertz Optoelectronics of Education Committee in the Capital Normal University. We also present the future trend of space technology of china including the terahertz imaging technology. Finally the cooperation between China and Europe is suggested with concerning on the basis of technology cooperation of other field. It is helpful for all us to exchange the idea on the application of terahertz technology on the space research.

* This work is supported by the Basic Research Program of China (973, Grant No. 2007CB310408 and 2006CB302901) and Natural Science Foundation of Beijing (Grant No. 4073030)).

Superconducting contacts and NbN HEB mixer performance

Tarun Aggarwal[1,2*], Pourya Khosropanah[1], Wen Zhang[1,3], Frans D. Tichelaar[2], Jian-Rong Gao[1,2], T. M. Klapwijk[2]

[1]SRON Netherlands Institute for Space Research, Groningen/Utrecht, the Netherlands

[2]Kavli Institute of Nanoscience, Delft University of Technology, Delft, the Netherlands

[3]Purple Mountain Observatory, Chinese Academy of Sciences, Nanjing, China

* Contact: T.Bansal@tudelft.nl, phone +31-(0)6-14160457

***Abstract*— We demonstrate that the performance of phonon cooled NbN hot electron bolometer mixers depends on the superconducting interlayer between the NbN bridge and the Au antenna. This interlayer is either a superconducting Nb layer or a NbTiN layer. We find that, for given interface cleaning conditions, the mixers with a Nb interlayer show a similar or even a slightly better noise temperature in comparison with the mixers with a NbTiN interlayer. The best receiver noise temperature is 1230 K at 2.5 THz and becomes 980 K corrected for reflection loss due to the use of a Si lens. An important outcome of this study is that the Nb interlayer can lead to excellent performance of HEB mixers. Unlike NbTiN, a Nb sputtering process is widely available and easy to use. In addition, we also inspect the interfaces of the contact structures using HRTEM and find that the interfaces of NbN/Nb and NbN/NbTiN after Ar^+ cleaning are excellent.**

I. INTRODUCTION

Phonon-cooled superconducting NbN hot electron bolometer (HEB) mixers are so far the only sensitive detector at high frequencies beyond 1.5 THz [1], [2]. It is known that under operating conditions the parabolic electron temperature profile due to the absorbed LO power and DC power depends on the boundary conditions, related to the interface between antenna and bridge (contact pads) [3]. Earlier we have reported that the sensitivity and reproducibility of such a mixer depend on the contact pads. The best sensitivity has been obtained using a NbTiN superconductor interlayer between NbN and Au in the contacts [4]. In this work we revisit the issue of the contact structure for NbN HEB mixers and explore the use of Nb as an interlayer instead of NbTiN. The motivations are: a) gaining new insight into the role of the contacts and hence the device physics; b) Nb process is more widely available and easy to use; c) establish a more reliable fabrication process.

The performance and reproducibility of a HEB mixer are mostly limited by the contact resistance caused by the poor interface between NbN and Au layer. It has been reported [5] that NbN can form a protective layer on its surface which causes a contact resistance. This contact resistance can be as high as a few kΩ. That is why in our earlier study [4] we have introduced an Ar^+ sputter cleaning to remove this layer. We study the contact structures by measuring DC characteristics and RF performance. In particular, we have examined the interfaces of different contacts by using high resolution transmission electron microscopy (HRTEM).

II. DEVICE FABRICATION

The HEB devices are fabricated using sputtered ultrathin NbN films (the film thickness is around 5.5 nm) on highly resistive, silicon substrates, with a native oxide, prepared at Moscow State Pedagogical University, Moscow, Russia. Figure 1 shows a SEM photo of a NbN HEB mixer with a spiral antenna. The size of the bridge is 2 µm (width) x 0.2 µm (length) and hence requires the use of electron beam lithography. In the first lithography step we realise the

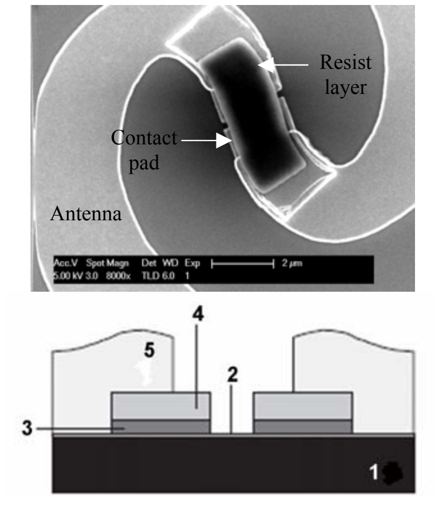

Figure 1: An SEM of spiral antenna coupled HEB mixer (Upper panel), and the lower panel shows the detailed layer structure of device: 1. Silicon wafer, 2. NbN film, 3. Superconducting layer (Nb or NbTiN), 4. Au of contact pad, 5. Au of antenna.

contact pads which also define the length of a bridge. Figure 1 also shows the layered structure of the device and emphasizes the contact pad between antenna and bridge. After e-beam writing and the development of contact pad patterns, short oxygen plasma cleaning (20 W RF, 20 sccm

O_2 and 20 μbar pressure for 5 seconds) is performed to remove the residual resist. After this step we perform an Ar^+ sputter cleaning for 32 sec using the same condition as in Ref. [6] to clean the surface of NbN and then sputter in situ a Nb or NbTiN superconducting interlayer and a gold layer on top of it. For a comparative study we prepare devices which have two different types of interlayer in the same batch. After the contact pad step we have a second lithography step for the antenna. The antenna is made of an evaporated gold layer of 150 nm thick. In the final lithography step a resist mask is patterned which defines the width of the bridge. We use this mask to selectively etch away NbN everywhere else.

TABLE I
KEY PARAMETERS OF THE CONTACT PAD STRUCTURE TYPE I & II FOR THE HEB MIXERS AND TYPE III ONLY FOR HRTEM STUDY.

Parameters	**Type of contacts**		
	Type I	**Type II**	**Type III**
Ar^+ etch clean	32 Sec.	32 sec.	No clean
Interlayer	Nb (6-7 nm) $T_C = 6.45K^*$	NbTiN (6-7 nm), $T_C = 8.8K^*$	NA
Gold	50-60 nm	50-60 nm	50-60 nm

* The T_C values are for the single layer Nb and NbTiN films grown on Si substrate and the thickness of these films indicated here is extracted from HRTEM pictures. From an α-step and AFM measurement the thickness is 10 nm for both films.

For HRTEM study we fabricate structures containing three different types of contact pads: Nb/Au with a 32 sec Ar^+ cleaning, the NbTiN/Au with 32 sec Ar^+ cleaning, and only Au layer without Ar^+ cleaning. It is important to note that the first two were the same as used for HEB devices.

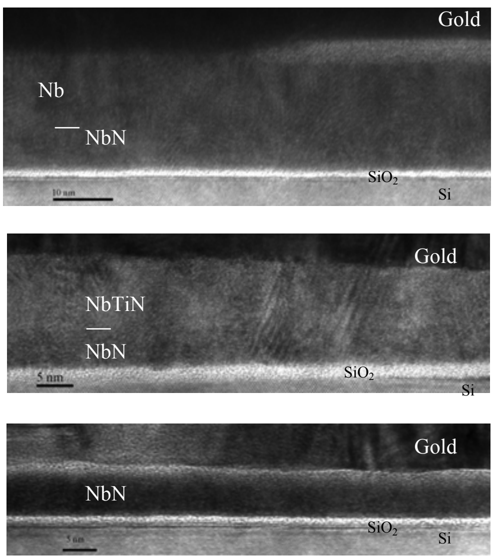

Figure 2: TEM pictures of three types of contact pads all on Si with a native oxide: a) Au/Nb contact to NbN with Ar etch, b) Au/NbTiN contact to NbN with Ar etch, and c) Au contact to NbN without Ar etch clean.

Table 1 indicates all key parameters used for the contact pads. Figure 2 shows HRTEM pictures of all three types of contact pads. Figures 2a and 2b show that after cleaning the growth of NbTiN and Nb follows the lattice structure of the NbN layer and both interfaces look excellent. In contrast, as shown in figure 2c there is always a white amorphous layer on top of NbN without Ar^+ cleaning. Very likely the reported poor reproducibility and high contact resistance for HEB mixer without Ar^+ cleaning is caused by the presence of this additional interfacial layer. We also find that without Ar^+ cleaning, the adhesion of the gold layer to NbN is poor.

III. MEASUREMENTS AND RESULTS

We measured several devices with both type of contact pads and also test structures to know the T_C of individual layers [7]. Test structures are fabricated in the same batch and simulate the real devices. Both DC and RF analysis of devices have been done.

A. DC characterization and analysis

Here we discuss the DC property of devices. The resistance versus temperature (RT) curve is shown in Fig. 3. The HEB device has three resistive transitions with respect to temperature because of the proximity effect at different multilayers [7]. T_{C1} is the transition temperature for the Nb contact pads, T_{C2} is for the antenna layer and T_{C3} for the bridge. The bridge has a T_c which is equal to that of the NbN film. Contact pads involve an Ar cleaning step and in situ

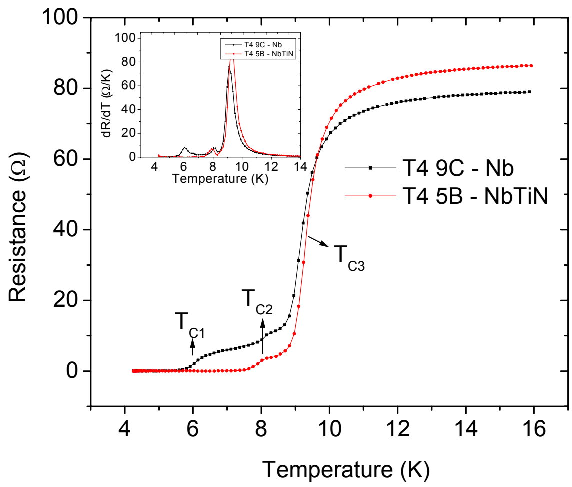

Figure 3 Resistance versus temperature curve of two HEBs with either Nb or NbTiN interlayer in the contacts. Inset shows corresponding differential resistances in log-scale.

sputtering of Nb or NbTiN and a gold layer on top of it. Hence, we expect a different transition temperature for the contact pads than for the bridge. The antenna layer has the thin NbN under the 150 nm gold layer. Since no Ar^+ cleaning is applied before the gold layer, we expect the interface to be poor and thus a weak proximity effect.

As we see clearly from the inset of figure 3, a transition at 8 K is common for both type of devices (Nb and NbTiN interlayers), and in the case of Nb device T4-9C we see a transition at 6 K. This gives us the first indication that T_{C1} is the transition temperature for the contact pads and T_{C2} is for the antenna layer which is the same for both types of devices. To confirm this we study the RT of a test structure, containing the same individual multilayers as the contact pads and antenna, which are also fabricated in the same batch. Fig. 4

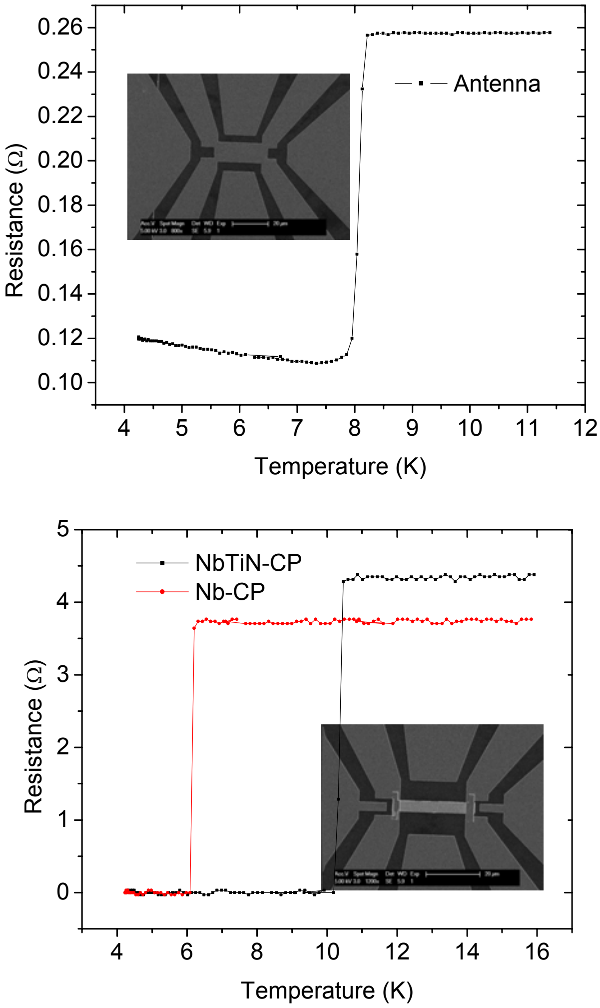

Figure 4. RT curve of the antenna test structure (upper panel) and the RT curves of Au/Nb/NbN and Au/NbTiN/NbN multilayers from the test structures (lower panel). Insets show the corresponding SEM pictures of the test structures

shows RT curves of the test structure while the insets show the corresponding SEM pictures of the test structure. The results indicate that the Nb contact pads have a T_C of 6 K, and the NbTiN contact pads have a T_C of 10.3 K. The latter explains why we do not see the transition T_{C1} in the case of NbTiN HEB devices, as it is merged with T_{C3}. We note that the present results do not agree with our previous analysis in [7] about the differences in T_C.

B. RF characterization and analysis

We study the RF property, primarily the receiver noise temperature, of the HEB devices with both contact structures at 2.5 THz. We use a standard lens–antenna quasi-optical coupling method to couple THz radiation to a HEB. We stress that all the measurements were done with a Si lens without antireflection coating. As local oscillator, we employ a far-infrared gas laser. We use the Y-factor method and the Callen-Welton definition to obtain the DSB receiver noise temperature ($T_{N,rec}$). Furthermore, we apply a new characterization method to obtain a noise temperature as discussed by Khosropanah et al in Ref. [8]. This method gives

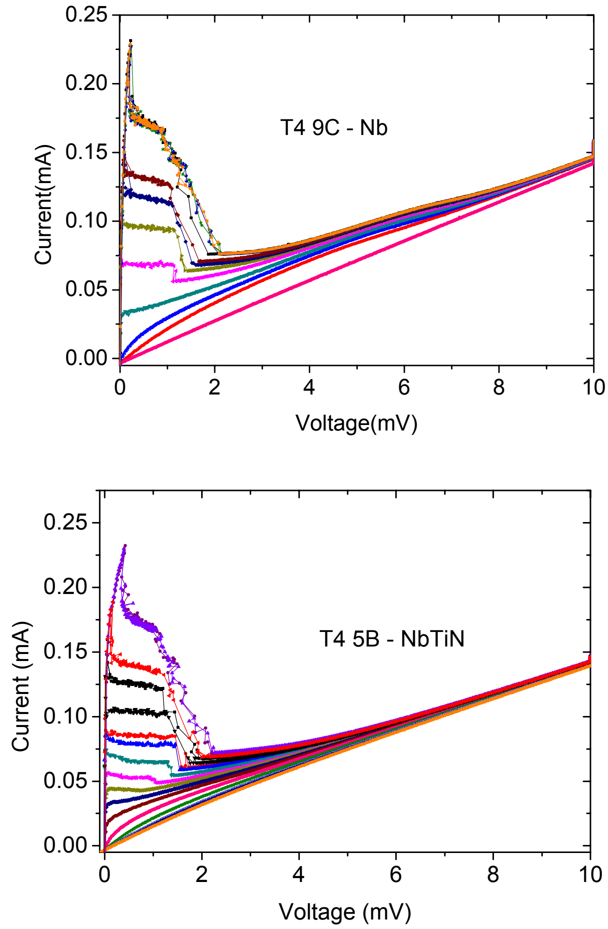

Figure 5. Pumped IV curves of a NbN HEB mixer with NbTiN/Au contacts (upper panel). Pumped IV curves of a NbN HEB mixer with Nb/Au contacts. The LO is operated at 2.5 THz.

us a Y-factor and hence the noise temperature which is not influenced by the direct detection effect and not affected by the instability of local oscillator power. Thus, the data obtained in this way are more accurate. Fig. 5 shows pumped IV curves of two HEBs with either Nb or NbTiN contacts. We find an optimum operating bias point for devices T4-9C and T4-5B around 0.8 mV and 0.6 mV respectively.

We obtain a minimum receiver noise temperature of 1230 K at optimal operating conditions for device T4 9C (Nb contacts) and 1300 K for device T4 5B (NbTiN contacts). These noise temperatures were obtained at an IF frequency of 1.4 GHz and at 4.2 K. We notice that the noise temperature of the HEB with Nb contacts seems slightly better than the HEB with NbTiN contacts. Since the difference is only 6 %, we consider both devices having equal performance. This result suggests that HEBs with Nb contacts are not necessarily worse than HEBs with NbTiN contacts, as reported earlier [7]. The lowest value of 1230 K from the HEB with Nb contact pads can be reduced to 980 K if we would apply a lens with anti-reflection coating layer (20% reflection loss is assumed). This value is essentially the same as the best performance reported in a HEB with NbTiN contacts at the same frequency [4].

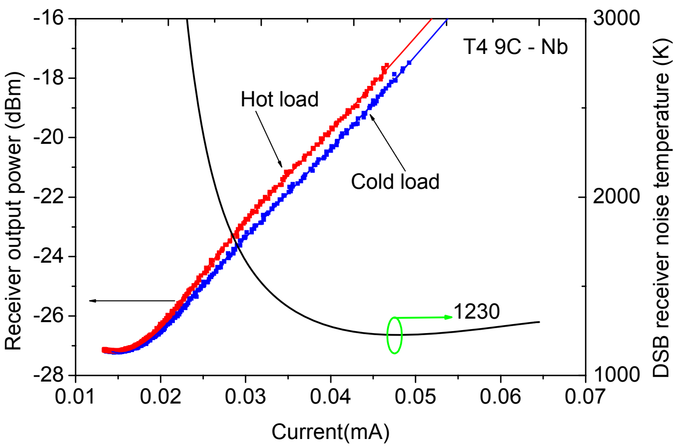

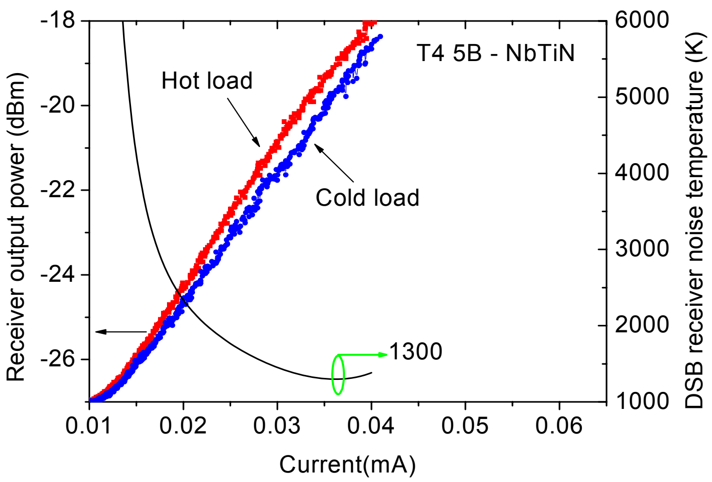

Figure. 6 Receiver output power (left axis) to hot/cold loads and resulting noise temperature versus current at an optimum bias voltage for a HEB mixer with Nb contacts (upper panel) and for a HEB mixer with NbTiN contacts (lower panel). The lowest noise temperature is indicated

CONCLUSIONS

We successfully demonstrated that NbN HEB mixers using a superconducting Nb interlayer for the contacts show a comparable or even slightly better sensitivity than with the HEBs with an NbTiN interlayer. The lowest receiver noise temperature at 2.5 THz for the HEB with Nb contact pads is 1230 K, which becomes 980 K if we would apply a lens with an anti-reflection coating. This value is the same as the best performance reported in a HEB with NbTiN contacts at the same frequency [4]. Since Nb is easier to sputter, high performance HEB mixers can be realized in different labs, which usually do not have a NbTiN process.

We have performed HRTEM inspections of various types of contact pads. We find that the interface between NbN and an interlayer of either a Nb or NbTiN after Ar^+ sputter cleaning is nearly perfect, implying no contact resistance. We also confirmed that there is an interfacial layer on the top of NbN if we do not perform Ar^+ sputter cleaning, which is the origin of the high contact resistance.

We have also identified the different transition temperatures in HEB devices. This helps to understand the physics of HEB devices as this affects the boundary conditions for the cooling mechanism. Thus we expect that IF bandwidth in HEBs with Nb contacts might be larger than those using NbTiN contacts.

ACKNOWL EDGEMENT

We acknowledge M. Hajenius for his help and useful discussions, Sheng-Cai Shi at Purple Mountain Observatory, Nanjing, China for his support to this joint research project. W. Zhang is supported by China Exchange Programme, which is the framework of the scientific cooperation between the Netherlands and P.R. China, and is executed by KNAW and CAS.

REFERENCES

[1] E. M. Gershenzon, G. N. Gol'tsman, I. G. Gogidze, A. I. Eliantev, B. S. Karasik, and A. D. Semenov, Sverkhprovodimost' (KIAE) 3, 2143 (1990) [Sov. Phys. Superconductivity 3, 1582]

[2] J.R. Gao, M. Hajenius, Z.Q. Yang, J.J.A. Baselmans, P. Khosropanah, R. Barends, and T.M. Klapwijk, "Terahertz superconducting hot electron bolometer heterodyne receivers", IEEE transactions on applied superconductivity, **17**, 252(2007).

[3] R. Barends, M. Hajenius, J. R. Gao, and T. M. Klapwijk,"Current-induced vortex unbinding in bolometer mixers', Appl. Phys. Lett. 87, 263506 (2005)

[4] J. J. A. Baselmans, M. Hajenius, J. R. Gao, T. M. Klapwijk, P. A. J. de Korte, B. Voronov and G. Gol'tsman "Doubling of sensitivity and bandwidth in phonon cooled hot electron bolometer mixers" Appl. Phys. Lett, 84, 1958-1961 (2004).

[5] G. N. Gol'tsman 19th ISSTT talk and abstract 'Fabrication and characterization of NbN HEB mixers with in situ gold contacts'

[6] M. Hajenius - Ph.D. thesis 'Terahertz heterodyne mixing with a hot electron bolometer and a quantum cascade laser'.

[7] M. Hajenius, J.J.A. Baselmans, A. Baryshev, J.R. Gao, T.M. Klapwijk, J.W. Kooi, W. Jellema, and Z.Q. Yang, "Full characterization and analysis of a THz heterodyne receiver based on a NbN hot electron bolometer", J. Appl. Phys., 100, 074507(2006).

[8] P. Khosropanah, J. R. Gao, W. M. Laauwen, M. Hajenius, and T. M. Klapwijk, " Low noise NbN hot electron bolometer mixer at 4.3 THz", Appl. Phys. Lett. 91, 221111 (2007).

NbN HEB for THz Radiation: Technological Issues and Proximity Effect

Konstantin S. Il'in[1,*], Axel Stockhausen[1], Michael Siegel[1], Alexei D. Semenov[2], Heiko Richter[2], Heinz-Wilhelm Hübers[2]

[1]Institute for Micro- and Nanoelectronic Systems University of Karlsruhe, Karlsruhe, Germany

[2]DLR Institute of Planetary Research, Berlin, Germany

* Contact: k.ilin@ims.uni-karlsruhe.de, phone +49-721-6084447

***Abstract*— Superconducting phonon-cooled hot-electron bolometer (HEB) detectors are complex multi-layer devices consisting of an ultra-thin superconducting film (mostly NbN) and a thick normal metal layer. We present results on the development of NbN ultra-thin film technology and the systematic study of superconducting and transport properties of NbN bridge-structures with different thickness (4 – 10 nm) and width (0.1 – 10 μm). The NbN films are deposited onto heated Si substrate by magnetron sputtering of Nb target in the reactive gas mixture of argon and nitrogen. A critical temperature of about 9.5 K is reached for NbN films with a thickness between 5 and 6 nm. Twofold increase of the film thickness increases the critical temperature to 12 K. Reducing the bridge width below 0.5 μm leads to a decrease in its critical temperature that is similar to the effect of the film thickness. The model of intrinsic proximity effect in ultra-thin films explains fairly well the degradation of superconductivity in NbN bridges with the decrease of either film thickness or bridge width. Moreover, the proximity effect theory agrees well with experimental data on the critical temperature variations in NbN/Au bi-layers with different thickness of the Au layer. We have shown that an 18 nm thick buffer layer of NbN under much thicker Au layer is sufficient to ensure a bi-layer critical temperature of 8.5 K that is close to the critical temperature of 5 nm thick HEB devices. Presented results demonstrate challenges of further developing HEB detectors for THz spectral range.**

I. Introduction

The hot-electron bolometer detectors and mixers are widely used devices with low noise level and high detection speed that make them suitable for operation in the THz spectral range. In spite of the more than two decades development history their performance still has to be improved to meet requirements of particular applications in astronomy, spectroscopy, imaging and security. Further optimization of these complex multi-layer devices can only be done with the deep understanding of properties of each layer, their mutual influence, and interrelation between layer properties and technology. Typical phonon cooled HEB device consist of at least four layers (from bottom to top):

- Substrate is usually made of Si owing to its transparency for THz radiation, low price, well developed micro-machining technique and prospective ease of integration
- Ultra-thin NbN film, which is a key element of the device, should have a thickness equal or less than 5 nm and should therefore be deposited onto the heated substrate
- Buffer layer of some getter material is required to improve electrical and mechanical contact between NbN film and a planar THz antenna
- A few hundred nanometer thick Au layer from which the antenna is made.

In this multi-layer structure we have to consider three interfaces, each of them is important to assure proper operation of the HEB device. Transparency of the interface between Si substrate and NbN film for phonons is the major factor determining the efficiency of device cooling and hence the speed of the HEB detector or the intermediate frequency (IF) bandwidth of the HEB mixer [1]. The quality of the substrate surface substantially contributes to the interface transparency and also determines the superconducting and crystalline properties of the ultra-thin NbN film [2].

Gold layer is usually deposited *ex-situ* on top of the NbN film. With this technique one can not avoid contamination of the surface of the NbN film, which results in worsening of both Au adhesion to NbN and the electrical contact between them. Weak adhesion results in mechanical instability and shortens the life time of the device. Worse electrical contact introduces extra resistance in the AC and DC current path from the antenna to the HEB [3]. These problems are partly compensated by deposition of a thin buffer layer from a getter material on top of NbN film *in-situ* with gold layer. Further improvement of electrical quality of this interface can be achieved by *in-situ* pre-cleaning of the surface of the NbN film before deposition of the buffer layer [4]. Reduction of the noise temperature of NbN HEB mixers due to pre-cleaning of the NbN surface has been recently observed.

In spite of *in-situ* deposition, the interface between buffer and gold layers should be taken into consideration in the course of optimizing HEB performance. RF properties of the antenna structure are also dependent on the quality of this interface that makes a significant contribution to the overall performance of the HEB device. Because of the difference between crystalline lattices of the buffer and the gold layer this interface cannot be a priory considered to be ideal with 100% transparency for electrons.

Optimizing multi-layer structure of HEB devices we have also to keep in mind that we put in "good" contact a thick normal-metal layer and an ultra-thin superconducting NbN film with a thickness close to the coherence length in this material. In such proximity system superconductivity in the NbN film under the metal layer will be effectively depressed or even completely destroyed. Similarly, the proximity effect between the HEB and the antenna terminals decreases the superconducting order parameter in the HEB itself [5]. The HEB is a rectangle from ultra-thin NbN film which has the width of several micrometers and the length of a few hundred nanometers defined by the distance between antenna terminals. For proper operation the critical temperature of this rectangle should be at least two times higher than the ambient temperature of the HEB device, which is usually close to 4.2 K. In this longitudinal proximity system a hot-spot has a high probability to appear in the vicinity of normal contacts, where it has less mobility and where both the spot formation and dynamics are almost unpredictable and non-reproducible.

Usually good getter materials like Ti or Cr are used to create a buffer layer for further deposition of gold. Both materials are normal metals at typical operation temperatures of NbN HEB devices, which is about the liquid helium temperature. It has been suggested [4] to use superconducting Nb and NbTiN layers as buffer layers in order to weaken the proximity effect and to support superconductivity in NbN films.

The sensitivity of the bolometer can be enhanced by reducing its volume. This means possible reduction of all three dimensions of the HEB: the thickness of NbN film, the width and the length of the HEB rectangle. This is not only a technological challenge that is a big issue by itself. The dimensions become comparable with characteristic lengths in superconductor (the film thickness is already about the coherence length in NbN film) that might result in different quantum effects in these mesoscopic devices.

In this paper we present results on the systematic study of the three aspects directly affecting the performance of the sophisticated system that is the phonon cooled NbN HEB detector for THz radiation. We shall start with technology and the analysis of superconducting properties of NbN films with different thicknesses deposited on Si substrate. Then we analyze the superconducting transition temperature and the density of the critical current in NbN bridges with different width and thickness. We shall consider the influence of only two dimensions, thickness and width, on superconducting properties of HEB devices. The effect of the bridge length has to be analyzed accounting for the proximity effect between the bridge and the normal-metal contacts that requires knowledge on the transparency of their interface for Cooper pairs and quasiparticles. These problems are out of the scope of the present paper. Finally, we present properties of superconducting/normal metal (NbN/Au) bi-layers with different Au thickness which model the antenna structure of HEB devices. In both cases, for NbN/Au bi-layers and for NbN bridges, analysis will be done using the proximity effect theory.

II. NbN Thin-Film Technology and Characterization

The NbN films were deposited on 10×10 mm^2 two-side polished single-crystalline (100) oriented Si substrates which were fabricated by the floating-zone method. The base pressure in the deposition chamber was created by a turbomolecular pump. It was about 2×10^{-7} mbar at the ambient temperature. To deposit of NbN films the substrates were directly placed on the surface of a heater without any thermo-conducting glue. During deposition the temperature of the heater was kept at 750 °C. The pressure in the chamber rose with the increase of the heater temperature and reached a value of about 10^{-6} mbar. Before deposition a two inch diameter Nb target was cleaned by sputtering the target surface layer in pure Ar atmosphere at a pressure $P_{\mathrm{Ar}} \approx 3\times10^{-3}$ mbar. A flow of nitrogen gas was then added resulting in a N_2 partial pressure $P_{\mathrm{N2}} \approx 6\times10^{-4}$ mbar. After stabilization of a discharge voltage the shutter was opened to deposit an NbN film onto the substrate with a deposition rate approximately 0.2 nm/sec. We varied deposition times from 18 to 40 s. After cooling the heater down to the ambient temperature, the substrate with the deposited film was taken out of the chamber. The thickness of the films was estimated using ellipsometry and crosschecked by means of the high resolution transmission electron microscopy [2] that was performed on the NbN films deposited under the same nominal conditions.

Right after deposition the temperature dependence of the film resistance $R(T)$ was measured in the temperature range from 4.2 K up to the room temperature by the standard four-probe technique. The films show negative dependence $R(T)$, i.e. an increase of the resistance with the decrease of temperature. At temperatures ≈ 20 - 30 K the resistance reaches the maximum, which is a factor of 1.2 - 1.4 larger than the resistance measured at room temperature. Below the maximum the resistance gradually decreases until the superconducting transition is reached. The width ΔT of the transition, which was defined as the temperature difference between the states with 10% and 90 % of the resistance just above the superconducting transition, varied from ≈ 1 K for thickest films with $d \approx 9$ nm and to ≈ 2 K for thinnest films ($d < 4$ nm). The thickness dependence of the zero resistance critical temperature, which was measured using a Si-diode temperature sensor with an accuracy of ± 0.5 K [6], is shown in Fig. 1. The T_C value increases with the thickness and does not show clear saturation even at largest values of d.

The critical temperature of our NbN film on Si is lower than the T_C value ≈ 17 K of bulk samples. Reduction of T_C in thin superconducting films was experimentally observed [7] -[9] and described in terms of the intrinsic proximity effect theory which was first suggested by Cooper [10] and generalized by Fominov and Feigel'man [11]. In the framework of this theory the NbN film is considered as a superconductor (S) sandwiched between two normal-metal (N) layers. The superconductivity is destroyed in the surface layer of the film and in the layer near the interface between the film and the substrate. In such three-layer NSN system, the superconductivity of the central part of the film is depressed and the measured T_C of the whole structure is lower than in the superconducting film without normal layers. According to [11] T_C of a NSN structure can be estimated from

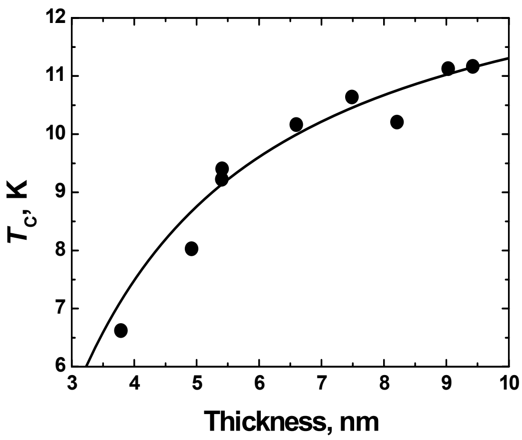

Fig. 1 Dependence of the zero-resistance critical temperature of NbN films on their thickness. The solid line is the best fit according to equation (1).

$$\ln\frac{T_C^0}{T_C}=\frac{\tau_N}{\tau_S+\tau_N}\left[\psi\left(\frac{1}{2}+\frac{(\tau_S+\tau_N)\hbar}{k_B T_C \tau_S \tau_N}\right)-\psi\left(\frac{1}{2}\right)-\ln\sqrt{1+\left(\frac{\tau_S+\tau_N}{\tau_S\tau_N\omega_D}\right)^2}\right], \tag{1}$$

where $\psi(x)$ denotes the digamma function, T_C^0 is the critical temperature of a pure superconductor, ω_D is the Debye frequency of the superconducting material, k_B and $\hbar$ are the Boltzmann and Planck constants. The τ_S and τ_N quantities for the NSN three-layer system are

$$\tau_S=\pi\frac{d_S}{V_S}\rho_{\text{int}}, \quad \tau_N=2\pi\frac{V_N d_N}{V_S^2}\rho_{\text{int}} \tag{2}$$

with $d_{S,N}$, $V_{S,N}$ being the thickness and the Fermi velocity of the S and N layers, correspondingly, and ρ_{int} is the dimensionless resistivity of the SN interface.

Superconductivity in surface and interface layers of the NbN films is destroyed due to formation of niobium monoxide, which is a normal metal above 1.38 K [12]. Following the theoretical approach [10], [11] and assuming that the superconductivity inside the films is of the same strength as in bulk NbN, we estimate for our NbN film the effective thickness d_N of surface and interface layers with destroyed superconductivity. Calculations were made assuming ideal interfaces between superconducting and non-superconducting parts of NbN film, i.e. in the Cooper's limit $\rho_{int}\rightarrow 0$ (the transparency of the interface approaches unity). We obtained $d_N \approx 0.6$ nm using the Debye temperature $\Theta_D = 300$ K, and the critical temperature of infinitely thick film $T_C^0 = 13.8$ K which provided the best fit of our experimental data (Fig.1) with equation (1). Thus the effective superconducting thickness of our films is about 1.2 nm smaller than the physical/geometrical one. The value of T_C^0 is lower than critical temperature reported for bulk NbN. There are several possible reasons for the reduction of the T_C^0 value. One of them is a deviation of the composition of the deposited material from the optimal one that results in weakening of the superconductivity in the film. Nano-crystallite structure of the deposited NbN films [2] can be also considered as a cause of lower T_C^0. It has been shown in [13], [14] that the critical temperature of NbN films with different thickness (up to several hundreds nanometer) depends on the diameter of grains, which is determined by the deposition conditions. Nevertheless, the T_C^0 value of NbN films studied in this paper is higher than the transition temperature of infinitely thick NbN films, which we have earlier deposited onto substrates kept at room temperature during deposition [15].

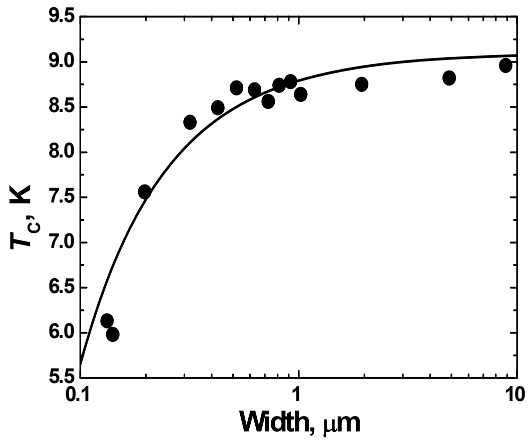

Fig. 2 Dependence of the zero resistance critical temperature of NbN thin-film bridges on their width. The thickness of NbN film is about 5.5 nm. The solid line is the best fit according to equation (1).

III. Single Bridge Structure: Fabrication and Characterization

Typical dimensions of the HEB rectangle are 1 – 2 μm (width) times 0.1 – 0.3 μm (length) that is required to match the impedance of the detector to the impedance of the antenna. Improvement of the detector sensitivity will require further shrinking of all dimensions keeping the value of the normal state resistance constant. An influence of the film thickness on the superconducting transition temperature was analysed in the previous section. Experimental observation of the dependence of T_C on the width of the NbN rectangle has been made on single bridge structures in the four probe configuration. The NbN films were patterned using a combination of electron-beam lithography to form a centre part of a sample and photolithography to form large contact pads. The image created in the photo- or the electron-beam resist was transferred into NbN film using ion milling technique. The width of bridges was varied from about 100 nm up to 10 μm. The actual width of each bridge was measured after patterning by SEM imaging.

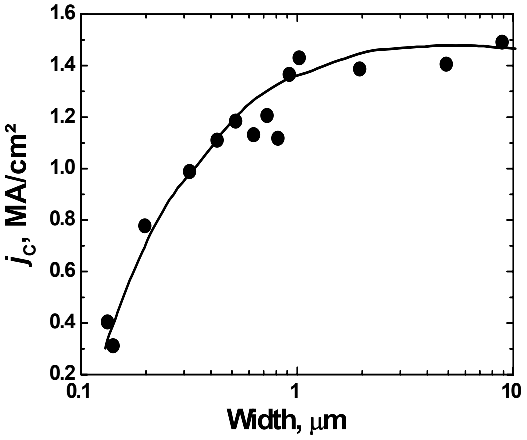

Fig. 3 Dependence of the nominal density of the critical current at $T = 4.2$ K on the bridge width. Bridges were made from the NbN film with a thickness of ≈ 5.5 nm. The solid line is to guide the eye.

The temperature dependencies of the resistance were measured on all bridges. Typical dependence of the zero resistance critical temperature on the width of NbN bridges is shown in Fig. 2. Reduction of the bridge width results in the significant decrease of T_C for bridges with a width smaller than half a micrometer. For wider bridges the T_C value is almost independent on the width. The small variation of T_C in this range might be due to spatial non-homogeneity of the film.

To describe reduction of the transition temperature T_C in narrow bridges, we suggest that the edges of each bridge were mechanically damaged by Ar ions during patterning of the film. The damaged areas oxidised later on after the bridges had been exposed to air. We speculate that these damaged edges became normal. We further consider the bridge as a planar NSN structure and apply to our experimental data on T_C the same approach as we used in order to describe the dependence of the superconducting transition temperature on the film thickness. The results of the fitting of the T_C dependence on the bridge width (W) are shown in Fig. 2 by the solid line. We used the only one fitting parameter W_N (instead of d_N in Eq. 2), which is the effective width of a normal strip running along both edges of the bridge. The value of T_C^0, which has been used for evaluation of $T_C(W)$ by means of equation (1), is equal to the value of T_C on plateau of the $T_C(W)$ dependence. We found $W_N \approx 15$ nm for NbN bridges made from the film with the thickness 5.5 nm.

The reduction of the bridge width and damage of the edges also influence the current carrying ability of the NbN thin film structures. Figure 3 shows the dependence of the nominal value of the critical current density $j_C = I_C(4.2\text{ K})/(W\,d)$ on the bridge width that was evaluated from the current voltage characteristic measured at $T = 4.2$ K. The critical current value I_C was defined as the current corresponding to the full switching of the structure from the superconducting to the resistive state. The value of $j_C(4.2\text{ K})$ is almost constant for bridges with a width larger than about 1 μm and decreases by a factor

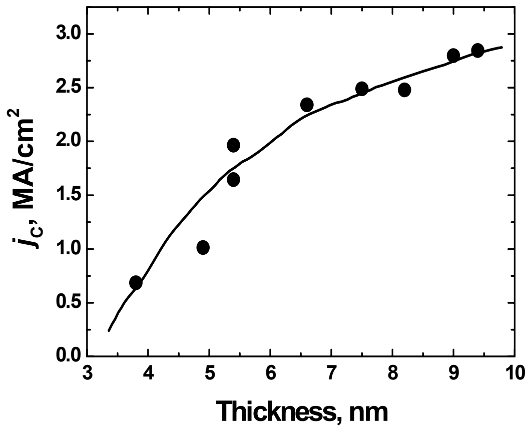

Fig. 4 Dependence of the nominal density of the critical current at 4.2 K on the thickness of the NbN film. The measurements were performed on bridges with a width larger than 1 μm. The solid line is to guide the eye.

of 4 for the smallest width (≈ 0.12 μm). There are at least two factors resulting in such strong decrease of j_C value. The first one is T_C of the bridge, which decreases with the width (see Fig. 2). The difference in the transition temperature between micrometer wide and 120 nm wide bridges amounts at 3 K. The second reason is a real superconducting width of the bridge, which is smaller than the geometric width measured by SEM. Both factors are not accounted in the estimations of j_C. This has been purposely done in order to get a feeling about directly measured transport properties of NbN bridges, which were fabricated by the above described technology.

The value of the critical current density on the plateau of its dependence on the width, i.e. the critical current density in micrometer wide bridges, was taken as the characteristic j_C value for unpatterned films. With this characteristic value we have found the dependence of the density of the critical current at 4.2 K on the thickness of NbN films deposited on Si substrates. The data are shown in Fig. 4. The j_C value gradually increases with the thickness. The rate of the increase weakens at larger thicknesses similar to the dependence of the critical temperature on the film thickness (see Fig. 1).

IV. Artificial Proximity Effect in NbN/Au Bi-Layer Systems.

Antenna structure for THz HEB mixers is usually made using lift-off technique. This limits the technological freedom via unavoidable *ex-situ* gold deposition at low temperatures that is required in order to avoid overbaking of the resist. Thus the only way to realise good enough mechanical and electrical contact between the gold layer and the contaminated surface of the NbN film is to deposit *in-situ* a buffer layer of any getter material. Usually used Ti and Cr are normal metal at operation temperatures of NbN HEB devices. Therefore, improving electrical contact immediately results in strong depression of superconductivity in underlying areas of the ultra-thin NbN film. Further reduction of RF losses at the interface between the superconductor and the antenna and, consequently, lower noise figure of the mixer can be reached via *in-situ* pre-cleaning of the NbN surface before

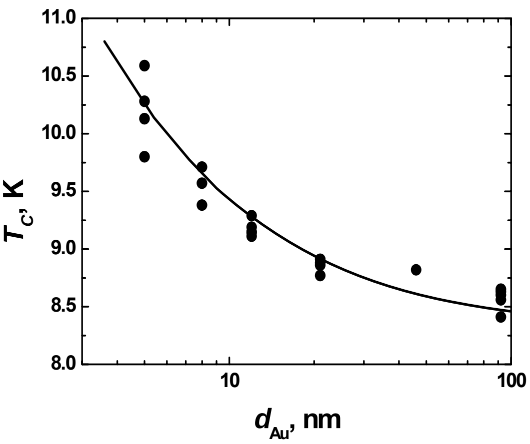

Fig. 5 Dependence of the zero-resistance critical temperature of the NbN/Au bi-layer structure on the thickness of the gold layer. The thickness of NbN film is 18 nm. The solid line is the best fit by means of Eq. (1).

deposition of the antenna [4]. However, the more transparent interface will result in stronger depression of the superconductivity in the NbN film.

To avoid this side effect, a superconducting material can be used as a buffer layer instead of the normal-metal getter. Criteria for choosing such material are high intrinsic critical temperature, low resistivity, good getter properties for small layer thickness and finally the T_C value of the bi-layer (buffer/Au), which should be about the critical temperature of the NbN film used for the device fabrication. It is hard to fulfil simultaneously all requirements since they are contradicting each other. It is well known that superconductors are usually bad metals and higher T_C generally means larger resistivity. If we consider the pair of Nb and NbN (both are reasonable candidates for NbN based HEB) the first material will be the winner as a getter and due to its lower resistivity in comparison to NbN. However, niobium nitride can be a better choice since it has higher T_C value for the same thickness of the buffer layer [15]. Another advantage of the NbN buffer is that it will be deposited onto the same material and will most likely have better superconducting and crystalline properties and make better interface to the underlying NbN film.

The NbN and gold layers were deposited *in-situ* on Si substrate kept at ambient temperature. DC magnetron sputtering was used for deposition of both layers. First Nb was reactively sputtered in argon/nitrogen atmosphere, then the gold film was deposited in pure Ar. Figure 5 shows the dependence of the transition temperature of NbN/Au bi-layers with 18 nm thick NbN layer on the thickness of the gold layer. The superconducting transition temperature of the 18 nm thick NbN film without gold was about 12 K. Subsequent deposition of the gold layer with approximately the same thickness resulted in about 3 K decrease in the T_C value of the bi-layer system. The increase of the thickness of the gold layer up to several hundred nanometers caused further decrease in the bi-layer T_C that levelled off at about 8.5 K and did not depend any more on the thickness of the gold layer. This value of the bi-layer transition temperature is only 0.5 – 1 K less than T_C of 5 to 6 nm thick NbN films which we used in the fabrication of THz HEB mixers [16]. The experimental dependence of the bi-layer T_C on the thickness of the gold layer agrees well with the result of the proximity effect theory [11], which is shown by the solid line in Fig. 5. The best fit was reached for the value of the interface resistivity ρ_{int} = 17 and T_C^0 = 12.8 K.

This T_C^0 value is larger than the transition temperature of bare NbN films with the same thickness. The possible reason can be the difference in the strength of the intrinsic and the artificial proximity effects. Nominally the strength is characterised by the value of ρ_{int}, which is much smaller in the case of the intrinsic proximity effect. In the case of bare NbN films, exposing the film to normal air after deposition contaminates the surface layer and makes it either "normal" or weakly superconducting. The interface between the "normal" surface layer and the superconducting core part of the film is almost ideal with $\rho_{int} \rightarrow 0$, that is demonstrated by very good agreement between experimental results and the theory for $T_C(d)$ dependence of bare NbN film (see Fig. 1). There are two remarkable differences between NbN/Au bi-layers and the intrinsic proximity effect in bare NbN films. One is that the interface transparency between NbN and Au is not perfect due to the difference in material (electron and phonon) properties of NbN and Au. This mismatch reduces mutual influence of the normal metal and the superconducting layer (weaker proximity effect). Another difference is that the surface of NbN layer was *in-situ* passivated by gold and hence was not contaminated/oxidized. The above arguments suggest that the effective transition temperature of a gold covered NbN layer might be larger than T_C of a bare NbN film that has a surface layer with destroyed superconductivity.

CONCLUSION

Systematic study of three objects forming together a phonon cooled HEB detector for THz frequencies – an ultra-thin NbN film on Si substrate, a narrow bridge made from such film, and a NbN/Au superconducting/normal metal bi-layer - has shown the strong influence of intrinsic and artificial proximity effects on their superconducting and transport properties. The following effects have been found experimentally and explained invoking the theory of the proximity effect. (i) Reduction of the film thickness, which is required to improve sensitivity and to increase speed of HEB detectors, is limited due to suppression of superconductivity in thinner films. A decrease in T_C worsens also the electron transport properties of NbN thin-film structures and hence the performance of the detector. (ii) Reducing the width of the NbN thin-film bridge below approximately 0.5 μm leads to further suppression of T_C. Structural damage of the bridge edges, which occurs in the patterning process, destroys superconductivity in narrow strips along the bridge edges. The NbN bridge can be considered as a superconducting core surrounded by non-superconducting, normal shell. Consequently, superconductivity in the core of the bridge is depressed due to proximity between the core and the normal shell. (iii) Superconducting buffer layer under the antenna structure of HEB detectors has to be thick enough to make the T_C of the entire bi-layer system with 200 - 300 nm thick gold comparable to the transition temperature of the NbN ultra-thin film. We have found that the optimal thickness of the NbN buffer layer deposited at ambient temperature should be about 20 nm which allows one to reach $T_C \approx 9$ K of the NbN/Au bi-layer.

The optimal thickness of the NbN buffer layer is 2 to 4 times larger than the thickness of commonly used Ti buffer layers while the resistivity of NbN is larger than the resistivity of Ti. Therefore, this way of improving AC superconducting properties of the device may increase RF losses since currents flow from the antenna through the buffer layer to the HEB made from ultra-thin NbN film. However, we believe that further optimisation of the room temperature deposition of NbN buffer layers aimed at the enhancing superconductivity and/or decreasing resistivity will improve performance of the phonon cooled NbN HEB detectors.

More complicated consequences of the proximity effect in a three-layer structure (ultra-thin NbN/ buffer NbN/ Au), which is closer to real THz HEB devices, has to be further investigated. The influence of the thickness and the material of the buffer layer on superconducting properties of the entire system containing normal metal contact pads and short superconducting bridge between them have to be studied in detail. The main criteria for the development and optimisation of technology of multi-layer structures are lower noise temperature and wider IF bandwidth of HEB THz mixers. Another important requirement coming from applications is the stability of HEB devices in time that includes mechanical rigidity and a low degradation rate of superconducting and transport properties and the sensitivity.

ACKNOWLEDGMENT

Authors thank S. Noll, P. Probst, A. Heller, and C. Prohm for the assistance in fabrication and characterisation of NbN thin film structures. This work is supported by DFG-CFN and BMBF project 13N9305.

REFERENCES

[1] S. Cherednichenko, P. Khosropanah, E. Kollberg, M. Kroug, H. Merkel, Terahertz superconducting hot-electron bolometer mixers, *Physica C*, vol. 372-376, pp.407-415, 2002.

[2] K. Ilin, R. Schneider, D. Gerthsen, A. Engel, H. Bartolf, A. Schilling, A. Semenov, H.-W. Hübers, B. Freitag, and M. Siegel, Ultra-thin NbN films on Si: crystalline and superconducting properties, *Journal of Physics: Conference Series*, vol. 97, 012045, April 2008.

[3] A.D. Semenov, H.-W.Hübers, J. Schubert, G.N. Gol'tsman, A.I. Elantiev, B.M. Voronov, E.M. Gershenzon, Design and performance of the lattice-cooled hot-electron terahertz mixer, *Journal of Applied Physics*, vol. 88 (11), pp. 6758-6767, 2000.

[4] J.J.A. Baselmans, M. Hajenius, J.R. Gao, T.M. Klapwijk, P.A.J. de Korte, B. Voronov, G. Gol'tsman, Doubling of sensitivity and bandwidth in phonon cooled hot electron bolometer mixers, *Appl. Phys. Lett.*, vol. 84, pp. 1958-1960, March 2004.

[5] D. Doenitz, R. Kleiner, D. Koelle, T. Scherer, K.F. Schuster, Imaging of thermal domains in ultrathin NbN films for hot electron bolometers, *Appl. Phys. Lett.*, vol. 90, 252512, June 2007.

[6] LackShore Si diode model DT-470-BO-12°

[7] S. A. Wolf, J. J. Kennedy, M. Nisenoff, Properties of superconducting rf sputtered ultrathin films of Nb, *J. Vac. Sci. Technol.*, vol. 13, pp. 145-147, Jen./Feb. 1976.

[8] S.A. Wolf, F.J. Rachford, M. Nisenoff, Niobium nitride thin-film SQUID's biased at 20 MHz and 9.2 GHz, *J. Vac. Sci. Technol.* 15(2), pp. 386-388, March/April 1978.

[9] S.I. Park, T.H. Geballe, T_c depression in thin Nb films, *Physica,* vol. 135B, pp. 108-112, 1985.

[10] L.N. Cooper, Superconductivity in the neighborhood of metallic contacts, *Phys. Rev. Lett.*, vol. 6, pp. 689-690, June 1961.

[11] Ya.V. Fominov, M.V. Feigel'man, Superconducting properties of thin dirty superconductor-normal-metal bilayers, *Phys. Rev. B*, vol. 63, 094518, Feb. 2001.

[12] K.E. Gray, ISS depth profile analysis of anodized niobium, *Appl. Phys. Lett.*, vol. 27,pp. 462-464, Oct. 1975.

[13] K.S. Keskar, T. Yamashita, Y. Onodera, Superconducting transition temperature of RF sputtered NbN films, *Jap. J. of Appl. Phys.*, vol. 10, pp. 370-374, March 1971.

[14] J.C. Villegier, L. Vieux-Rochaz, M Goniche, P. Renard, M. Vabre, NbN tunnel junctions, *IEEE Transactions on Magnetics*, vol. 21, pp. 498–504, March 1985.

[15] A. Engel, A. Semenov, H.-W. Hübers, K. Il'in, M. Siegel, Electric Noise and Local Photon-Induced Nonequilibrium States, ser. New Frontiers in Superconductivity Research, B. P. Martins ed., New York: Nova Science Publishers, Inc. 2006

[16] H. Richter, A.D. Semenov, S.G. Pavlov, H.-W. Hübers, L. Mahler, R. Green, A. Tredicucci, H.E. Beere, D.A. Ritchie, K.S. Il'in, M. Siegel Terahertz heterodyne receiver with quantum cascade laser and hot electron bolometer mixer in a pulse tube cooler, Submitted to *Phys. Rev. Letters*

Development of 0.8 THz and 1.5 THz Waveguide NbTiN HEB Mixers

L. Jiang[1], S. Shiba[1], K. Shimbo[1], M. Sugimura[1], P. G. Ananthasubramanian[2], H. Maezawa[3], Y. Irimajiri[4], S. C. Shi[5], S. Yamamoto[1]

[1]*Department of Physics, Faculty of Science, The University of Tokyo, Tokyo, Japan*

[2]*Raman Research Institute, Bangalore, India*

[3]*Solar-Terrestrial Environment Laboratory (STEL), Nagoya University, Nagoya, Japan*

[4]*National Institute of Information and Communications Technology (NICT), Japan*

[5]*Purple Mountain Observatory, NAOC, CAS, Nanjing, China*

* Contact: ljiang@taurus.phys.s.u-tokyo.ac.jp, phone +81-3-5841-4217

***Abstract*— In this paper, we present results on the noise performance of the waveguide Niobium Titanium Nitride (NbTiN) superconducting hot electron bolometer (HEB) mixers, cryogenically cooled by a 4-K close-cycled refrigerator. The NbTiN superconducting HEB mixer is fabricated on a crystalline quartz substrate, and is mounted in a waveguide mixer block for RF and LO coupling. At 0.81 THz, the uncorrected DSB receiver noise temperature is measured to be 500 K and the noise bandwidth is 1.4 GHz. The same mixer shows the DSB receiver noise temperature of 640 K at 0.65 THz. We also investigate the DC performance of superconducting NbTiN HEB mixer designed for 1.5 THz.**

I. Introduction

Astronomy in the submillimeter-wave to far infrared region is very attractive. In this wavelength region, there exist various spectral lines of fundamental atoms and molecules, which provide us with rich information on physical conditions and chemical compositions of interstellar clouds and circumstellar envelopes [1]. With this in mind, we are developing the superconducting HEB mixer, which is demonstrated as the most sensitive detector above 1 THz. Currently, state-of-the-art phonon-cooled HEB mixers are usually made of Niobium Nitride (NbN) [2, 3, 4]. However, the Niobium Titanium Nitride (NbTiN) HEB mixer is promising as well in the THz region, because physical and chemical properties of the NbTiN and NbN thin films are closely related to and quite similar to each other. Since the NbTiN film can readily be fabricated on a quartz substrate, the waveguide coupling, which gives a well defined beam pattern, is possible for the NbTiN HEB mixer. This is an important merit for astronomical applications. In fact, the NbTiN HEB mixer receiver has been successfully installed to the APEX telescope to observe the CO *J*=13-12 emission line [5]. We here report the performance of the waveguide NbTiN HEB mixer fabricated in our laboratory.

II. Device Fabrication

The NbTiN thin film is deposited at the room temperature on a Z-cut crystalline quartz substrate by the RF plasma assisted sputtering system using an NbTi (weight ratio of Nb:Ti = 4:1) alloy target in the Ar and N_2 buffer gas. The film thickness is measured to be about 12 nm, where the deposition rate of the NbTiN superconducting thin film is about 6 nm per minute. We found that the N_2 mass flow sensitively affects the critical temperature T_c of the NbTiN superconducting thin film. The optimized N_2 mass flow is 0.94 sccm and the total chamber pressure is 0.42 Pa. When the N_2 flow is changed by 5 %, T_c significantly degrades. The film has a normal state sheet resistance of approximately 250 Ω per square. The NbTiN and Ti/Au layers are successively deposited on the crystalline quartz substrate without breaking vacuum in order to ensure a good contact between the two layers without suffering from natural oxidation of the NbTiN film surface.

The active area of the HEB mixer is defined by electron beam lithography and ICP (inductively coupled plasma) RIE (reactive ion etching) system to form a microbridge structure whose length and width are about 0.2 μm and 2 μm, respectively. The fabricated HEB mixer has a room temperature resistance of 25 Ω and a critical current of higher than 500 μA at 4.2 K. We are unable to obtain exact critical

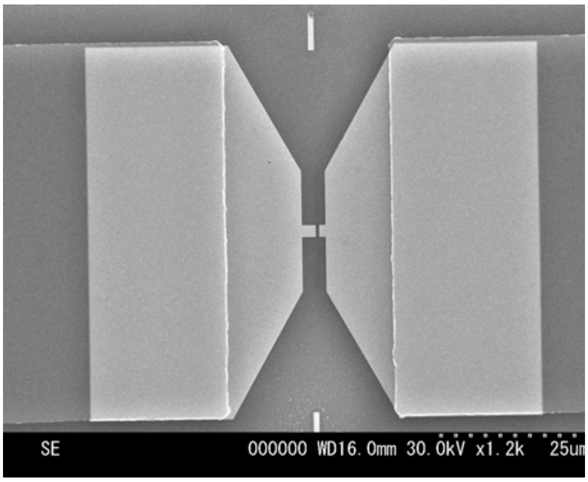

Fig. 1 SEM micrograph of a waveguide NbTiN HEB mixer.

current value due to the amplitude limit of our bias supply. Fig. 1 shows a SEM micrograph of an example of our HEB mixers.

In our past experiments, the structure of the HEB elements including choke filter, device thickness and width is simply taken from the design of the SIS mixers except for the microbridge part. This old design is found to have serious mismatching between the waveguide embedding impedance and the HEB mixer impedance. Therefore, the choke filter of the waveguide circuit is optimized so as to minimize the reflection loss between the RF circuit and the NbTiN superconducting HEB mixer.

III. Measurement Setup

Fig. 2 shows a schematic view of the measurement setup. The waveguide NbTiN superconducting HEB mixer chip is housed in a waveguide mixer block mounted on the cold plate of a GM two-stage 4-K close-cycled refrigerator. A Gunn oscillator, operating at 90 GHz, followed by two solid state frequency triplers, provides local oscillator (LO) power at a frequency of 810 GHz. The blackbody radiation from a slab of Eccosorb at 295 K (hot load) and 77 K (cold load) is used as an RF signal. The LO signal is collimated with a parabolic mirror, and is further combined with the RF signal by a beamsplitter. The combined signal passes through a parabolic mirror, a 7.5 µm thick Kapton vacuum window, and two Zitex G106 infrared filters mounted on the 50 K shield, and is finally directed into the diagonal horn of the mixer block by a parabolic mirror mounted on the cold plate of the cryostat.

The IF output signal of the HEB mixer with the frequency range 0.9-1.3 GHz goes through a bias-tee and an isolator to the cryogenic amplifier, and it is further amplified by a room-temperature amplifier chain. The latter consists of two amplifiers and a band pass filter. The IF power is finally measured by a square-law detector. The band pass filter has a bandwidth of 200 MHz at the center frequency of 1.1 GHz. The entire IF chain has a gain of 87 dB and a noise temperature of 9.5 K.

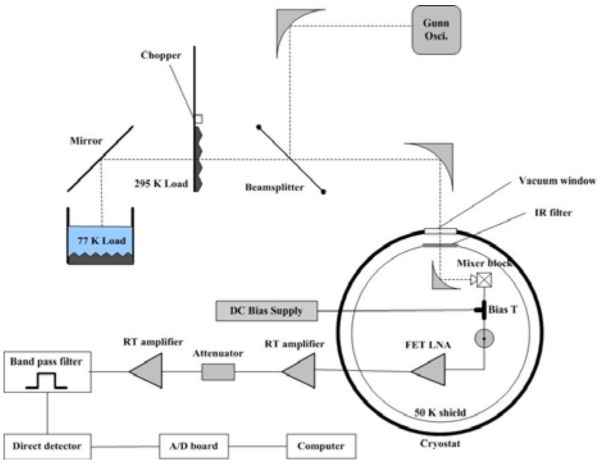

Fig.2 Schematic of measurement setup.

IV. Measurement Results

We used the conventional Y-factor method to measure the noise performance of the waveguide NbTiN superconducting HEB mixer, taking the ratio of the receiver output power corresponding to the hot and cold loads. The current-voltage curves of the HEB for different absorbed LO power levels are shown in Fig. 3.

Fig. 4 shows the measured IF output power corresponding to the hot and cold loads respectively, as a function of the bias voltage at optimum LO pumping level. The measured minimum receiver noise temperature is 500 K, where the bias voltage and current are 0.8 mV and 93 µA, respectively. This is a comparatively low noise performance when it is compared with results published previously [6], even though we use relatively thick NbTiN film of 12 nm. It should be

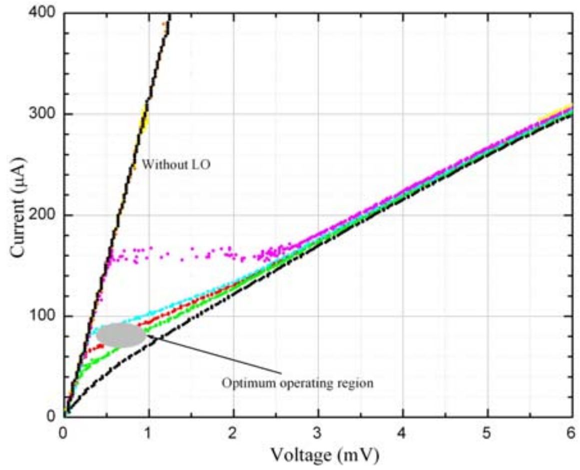

Fig. 3 Current-voltage curves of the waveguide superconducting NbTiN HEB mixer for different LO pumping levels. The optimum working region is 0.4-1 mV and 70-95 µA with the absorbed LO power is about 290 µW.

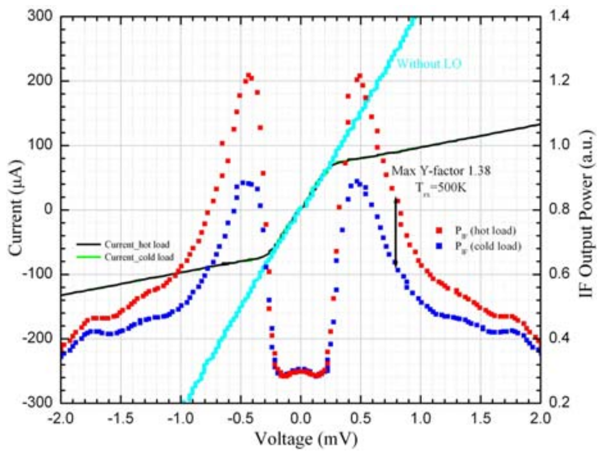

Fig. 4 Current-voltage curves of HEB mixer with and without LO at 0.81 THz, and receiver IF output power corresponding to the hot (295 K) and cold (77 K) loads as a function of bias voltage at optimum LO pumping level. The maximum Y-factor determined by the ratio of the IF output power levels corresponding to the hot and cold loads is 1.38.

noted that the flat region of IF output power around zero bias voltage is caused by residual series resistance of 3 Ω.
We also measured the DSB receiver conversion gain of the waveguide NbTiN superconducting HEB mixer using a U-factor technique [7], as shown in Fig. 5. The HEB mixer gain is obtained after correcting the losses in the quasi-optical path and the IF amplifier chain. Since the bandwidth of IF amplifier chain is 0.9-1.3 GHz, the accurate receiver and mixer gains can't be obtained below 0.9 GHz. The IF gain bandwidth of the superconducting NbTiN HEB mixer is supposed to be around 1.2 GHz. The measured receiver noise bandwidth of superconducting HEB mixer is about 1.4 GHz.

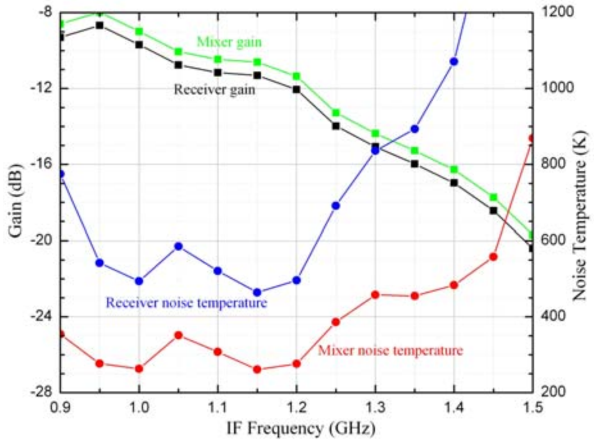

Fig. 5 Measured receiver noise temperature and conversion gain. The mixer noise temperature and gain are obtained after correcting the losses of the quasi-optical path and the IF amplifier chain.

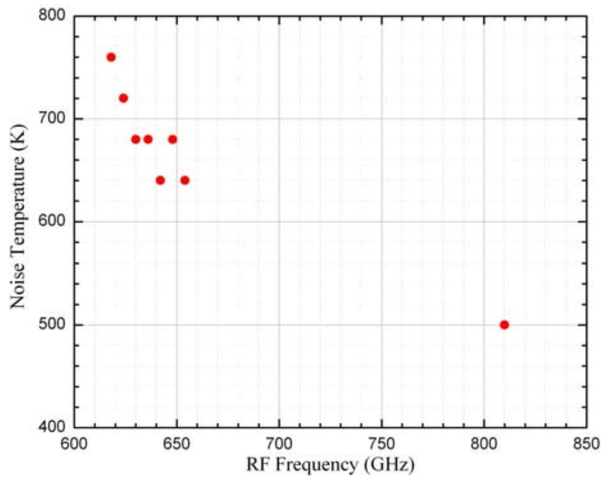

(a)

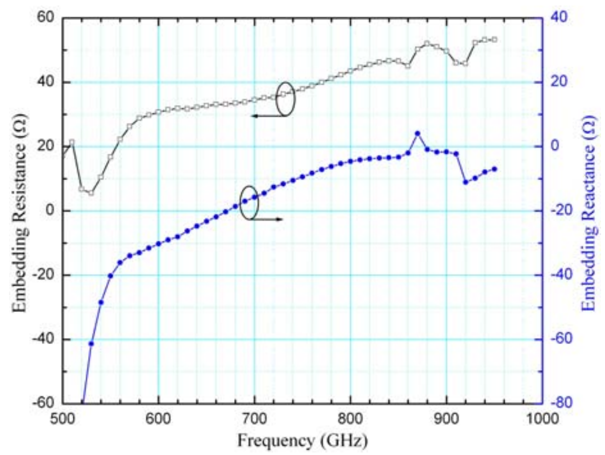

(b)

Fig. 6 Measured DSB receiver noise temperature at 0.62-0.65 and 0.81 THz for the same HEB device (a) and simulated embedding impedance with HFSS in the frequency range of 0.5-1 THz (b).

Our NbTiN HEB mixer designed for 0.81 THz is found to be still sensitive at 0.62 THz. The receiver noise temperature is measured to be 640 K at 0.65 THz and 760 K at 0.62 THz, as shown in Fig. 6 (a). Fig. 6 (b) shows that the degradation of the receiver noise temperature at 0.62 THz partly results from the impedance mismatching between the superconducting HEB microbridge and the waveguide embedding circuit. The calculated coupling efficiency between the HEB mixer and the waveguide embedding circuit reduces from 92 % at 0.81 THz to 80 % at 0.62 THz.

The structure of the superconducting HEB mixer for the 1.5 THz region is designed with the HFSS simulator, and is fabricated by the same process as the 0.81 THz HEB mixer element. The thickness of the quartz substrate is 30 μm, the microbridge width 1.5-4 μm, and the length 0.2-0.6 μm. The HEB chip is housed into a waveguide of 180 μm wide and 70 μm high. Current-voltage curves of 1.5 THz superconducting NbTiN HEB mixers with different chip volumes are measured by a liquid-helium dip test, as shown in Fig. 7. The measurement of the RF performance of the NbTiN HEB mixer at 1.5 THz is ongoing.

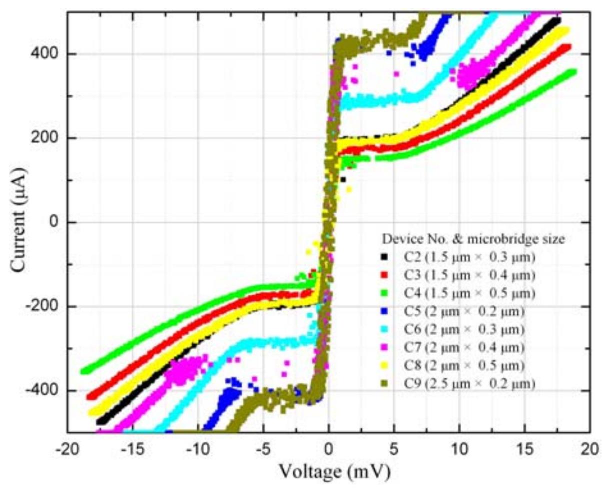

Fig. 7 Current-voltage curves of 1.5 THz superconducting NbTiN HEB mixers without LO pumping power for different element sizes.

CONCLUSIONS

In conclusion, we successfully fabricated the waveguide superconducting NbTiN HEB mixer, and characterized its DSB receiver noise temperature and conversion gain at 0.81 THz. A uncorrected DSB receiver noise temperature is measured to be 500 K at 0.81 THz, and the calibrated mixer noise temperature is 260 K after the correction of the losses of quasi-optical path and IF amplifier chain. The measured noise bandwidth is about 1.4 GHz, and the IF gain bandwidth is about 1.2 GHz. Although our mixer employs a relatively thick NbTiN film (12 nm), the performance obtained is comparable to those reported previously. The superconducting NbTiN HEB mixer designed for 0.81 THz still has high sensitivity even down to 0.65 THz, where the measured DSB receiver noise temperature is 640 K. In addition, we obtained good DC characteristics of superconducting NbTiN HEB mixers at 1.5 THz, and their RF performance tests are in progress.

ACKNOWLEDGMENT

LJ thanks Japan Society for the Promotion of Science, for financial support. This study is supported by Grant-in-Aid from the Ministry of Education, Culture, Sports, Science, and Technologies (14204013 and 15071201).

REFERENCES

[1] T. G. Phillips and J. Keene, "Submillimeter astronomy," *Proceedings of the IEEE*, vol. 80, no. 11, pp. 1662-1678, November, 1992.

[2] J. J. A. Baselmans, M. Hajenius, J. R. Gao, T. M. Klapwijk, P. A. J. de Korte, B. Voronov, and G. Gol'tsman, "Doubling of sensitivity and bandwidth in phonon cooled hot electron bolometer mixers," *Applied Physics Letters*, vol. 84, no. 11, March, 2004.

[3] W. Zhang, P. Khosropanah, J. N. Hovenier, J. R. Gao, T. Bansal, M. Hajenius, T. M. Klapwijk, M. I. Amanti, G. Scalari, and J. Faist, "Demonstration of a heterodyne receiver for detection of OH line at 3.5 THz based on a superconducting HEB mixer and a distributed feedback quantum cascade laser," *Proceedings of 19th International Symposium on Space Terahertz Technology*, Groningen, The Netherlands, April, 2008.

[4] P. Khosropanah, J. R. Gao, W. M. Laauwen, M. Hajenius, and T. M.Klapwijk, "Low noise NbN hot electron bolometer mixer at 4.3 THz," *Applied Physics Letters*, vol. 91, 221111, 2007

[5] M. C. Wiedner, G. Wieching, F. Bielau, K. Rettenbacher, N. H. Volgenau, M. Emprechtinger, U. U. Graf, C. E. Honingh, K. Jacobs, B. Vowinkel, K. M. Menten, L.-A. Nyman, R. Gusten, S. Philipp, D. Rabanus, J. Stutzki, and F. Wyrowski, "First observations with CONDOR, a 1.5 THz heterodyne receiver," *Astronomy and Astrophysics* 454, L33-L36, 2006.

[6] D. Loudkov, C.–Y. E. Tong , R. Blundell, K. G. Megerian, and J. A. Stern, "Performance of the NbTiN hot electron bolometer mixer with AlN buffer layer at terahertz frequency range," *IEEE Transactions on Applied Superconductivity*, vol. 15, no. 2, June, 2005.

[7] Ling Jiang, Wei Miao, Wen Zhang, Ning Li, Zhen Hui Lin, Qi Jun Yao, Sheng-Cai Shi, Sergey I. Svechnikov, Yury B. Vakhtomin, Sergey V. Antipov, Boris M. Voronov, Natalia S. Kaurova, and Gregory N. Gol'tsman, "Characterization of a quasi-optical NbN superconducting HEB mixer," *IEEE Transactions on Microwave Theory and Techniques*, vol. 54, no. 7, July, 2006.

Development of membrane based NbN-HEBs for submillimeter astrophysical applications

R. Lefèvre[1*], Y. Delorme[1], A. Féret[1], F. Dauplay[1], W. Miao[1,2], L. Pelay[1], B. Lecomte[1]
B. Guillet[3], G. Beaudin[1] and J.-M. Krieg[1]
[1]LERMA, Observatoire de Paris, UPMC, CNRS, 77 av. Denfert-Rochereau, 75014 Paris, France
[2] Purple Mountain Observatory, NAOC, CAS, China
[3] GREYC ENSICAEN, 6 bd Maréchal Juin, 14050 Caen, France
* Contact: roland.lefevre@obspm.fr, phone +33-1-40-51-20-72

***Abstract* — We are developing membrane based Nb N hot electron bolometer (HEB) arrays for sub-millimeter astrophysical applications. Here we report in detail on the device fabrication process using a silicon oxide based resist (HSQ). The e-beam patterned HSQ is used as a mask in reactive ion etching for HEB definition and then remains on top of the HEB providing protection against contamination. This process is relatively simple since it requires less steps than previously reported and therefore reduces the risk of degradation of the ultra thin NbN film. To get good quality membranes for THz-HEB applications, different membrane process have been investigated. Electrical characterisations have been performed at room and cryogenic temperatures to compare the quality of the devices with membranes made up of Si/SiO$_2$ or Si$_3$N$_4$/SiO$_2$ and processed with either dry or wet etching methods.**

I. Introduction

There are many astrophysical relevant molecular transitions in the frequency window between 2.3-2.8 THz. Observations of the rotational transition of the deuterated hydrogen molecule, HD, at 2.7 THz, will provide critical information on the star formation history across the Galactic disk and nearby galaxies. OH (2.5 THz), the hydroxyl radical is one of the most important molecules in interstellar chemistry. It is vital for understanding the water chemistry, and its observations will be used to derive information about shocked molecular gas and will allow to discriminate between different shock models.

Our laboratory is developing a prototype of a 4 pixels camera using NbN Hot Electron Bolometer (HEB) mixers with a membrane based quasi-optical design in the frame of the balloon project CIDRE (Campagne d'Identification du Deutérium par Réception hÉterodyne), proposed to the CNES (Centre National d'Études Spatiales).

.

II. Membrane-based quasi-optical structure

The proposed quasi-optical structure[1,2] for each pixel of the camera is illustrate in the Fig. 1. A parabolic mirror collects and focuses the incoming signal on the membrane where is placed an integrated planar antenna connected to the HEB. A metallic back reflector on the second membrane allows to increase the gain of the antenna. This design, in comparison with the conventional coupling structure employing lens and thick substrates, will provide particular features such as larger antenna size, absence of the substrate mode and lower request for P_{LO} and then will help to achieve higher coupling efficiency.

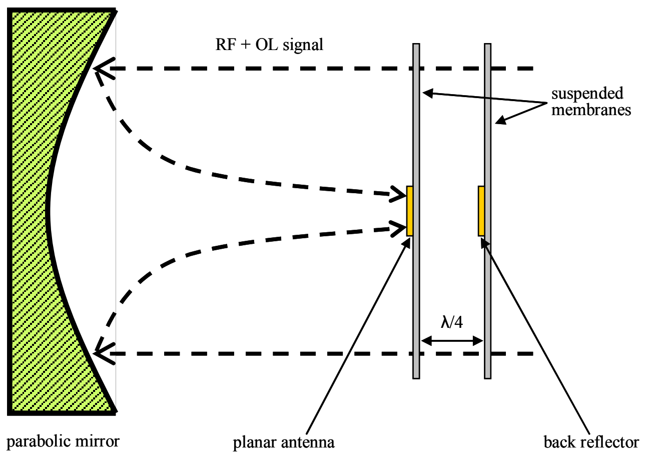

Fig. 1 Schematic view of the quasi-optical structure for one pixel of the camera.

III. Fabrication process

We have selected two kinds of membrane for this study: 1.4 µm thick Si$_3$N$_4$/SiO$_2$ membrane and 3.5 µm thick SOI membrane. Both membranes are deposited on Si substrates with a thickness around 500 µm.

The fabrication process concerns first the HEB and all circuits on the membrane side of the substrate and second the suspended membrane formation through the backside of the substrate. We'll illustrate (Fig. 2) and describe step by step the whole fabrication process developed in our lab.

(a) Deposition (realized by Moscow State Pedagogical University) by sputtering of an ultra thin superconducting film of NbN (3.5 nm expected, while 5 – 10 nm measured[3]) with or without a buffered layer of MgO (200 nm) underneath.

(b) One step e-beam lithography to pattern the whole circuits: the antenna, the electrodes as well as the length of the HEB, the RF choke filter, the CPW and the bonding pads. By this way, we avoid additional lithography steps (e-beam or optical) and then limit the risk of layer degradation.

(c) Use of FOx, an inorganic negative resist, to define by e-beam lithography the width of the HEB and the passivation area above the HEB. FOx, based on hydrogensilesquioxane (HSQ), contains atoms of H, Si and O and will form during lithography a kind of SiO mask. This mask is used for next etching and is left on the substrate to protect the bolometer from aging. In addition, the FOx mask is compatible with organic solvents, so we can clean the chip before bonding using many standard solvents like acetone for example.

(d) Etching of NbN film by RIE with SF_6 and O_2. This step defines the HEB. Fig. 3 shows images of the HEB taken by SEM and AFM.

(e) Pattern of the etching mask on the backside of the substrate. It can be a thick organic resist, a thin Au layer or a Si_3N_4/SiO_2 bilayer.

(f) Making of the suspended membrane by etching the Si substrate through the backside mask, which is removed at the end.

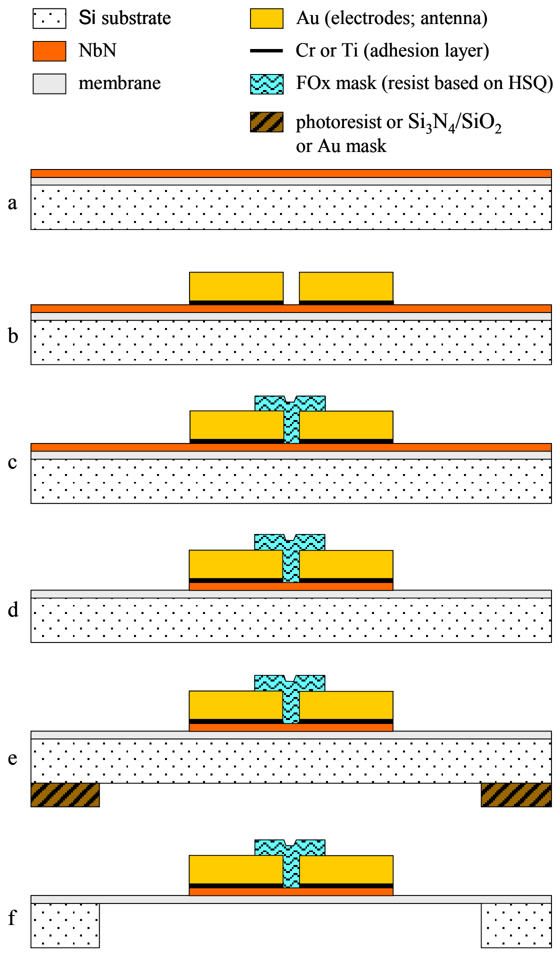

Fig. 2 Fabrication steps of a HEB on suspended membrane with a FOx mask.

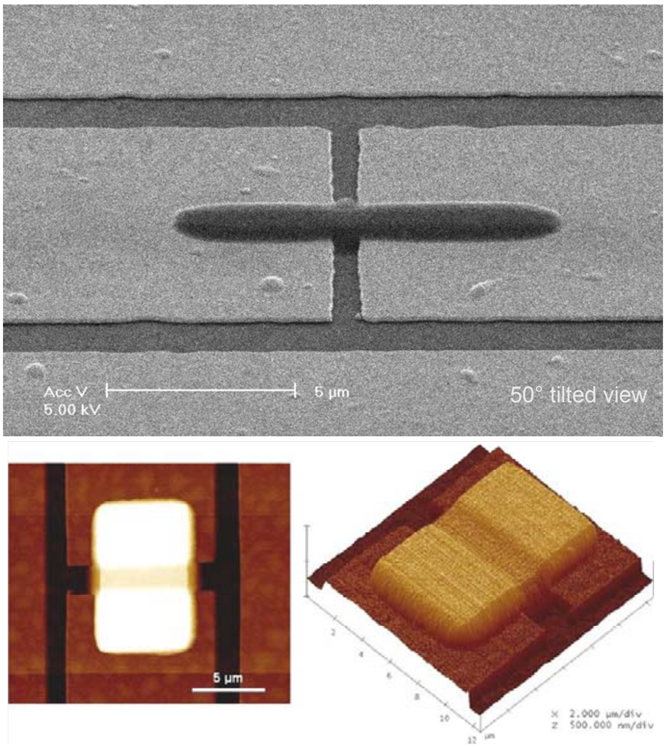

Fig. 3 Top: SEM image of a 'standard dimensions' NbN HEB. The dark pattern is a FOx resist mask. Dimensions of the HEB: L = 680 nm and W = 2.7 µm. Bottom: AFM images of a 'large' NbN HEB. The clear pattern is a FOx resist mask. Dimensions of the HEB: L = 2 µm and W = 8 µm.

IV. Process for Substrate Etching

Different wet and dry etching methods have been explored (KOH, standard DRIE and cryo-DRIE) to make suspended membranes (either Si_3N_4/SiO_2 or SOI) through backside masks made of different materials. Conditions and results are presented in the Table 1.

TABLE II
CONDITIONS AND RESULTS OF ETCHING METHODS

wet	**etching**	**DRIE Bosch process**	**cryo-DRIE**
membrane material	Si_3N_4/SiO_2	SOI	SOI
temperature	90°C	10°C	- 85°C
etchant	KOH (aq) 20 wt.%	$SF_6 + 0_2$ (g)	$SF_6 + 0_2$ (g)
passivation	n.a.	C_4F_8 (g)	autopassivated
frontside protection	resist + special chuck	resist + cool grease	resist + grease
rate	1.5 µm/min	7 µm/min	10 µm/min
membrane shape	square	all shape	all shape
compatible mask	Si_3N_4/SiO_2; Au	resist	Si_3N_4/SiO_2; Au
sidewall	angular	vertical	random
protection stripping	easy	difficult	easy

Fig. 4 shows a chip with 4 pixels on suspended membrane obtained by wet etching. At the moment we process with all these three methods since a large number of samples is necessary to determine which method will be the most suitable for our applications.

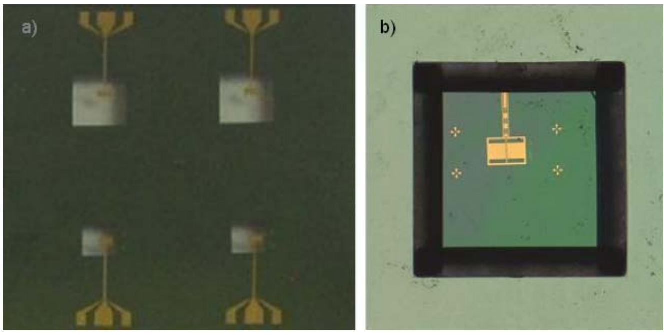

Fig. 4 a) Top view of a chip (10 x 10 mm²) with 4 pixels on suspended membranes obtained by wet etching of the Si substrate (400 µm thick). b) Back view of one pixel with the antenna, the RF choke filter and the CPW seen through the Si_3N_4/SiO_2 membrane.

V. DC MEASUREMENTS

DC measurements have been performed on several devices with thick substrates (i.e. without suspended membrane) in a cryostat at the liquid He temperature (Fig. 5). The critical temperature T_c was about 10 K. From the IV characteristics (shown in Fig. 6), the critical current I_c was around 300 µA for 'normal' and 600 µA for 'large' HEBs. The sheet resistances of different devices at 300 K range from 1000 to 5000 Ω/□, quite scattered and higher than expected values. Investigations are underway in order to find out the reasons which could affect the measured resistances.

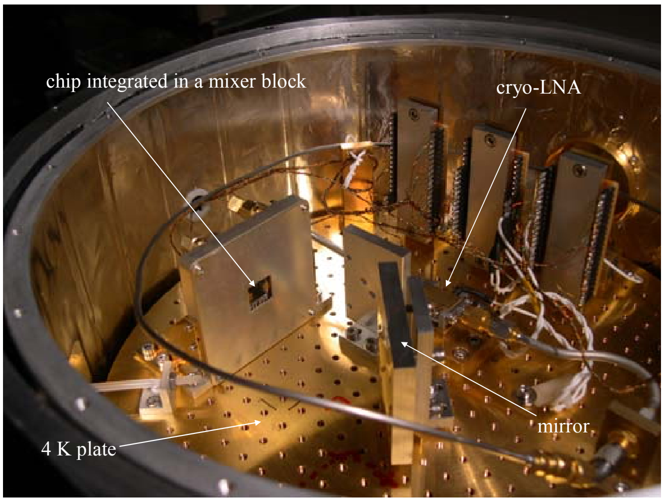

Fig. 5 Inner view of the cryostats used for DC measurements.

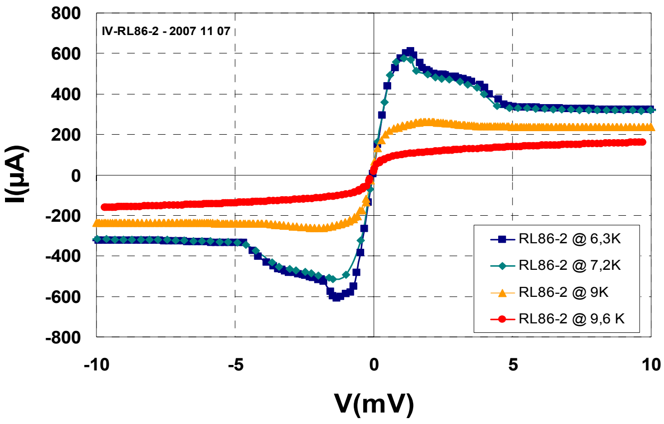

Fig. 6 Measured I-V curves of a 'large' HEB (on thick substrate).

CONCLUSION & PERSPECTIVES

We've developed a relatively simple fabrication process for a membrane based NbN Hot Electron Bolometer array. By using the Fox resist as etching mask and passivation layer, we reduce the number of process steps and then the risk of layer degradation. Different wet and dry etching ways have been explored to get suspended membranes by Si substrate etching. The fabrication process is being enhanced; efforts will be made to improve the quality of suspended membranes and the quality of substrate cleaning during the process.

First DC measurements of HEBs before membrane process have shown normal IV characteristics. We are planning to perform both DC and RF characterizations of HEBs on suspended membranes and make comparison with those on thick substrates.

ACKNOWLEDGMENT

This work is supported by CNES under a R&T contract.The fabrication process was partly performed in the cleanrooms of CTU-IEF at Orsay and CEA/SPEC at Saclay.

Thanks to J. Spatazza from CNRS/DT-INSU for his support in mechanical design.

REFERENCES

[1] Baubert J.; Salez M.; Merkel H.F, "Simulations for membrane-based HEB mixers in array configuration for SHAHIRA", *Astronomical Telescopes and Instrumentation Proc. SPIE*, vol. 5498, pp. 667-674, 2004.

[2] Baubert J., "Récepteur hétérodyne HEB 2.5 THz et caméra 16 pixels à 2.5 et 4.7 THz", PhD Thesis, Observatoire de Paris, Paris, 2005.

[3] B. Guillet, Ö. Arthursson, L. Méchin, M.N. Metzner, M.P. Chauvat, P. Ruterana, V. Drakinskiy, S. Cherednichenko, R. Lefèvre, Y. Delorme and J.M. Krieg, "Properties of ultra-thin NbN films for membrane-type NbN THz HEB", *J. Low Temp. Phys.*, vol. 151, pp. 570-574, 200

Integration of IF Amplifiers with NbTiN SHEB Mixers

P. Pütz[1], C.E. Honingh[1], M. Justen[1], K. Jacobs[1]
J. Bardin[2], H. Mani[2], S. Weinreb[2]

[1]*KOSMA, 1. Physikalisches Institut der Universität zu Köln, Germany*
[2]*Department of Electrical Engineering, California Institute of Technology, Pasadena CA 91125*

For the 1.4 THz and 1.9 THz channels of the GREAT instrument for SOFIA we have developed waveguide mixers with NbTiN superconducting Hot Electron Bolometer (SHEB) devices on low stress silicon nitride membranes. Comparable mixers will also be used in the balloon-borne Stratospheric Terahertz Observatory (STO). In the current baseline approach for these receivers, the mixer is connected to the low noise IF amplifier by a narrow-band (1.2–1.8 GHz) cryogenic isolator to prevent interactions between the 1–2 GHz amplifier and the mixer. Previous tests have indicated that an isolator is necessary for a stable receiver performance with minimal variations of noise and gain vs. IF frequency. Unfortunately, the isolator has the disadvantage that a significant fraction of the potential IF bandwidth of the mixer and low noise IF amplifier is wasted.

Several approaches are currently being pursued for wide-bandwidth integration of mixers and IF amplifiers and experimental results will be reported at the conference. A first approach is a connection of a Caltech 0.5–11 GHz indium-phosphide LNA directly to the mixer without an isolator; initial results have shown large frequency ripple in the measured receiver noise temperature. The amplifier has excellent noise and flat gain when driven from a 50 ohm generator but does not present a 50 ohm load to the HEB mixer at IF frequencies below 4 GHz. The use of a small attenuator between LNA and mixer will be investigated. Finally, a new silicon-germanium (SiGe) LNA for the 0.3 to 5 GHz range with good input match is under test at Caltech and further tests of integration with the HEB mixer are planned prior to the conference.

Development of a 1.8-THz Hot-Electron-Bolometer Mixer for TELIS

Alexei D. Semenov[1,*], Heiko Richter[1], Heinz-Wilhelm Hübers[1], Pourya Khosropanah[2], Merijn Hajenius[2,3], Jian-Rong Gao[2,3], and Teun M. Klapwijk[3]

[1]German Aerospace Center (DLR), Institute of Planetary Research, Germany

[2]SRON Netherlands Institute for Space Research, Groningen, the Netherlands

[3]Kavli Institute of NanoScience, Delft University of Technology, the Netherlands

Contact: Alexei Semenov@dlr.de, phone +49-30-670 5505

***Abstract*— We rep ort on th e fu rther d evelopment of th e superconducting NbN hot-electron bolometer mixer for the 1.8 THz channel of the T erahertz and susbmillimeter Limb Sounder that has r esulted in an e xtension of the intermediate frequency band and a de crease in the mixer noise temperature.**

I. Introduction

Terahertz and susbmillimeter Limb Sounder (TELIS) is a new balloon borne three channel (0.5, 0.6, and 1.8 THz) cryogenic heterodyne spectrometer, which will allow limb sounding of the Earth's atmosphere within the submillimeter and far-infrared spectral range [1]. The instrument is being developed by a consortium that includes the Space Research Organization of the Netherlands (SRON), the Rutherford Appleton Laboratory (RAL) in the United Kingdom and the German Aerospace Center (DLR, leading institute). TELIS will utilize the state-of-the-art superconducting heterodyne technology and is designed to be compact and lightweight, while providing broad spectral coverage, high spectral resolution and an operation time larger than the typical flight duration (≈24 hours) in a single campaign. The combination of high sensitivity and extensive flight duration will allow investigation of the diurnal variation of key atmospheric short-lived radicals such as OH, HO_2, ClO, and BrO together with stable constituents such as O_3, HCl and HOCl. In the present flight configuration the 1.8 THz channel is equipped with the replica of the mixer that has been developed for the 6H-band (coverage 1410-1910 GHz) of the Heterodyne Instrument for the Far Infrared (HIFI) [2] onboard of the Hershel Space Observatory. The HIFI mixer [3] is a phonon cooled hot electron bolometer (HEB) fabricated from a NbN film that has been grown on a high resistivity silicon substrate at the Physical Department of the State Pedagogical University (Moscow). The bolometer is integrated with a planar double-slot antenna and a 5-mm diameter elliptical lens.
The DSB noise temperature of the TELIS receiver with the HIFI mixer measured in the lab at 1.8 THz was slightly larger than 3000 K at the intermediate frequency 4 GHz and raised to 5000 K at the upper edge (6 GHz) of the usable IF band. The noise temperature corrected for optical losses was 1700 k at 4 THz [4]. Although this performance complies with the baseline figures of merit of the TELIS 1.8-THz channel, an improvement of the noise temperature and a decrease of the required local oscillator power would ease the instrument operation and increase the throughput of scientific date during the flight time.

II. The HEB Mixer

Hot-electron bolometers were made from NbN films with a nominal thickness of 5.5 nm deposited by magnetron sputtering on highly resistive 340 µm thick Si optically polished substrates with native oxide (Films were provided by he Physical Department of the State Pedagogical University in Moscow, B. Voronov and G. Gol'tsman). The films typically had a superconducting transition temperature of 9.5 K and a square resistance of approximately 600 Ω at room temperature. To define the film thickness, a few micrometers thick slice of a similar film made at right angles to the film surface was studied by means of high resolution transmission electron microscopy (HRTEM). The image obtained with HRTEM is shown in Fig. 1. The native oxide layer (SiO_2) clearly seen in the picture makes a poorly defined interface between the film and the substrate. There is also a niobium oxide layer on the top of the film which causes additional resistance at the interface between the film and the planar antenna. Results of the HRTEM study show a consistency with the previously reported data [5].

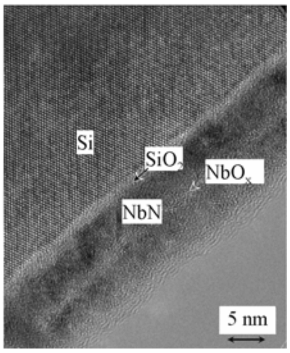

Fig. 2 HRTEM image of a typical NbN film on silicon substrate. Courtesy R. Schneider and D. Gerthsen, University of Karlsruhe.

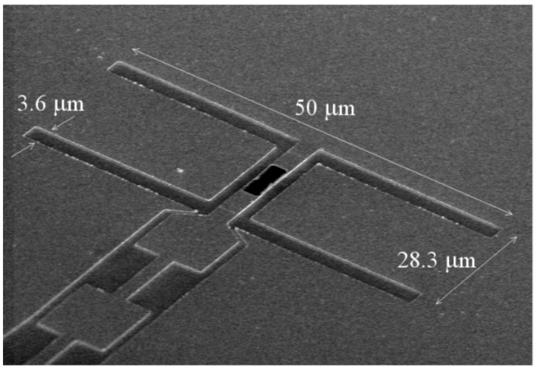

Fig. 3 Picture made with scanning electron microscopy shows the layout of the twin-slot antenna with the HEB mixer and a part of the filter structure [5].

The HEB and the planar twin-slot antenna are made by a few deposition and lithographic steps from the multiplayer system including NbN film, matching getter film and a gold layer. Details of the technological approach have been described elsewhere [6]. The HEB is located in the middle of a co-planar waveguide (CPW) connecting two slots of a twin-slot antenna. The quasioptical twin-slot antenna was designed for a center frequency of 1.8 THz. The dimensions of the important antenna defining the center frequency are shown in Fig.2. The CPW transformer has a central line width of 2.8 μm and a gap of 1.4 μm, yielding a characteristic waveguide impedance of 51 Ω. The HEB is connected to CPW via gold contact pads consisting of 10 nm NbTiN and 40 nm Au on top. Fig. 3 shows schematically the sequence of contact layers. The contact pads are fabricated by cleaning the NbN surface that is followed by in situ sputter deposition of the metal layers. The precise contacting to the NbN film by the contact pads turns out to be essential for the mixer performance of HEBs. The antenna is defined by lift-off using a negative e-beam resist mask and in situ evaporation of 5 nm Ti for adhesion, 150 nm Au, and on top 10 nm Ti to avoid redepositing Au during later etches steps. As a last step, the bridge width is defined between the contact pads by a negative e-beam resist etch mask and subsequent reactive ion etching. The final HEB

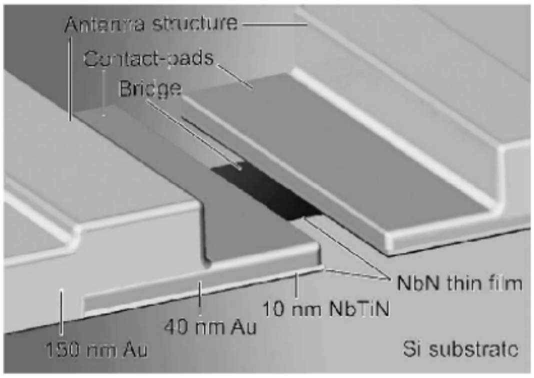

Fig. 4 Schematics of the contact pads fabricated between the NbN film and the gold antenna layer in order to minimize the contact resistance and thus improve the noise temperature of the HEB mixer [5].

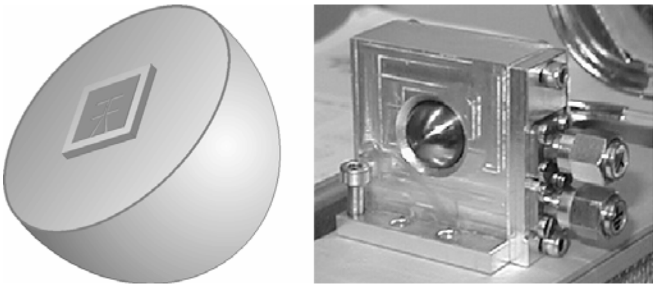

Fig. 5 Mixer chip on the rear side of the silicon elliptical lens (left) and the photo of the mixer block (right).

dimensions were 1.5 x 0.2 μm^2. It was covered with a passivating SiO_2 layer.

The 2×2 mm^2 substrate with the planar antenna and the HEB was glued to the rear side of a silicon elliptical lens (Fig. 4). The planar antenna appeared at the second geometric foci (looking along the propagation vector of the incident radiation) of the lens ellipse with the elliptical axes $a = 6.27$ mm and $= 6.0$ mm. The lens had an antireflection coating from Paryhlene-C optimized for 1.8 THz. The positioning accuracy of the HEB with respect to the lens center was better than 20 micrometers limiting the deviation of the mixer beam from the geometrical axis of the lens to 0.55°.

III. Laboratory Test

The mixer was characterized in the laboratory test receiver [7] shown schematically in Fig.5. The mixer with the lens was mounted in a mixer block (Fig. 4) that was thermally anchored to the cold plate in the vacuum chamber of an IRlabs HDL-5 dewar. The mixer operation temperature was 6.5 K at which the critical current of the HEB was 113 μA. The HEB was dc voltage biased through the bias chip designed to cover the IF band from 1 to 7.5 GHz. The radiation was coupled through a 2-mm thick wedged TPX window and a blocking quartz filter with diamond powder. The filter (C-45; IRlabs) cut off the radiation with a wavelength smaller than 45 μm. The LO radiation was provided by an infrared gas laser at the frequency 1.89 THz. A diplexer was used to match the LO polarization to the

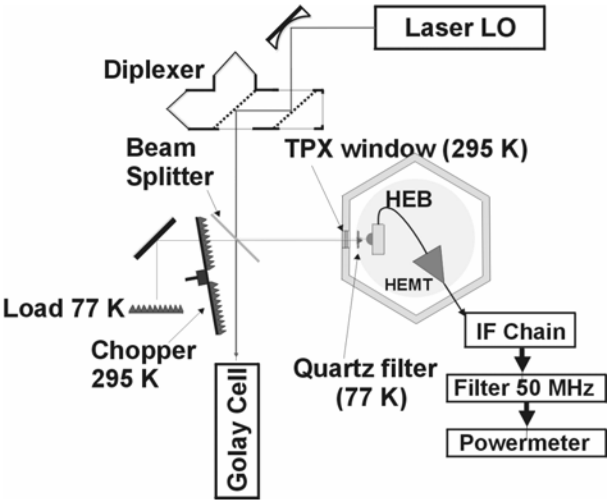

Fig. 6 Schematics of the laboratory test setup. HEMT denotes the amplifier.

polarization of the twin-slot antenna. The LO and signal radiation were superimposed wit a 6-μm thick Mylar beam splitter in the p-polarization. The IF signal was enlarged with a cooled low-noise microwave amplifier (30 dB gain, 1-12 GHz bandwidth, 4 K noise temperature) and guided out of the dewar with a coaxial cable. The spectrum of the IF signal was recorded by a power meter in the bandwidth 50 MHz that was defined by the microwave filter with electrically controlled center frequency. The system noise temperature was computed in the Collen-Welton formulation (quantum noise theory) from the Y-factor that was measured in the common way by alternating the cold (77 K) and hot (297 K, chopper wheel) black body (Eccosorb) covering the field of view of the mixer. The 3-dB IF bandwidth of the mixer was measured using the signal produced by alternating loads [7]. The optical path between the loads and the dewar window was 70 cm. Optical losses associated with the setup are summarized in Table I. The directional beam pattern of the mixer antenna was measured with a high-pressure metal-halide lamp having a diameter of 5 mm. The lamp was moved in the far field of the antenna, typically at a distance from 1.5 m to 2 m from the feed. The corresponding angular resolution was better than 0.2 degree. The signal at the intermediate frequency was recorded as a function of the lamp position [8].

TABLE III
SUMMARY OF THE OPTICAL LOSSES AT 1.89 THZ

Element Los	**ses, dB**	**Method**
Signal path (35% humidity)	0.9	Computed
Mirror	0.46	Measured
Beam-splitter	0.06	Computed
TPX window	0.67	Computed
Filter at 77 K	1.3	IRlabs specs
Si lens with Paryhlene	2.1	Measured

IV. MIXER PERFORMANCE

The major mixer parameters measured with the lab receiver are collected in Table II. The measured system noise

TABLE IV
MIXER PERFORMANCE IN THE LAB RECEIVER

Measured DSB noise temperature	1500 K @ 1.5 GHz 3050 K @ 4.0 GHz 4400 K @ 6.0 GHz 5400 K @ 7.0 GHz
Corrected for optical losses noise temperature (at the tip of the lens)	690 K @ 1.5 GHz 1390 K @ 4.0 GHz
T_n variations in the 4-6 GHz band	Less than 2 dB
HEB conversion gain @ 1.5 GHz	-9.8 dB
Gain bandwidth (3 dB)	2.7 GHz
LO power in front of the window	0.6 μW
Directional beam pattern: Waist (ω_0) Width (θ_0) Side-lobes	3.3 mm 0.88 degree Less than -14 dB

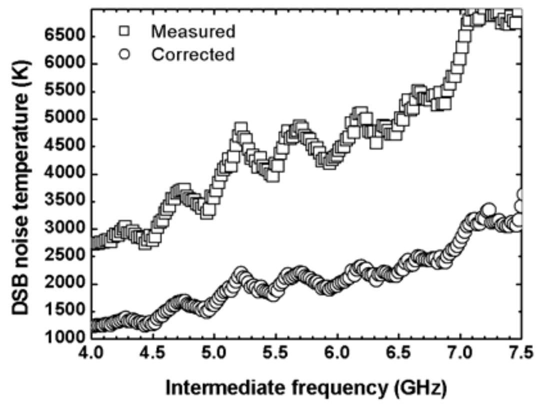

Fig. 7 Measured and corrected noise temperature in the 4 to 7.5 GHz band.

temperature, as well as the noise temperature corrected for optical losses (see Fig. 6), increases with IF frequency. This observation rules out possible shrinking of the usable mixer bandwidth due to optics. According to the conventional mixer model, the rate of the noise temperature increase is controlled by the zero-frequency ratio of the thermal fluctuation noise to the Johnson noise. The ratio is directly connected with the steepness of the superconducting transition of the NbN film. Excluding film degradation during device manufacturing, one should expect the same rate of the noise temperature increase for all devices made from films with the same quality. However, the IF wiring and microwave lines guiding the signal to the amplifier may introduce resonances directly affecting the measured noise temperature. Thus a better design of the IF mixer readout can extend the usable bandwidth. Doing that we achieved the IF coverage from 1 to 7.5 GHz with less that 2 dB ripples in the measured noise temperature.

The directional pattern of the antenna beam shows an almost perfect coincidence with the pattern modeled by

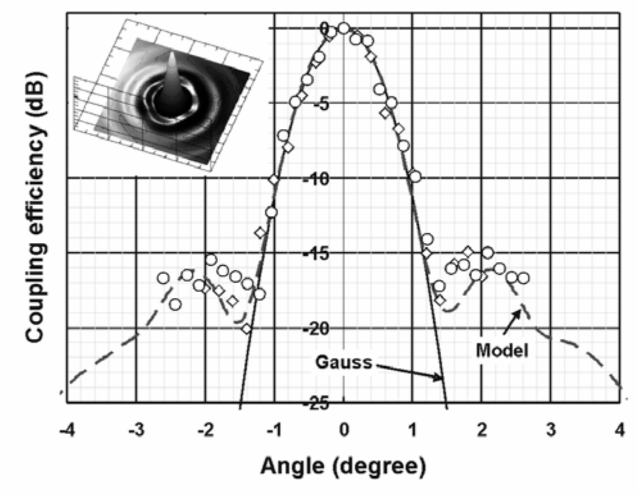

Fig. 8 Directional pattern in the E-plane (symbols) and the best fit with the Gaussian profile. Also shown is the E-plane cut of the modeled beam profile. Inset shows the modeled 3-dimentional directional beam pattern.

means of the physical optics and ray tracing technique [8]. The modeled pattern is shown in Fig. 7 along with the experimental E-field cut of the beam. The noise of the setup limited the lowest available level to –17 dB, just sufficient to confirm that the first side lobes appear below –14 dB. Fitting of the measured pattern with the Gaussian profile returned the position and the size of the beam waist along with the angle of divergence. The beam waist is located in front of the lens at a distance of approximately 6 mm from the tip of the lens.

In conclusion, we have demonstrated the superconducting hot-electron bolometer mixer satisfying the goal performance of the TELIS 1.8 THz channel and having slightly better noise temperature and an extended IF coverage as compared to the mixer of the present flight configuration.

ACKNOWLEDGMENT

Authors would like to thank A. M. Selig, R. Hoogeveen, and H. Hoevers at SRON for their support and inputs regarding TELIS.

REFERENCES

[1] M Birk, U. Mair, M. Krocka, G. Wagner, P. Yagoubov, R. Hoogeveen, T. de Graauw, H. van de Stadt, A. Selig, H.-W. Hübers, H. Richter, A. Semenov, V. Koshelets, S. Shitov, B. Ellison, D. Matheson, B. Alderman, M. Harman, B. Kerridge, R. Siddans, J. Reburn, A. Duric, A. Murk, A. Magun, N. Kämpfer, D. Murtagh, "TELIS – development of a new balloon borne THz/submm heterodyne limb sounder," Digest of the 35th COSPAR Scientific Assembly, Paris, France, 18-25.7.2004, p. 352, 2004.

[2] S. Cherednichenko, V. Drakinskiy, T. Berg, P. Khosropanah, E. L. Kollberg, "Hot-electron bolometer terahertz mixers for the Herschel Space Observatory," *Review of Scientific Instruments*, Vol. 79, pp. 034501-(1-10), 2008. Digital Object Identifier: 10.1063/1.2890099

[3] T. de Graauw, E. Caux, R. Gusten, W. Jellema, W. Luinge, J. Pearson, T. Phillips, R. Schieder, J. Stutzki, K. Wafelbakker, N. Whyborn, K. Wildeman, "The Herschel-Heterodyne Instrument for the Far-Infrared (HIFI)," Conference Digest of the Joint 29th International Conference on Infrared and Millimeter Waves, and 12th International Conference on Terahertz Electronics, pp. 579-580, October 2004. Digital Object Identifier: 10.1109/ICIMW.2004.1422223

[4] M. Birk, private communication.

[5] J. R. Gao, M. Hajenius, F. D. Tichelaar, T. M. Klapwijk, B. Voronov, E. Grishin, G. Gol'tsman, C. A. Zorman and M. Mehregany, "Monocrystalline NbN nanofilms on a 3C-SiC/Si substrate," *Applied Physics Letters*, Vol. 91, pp. 062504 (1-3), (2007).

[6] M. Hajenius, J. J. A. Baselmans, A. Baryshev, T. M. Klapwijk, J. W. Kooi, W. Jellema and Z. Q. Yang, "Full characterization and analysis of a terahertz heterodyne receiver based on a NbN hot electron bolometer," *Journal of Applied Physics*, Vol. 100, pp. 074507 (1-10), 2006.

[7] A. D. Semenov, K. Ilin, M. Siegel, A. Smirnov, S. Pavlov, H. Richter and H.-W. Hübers, "Evidence of non-bolometric mixing in the bandwidth of a hot-electron bolometer," *Supercond. Sci. Technol.*, Vol. 19 pp. 1051–1056, September 2006.

[8] A. Semenov, H. Richter, H.-W. Hübers, B. Günther, A. Smirnov, K. Ilin, M. Siegel and J. Karamarkovic, "Terahertz performance of integrated lens antennas with a hot-electron bolometer," *IEEE Transactions on Microwave Theory and Technique*, vol. 55, pp. 239-247, February 2007

AlN Barrier SIS Junctions in Submm Heterodyne Receivers: Operational Aspects

J. Bout[2], A. Baryshev[1,2], J. Barkhof[1,2], F.P. Mena[1,2], R. Hesper[1,2], B. Jackson[2], W. Wild[1,2],

C.F.J. Lodewijk[3], D. Ludkov[3], T. Zijlstra[3], E. van Zeijl[3], T.M. Klapwijk[3]

[1]*SRON Netherlands Institute for Space Research, Groningen, the Netherlands*

[2]*University of Groningen, Kapteyn Astronomical Institute, Groningen, the Netherlands*

[3]*Kavli Institute of Nanoscience, Faculty of Applied Sciences, Delft University of Technology, Lorentzweg 1, 2628 CJ Delft, The Netherlands*

* Contact: bout@astro.rug.nl, phone +31-50-363 4061

***Abstract*— The Atacama Large Millimeter Interferometer (ALMA) [1] site is an observatory which consists of more than fifty 12 meter diameter sub-mm telescopes, located at an altitude of 5000 m in the Atacama desert in Chile. It covers the 30-950 GHz frequency range which is divided into ten bands following the atmospheric transmission windows. ALMA front-ends will be using Superconductor-Insulator-Superconductor (SIS) heterodyne mixers as the key sensitive elements for all of its high frequency bands.**

The ALMA band 9 receiver which covers 600-720 GHz is being developed in the Netherlands. The first eight receivers have already been built based on AlO_x barrier SIS junctions mixers. These mixers have excellent noise temperature but show limited RF and IF bandwidth. Using new AlN barrier higher current density SIS junctions, it is possible to improve on the RF and IF bandwidth of SIS mixers thus making this technology significantly more attractive for the use in large series of SIS receivers. Currently, a good sensitivity and band coverage has already been achieved for AlN mixers [2]. However, performance of AlN mixers at higher frequencies depends highly on Josephson noise suppression and is only optimal if a precise magnetic field is applied on the barrier. Present routines for Josephson noise suppression in AlO_x barrier mixers were not sufficient. In this paper these routines will be discussed in detail and its adaptation to AlN barrier mixer operation will be reported.

I. Introduction

AlO_x barrier SIS junctions mixers developed for ALMA band 9 (600–720 GHz) [3], [4] have excellent noise temperature but show limited RF and IF bandwidth. Using a new AlN barrier higher current density SIS junctions [5], it is possible to improve on the RF and IF bandwidth of SIS mixers (see Figures 1 and 2), thus making this technology significantly more attractive for the use in large series of SIS receivers. As AlN junctions are relatively small and thin, a flux quantum at the barrier is already created if the bias voltage exceeds 3 mV. This does not disturb its operation as the bias voltage operation point lays at 2 mV.

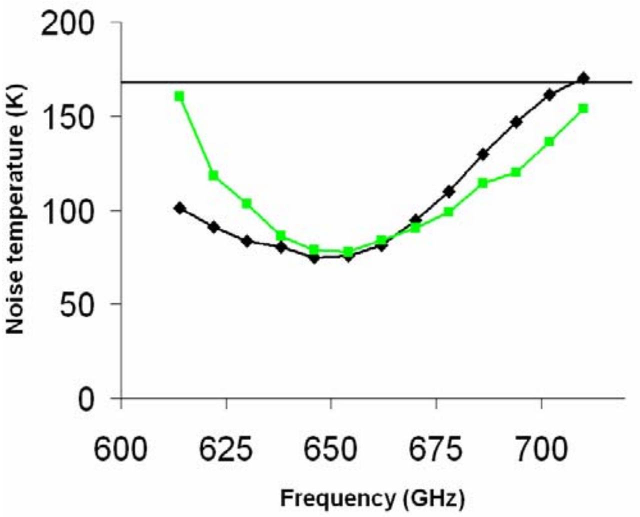

Fig. 9 Noise temperatures of present mixers based on AlO_x (green line) and AlN (black line) barriers. The AlO_x barrier mixer is one of the delivered junctions for ALMA. It has a size of 1 μm^2 and a resistance times area of 25 $\Omega\ \mu m^2$. The AlN barrier mixer has a size of 0.25 μm^2 and a resistance times area of 3.7 $\Omega\ \mu m^2$. The AlN mixer has a lower minimum noise temperature.

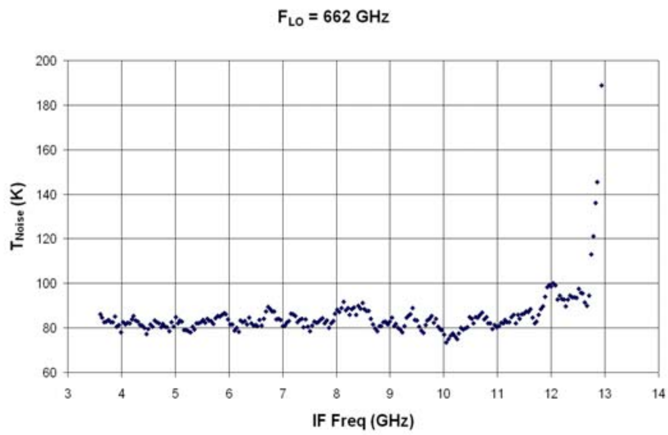

Fig. 2 IF coverage for the AlN mixer using an LO frequency of 662 GHz. For obtaining data over the whole 600 - 720 GHz range, the LO frequency

can be altered in steps of 8 GHz as the IF coverage is nicely flat over an 8 GHz range (from 4 to 12 GHz).

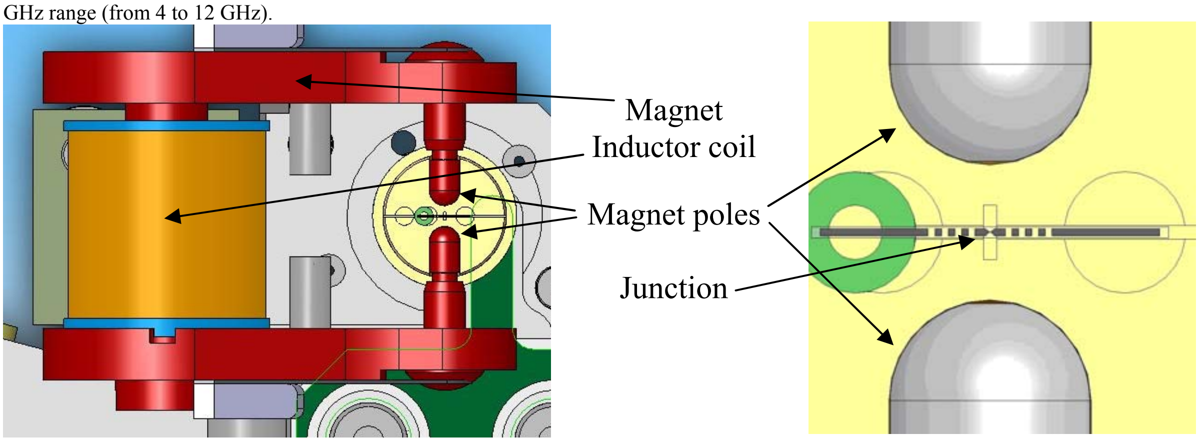

Fig. 3 Overview and detail of the Vacoflux 50 ferromagnetic construction for generating a magnetic field at the junction. Within the overview picture the ferromagnetic material is shown in red. Tuning and demagnetizing it is done using the inductor (coil made of 4600 turns of 30µm NbTi wire), shown in orange. The junction is positioned in between the two poles as shown in the detail picture. At the junction, the magnetic field can be considered uniform and the field lines are in the same plane as the barrier (Figures by Gerrit Gerlofsma).

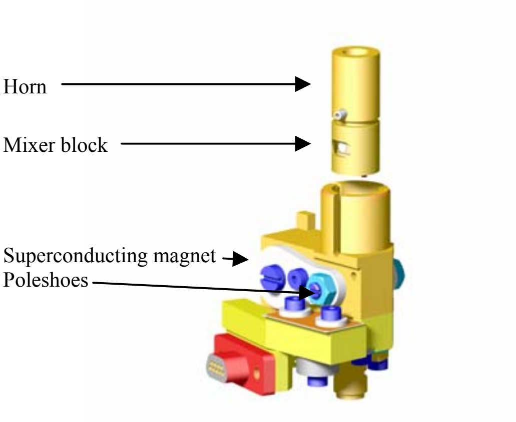

Fig. 4 Mixer holder with superconducting magnet, poleshoes, heater contact, thermometer and IF connector. To operate an AlN barrier mixer the remanent field inside the magnet and the flux inside the superconducting material should be removed. After this, the right magnetic field can be set to suppress the Josephson effect (Figure by Gerrit Gerlofsma).

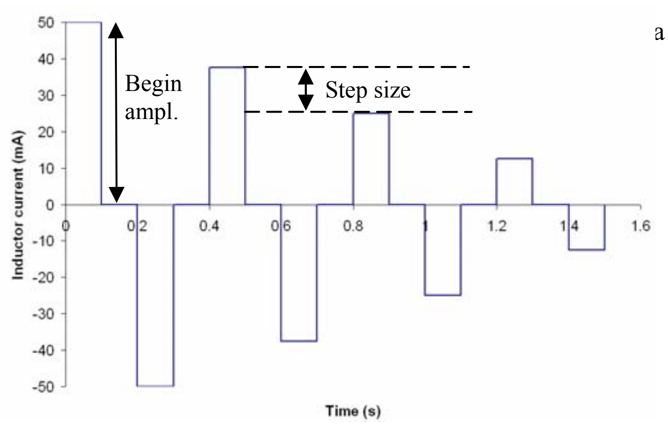

Fig. 5 Block shaped current function with decreasing amplitude used for demagnetizing the magnet. The step size is the amplitude decrease between two succeeding current pulses of the same sign. Each negative current pulse has the same amplitude as the previous positive pulse.

To get a small and repeatable noise temperature and stable operation for AlN SIS mixers operating at 600–720 GHz, the Josephson effect should be properly suppressed by applying a specific magnetic field over the junction. An external magnet consisting of a superconducting coil and a ferromagnetic core is in our mixer. Here, the coil is made of 4600 turns of 30µm NbTi wire and the ferromagnetic core is made of Vacoflux 50 (49% cobalt and 49% iron, having a high saturation induction) and its poles are positioned near the junction (see Figure 3, 4). At the junction the magnetic field can be considered uniform and the field lines are in the same plane as the barrier.

Due to hysteresis a magnet can produce a remanent field. This remanent field can be removed by demagnetization of the magnet. Only after demagnetization a current through the inductor will result in a predictable magnetic field delivered by the magnet. Also flux quanta trapped in the superconducting material in or around the SIS junction will able to set the right magnetic field for maximum Josephson effect suppression.

Demagnetizing a magnet core is ordinary done by putting a block shaped current with decreasing amplitude through the inductor surrounding the magnet (see Figure 5). With each current pulse a magnetization is created inside the magnet which will be replaced by a magnetization of opposite direction during the preceding current pulse of opposite sign. This magnetization will be replaced by a magnetization of opposite sign and smaller magnitude during the next pulse which has a smaller magnitude.

Defluxing superconducting material is done by temporarily taking it out of superconducting state by heating it up. Once it is out of superconducting state the flux will vanish due to resistance of the film. If there is no magnetic field during the proceeding cooling down (proper demagnetized required) no new flux will be trapped and the defluxing procedure was successful.

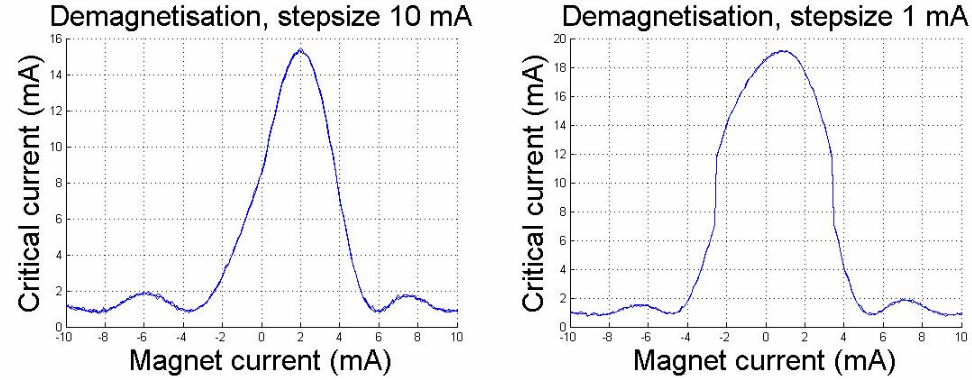

Figure 6: Demagnetization with a step size of 10 mA (common for ALMA AlO_x mixers) results in a asymmetric curve (left hand side). Demagnetization with a step size of 1 mA results in an almost symmetric curve (right hand side). Both curves were obtained using an AlO_x barrier and a starting amplitude of 40 mA. Demagnetizing was always followed by defluxing.

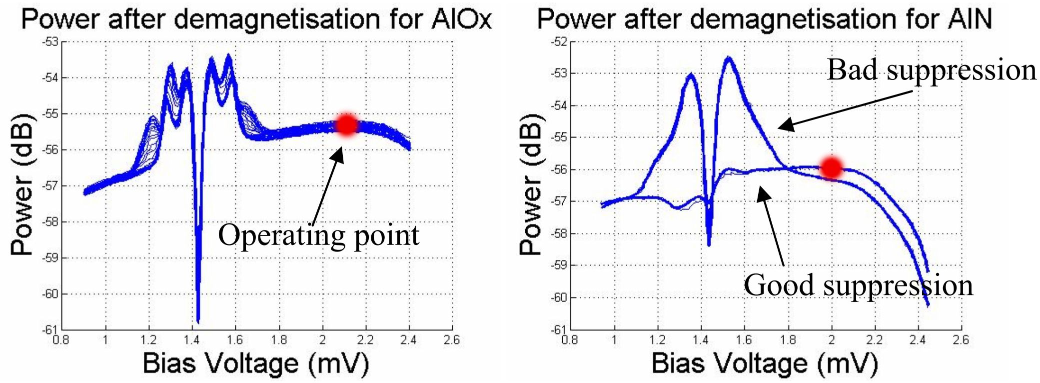

Figure 7: Measured power v.s. bias voltage profile after demagnetization and defluxing for an AlO_x and the AlN mixer. The operation procedure was repeated 40 times for each mixer. For AlO_x all attempts did result in a good operating point (the red dot). For AlN in 21 cases the Josephson effect was insufficiently suppressed. The starting amplitude of demagnetization was 40 mA and the step size was 1 mA.

II. Used methods & results

The quality of the defluxing and demagnetizing procedure can be studied by measuring the critical current as a function of the magnet current afterwards. If this function is symmetrical around zero, there was no flux or remanent field. As this involves applying magnet currents of opposite signs a remanent field will be introduced somewhere and influence part of the measurement. To overcome this problem, the measurement is done in two parts: first magnet currents from zero to a negative minimum value are applied (and critical currents are measured), then the defluxing and demagnetizing procedure is repeated and finally magnet currents from zero to a positive maximum value are applied. The whole measurement was done twice to show its repeatability.

Demagnetization AlO_x mixers for ALMA is currently done using a step size of 10 mA. Using this step size did result in an asymmetric curve. Decreasing the step size to 1 mA did result in a more symmetric curve, showing a better quality demagnetization.

If the demagnetizing and defluxing was performed correctly, a specific magnetic field can be obtained by putting a specific current through the inductor. The Josephson effect then gets properly suppressed and the measured power gets predictable for a given bias voltage (an operating point, see Figure 7). If the Josephson is not suppressed properly, the measured power will differ which will result in a bad noise temperature.

The repeatability of demagnetizing and defluxing can be tested by retrieving the power v.s. bias voltage profile afterwards for a specified magnet current and repeat the whole procedure many times. This was done 40 times for both the AlO_x and the AlN mixer (see Figure 7). For AlO_x all attempts did result in a good operating point (indicated in the Figure). For AlN in 21 cases the Josephson effect was insufficiently suppressed, because the AlN junction is more sensitive to small deviations from the optimal magnetic field. This is due to the small dimensions of the AlN junction: it is small and thin when compared with AlO_x junctions. So for the AlO_x mixer one can assume that the Josephson effect is properly suppressed, while for AlN one has to test this and repeat the demagnetizing and defluxing procedure in case the

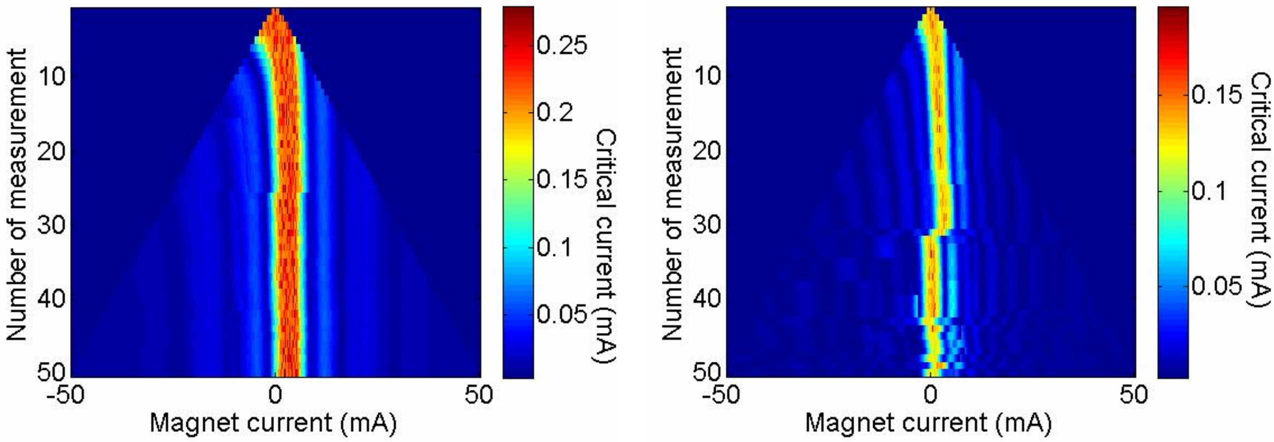

Figure 8: 50 measurements (measurement number on the vertical axis) of the critical current (intensity) as a function of magnet current (in mA, horizontal axis). Data for 0.25 μm^2 AlN barrier junction is presented on the left hand side and data for 1 μm^2 AlO_x is on the right hand side. For each measurement the magnet current was varied between a negative and a positive value with increasing magnitude. The junction was demagnetized and defluxed before doing these measurements. The measurements show the critical current response to different magnet current extrema. With increasing magnet current extrema the intensity patterns first start to look similar as the magnet will move towards its saturation level. If the magnitude of the extrema gets above 20 mA the patterns can get shifted. This is not explained yet. One possibility can be that a flux in the film can be generated relatively far from the junction location that shifts the curve, but does not decrease the maximum critical current.

Josephson effect was not properly suppressed. This is a big drawback for AlN mixers right now and requires further investigation.

The response to high magnet currents and the saturation level of the magnet was studied. This was done by doing 50 measurements of the critical current as a function of magnet current (see Figure 8). For each measurement the magnet current was varied between a negative and a positive value with increasing magnitude. The junction was demagnetized and defluxed before doing these measurements and both AlN and AlO_x barriers were used. The measurements show the critical current response to different magnet current extrema. With increasing magnet current extrema the intensity patterns first start to look similar as the magnet will move towards its saturation level. If the magnitude of the extrema gets above 20 mA the patterns can get shifted. One possibility can be that a flux in the film has been created that shifts the curve but does not decrease the maximum critical current. This effect does not prevent operation of the ALMA detectors, but it does occur during the demagnetization procedure now used on the ALMA mixer.

CONCLUSIONS

We succeeded in operating an AlN barrier SIS junction. This junction is the result of very recent developments and shows a top sensitivity. AlN barrier junctions do have some drawbacks. It is relatively difficult to suppress the Josephson noise. Also, bias voltages of over 3 mV will introduce flux in the junction. Finally, to properly deflux the junction, AlN barrier junctions should also be symmetrically shaped. This puts lower limits on the sizes of fabricated junctions.

We developed an automatic operating procedure for the junction which includes demagnetizing and defluxing. Executing this procedure statistically results in about 50% chance of success. When attempts are unsuccessful, subsequent attempts also have 50% chance of success.

ACKNOWLEDGMENT

We would like to thank G. Gerlofsma for preparing SIS junctions.

This work has been partially funded by the European Organization for Astronomical Research in the Southern Hemisphere (ESO), under ESO contract numbers 73072/MAP/03/8632/GWI and 16173/ESO/07/14997/YWE. The work was also supported by the Dutch Astronomical Research School (NOVA) within a NOVAII grant. The work has also benefited from research funding from the European Community's sixth Framework Programme under RadioNet R113CT 2003 5058187

REFERENCES

[1] http://www.alma.cl

[2] Jacob W. Kooi, Attila Kovács, Matthew. C. Sumner, Goutam Chattopadhyay, Riley Ceria, Dave Miller, Bruce Bumble, Henry G. LeDuc, Jeffrey A. Stern, and Tom G. Phillips, “A 275–425-GHz Tunerless Waveguide Receiver Based on AlN-Barrier SIS Technology”, *IEEE trans. On Microwave Theory and Techniques*, vol. 55, NO. 10, Oct 2007

[3] C. F. J. Lodewijk, M. Kroug, and T. M. Klapwijk, “Improved design for low noise Nb SIS devices for band 9 of ALMA (600–720 GHz),” *Proc. 16th Int. Space Terahertz Technol. Symp., Göteborg, Sweden*, 2005, paper S03-05.

[4] Hesper, R., Jackson, B.D., Baryshev, A., Adema, J., Wielienga, K., Kroug, M., Zijlstra, T., Gerlofsma, G., Bekema, M., Keizer, K., Schaeffer, H., Barkhof, J., Mena, F.P., Rivas, R., Klapwijk, T.M., Wild, W., “Design and Development of a 600-720 GHz Receiver Cartridge for ALMA Band 9”, *16th Int. Symp. on Space Terahertz Technology*, 2005

[5] T. Zijlstra, C. F. J. Lodewijk, N. Vercruyssen, F. D. Tichelaar, D. N. Loudkov, and T. M. Klapwijk, “Epitaxial aluminum nitride tunnel barriers grown by nitridation with a plasma source”, *Appl. Phys. Lett.*, 91, 233102 (2007)

Formation of High Quality AlN Tunnel Barriers via an Inductively Couple Plasma

Thomas W. Cecil[1*], Arthur W. Lichtenberger[1], and Anthony R. Kerr[2]
[1]Univeristy of Virginia, Charlottesville, VA 22901, USA
[2]National Radio Astronomy Observatory, Charlottesville, VA 2290X, USA
* Contact: twc7c@virginia.edu, phone 434-924-8940

***Abstract*— Increasing operating frequencies of SIS receivers requires junctions that can operate at higher current densities. A major limiting factor of higher current density junctions is the increase in subgap leakage that occurs in AlO_X barriers as current densities approach and exceed 10kA/cm^2. AlN insulators are a promising alternative due to their lower leakage current at these high current densities. In this paper we present a more detailed analysis of the formation of AlN barriers using our previously reported inductively coupled plasma (ICP) source growth technique. The ICP allows for independent control of ion energy and current density in the plasma. Additionally, plasmas with very low ion energy (~20eV) and a high degree of dissociation (~80%) can be achieved. This improved control allows for the repeatable formation of high quality barriers. In particular, we report on the relationship between barrier thickness and plasma conditions as determined by in-situ discrete ellipsometry. Ellipsometry results were verified by fabricating Nb/Al-AlN/Nb junctions and measuring current-voltage, I(V), curves. dc I(V) curves for a range of current densities are presented.**

I. Introduction

The terahertz region of the electromagnetic spectrum contains large amounts of information of interest to radio astronomers. In order for much of this information to analysed it must be frequency down converted prior to analysis. For frequencies below 1THz, SIS junctions offer the lowest noise temperatures; Nb/Al-AlO_X/Nb junctions have been fabricated with noise temperatures of 2 to 5 times the quantum limit for frequencies below 700GHz. As the design frequency of an SIS junction increases, the desired current density increases. Unfortunately, as current densities increase beyond ~ 10kA/cm^2 the commonly used aluminium-oxide (AlO_X) barrier shows an increase in leakage current. The increase in leakage current is attributed to an increase in pinhole defects in the barrier. For projects intended to operate at even high frequencies and current densities, for example ALMA Bands 8, 9, and 10, an alternative barrier material is required to reduce subgap leakage and mixer noise temperatures.

Reference [1] first attempted to use an aluminium-nitride (AlN) barrier for SIS junctions after noticing an improvement in thermal stability after performing a nitridation of the Nb electrodes. The AlN barrier was fabricated using a process similar to that for AlO_X. A thin layer of aluminium (Al) was exposed to a nitrogen plasma generated by a set of parallel plates. The plasma is necessary to crack the nitrogen molecule which will not spontaneously react with the Al layer. This work was reproduced by [2] who found that while their high j_C junctions displayed excellent I(V) curves, their low j_C junctions displayed poorer I(V) curves. The poor quality of these junctions was attributed to damage caused by energetic ions from the plasma striking the growing barrier. Reference [3] improved the fabrication process by moving the device wafer to the grounded electrode, a step that has been adapted by many groups [4]–[6]. Although this has yielded improved junction quality, the process still suffers from increased sub-gap leakage at higher current densities and issues of repeatability with wafers fabricated using the same processing conditions displaying current densities ranging over an order of magnitude or more.

Previously at the 2006 Applied Superconductivity Conference we reported on the first ever use of a novel technique for fabricating AlN-based tunnel junctions via a COPRA inductively coupled plasma (ICP) source [7]. An ICP enables independent control of the ion energy and current density of a plasma; this is not possible in a plasma formed via a parallel plates. Initial results of AlN formation characterized by in-situ ellipsometry indicated improved control over the AlN formation dynamics when using the ICP. Reference [8] has since also adapted our ICP approach using the same COPRA ICP. By operating in a high pressure regime they have achieved reproducible, high quality AlN barriers. In this paper we present further studies of the AlN formation dynamics via ellipsometry along with dc I(V) curves of AlN-based SIS junctions fabricated using an ICP source.

II. Experimental Methods

The AlN barriers described in this paper were formed using an Al over-layer process: a thin film of Al is exposed to a nitrogen plasma to form a layer of AlN. We examine plasmas formed at higher pressures with lower ion energies and current densities than our previous work. These conditions should yield a higher quality barrier and a more reproducible process. The nitrogen plasma was created using a COPRA inductively coupled plasma source from CCR Technology of Germany [9]. The COPRA source is part of the loadlock of a sputtering deposition system solely used for depositing SIS trilayers. The wafer sits on a ground platter 10cm above the extraction grid of the ICP. The current density of the plasma is primarily determined by the rf power applied to the ICP. The ion energy can be varied by applying a bias to the bottom of the ICP plasma chamber through a series of capacitors. The capacitance is controlled by an energy knob with settings ranging from E(0) to E(10); E(0) is the lowest ion energy and E(10) the highest. At this moment we do not know the exact value of ion energy generated by the source, but it is believed to range from approximately 20eV to 200eV based upon measurements from the manufacturer.

A Digisel [10] discrete ellipsometer from HORIBA Jobin Yvon is attached to the loadlock of the deposition system such that measurements can be made while the wafer is sitting on the platter above the ICP during the nitridation process. The Digisel is attached at an angle of incidence of 70° and operates at a wavelength of 632.8nm. Data collection rates of up to 5 samples per second allow for real-time analysis of the AlN formation dynamics. During some sample runs the ellipsometer was set to collect data before and after the nitridation plasma was run. This was used to verify that any radiation generated by the plasma did not alter the ellipsometry data. No such alteration was found.

A. Ellipsometry Characterization

The formation dynamics of the AlN tunnel barriers were studied using in-situ ellipsometry. Ellipsometry is a non-destructive optical method to determine the thickness and optical properties (refractive index and extinction coefficient) of thin films. Ellipsometry measures the change in polarization of light reflected from the film. These values are compared to values calculated using first principles and a model of the film's presumed thickness and optical properties. Adjusting the properties of the model until the calculated and measured polarization values agree yields the film's properties. This method requires some a prior knowledge of the films properties, such as either the film thickness or optical properties. When the optical properties are know, film thicknesses can be determined to within an angstrom when used in-situ.

Samples used for AlN formation analysis were made by first deposition ~1000Å of Al on a Si/SiO_2 wafer. At this thickness the Al layer is more than four times the thickness of the penetration depth of 632.8nm light in Al and the Al layer is opaque to the light. Thus the sample can be modelled as an Al substrate upon which an AlN layer is grown (Here after the AlN formation process will be referred to as growth). Although the formation of the AlN layer does consume some of the Al layer, it is not enough to alter the model. For film thicknesses below ~100Å, the change in polarization is a product of the film thickness and refractive index. We used a value of 2.12 as found in ref [11]. This value was determined from much thicker films and to our knowledge no data is currently available on extremely thin AlN films. Ultimately, the thickness determined by ellipsometry is derived from a model and will need to be calibrated (discussed below).

B. Junction Fabrication and Testing

Nb/Al-AlN/Nb SIS junctions were fabricated using a self-aligned junction process. This process has recently been improved to yield better control over the final junction size and improved insulation around the top electrode [12]. The base electrode Nb thickness is 1650Å, the counter electrode Nb thickness is 650Å, and the Al over-layer thickness is nominally 50Å. The base electrode for these devices have been fabricated using both a lift-off and trilayer etch process. The lift-off process helps to limit stress based degradation of the junction [13] while the trilayer etch process enables the use of the ellipsometer on wafers that will be fabricated into full devices. We observed no difference in the quality of the devices fabricated by the two methods.

Measurements of the thickness of AlN barriers of fabricated devices is not possible. The thin Al over-layer is transparent and it's thickness must be accounted for in the model. As the AlN layer forms, it consumes some Al and thus the thickness of both the AlN and Al layers are simultaneously changing. The Digisel system is only capable of monitoring a change in thickness of a single layer. However it is still possible to measure the change in polarization parameters, which do not depend on a material model, and compare these to AlN thicknesses measured on 1000Å Al films or calculated from current density measurements.

III. Results

A. Barrier Thickness Measurements

The suitability of the COPRA ICP source for forming AlN tunnel barriers was first examined via in-situ ellipsometry. Plasmas with a range of ion energies and current densities were examined. Some initial earlier results are described elsewhere [7] and have been summarized in Figure 1 for the benefit of the reader. Barriers A, B, and C were grown with rf power of 150W and energy settings of E(2), E(5), and E(8); ~50eV, ~100eV, and ~150eV respectively. Barriers D and E were grown at an energy setting of E(2) with rf power of 300W and 450W respectively. The nitrogen pressure for all of the barriers was 2mTorr. The portions of the Figure to the left and right of the vertical lines (0 - 60 sec and 360 - 420 sec) represents the time before the plasma is turned on and after the plasma is turned off. It is important to note that the pre-plasma curves all closely overlap and the post growth curves are relatively flat. This indicates that radiation from the plasma is not interfering with the ellipsometry measurements and that the barriers are stable after the plasma is shut off.

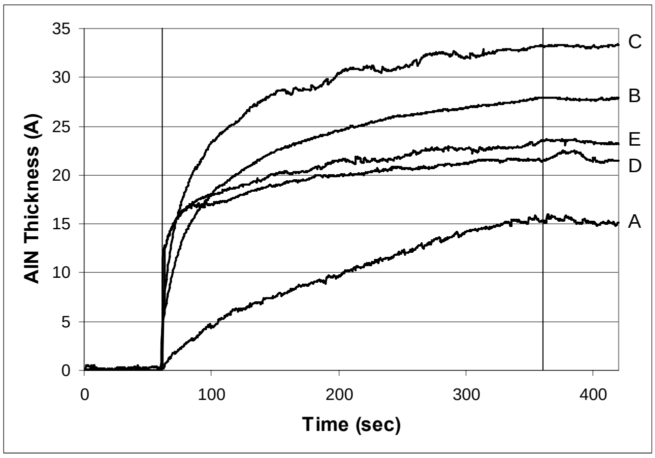

Fig. 10 AlN barrier thickness as a function of time for a wide range of applied rf power (ion current density) and energy setting (ion energy).

As expected we see an increase in barrier thickness with both ion energy and current density after 5 minutes; higher energy ions can implant deeper into the Al layer while a higher current density provides more ions to react with the Al layer. Barriers B, C, D, and E show an faster initial growth rate that slows over time. For Barriers D and E this initial growth is very rapid yielding a ~15Å thick layer in less than 20 seconds. This is followed by a much slower growth with both barriers roughly 22Å thick after 5 minutes. This suggests the possibility that the barrier thickness may be saturating over time, but longer growth periods will need to be examined. Barrier A, formed at the lowest ion energies and current densities examined, shows a mostly linear growth curve with a thickness of 15Å after 5 minutes. Unfortunately, all of these growth curves rapidly yield thicknesses greater than the ~10Å which is likely necessary to yield high current density junctions. Additionally, the rapid increase in thickness will make it difficult to repeatedly fabricate junctions with the same barrier thickness and current density. However, the thickness of these barriers as determined by ellipsometry must be calibrated and thus these conditions can not be completely ruled out.

To achieve slower growth rates and smaller ultimate thicknesses, the applied rf power was greatly reduced. At a pressure of 2mTorr and energy setting E(2) the plasma was stable down to rf powers of 25W. By raising the pressure to 5mTorr the plasma was stable down to 10W. Figure 2 below shows the thickness-time curves for AlN barriers grown at 10W, 25W, and 50W; Barriers F, G, and H respectively.

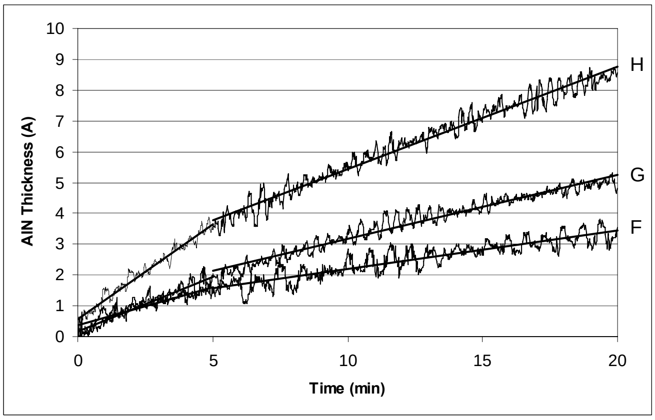

Fig. 2 AlN barrier thickness as a function of time for low applied rf power (ion current density). The superimposed lines are best-fit trendlines.

The curves in Figure 2 are highly linear when compared with those in Figure 1. After 5 minutes the barriers are all still less than 4Å thick. Two different growth periods can be observed with the first period lasting for 5 minutes. This growth period is slightly faster than the second period with growths rates of 0.25Å/min, 0.35Å/min, and 0.62Å/min - for barriers F, G, and H respectively – compared with 0.13Å/min, 0.21Å/min, and 0.33Å/min for the following 15 minutes. Although these conditions would lead to longer growing times, the ability to control the magnitude of the rate of growth while maintain a constant growth rate should improve reproducibility with variations in the nitridation time of a few seconds having a much smaller affect on the overall thickness. Additionally, there appears to be no affect on the growth process by moving to higher pressures, although further study is needed. Importantly, with all other conditions remaining constant, higher pressures should yield lower ion energies due to thermalization in the plasma and may reduce barrier damage caused by energetic ions.

While the growth curves in Figure 2 for lower rf power show promise, there is still concern over damage to the growing barrier from high energy ions. The barriers were grown at E(2), which corresponds to an ion energy of ~50eV. This was the lowest energy setting examined previously because no conditions were found at which the plasma would start for lower energy settings. However, after developing a process for starting the plasma at higher energy settings and then raising the pressure and lowering the energy setting, stable plasmas at an energy setting of E(0) were achieved. This required a pressure of 5mTorr and rf powers of 100W or higher. These conditions should yield the lowest possible energy from the source, although because there is a small correlation between ion energy, rf power, and pressure, these may not be the absolute lowest values. In this process the plasma is started with the wafer in a separate portion of the loadlock chamber away from the plasma. After the plasma has stabilized at the desired conditions the wafer is moved into place. Thickness-time curves for barriers grown at 5mTorr, energy setting E(0), and rf powers of 100W, 200W, and 300W – Barriers I, J, and K respectively – are shown in Figure 3.

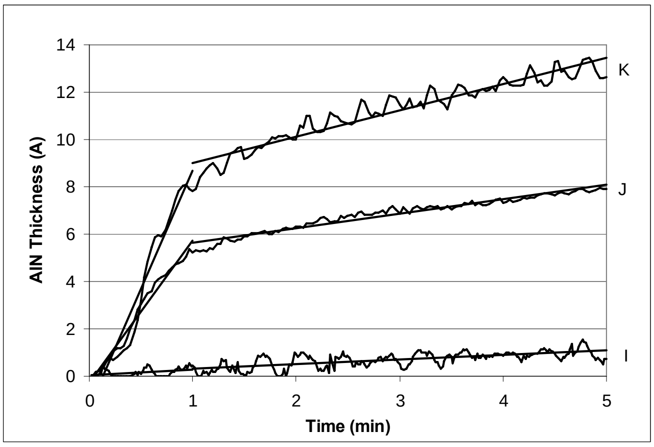

Fig. 3 AlN barrier thickness as a function of time for energy setting, E(0): ion energy of ~20eV. The superimposed lines are best-fit trendlines.

For Barriers J and K there is again an initial period with a high growth rate followed by a slower growth rate. It is likely that the two periods this still occur for Barrier I but the second period does not occur during the first 5 minutes. Although at a lower ion energy than in Figure 2, the higher rf powers yield higher growth rates such as those in Figure 1. Barriers J and K display initial rates of 6Å/min and 10Å/min followed by 0.6Å/min and 1.1Å/min. This yields barriers thicknesses of 8Å and 13Å respectively after 5 minutes. (The 0.2Å/min growth rate for Barrier I would require a nitridation times in excess of 50 minutes to yield a 10Å barrier.) The conditions for Barriers J and K are promising due to the combination of high initial growth rate to yield a thickness on the order of the desired thickness follow by a much slower growth rate to allow finer control over the final barrier thickness.

One unresolved question regarding the growth of AlN barriers is whether the barrier thickness saturates over time [3], [4]. If the AlN barrier were to saturate as a function of ion energy, the desired thickness could be controlled by selecting the necessary ion energy and thereby removing the issues of ion current density and nitridation time. Because much of the work in this area has been done using parallel plate plasmas it is difficult to isolate the contribution of ion energy to barrier thickness. Additionally, since many of the reports in the literature have been based upon current density measurements, if the barrier saturates at a thickness outside of the range useful for tunnel junctions it may not be fully observed. We examined this question with a series of long (90 min) plasma exposures. The resulting thickness-time curves are shown in Figure 4. Barriers J and K were grown at E(0) and rf power of 200W and 300W, respectively. Barriers L, M, and N were formed at E(2) and rf power of 100W, 200W, and 300W, respectively. A pressure of 2mTorr was used for all the barriers.

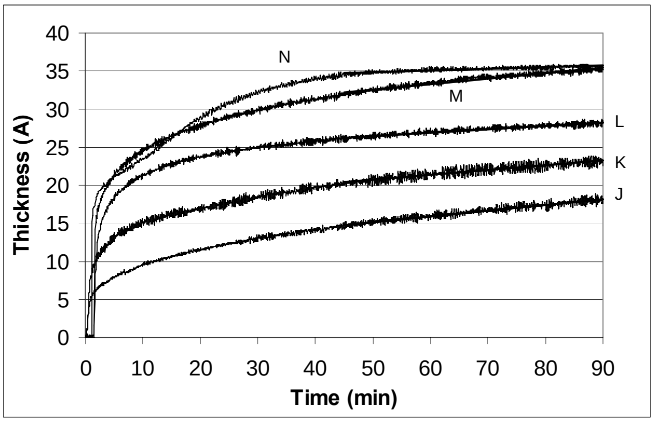

Fig. 4 AlN barrier thickness as a function of time for various plasma conditions.

After 90 minutes all of the barriers continue in increase in thickness and also display thicknesses above those desirable for high current density junctions. Barriers N and M appear close to saturating and it is possible that after nitridation times of several hours they may reach a final thickness. However Barriers J, K, and L all have significant growth rates after 90 minutes. Should it be possible to reach saturation at thickness desirable for tunnel junctions, the long time that are required increase the likelihood of contamination from background gases. It is likely that the reports of saturation in the literature were for devices fabricated in the two growth periods. When comparing devices fabricated in these two periods it would likely appear that those from the second period had achieved a saturation level when compare with the rapidly changing barrier thickness and current density of those fabricated in the initial growth period.

B. dc Current-Voltage Curves

Although ellipsometry measurements can speak to the thickness of the AlN barrier, dc current-voltage, I(V), curves are necessary to speak to the quality of the barrier. Nb/Al-AlN/Nb junctions were fabricated as described above in Section II. Junctions were fabricated with barriers grown from a range of plasmas conditions. The plasma conditions were chosen based upon the results of the ellipsometry data from figures above, beset represented by Barrier J. All the barriers were formed with a nitrogen pressure of 5mTorr and rf power of 200W. The nitridation times ranged from 15 to 25 minutes and energy settings of E(0) to E(2). As expected the current density decreased for increases in both nitridation time and energy setting. The highest quality junctions were formed with a nitridation time of 25 minutes and energy settings of E(0) and E(1). The resulting current densities ranged from 0.14kA/cm^2 to 32.5kA/cm^2. Typical I(V) curves for these junctions are shown in Figure 5.

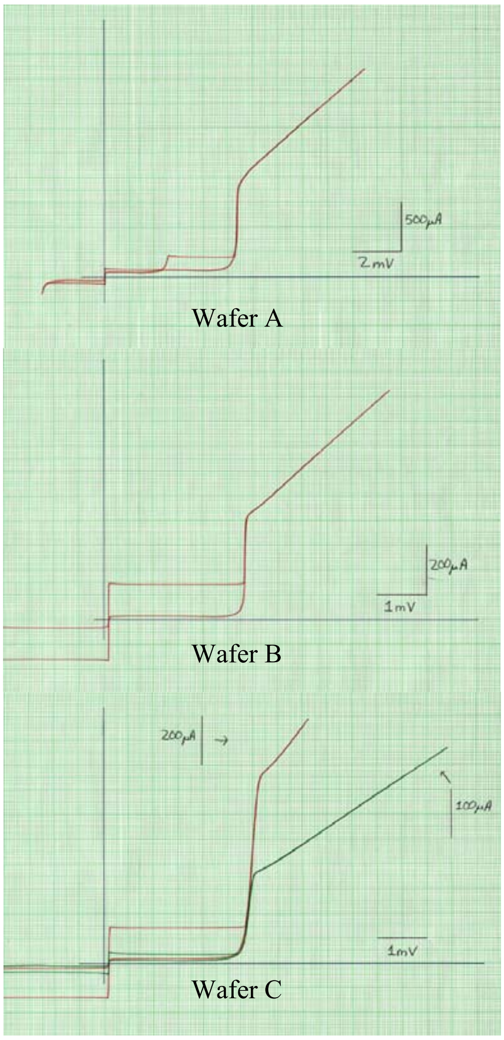

Fig. 5 dc I(V) curves for Wafer A: top, E(0), 25min, 32.5kA/cm^2, Wafer B: middle, E(0), 25min, 4.2kA/cm^2 and Wafer C: bottom E(1), 25min, 0.14kA/cm^2. Wafer A has two series junctions. Wafers B and C have single junctions.

Uniformity of current density over a 2" diameter wafer is +/-15% while neighbouring junctions are nearly identical. Run to run reproducibility has shown some irregularities. Wafers A and B were fabricated with the same plasma conditions, but two months apart. Their current densities are 32.5kA/cm^2 and 4.2kA/cm^2 respectively. However, a wafer fabricated the day after wafer B with the same conditions had a current density of 4.1kA/cm2. We believe that these irregularities likely arise from two sources: 1) small changes in the energy setting from run-to-run and 2) changes in the plasma conditions over time.

As discussed above the ion energy is set by turning a knob attached to a bank of capacitors. This knob does not have a physical "stop" and thus is likely to be in a slightly different location each run. Barriers made in consecutive run during which the energy knob was not moved showed thickness variation of less than 1Å. It is not possible to do this for real devices; the energy setting is increased at the beginning of a trilayer deposition for argon plasma substrate cleaning. Because nitrogen is a reactive gas it can attack the extraction grid of the ICP and cause the grid to breakdown over time. This may lead to changes in the ion energy and current density of the plasma over time despite using the settings. We have recently installed a Faraday cup plasma monitor on our deposition system and are examining both possible causes. WE believe the plasma monitor will allow use the set the exact plasma conditions prior to each nitridation.

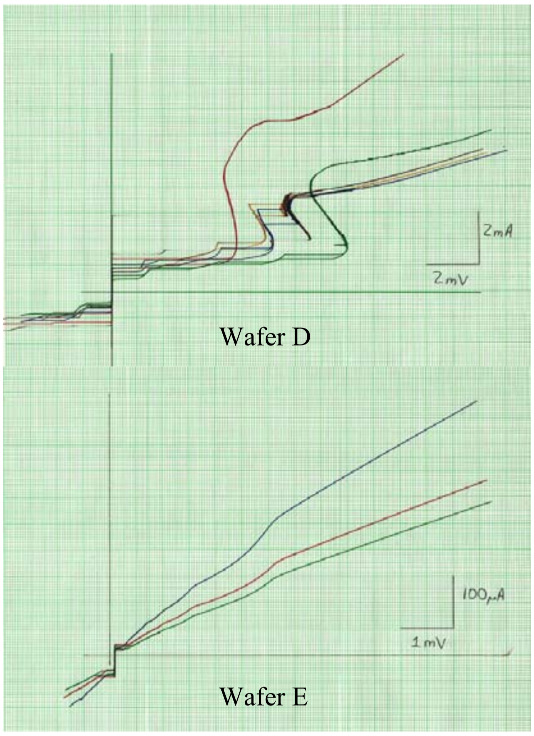

Fig. 6 dc I(V) curves for Wafer D top (E(0), 15min), and Wafer E top (E(2), 25min). Wafer D has up to 4 junctions in series. Wafers E has single junctions.

Decreasing the nitridation time from 25 minutes with an energy setting of E(0) results in very high current densities (above 100kA/cm^2) and I(V) curves that display junction heating and large subgap leakage. For energy settings above E(1) the barriers shows signs of damage from the higher energy ions. Examples of both of these problems are shown above in Figure 6. Although Wafer C, fabricated with E(1) has a high quality I(V) curve, it is desirable to operate at the lowest possible energy setting to avoid the possibility of damage.

Although some questions remain about the reproducibility of this process, it is important to note the high quality of this process. Table 1 list the quality factor (R_{sg}/R_N) for these devices over a range of current densities (in kA/cm^2) compared with those from other groups made using both ion gun and parallel plate sources.

TABLE V
JUNCTION QUALITY COMPARISONS

	UVa		JPL [14]		Delft [15]	
Wafer	j_C	R_{sg}/R_N	j_C	R_{sg}/R_N	j_C	R_{sg}/R_N
A	32.5	15.5	---	---	38	9
	---	---	9.4	12.6	---	---
B	4.2	22.5	4	28	4.75	22.5
C	0.14	25	0.55	50	---	---

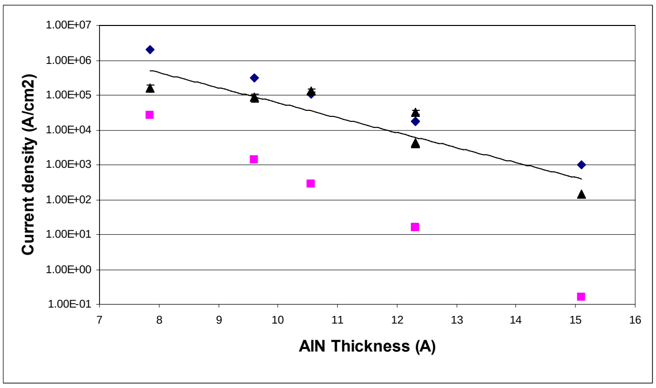

Fig. 7 Current density as a function of AlN barrier thickness for measured data (triangle), values calculated for Φ_B = 0.88eV (diamond) and Φ_B = 2.35eV (square). The line is a best-fit trendline for the measured data.

C. Ellipsometry Calibration

As discussed above, ellipsometry does not directly measure the thickness of a material layer but rather determines it based upon a model of the layer's optical properties. We examined the validity of our AlN model by comparing the calculated thickness with current densities from fabricated devices. The thickness of an AlN layer formed on a thick Al layer, 1000Å, was first measured. Next an SIS junction was fabricated using the same plasma conditions. The current density of the fabricated device was then measured and compared to a theoretical current density calculated using the thickness determined by ellipsometry. The measured current density was determined from the quasi-particle rise of the dc I(V) curve. The theoretical current density was calculated using the equation derived by Simmons [16]

$$j_C = 3.16 * 10^{10} \frac{\sqrt{\Phi_B}}{d} \exp(-1.025\sqrt{\Phi_B}d$$

where j_C is the current density in A/cm^2, d is the barrier thickness in Å and Φ_B is the barrier height in eV.

Figure 7 plots the measured current density of our AlN junctions based upon their measured barrier thickness along with theoretical curves for two values of barrier height. Reference [17] reported two different values of AlN barrier height depending upon the current density of the junction. Junctions with current densities above 5kA/cm^2 had a barrier height of 0.88eV while those with current densities below 5kA/cm^2 had a barrier height of 2.35eV. Our measured data fits much better with the barrier height for the higher current density which may be expected given that all of our junctions but one had current densities roughly at our above 5kA/cm^2. Our data can be fit with an exponential trendline defined by the equation j_C = C*exp(-0.99d) where C is a constant. This matches well to the equation j_C = C*exp(-0.96d) reported in [17].

The fit between the measured and calculated data can be improved by adjusting the thickness against which the measured data is plotted. An increase in the thickness shifts the curve for the measured data to the right. In Figure 8 the measured current densities are plotted with a AlN thickness increased by a factor of 1.1. This yields the best fit between the theoretically calculated data (diamond points and dotted line) and corrected data (circle points and dashed line). For very thin layers, <100Å, the change in polarization parameters measured by ellipsometry is a product of layer thickness and index of refraction. Thus an increase in thickness is proportional to a decrease in the value of index of refraction used in the model from 2.12 to 1.91. This range of values has been seen in thicker films with the variation attributed to changes in film structure [18].

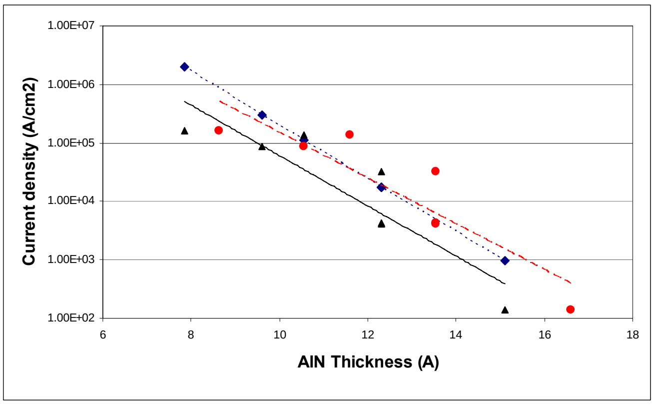

Fig. 8 Current density as a function of AlN barrier thickness for measured data (triangle, solid line), calculated data for Φ_B = 0.88eV (diamond, dotted line), and measured data with AlN thickness adjusted by a factor of 1.1(circle, dashed line). The lines are a best-fit trendline for the measured data.

CONCLUSIONS

We presented recent results on our technique for fabricating AlN tunnel barrier for SIS junctions via inductively coupled plasma. Using in-situ ellipsometry we have studied the growth dynamics of AlN layers formed via ICP at higher pressures with lower ion energies and current densities. The ICP technique is highly versatile and capable of altering the characteristics (rate and curvature) of the AlN growth curve. In the range of interest these curves can be described by two distinct growth periods: a shorter initial period with high growth rate followed by a longer period with slower growth rate. At lower plasma energy settings and rf powers both of these regions can be roughly approximated as linear. The issue of AlN thickness saturation was examined, and while it appears possible that the thickness may eventually saturate, this occurs outside the range of desirable thicknesses for SIS junctions.

We have fabricated and tested Nb/Al-AlN/Nb SIS junctions. Using nitridation conditions determined through the use of in-situ ellipsometry very high quality junctions with current densities ranging from 0.14kA/cm2 to 32.5kA/cm2 have been achieved with high quality factors of 25 to 15.5. Importantly even at current densities above 10kA/cm^2, when AlN barriers become technologically important, the quality factor of these devices remains high. Comparing the measured current density of these devices to theoretically calculated values we have confirmed the AlN thickness determined by ellipsometry to within 10%. An in-situ plasma monitor is currently being installed in the deposition system to monitor changes in the plasma over time and answer questions regarding process reproducibility.

ACKNOWLEDGMENT

The authors would like to thank Jian-Zhong Zhang, Jie Wang, and Greg Stronko for their help with device fabrication.

REFERENCES

[1] T. Shiota, T. Imamura, and S. Hasuo, "Nb Josephson junction with an AlNx barrier made by plasma nitridation," *Applied Physics Letters*, vol.61, no. 10, Sep. 1992, pp. 1228-1230.

[2] A.W. Kleinsasser, W.H. Mallison, and R.E. Miller, "Nb/AlN/Nb Josephson Junctions with high critical current density," *IEEE Transactions on Applied Superconductivity*, vol. 5, no. 2, Jun. 1995, pp. 2318-2321.

[3] B. Bumble et. al., "Fabrication of Nb/Al-N$_x$/NbTiN junctions for SIS mixer applications," *IEEE Transactions on Applied Superconductivity*, vol. 11, no.1, March, 2001., pp. 76-79.

[4] N.N. Iosad et. al., "Characterization of the fabrication process of Nb/Al-AlN$_x$/Nb tunnel junctions with low R$_N$A values up to 1 Ω μm^2," *Superconducting Science and Technology*, vol. 15, 2002, pp. 945-951.

[5] P.N. Dmitriev et. al., "High Quality Nb-based Tunnel Junctions for High Frequency and Digital Applications," *IEEE Transactions on Applied Superconductivity*, vol. 13, no. 2, Jun. 2003, pp. 107-110.

[6] J. Kawamura et. al., "Very high-current-density Nb/AlN/Nb tunnel junctions for low-noise submillimeter mixers," *Applied Physics Letters*, vol. 76, no. 15, Apr. 2000, pp. 2119-2121.

[7] T. Cecil et. al., "Investigation of NbTiN Thin Films and AlN Tunnel Barriers with Ellipsometry for Superconducting Device Applications," *IEEE Transaction on Applied Superconductivity*, vol. 17, no. 2, Jun 2007, pp3525-3528..

[8] T. Zijlstra et.al., "Epitaxial aluminium nitride tunnel barriers grown by nitridation with a plasma source," Applied Physics Letters," vol. 91, Dec 2007, pp. 233102.

[9] "COPRA" Plasma Source. CCR Technology Gmbh., Maarweg 30, D-53619 Rheinbreitbach, Germany.

[10] HORIBA Jobin Yvon Inc., 3880 Park Avenue, Edison, NJ. 08820-3012. USA

[11] S. Loughin and R.H. French, "Aluminum Nitride," *Handbook of Optical Constants of Solids III*, E.D. Palik Ed., Academic Press, 1998, pp. 391.

[12] A. Lichtenberger et. al., "Pentalevel Resist Process for the Precise Fabrication of SIS Junctions," Submitted to 2008 Applied Superconductivity Conference, Chicago, IL, USA. August 17-22.

[13] T. Imamura, T. Shiota, and S. Hasuo, "Fabrication of high quality Nb/Al-AlO$_x$-Al/Nb Josephson junctions: I – Sputtered Nb films for junction electrodes," *IEEE Transactions on Applied Superconductivity*, vol. 2, no. 1, Mar. 1992, pp. 1-14.

[14] A.B. Kaul et. al., "Aluminum Nitride Tunnel Barrier Formation with Low-energy Nitrogen Ion Beams," *J. Mater. Res.*, vol. 20, no. 11, Nov. 2005, pp. 3047-3053.

[15] N.N. Iosad et. al., "Analysis of the Fabrication Process of Nb/Al-AlNx/Nb Tunnel Junctions with Low R$_N$A Values for SIS Mixers," *IEEE Transactions on Applied Superconductivity*, vol. 13, no. 2, Jun. 2003, pp. 127-130.

[16] J.G. Simmons, "Generalized Formula for the Electric Tunnel Effect between Similar Electrodes Separated by a Thin Insulating Film," *Journal of Applied Physics*, vol. 34, no. 6, Jun. 1963, pp. 1793-1803.

[17] Z. Wang et. al., "Interface and Tunnel Barrier Heights of NbN/AlN/NbN Tunnel Junctions," *Applied Physics Letters*, vol. 75, no. 5, Aug. 1999, pp. 701-703.

[18] H.Y. Joo et. al., "The Optical and Structural Properties of AlN Thin Films Characterized by Spectroscopic Ellipsometry," *Thin Solid Films*, vol. 368, 2000, pp. 67-73.

Design of SIS finline mixers with ultra-wide IF bands

Paul K. Grimes[1*], Ghassan Yassin[1], Karl Jacobs[2] and Jamie Leech[1]

[1]*Astrophysics, Dept. of Physics, University of Oxford, Denys Wilkinson Building, Keble Road, Oxford, OX1 3RH, UK*

[2]*KOSMA, I Physikalisches Institut, Universität zu Köln, Zülpicher Straße 77, 50937, Köln, Germany*

* Contact: P.Grimes1@physics.ox.ac.uk, phone +44 1865 273304

***Abstract*— We present the design of a 230 GHz finline SIS mixer with a 2-20 GHz IF bandwidth. The mixer is intended for use in a prototype high brightness sensitivity, low spatial resolution heterodyne interferometer currently under construction at Oxford[1]. The sensitivity of the instrument will be sufficient for measuring the spectrum of the Sunyaev-Zel'dovich effect in the brightest galaxy clusters.**

The mixer design is based on a previously reported 230 GHz finline mixer design[2], with a number of improvements and features added to achieve the very demanding IF bandwidth requirements. An RF bandpass filter is included on the chip to isolate the IF signals from the finline transition, and the mixer tuning circuits, RF choke and IF connections have been carefully designed to exhibit very low parasitic reactances in the IF band.

The first two batches of these mixers were recently fabricated at Cologne University, and are currently being tested.

I. Introduction

SIS mixers now routinely achieve noise temperatures of a few times the quantum limit in the mm-wave band. It is therefore difficult to make significant improvements in SIS millimetre receiver sensitivity by improving the noise temperature. However, the performance of SIS receivers can be improved in a number of other ways, such as the use of sideband separation, improvements in stability and the construction of large arrays of mixers.

For observations of continuum sources, the sensitivity of a receiver does not depend on the raw noise performance only, but also on the available instantaneous bandwidth over which detected power is integrated. The instantaneous bandwidth of heterodyne receivers is defined by their IF bandwidth. Increasing the IF bandwidth may also be useful for spectroscopic observations, as it allows the simultaneous observation of several spectral lines and with a wider range of Doppler shifts. Wider IF bands can also provide more data for determining baseline signal levels.

SIS mixers have traditionally had relatively small IF bandwidths (e.g. 4.2-5.8 GHz for SIS receivers on the JCMT) although wider IF bandwidths are now being used on newer instruments (e.g. 4-8 GHz for the HIFI instrument on Herschel and 4-12 GHz for ALMA). This is because a number of key problems have to be solved in designing mixers with very wide IF bandwidths.

Each of the sidebands have bandwidths equal to the IF bandwidth, and so the RF signals must be well coupled to the mixer over a relatively large frequency range. The SIS junction must see a reasonably constant embedding impedance throughout the IF band, and IF signals can not be allowed to leak into the RF feed when the IF frequency becomes a significant fraction of the RF. The IF signals must be efficiently coupled from the mixer chip to an IF amplifier with good performance over a large fractional bandwidth. Other IF components, such as bias tees, must also have good performance over large fractional bandwidths. Finally it is necessary that the backend electronics can handle the large bandwidth signals output by the receiver.

We have designed a finline SIS mixer with an RF bandwidth of 185-275 GHz and a target IF bandwidth of 2-20 GHz. This mixer will be used in our prototype interferometer GUBBINS, described in these proceedings [1].

II. Mixer Design

The mixer chip described in this paper is based on a design that has been described previously [2], with the following significant modifications to allow the ultra-wide IF bandwidth:

(i) An RF bandpass filter has been added to block the IF signal from the finline taper. This is necessary because the top end of the IF band is higher than the cutoff frequency of parts of the finline taper. (ii) The IF connection has been optimised to minimise the reactance of the IF bondwires, and (iii) a multi-stage microstrip IF transformer is used to match the IF output of the mixer to the input of the IF amplifier.

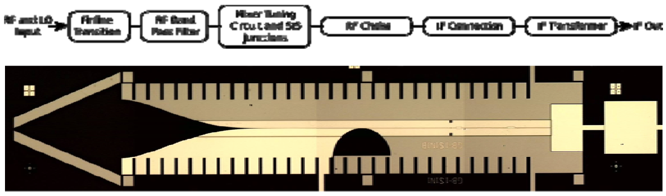

Fig. 11. (Top) circuit components making up the ultra-wide IF band finline SIS mixer. (Bottom) photo of an ultra-wide IF band finline SIS mixer chip prior to dicing and mounting in the mixer block. Apart from the finline taper, left, and the IF bond pads, right, the circuit components are too narrow to be seen in the photo.

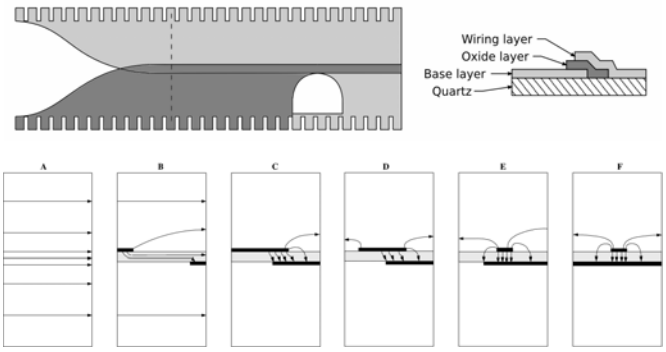

Fig. 12. (Top) Schematic of the modified antipodal finline taper used on these mixers. (Bottom) Cross-sections through an antipodal finline transition, showing E-field lines. **A** Loaded waveguide. **B** Unilateral finline section. **C** Antipodal finline section. **D** 1st half of circular finline to microstrip transition. **E** 2nd half of circular finline to microstrip transition. **F** Output microstrip.

The mixer is fabricated on 225 µm thick Infrasil fused quartz and uses a 200/10/100 nm thick Nb-AlO_x-Nb trilayer, a 425 nm thick SiO dielectric evaporated in two layers with a dielectric constant $\varepsilon_r = 5.8$ and 400 nm thick Nb wiring layer.

A schematic of the components on the completed mixer chip are shown in Fig. 11. In the rest of this section we shall describe the details of the mixer components.

A. Finline transition

An modified antipodal finline transition [3] is used to couple RF power into the mixer chip. The antipodal finline taper transforms the waveguide mode into the TEM microstrip mode using overlapping superconducting niobium films, separated by 425 nm of silicon monoxide. The taper is deposited on a 180 µm quartz substrate which supports the structure in the E-plane of a rectangular waveguide. Before the fins overlap, the taper acts as a unilateral finline since the oxide is much thinner than the quartz substrate. When the fins start to overlap it behaves like an antipodal finline, and when the overlap becomes larger than the oxide thickness the transition to microstrip is performed using a semicircular taper. A schematic of the tapering is shown in Fig. 12.

The mixer chip is mounted in the E-plane split mixer block, supported by grooves in the waveguide wall. Quarter wavelength serrations are added to each side of the finline to prevent RF power propagating in the grooves. These serrations provide a virtual RF short for finline at the waveguide wall, while allowing the mixer chip to remain DC isolated from the mixer block.

The finline taper is designed in several sections. The approximately unilateral section (before the fins overlap) was designed using the transverse resonance technique in conjunction with an optimum taper method, as described in [4].

The overlapping fin section is designed using HFSS simulations to calculate the wave impedance as a function of fin overlap and then using an impedance tapering method to synthesize the taper. A similar technique is used to taper the fin overlap and microstrip width in the semicircular transition from antipodal finline to microstrip.

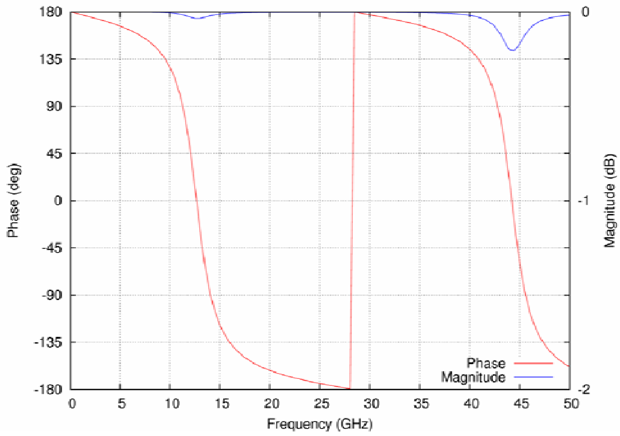

Fig. 13. Phase and magnitude of the reflection back from the finline taper towards the SIS junction in the IF band, as calculated by HFSS.

The profiles generated by each of the methods are combined by overlapping the sections, and matching the impedances, fin widths and gradients of each section at the join.

This rigorous design method generates finline tapers that are significantly shorter than those previously used, and allows the scattering parameters of the full transition to be calculated in the RF band. The resulting design of both the tapers and serrations has been validated by both scale model measurements at 15 GHz and by HFSS simulations of the complete tapers.

Ansoft HFSS was used to calculate the scattering parameters of the finline transition in the IF band of the mixer. The cut-off frequency varies smoothly along the finline transition, from zero in the microstrip output to the waveguide cut-off frequency at the front of the chip. This means that although all of the IF power is reflected from the finline, the point at which it is reflected varies with frequency, giving a large variation in the phase of the reflected signal across the IF band. This would limit the IF bandwidth of our mixer to around 10-12 GHz if IF signals were allowed to leak into the finline taper.

B. RF band-pass filter

To prevent the IF signal from leaking into the finline transition, we place an RF band-pass filter between the finline transition and the mixer tuning circuit. This filter transmits fully the RF signals, but reflects the IF signals from a fixed point, close to the mixer tuning circuit. The RF filter is made up of three sections of microstrip line and two parallel plate capacitors in series. The design was initially modelled and optimised as a lumped element and ideal transmission line circuit in the Ansoft Designer, before being verified in Sonnet *em* Suite. The final design and simulated performance are shown in Fig. 14.

The parallel plate capacitors are fabricated by depositing the lower plates as part of the first niobium wiring layer, before anodising the plates to form niobium oxide. The second wiring layer is then deposited to form the two top plates and the central microstrip of the band-pass filter.

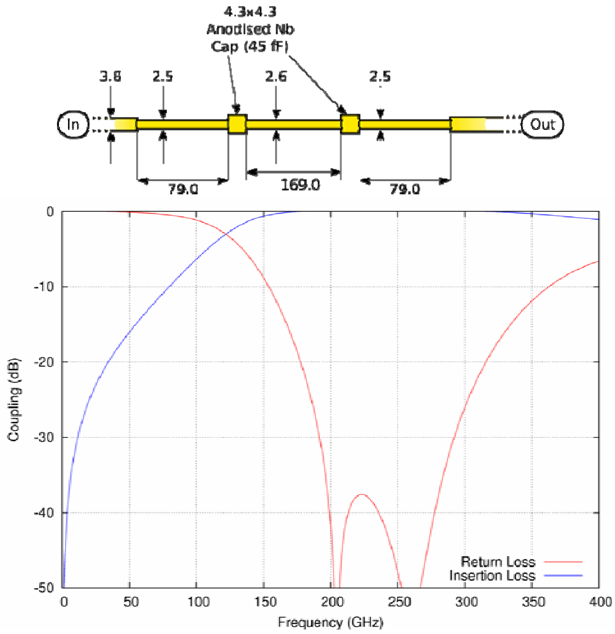

Fig. 14. (Top) Diagram of the RF band-pass filter. Dimensions are in microns. (Bottom) Calculated scattering parameters of the RF band-pass filter.

One potential problem with this design is that the dielectric constant of niobium oxide depends somewhat on the degree of oxidation which in turn affects the capacitance of the parallel plate capacitors. The wet anodisation process used to produce the niobium oxide gives us good control of the oxide thickness, so it should be possible to adjust this process to give the correct capacitances.

C. Tuning circuits

We have designed two tuning circuits for these mixers, both of which use identical 16.5 Ω, 1.25 μm diameter (area 1.21 μm^2) SIS junctions with a critical current density of 14 kA/cm^2 and a specific capacitance of 75 $fF/\mu m^2$. The first design uses a single SIS junction tuned by a single microstrip stub terminated by the RF choke (Fig. 15). This design gives relatively narrow band tuning, but is reliable and relatively simple to design and analyse.

The second design uses two SIS junctions in a single-ended dual-junction tuning circuit [5], with the IF output end terminated by a microstrip stub and stepped microstrip line RF choke (Fig. 16). This design gives very wide RF bandwidth, but is somewhat more difficult to integrate, as it relies on the successful fabrication of two identical SIS junctions on the chip.

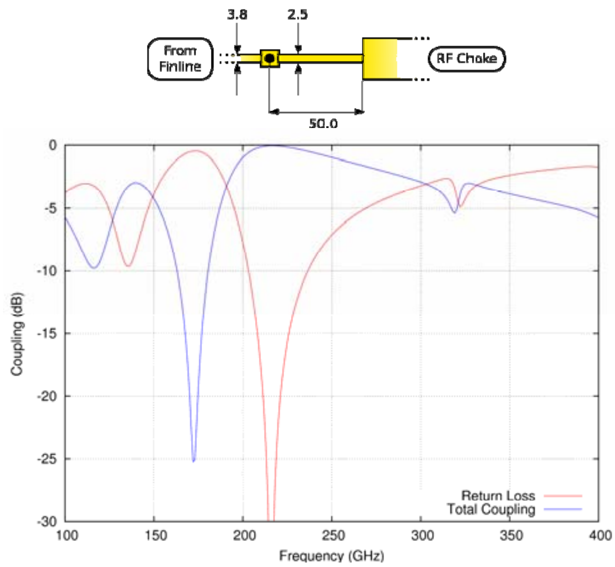

Fig. 15. (Top) Diagram of the single junction tuning circuit. Dimensions are in microns and the SIS junction is shown as a black circle. (Bottom) SuperMix calculated scattering parameters for the single-junction tuning circuit.

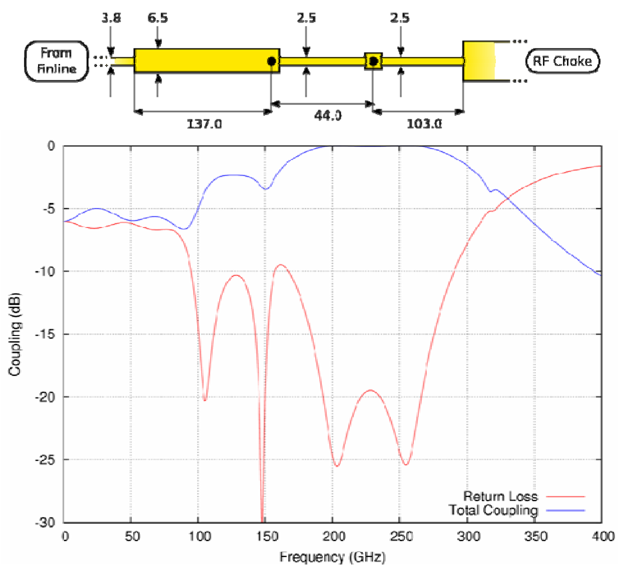

Fig. 16. (Top) Diagram of the dual junction tuning circuit. Dimensions are in microns and the SIS junctions are shown as black circles. (Bottom) SuperMix calculated scattering parameters for the dual-junction tuning circuit.

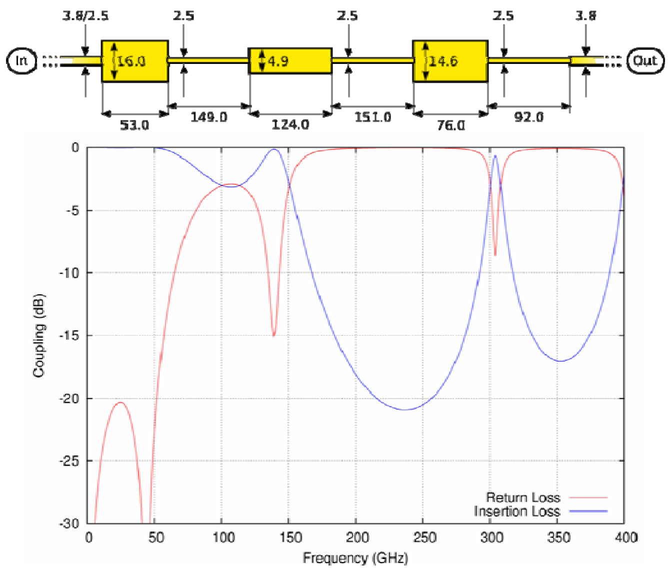

Fig. 17. (Top) Diagram of the stepped width microstrip RF choke. Dimensions are in microns. (Bottom) Sonnet *em* calculated performance of the RF choke.

D. *RF choke*

The RF choke is made up of six stepped width sections of microstrip in series (Fig. 17). The lengths and widths of these sections were optimised in Ansoft Designer and Sonnet *em* Suite to give the best possible transmission in the IF band, while still blocking the RF signal at a relatively high level. Some RF performance was sacrificed in order to obtain very wide IF bandwidth. The RF choke also acts as the microstrip stub termination in both of the tuning circuits.

This stepped microstrip line design was found to give significantly better IF bandwidth than the radial stub chokes used in previous finline mixers.

E. *IF connection and transformer*

IF signals from the mixer are transmitted through the RF choke to the wiring layer bond pad at the rear of the chip. This bond pad is connected to an IF connection circuit fabricated from 17 µm thick copper microstrip on 0.254 mm thick Rogers' Duroid 6010LM by three 50 µm diameter aluminium bond wires (Fig. 18). In order to minimise the inductance of the bond wires, the bonds are kept as short and low as possible. Two bond wires on each side of the chip provide the ground connection to the mixer block.

The IF connection has been carefully modelled in HFSS and various aspects tuned to achieve good performance at high IF frequencies. In particular, the width of the bond pad was increased, and the gap between the wiring layer bond pad and ground layer was reduced. This appears to reduce the mismatch between the 16.5 Ω microstrip output of the RF choke and the bond pad.

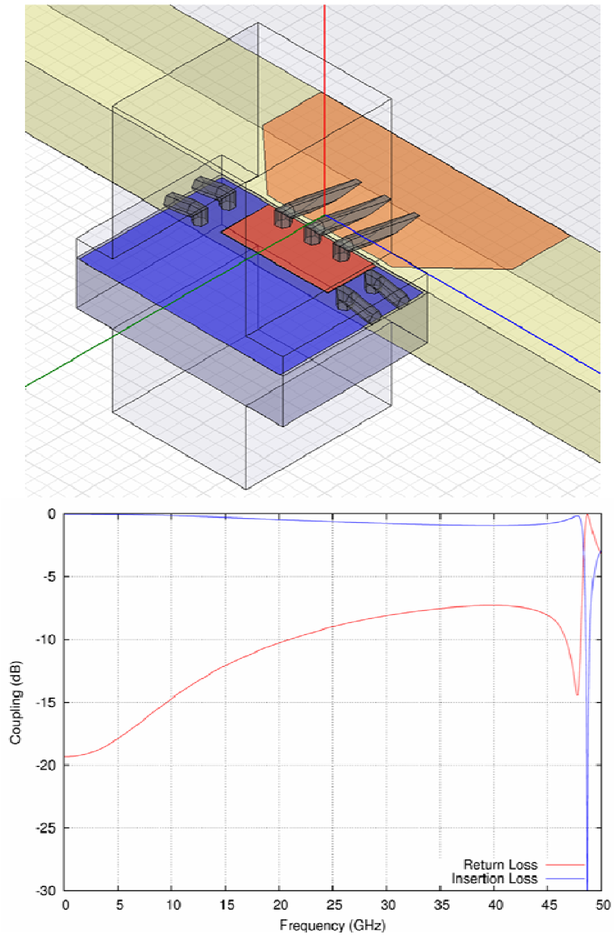

Fig. 18. (Top) HFSS model of the IF bond pads (blue and red), bond wires (grey) and IF output microstrip (pink). Three bond wires connect the mixer wiring to the IF output, while two wires are used on each side to ground the chip to the mixer block. (Bottom) HFSS calculated scattering parameters of the IF connection, normalised to the mixer output impedance of 16.5 Ω.

A five step quarter-wave microstrip transformer is incorporated onto the IF connection board to match the mixer output to the 50 Ω SMA connector and IF amplifier input over the 2-20 GHz IF band (Fig. 19). The first section of this transformer is shortened to cancel some of the inductance due to the bond wires and pad, and the whole transformer design is optimised in Ansoft Designer in conjunction with the HFSS results for the IF connection above. This allows an excellent match to be achieved between the 16.5 Ω SIS junction and the 50 Ω IF amplifier.

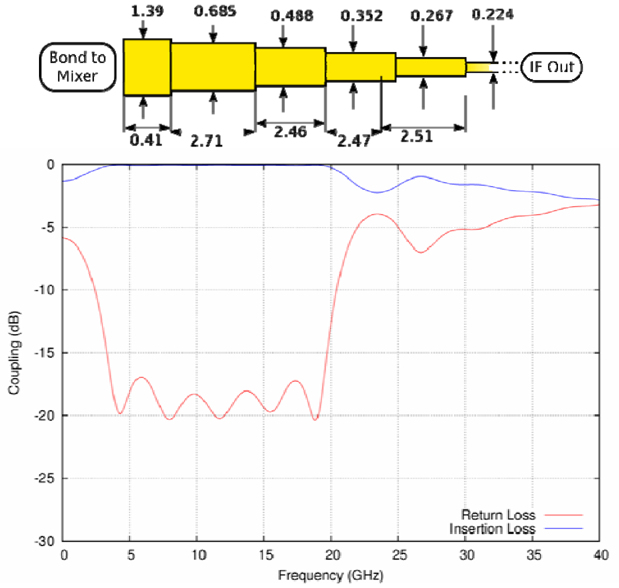

Fig. 19. (Top) Diagram of the IF output transformer, fabricated on 0.254 mm thick Duroid 6010LM. Dimensions are in mm. (Bottom) Combined scattering parameters of the IF connection and output transformer, normalised to 16.5 Ω at the input and 50 Ω at the output.

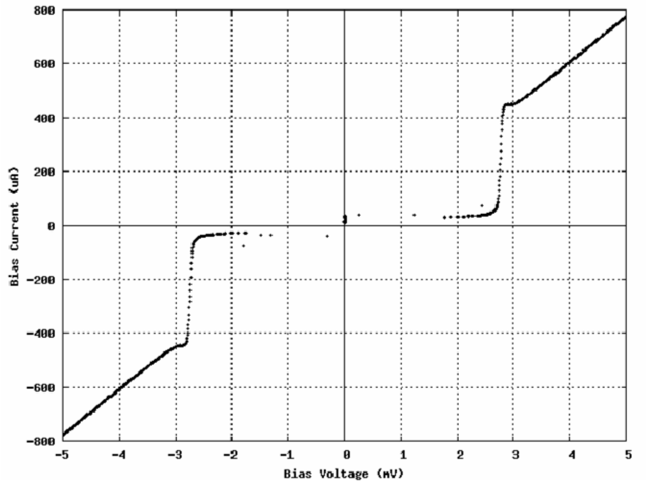

Fig. 20. Measured I-V curves for a dual-junction mixer from the first fabrication batch.

III. Fabrication

The mixers were fabricated on 225 µm thick Infrasil fused quartz with a 20 nm AlN etch-stop layer using UV photolithography to define all features except the junctions, which are defined by E-beam lithography.

Fabrication takes place in seven fabrication steps:

1. Deposition of 200/10/100 nm thick Nb-AlO$_x$-Nb trilayer and lift-off to form the lower finline and mixer ground plane.
2. Definition of areas to covered by first SiO dielectric layer (including junction areas to be defined by E-beam), and definition of junctions by E-beam lithography. Reactive ion etching to form junctions.
3. Evaporation of first 200 nm SiO layer followed by lift-off of SiO over junctions.
4. Evaporation of 225 nm second SiO layer and lift-off.
5. Deposition of first 400 nm Nb wiring layer and lift-off
6. Anodisation of wiring layer to form capacitors for RF band-pass filter.
7. Deposition of second 400 nm Nb layer and 25 nm Au protection layer and lift-off to form RF band-pass filter centre section and bond pads.

The junction definition and first SiO layer steps (2 and 3 above) use both UV and E-beam lithography to define the area of the trilayer to be reactive ion etched and covered in SiO. First the outside edge of the area to be etched and covered in SiO is defined by UV lithography, before the junctions are defined by E-beam lithography and reactive ion etching through the top Nb layer. SiO is then evaporated onto the wafer. A chemical mechanical polishing step was used with these wafers to remove the E-beam charge dissipation layer from the junction areas before lifting off the E-beam resist and SiO covering the junctions.

The niobium oxide insulating layers in the capacitors in the RF band-pass filter are anodised in $C_2H_2O_6/NH_4B_{10}O_{16}$ solution under a constant current until the anodisation voltage indicates that the required thickness has been achieved.

Two batches of 18 devices were fabricated in the first fabrication run at KOSMA, Cologne in December 2007. The second batch used an alternative wiring layer mask that does not have the RF band-pass filters, so that the RF coupling with and without this component can be compared.

The yields from the two batches were excellent, and apart from some problems with the wiring layer photoresist in the second batch, all fabricated devices showed excellent I-V characteristics (Fig. 20) and consistent normal resistances and Fiske resonances across the wafers.

IV. Simulated Mixer Performance

The mixer designs have been extensively simulated throughout the design process with software based on Caltech's SuperMix simulation library[6]. In this section we present simulation results for both single and dual junction mixer designs.

The simulations include all of the components on the chip as well as the IF connection and IF transformer board, and the 4 K input noise of the IF amplifier. Other receiver components such as the cryostat window, IR shields and LO injection beamsplitter are not included. Additionally, RF losses in the finline are not included, although these are expected to be small at frequencies below the energy gap of niobium.

In both cases the unpumped junction I-V curve is taken from a 700 GHz finline mixer fabricated in the KOSMA facility in December 2002, using a similar process to these mixers, apart from the junction definition, which used UV lithography. This junction should give a very similar I-V curve to these new devices.

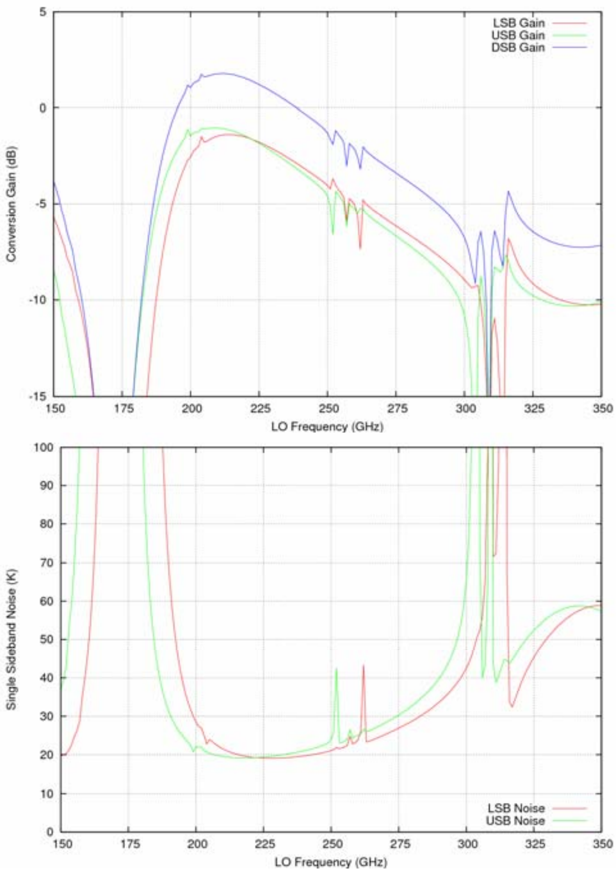

Fig. 21. SuperMix calculated mixer conversion gain (top) and noise temperature (bottom) against LO frequency for the complete single-junction mixer. The mixer is biased at a fixed bias voltage of 2.2 mV, and pumped with a fixed LO power of 50 nW. The IF frequency is 5 GHz. The narrow spikes in the performance just above 250 GHz and 300 GHz are artefacts caused by running the simulation at a fixed bias voltage and LO power.

F. *Single-junction mixer*

The mixer performance for the single-junction mixer as a function of LO frequency is shown in Fig. 21. In these plots the mixer is biased at a fixed voltage of 2.2 mV and pumped by a fixed LO power of 50 nW, while the performance calculated at a fixed IF frequency of 5 GHz.

The mixer performance as a function of IF frequency is shown in Fig. 22. The mixer bias voltage and LO power are again 2.2 mV and 50 nW respectively, while the LO frequency is 220 GHz, the centre of the mixer's tuning resonance.

The reduction in the mixer conversion gain (and associated increase in noise temperature) with increasing IF is mainly due to the narrowness of the RF coupling response of the mixer tuning circuit. This reduces the coupling of the sidebands to the mixer as the IF frequency increases, since the sidebands are now further from the centre of the coupling response.

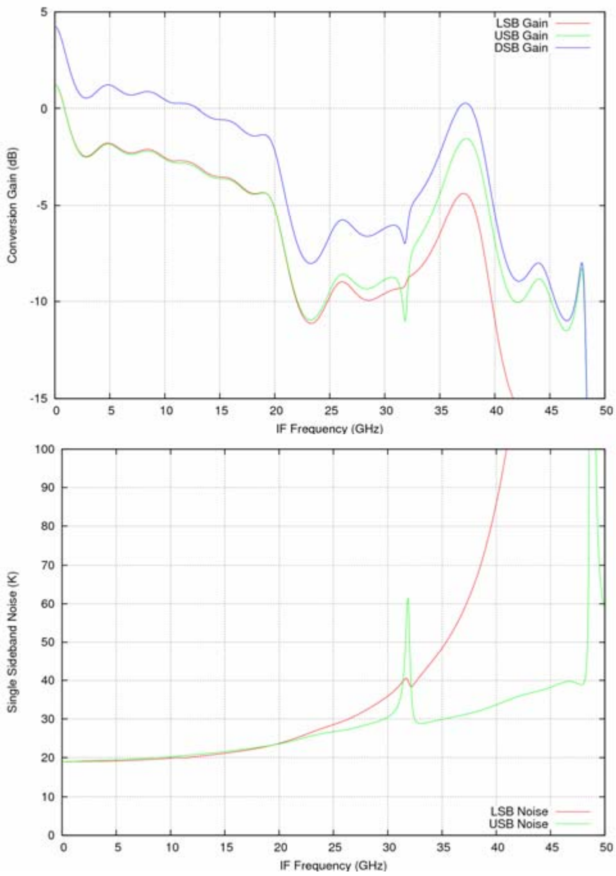

Fig. 22. SuperMix calculated mixer conversion gain (top) and noise temperature (bottom) against IF frequency for the complete single-junction mixer. The mixer is biased at 2.2 mV, and pumped by 50 nW of LO power at a frequency of 220 GHz.

G. *Dual-junction mixer*

The mixer performance for the dual-junction mixer as a function of LO frequency is shown in Fig. 23. In these plots the mixer is biased at a fixed voltage of 2.2 mV and pumped by a fixed LO power of 100 nW, while the performance calculated at a fixed IF frequency of 5 GHz.

The mixer performance as a function of IF frequency is shown in Fig. 24. The mixer bias voltage and LO power are again 2.2 mV and 100 nW respectively, while the LO frequency is 220 GHz, for comparison with the single-junction mixer above.

In this case the reduction in mixer conversion gain with increasing IF (up to 20 GHz) is due to the mismatch between the two parallel 16.5 Ω junctions and the 16.5 Ω IF output. This leads to a much lower increase in noise temperature than for the RF mismatch in the single-junction case above, as the mixer noise is also mismatched.

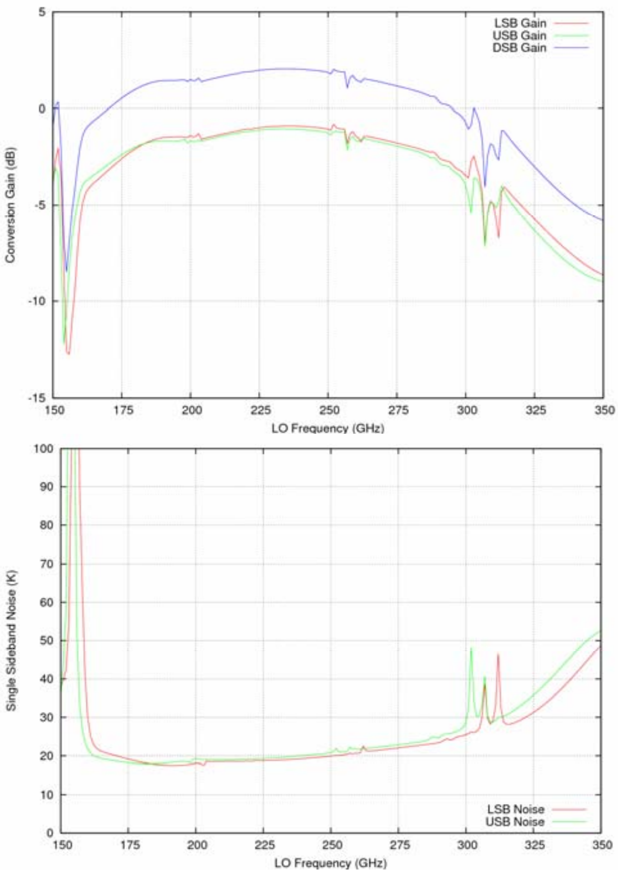

Fig. 23. SuperMix calculated mixer conversion gain (top) and noise temperature (bottom) against LO frequency for the complete single-junction mixer. The mixer is biased at a fixed bias voltage of 2.2 mV, and pumped with a fixed LO power of 100 nW. The IF frequency is 5 GHz. The narrow spikes in the performance just above 250 and 300 GHz are artefacts caused by running the simulation at a fixed bias voltage and LO power.

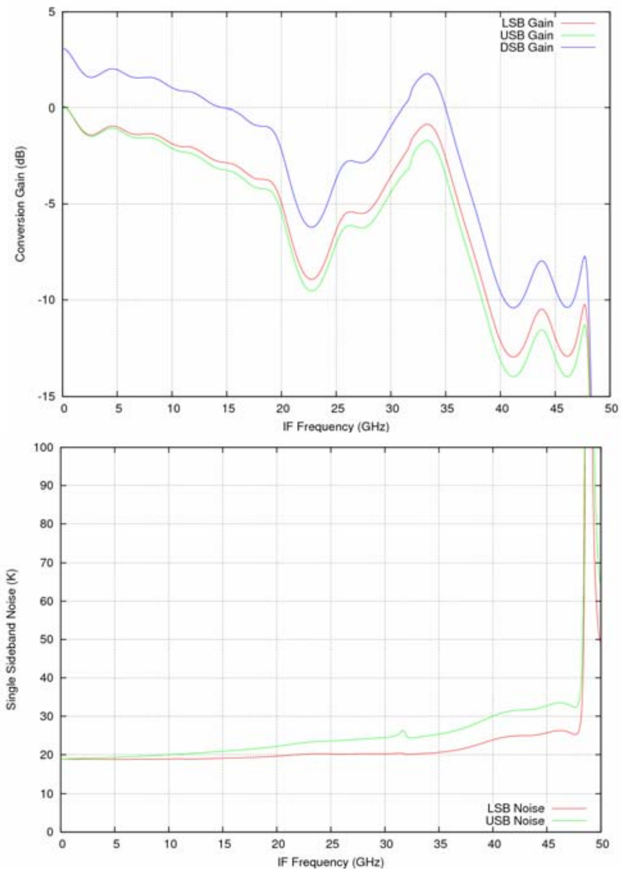

Fig. 24. SuperMix calculated mixer conversion gain (top) and noise temperature (bottom) against IF frequency for the complete single-junction mixer. The mixer is biased at 2.2 mV, and pumped by 100 nW of LO power at a frequency of 220 GHz.

CONCLUSION AND FUTURE WORK

We have presented an SIS mixer design with a very wide IF bandwidth covering the range of 2-20 GHz. The employment of the finline design permitted elegant integration of circuits to allow efficient operation at these high IF frequencies and minimise parasitic reactances. Our RF simulations demonstrate that operation at these high IF frequencies is feasible, while our SuperMix simulations show that both the wideband RF and IF operation can be achieved in conjunction with a high performance mixer.

So far we have only tested the narrow-band devices with a narrow-band IF system in order to set a benchmark for the more complicated wide-band mixers. Preliminary results have confirmed the integrity of our design method.

Testing of the broadband devices will follow after the benchmark tests are completed.

Once these mixers have been characterised, we will develop single chip balanced and image separating mixers with very wide IF bandwidth based on our back-to-back finline layout. These devices will be particularly suitable for use with photonic LOs as they require much less LO power than single-ended designs.

REFERENCES

[1] P.K. Grimes, C. Holler, M.E. Jones, O.G. King, J. Leech, A.C. Taylor and G. Yassin, “A novel heterodyne interferometer for millimetre and submillimetre astronomy”, in *Proc. 19th Int. Symp. Space THz Tech.*, Groningen, 2008.

[2] G. Yassin, R. Padman, S. Withington and K. Jacobs, “A broad band antipodal finline mixer for astronomical imaging arrays”, *Electron. Lett.*, vol. 33, pp 498-500, 1997.

[3] G. Yassin, S. Withington, K. Jacobs and S. Wulff, “A 350 GHz antipodal finline mixer”, *IEEE Trans. Microwave Theory Tech.*, vol. 48, pp662-669, 2000.

[4] C.E. North, G. Yassin and P.K. Grimes, “Rigorous analysis of antipodal finline tapers for high performance millimetre and submillimetre detectors”, in *Proc. 17th Int. Symp. Space THz Tech.*, Paris, 2006.

[5] J. Zmuidzinas, H.G. LeDuc, J.A. Stern and S.R. Cypher, “Two-junction tuning circuits for submillimetre SIS mixers”, *IEEE Trans. Microwave Theory and Tech.*, vol. 42, pp 698-706, 1994.

[6] J. Ward, F. Rice, G. Chattopadhyay and J. Zmuidzinas, “SuperMix: A flexible software library for high-frequency circuit simulation, including SIS mixers and superconducting elements”, in *Proc. 10th Int. Symp. Space THz Tech.*, pp 269, 1999.

A 0.5 THz Sideband Separation SIS Mixer for APEX Telescope

R. R. Monje[1,*], V. Belitsky[1], V. Vassilev[1], A. Pavolotsky[1], I. Lapkin[1,2], V. Desmaris[1], D. Meledin[1], D. Henke[1] and D. Dochev[1]

[1]Group for Advance Receiver Development with Onsala Space Observatory, Chalmers University of Technology, Gothenburg, Sweden

[2]Russian Academy of Science, Institute of Applied Physics, Russia

* Contact: raquel.monje@chalmers.se

***Abstract*— We present the design and the experimental results of a fixed-tuned sideband-separating superconductor-insulator-superconductor (SIS) mixer for 385 - 500 GHz. The sideband separation is achieved using a quadrature scheme, where two separate DSB mixer blocks are combined with an intermediate waveguide component containing the LO waveguide distribution circuitry and RF waveguide hybrid. The intermediate waveguide piece is fabricated by using copper micromachining, which gives dimensions' accuracy better than 1 µm. The RF signal coming from the waveguide hybrid is coupled to the SIS junctions through an E-probe with integrated bias-T. We implemented an on-chip LO injection solution, where the LO coupler is integrated onto the mixer chip and fabricated together with the SIS junction and the tuning circuitry. The on-chip LO coupler is made as a combination of superconducting microstrip lines and slot-lines (branches), which gives almost a lossless solution. With the fabrication accuracy better than 0.5 µm by using optical lithography, the circuitry is proven to give a good performance following the simulations expectations.**

I. INTRODUCTION

The Atacama Pathfinder EXperiment (APEX) [1] is a radio telescope using a 12 m ALMA prototype antenna operating at the Atacama Desert on the Chilean Andes at about 5100 m altitude. The site is one of the best places for submillimeter astronomy on the Earth because of the extremely low content of water vapour. For spectroscopy studies APEX houses single pixel heterodyne receivers covering the frequency range of 211 GHz up to 1.5 THz.

The APEX single pixel heterodyne sideband separation receiver for 385 – 500 GHz (APEX band 3) is presented in this paper. The sideband separation is achieved using a quadrature scheme where the RF signal is divided equally with 90˚ phase difference through a 3 dB directional coupler, and the LO is symmetrically split by an in-phase power divider and fed to two identical double sideband (DSB) mixers. The intermediate frequency (IF) outputs from mixer 1 and mixer 2 are connected to quadrature 3 dB hybrid which enables the sideband separation, into upper sideband (USB) and lower sideband (LSB) signals, through phase cancellation. The sideband separation scheme can be better explained using the phase diagrams for USB and LSB presented in Figure 1. Sideband separation technology provides better sensitivity for spectral line observation than DSB [2]. Besides, DSB observations may lead to spectral line-confusion or degrade the system noise temperature and the receiver sensitivity with strong atmospheric absorption bands falling into the image band. This is a driving reason to choose this technology considering that some of the important molecules for this band are very close to telluric absorption line, as in the case of deuterated water, HDO, with its fundamental transition frequency at 465 GHz.

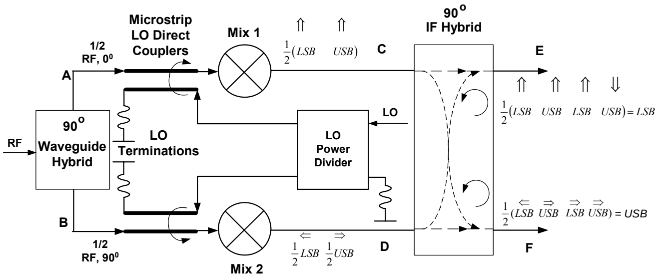

Fig. 1 Block diagram of a sideband-separating mixer. The signal vectors around every component illustrate principles of sideband separation.

Ultimately, the desired sideband separation receiver design would fully integrate all components, such as RF 3-dB hybrid, LO power divider, 16 dB coupler and SIS tuning circuit, onto a single chip. This very compact design would allow the reduction of overall receiver dimensions, being extremely important for multi-pixel array receivers or multi-channel receivers, such as the APEX or ALMA [3] receivers where several bands are integrated into a single cryostat making the space and cooling capacity critical. Furthermore, a single chip approach should facilitate fabrication and potentially improve the yield, since the chips can be done with lithography which would provide accuracy better than 1 µm. However, the drawback of this approach has been proven to be a challenge by increasing complexity and difficulty to identify the possible problems in the case of unexpected performance [4].

We propose a less complex sideband separation mixer design, yet still with the benefit from the combination of low-loss waveguide components with integrated on-chip solutions; as for example LO injection with a planar ellipse termination for the through port of the LO coupler.

II. Mixer Design

A. *Mixer Chip Design*

The mixer chip design for the frequency range of 385 – 500 GHz uses the on-chip LO injection design described in [5 - 6]. Therefore, both the RF and LO signals should be coupled from the waveguide to the microstrip propagating mode. For the RF probe we used the novel approach presented by [7], which consists of a waveguide-to-microstrip transition with integrated bias - T. The advantage of this probe comes from the fact that it couples the input waveguide signal to the SIS junction and tuning circuitry lines via and E-probe while having an isolated port at the opposite side of the substrate for the IF extraction and DC biasing. The RF probe is shaped in order to achieve a broadband matching and to obtain as low impedance as possible at the microstrip port. The LO signal is coupled from the waveguide to the chip by the use of a simpler waveguide-to-microstrip transition, see Figure 2.

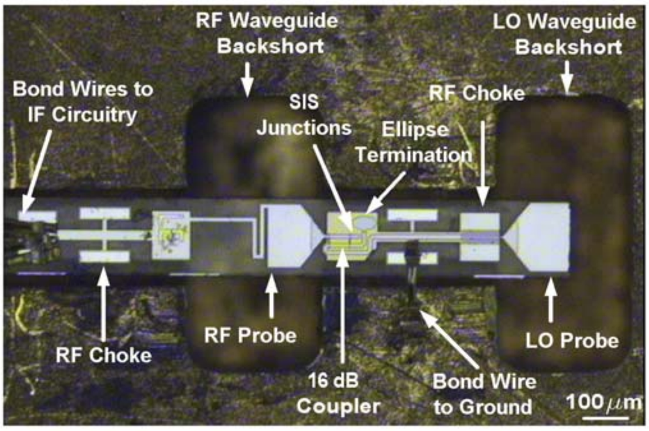

Fig. 2 Photograph of the mixer chip mounted into the mixer block in the back-piece layout.

Typical tuning circuits incorporate one or more microstrip transformer sections to match the characteristic impedance from the E-probe to the impedance of the active component. In this design we use a quarter wavelength transformer which also forms part of a 16 dB directional coupler to couple the LO signal into the RF signal.

The on-chip LO coupler is made with superconducting lines coupled via lumped links; two perforations forming skit-holes in the ground plane on the same SiO_2 dielectric (ε_r = 3.74) as the SIS junction and the RF tuning circuitry. The RF signal comes from the waveguide-to-microstrip probe and the LO signal comes from another probe on the other side of the mixer chip. One of the output signals goes to the SIS mixer and the idle port of the LO coupler is terminated with an elliptical termination [8]. The termination is made of resistive material by sputtering titanium mixed with nitrogen in order to reach the required resistivity.

The SIS junctions are made in-house using the Chalmers MC2 clean room facility. The designed Nb-AlOx-Nb SIS junctions have an area of 3 μm^2 and a normal resistance (R_n) of ~ 7 Ω. The design uses two junctions connected through a short line [9] equivalent to inductance, L_t, at RF. The junctions resulting complex impedance is designed to be real and is then matched to the RF source impedance.

B. *DSB Mixer Block*

The DSB mixer block consisting of the following elements: a mixer back piece that houses the mixer chip with the DC and IF circuitries, an intermediate piece containing the waveguides for the RF and LO signal injection, a magnetic coil with two magnetic concentrators, a diagonal LO horn and a corrugated RF horn (see Figure 3 left). This configuration enables the use of the same mixer back piece for both DSB and 2SB modes. The mixer back piece (Figure 3 right) and the intermediate piece are manufactured by direct milling (the split-block technique is used when machining the intermediate piece). The blocks are fabricated using copper-tellurium alloy, which has a similar conductivity to pure copper at room temperature but is easier to machine, and plated with a thin layer of gold (~ *2 μm*). Although gold has worse conductivity than copper, it facilitates bonding with gold wires and protects the blocks from corrosion.

For the Gaussian beam-to-waveguide converter at the RF side, a corrugated feedhorn is preferred since it provides wider bandwidth and a higher coupling efficiency. The feedhorn is coupled through a circular to full-height waveguide transition. For the LO side, a diagonal horn was used instead, since the coupling efficiency is not so critical and they are easier to manufacture, allowing in-house fabrication.

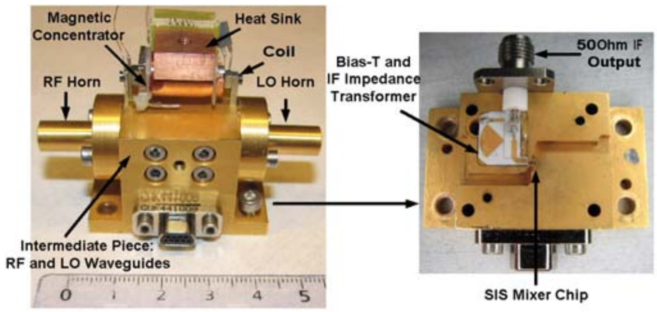

Fig. 3 The left picture shows the DSB mixer block. Two magnetic iron concentrators guide the magnetic field from an external coil to the vicinity of the junctions. On the right, the mixer back piece is pictured, containing the mixer chip, the bias-T with 20 to 50 Ohm transformer and the DC circuitry in the back side; this piece is compatible with the 2SB mixer.

For the suppression of the Josephson Effect a magnetic coil extracted from a commercial relay with approximate number of turns around 10,000 was used. The coil is thermally isolated from the mixer block through a fiberglass bracket, and furthermore, the coil was embedded into a copper block that was thermally connected to the 4 K plate to sink any heat generated by the coil. The magnetic field is guided from the coil to the SIS junctions through two iron magnetic field concentrators.

The mixer chip with dimensions 1200 x 150 x 65 μm^3, was placed on a suspended microstrip channel and glued to the mixer block through a non-conductive wax. This approach gave the advantage of shorter overall waveguides since the mixer back piece housed only the mixer channel and the waveguide backshorts. One bond wire connected from the mixer block to the RF choke provides DC ground, as shown in Figure 2, and several bond wires connect the mixer chip to the IF/DC circuitry. The DC circuitry for the SIS biasing is placed on the backside of the mixer block.

C. 2SB Mixer

The sideband separation mixer was built with two mixer back pieces described in previous section, being common for the DSB and 2SB designs, and an intermediate piece. On the contrary to the DSB mixer, the intermediate waveguide piece contains the LO in-phase power divider and the 3 dB 90-degree waveguide RF hybrid in order to achieve sideband separation using the quadrature scheme. Similar to the DSB receiver, the mixer block was fabricated using Copper-Tellurium alloy. The intermediate piece was fabricated using micromachining, a novel approach developed at GARD. This innovative technique combines photolithography with electroplating to fabricate the waveguide structure, providing an accuracy better than 1 µm [10–11].

Figure 4 illustrates the 2SB receiver assembly; note that the top mixer back piece is a mirrored version of the bottom mixer block. Hence, the SMA connectors face the same side and this configuration provides a more compact IF chain, optimizing the space inside the dewar.

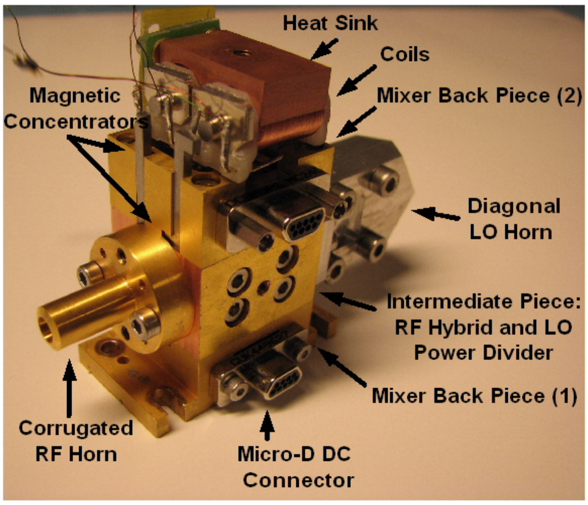

Fig. 4 The 2SB mixer block consists of two mixer back pieces, where the mixer chip is placed together with the DC input and IF output, and two intermediate pieces, containing the LO power divider and the RF 3dB 90° hybrid.

III. Results

This section presents the measurement configuration and experimental results for the noise temperature and sideband rejection of the sideband separation mixers, over the frequency ranges of 385 – 500 GHz, corresponding to APEX band 3.

A. Receiver Characterization

Figure 5 shows a photograph of the laboratory test cryostat, a liquid helium Oxford Instrument cryostat, used for our measurements. The measurement setup contains both warm and cold components. Internal to the dewar, the cold items include the DSB or SSB mixer, the optical components (lens, IR filter, windows), isolator, low noise amplifier (LNA), thermal links to provide necessary cooling to low temperature to all components and stainless steel coaxial cables. The warm components are a room temperature amplifier, a filter (when necessary) and the IF power detector.

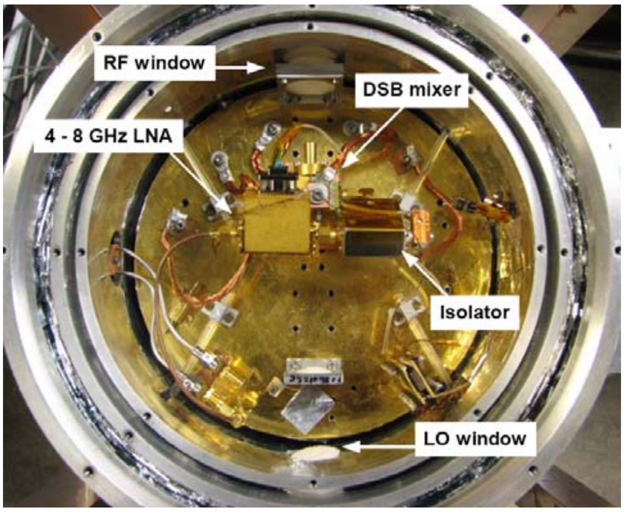

Fig. 5 View of the DSB receiver installed in the cryostat

The mixer is attached to a copper support that ensures optical alignment with the cryostat windows and good thermal contact with the 4.2 K plate. A corrugated feedhorn, followed by a cold Teflon lens with a focal distance of *25 mm*, provides the desirable coupling of the RF power. The cryostat vacuum windows, for both RF and LO, are made of 1.5 mm high density polyethylene (HDPE) with an anti-reflecting grooved surface optimized for these frequencies. Infrared filters made of 200 µm Zitex placed on the 77 K stage, minimize radiative thermal coupling through the windows.

The local oscillator is an x36 frequency extension module from VDI giving an average output power across the band around 0.6 mW (-2.22 dBm). The local oscillator is coupled quasioptically to minimize the power loss.

B. Measurement of Receiver DSB Performance

The noise temperature measurements were performed with the standard Y-factor technique using a hot (293 K) and cold load (77 K) placed in front of the RF window. Figure 6 shows the measured receiver noise. The measurements give an equivalent DSB receiver noise temperature within 5 to 9 quanta across the band of interest. For local oscillator frequencies between 370-400 GHz the noise temperature is within 80-150 K. The upper side of the LO frequency band 410-480 GHz presents a noise temperature in the range of 180-210 K. There is a rapid increase in the noise for LO frequencies above 480 GHz.

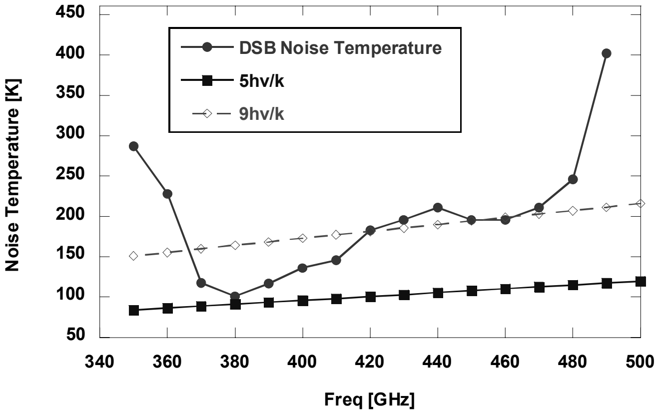

Fig. 6 DSB receiver noise temperature

C. 2SB Measurement Results

After completing the DSB tests, and selecting two chips with similar performance, the two blocks were then used to construct the sideband separating receiver assembly. Figure 7 shows the single sideband noise of the receiver. The 2SB noise temperature is consistent with the DSB noise measurements for the lower band of the LO frequency (370 – 420 GHz). At the frequencies where the 2SB noise is greater than twice the DSB noise temperature of the individual mixer blocks, this may indicate a dependence on the RF loss in the waveguide hybrid and added IF noise due to the additional components required for sideband rejection, such as the IF hybrid.

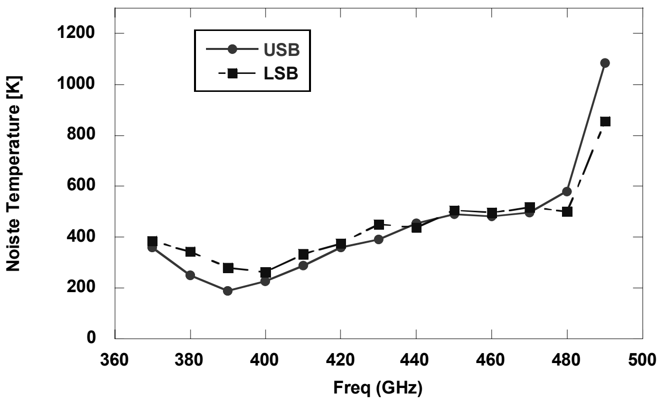

Fig. 7 2SB receiver noise temperature for the upper and lower sideband.

The sideband ratio of a receiver can be measured by injecting a continuous wave (CW) signal into the upper and lower sidebands and measuring the IF response at each band. Since we can not accurately determine the amplitude of the CW signal, the conversion gains of the sidebands can be determined using an interfering source (of unknown amplitude) and measuring the resulting power ratios, combined with hot/cold measurements, as described in [12]. Ideally, the sideband ratio is infinite however in practice cases the ratio is on the order of 10 dB. Figure 8 shows the sideband separation ratio for this receiver. It can be seen from the figure that the rejection ratio is typically worse for one of the sidebands outputs (USB). However, if we take only the LSB output, results are better than 10 dB for most of the band with the worst cases better than 7 dB otherwise.

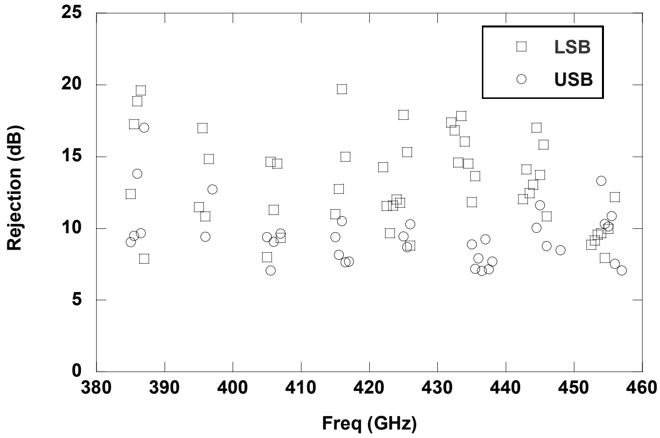

Fig. 8 Corrected sideband rejection ratios for the USB and LSB.

CONCLUSIONS

In this paper, we present the design and first measurements of a 2SB fixed-tuned SIS mixer for APEX band 3 (385-500 GHz). The mixer design introduces novel components such as a waveguide probe with integrated bias-T, allowing to extract IF signals and to inject DC current, and an on-chip integrated LO injection circuitry employing a high-performance ellipse termination for the directional coupler idle port. All these components are fabricated together with the SIS junction and the tuning circuitry. The demonstration of all these new technologies was achieved via successful mixer measurements resulted with competitive double sideband and sideband separation noise temperature better than 180 K and 400 K, respectively, measured at the center frequency 442 GHz. Furthermore the sideband separation mixer presents a rejection ratio better than 10 dB for most of the band.

ACKNOWLEDGMENT

The authors would like to acknowledge Dr. Christophe Risacher, now at European Southern Observatory, for very interesting and useful discussions. Professor Hans Olofsson for providing us with remarkable encouragement and support during this project. This work is related to APEX Project and is funded by the Swedish Research Council and the Wallenberg Foundation by their respective grants. Part of this work was supported by research grant via EU FP6 AMSTAR Program.

REFERENCES

[1] APEX homepage: http://www.apex-telescope.org

[2] P. R. Jewell and J. G. Mangum, "System temperatures single versus double sideband operation and optimum receiver performance", International Journal of Infrared and Millimeter Waves, Vol. 20, No 2, pp. 171-191, May 1999.

[3] Booth R. S., "ALMA, the Atacama Large Millimetre Array", *European Space Agency* (Special Publication) SP-451, 107-114, May 2000. See also ALMA project in ESO homepage: www.eso.org/projects/alma/index.html.

[4] Kerr A. R., Pan S.–K., "Design of planar image separating and balanced SIS mixers", *Proceedings of the Seventh International Symposium on Space Terahertz Technology,* pp. 207-219, March 12-14, 1996.

[5] Vassilev V., Henke D., Lapkin I., Nyström O., Monje R., Pavolotsky A., Belitsky V., "Design and Characterization of a 211-275 GHz Sideband Separating Mixer for the APEX Telescope", *IEEE Microwave and Wireless Components Letters*, 18, 58 – 60, 2008.

[6] Monje R., Belitsky V., Risacher C., Vassilev V. and Pavolotsky A., "SIS Mixer for 385 – 500 GHz with On-Chip LO injection", *Proceedings of the 18th International Symposium on Space Terahertz Technology***,** California Institute of Technology, Pasadena, California, USA, March 21 -23, 2007.

[7] Risacher C., Belitsky V., Vassilev V., Pavolotsky A., "A Waveguide to Microstrip Transition with Integrated Bias-T", *IEEE Microwave and Wireless Components Letters*, 13, 7, 262-246, 2003.

[8] Monje R. R., Vassilev V., Pavolotsky A., Belitsky V., "High Quality Microstrip Termination for MMIC and Millimeter-Wave Applications", *IEEE MTT-S International Microwave Symposium 2005*, pp. 1827- 1830, Long Beach, California, June 12-17, 2005.

[9] Belitsky V., Tarasov M., "SIS Junction Reactance Complete Compensation", *IEEE Trans. on Magnetic*, MAG- 27, 2, 4, 2638-2641, 1991.

[10] Pavolotsky A., Meledin D., Risacher C., Pantaleev M., Belitsky V., "Micromachining approach in fabricating of THz waveguide components", *Microelectronics Journal,* 36, 683-686, 2005.

[11] Demaris V., Meledin D., Pavolotsky A., Monje R., Belitsky V., "All Metal Micromachining for Fabrication of Sub-millimeter and THz waveguide Components and Circuits", accepted for publication at *Journal of Micromechanics and Microengineering,* 2008.

[12] Kerr A. R., Pan S.–K., Effland J. E., "Sideband Calibration of Millimeter-Wave Receivers" *ALMA Memo 357*, May 2004, available at www.alma.nrao.edu/memos/.

Balanced SIS Mixer System with Modular Design for 490 GHz

M. Justen[1,*], C.E. Honingh[1], T. Tils[1], P. Pütz[1], K. Jacobs[1]

[1]KOSMA, I. Physikalisches Institut, Universität zu Köln, Zülpicher Strasse 77, 50937 Cologne, Germany

* Contact: justen@ph1.uni-koeln.de, phone +49-221-370 3489

***Abstract*—We present measurements on a balanced mixer for 490 GHz. The system consists of a central -3 dB waveguide branchline coupler, which has been fabricated in split block technique in the KOSMA workshop. It is connected to two SIS mixers and two feed horn antennas. A corrugated horn is used for the signal and a diagonal horn with the same beam parameters is used to feed the coupler with the LO signal.**

The modular design allows to characterize every component separately. In particular, various waveguide couplers have been investigated with a vector network analyzer at their respective operating frequencies at the university of Bern [1]. The SIS mixers have been tested in standard double sideband mode and show 60-80K DSB noise temperature over the RF band.

These results can be compared with simulations and with measurements of the entire balanced mixer in order to gain insight into function and interaction of the different components as well as into critical fabrication tolerances.

I. Introduction

A balanced mixer configuration has many advantages compared to a simple mixer, in particular a very efficient and stable LO coupling, cancelation of LO amplitude noise and, resulting from the latter, an improved system stability [2]. Because of these advantages, which become more and more essential with increasing frequency, it is worth to study the much more complex design of a balanced mixer in praxis, in order to gain insight into the interactions of the different components of the mixer.

As a first step towards more compact and integrated mixers we have chosen a modular design for a balanced mixer, operating at 490 GHz. The modularity allows to measure performance for each component separately.

II. Balanced Mixer System

A. Overview

The mixer consists of a central waveguide directional coupler, fabricated in split block technology. Two standard mixer blocks from the SMART receiver [3] and two horns, one for signal and one for LO feed, are mounted at the four ports of the coupler, as shown in Fig. 2. The modularity allows to measure the performance for each mixer block separately. Also the S-parameters of the coupler can be studied with a vector network analyser.

Both IF output signals of the mixer blocks are amplified and recombined outside the cryostat by a very broadband 4-stage Wilkinson power combiner, which also has been tested separately.

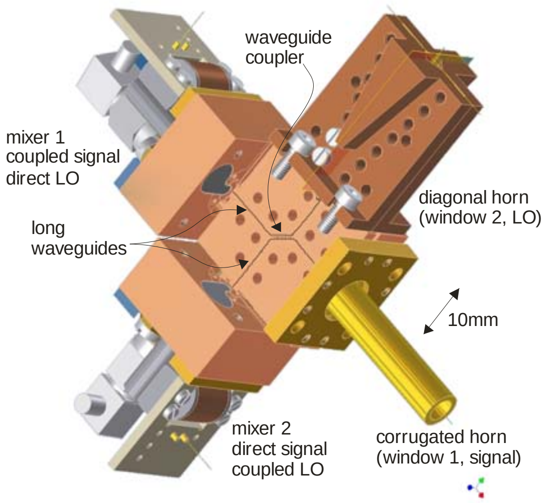

Fig. 25 3D model of the balanced mixer unit. The upper split block half is blanked out in order to allow a view to the waveguide arms and the waveguide coupler.

B. Waveguide Coupler for 490 GHz

The split block waveguide coupler for 490GHz, fabricated in the KOSMA workshop, was micromilled on a *Deckel FP 2* with a 60krpm spindle. With the machines 1µm resolution xyz stages, an absolute precision of ~10µm can be obtained. Prior to every milling process, a test slot has been milled in order to measure the actual tool dimensions. This way, an overall precision better 20µm was achieved.

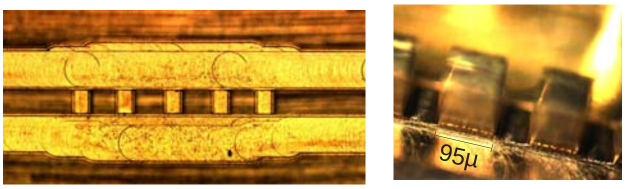

Fig.2 Split block waveguide coupler for 490GHz, fabricated in the KOSMA workshop.

Simulations and measurements with a vector network analyzer of a similar waveguide coupler for 345GHz revealed degradation of the coupler performance due to the fabrication tolerances [1]. Likewise a strong imbalance of the 490 GHz coupler could be observed in the measurements presented in this paper.

C. 4-Stage Wilkinson Power Combiner for 2-12 GHz

A 4-stage Wilkinson power combiner was used to recombine the IF signal coming from the two LNAs. The TMM10 board of the power combiner has been manufactured also in house with an LPKF surface milling machine. Ultra miniature resistors (0402) have been used in order to keep parasitics as small as possible. High isolation (-20...-15dB) between the input ports and a high symmetry in power and phase could bee obtained over a very broad band (2...12GHz).

III. MEASUREMENTS

A. Asymmetry in LO Power and Sensitivity

Heterodyne measurements revealed a strong imbalance in the RF waveguide system. The pump level (DC current at the optimum bias voltage) (Fig. 3) of the mixer shows an imbalance depending on LO frequency and depending on which port (horn) has been used for LO injection. In contrast, in the separate measurement, the optimum pump level of the mixers was very similar and at approximately the same LO input power (measured with a Golay).

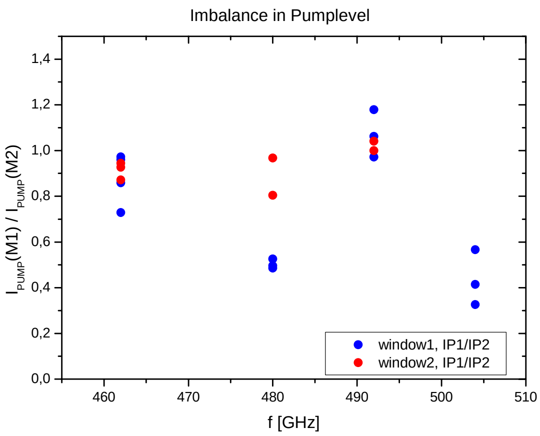

Fig. 3 Variations in the pump level ratio I_{PUMP}(M1) / I_{PUMP}(M2) in dependence of frequency and LO injection port (window 1 and window 2). The variations are probably due to asymmetry of the coupler and due to standing waves in the RF system.

The coupled signal is observed to be stronger than the signal in the direct path at some LO frequencies.

Also the noise temperature, measured separately for each mixer in the balanced configuration, shows a comparable imbalance, even if the LO power is adjusted for each mixer to its optimum level. For instance, the noise temperature, measured with mixer 1, is lower when the signal is injected via window 1 (Fig. 4), compared to the noise temperature via window 2, which is the direct path (compare Fig. 1). This unexpected coupling factors are in contrast to the measurements on the 345GHz waveguide coupler with the NWA.

In addition strong standing waves in the RF system could be observed over the whole frequency range.

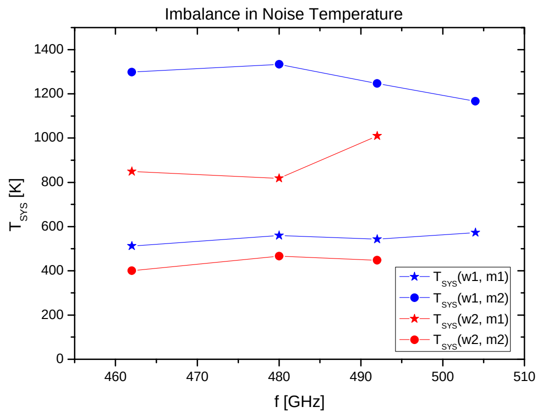

Fig. 4 Noise temperatures of each mixer have been recorded in dependence of LO frequency and signal injection (via window 1 or window 2). The noise temperatures should be doubled in comparison to a single mixer configuration, because only about 50% of the signal is coupled in one mixer block. The further increase of noise temperature is due to absorption of the signal in (the long waveguide arms of) the split block coupler. Furthermore the performance of the SIS mixers is reduced by a somewhat higher bath temperature, resulting in higher noise levels (compare Fig. 5).

Fig. 5 shows pumped and unpumped I(V)- and P(V)-curves of mixer 1, on one hand measured separately in a standard DSB measurement setup and on the other hand measured while being use as part of the balanced mixer (bold lines). The reduced gap voltage in the balanced mixer configuration indicates a higher temperature of the mixer chip due to an increased thermal resistance via the split block coupler.

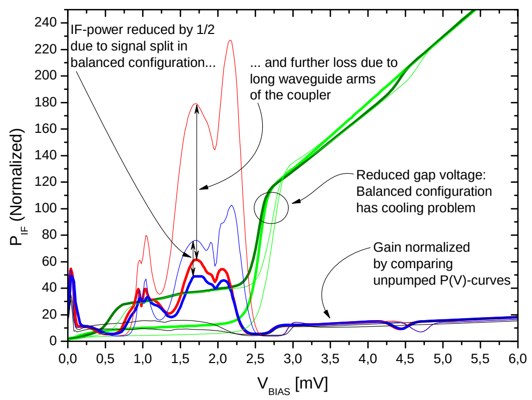

Fig. 5 Pumped and unpumped I(V)-curves (green) and P(V)-curves (red and blue) of mixer 1, measured separately in a standard DSB measurement setup (thin lines) and measured while being used as part of the balanced mixer (bold lines). The IF output power at the hot load is strongly reduced compared to the measurements without waveguide coupler in simple DSB mode. This is attributed to the attenuation of the long waveguide arms in the coupler.

Comparing the unpumped P(V)-curves above the gap voltage, the gain of both measurements can be normalized. This allows the comparison of the pumped P(V)-curves in both, separate and balanced setup. It would be expected that in the balanced setup the IF output power for the hot load would be approximately 50% of that measured in the separate DSB set-up. In Fig. 5 the level in the hot P(V)-curve of the balanced setup is only about 33% of that of the P(V)-curves of the single mixers (Fig. 5). This cold loss, in the long waveguide connecting to the coupler or in the coupler itself results in an additional 50% higher noise temperature for the individual mixer in the balanced mixer setup. This effect, combined with the imbalance, results in a best noise temperature of approximately 500K for the balanced mixer (Fig. 6).

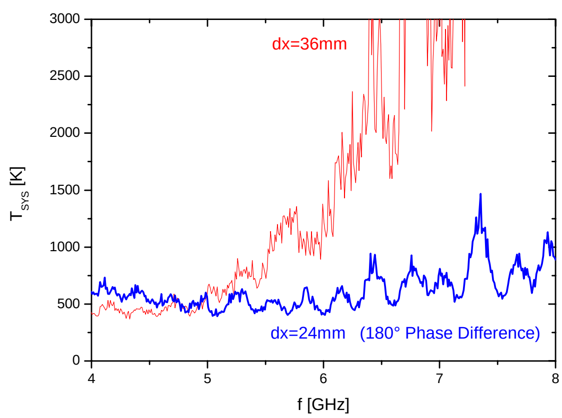

Fig. 6 Noise temperature of the balanced mixer over the IF band.. The IF signals are combined with 180° phase difference in order to obtain the balanced signal. With proper path length compensation, balance over the whole 4-8GHz IF range can be achieved.

Fig. 6 shows the noise temperature of the balanced mixer behind the Wilkinson power combiner. When the phase difference in both IF-chains is compensated by an additional 24mm SMA cable, the balanced operation is achieved over the whole IF range from 4-8GHz. The phase compensation does not depend on LO frequency and results from different IF path lengths inside the dewar.

IV. Discussion

The strong standing waves in the RF system are believed to come from the fact that the mixer blocks and the corrugated horn use half height waveguides (which improves the performance of the waveguide probe of the mixer chip) whereas the full height waveguides are used in the split block coupler in order to afford the milling process.

The strong reduction of the RF power which can be observed by comparing the P(V)-curves, can probably not only attributed to the power splitting in the coupler, but may be due to (cold) absorption in the long waveguide arms.

The observed coupler imbalance can not be explained only by the influence of standing waves in the waveguide system, but comes most likely by fabrication tolerances in the coupling slits, which are to high compared to the operating wavelength ($\Delta x / \lambda \approx 0.03$).

Conclusions

A balanced SIS-mixer at 490GHz with modular design has been investigated by heterodyne measurements.

Balanced operation could be achieved over the whole 4-8GHz IF range.

The measurements revealed a strong RF power imbalance most likely due to unacceptable tolerances of the central waveguide coupler manufactured in split block technology.

Cold attenuation due to the long waveguide arms which had to be used in a modular design, result in high noise temperatures of the balanced system, although a separate testing showed good performance of the individual mixer blocks.

Strong standing waves in the RF paths are partly the result of untapered transitions from half height to full height waveguides used in the mixer blocks and the waveguide coupler respectively.

The advantages of separate testing of a modular design are partly thwarted by the signal damping in the waveguide arms and the reflections due to waveguide transitions which could not be measured directly. Nevertheless, the measurements could show that the fabrication of the waveguide coupler on a standard milling machine, although carried out with highest elaborateness, does not give the required accuracy which is necessary to manufacture a coupler for 490GHz. A similar result has been obtained by comparing two split block couplers for 375GHz, fabricated on a *Deckel FP2* and a *Kern MMP* with a higher milling precission [1,2].

An integrated system with a more accurate fabrication, especially of the waveguide coupler, could avoid attenuation and imbalance and significantly improve the noise temperatures.

ACKNOWLEDGMENT

This work was supported by the research funding from the European Community's sixth Framework Program under RadioNet R113CT 2003.

REFERENCES

[1] M. Justen, T. Tils, P. Pütz, A. Murk, C.E. Honingh, K. Jacobs. RF and IF couplers for a sideband separating SIS waveguide mixer for a 345 GHz focal plane array. ISSTT 2006.
[2] T. Tils. Design and 3-D electromagnetic modeling of terahertz waveguide mixers and components. Dissertation. ISBN: 9783865379146 3865379141. Köln 2006
[3] S.A. Maas, Microwave Mixers. Norwood, MA, Artech House. 1992
[4] U. U. Graf, S. Heyminck, E. A. Michael, S. Stanko, C. E. Honingh, K. Jacobs, R. T. Schieder, J. Stutzki, B. Vowinkel. SMART: The KOSMA Sub-Millimeter Array Receiver for Two frequencies. Proc. SPIE, Vol. 4855, 322. 2003

The HIFI Focal Plane Beam Characterization and Alignment Status

Willem Jellema[1,2,*], Marinus Jochemsen[3], Tully Peacocke[4], Lenze Meinsma[5], Paul Lowes[6], Stafford Withington[7] and Wolfgang Wild[1,2]

[1]SRON Netherlands Institute for Space Research, P.O. Box 800, 9700 AV, Groningen, the Netherlands

[2]Kapteyn Astronomical Institute, University of Groningen, P.O. Box 800, 9700 AV, Groningen, the Netherlands

[3]currently at ASML Netherlands B.V., De Run 6501, 5504 DR, Veldhoven, the Netherlands

[4]Department of Experimental Physics, National University of Ireland Maynooth, Co Kildare, Ireland

[5]Ontwerpburo ANNEX, Bellingeweer 16, 9951 AM, Winsum, the Netherlands

[6]SRON Netherlands Institute for Space Research, Sorbonnelaan 2, 3584 CA, Utrecht, the Netherlands

[7]Cavendish Laboratory, University of Cambridge, JJ Thomson Avenue, Cambridge CB3 0HE, United Kingdom

*Contact: W.Jellema@sron.nl, phone +31-50-363 4058

***Abstract*— In this paper we present the results of the characterization program of the beams in the focal plane of the HIFI flight model. We discuss the beam properties, quality of alignment, instrument footprint, performance impact and compliance and compare the results to predictions based on lower-level characterization results and simulations. We finally conclude by presenting the expected properties at the sky by forward propagation through a telescope model.**

I. Introduction

Prior to final characterization of the flight model of the HIFI Focal Plane Unit [1-6], the design and sub-units have been thoroughly analysed and verified in several studies and measurement campaigns [7-12]. In the development model phase of HIFI the long wavelength limit of the instrument has been modelled and verified experimentally as part of an ESA-TRP study [13-17]. In these early activities we validated the design and green light was given for flight production, alignment and test of the flight hardware. A crucial part of the flight alignment and integration concerned the tests of the high-frequency bands of HIFI involving the measurement and mechanical corrections for the lens-antenna mixers employing small Si lenses [18-22]. Several corrections were applied to properly align and correct the optical interfaces of mixer-units in band 5, 6 and 7. These beam pattern measurements and shimming activities took place at sub-unit level where we tested individual Mixer-Sub Assemblies containing a single polarization flight mixer [6]. The final verification step carried out during the Instrument Level Test program was the experimental end-to-end verification of the optical chain from mixer-unit to the focal plane where the individual HIFI beams interface to the Herschel telescope. Since beyond this level no additional testing is planned involving the actual telescope, great effort was put to ensure proper mechanical referencing of the HIFI beams relative to optical alignment devices, which are later used by industry to align the FPU to the Herschel optical bench and telescope [7].

In this paper we provide a compact summary of the verification results obtained prior to flight tests. We then focus mainly on the results obtained during the ILT phase of HIFI [40], we shortly summarize the experimental system used, and present the measured footprint of the instrument in the focal plane. We discuss compliance and conclude by projected performance at the sky and a brief outlook at future pointing calibration activities planned in space [47].

II. Quasi-Optical Alignment Approach

The main philosophy behind the end-to-end alignment of the HIFI Focal Plane Unit (FPU) is to use visible laser light alignment methods whenever possible. This is driven by the complexity of the optics, consisting of a common optics assembly including the telescope pick-off mirror, the chopper mirror and relay optics to the individual mixer bands in a compact, wide-field and off-axis arrangement [5-7, 23-26]. Central to the instrument there exist an optical-mechanical interface at which the smallest self-contained receiver units, the Mixer Sub-Assemblies (MSA's), can be mounted [7]. The MSA optics only contains three off-axis mirrors in a compact near-field off-axis arrangement and finally the Mixer Unit (MU) in which the mixers are located [6, 9]. The beams from the mixer units hit in some cases as many as 15 optical elements before they interface to the Herschel telescope in the focal plane [7]. To get this complex system under full control we decide to first pre-align all mirrors but the mixer units by visual laser light. All the reflective elements are compatible with use of visible light and are of optical quality. The main optics of the FPU, containing the common optics to all receiver bands, are fully pre-aligned before being interfaced to individual MSA modules. The MSA modules are also fully pre-aligned prior to integration of the MU modules. The visual alignment can be done very accurately as the image quality is diffraction limited. This eliminates the need of adjustment of mirrors after integration of the mixer units. The measurement campaign then relies only on ensuring that a) the MU has a proper optical interface in terms of beam properties, location and direction, b) a properly mounted MU has still good performance when remeasured at MSA level and c) a verified MSA in terms of radio alignment and beam quality still show good performance after passing through the common optics of the FPU. The advantage of this modular approach is that once the smallest self-contained module is properly verified it can simply be mounted on the FPU and performance is ensured. This will in principle allow for easy exchange of Mixer Sub-Assemblies when necessary and is preferred in terms of project AIV logistics.

III. Pre-flight Model Verification Results

The suppliers of the mixer units carried out a unit level verification program verifying either by test and/or analysis [27-28] that the mixer units comply with their optical interfaces. In the high-frequency bands 6 and 7 the MU level verification was combined with the MSA level verification in close collaboration with the supplier [18-19]. The design of the MSA optics was verified independently by analysis and test prior to integration with the MU. For that purpose dedicated electromagnetic simulations were carried out by Neil Trappe, Massimo Candotti, Gary Cahill, Tim Finn, and Tully Peacocke using a variety of modelling techniques and simulation packages [8, 11-17]. A few striking simulation and measurement results obtained for the long wavelength limit of HIFI are shown in Fig. 1 to 4 and described in more detail and extent in [7]. In Fig. 1 the simulated beam pattern of a band 1 MU after passing through the three-mirror system of the MSA [7, 9] is shown. The beam map is obtained in a plane where we interface to the common optics of the FPU. The measured beam profile in the same plane is shown in Fig. 2. Both patterns are shown on a logarithmic scale. The apparent visual agreement is striking. When taking a closer look at the patterns and comparing two orthogonal cuts taken through the centre of the maps in phase and amplitude, this agreement can indeed be confirmed. In Fig. 3 the measured and simulated intensity is compared and quantitative agreement down to -40 to -50 dB is obtained. In Fig. 4 we see that also in phase there exists excellent agreement. The observed structure both in intensity as well as in phase matches nicely to the predicted shapes. The differences are believed to originate from the applicable manufacturing tolerances. Differences in for example coupling efficiencies calculated on the basis of measured and simulated patterns agree within tenths of a percent.

In [7] and [9] we present all results obtained for the long wavelength limit design verification at 480 GHz. This paper also includes measurements and simulation for the Local Oscillator path and includes the telescope optics.

From these verification activities we concluded that once a mixer itself is compliant to the optical interface good end-to-end performance for a perfectly pre-aligned optical chain can indeed be ensured and that powerful analysis tools are available to predict and simulate expected performance at higher level of integration. It is therefore safe to limit further testing to end-to-end verification at MSA and FPU level only.

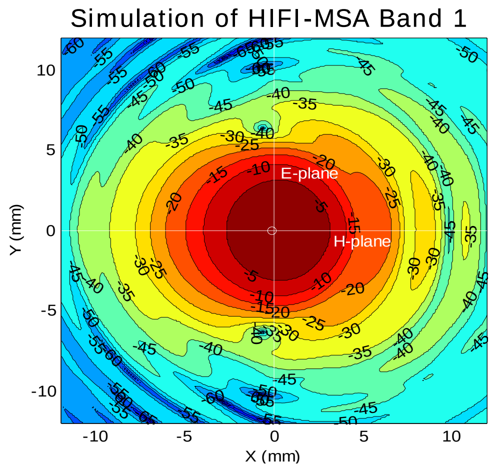

Fig. 1 Simulated beam pattern of HIFI MSA band 1 at 480 GHz.

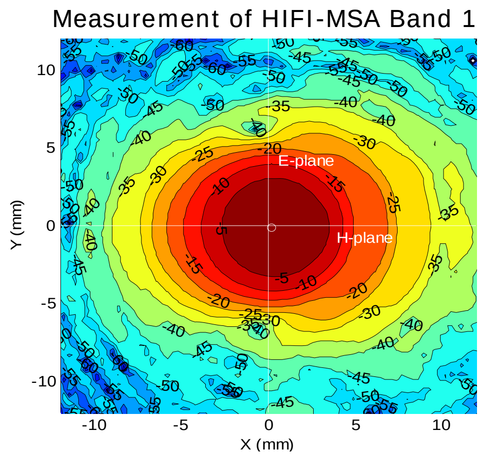

Fig. 2 Measured beam pattern of HIFI MSA band 1 at 480 GHz.

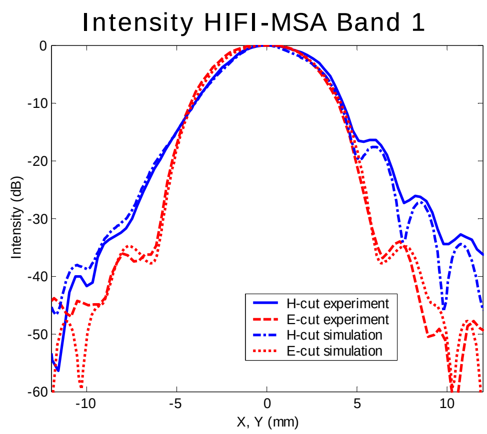

Fig. 3 Simulated and measured intensity along the E- and H-planes of the maps in Fig. 1 and 2.

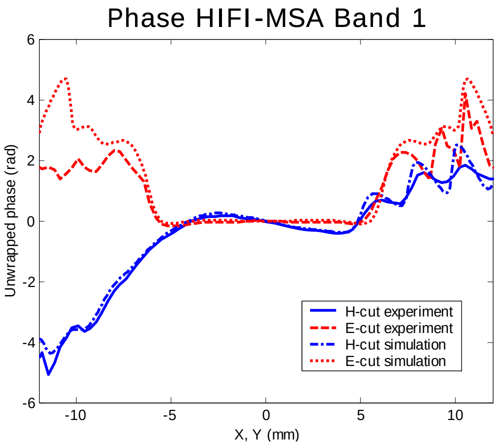

Fig. 4 Simulated and measure phase cuts of MSA band 1 at 480 GHz.

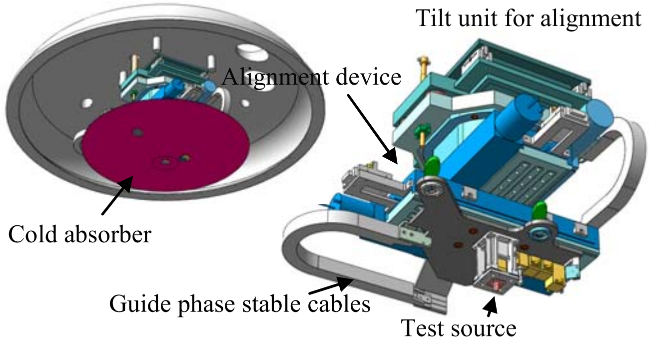

Fig. 5 Artist impression of vacuum scanner system used for the measurement of the focal plane beams of HIFI.

IV. Experimental System

We measure the HIFI beams in phase and amplitude as becomes clear in Fig. 3 and 4. This has the clear advantage that all information is contained in a single planar measurement[36-38]. From the measured complex field distribution the relevant parameters such as beam width, phase centre location and direction of propagation can be determined. Furthermore measured datasets can be included in electromagnetic simulation software and forward propagated to a higher level of integration. The measurement technique and system architecture employed is described in detail in [29-38]. We obtain a signal-to-noise ratio over 90 dB and phase resolution below 5º at frequencies as high as 1.6 THz.

For Instrument Level Tests at Focal Plane Unit level we use a rather involved system. Since the Herschel telescope has a focal ratio of 8.7 the spatial extent of the HIFI beams is already significant at the gate valve flange on the FPU cryostat which is roughly at half a meter from the optical bench. In order to reduce the heat load on the instrument we developed a vacuum scanner system which is mounted on top of the FPU cryostat. Once pressures at both sides of a gate valve system are equalized, the gate valve is opened and the scanner system can see the FPU. The scanner system is composed of a X- and Y-stage for horizontal and vertical translation, contains mechanical interfaces for coherent test sources and alignment devices and a cold absorber screen [39] which is cooled by liquid nitrogen. The cold absorber screen is mechanically supported from the moving stage and moves with the test source and is contained in a floating thermal shield construction in the vacuum scanner box. An artist impression of this system is shown in Fig. 5. See also section III of the paper by Teyssier et al in these proceedings [40]. In Fig. 6 we show the FM FPU as it would sit on the baseplate of the FPU cryostat. The scanner system shown in Fig. 5 scans the beam in a radial pattern in an on-the-fly-mapping mode measuring the two polarization channels in each mixer band simultaneously. We finally show a close-up of the actual scanner system in which a test source and the thermal-mechanical interface to which the cold absorber screen is mounted can be seen.

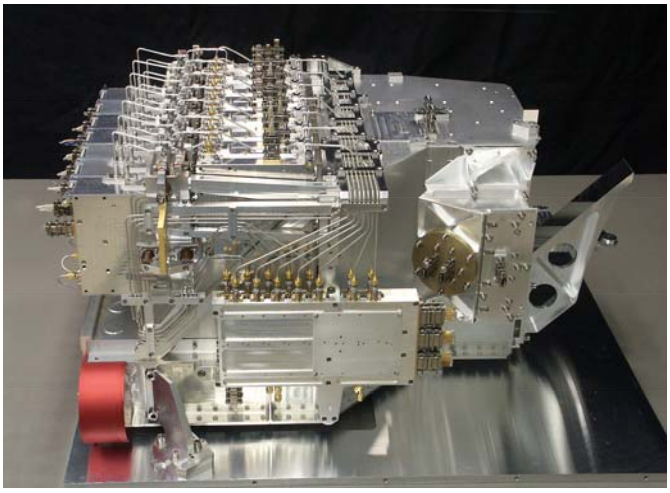

Fig. 6 Flight model FPU of HIFI. On the right hand side the telescope pick-off mirror M3 can be seen. On the top of the instrument the alignment cube used for Herschel optical bench integration and telescope alignment is visible.

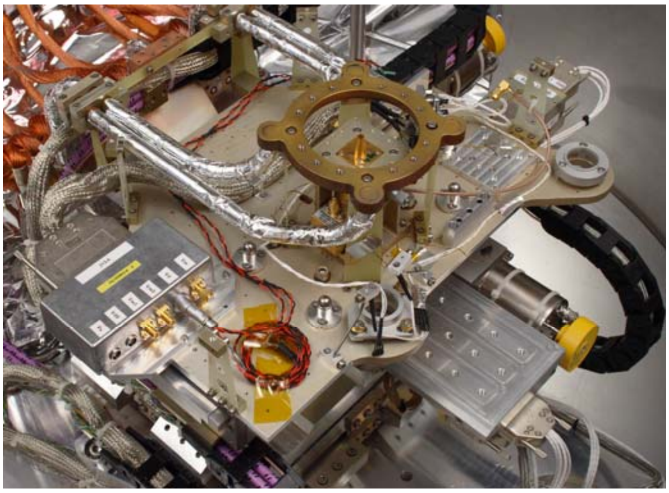

Fig. 7 View on the vacuum scanner system. In the centre the horn of a coherent test source and the thermal interface to the cold absorber screen are visible.

V. ILT RESULTS AND FOCAL-PLANE FOOTPRINT

During the ILT test campaign we measure the HIFI focal plane beams in 4 clusters. By using a test source that operates at the edges between bands a simultaneous measurement of 4 mixers can be done in one cooldown. For band 1 we use a source operating at 480 GHz and measure the beams of mixers 1H and 1V. Using a test source at 800 GHz we measure the beams of 2H, 2V, 3H and 3V resp. A source tuned at 1128 GHz is used to measure 4H, 4V, 5H and 5V. Finally we measure 6H, 6V, 7H and 7V at a frequency of 1619 GHz. Note that for band 7 this is formally an out-of-band frequency and some care has to be taken when interpreting the beam characteristics. Note that in all cases we use phase-locked or direct multiplied lab LO sources instead of the FM Local Oscillator Unit.

An example of a measurement for mixer band 5H is shown in Fig. 8 and 9 in amplitude and phase respectively. We obtain excellent signal-to-noise ratio, however the measured profiles show some scatter due to multiple reflections from shiny thermal shields in between the source and instrument. These multiple reflections can be partially removed by frequency switched measurements as well as in the analysis software. In our analysis we find that the scattering effect does not bias the determined beam properties. We observe that high spatial frequencies are filtered out by propagating the raw data to the focal plane.

We obtain identical results when fitting a fundamental Gaussian beam mode to our data, both in the initial measurement plane as well as in the focal plane after field propagation. The result of the propagation [44-46] of the measured field shown in Fig. 8 and 9 to a reconstructed distribution in the focal plane is shown in Fig. 10. In Fig. 10 we show the reconstructed field of mixer band 5H.

The fitted Gaussian beam that provides highest coupling to the complex field distribution is shown in Fig. 11. In Fig. 11 we show two orthogonal cuts through the field and compare the measured and fitted intensity and phase. The Gaussian fit provides the beam width, the propagation direction and the location of the phase centre and is used to verify compliance with the telescope interface. The Gaussian fitting procedure is explained in detail in [7]. In all cases we measure excellent Gaussian beam coupling well above 90% and in most cases between 93% and 95% We furthermore find that analysis on the measured maps yields similar numbers as compared to analysis on forward propagated model data taken from MSA measurements assuming perfectly aligned FPU optics. Differences we find can be understood in terms of alignment errors, both in the actual flight hardware as well as in the relative alignment between scanner system and FPU.

Finally we directly measure the co-alignment between the mixers operating on orthogonal polarizations. As both mixer are sampled simultaneously the co-alignment can be measured very precisely independent of alignment errors in the scanner system and FPU optics. We find that co-alignment is best in HIFI bands 6 and 7, reflecting the great effort that was put in shimming these lens-antenna based mixers. We discuss compliance further in section VI.

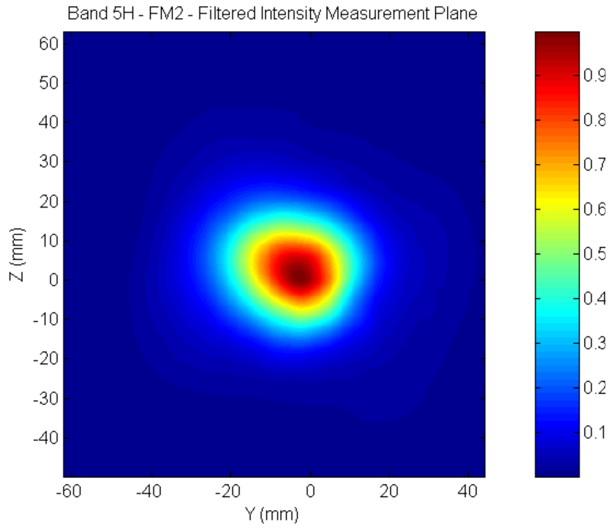

Fig. 8 Measured intensity distribution of band 5H.

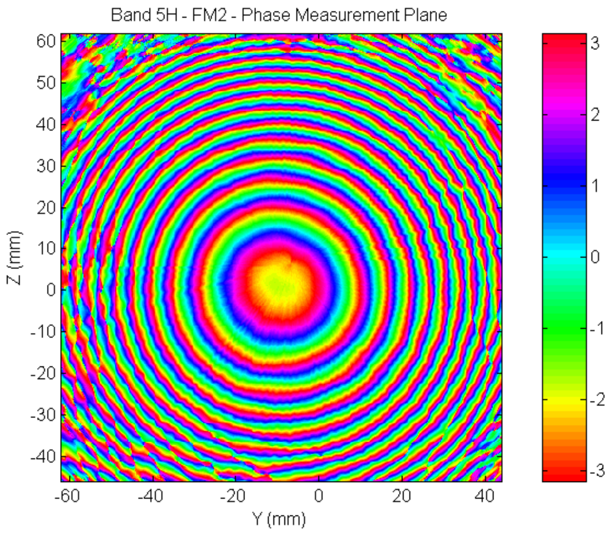

Fig. 9 Measured phase distribution of band 5H.

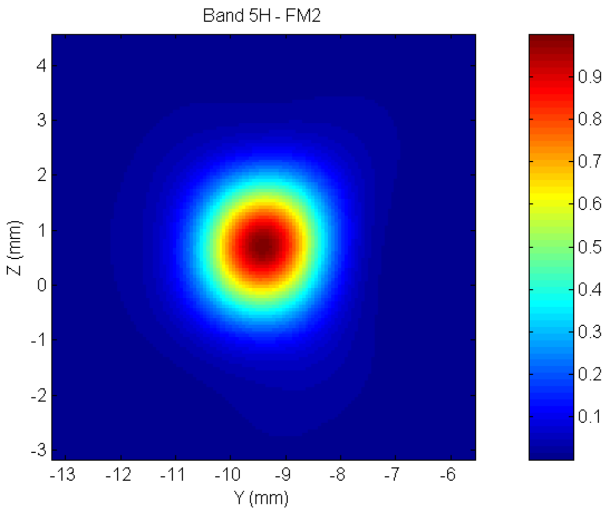

Fig. 10 Reconstructed focal plane field distribution in band 5H.

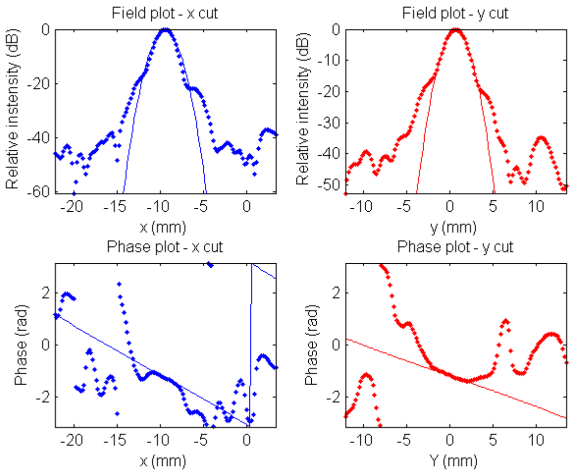

Fig. 11 Measured and fitted intensity and phase cuts in the focal plane for mixer band 5H.

A composite plot showing the results of all beams propagated to the focal plane are shown in Fig. 12. From left to right the bands 1 to 7 are covered. The size of the plot area reflects the actual size of mirror M3 as shown in Fig. 6. Indicated in the plot are the clusters of beam measurements. Within each cluster excellent relative alignment accuracy is available. Between clusters the reproducibility of the alignment procedure between scanner system and FPU optics is applicable as carried out for different configurations and time intervals. For all clusters the absolute alignment between scanner and FPU optics is dominant and is of order of a few mm. Note that a lateral error of a few mm in the focal plane only presents initial pointing inaccuracy but is insignificant as far as the alignment to the secondary mirror of the Herschel telescope is concerned. The systematic nature of alignment errors in the beam measurement is reflected in the pointing calibration plan [47] which we shortly outline in section VIII.

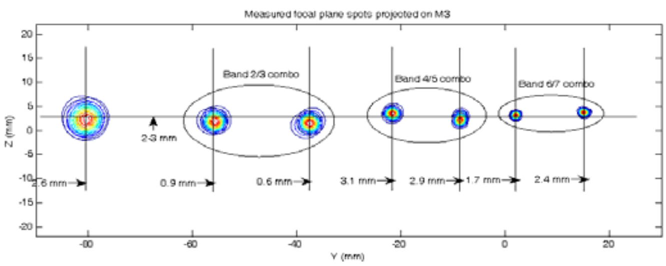

Fig. 12 Measured HIFI beams propagated to the focal plane.

VI. Compliance of Optical Performance

The Gaussian beam fitting results provide propagation direction and location of phase centre as well as the beam properties of the measured field. We compare the measured position (X, Y and Z coordinates) of the waist to the design values. We find that the location of the phase centre nicely follows the focal plane curvature and conclude that all beams are within focus of the Herschel telescope within the wavelength dependent tolerances [42]. Losses due to defocus are generally below 1%.

As explained in the previous section a direct comparison between measured and predicted lateral positions in the focal plane fails because of alignment errors between scanner plane and instrument. On the basis of forward propagated data obtained at MSA level, and knowledge of the visual laser light alignment of the FPU optics, we belief that the absolute errors of the beams in the focal plane are as small as 0.5 mm which corresponds to 3.5" at the sky. The absolute positions of the HIFI beams will anyhow be calibrated in-orbit as described in section VIII. As far as compliance is concerned the observed lateral deviations are insignificant as compared to the pupil alignment requirement [42] (illumination of the secondary mirror of the Herschel telescope).

As far as co-alignment is concerned we observe in general that mixer bands 6 and 7 show best co-alignment figures. This reflects the mechanical shimming corrections applied at MSA level [19]. For band 1 to 4 no mechanical corrections have been applied and co-alignment figures are generally worse and do not generally satisfy a 10% of waist radius co-alignment goal. We therefore decide to make default use of a telescope pointing in between the sky positions of the two polarizations. Worst-case coupling losses for a point source are then reduced by a factor of 4 as compared to using one polarization only. The co-alignment results are summarized in Table I. For each band we list the measured lateral offset in Y and Z (spacecraft coordinates) in mm. The fourth column indicates the total lateral offset. Note that 1 mm in the focal plane corresponds to roughly 7" at the sky. The waist radius is listed in the fifth column followed by the co-alignment error as a fraction of the waist radius. The last two columns indicate the coupling loss for a point source. $L_{H,V}$ indicates the coupling loss observed for one polarization channel when pointing the telescope at the other polarization. The last column indicates L_S, the coupling loss for synthesized pointing, where the telescope is pointed in between the H and V sky positions. As can be seen from the table the associated coupling losses are a factor of four lower, but losses are now present for both polarizations. When co-adding spectra, which is the default mode of scientific operation, there is a clear advantage to use a synthesized pointing approach.

TABLE VI
CO-ALIGNMENT RESULTS OBTAINED DURING ILT

Band	**ΔY**	**ΔZ**	**ΔR**	**W_0**	**$\Delta R/W_0$**	**$L_{H,V}$**	**L_S**
1	2	0.2	2	3.87	0.52	0.27	0.07
2	0.6	0.2	0.6	2.32	0.26	0.07	0.02
3	0.7	0.6	0.9	2.32	0.39	0.15	0.04
4	0.2	0.3	0.4	1.65	0.24	0.06	0.01
5	0.1	0.6	0.6	1.65	0.36	0.13	0.03
6	0.1	0	0.1	1.15	0.09	0.01	0.00
7	0.1	0.1	0.1	1.15	0.09	0.01	0.00

Next we discuss the alignment on the secondary mirror of the Herschel telescope. Alignment on M2, or pupil alignment, is important for the aperture efficiency and sidelobes of HIFI. The general requirement is to satisfy pupil alignment within

10% of the beam radius. Measured in the focal plane, M2 pupil alignment errors translate to tilt errors of the propagation direction of the beams. We observe that M2 pupil alignment generally satisfies 10-15% of the waist radius [41].

Finally we find that the measured waist size is within 10% from the design value. We conclude therefore that all HIFI bands are compliant with the quasi-optical alignment budget [42-43]. Expected aperture efficiencies, assuming an ideal telescope, should be within 10% from the design values.

VII. Beam Properties at the Sky

Finally we simulate the expected beam patterns at the sky by propagating [44-46] the measured results through a telescope model and applying a pupil mask representing the obscuration by the secondary mirror and support structure. An example of the masked telescope aperture field is shown in Fig. 13. The example is given for band 7 at 1.8 THz. An example of the wavefront error map in band 1 is shown in Fig. 14. By a Fourier Transform of the complex aperture field distribution at the primary mirror we obtain the far-field distribution.

The as-determined far-field profiles show generally good performance. We find highly symmetric beams which nicely follow a Gaussian distribution down to -20 dB. Sidelobes usually appear at the -20 dB level. Sidelobes are not always symmetric. Aberrations, astigmatism and coma originating from the focal plane beams causes this asymmetry [24-25]..

An example of a far-field cut obtained for band 1 is shown in Fig. 15. In this figure we show two orthogonal intensity cuts obtained in the principal planes of the satellite coordinate system together with the expected pattern on the basis of a truncated Gaussian beam. Although there are some differences in the sidelobes, the general agreement is excellent.

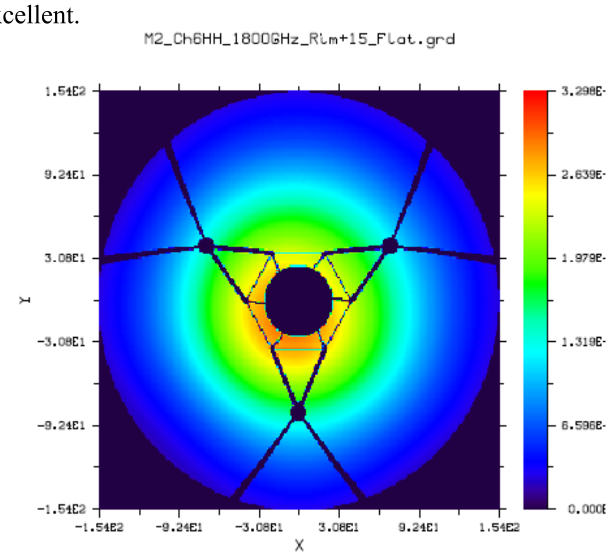

Fig. 13 Example of an obscured telescope aperture field.

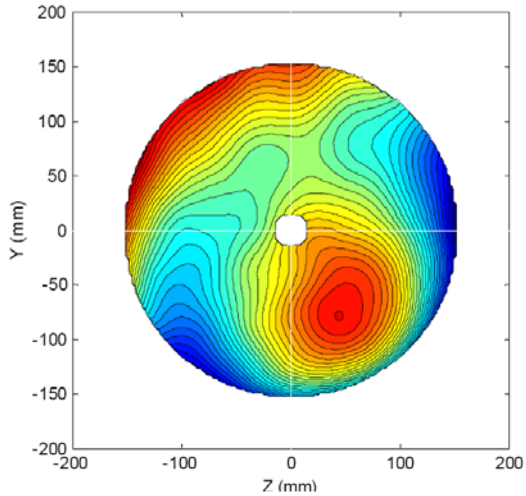

Fig. 14 Example of a measured wavefront error map in band 1.

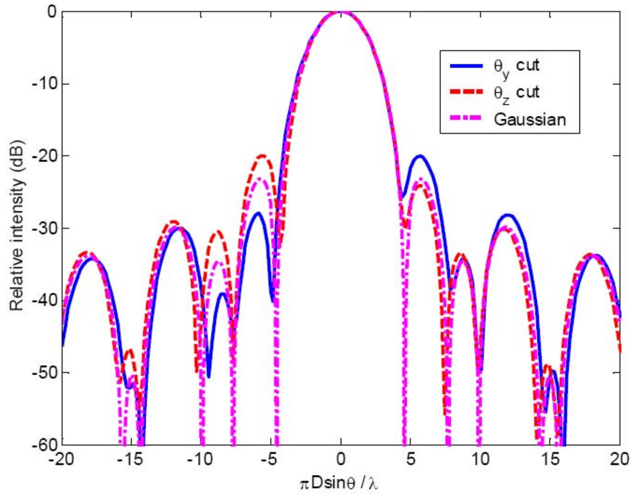

Fig. 15 Example of a far-field cut obtained for band 1

VIII. In-Orbit Calibration

In the previous sections it is explained that the absolute knowledge of initial pointing performance is limited by the metrology available during ILT. Consequently our initial estimate is not better than 3 to 4”. This is however a fairly good number to start with given the size of the FWHM beam width ranging from typically 40” in band 1 to 10” in band 7. In close collaboration with the other Focal Plane instruments PACS and SPIRE on Herschel, the Herschel pointing calibration working group has issued a calibration plan in which a procedure is presented to calibrate the pointing direction for each individual aperture in HIFI [47]. For HIFI two Focal Plane Geometry calibration activities are foreseen. In the initial step a relatively large beam map is taken for one band at one frequency in each cluster mentioned in section V. Together with the results obtained in ILT, the relative knowledge of the other beams in each cluster is used to refine the initial estimate for a second calibration step. In the second finer calibration measurement, a smaller map of two times the FWHM is taken to obtain the final pointing calibration. For pointing calibration we will use planets as test sources. An example of the planned coarse and fine maps is illustrated in Fig. 16. In Fig. 16 all apertures of HIFI are shown, from right to left bands 1 to 7 projected on the sky can be recognized. The central row is for the central position of the focal plane chopper, the upper and lower rows correspond to the chopped positions which are separated by the chopper throw of 3'. The raster for the FPG coarse calibration is shown on the top row, whereas the final FPG fine calibration is shown on the bottom row.

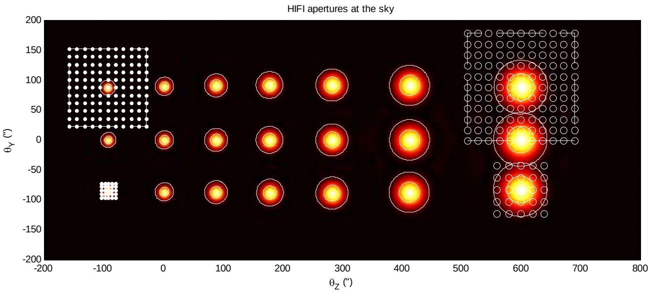

Fig. 16 Focal Plane Geometry calibration rasters shown on top of the nominal aperture positions for HIFI.

In addition to in-orbit pointing calibration we eventually measure in detail the beam patterns of all HIFI beams and determine aperture efficiencies at a number of frequencies as part of the spatial framework calibration activity for HIFI [48].

SUMMARY AND CONCLUSIONS

In this paper we provide an overview of simulation, alignment and beam measurement results obtained for HIFI. We present the alignment approach adapted and pre-flight model verification results supporting the selected verification method. We present the experimental setup and summarize results obtained during the Instrument Level Test program. We conclude that HIFI is fully compliant with the quasi-optical alignment budget. This implies that the total loss due to optical coupling loss is limited to 6% and the aperture efficiency for a nominal telescope is within 10% from the expected value. We furthermore observe that co-alignment is generally within 20-30% of the waist radius or within 10-15% of the FWHM. When pointing at the average sky position the loss per polarization channel is worst-case 7% and more typically 2-4%. In band 6 and 7 we achieve nearly perfect co-alignment, reflecting the careful mechanical shimming work done at Mixer Sub-Assembly level. We furthermore predict expected beam patterns at the sky by propagation of measurement results through a telescope model. Final pointing and beam pattern calibration will be carried out in space.

ACKNOWLEDGEMENT

The authors want to acknowledge the contribution by NASA-JPL. Without the technical support and loaner hardware provided by John Pearson, Frank Maiwald and John Ward, high-quality phase sensitive beam measurements up to 1.6 THz, corrective actions in band 5, 6 and 7, reflected in the excellent co-alignment achieved in the lens-antenna bands 6 and 7, would not have occurred.

REFERENCES

[1] Th. de Graauw, N.D. Whyborn, P. Dieleman, W. Jellema, J. Kooi, W. Luinge, T. Marston, T. Peacocke, D. Teyssier, "The Pre-flight Performance of the Herschel-Heterodyne Instrument for the Far-Infrared (HIFI)", *Bulletin of the American Astronomical Society*, Vol. 37, p.1197, Dec 2005.

[2] T. de Graauw, E. Caux, R. Guesten, W. Jellema, W. Luinge, J. Pearson, T. Philips, R. Schieder, J. Stutzki, K. Wafelbakker, N. Whyborn, K. Wildeman, "The Herschel-Heterodyne Instrument for the Far-Infrared (HIFI)", *Proceedings of the 2004 29th International Conference on Infrared and Millimeter Waves and 12th International Conference on Terahertz Electronics*, September 27 – October 1, 2004, Karlsruhe, Germany.

[3] T. de Graauw, N. Whyborn, W. Jellema, E. Caux, T. Philips, J. Stutzki, "Development Status of the Herschel-Heterodyne Instrument for the Far-Infrared (HIFI)", *Proceedings of the 15th International Symposium on Space TeraHertz Technology*, April 27-29, 2004, Northampton, USA.

[4] T. de Graauw, F. P. Helmich, "Herschel-HIFI: The Heterodyne Instrument for the Far-Infrared", *in The Promise of the Herschel Space Observatory*, edited by G. L. Pilbratt et al., ESA SP-460, pp. 45-51, 2001.

[5] N.D. Whyborn et al, "The Focal Plane Optics of HIFI, a Heterodyne Instrument for the Herschel Space Observatory", *to appear in the Proceedings of the 5th International Conference on Space Optics*, March 30-April 2, 2004, Toulouse, France

[6] B. D. Jackson, K. J. Wildeman, N. D. Whyborn on behalf of the HIFI Focal Plane Consortium, "The HIFI Focal Plane Unit", *Proc. 13th International Symposium on Space Terahertz Technology*, pp. 339-348, 26-28 March 2002, Harvard University, Cambridge, Massachusetts, USA.

[7] W. Jellema, R. Huisman, N. Trappe, T. Finn, S. Withington, J. A. Murphy, "Comparison of Near-Field Measurements and Electromagnetic Simulations of the Focal Plane Unit of the Heterodyne Instrument for the Far-Infrared", *Proceedings of the 5th International Conference on Space Optics*, March 30 – April 2, 2004, Toulouse, France.

[8] N. Trappe, W. Jellema, J. A. Murphy, P. R. Wesselius, B. Kruizinga, H. Visser, T. Finn, "Validation of the Quasi-Optical Analysis of HIFI for the Herschel Space Observatory", *Proceedings of the 11th IEEE International Conference on Terahertz Electronics*, September 24-26, 2003, Sendai, Japan.

[9] W, Jellema, P. R. Wesselius, S. Withington, G. Yassin, J. A. Murphy, C. O'Sullivan, N. Trappe, T. Peacocke, B. Leone, "Experimental Verification of Electromagnetic Simulations of a HIFI Mixer Sub-Assembly", *Proceedings of the 14th International Symposium on Space Terahertz Technology*, Tucson, USA, April 22-24, 2003.

[10] Neal Trappe, J. Anthony Murphy, Bob Kruizinga, Huib Visser, Willem Jellema, Klaas J. Wildeman, Herman van der Stadt, "Quasi-optical analysis of the HIFI instrument for the Herschel Space Observatory", *Proceedings of SPIE - Volume 4876 Opto-Ireland 2002: Optics and Photonics Technologies and Applications*, Thomas J. Glynn, Editor, March 2003, pp. 1091-1099.

[11] N. Trappe, J.A. Murphy, B. Kruizinga, H. Visser, W. Jellema, K. Wildeman, H. van de Stadt, "Quasi-Optical Analysis of the Front-End Optical System of the HIFI Instrument for the Herschel Space Observatory", *Proceedings of the 25th Antenna Workshop on Satellite Antenna Technology*, ESA, Noordwijk, The Netherlands, Sept. 2002.

[12] N. Trappe, J.A. Murphy, B. Kruizinga, H. Visser, W. Jellema K. Wildeman, H. van de Stadt, "Quasi-Optical Analysis of the HIFI Instrument for the Herschel Space Observatory", *SPIE Proceedings Optoelectronics*, Photonics and Imaging, Galway, Sept. 2002.

[13] O'Sullivan, C. J.A. Murphy, G. Cahill, M.L. Gradziel, N. Trappe, D. White, V. Yurchenko, S. Withington, W. Jellema, "Developments in Quasi-Optical Design for THz", *Proc. SPIE-04*, Glasgow, UK, 21-25 June 2004, #5498-39, June 21-25, 2004.

[14] P. R. Wesselius et al, " Far-Infrared Optics Design and Verification Tools*", Final Report Phase II ESA TRP Study 13043/98/NL/PB*, March 2003, to be made available by ESA.

[15] O'Sullivan C., Atad-Ettedgui E., Duncan W., Henry D., Jellema W., Murphy J.A., Trappe N., van de Stadt H., Withington S. and Yassin G., "Far-IR Optics Design and Verification", *International Journal of Infrared & Millimeter Waves*, pp. 1029-1045, Vol. 23, No. 7, July 2002.

[16] G. Yassin, S. Withington, C. O' Sullivan, J. A. Murphy, W. Jellema, P. R. Wesselius, T. Peacocke, "Far-Infrared Optics Design and Verification Phase II", *Proceedings of the 13th International Symposium on Space Terahertz Technology*, pp. 525-536, 26-28 March 2002, Harvard University, Cambridge, Massachusetts, USA.

[17] O'Sullivan C., Murphy J.A., Withington S., Yassin G., Atad-Ettedgui E., Duncan W., Henry D., Jellema W. and van de Stadt H., "MM-Wave Optics Design & Verification", *2K1BC Workshop Experimental Cosmology at Millimetre-waves*, Breuil-Cervinia (AO) Italy, July 9 - 13, 2001, *AIP Conference Proceedings 2002 (Vol. 616)*, M. De Petri & M. Gervasi eds., p.290-294.

[18] M. Hajenius, J.J.A. Baselmans, A. Baryshev, J.R. Gao, T.M. Klapwijk, J.W. Kooi, W. Jellema, and Z.Q. Yang, "Full characterization and analysis of a THz heterodyne receiver based on a NbN hot electron bolometer", *Journal of Applied Physics*, Volume 100, Issue 7, pp. 4507, October 2006.

[19] Willem Jellema, Timothy J. Finn, Andrey Baryshev, Maarten van der Vorst, Stafford Withington, J. Anthony Murphy and Wolfgang Wild, "Phase-Sensitive Near-Field Measurements and Electromagnetic Simulations of a Double-Slot HEB Integrated Lens-Antenna at 1.1, 1.2 and 1.6 THz", *to appear in Proceedings of the 16th International Symposium on Space Terahertz Technology*, Gothenburg, Sweden, May 2-4, 2005.

[20] A. Baryshev, M. Carter, W. Jellema, R. Hesper, "Design and Evaluation of ALMA Band 9 Quasioptical System", *Proceedings of the 5th International Conference on Space Optics*, pp. 365 – 371, 30 March – 2 April 2004, Toulouse, France.

[21] M .J. M. van der Vorst, "Integrated Lens Antennas for Submillimetrewave Applications", *Ph.D. dissertation*, Eindhoven University of Technology, the Netherlands, 1999.

[22] D. F. Filipovic, S. S. Gearhart and G. M. Rebeiz, "Double-slot Antennas on Extended Hemispherical and Elliptical Silicon Dielectric Lenses", *IEEE Trans. Microwave Theory Tech*., Vol. 41, 1993, pp. 1738-1749.

[23] Offner A., "Annular Field Systems and the Future of Optical Microlithography", *Optical Engineering*, Vol. 26, 294-299, 1987.

[24] J.A. Murphy and S. Withington, "Perturbation Analysis of Gaussian-beam-mode Scattering at Offaxis Ellipsoidal Mirrors", *Infrared Physics Technology*, Vol. 37, pp. 205-219, March 1996.

[25] J.A. Murphy, "Distortion of a Simple Gaussian Beam on Reflection from Off-axis Ellipsoidal Mirrors", *International Journal of Infrared & Millimeter Waves*, Vol. 8, pp. 1165-1187, September 1987.

[26] D.H Martin and E. Puplett, "Polarized Interferometric Spectrometry for the Millimetre and Submillimetre Spectrum", *Infrared Physics*, Vol. 10, pp. 105-109, 1969.

[27] A.D. Olver, P.J.B. Clarricoats, A.A. Kishk and L. Shafai, *Microwave Horns and Feeds*, IEEE Press, 1994.

[28] Richard J. Wylde and Derek H. Martin, "Gaussian beam-mode analysis of corrugated feed horns", *IEEE Transactions on Microwave Theory and Techniques*, Vol. MTT-41(10), 1691–1699, October 1993

[29] Willem Jellema, Andrey Baryshev, Dimitri Paveliev, Jeffrey Hesler, Wolfgang Wild and Stafford Withington, "Development Status of a 420-1980 GHz Vector Network Analyzer for Time-Domain Reflectometry and Imaging Applications*", Proc. of the 32nd Int. Conf. on Infrared and Millimeter Waves and 15th Int. Conf. on Terahertz Electronics*, Cardiff, United Kingdom.

[30] W. Jellema, S. J. Wijnholds, P. R. Wesselius, S. Withington, G. Yassin, J. A. Murphy, C. O'Sullivan, N. Trappe, T. Peacocke, B. Leone, "Performance Characterisation and Measurement Results of a Submillimeter-Wave Near-Field Facility for the Heterodyne Instrument for the Far-Infrared", *Proceedings of the 3rd ESA Workshop on Millimeter Wave Technology and Applications*, Millilab, Espoo, Finland, May 21-23, 2003.

[31] A. Baryshev, M. Carter, R. Hesper, S. J. Wijnholds, W. Jellema, T. Zijlstra, "Use of Subharmonically Pumped SIS Mixer with High Harmonics Number for Phase and Amplitude Antenna Measurements", *Proc. 13th International Symposium on Space Terahertz Technology*, pp. 551-558, 26-28 March 2002, Harvard University, Cambridge, Massachusetts, USA.

[32] M. Carter, A. Baryshev, R. Hesper, S. J. Wijnholds, W. Jellema, T. Zijlstra, "Phase and Amplitude Antenna Measurements on an SIS Mixer Fitted with a Double Slot Antenna for ALMA Band 9", *Proceedings of the 13th International Symposium on Space Terahertz Technology*, pp. 515-524, 26-28 March 2002, Harvard University, Cambridge, Massachusetts, USA.

[33] P. Goy, M. Gross, "Vector Transceiver for mmWave Antennas", *Proc. 20th ESTEC Antenna Wokshop on Millimetre Wave Antenna Technology and Antenna Measurement*, pp. 289-294, 18-20 June 1997, ESTEC, Noordwijk, The Netherlands.

[34] N. Erickson, V. Tolls, "Near-Field Measurements of the Submillimeter Wave Astronomy Satellite Antenna", *Proc. 20th ESTEC Antenna Wokshop on Millimetre Wave Antenna Technology and Antenna Measurement*, pp. 313-319, 18-20 June 1997, ESTEC, Noordwijk, The Netherlands.

[35] C. E. Tong, S. Paine, R. Blundell, "Near-Field Characterization of 2-D Beam Patterns of Submillimeter Superconducting Receivers", *Proc. 5th International Symposium on Space Terahertz Technology*, pp. 660-673, 1994.

[36] A. C. Newell, "Error Analysis Techniques for Planar Near-Field Measurements", *IEEE Transactions on Antennas and Propagation*, vol. 36, No. 6, pp. 754- 768, June 1988.

[37] A. D. Yaghjian, "An Overview of Near-Field Antenna Measurements", *IEEE Transactions on Antennas and Propagation*, vol. AP-34, No. 1, pp. 30-45, January 1986.

[38] D. M. Kerns, Plane-Wave Scattering-Matrix Theory of Antennas and Antenna-Antenna Interactions, *NBS Monograph 162*, pp. 89, June 1981.

[39] M. C. Diez, T. O. Klaassen, C. Smorenburg, K. J. Wildeman, "Reflectance Measurements on Absorbing coating for Sub-Millimeter Radiation", *Proc. 4th Annual Symposium IEEE/LEOS (Benelux Chapter),* pp. 107-110, 15 November 1999, Mons, Belgium.

[40] D. Teyssier, N.D. Whyborn, W. Luinge, W. Jellema, J. Kooi, P. Dieleman and T. de Graauw, "HIFI Pre-Launch Calibration Results", *these proceedings.*

[41] Tully Peacocke, "Gaussian beam properties derived from the Hifi beam measurements", Version 0.1, June 13, 2006.

[42] Nick Whyborn, "HIFI Quasi-Optical Alignment Budget", HIFI technical note, SRON-G/HIFI/TN/2000-004, October 13, 2000.

[43] Willem Jellema, "Optical Design Criteria and Definitions", HIFI technical note, SRON-G/HIFI/TN/1999-002, December 15, 1999.

[44] P. F. Goldsmith, Quasioptical Systems: Gaussian Beam Quasioptical Propagation and Applications, IEEE Press: New York.

[45] J. W. Goodman, Introduction to Fourier Optics, 2nd Edition, McGraw-Hill, New York, 1996.

[46] D.H. Martin and J.W. Bowen, "Long-wave Optics", IEEE Transactions on Microwave Theory and Techniques, Vol. MTT-41(10), pp. 1676-1690, October 1993..

[47] Tony Marston on behalf of the Herschel Pointing Calibration Wokring Group, "Herschel Pointing Calibration Plan – Calibration Plan for Commissioning and PV Phases", HERSCHEL-HSC-DOC-1139, Issue 0.91, June 11, 2008.

[48] Carsten Kramer on behalf of the HIFI/Herschel Calibration group, "Spatial response framework document", Version 1.8, May 10, 2006.

A Compact, Modular Package for Superconducting Bolometer Arrays

Dominic J. Benford[1*], Christine A. Allen[1], and Johannes G. Staguhn[1,2]
[1]NASA / Goddard Space Flight Center, Greenbelt, MD 20771, USA
[2] University of Maryland: Department of Astronomy, College Park, MD 20742-2421 USA
* Contact: Dominic.Benford@nasa.gov, phone +1 301.286.8771

***Abstract*— As bolometer arrays grow to ever-larger formats, packaging becomes a more critical engineering issue. We have designed a detector package to house a superconducting bolometer array, SQUID multiplexers, bias and filtering circuitry, and electrical connectors. The package includes an optical filter, magnetic shielding, and has well-defined thermal and mechanical interfaces. An early version of this package has been used successfully in the GISMO 2mm camera, a 128-pixel camera operating at a base temperature of 270mK. A more advanced package permits operation at lower temperatures by providing direct heat sinking to the SQUIDs and bias resistors, which generate the bulk of the dissipation in the package. Standard electrical connectors provide reliable contact while enabling quick installation and removal of the package. The design compensates for differing thermal expansions, allows heat sinking of the bolometer array, and features magnetic shielding in critical areas. It will be scaled to 1280-pixel arrays in the near future.**

I. Introduction

The state of the art for far-infrared and submillimeter instruments being developed for ground-based, airborne, and space-based observations now consists of arrays of broadband detectors containing at least a thousand elements. The largest operational cryogenic detector array from NASA's Goddard Space Flight Center to date is the 384-pixel bolometer array manufactured for the Caltech Submillimeter Observatory (CSO) SHARC-II instrument [i]. This array uses a design for close-packing detectors to achieve a near unity filling factor. However, the bolometers use semiconducting thermistors read out by individual FETs for every pixel. Future instruments require bolometer arrays with many more pixels, and may require sensitivity of 100 times better. A design using superconducting transition edge sensor (TES) bolometers and multiplexed SQUID readouts can achieve this, in part due to the scalability of a suitable multiplexed readout. A TES bolometer has a faster response time than an identically designed, same sensitivity semiconducting bolometer (or a more sensitive bolometer for the same response time) due to the strong negative electrothermal feedback intrinsic to a voltage-biased TES [ii]. TES bolometers are inherently low impedance devices, so they are well matched to being read out by DC SQUID amplifiers [iii]. These amplifiers have a large noise margin over the TES Johnson noise and bolometer phonon noise. This permits the bolometer to be read out in a multiplexed fashion by a suitable SQUID multiplexer [iv], thereby reducing the amplifier size and the wire count. Because SQUID multiplexed amplifiers operate at the base temperature of the bolometer, they can be coupled very closely, removing the complex interfaces necessary with semiconducting bolometers. Past work by our group has resulted in the demonstration of such detector systems operating using SQUID multiplexers [v], optical detection of light while multiplexing [v], Johnson-noise-limited readout by SQUID multiplexers [vi], near-phonon-noise-limited bolometers [vii]. Recently, we have fielded the largest superconducting bolometer array to be used at a telescope [viii]. This paper details our design of a package to house an array of multiplexed TES bolometers that is compact, modular, and scalable to at least 1,280 detector elements.

II. The GISMO Camera

We began work in late 2005 on a new bolometer camera that became GISMO, the Goddard-IRAM Superconducting 2 Millimeter Observer [ix]. Optimized to operate in the 2mm atmospheric window at the IRAM 30m radio telescope on Pico Veleta, Spain, this camera was conceived as a means of field-testing superconducting bolometer arrays fabricated using the recently-developed backshort-under-grid architecture [x, xi, xii]. GISMO can also produce cutting-edge scientific results, being optimized for large-area surveys of the very high redshift ($z \geq 5$) universe [xiii]. The bolometer array was designed with 128 pixels arranged in an 8×16 format, with wiring brought out along the beams between pixels to connect to a 4×32 array of SQUID multiplexers. In order to simplify the assembly and test of the instrument, we wished to develop an integrated, compact cryogenic detector package that contained the detector array, SQUID readouts, all necessary thermal and mechanical structures, magnetic shielding, an optical bandpass filter to limit the wavelength range of light entering the package, and a set of electrical connectors to communicate into the package. We also sought to use several aspects of this package as the point of departure in designing a detector package able to accommodate 32×40 bolometer arrays based on the SCUBA-2 multiplexer developed by NIST/Boulder [xiv].

III. Schematic Diagram

The design of the 4×32 readout is based on heritage to earlier instrument developments using the NIST/Boulder 1×32 time-domain SQUID multiplexers [xv, xvi]. This includes both readout electronics development [xvii, xviii] and instruments that have been successfully used on ground-based telescopes [xix, xx]. One important property of these SQUID readouts is that they operate naturally at the very low temperatures required by sensitive bolometers (in this case, at 300 mK). They dissipate little power (4 nW per 1×32 multiplexer, only a few times more than the dissipation in the bolometers themselves), and can therefore be closely coupled to the bolometer array wafer. In addition to the multiplexer, a superconducting Nyquist filter inductor and a bias shunt resistor must be included for each pixel.

The schematic diagram of the electrical wiring in the 4×32 package is shown in Figure 1. The diagram for a 32×40 package is very similar, with the addition of a dark SQUID channel that acts like row 41, but has no TES, bias, or filter on the input. Designed as a three-stage amplifier, the high gain third stage requires of order 1 μW of power and hence is located in a physically separated package, which is thermally connected to the ^{4}He bath. The first stage SQUID multiplexer inputs are shown (in green in color versions of this paper), along with the input coil, feedback coil, and transformer coil. Feedback provided by the room temperature electronics exactly nulls the signal from the input coil, so that the input SQUID is operating at a nearly constant locus on its flux-voltage characteristic. This provides, to first order, linear response from the SQUID, and results in the error term being the flux transformed out into the summing loop that couples to the second stage SQUID. It should be noted that the transformer coil does not couple directly to the SQUID, but instead is used to sense the changing voltage across the SQUID with flux by the changing current through the parallel address resistor.

Multiplexer-compatible chips consisting of 32 $L \approx 1$ μH superconducting inductors and 32 low-value bias resistors ($R \approx 2$ mΩ) are fabricated by NIST/Boulder and NASA/GSFC, respectively. The inductors, shown in purple in Figure 1, have a pass-through aspect not emphasized in the figure, and with a coil on the side connected to the shunt resistor and a coil on the side connected to the TES. This balancing provides symmetry while achieving the function of bringing the integrated signal to the multiplexer. The bias shunt resistors, shown in blue, have a pass-through provided by bridging wirebonds over the bias loop (the vertical portion of the wiring in the blue area). These accommodations allow the compact arrangement of the readout circuit, which is the subject of Section V.

IV. The 8x16 Bolometer Array

The detector array design and performance has been detailed elsewhere [xxi], and so only a brief summary will be made here. For orienting the reader, a photo of two arrays is shown in Figure 2. The pixel pitch is 2 mm to avoid complicated optical coupling at pitches <λ while keeping a small overall size. The detector chip is 32 mm × 48 mm and has a pair of 3 mm diameter holes spaced by 41 mm to enable mounting. Gold heat sink pads next to the holes are used to enable gold wirebonds to make thermal attachment to the array. In Figure 3 we show an enlarged view of a single pixel. Each corner of a pixel connects to the beams that make up the structural grid of the suspended bolometer at two places, so there are a total of eight legs providing a saturation power of ~32 pW between 300 mK and T_C~450 mK. The TES is the small gold rectangle near the upper edge, located so as to minimally interfere with the optical absorption. A back-side coating of bismuth provides high efficiency absorption at many wavelengths, and a reflective λ/4 backshort tunes this absorption to peak efficiency at the desired 2 mm wavelength.

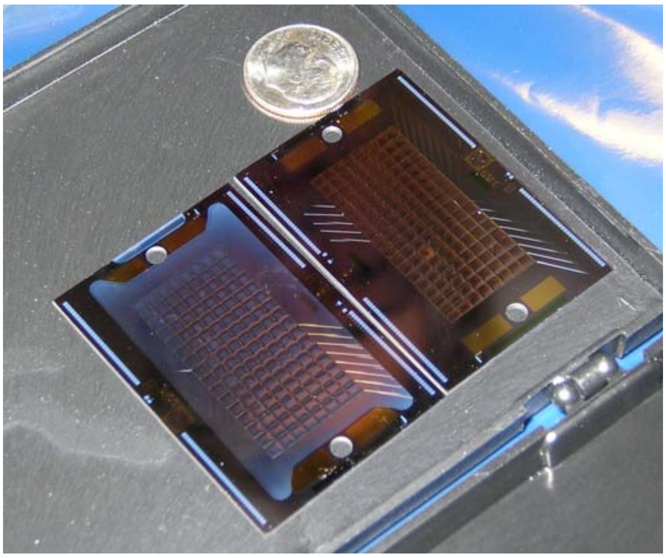

Figure 2. A photo of two transition edge sensor bolometer arrays for GISMO shows the scale of the active area as well as the areas for signal connections and heat sinking or mechanical attachment.

Figure 3. This micrograph of a single pixel shows the style of thermal attachment to the beams making up the bolometer array grid. The TES is the small gold rectangle at the top edge

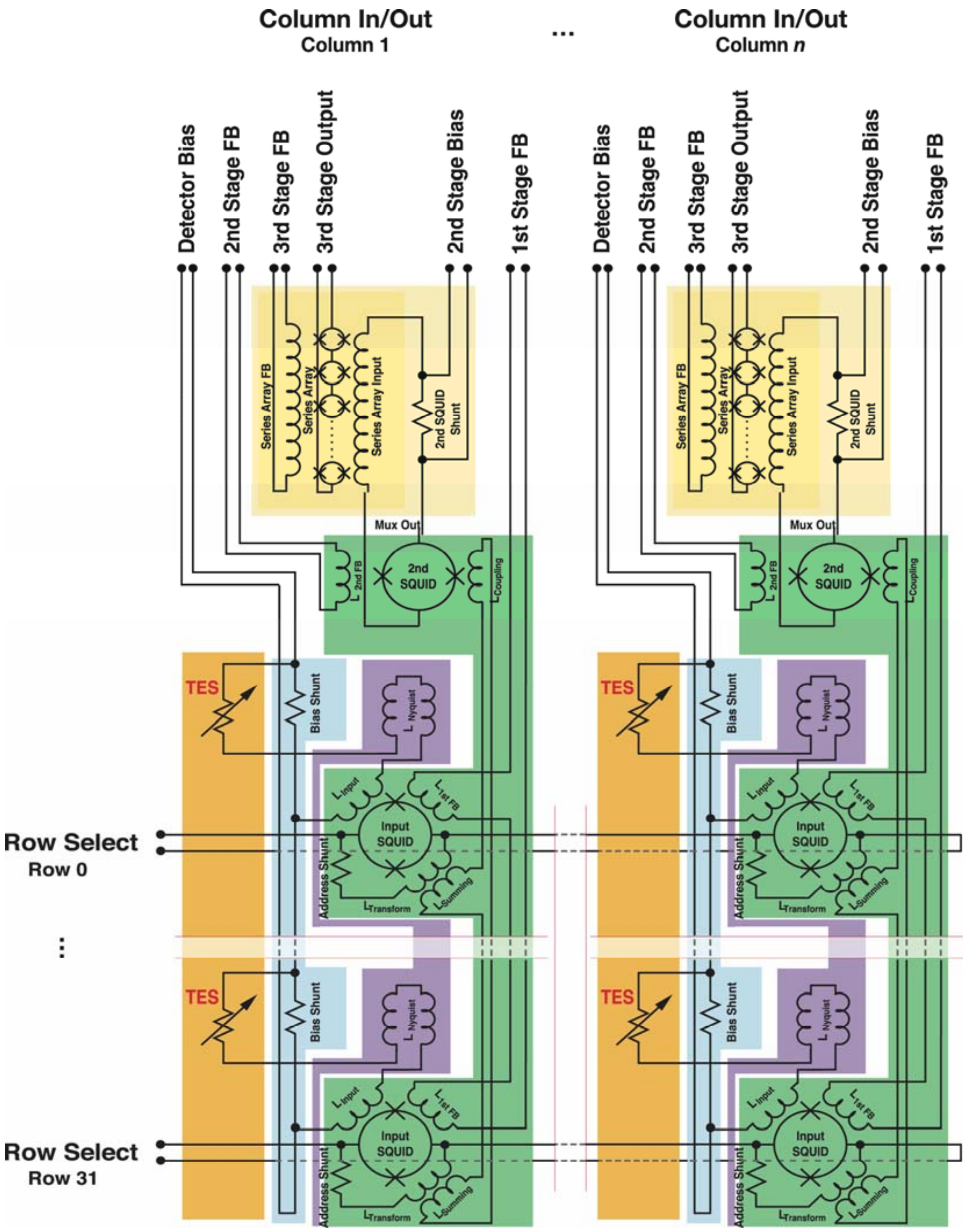

Figure 1. The schematic diagram of the multiplexed system shows that each column requires six pairs of wires for bias and readout, while the total number of address pairs is 32 when wired directly or 8 when wired using a demultiplexing address driver [xviii]. The readout unit consists of a single set of the SQUID/Nyquist/Shunt (green/purple/blue) chips as detailed in Section V. The series array amplifier (yellow) chips at the top are located in a different housing at a higher temperature.

V. Readout Unit

We have designed the readout circuit above to enhance its modularity and robustness. The overall goal is to produce a small-volume modular readout unit to provide multichannel cryogenic readout within the GISMO detector package and also within other future detector packages. At the same time, we sought to provide well-engineered electrical, mechanical, magnetic, and thermal interfaces.

To ease the electrical interfaces, we have designed a ceramic circuit board that brings wire bonds out to large, reusable pads for more bond cycles and improved chip heat sinking. The circuit board traces also bring pads to only two edges as opposed to the three necessary before. The circuit boards, shown in Figure 4, consist of 99.6% alumina ceramic 0.5mm thick with silkscreened gold traces, custom manufactured by Emtron Hybrids [xxii]. Mounting holes at the corner permit attachment to a thermal/mechanical

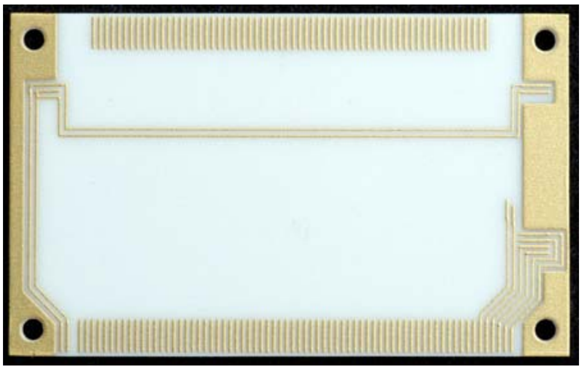

Figure 4. An alumina ceramic readout circuit board with gold traces prior to adding superconducting shorts to reduce stray resistance. The board measures 15 mm by 25 mm.

structure, discussed below. The design requires superconducting traces to prevent loss and heating; this effect is particularly important for the second stage output and detector bias lines, respectively, where the impact is most notable. It proved challenging to achieve very low total loop resistances in these boards, as the requirement of ≤10 mΩ necessitates high purity normal metals for the bond pads and superconducting traces for the wiring runs. We used pure gold wiring and shorted many of the traces with superconducting aluminium bond wires to ensure the lowest possible parasitic stray resistance. Aluminum wirebonds within the readout chips and to traces on the circuit board carry all signals. A photo of an assembled readout board is shown in Figure 5, along with an enlargement showing some of the trace-shorting wirebonds in Figure 6.

In the earlier GISMO detector packages, the ceramic carrier was glued directly to a metalized fiberglass board. While the coefficient of thermal expansion (CTE) mismatch is not exceptional, being on the order of 3 mm/m total, some failures were seen on repeated thermal cycling. It is possible that the combined CTE mismatch including the Nb foil was too great, producing large shears across a very small volume. We therefore designed a flexible metal bracket to hold the

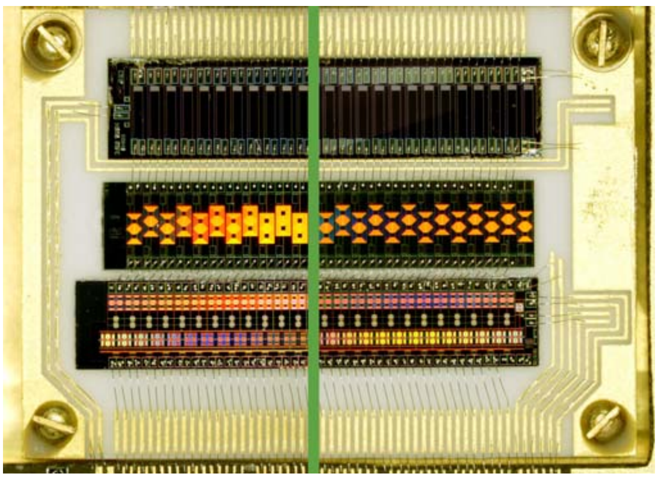

Figure 5. A composite photograph of a completed readout unit; several of the 32 channels have been cropped out of the middle. The chips are, from top to bottom, the shunt, Nyquist inductor, and SQUID multiplexer.

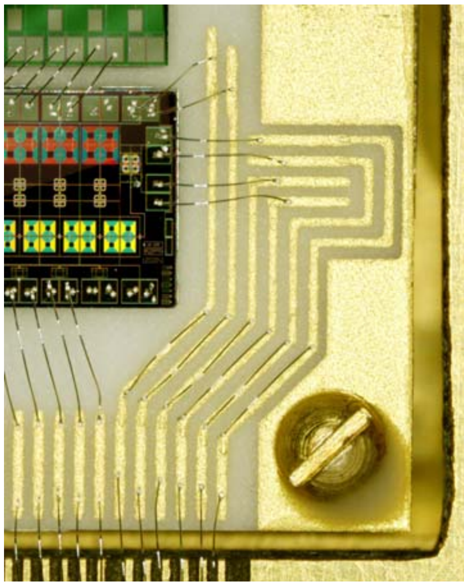

Figure 6. This in-progress photo of the wirebonding shows the first leg of superconducting bonds to short out critical gold traces.

ceramic circuit board (Figure 4) and the Nb foil separately. This grappler bracket, shown in Figure 7, uses flexures to accommodate the CTE mismatch between the ceramic and the copper of the bracket. The circuit board is attached to the grappler bracket by means of four 000-120 brass screws, nuts, and washers. A three-point 0-80 screw mount to the bottom side permits a quasi-kinematic mounting of the readout assembly. The Nb foil is glued to the back side of the ceramic board, alleviating the CTE problems across the foil. The assembly process is shown in Figure 8.

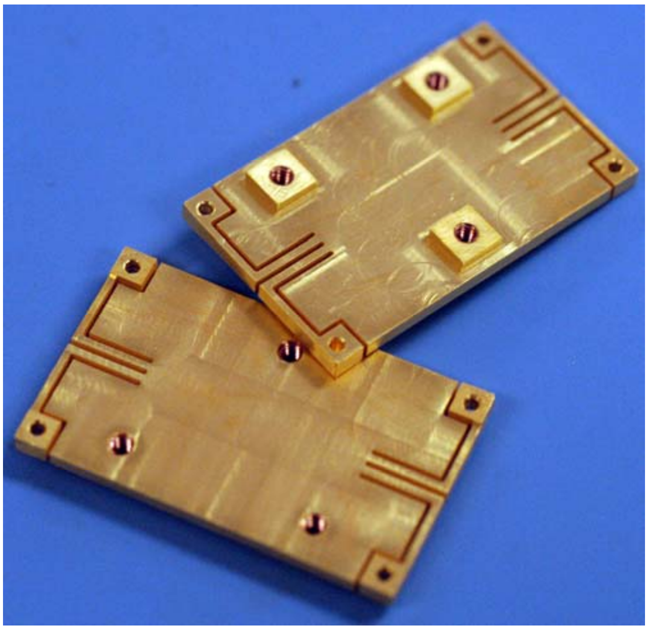

Figure 7. The grappler brackets are made from OFHC copper with wire EDM flexures, gold plated to provide good thermal contact to both the ceramic circuit board and the copper detector package box. Parts made by Zen Machine and Scientific Instrument [xxvi].

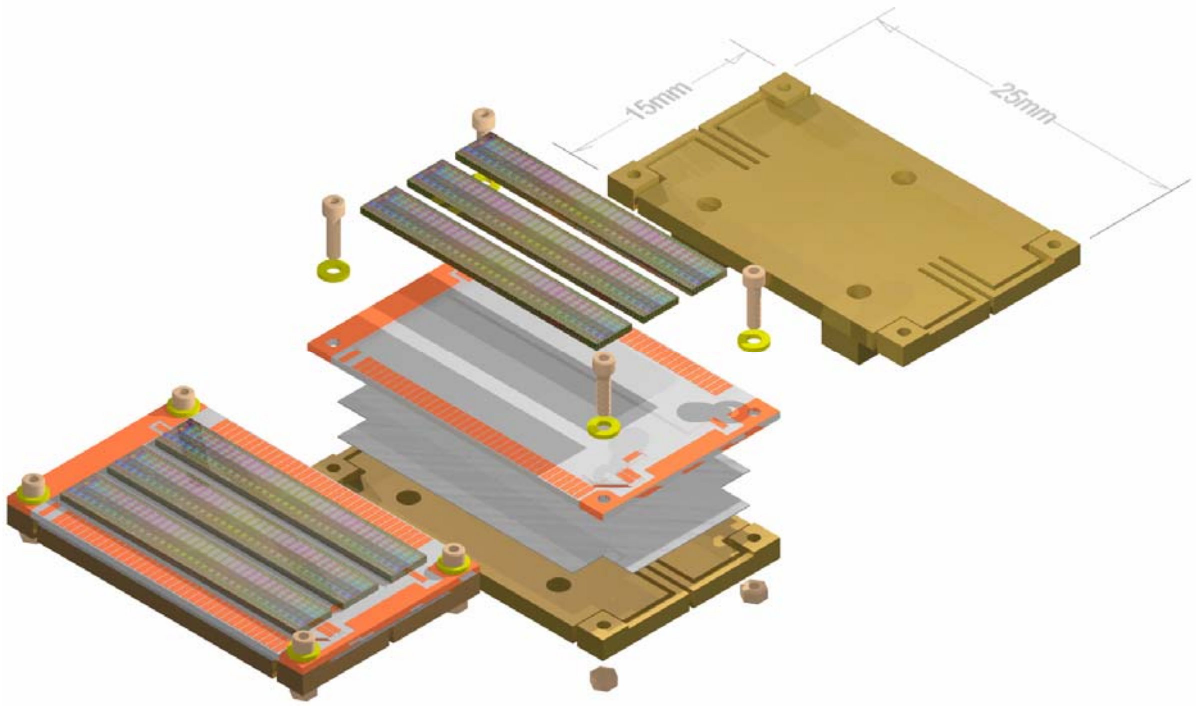

Figure 8. The assembly drawing of the readout circuit shows the parts described in the text.

VI. DETECTOR PACKAGE DESIGN

Our design for the GISMO 4×32 detector package incorporates several key elements that contribute to its proper function. It was designed for small overall volume (11.9 cm × 8.8 cm × 1.9 cm) and mass. Simple electrical connections were required for an easily mateable/demateable interface to the detectors and readouts. Robust thermal interfaces were necessary to enable heat sinking of the critical parts. We also needed to provide magnetic shielding at several levels and to maintain a light-tight package except for a window with a bandpass filter [xxiii], so that the environment inside the package would be free of both stray magnetic fields and stray light.

A. First Generation Package

The first generation GISMO detector package was used for an engineering observing run in November 2007 [viii]. For this package, we used small but readily available connectors for the electrical interface: microminiature D connectors with a dense footprint, with three connectors providing cable attachments to three 4K electronics boards. The detector package volume is to a certain extent determined by the connectors; they limit both the length and height of the overall package.

Magnetic shielding was accommodated by means of a niobium foil (see section 2.1), but augmented by an overall shield made of lead tape that was wrapped around the detector package after assembly. The entire cryostat is magnetically shielded with high permeability material [xxiv], and hence the superconducting shields should operate in a small magnetic field environment. Unfortunately, residual magnetic susceptibility was seen during the observing run; some pickup of the Earth's magnetic field was seen on all SQUID channels. The GISMO cryostat has a very large (~20cm) window with the detector package roughly one window diameter inside. It is most likely that magnetic flux penetrates far down into this region. In this case, flux trapping would occur when the insufficiently shielded Nb foil goes through its superconducting transition, leading to degraded performance from the SQUID amplifiers.

The three microminiature D connectors are a large fraction of the total heat capacity of the detector package, and additionally require large penetrations through the magnetic shielding. The second-generation package uses two Nanonics [xxv] connectors for the same wiring, reducing the volume of connectors by around an order of magnitude and shrinking the penetration area by a factor of several.

The detector array is mounted on a copper-plated alumina ceramic board that is epoxied to four flexure mounts built into the base of the copper detector package. The array is surrounded by a fiberglass circuit board with eight copper wiring layers, plated on both sides with bondable gold. The readout assemblies are glued to this board and are wirebonded to both it and the detector array. The array is heat sunk by means of many gold wire bonds to the upper layer of the fiberglass board, which is attached to a copper braid that penetrates the package and is used to provide direct cooling from the 300 mK ^{3}He cooling system to the detector package interior. An overall view of the completed detector package is shown in Figure 9 (with no lid) and Figure 10 (with lid, optical filter, and magnetic shielding applied).

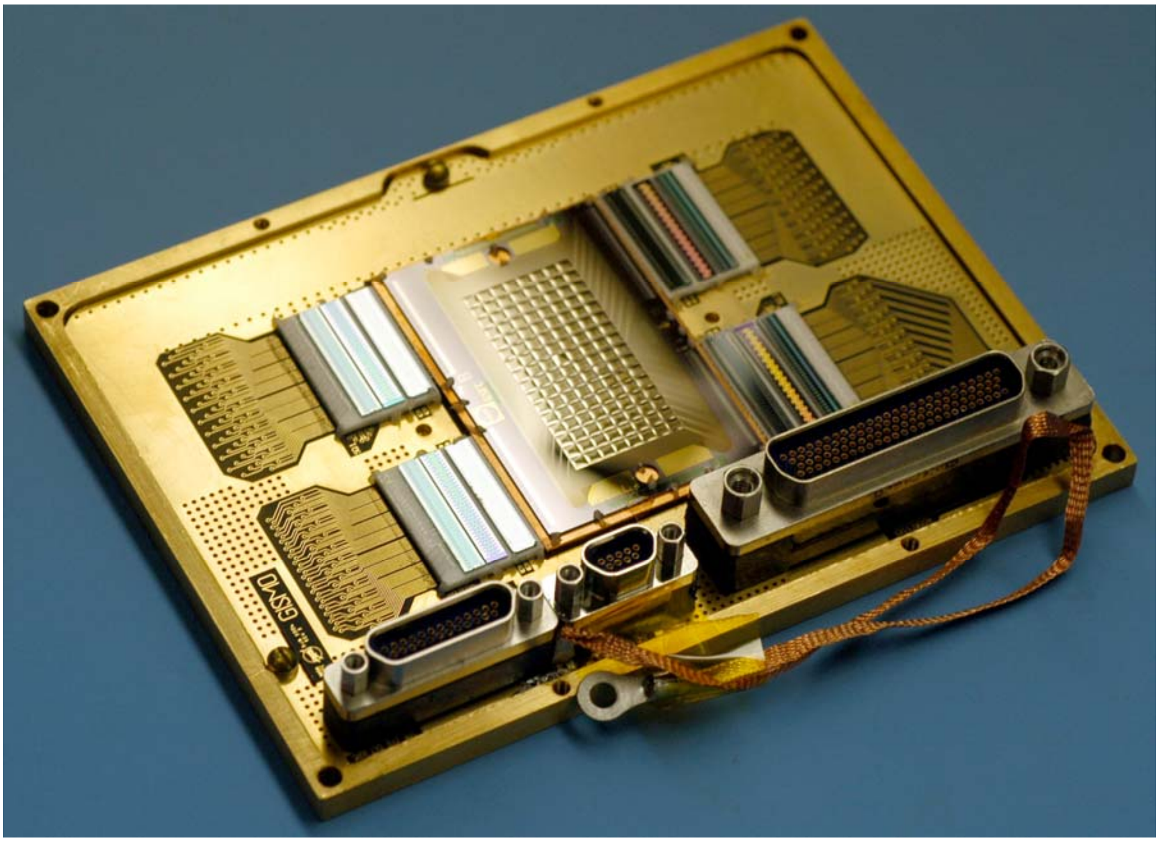

Figure 9. View of the first-generation detector package with the lid, filter, and magnetic shielding removed. The copper braid thermal connections are near the bottom; three connectors sit at the edge of the package; a gold-plated fiberglass circuit board handles the interconnections and holds the readouts.

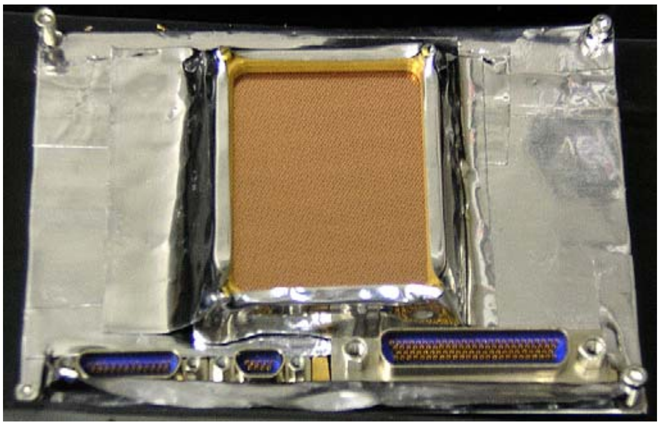

Figure 10. Completed first-generation detector package, showing the connectors, bandpass filter, and overall lead tape shielding.

B. Second Generation Package Design

Our second-generation detector package is designed to maintain most aspects of the interface while improving several aspects of its performance. The robust mechanical connection and heat sinking of the readout chips was discussed in Section V. This design reduces the overall surface area of the fiberglass board, which permits larger arrays to be mounted in the center. There is enough space to situate our prototype 32×40 detector arrays, which have a footprint of around 41×51 mm, easily within its 53×65 mm central space, with the extra area to be used by a suitably designed heat sinking ceramic board. As mentioned above, the connectors were changed to Nanonics type, which are much smaller. In the near future we plan on implementing superior stray light rejection by blackening the inside of the detector package lid, and superior magnetic field rejection by placing symmetric layers of Nb foil and Metglas [xxiv] on the top (where possible) and bottom surfaces. We have also made the detector array’s ceramic board screw-mounted onto flexures to permit more accurate and reliable attachment to the detector package base.

This package was fabricated by Zen Machine & Scientific Instrument [xxvi] and has been tested with a 128-pixel array in August 2008, for an expected observing run in the October 2008. A 1,280-pixel version will be produced following this. Pictures of the package design and assembly and several key components are shown below in Figure 11-15.

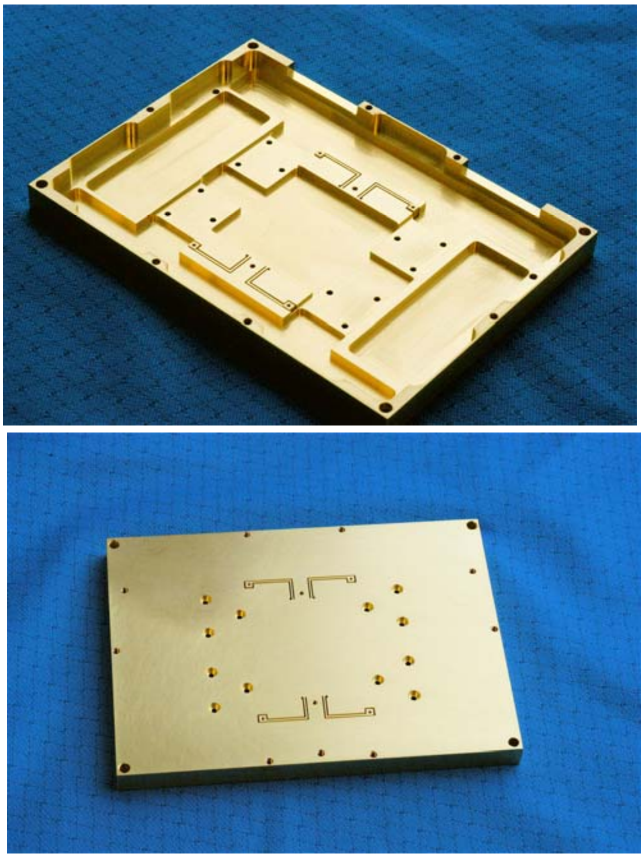

Figure 11. Second-generation detector package box base, as seen from the inside (top) and outside (bottom). Many internal features are lightweighting.

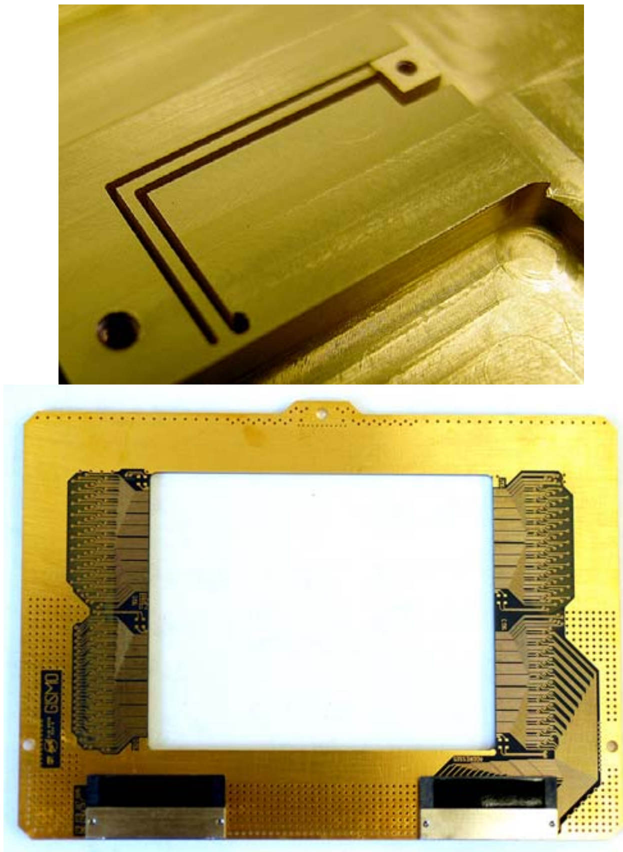

Figure 12. (Top) Close-up of a detector array flexure mount (1 of 4); (Bottom) Fiberglass circuit board with Nanonics connectors.

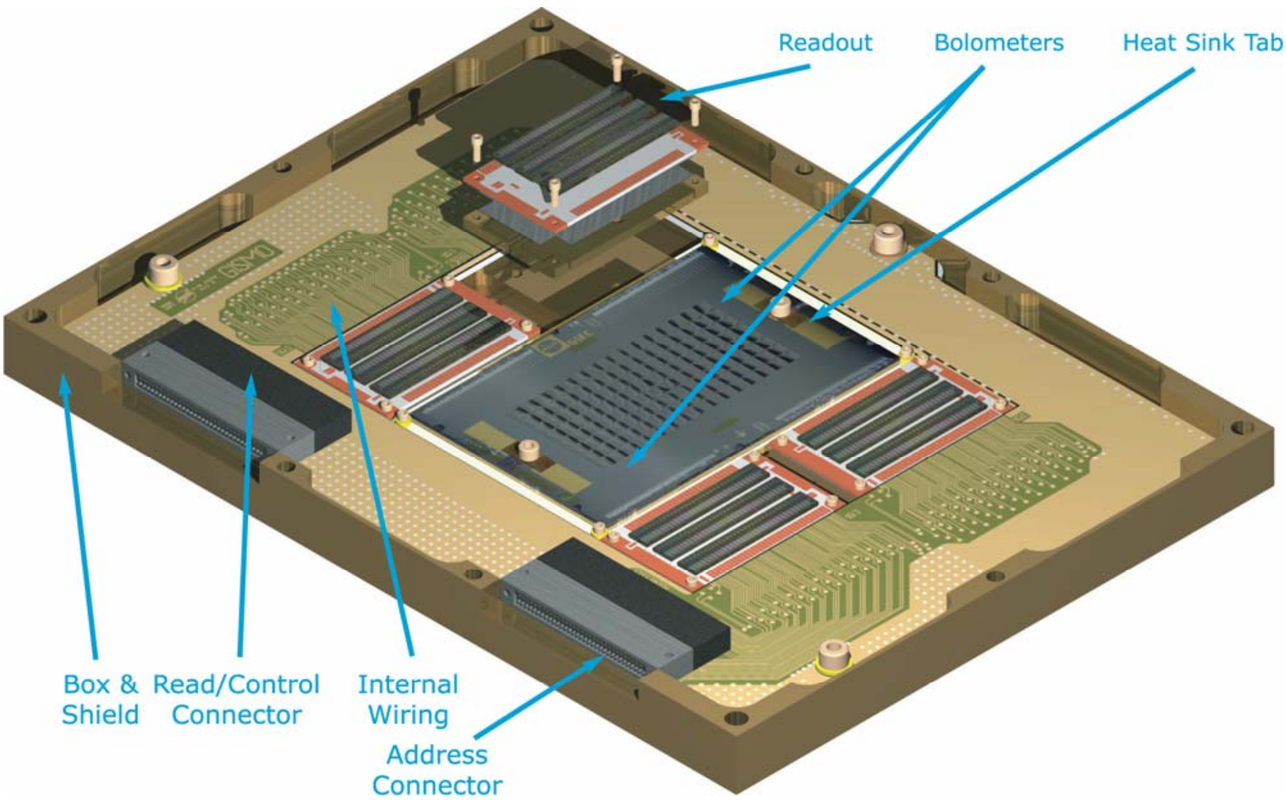

Figure 13. This rendered drawing shows the layout of each element in the detector package.

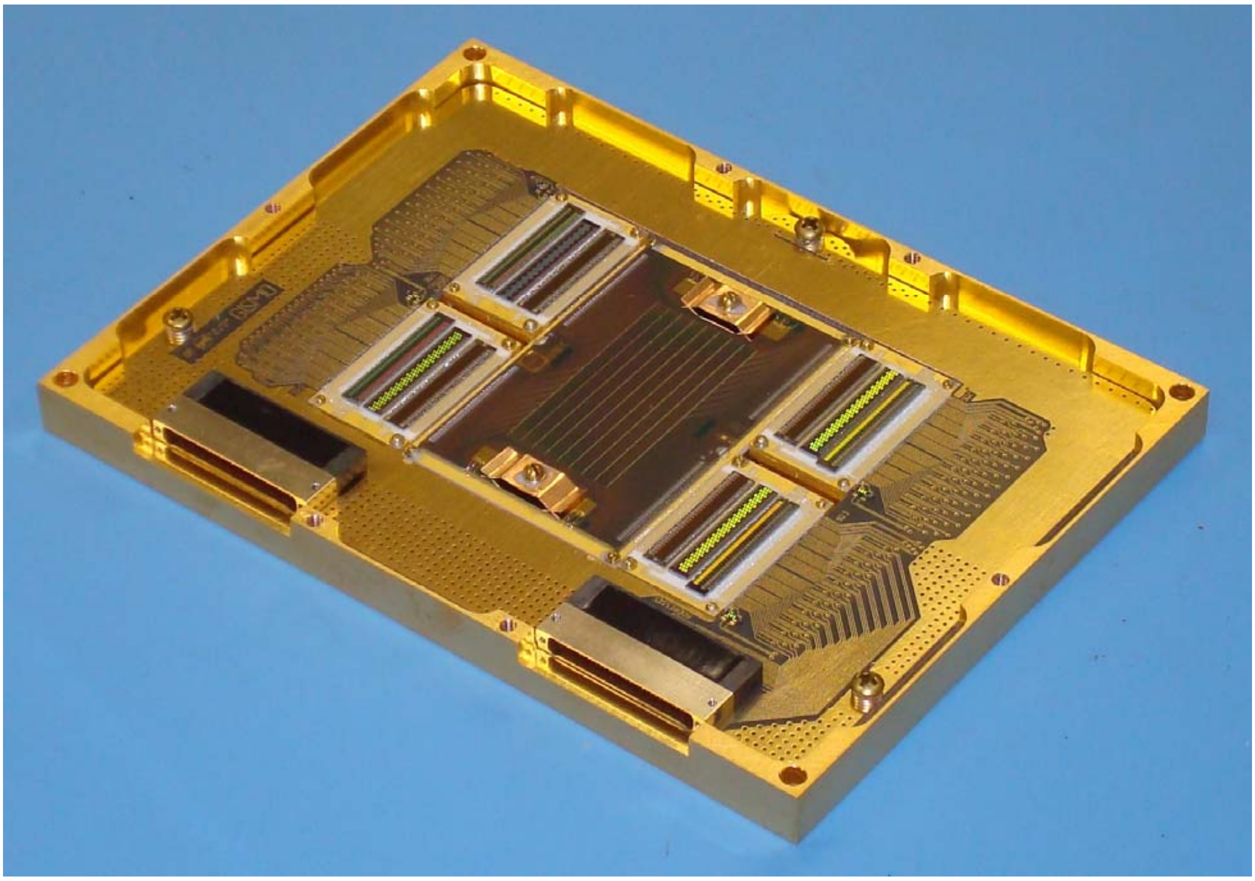

Figure 14. When completed, the detector package bears a strong resemblance to the design.

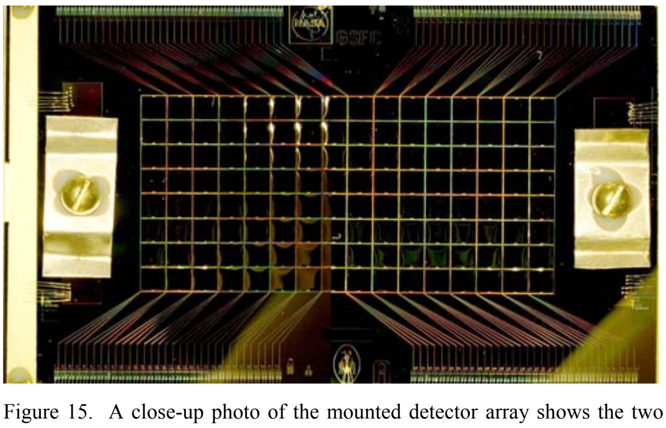

Figure 15. A close-up photo of the mounted detector array shows the two spring clips that hold the array in place, the aluminium TES connection bonds along the top and bottom edges, and the gold heat sink wirebonds at the left and right edges. A vertical seam is visible at the center where two photos were joined.

CONCLUSIONS

We have designed and constructed a package for low temperature superconducting bolometer arrays that performs several optical, thermal, mechanical, electronic, and magnetic roles. It has been successfully used in the GISMO 128-pixel camera for an observing run that yielded novel astronomical data. A second-generation package has been developed and is under construction to improve upon the design in ways meant to improve performance and enhance reliability. A third generation package is currently being worked out that will provide similar capability for arrays in formats up to 1,280 pixels.

ACKNOWLEDGMENTS

The authors thank Elmer Sharp, Carol Sappington, and Tim Miller for their significant contributions in the assembly of the detector packages, without which this paper could never have been written. Further thanks are due to Ed Wollack, George Voellmer, and Steve Snodgrass for useful discussions that helped improve the designs.

REFERENCES

[1] Voellmer, G. M., et al. 2003, Proc. SPIE #4855, pp.63-72; "Design and fabrication of two-dimensional semiconducting bolometer arrays for HAWC and SHARC-II"

[2] Irwin, K.D. 1995, Applied Physics Letters 66 (15), pp. 1998-2000; *"An application of electrothermal feedback for high resolution cryogenic particle detection"*

[3] Welty, R.P. & Martinis, J.M. 1993, IEEE Trans. On Applied Superconductivity 3 (1), pp.2605-2608; *"Two-stage integrated SQUID amplifier with series array output"*

[4] Chervenak, J.A., Irwin, K.D., Grossman, E.N., Martinis, J.M., Reintsema, C.D. & Huber, M.E. 1999, Applied Physics Letters 74 (26), pp.4043-4045; *"Superconducting Multiplexer for Arrays of Transition Edge Sensors"*

[5] Benford, D.J. et al. 2000, IJIMW 21 (12), pp. 1909-1916; *"Multiplexed Readout of Superconducting Bolometers"*

[6] Staguhn, J.G. et al. 2001, AIP Conference proceedings #605, "Low Temperature Detectors", F.S. Porter et al., eds., pp. 321-324; *"TES Detector Noise Limited Readout Using SQUID Multiplexers"*

[7] Staguhn, J.G., Moseley, S.H., Benford, D.J., Allen, C.A., Chervenak, J.A., Stevenson, T.R., & Hsieh, W.-T. 2004, Nuclear Instruments and Methods in Physics Research A, 520, pp.336-339; *"Approaching the fundamental noise limit in Mo/Au TES bolometers with transverse normal metal bars"*

[8] Staguhn, J.G., Benford, D.J., Allen, C.A., Maher, S.F., Sharp, E.H., Ames, T.J., Arendt, R.G., Chuss, D.T., Dwek, E., Fixsen, D.J., Miller, T.M., Moseley, S.H., Navarro, S., Sievers, A & Wollack, E.J. 2008, these proceedings; *"Instrument Performance of GISMO, a 2 Millimeter TES Bolometer Camera used at the IRAM 30 m Telescope"*

[9] Staguhn, J.G., Benford, D.J. Allen, C.A. Moseley, S.H., Sharp, E.H., Ames, T.J., Brunswig, W., Chuss, D.T., Dwek, E., Maher, S.F., Marx, C.T., Miller, T.M., Navarro, S. & Wollack, E.J. 2006, Proceedings of the SPIE, Volume 6275, pp. 62751D;*"GISMO: a 2-millimeter bolometer camera for the IRAM 30 m telescope"*

[10] Allen, C. A.; Benford, D. J.; Chervenak, J. A.; Chuss, D. T.; Miller, T. M.; Moseley, S. H.; Staguhn, J. G.; Wollack, E. J. 2006, Nuclear Instruments and Methods in Physics Research Section A, Volume 559, Issue 2, p. 522-524; *"Backshort-Under-Grid arrays for infrared astronomy"*

[11] Allen, Christine A.; Benford, Dominic J.; Miller, Timothy M.; Moseley, S. Harvey; Staguhn, Johannes G.; Wollack, Edward J. 2007, Infrared Spaceborne Remote Sensing and Instrumentation XV. Edited by Strojnik-Scholl, Marija. Proceedings of the SPIE, Volume 6678, pp. 667806; *"Technology developments toward large format long wavelength bolometer arrays"*

[12] Miller, T. M., Costen, N. & Allen, C. 2008, Journal of Low Temperature Physics v.151, pp. 483-488; *"Indium Hybridization of Large Format TES Bolometer Arrays to Readout Multiplexers for Far-Infrared Astronomy"*

[13] Benford, D.J., Staguhn J.G., Allen, C.A., Ames, T.J., Buchanan, E.D., Maher, S.F., Moseley, S.H., Sharp, E.H & Wollack, E.J. 2007, Proceedings of the 18th International Symposium on Space Terahertz Technology, pp. 82-87; *"Development of a Large Format Fully Sampled Bolometer Camera for 2 mm Wavelength"*

[14] Irwin, K.D., Audley, M.D., Beall, J.A., Beyer, J., Deiker, S., Doriese, W., Duncan, W., Hilton, G.C., Holland, W., Reintsema, C.D., Ullom, J.N., Vale, L.R. and Xu, Y. 2004, Nuclear Instruments and Methods in Physics Research Section A, Volume 520, Issue 1-3, p. 544-547; *"In-focal-plane SQUID multiplexer"*

[15] Irwin, K.D., Vale, L.R., Bergren, N.E., Deiker, S., Grossman, E.N., Hilton, G.C., Nam, S.W., Reintsema, C.D., Rudman, D.A. & Huber, M.E. 2002, AIP Conference Proceedings, Volume 605 (Ninth International Workshop on Low Temperature Detectors), pp. 301-304; *"Time-division SQUID multiplexers"*

[16] de Korte, P.A.J., Beyer, J., Deiker, S., Hilton, G.C., Irwin, K.D., Macintosh, M., Nam, S.W., Reintsema, C.D., Vale, L.R. & Huber, M.E. 2003, Review of Scientific Instruments, Volume 74, Issue 8, pp. 3807-3815; *"Time-division superconducting quantum interference device multiplexer for transition-edge sensors"*

[17] Reintsema, C.D., Beyer, J., Nam, S.W., Deiker, S., Hilton, G.C., Irwin, K., Martinis, J., Ullom, J., Vale, L.R. & Macintosh, M. 2003, Review of Scientific Instruments, Volume 74, Issue 10, pp. 4500-4508; *"Prototype system for superconducting quantum interference device multiplexing of large-format transition-edge sensor arrays"*

[18] Forgione, J.B., Benford, D.J., Buchanan, E.D., Moseley, S.H., Jr.; Rebar, J., & Shafer, R.A. 2004, Proceedings of the SPIE, Volume 5498 (Millimeter and Submillimeter Detectors for Astronomy II), pp. 784-795; *"Enhancements to a superconducting quantum interference device (SQUID) multiplexer readout and control system"*

[19] Benford, D.J., Dicker, S.R., Wollack, E.J., Supanich, M.P., Staguhn, J.G., Moseley, S.H., Jr., Irwin, K.D., Devlin, M.J., Chervenak, J.A. & Chen, T.C. 2004, Proceedings of the SPIE, Volume 5498 (Millimeter and Submillimeter Detectors for Astronomy II), pp. 208-219; *"A planar two-dimensional superconducting bolometer array for the Green Bank Telescope"*

[20] Benford, D.J. Staguhn, J.G., Ames, T.J., Allen, C.A., Chervenak, J.A., Kennedy, C.R., Lefranc, S., Maher, S.F., Moseley, S.H., Pajot, F., Rioux, C., Shafer, R.A. & Voellmer, G.M. 2006, Proceedings of the SPIE, Volume 6275 (Millimeter and Submillimeter Detectors and Instrumentation for Astronomy III), pp. 62751C; *"First astronomical images with a multiplexed superconducting bolometer array"*

[21] Staguhn, J.G., Allen, C.A., Benford, D.J., Chervenak, J.A., Chuss, D.T., Miller, T.M., Moseley, S.H. & Wollack, E.J. 2006, Nuc. Inst. & Methods in Phys. Research Section A, Volume 559 (2), pp. 545-547; *"Characterization of TES bolometers used in 2-dimensional Backshort-Under-Grid (BUG) arrays for far-infrared astronomy"*

[22] Emtron Hybrids Inc., 86 G Horseblock Rd. Yaphank, NY 11980 USA; +1 631.924.9668

[23] C. Lee, P.A. Ade & C.V. Haynes 1996, Proc. 30th ESLAB Symposium, ESA SP-388, p.81; *"Self-Supporting Filters for Compact Focal Plane Designs"*

[24] Metglas 2605 SA1; Metglas®, Inc., 440 Allied Drive, Conway, SC 29526; Tel: (800) 581-7654; Email: metglas@metglas.com; http://metglas.com/products/page5_1_2_4.htm

[25] Nanonics connectors of type STM065; Tyco Electronics; 1050 Westlakes Drive, Berwyn, PA 19312 USA; Tel: 610-893-9800; http://www.tycoelectronics.com/components/

[26] Zen Machine & Scientific Instrument, 1568 Steamboat Valley Rd., Lyons CO 80540-1658 USA; +1 303.823.5842

A Novel Thermal Detector for Far-Infrared and THZ imaging Arrays

Pekka Rantakari and Arttu Luukanen
Millimetre Wave Laboratory of Finland – MilliLab, Espoo, Finland
Steven Deiker, Lockheed Martin Solar and Astrophysics Laboratory, Palo Alto, U.S.A.

This paper reports on novel MEMS based thermal detector architecture, which could allow the construction of very large focal plane arrays of bolometers for far-infrared and THz imaging. The principal challenge in developing large format cryogenic bolometer arrays is related to the multiplexing and readout of cryogenic detectors. The readout architectures that are being developed and deployed are mostly based on Superconducting Quantum Interference Devices (SQUIDs), which are highly sensitive but also relatively complex devices and have shortcomings with respect to the robustness of SQUIDs for operation in nonideal condition.

The detector architecture presented here is based on the transition-edge sensor (TES), which is integrated on the surface of a freestanding micro electro mechanical (MEM) switch (Fig. 1). The key idea in this architecture is in thermal switching and in transformation of TES output to voltage pulses for faster detection and simpler multiplexing and readout of detectors.

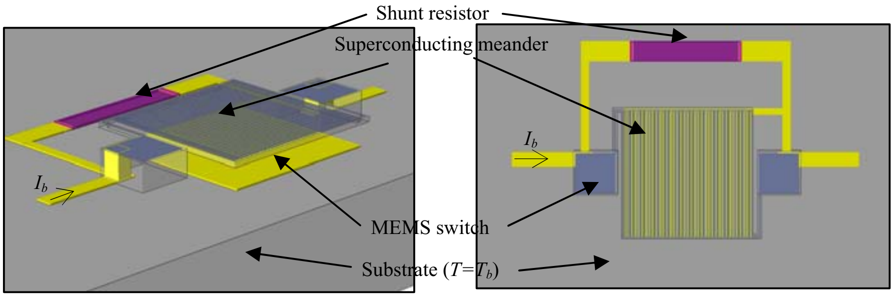

Fig.1 Schematic drawing of the novel thermal detector architecture. Transition-edge sensor, consisting of superconducting thin film meander, is integrated on top of the MEMS switch.

The TES on top of the MEMS switch is current biased slightly below its critical current. A shunt resistor is in parallel with the meander on the substrate. In the up-state of the MEMS switch, the TES is thermally well-isolated from the substrate at bath temperature of T_b. Incident optical power absorbed to the film increases the temperature of the TES with time. The critical current of the superconducting meander get decreased with increasing temperature and when reaching the value of the bias current I_b, the meander quenches and becomes dissipative causing voltage to build up across the meander and shunt resistor. This voltage is used for triggering the MEMS switch and when reaching the pull-in voltage of the switch, the switch closes and the thermal conductance between the TES and the substrate get increased causing a fast cool-down of the film. As the film cools near to the bath temperature, it returns back to the superconducting state and the voltage disappears releasing the MEMS switch and the new thermal integration cycle begins again. The frequency of the voltage pulses generated in the detector is proportional to the incident optical power and the array of detectors can be read out through common readout line by amplitude multiplexing of the pulses facilitated by the choice of shunt resistance values. Figure 2 shows simulated voltage and displacement responses of the detector at $T_b = 4K$ for incident optical power of 4 pW.

(a)

$$f_0(P_{opt}) = \frac{P_{opt}}{T_c C_{th}\left(1 - T_b/T_c - (I_b/I_{c0})^{2/3}\right)}$$

P_{opt} = incident optical power
C_{th} = the thermal capacitance of the detector
T_c = critical temperature of TES
T_b = bath temperature of the detector
I_{c0} = critical current density of thin film meander
I_b = bias current

(b)

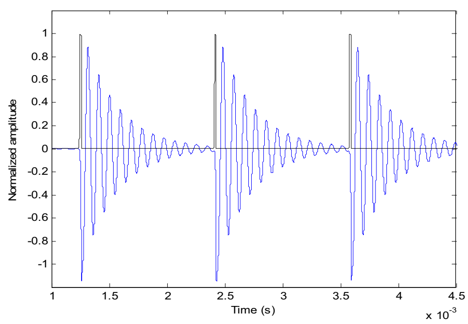

Fig. 2 The switching frequency of the detector with certain assumptions (a) and the simulated normalized voltage (solid line) and displacement (dodded line) of the MEMS based thermal detector (b).

In this paper, we will introduce the detector architecture and show the detector operation principle with analytical methods and with time domain simulations. Also, a noise model for the detector will be derived.

Design of Superconducting Terahertz Digicam

Hiroshi Matsuo[1], Yasunori Hibi[1], Hirohisa Nagata[2], Seiichiro Ariyoshi[3], Chiko Otani[3], Hirokazu Ikeda[2] and Mikio Fujiwara[4]

[1]*National Astronomical Observatory of Japan, Mitaka, Tokyo 181-8588, Japan*

[2]*Institute of Space and Astronautical Science, Sagamihara, Kanagawa 229-8510, Japan*

[3]*RIKEN, Sendai, Miyagi 980-0845, Japan*

[4]*National Institute of Information and Communications Technology, Koganei, Tokyo 184-8795, Japan*

* Contact: h.matsuo@nao.ac.jp, phone +81-422-34-3915

***Abstract*— Imaging array design for 650 GHz SIS photon detector array, which we call superconducting terahertz digital camera, is discussed. Focal plane optics and cryogenic readout electronics are two major topics for the array developments. Lens arrays are discussed to make high optical efficiency and compact focal plane assembly. Cryogenic readout electronics were designed and fabricated based on GaAs-JFET technologies. These designs are similar to CMOS digital camera, but operate at cryogenic temperature, and we can make use all the advantage of the digital camera technologies for the superconducting terahertz digicam.**

I. Introduction

Development of large format imaging array in terahertz frequencies are crucial for future space terahertz community for imaging large field of view with high dynamic range. Variety of imaging array techniques are employed in this field: transition edge sensor bolometers, kinetic inductance detectors, hot/cold electron bolometers and superconducting tunnel junction detectors [1].

We have been working on superconducting direct detectors with niobium tunnel junctions, the SIS photon detectors. The detectors have high dynamic range and fast response, and operate at higher temperature than bolometric detectors. But, there are some issues before we can apply the detector technology to future instrumentations. One is how to realize large format array with efficient focal plane optics and cryogenic readout electronics, others are how to improve sensitivity and wavelength coverage for low background space-born instrumentations.

In this paper we describe the design of focal plane optics for large format imaging array and integrated readout electronics for the superconductive imaging submillimeter-wave camera for 650 GHz observation.

II. Imaging Array Design

Our imaging array is based on submillimeter-wave SIS photon detectors which are a kind of tunnel junction detectors with their photo response due to the photon assisted tunnelling process [2]. Because the tunnel junction detectors are relatively high impedance detectors they can be readout using semiconductor readout circuits. Our plan is to implement two imaging array technologies of CMOS digital camera to our superconducting imaging arrays; lens array and semiconductor integrated circuits. Schematic diagram of the imaging array is shown in figure 1, which is similar to cryogenic infrared imaging array with CMOS integrating amplifier and multiplexer bonded to the detector array. Two major differences to the infrared arrays are that the input radiation is coupled to antenna behind each lens, and that the readout circuits operate at less than 1 K. Key parameters of the camera are listed in table I, which will be addressed into detail in the following sections; the detector, focal plane optics and readout electronics.

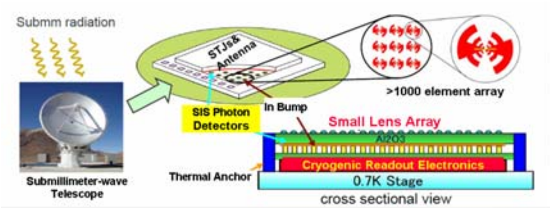

Fig.1. Schematic diagram of the superconducting terahertz digicam [3].

TABLE VII
KEY PARAMETERS OF THE DIGICAM

Detectors	SIS photon detectors at 650 GHz
Focal Plane Optics	Hexagonal lens array with 1.0 Fλ spacing 1027 pixels ϕ37 mm FPA at F2.0 focus
Readout Electronics	GaAs-JFET CTIA at < 1.0 K Multiplexed Readout Low noise < 1 μV/√Hz @ 1H Low power dissipation < 10 μW/ch

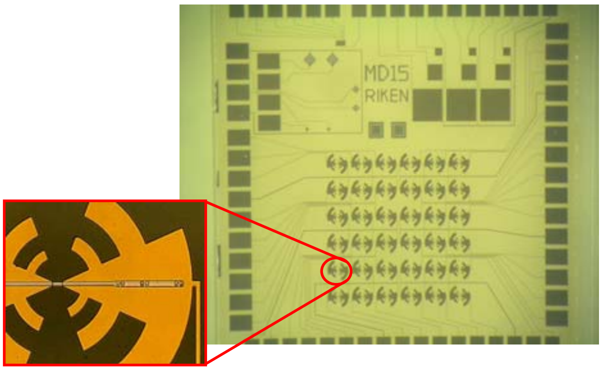

Fig.2. 36-element 650 GHz SIS photon detectors on 5mm x 5mm sapphire substrate [5].

A. *SIS Photon Detectors*

The SIS photon detectors are antenna coupled superconducting tunnel junction direct detectors based on photon assisted tunnelling process. Their operational frequency is below the superconducting energy gap, which is same as the SIS mixer. Since the SIS photon detectors are quantum detectors, their response is much faster and their dynamic range is higher that bolometric detectors. The detector performance is limited by the leakage current of the tunnel junctions. Sensitivity and noise of SIS photon detector is expressed by the following equations [4]:

$$S = \eta \cdot \frac{e}{h\nu} \quad \text{[A/W]}$$

$$N = \sqrt{2eI_0} \quad [\text{A}/\sqrt{\text{Hz}}]$$

$$NEP = N/S = \frac{h\nu}{\eta} \cdot \sqrt{\frac{2I_0}{e}} \quad [\text{W}/\sqrt{\text{Hz}}]$$

where η is quantum efficiency, ν is frequency and I_0 is the leakage current. Current performance of submillimeter-wave SIS photon detector is limited by leakage current of about 100 pA and quantum efficiency of about 20%, which result in NEP of about 10^{-16} W/Hz$^{0.5}$ at 650GHz. Our goal is realize leakage current of less than 10 fA and NEP of less than 10^{-19} W/Hz$^{0.5}$ for future space-born instrumentations.

Figure 2 shows the 36-element array of SIS photon detectors fabricated in RIKEN that operates at 650 GHz with 10% bandwidth [5]. One detector element consists of log-periodic antenna and a series of 6-element distributed parallel junctions, totally 12 tunnel junctions on one detector element which forms matching circuits for 650 GHz input radiation.

Table II summarizes the performance of SIS photon detectors [6]. It is characterized as large voltage response detector with short time constant and large dynamic range. When the detector temperature is higher than 0.7 K, their performance is limited by the thermally excited quasi-particle current, but have good performance even at 4.2 K compared to bolometers operating at the same temperature [2]. If their leakage current further decreased down to 0.5 K following the BCS theory, leakage current of 10 fA would give NEP of 10^{-19} W/Hz$^{0.5}$.

TABLE VIII
PERFORMANCE OF SIS PHOTON DETECTORS AT 650 GHZ

NEP	10^{-16} W/Hz$^{0.5}$
Temperature	< 0.7 K
Voltage Response	10^{9}
Time Constant	<< 10^{-3} second
Dynamic Range	> 10^{7}
Limit of NEP	Leakage current

Before implementing multiplexed readout circuit for SIS photon detectors, we have confirmed operation of a detector with an integrating amplifier [7]. For this experiment we used conventional operational amplifier at room temperature to make resistive or capacitive trans-impedance amplifier (TIA or CTIA). Figure 3 shows the I-V characteristics measured with TIA and output signal from CTIA under background illumination from 300 K and 77 K blackbody, respectively. From the experiment we have found that stable operation of SIS photon detector is realized when feedback amplifier gain is more than 2000.

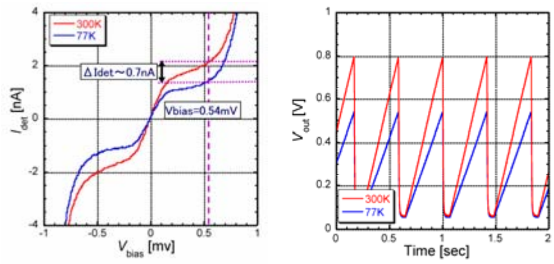

Fig. 3. (left) I-V characteristics of an SIS photon detector under radiation input from 300 K and 77 K blackbody source. (right) Signal output from integrating amplifier under the same radiation conditions [7].

B. *Focal Plane Optics Design*

High efficiency and compact focal plane optics is important for the large format array design. First we discuss briefly on the figure of merit of focal plane optics and then show possible design to install a large format array of SIS photon detectors in a compact cryostat.

There are two obvious approaches for focal plane optics design, one is optical design approach and another is microwave approach. Thin film absorber is commonly used for bolometric detectors and often used in a small cavity or with multi-mode waveguides connected to a conical horn or a Winston cone. This could be a combination of microwave horn technologies and optical thin film technologies, which has been used extensively for semiconductor bolometers. Filled array with thin film absorber is another approach often used for TES bolometers such as SCUBA-2 [8] and ones made in NASA GSFC [9]. In this design, pixel spacing of half beam width or Nyquist sampling is adopted. The filled array is like CCD, for which incoming radiation from any angle of incidence is absorbed. Other approaches use thin film antennas with lens or without lens. In this approach, distributed antenna array [10] or quasi-optical technology [11] is adopted, where Gaussian beam mode analysis is often used to achieve high beam-mode coupling to telescope optics.

To compare the different focal plane optics design, the following figures of merits are discussed: 1) focal plane coverage, 2) number of pixels, 3) beam efficiency, 4) size of focal plane. Table III lists some of the parameters to show the characteristics of different focal plane optics design.

The focal plane coverage means the efficiency of focal plane usage or the ratio of detected radiation and total radiation from telescope aperture within field of view of the array. Horn array results in small coverage because the horn aperture size limits the spacing between pixels. Other planar structure can cover most of the focal plane area in principle. The number of pixels is the required number of detectors to cover the focal plane normalized by focal plane area divided by half power beam area. For the horn array number of pixels is limited by the focal plane coverage. For filled array, Nyquist sampling is preferred and four times larger number of pixels is required than the full sampling arrays. Beam efficiency means the coupling efficiency of one detector element to telescope optics. Horn arrays have high beam efficiency, but filled array have low efficiency due to large side lobe which should be terminated by cold stop inside a cryostat. Size of arrays is also dependent on re-imaging optics. Horn array tend to have longer focal length and the array size becomes larger. On the other hand, filled arrays prefer small sizes for better optical coupling and smaller absorber volume. The distributed antenna and lens arrays with full beam sampling design could achieve high focal plane coverage with smaller number of pixels compared to the filled array design.

TABLE IX
COMPARISON OF FOCAL PLANE OPTICS DESIGN

	Horn array	Filled array	Antenna array	Lens array
Focal plane coverage	20-30%	~100 %	80-100%	80-100%
Number of pixels	0.2-0.3	4	0.8-1	0.8-1
Beam efficiency	high	low	medium	medium
Size of array	large	small	medium	medium

From the above consideration, distributed antenna array or lens array seems to be a good compromise for optical performance and number of pixels required. In this paper we propose to use lens array for the imaging array. The lens array is designed using Al_2O_3 ceramic lens with low absorption coefficient and large index of refraction. We are going to use planar antennas at focus of each lens. In front of the lens, incoming beams are overlapped at -3dB at lens edges and each lenses focus the beams onto planar antennas at the backside of the lens array. Figure 4 shows the ZEMAX calculation of beams inside the 0.4-K cryostat for ASTE. Fore-optics and the cryostat is the same as in reference [4]. Aberration within the 7 arcmin field-of-view is within the Airy radius. The lens diameter and thickness are both 1 mm. Lenses are placed in a hexagonal pattern to make the distance between beams as small as possible. With this configuration the array would cover the

6.8 arcmin field-of-view with 1027 detectors, which correspond to the physical size of 37 mm in diameter at F2 focal plane of 10-m diameter telescope.

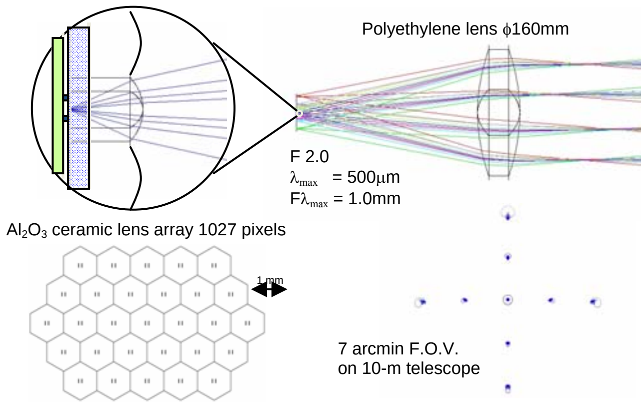

Fig.4. (top) Focal plane optics design with lens array at focal plane. SIS photon detectors are at the backside of sapphire substrate with planar antenna such as double-slot antennas. (bottom) Front view of the hexagonal lens array and spot diagram calculation within a field of view of 7 arcminues on 10-m diameter telescope.

III. Cryogenic Readout Electronics

The cryogenic readout electronics is based on junction field effect transistor of gallium arsenide semiconductors (GaAs-JFETs). First we explain the property of SONY GaAs-JFETs and then describe the design and recent measurement results of cryogenic readout electronics both analogue and digital circuits for the superconducting terahertz digicam.

A. GaAs-JFETs

GaAs-JFETs have good I-V and noise characteristics at cryogenic temperature [12]. We have been working on SONY GaAs-JFETs at cryogenic temperature below 4.2 K that show identical performance even down to 0.3 K [13]. Figure 5 shows I-V characteristics and noise spectrum of a depletion-type GaAs-JFET.

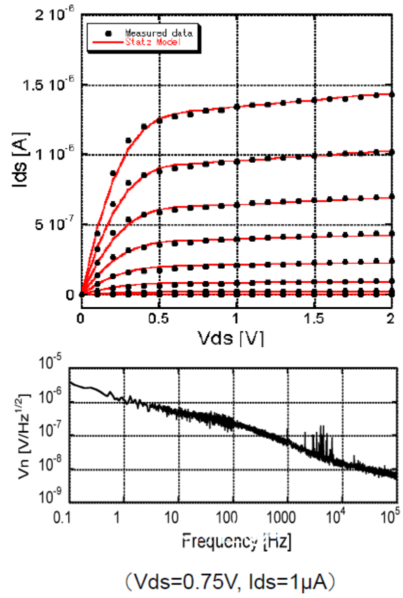

Fig.5. I-V characteristics and noise performance of SONY GaAs-JFET (W/L=5/50um) at 4.2K. A Statz model well fits to the I-V characteristics [7].

The I-V curve show a good fit to a standard Statz model, which makes the design of circuits very flexible and low power dissipation circuits can be designed relatively easily. They show no hysteretic or kink behavior like silicon MOSFETs. Unlike GaAs-MESFETs, the gate leakage current of p-n junction of GaAs-JFET is extremely low and also have low noise performance [14]. The SONY GaAs-JFETs show gate leakage current of an order of 10^{-19} A, and low voltage noise of less than 1 $\mu V/Hz^{0.5}$ at 1Hz were measured. We can design integrated circuits both with depletion and enhancement type JFETs on the same wafer, so we can control DC offset of amplifier and normal state of switching circuits. The flexible circuit design also serves to lower the power dissipation.

B. Design of CTIA amplifiers

The analogue electronics for the imaging array is based on ac-coupled capacitive trans-impedance amplifier (AC-CTIA). We decided to use AC-CTIA because of the following reasons: 1) SIS photon detectors are low current and high impedance device, 2) SIS photon detectors require low and constant bias voltage of about 1 mV, 3) output signal should be multiplexed. Figure 6 shows the schematic diagram of the readout electronics. It is composed of AC-CTIAs, sample-and-holds, a multiplexer and shift registers.

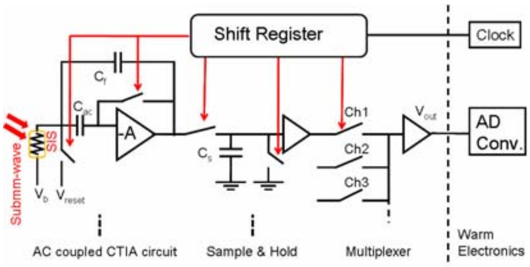

Fig.6. Schematic diagram of the cryogenic readout electronics [3].

Bias voltage of SIS photon detector is kept constant at V_b by the feedback amplifier and quasi-particle current is integrated on feedback capacitor (C_f). Because of relatively large offset voltage of GaAs-JFET and small voltage bias to the detector of about 1 mV, the amplifier is ac-coupled (C_{ac}) to cancel the offset voltage. The AC-CTIA amplifier is followed by a sample-and-hold circuit and a multiplexer that is addressed by a shift register. Full explanation of the analogue integrated circuits are given by Nagata et al. [15].

We have designed high gain amplifier circuits and fabrication of test circuits is made using a standard GaAs-JFET process by SONY. Figure 7 shows one of the test circuits; a cascode active-load amplifier with differential input and output source follower. The measured gain of the amplifier was 170, power dissipation was 4 μW, input referred noise 8 $\mu V_{rms}/Hz^{0.5}$ at 1Hz, and output voltage swing 0.8 $V_{p\text{-}p}$. Since input stage FETs are enhancement type in this circuit, the noise tend to be larger than the depletion type FETs.

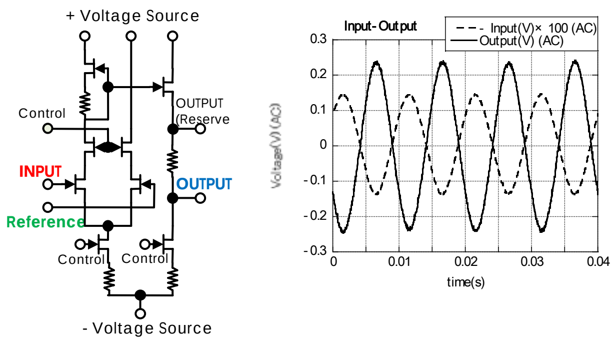

Fig.7. Demonstration of GaAs-JFET single stage amplifier with gain of about 200.

Circuit design of one of the ac-coupled CTIA amplifiers is shown in figure 8. FETA is an enhancement type JFETs and the other FETs are depletion types. The gate sizes of these FETs are W(μm)/L(μm)=5/5, 5/10, 5/50 5/100 for both FETA and B, FETC, FETD, and FETE. CTIAs with other combinations of the GaAs-JFETs are also designed and fabricated. The resistance of Ra, Rb, Rc, and Rd are 2 MΩ, 1 MΩ, 200 kΩ, and 300 kΩ, respectively. Capacitance for C_{ac} and C_f are 20 pF and 10 pF. A resistor, R, and capacitor, C, series placed in parallel with FETD is a phase compensation circuit. The resistance R is 30 kΩ, and the capacitance C is selectable from 2 pF to 20 pF because we have only upper limit values of stray capacitances for the GaAs-JFETs (gate-drain, drain-source, and gate source capacitance).

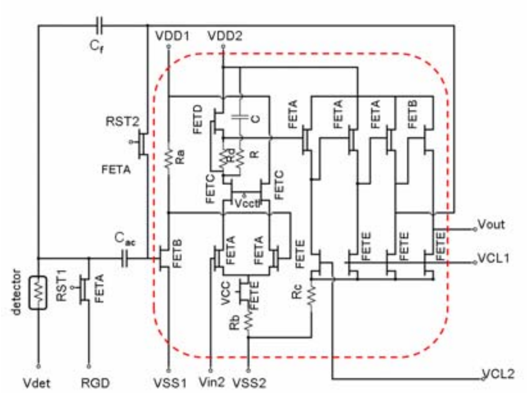

Fig.8. Circuit diagram of AC-CTIA circuits. The area covered by the dashed line is high gain amplifier with gain of more than 2000, that is composed of two stage amplifiers with output level shift source followers. FETAs are enhancement-type and others are depletion-type [15].

PSPICE simulations have shown that open loop gain is more than 2000, the gain bandwidth product of the amplifier is around 250 kHz, voltage swing is 0.5 V, and power consumption is 1.4 μW.

C. *Design of Digital Circuits*

To decrease the number of readout cables, we designed multiplexer circuit made of sample-and-hold and a multiplexer that are addressed by shift registers operating at the same detector temperature. GaAs-JFETs have good switching performance at low current region, which is advantageous for various switching elements in readout electronics. Accompanied with low gate capacitance of GaAs-JFETs, we can operate GaAs-JFET circuit much faster than silicon MOSFET circuits.

The digital circuit is based on direct-coupled FET logic (DCFL). Since we can use depletion and enhancement type FETs on the same wafers, we used depletion-type FETs (DFET) as current sources and enhancement-type (EFET) as switches to make various logic circuits with low power dissipation. We designed with the DCFL logic level of 0 V (low) and 1 V (high) and source current of 0.12 μA. Figure 9 shows the switching characteristics of the NAND and NOR gates. From the figure, we estimated the voltage margin for our DCFL circuits are more than 0.3 V. This voltage margin is large enough compared to the variation in threshold voltage of GaAs-JFETs.

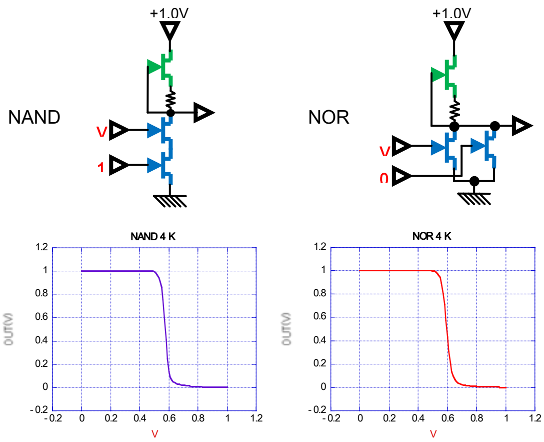

Fig.9. (top) NAND and NOR gates of GaAs-JFET DCFL circuits. DFET as current source and two EFETs for switch for both NAND and NOR gates. (bottom) Input and output voltages of NAND and NOR gates at 4 K. Voltage margin for logic gates are larger than 0.3 V [3].

Figure 10 shows a circuit of a master-slave type flip-flop using NAND gates. Combination of NAND gates is advantageous for low power operation of the circuit. Using 4 flip-flop circuits, we have designed a 4-channel shift register, which can be used to address 4 detector pixels in series.

We have confirmed basic operation of analogue and digital circuits and designed all the cryogenic readout components using n-type GaAs-JFETs only. Based on these experiments and simulations, we now have designed and fabricated 4-channel AC-CTIA amplifiers, 8 channel sample-and-hold circuits and 2 sets of 4 channel shift registers on each chips for evaluation. We are going to measure operation of shift registers, measure their speed and combine with sample-and-hold and multiplexers to make a readout circuits for the imaging array.

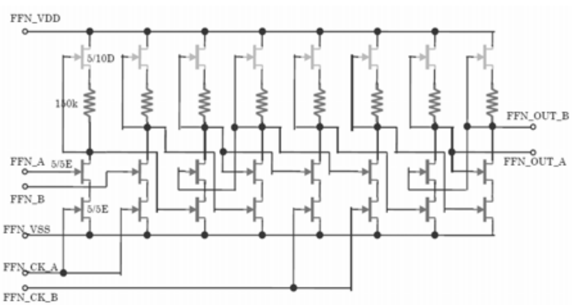

Fig.10. Circuit diagram for a master-slave type flip-flop circuit with NAND gates. Series connection of this flip-flop circuit is used for a shift register. [3]

Although details of clock timing and addressing scheme are not decided yet, we can use similar schemes to CMOS camera or infrared imaging arrays as shown in figure 11, where much larger arrays have been operational and we can use all the developed technologies of the readout electronics.

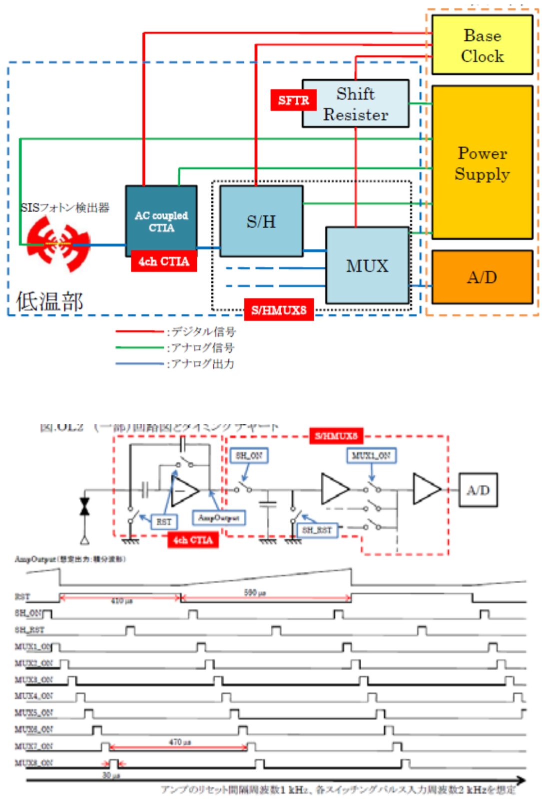

Fig.11. (top) Block diagram of readout electronics of the imaging array. This readout scheme is much like CMOS optical imager except that all analogue and digital electronics operate at cryogenic temperature at less than 1 K. Interface to the room temperature electronics are clock, power supply and a signal line to an A/D converter. (bottom) Timing diagram for 8 channel readout circuit.

.

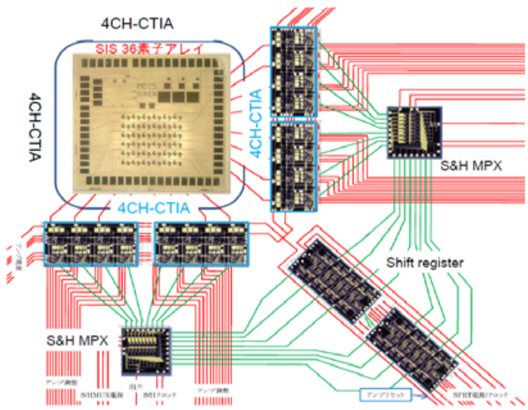

Fig.12. Configuration of SIS photon detectors and readout electronics when all the test circuits are combined together. Size of the each test chips are either 1.9 mm square or 1.9 mm by 3.8 mm, with total size of less than 20 mm square [15].

Figure 12 shows possible configuration of hybrid readout circuit when all test chips are connected together to make 16-channel cryogenic readout electronics. We still have large number of power supply lines for tuning each amplifier, but most lines can be in common

CONCLUSIONS

In this paper we discussed two major topics to realize large format arrays of submillimeter-wave SIS photon detectors; focal plane optics and cryogenic readout electronics.

Focal plane optics is important to define the size of the system (number of pixel, pixel separation, cryogenic optics and beam quality), so trade-off between different technologies is important. Compact lens array is discussed in this paper to make efficient focal plane sampling with smaller number of detectors, which is sensible when number of detector and field of view are limited.

Our readout electronics is based on integrating amplifiers with semiconductor device that is identical to infrared imaging arrays, and implementation of readout circuits are straight forward up to 1-k pixel arrays. For larger format arrays and for space-born applications, further development to decrease power consumption of readout electronics or low thermal conductivity interconnect between detector and readout electronics becomes important. When pair-breaking detector in far-infrared region is demonstrated, application fields of superconducting direct detectors will grow including far-infrared space-born instrumentations and various application fields of terahertz technologies.

ACKNOWLEDGMENT

This work was supported by the Grant-in-Aid for the Scientific Research from the Japan Society for the Promotion of Science (No. 18206042).

REFERENCES

[1] Zmuidzinas, J. and Richards, P.L., "Superconducting Detectors and Mixers for Millimeter and Submillimeter Astrophysics," Proc. of IEEE, 92, 1597-1616 (2004).

[2] Matsuo, H., Nagata, H., Mori, Y., Kobayashi, J., Okaniwa, T., Yamakura, T., Otani, C., Ariyoshi, S., "Performance of SIS photon detectors for superconductive imaging submillimeter-wave camera (SISCAM)", Proc. SPIE 6275, 627504 (2006).

[3] Matsuo, H., Hibi, Y., Nakahashi, M., Murakoshi, Y., Arai, H., Ariyoshi, S., Otani, C., Ikeda, H., Fujiwara, M., "System design of submillimeter-wave imaging array SISCAM", Proc. SPIE 7020, 702015 (2008).

[4] Matsuo, H., Ariyoshi, S., Otani, C., Ezawa, H., Kobayashi, J., Mori, Y., Nagata, H., Shimizu, H.M., Fujiwara, M., Akiba, M., Hosako, I., "Design of wide-field submillimeter-wave camera using SIS photon detectors", SPIE 5498, 371-380 (2004).

[5] Ariyoshi, S., Otani, C., Dobroiu, A., Sato, H., Kawase, K., Shimizu, H.M., Taino, T., Matsuo, H., "Terahertz imaging with a direct detector based on superconducting tunnel junctions", Appl. Phys. Lett. 88, 203503 (2006).

[6] Ariyoshi, S., Matsuo, H., Otani, C., Sato, H., Shimizu, H.M., Kawase, K., Noguchi, T., "Characterization of an STJ-Based Direct Detector of Submillimeter Wave", IEEE Trans. Applied Supercond.14, 920-923 (2005).

[7] Nagata, H., Kobayashi, J., Matsuo, H., Fujiwara, M., "Progress on GaAs cryogenic readout circuits for SISCAM", SPIE 6275, 627527 (2006).

[8] Woodcraft, A.L. et al., "Characterization of a prototype SCUBA-2 1280-pixel submillimetre superconducting bolometer array", SPIE 6275, 62751F (2006).

[9] Allen, C.A., Abraham, J., Benford, D.J., Chervenak, J.A., Chuss, D.T., Staguhn, J.G., Miller, T.M., Moseley, S.H. Wallack, E.J., "Far infrared through millimeter backshort-under-grid arrays", SPIE 6275, 62750B (2006).

[10] Day, P.K., LeDuc, H.G., Lee, R.A.M., Dowell, C.D., Zmuidzinas, J., "Distributed antenna-coupled transition edge sensors", SPIE 6275, 62751R (2006).

[11] Myers, M.J., Arnold, K., Ade, P., Engargiola, G., Holzapfel, W., Lee, A.T., Meng, X., O'Brient, R., Richards, P.L., Spieler, H., Tran, H.T., "Antenna-Coupled Bolometer Arrays for Measurement of the Cosmic Microwave Background Polarization", J. Low Temp. Phys. 151, 464-470 (2008).

[12] Fujiwara, M., Sasaki, M., Akiba, M., "Reduction method for low-frequency noise of GaAs junction field-effect transistor at a cryogenic temperature", Appl. Phys. Lett. 80, 1844-1846 (2002)

[13] Nagata, H., Kobayashi, J., Matsuo, H., Nakahashi, M., Kobayashi, K., Ikeda, H., Fujiwara, M., "Fabrication of cryogenic readout circuits with n-type GaAs-JFETs for low temperature detectors", J. Low Temp. Phys. 151, 1022-1027 (2008).

[14] Fujiwara, M., Sasaki, M., "Performance of GaAs JFET at a cryogenic temperature for application to readout circuit of high-impedance detectors", IEEE Trans. Electron. Devices 51, 2042-2047 (2004).

[15] Nagata, H., Kobayashi, J., Matsuo, H., Hibi, Y., Nakahashi, M., Ikeda, H., Fujiwara, M., "Development of cryogenic GaAs AC-coupled CTIA readout for far-infrared and submillimeter detectors", SPIE 7020, 70202Q (2008).

Recent work on a 600 pixel 4-band microwave kinetic inductance detector (MKID) for the Caltech Submillimeter Observatory

O. Noroozian[1], P. Day[2], M. Ferry[1], J.-S. Gao[1], J. Glenn[3], S. Golwala[1], S. Kumar[1], H. LeDuc[2], B. Mazin[2], H. T. Nguyen[2], J. Schlaerth[3], J. E. Vaillancourt[1], A. Vayonakis[1], J. Zmuidzinas[1]
[1]California Institute of Technology, [2]Jet Propulsion Laboratory, [3]University of Colorado

We report recent progress on a ~600 spatial pixel 4-band (750, 850, 1100, 1300 microns) camera (MKIDCam) for the Caltech Submillimeter Observatory (CSO). This work is based on extensive previous work on a 16 pixel 2-color demonstration camera tested at the CSO (see poster by A. Vayonakis et al.).

Our camera focal plane will make use of three novel technologies: Microwave kinetic inductance detectors (MKID), photolithographic phased array antennae, and on-chip band-pass filters. An MKID is a highly multiplexable photon detector that uses the change in surface impedance of a superconducting quarter-wave coplanar-waveguide (CPW) resonator to detect light. The resonator is weakly coupled to a CPW feed line. The amplitude and phase of a microwave probe signal (at the resonance frequency) transmitted on the feed line past the resonator changes as photons break cooper pairs. Hundreds to thousands of resonators tuned to slightly different frequencies may be coupled to a single feed line resulting in an elegant multiplexing scheme to read out a large array. Our phased array antenna design obviates beam-defining feed horns. On-chip band-pass filters eliminate band-defining metal-mesh filters. Together, the antennae and filters enable each spatial pixel to observe in all four bands simultaneously. Due to the large number of pixels the step and repeat capability of our photolithography system will be used to reduce the number of required masks and the field size in the fabrication process.

In order to reduce frequency noise due to fluctuations in the dielectric constant of the substrate, we are exploring new resonator designs that use interdigitated capacitors to lower electric field concentrations around the resonator lines.

Readout will be done with software-defined radio and will use microwave IQ modulation which has been demonstrated at the CSO. We are working on the implementation of an improved design using sixteen X5-400M commercial FPGA boards operating at room temperature.

Thermal characterization and noise measurement of NbSi TES for future space experiments

Y. Atik [1,2,*], F. Pajot [1], C. Evesque [1], B. Leriche [1], M. Chaigneau [1], B. Bêlier [2], L. Dumoulin [3],L. Bergé [3], M. Piat [4], E. Bréelle [4], D. Prêle [4], F. Voisin [4], G. Sou [5], G. Klisnick [5], M. Redon [5]

[1] *CNRS-IAS Bât. 121, Université Paris Sud-11, 91405 Orsay, France*

[2] *CNRS-IEF Bât. 220, Université Paris Sud-11, 91405 Orsay, France*

[3] *CNRS-CSNSM Bât 104, Université Paris Sud-11, 91405 Orsay, France*

[4] *CNRS-APC 10 rue Alice Domon et Léonie Duquet, 75205 Paris, France*

[5] *L2E UPMC Site "Raphael" BC 252 3 rue Galilée, 94200 Ivry-sur-Seine, France*

* Contact: youssef.atik@ias.u-psud.fr, phone +33-1-6985 8555

Abstract— **The principal observational demonstration of the theory of the Big Bang, the cosmic microwave background (CMB), has its maximum of intensity to the millimeter-length wavelengths. Instrumental progress allowed the development of bolometric detectors adapted to these wavelengths. Superconducting transition-edge sensors (TESs) are currentlyunder heavy development to be used as ultra sensitive bolometers. In addition to good performance, the choice of material depends on long term stability (both physical and chemical) along with a good reproducibility and uniformity in fabrication. For this purpose we are investigating the properties of NbSi thin films. NbSi is a well-known alloy for use in resistive thermometers. We are co-evaporating Nb and Si simultaneously. We present a full low temperature characterization of the NbSi films. In order to tune the critical temperature of the NbSi thermometers down to the desired range, we have to adjust the concentration of niobium in the NbSi alloy. In this experiment, we set for a Niobium concentration of 15%, to be able to run tested at a convenient temperature of 300mK. Tests are made using 4He-cooled cryostats, 300mK 3He mini-fridges, resistance bridge and a commercial SQUID. Parameters being measured are: critical temperature, resistance, sharpness of the transition and noise measurements.**

I. Introduction

Future generations of space experiments will require sensitivities better by a factor of 10 to 100. The only solution is an extensive coverage of the focal plane by large contiguous detector arrays of 10 000 pixels or more, with NEPs ranging from 1.10-17 W/Hz^1/2 for mapping instruments to 1.10-19 W/Hz^1/2 and better for spectrometers at the focus of cooled telescopes [1]. These improvements of sensibility are required for the mapping of the Cosmic Microwave Background polarized emission with high signal to noise ratio, as well as for spectroscopic observations of galaxies during their formation at high red shift. We present here the development and test of TES bolometers arrays and readout for this purpose. These detectors are included in the design of coming ground based instrument such as BRAIN (Dome C). The BRAIN experiment is a bolometric interferometer for B-modes of the Comic Microwave Background [2].
Besides, they may be candidate for future ESA missions: a cosmological mission like Bpol or a spectrometer such as in SPICA [3].

II. Arrays fabrication

The fabrication of arrays is developed in the microelectronics facility IEF/MINERVE of Paris Sud-11 University at Orsay. NbSi are in co-evaporators of CSNSM. Characterization and tests were conducted at IAS.
NbSi thin films are currently used as thermometers for different devices related to detection in astrophysics, be it for bolometer arrays for submillimetric or X-ray detection. They can act as high impedance or as TES thermometers. The material is in this form Nb_xSi_{1-x} : x higher than 12 % for superconductive detectors, or lower for high impedance detectors. The critical temperature Tc can be adjusted between approximately 50 mK and 1 K [4].
Our NbSi TES have been made with 15,55 % and 15,18 % of Nb. The fabrication process is composed of four steps with three lithography.

1. Deposit of membranes material by PECVD (SiO_2+Si_3N_4 SiO2/SiN/SiO2 = 290/230/100 nm thick)
2. Level 1 – lithography of the thermometers NbSi (100 nm)
3. Level 2 - lithography of the connection circuits (Nb, 50 nm)
4. Level 3 - lithography of the contact pads (Au, 150 nm)

In this study we have worked only on the NbSi TES, without opening the membranes. The optical lithography is a process used in microfabrication to selectively remove parts of a thin film (or the bulk of a substrate). It uses light to transfer a geometric pattern from a photomask to a light-sensitive chemical (photoresist or simply "resist") on the substrate.

The NbSi is co-evaporated by irradiating two targets of Nb and Si simultaneously. In order to lower the average resistance at the superconducting transition below 1 Ω, interleaved comb geometry is used. The contact pads make the electric interface between the Nb leads and the external system. Gold is used for the contacts because it offers the advantage of a compatibility with Nb connections. The layer of gold (100-150 nm) is deposited on the ends of the Nb tracks. We can see the metal layers on the periphery of the array (Fig. 1). After the process, we have obtained an array of 23 pixels.

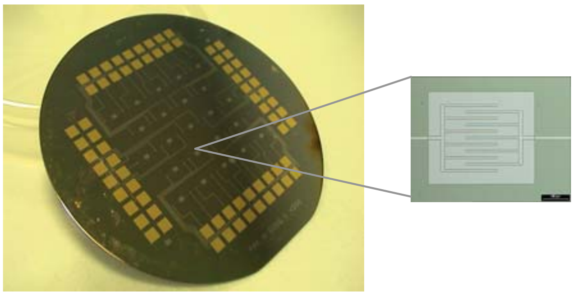

Fig. 1 23 Pixels TES array with the Nb lead comb structure

This 23 pixels array have 500 * 500 µm TES thermometers. Pixels center-to-center distance is 5.0 mm. The design of the TES is scaled down to 0.8*0.8 mm for this array. On the other hand, we also developed the complete process for the manufacture of superconductive bolometers arrays supported by membranes opened with XeF2. Tests will be made after the validation of NbSi as optimal material for bolometers

III. Thermal Characterizations

A. Test setup

Critical aspects in the fabrication of microcalorimeters are the reproducibility of the film characteristics, in particular transition temperature and their uniformity over sufficiently large areas. For that, we have fabricated two arrays with different Nb proportions for the NbSi TES. Two test benches are used in the collaboration for the measurement of the critical temperature Tc of the TES arrays (Fig. 2).

(a) (b)

Fig. 2 Test benches at APC (a) and at IAS (b)

The 3He fridge allows us to reach 300 mK. This system is integrated in a 4He cryostat. Resistance versus temperature curves were measured using this fridge, with an Air Liquide-ORPX and a Picowatt-AVS 47 resistance bridges. The array used has 23 NbSi TES. The thermometers arrays are thermally connected to the 300mK cold tip of He3 fridge.

B. First Results

Measurements are obtained during the cool down of the array down to 350 mK and then by heating the device up to 650 mK. Fig. 3 shows similar TES resistance curves during cool down and warm up on a given pixel. The thermometer is used at the transition between normal and superconducting state where sensitivity is maximum. Within the precision of the measurements, we see little hysteresis effect. Homogeneity of transitions of a set of pixels over the array is shown on Fig. 5 and Fig. 6. The pixels locations on the array are shown with the Fig. 4.

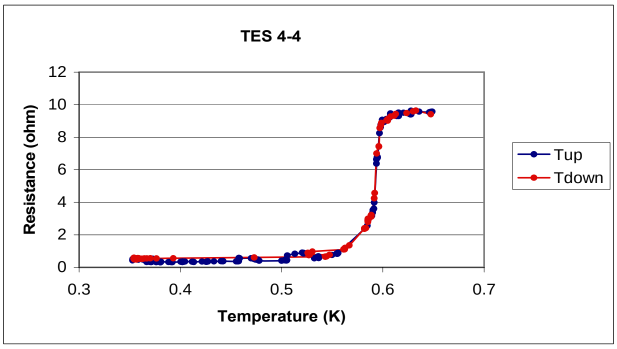

Fig. 3 Superconducting transition at the cooling (Tdown) and at the heating (Tup)

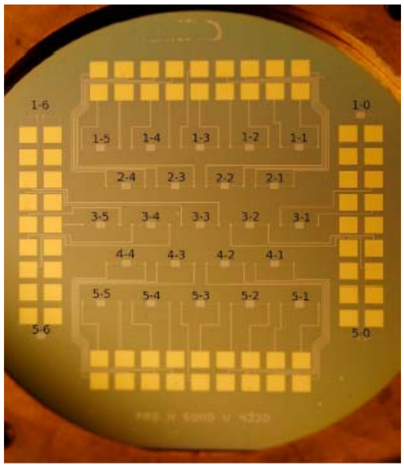

Fig. 4 Pixel numbering over the array

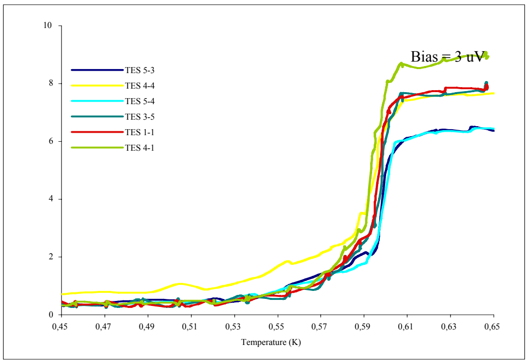

Fig. 5 Superconducting transition for different NbSi TES on 23 pixel array with 15,55% of Niobium

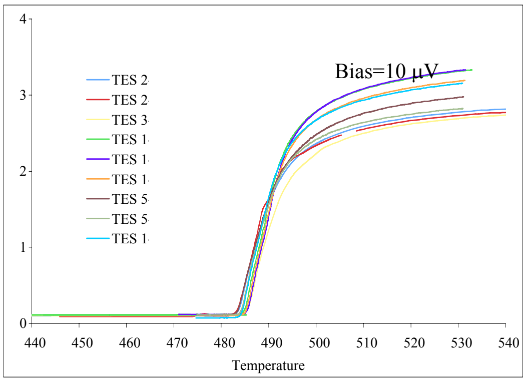

Fig. 6 Superconducting transition for different NbSi TES on 23 pixel array with 15,18% of Niobium

Results show a good homogeneity of the critical temperatures Tc accross the array. The average Tc obtained is about 595 +/- 3 mK (Fig. 5) and 486 +/- 1mK (Fig. 6). This difference in Tc dispersion can be explained by the noise of the measurements, larger for the test bench used for array showed in Fig. 6. We can notice that the normal state resistance is too high. This effect can be explained by the presence of a parasitic resistance in the setup.

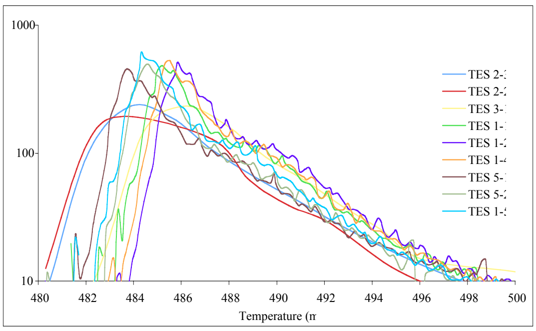

Fig. 7 Alpha parameter versus temperature with bias of 10 µV

The value of the transition remains the same for various biases applied to the resistance bridge (within +/- 2.5 mK). For all the characterized samples, the alpha parameter is larger than 100 within a 5 mK temperature interval starting from the foot of the transition (Fig. 7).

IV. Noise Measurements

Noise of the thermometric sensor is a key parameter in the performance of TES bolometers. For this measurement, we have developed a test bench with a commercial SQUID from Star Cryoelectronics. This test bench can characterize one pixel at a time. Fig. 8 shows a typical readout of the spectral density of the noise amplitude.

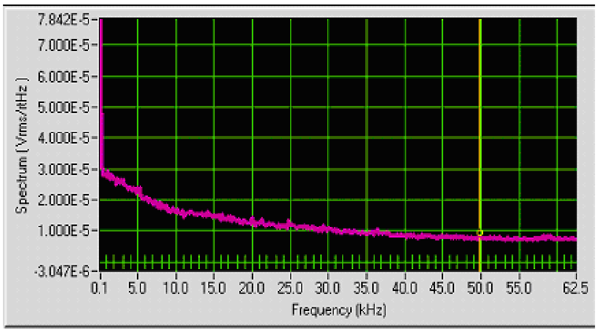

Fig. 8 Spectral density of the noise amplitude at 2 K

The noise measured at the output of the SQUID amplifier is 7.2 µV/√Hz at 50 kHz, corresponding to the specification of 3 pA/√Hz at the input. Characterisation of noise properties of a single NbSi superconducting thermometer is under progress.

V. Ultra Low Noise Readout Developed at APC

The future use of large number of very low Tc superconducting bolometers requires the development of ultra low noise amplification and multiplexing electronics operating close to the sensors, at cryogenic temperature. The ultra low noise performances required for the TES readout are obtained by SQUIDs driven by a SiGe Integrated Circuit (ASIC) operating at 4 K. Time domain SQUID multiplexing with SiGe ASIC allows to reduce drastically the number of wires between cryogenic and room temperature. A first cryogenic ASIC was developed to read out a 2*4 SQUID array demonstrator for 8 TES This ASIC combines switching biasing for time domain SQUID multiplexing and multiplexed input SiGe amplifier. An original topology avoiding the use of two switches along the signal path allowed a voltage white noise level of 0.2 nV/√Hz at 4 K at the input of this multiplexed amplifier [5].

A second version of the ASIC allows the readout of 3 columns of 8 SQUIDs (24 pixels). It is fully differential for better noise performances [6]. Thus, it is possible to use a standard integrated technology like BiCMOS SiGe with very interesting performances at 4 K.

ACKNOWLEDGMENT

The authors are grateful to M. Pairat and D. Broszkiewicz for their contribution. Our work was carried out within the framework of the partnership: Développement Concerté de Matrices de Bolomètres (DCMB) funded by the Centre National d'Etudes Spatiales (CNES), the CNRS, the participating universities and the Ministère de l'Enseignement Supérieur et de la Recherche. Y. Atik is under contract with CNES and Thales Alenia Space.

REFERENCES

[1] J.G. Staguhn, D.J. Benford and al., "Astronomical demonstration of superconducting bolometer arrays," in *Proc. SPIE*, 2003, paper 4855, pp. 100-107.

[2] G. Polenta and al., "The BRAIN CMB polarization experiment", *New Astronomy Reviews*, vol. 51, pp. 256–259, 2007.

[3] Takao Nakagawa, "SPICA and its Instrumentation", in *Proc. ISSTT*, 2008.

[4] Ukibe and al., "Fabrication of large NbSi bolometer arrays for CMB applications", *Nuclear instruments & Method in physics research*, vol. 559, pp. 554-556, 2006.

[5] F. Voisin and al., "Very Low Noise Multiplexing with SQUIDs and SiGe Heterojunction Bipolar Transistors", *Journal Low Temp Phys*, vol. 151, pp. 1028-1033, 2008.

[6] F. Voisin and al., "Cryogenic SiGe ASIC for readout and multiplexing of superconducting detector arrays", in *Proc. SPIE Astronomical Telescopes and Instrumentation*, 2008.

Distributed Correlator for Space Applications

A.W. Gunst*, L. B. Venema, and A. Bos

ASTRON Netherlands Foundation for Research in Astronomy, Dwingeloo, the Netherlands

* Contact: gunst@astron.nl, phone +31-521-59 5113

Abstract— **Earthbound radio telescopes use for the processing of the received signals a central correlator system. However, for interferometry in space using free flying units, where downlink bandwidth, the power dissipation and space per satellite is limited, a distributed correlator can be more advantageous. This distribution reduces the risk of failures as well.**

In this paper the proposed architecture for a distributed correlator in space is discussed.

I. Introduction

In radio astronomy interferometers are used to enhance the sensitivity and angular resolution for observations. Recently [1] an initiative was started to use interferometers in space for the submm regime. In space different requirements for the correlator apply. In this paper a correlator architecture is proposed for interferometry in space.

As a starting point the block diagram of a traditional telescope system is presented in Section II. From there on the requirements for a correlator in space, distributed over multiple satellites is discussed including a block diagram. The distributed correlator is more detailed in Section IV. The impact of a failing satellite is discussed in Section V.

II. A Ground Based Receiver System

The incoming radiation is measured using one or pairs of orthogonal dipoles in the focal plane of a dish. In the low frequency range this is often limited to just a large number of dipoles [2].

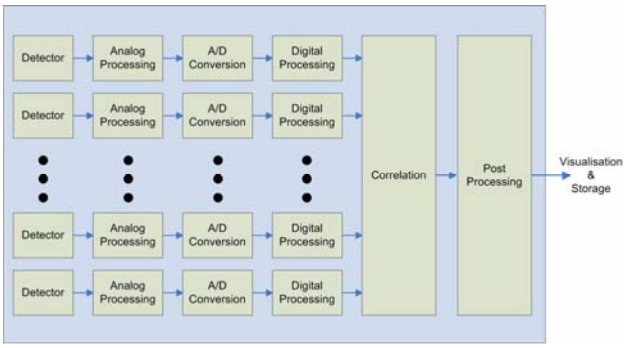

Figure 5 Block diagram of a ground based receiver system

The dipole signals are amplified, filtered and mixed down to baseband. The signal processing that follows involves generally down conversion to baseband, analog-to-digital (A/D) conversion, fringe- and delay tracking. Fringe tracking is often combined with the down conversion in the analog block. The number of bits to be used for A/D conversion is determined by the characteristics of the input signal, the required dynamic range and the loss in sensitivity allowed. Delay tracking is preferably done in the digital processing block. The digital signals from each antenna are send to a central correlator. The correlator computes the cross-correlation between all possible antenna pairs. This reduces the output data rate of the system by orders of magnitude. The WSRT correlator for example reduces its input data rate of 40 Gbits/sec to a maximum output data rate of 30 Mbits/sec.

After the correlation process the correlator products are e.g. calibrated, flagged, etc. in the post processing block. Finally the result is used to generate images.

III. Correlator Requirements in Space

The system concept consists of a number of satellites equipped with an antenna and a receiver system. This is depicted in Figure 6. The satellites are free flying. In this way the baselines in between the satellites can be varied as function of time, delivering an acceptable UV coverage even with a small amount of satellites.

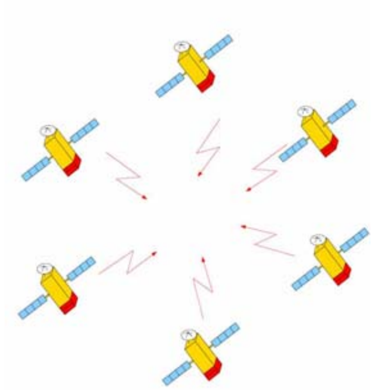

Figure 6 Satellite configuration for an interferometer in space

Observations in the submillimeter wave length range require a typical receiver bandwith in the 1-10 GHz range. The bandwidth available for the downlink will be insufficient to cope with the required data rates.

Since, the correlation process reduces the data significantly it is more efficient to implement the correlator in space as well. One of the consequences is that a communication is necessary between all satellites as is depicted in Figure 6.

Driven by risk reduction and the need to balance the power load over all satellites and to benefit from series production to have only one type of satellite it is desired to share the correlator over all satellites. Furthermore, the communication bandwidth in between the satellites should be minimized.

These requirements results in the block diagram as shown in Figure 7. The first blocks in Figure 7 are common with ground based telescopes, except the correlator block which is now distributed. Furthermore, the post processing can be done on earth because the amount of data in the correlator is reduced significantly to downlink this. An example of data rates is presented in [4].

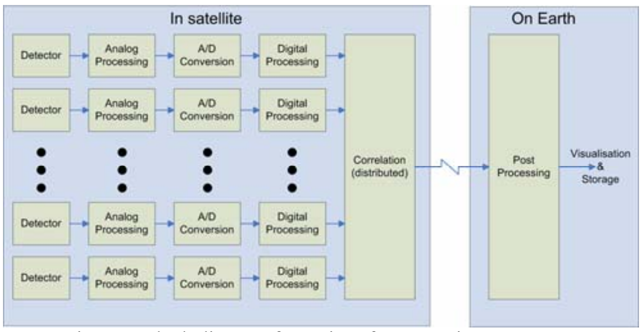

Figure 7 Block diagram for an interferometer in space

IV. Distributed Correlator

In principle there exists several ways to distribute the correlator functionality over the satellites. Amongst them are: distribution in antennas, time and basebands/subbands.

The correlator can be distributed over antennas, by calculating a subset of cross correlation products in each satellite. The correlation process can also be distributed in time, so that satellite 1 correlates the first time slot, satellite 2 the second time slot, … and satellite N the N^{th} time slot. The next time slot $N+1$ is again correlated by the first satellite. Finally, distribution in frequency can be done by splitting the frequency band up in N parts, where each satellite correlates its own frequency band.

In [3] all three concepts are compared. The communication data rate in between the satellites is minimized by adopting a distribution in time or basebands/subbands. For a correlator distributed in time extra buffer capacity is required. Furthermore, the number of correlator multipliers in a frequency distributed correlator is less. Hence, a distribution in frequency is proposed.

Many radio telescopes use an XF correlator, meaning that first the correlation and integration of the signals is done in time domain (X), after which the Fourier transform (F) is accomplished to get a cross power spectrum out of the correlator. This is an economically attractive technique for radio telescopes with a limited number of detectors. The number of multipliers required for an XF correlator equals

$$\frac{N \cdot (N+1)}{N} \cdot N_S$$

wherein N is the number of satellites and N_S is the total number of spectral channels. All multipliers in an XF correlator run at the input clock frequency f_s.

For systems with a large number of antennas it is more economical to use an FX architecture. A number of existing systems use a combination of the two architectures, the hybrid architecture (HXF).

In an FX architecture the input band is split in frequency such that the required spectral resolution after correlation is met, while in a HXF architecture the input band is split into basebands/subbands first. An XF correlator per baseband/subband is used to produce the final spectral resolution.

Both the FX and HXF correlator are a usefull architecture for a distributed correlator, since both splits up the band prior to correlation. The choice between both depends on detailed parameters like flexibility, power consumption, etc.

Also for a FX and HXF correlator the number of multipliers required for the correlation equals the number of spectral channels. However, the multipliers can run on a decimated clock rate, dependent on the baseband/subband width. If the filtering operation is implemented digitally, then also multipliers for this operation are required. The exact number depends on the required ripple, stopband attenuation and transistion region of the filter. Furthermore, in the FX architecture also the multipliers for the FFT should be counted.

Assuming a HXF architecture, then the number of correlator multipliers for a 1 GHz band sampled at f_s = 2 GHz is depicted in Figure 8 assuming 512 spectral channels. The band is split in four basebands with analog filters and the number of multipliers equals the number of spectral channels N_s. While in a XF correlator all multipliers are running at the input clock frequency of f_s, the multipliers in the HXF correlator run at the downsampled rate of f_s /4 in this case. This saves chip area or power consumption.

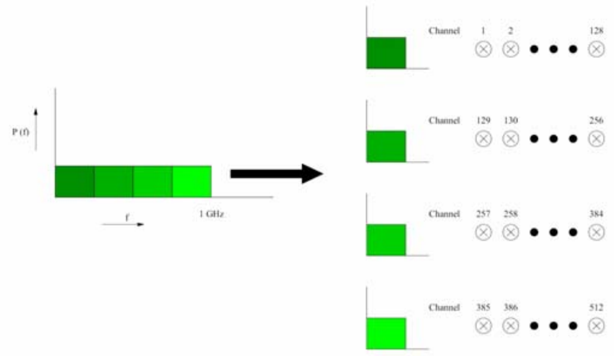

Figure 8 Number of correlator multipliers for a HXF correlator

With the proposed solution all satellites can be identical. Given N satellites each satellite processes $1/N$ of the total input bandwidth. Satellite i correlates band i, where i=1 … N. This means that all satellites have to transport their digitized signal in band i to satellite i. So, in this case satellite 1 transports band 2 to N to satellites 2 to N, while it receives band 1 from all the other satellites.

V. Satellite Failure

The proposed architecture is robust for satellite failures. When one of the N satellites fails, one detector fails and part of the correlator fails. That means that part of the bandwidth cannot be correlated anymore by the failed satellite. As a consequence the processing in the other satellites is more relaxed since the number of detectors to correlate is reduced by one. This extra capacity can be used to correlate the original bandwidth again. Even then processing power is left over because the number of multipliers required for the correlation relates quadratically with the number of detectors and linearly with the bandwidth.

Conclusions

In this paper a distributed correlator is proposed for interferometers in space. For a distribution in the frequency domain, a power efficient and robust solution is found. The internal data rates in between satellites are optimised in this configuration. Finally all satellites can be identical and no single point of failure is present in the proposed solution.

References

[1] W. Wild, Th. De Graauw, F. Helmich, J. Cernicharo, A. Baryshev, A. Bos, J.-W. den Herder, A. Gunst, B. Jackson, H-J. Langevelde, P. Maat, J. Martin-Pintado, J. Noordam. A. Quirrenbach, P. Roelfsema, L. Venema, P. Wesselius, N. Whyborn, P. Yagoubov, *Exploratory Submm Space Radio-Interferometric Telescope (ESPRIT),* URSI 2005, New Delhi, October 23-29, 2005.

[2] Gunst, A.W., Bentum, M.J., *Signal Processing Aspects of the Low Frequency Array*, IEEE International Conference on Signal Processing and Communications, 24-27 November 2007, Dubai, United Arab Emirates, p600-603.

[3] Gunst, A.W., *Correlator Configurations for Interferometers in Space,* New Perspectives for Post Herschel Infrared Astronomy for Space Workshop, Sept. 1-4, 2003, Madrid, Spain.

[4] Gunst, A.W., *Correlator for ESPRIT*, ESPRIT Workshop, Sept. 2, 2004, Utrecht, the Netherlands.

CASIMIR – Caltech Airborne Submillimeter Interstellar Medium Investigations Receiver

David Miller*, Michael L. Edgar, Alexandre Karpov, Sean Lin, Simon J. E. Radford,
Frank Rice, Jonas Zmuidzinas[1], and Andrew I. Harris[2]
[1] California Institute of Technology, Pasadena, CA 91125, USA
[2] University of Maryland, College Park, MD 20742, USA
* Contact: davem@submm.caltech.edu, phone(626)395-3668

Abstract— **CASIMIR, the Caltech Airborne Submillimeter Interstellar Medium Investigations Receiver, is a multiband, far-infared and submillimeter, high resolution, heterodyne spectrometer under development for SOFIA. It is a first generation, PI class instrument, designed for detailed, high sensitivity observations of warm (100 K) interstellar gas, both in galactic sources, including molecular clouds, circumstellar envelopes and protostellar cores and in external galaxies. Combining the 2.5-meter SOFIA mirror with state of the art superconducting mixers will give CASIMIR unprecedented sensitivity. Initially, CASIMIR will have two bands, at 1000 and 1250 GHz, and a further three bands, 550, 750, 1400 GHz, will be added soon after. Up to four bands will be available on each flight, contributing to efficient use of observing time. For example, searches for weak lines from rare species in bright sources can be carried out on the same flight with observations of abundant species in faint or distant objects.**

I. Introduction

CASIMIR, the Caltech Airborne Submillimeter Interstellar Medium Investigations Receiver, is a far-infrared (FIR) and submillimeter, very high-resolution, heterodyne spectrometer. It is being developed as a first generation, Principal Investigator (PI) class instrument for the Stratospheric Observatory For Infrared Astronomy, SOFIA [1], [2]. Observations with CASIMIR on SOFIA are expected to begin in mid-2010 and the instrument should be available to guest investigators soon after. It is anticipated SOFIA will eventually achieve a flight rate of up to 160 flights per year, with a lifetime of 20 years. During the initial flights, CASIMIR will have two bands available, 1.0 and 1.25 THz. Three additional bands will be added with ongoing instrument development, providing frequency coverage from 500 GHz up to 1.4 THz. The frequency coverage may be expanded up to 2 THz later. It will be capable of covering this frequency range with a resolution of $\sim 10^6$.

The FIR/submm is extraordinarily important for the investigation of both the galactic and extragalactic warm ($T \sim 100$ K), interstellar medium. This material is heated by shock waves or UV radiation, phenomena that are often associated with star formation or other high energy events, e. g., supernovae or active galactic nuclei. This excited material then re-emits either as dust continuum radiation or gas line emission. CASIMIR will be able to utilize recent advances in the sensitivity of superconducting mixers to study the fundamental rotational transitions of many astronomically significant hydride molecules. Even at excellent ground sites, such as Mauna Kea or the high Chilean Andes, the atmosphere is opaque to most of these lines. Observations of these species can provide critical tests of our understanding of interstellar chemical networks and reactions.

II. Scientific Objectives

A selection of significant spectral lines observable with CASIMIR is shown in Table I. It is expected that initial observations will concentrate on lines from this list. Most of these lines are completely unobservable from the ground. The atmospheric transmissions shown are for typical SOFIA operating altitudes, ~ 40,000 ft or 12 km. At the Caltech Submillimeter Observatory (CSO), on the summit of Mauna

TABLE X
OBSERVING LIST OF SIGNIFICANT SPECTRAL LINES FOR CASIMIR

Band [GHz]	Species	Line [GHz]	Atm. Trans. [%]
550	CH	532, 537	98, 97
	$H_2{}^{18}O$	547	81
	NH_3	572	94
	CO	576	80
750	$H_2{}^{18}O$	745	82
1000	H_3O+	985	65
	CH_2	946	99
	NH	975	96
	$H_2{}^{18}O$	995	73
	CO	1037	94
1200	$H_2{}^{18}O$	1137, 1181	70, 75
		1189, 1199	87, 81
	HF	1232	30
1400	H_2D+	1371	94
	N+	1461	92

Kea, at 4.1 km altitude, only two of the lines listed have an atmospheric transmittance more than 0%: CH (1%) and CH_2 (13%).

Oxygen is the third most abundant element, yet its chemistry in interstellar clouds is poorly understood. The atmosphere is opaque to many of its key species, such as O, O_2, H_2O, H_3O+ and OH, limiting detailed ground observations, but are prime candidates for investigation using CASIMIR. Also, the high *J* lines of CO will be observed with CASIMIR. These lines typically trace shocked gas and have been studied extensively with the Kuiper Airborne Observatory (KAO) with high-resolution, heterodyne spectroscopy.

A. Water

As can be seen from Table I, CASIMIR is exceptionally well suited to investigate the abundance and excitation of interstellar water, using a number of transitions of $H_2{}^{18}O$. Water vapor plays an important role in the energy balance of molecular clouds by mediating radiative heating and cooling through its rotational transitions in the far infrared and submillimeter [3]. Figure 1 shows the rotational energy levels for $H_2{}^{18}O$, indicating the large number of low excitation level transitions visible to CASIMIR. Only two relatively high energy transitions can be observed from the ground (i. e., CSO). Figure 2 shows the comparison between previous KAO observations at 547 GHz for $H_2{}^{18}O$ in SgrB2 and W51, and the line profiles and intensities predicted for CASIMIR on SOFIA, revealing the anticipated gain in sensitivity.

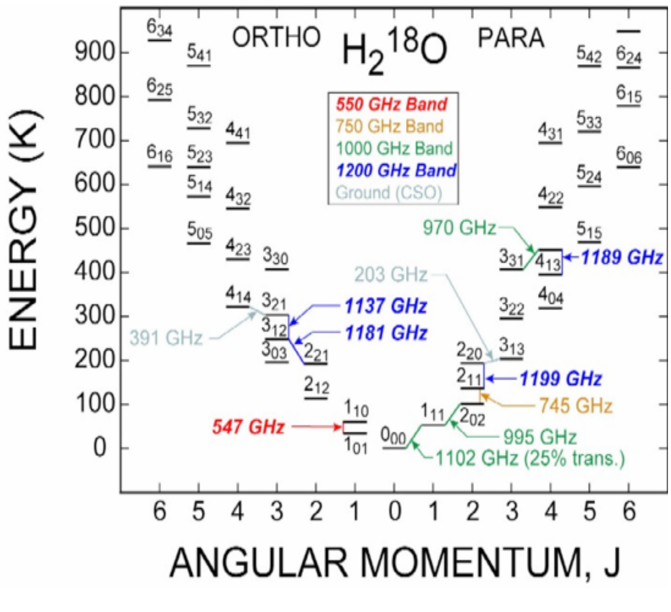

Fig. 1. The coverage by CASIMIR of the rotational energy levels of the $H_2{}^{18}O$ molecule. Four of the CASIMIR bands will be able to observe 9 of these transitions, including several low temperature lines

B. H_2D^+ and N^+

A 1.4 THz band is expected to be available soon after CASIMIR begins observations on SOFIA. This band will concentrate on the H_2D^+ 1370 GHz ground state line. The H_2D^+ ion is of particular interest, as it is the deuterated version of $H_3{}^+$, which is believed to be responsible for driving much of the chemistry of molecular clouds. The 372 GHz line of H_2D^+ now has been observed in several molecular clouds with the CSO [4] and the APEX telescope [5] on the Chajnantor plateau in Chile. However, this is an excited transition that traces hot, dense gas, which has more complicated chemistry. In addition, the abundance of the species is low. The ground state line at 1371 GHz will be a better choice for studying the overall distribution of this important molecule. To date, there has been only one tentative detection of the 1371 GHz line in Orion with the KAO [6].

Another transition of major importance is the 1461 GHz transition of the nitrogen ion, N+, which traces the warm, ionized interstellar medium. COBE has shown that, apart from the 1900 GHz C+ line, the two fine-structure N+ lines are the brightest emitted by our Galaxy.

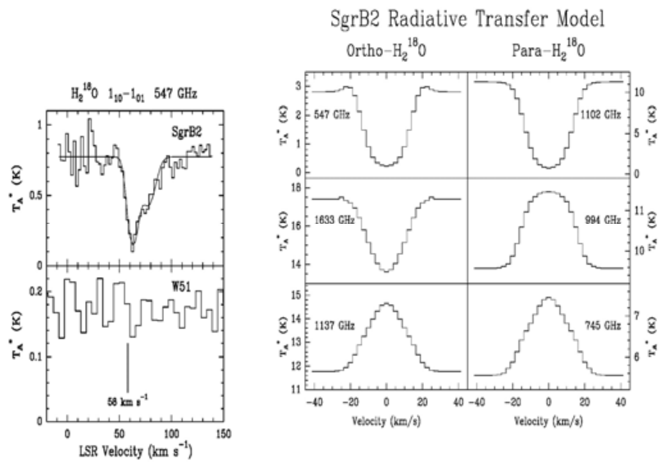

Fig. 2. Comparison of $H_2{}^{18}O$ line sensitivities obtained with the Kuiper Airborne Observatory (KAO) with these expected for CASIMIR. The left part of the figure shows 547 GHz observations of SgrB2 and W51, obtained on the KAO. The right part shows predicted performance for observations of SgrB2 with CASIMIR on SOFIA, for several lines. SgrB2 was modeled as a sphere, $n_{H2}(r) \sim r^{-2}$ and $T(r) \sim r^{-0.5}$, which matches existing CO, dust and $H_2{}^{18}O$ data.

III. Instrument Configuration

CASIMIR embodies a versatile and modular design, able to incorporate future major advances in detector, LO and spectrometer technology. It mounts on the SOFIA SI telescope flange. The entire instrument is about 1.5 m long and 1 m diameter, and weighs about 550 kg. Two separate cryostats each can hold two mixers – thus up to four mixers are available on each flight. The optics box supporting the cryostats is open to the telescope cavity and contains the relay optics and calibration systems. Besides the cryostat windows, all the optics are reflective and can accommodate the entire 8' telescope field of view. Bias electronics and warm IF amplifiers are mounted on the cryostats, while independent electronics racks contain backend spectrometers, control electronics, and power supplies.

The general layout of the CASIMIR instrument is shown in Figure 3. Two cryostats are mounted side by side on top of a box, which contains the relay optics. Two standard 19-inch racks are mounted directly behind this box. All the critical electronics components are mounted in these racks, such as the LO drive electronics and the microwave spectrometers. This ensures very short cable runs to the cryostats and prevents any differential rotation and twisting of the cables. All electronic systems for the instrument are packaged as 19-inch bins, which will allow easy replacement of any unit.

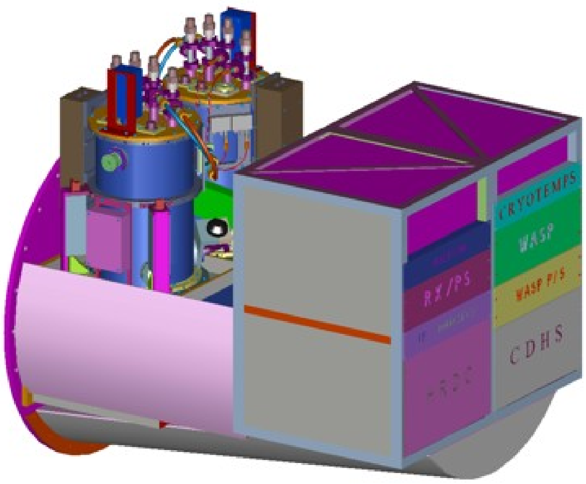

Fig. 3. The CASIMIR instrument. The instrument is mounted to the telescope via the round flange at extreme left of the figure. This flange forms the pressure interface between the telescope cavity and the aircraft's cabin. The portion of the instrument shown is located in the cabin with the observers. The telescope beam enters the instrument through the center of this round flange. The instrument structure is constructed almost exclusively of aluminum. It is approximately 1.5 m long by 1 m square. It weighs approximately 550 kg, including 150 kg of electronics mounted in the racks, at the right of the figure. Approximately 150 kg more of ancillary electronics are located nearby in the aircraft cabin

A. *Cryostats*

The cryostats are of conventional design with LN_2 and LHe reservoirs. For frequencies below 1 THz, the mixers will operate at ~ 4 K. At higher frequencies, the LHe reservoirs will be pumped to operate the receivers at ~ 2.5 K. There will be two cryostats per flight and up to two frequency bands in each cryostat, thus four bands will be available per flight. Observations can be made with only one band at a time, but any one of the four bands can be selected at anytime during the flight. This selection is made by software alone, and does not require caging of the telescope, any mechanical adjustment or physical access to the instrument.

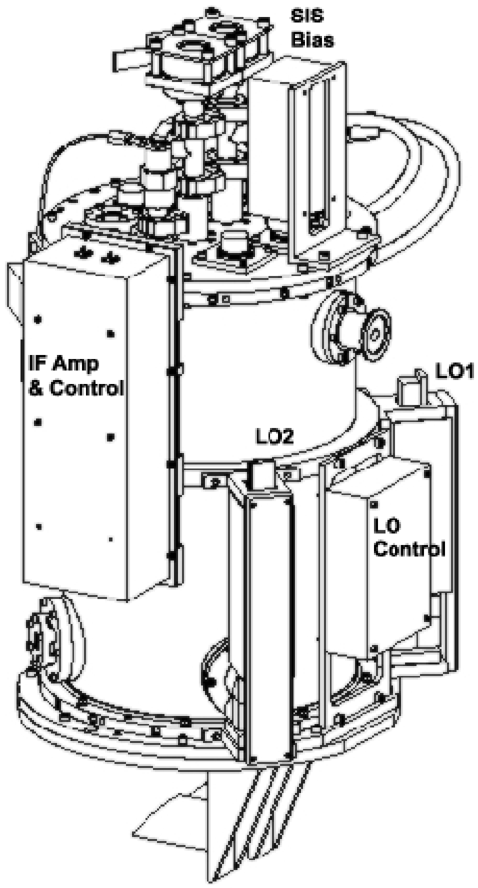

Fig. 4. The CASIMIR Cryostat. The cryostat contains 5 liters each of LN_2 and LHe and has a 250 mm diameter cold-work-surface. This is the maximum, practical diameter for cryostats that can be used in the side-by-side configuration for SOFIA. It is 60 cm high and weighs ~40 kg. The LOs, IF system, receiver and bias electronics are mounted directly to the sides of the cryostat. The rather impressive array of plumbing fixtures on the top of the cryostat prevents the formation of ice plugs or the rupture of the cryogenic reservoirs. This design was required to obtain airworthiness certification by the Federal Aviation Administration. The two elliptical mirrors of the relay optics, mounted on the base of the cryostat, can be seen at the bottom of the image.

Fig. 5. Receiver bias electronics developed in collaboration with CSO. These circuit boards are for biasing the low-noise amplifier (LNA) on the cold LHe work surface of the receivers. These electronics are fully automated and controlled via computer interface, and also have the capability for manual control, allowing them to be used during mixer development

As shown in Figure 4, all of the components specific to an individual frequency band are integrated directly onto the cryostat, i. e., the LOs, IF systems, relay optics, and bias electronics (see Figure 5). All systems mounted elsewhere on the instrument are common to all of the bands. Therefore, changing the selection of the four bands which are to be available on a given flight only requires swapping cryostats, which would be a straight-forward task between flights. In addition, this modular approach allows future upgrades and improvements to the bands to be incorporated completely independent of the rest of the instrument. This will allow continuous enhancements to the frequency bands throughout the life of the instrument.

B. Mixers

All of the receivers for the five bands of CASIMIR, up to 1.4 THz, use advanced Superconductor-Insulator-Superconductor (SIS) mixers fabricated with Nb/AlN/NbTiN junctions in the JPL Micro Devices Lab. These planar mixers are quasi-optically coupled with twin slot antennas, and silicon hyperhemisphere lenses with Parylene antireflection coatings. These mixers and their development are discussed in detail elsewhere [7]. Simulations show this mixer technology is usable up to 1.6 THz. With ongoing development, DSB noise temperatures of $3h\nu/k_B$ at frequencies below 1 THz (see Figure 6), and $6h\nu/k_B$ above 1 THz (see Figure 7) are expected.

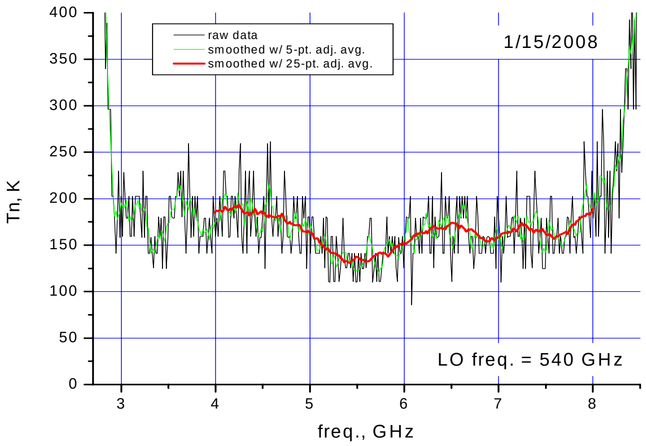

Fig. 6. Noise temperature results for the full 4 GHz IF band using an old-style quasi-optical SIS mixer with NbTiN/AlO_x/NbTiN junctions at LO frequency of 540 GHz. Input optics consisted of mylar beamsplitter, mylar pressure window, Zitex IR filters, HDPE focusing lens, and silicon hyperhemisphere lens. The IF output included cryogenic isolator, Chalmers LNA, and room-temperature IF amplifier module.

C. Intermediate Frequency System

The intermediate frequency (IF) is the output signal from the mixer. This is defined as 4 GHz bandwidth, centered at 6 GHz, for all bands on CASIMIR. This wide frequency

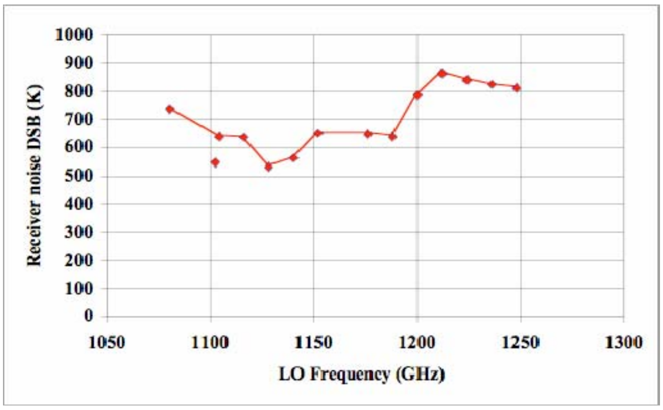

Fig. 7. Noise temperature results for 1.2 THz SIS mixer. The receiver noise is uncorrected for beamsplitter and cryostat window losses. With these corrections, the noise temperatures would fall to approximately $6h\nu/k_B$

range will allow observation of the broad lines from extragalactic sources.

The low noise amplifier in all bands is a Chalmers [8] design. It is a two-stage amplifier using InP transistors, with minimum gain of 27 dB and a nominal noise temperature of 3 K. It is mounted on the cold work surface of the cryostat at LHe temperature, and is connected to the mixer via a Passive Microwave Technologies (Pamtech) [9] cryogenic isolator, which reduces ripple in the IF due to impedance mismatches.

The room temperature IF electronics consist of a 4-8 GHz amplifier module. The bandwidth defined by this unit is shown in Figure 8. This is an integrated unit developed under contract by CTT Inc. [10], containing a low noise amplifier, a voltage variable attenuator (VVA), band defining filter, power amplifier, a directional coupler for monitoring

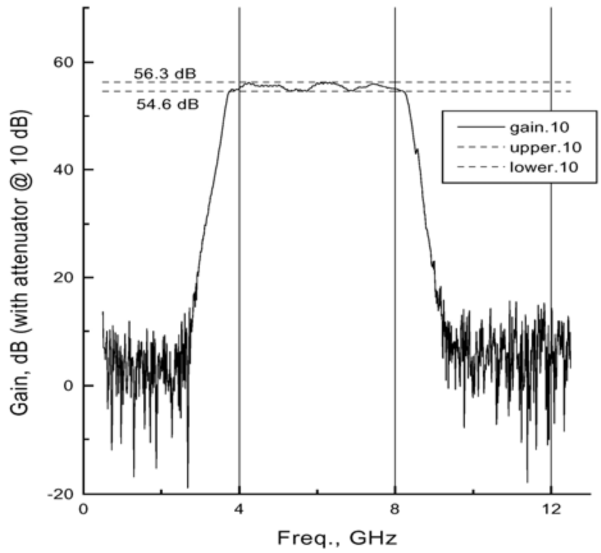

Fig. 8. IF bandwidth defined by bandpass filter within the room temperature IF unit. At a typical operating point, with the VVA set for 10 dB attenuation, the IF unit demonstrates excellent uniformity, < ± 1 dB, across the entire 4 GHz bandwidth.

the IF power level, and a switch for setting the IF power zero level. An integrated isolator at the input of the module minimizes standing wave ripples between the cryostat and amplifier module. The nominal gain of the unit is 65 dB with a typical noise temperature of 300 K. A diode is connected to the monitor port for measuring the signal strength and adjusting the VVA to prevent saturating the internal input amplifier stage. These units are mounted directly to the side of the cryostat and are designed for fully automatic operation.

D. Local Oscillators

The Local Oscillators (LOs) for all bands are tunerless and use solid state devices exclusively. At present, 550 GHz and 1.37 THz LOs made by Virginia Diodes [11], and a 1.2 THz LO developed at JPL, based on a Herschel/HIFI design [12], are used for mixer development. The 750 GHz LO will be acquired from Virginia Diodes, while the 1.0 THz and 1.4 THz flight LOs will be developed at JPL. All bands are driven from a single, commercial microwave synthesizer at a frequency in the range 26–40 GHz.

As shown previously in Figure 4, up to two LOs can be mounted directly on the outside of the cryostat. The LO output is via a feedhorn, with the output divergent beam reflected through 90° and converted into a ~ *f*/10 converging beam by an off-axis elliptical mirror mounted directly below the feedhorn (see Figure 9). The beam passes through a window in the cryostat wall to a cryogenically-cooled mylar beamsplitter mounted directly below the receiver elliptical mirror. The beamsplitter directs a fractional part (~ 10%) of the LO signal power towards the cryostat cold work surface and into the mixer, where it combines with the incoming, astronomical signal.

E. Spectrometers

CASIMIR will have a high resolution digital FFT spectrometer developed by Omnisys [13], [14] as a turnkey COTS system. This instrument consists of two processing modules, each with two high speed samplers and an FPGA engine. The spectrometer covers the entire 4 GHz IF bandwidth, providing over 16 k channels and a maximum resolution 250 kHz per channel, which corresponds to a velocity resolution 75 m s^{-1} at 1 THz observing frequency. Lower resolution is possible by averaging channels. Two single height, 3U, correlator cards will handle processing the full 4 GHz IF bandwidth, at a total power consumption of less than 50 W, which is a major advantage for an airborne instrument. The spectrometer is scalable to provide IF bandwidths of 8, 12, or 16 GHz, and we plan to be able to exploit this capability on CASIMIR in the future.

F. FIR Relay Optics

Figure 9 shows a schematic of the relay optics, which uses two off-axis elliptical mirrors to match the incoming telescope beam to the output beam of the mixer. Including the telescope, there are five mirrors at ambient temperature and one cryogenically cooled mirror, EM1, in the optical path. This includes the two off-axis elliptical mirrors, the rotating, beam selecting plane mirror in the Optics Box (see Figure 10) and the fully reflective tertiary of the telescope. The window in the base of the cryostat is the only pressure boundary in the optical path from the telescope. Therefore, this window and a lens in the mixer assembly are the only transmissive elements in the entire optical path from the telescope to the mixer.

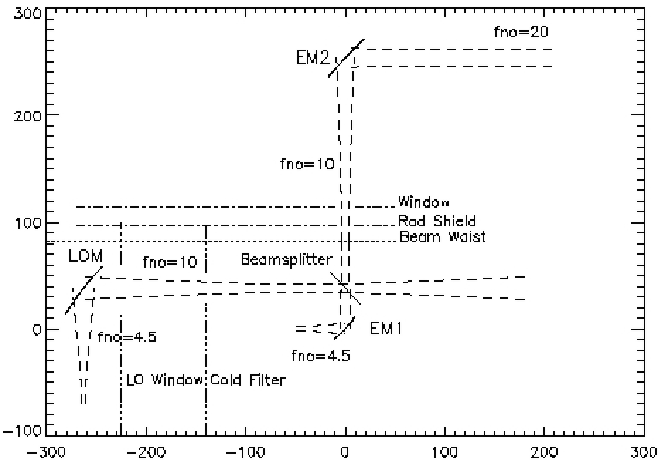

Fig. 9. CASIMIR Relay and LO Injection Optics. The up down orientation is reversed, as compared to the cryostat, meaning that the telescope beam, which is shown coming into the cryostat from the top in this figure, and enters the actual instrument from the bottom. The units on the scale are mm, with the origin at the center of EM1, the elliptical mirror mounted on the cryostat cold-work surface. EM2 is the elliptical mirror mounted below the base of the cryostat. EM2 is in the plane of the telescope beam, and it converts the incoming, diverging *f*/20 telescope beam into an intermediate *f*/10 beam and reflects it through 90°, through a window in the base of the cryostat. LOM is the LO elliptical mirror, which matches the LO output beam to the incoming intermediate beam. EM1 converts the intermediate beam to a converging ~ *f*/4.5 beam, which matches the output beam of the mixer

The relay optics for all bands are designed to have an edge taper of 10 dB. This corresponds to an aperture efficiency of 0.71. Initially, SOFIA will use an oversize tertiary mirror, which would reduce the aperture efficiency to 0.64; however, a smaller tertiary mirror may become available later, allowing for increased efficiency. All bands will have a main beam efficiency of 0.77. The beam size at 550 GHz (the largest beam) is 0.8 arcmin.

G. Optics Box

Since CASIMIR will use the fully reflective tertiary mirror on the telescope in SOFIA, none of the observatory's guiding cameras will be able to image the telescope's focal plane. Therefore, we have included an optical boresight camera inside the Optics Box for alignment and beamfinding. The boresight can also be used as a pupil imager by moving a biconcave lens into the optical path. The camera has a 6' × 6' field of view and uses a 1024 × 1024 pixel, optical wavelength CCD. The rotating mirror also selects this camera.

Stepper motors are used to move all the optical components. All of these motors are mounted inside the Optics Box and are controlled remotely via software. Besides the electronic feedthroughs mounted in the sides of the box, there are no mechanical motions through the pressure boundary, thus avoiding the possibility of dynamic motion seals failing during observations. Physical access to the Optics Box will not be required at any time during the flight.

Apart from providing the pressure boundary between the inside and outside of the aircraft and being the mechanical mount for the two cryostats, the Optics Box also contains all of the optics that is common for all FIR/submm bands. Figure 10 shows a 3D model of the interior of the Optics Box and these optics. Figure 11 shows the Optics Box with the flight cryostats mounted on top.

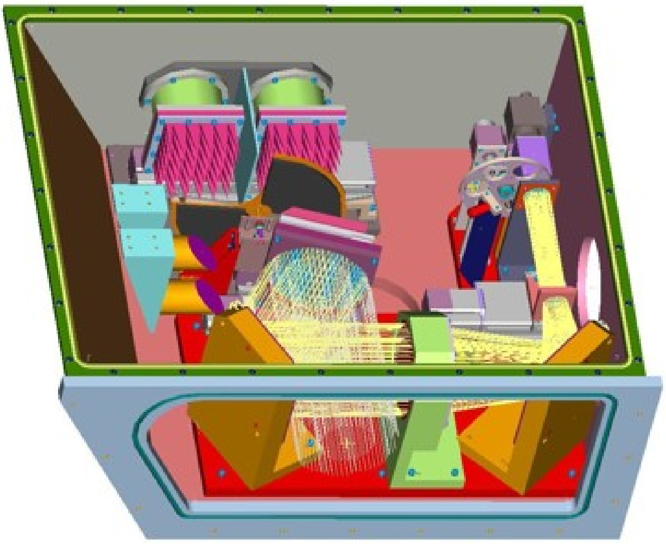

Fig. 10. The Optics Box interior. The cryostats are bolted directly to the lid of this box, which has been removed for this image. The elliptical mirrors mounted on the base of the cryostats (see Figure 4) protrude trough an aperture in the lid and are located in the plane of the telescope beam. The two elliptical mirrors for one of the cryostats are shown in the left part of the image. The telescope beam enters from the front of the figure. In this image, the rotating mirror, at the center of the figure, directs the telescope beam to the optical boresight, at the far right rear corner. The calibration chopper wheel and the two loads are shown in the rear of the figure.

The central feature is a plane mirror, which can be commanded to rotate through ± 180° in the plane of the telescope and up to ± 5° in tilt. This rotating mirror directs the telescope beam to one of the four elliptical mirrors mounted on the two cryostats, selecting the frequency band.

The calibration system consists of a chopper wheel at ambient temperature plus hot and ambient temperature loads. Moving the rotating mirror by ~ 180°, allows any of the frequency bands to be first illuminated with the sky signal and then the signal from a known temperature calibration load.

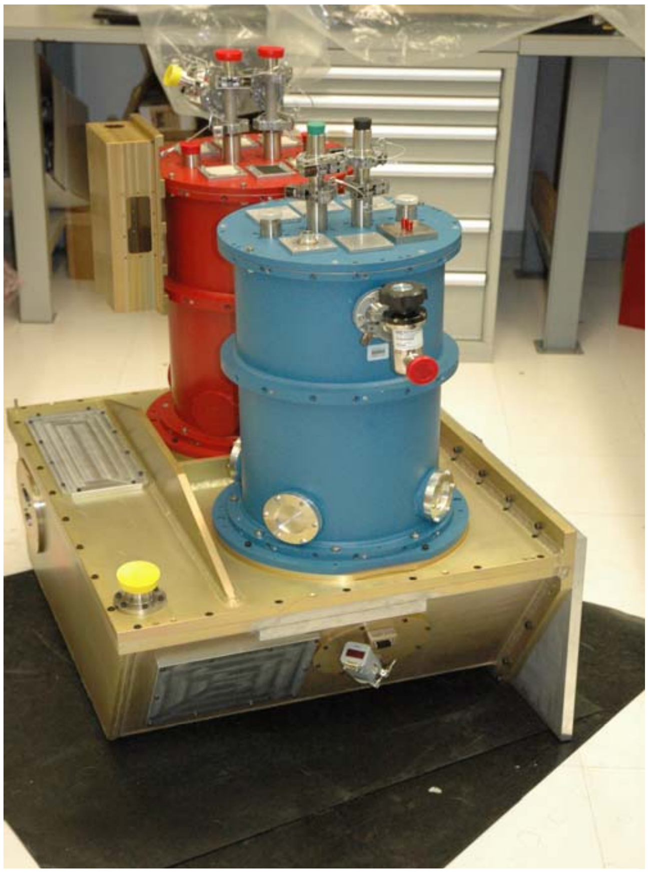

Fig. 11. The Optics Box with Cryostats Mounted. The cryostats mount directly to the top of the Optics Box. The Optics Box is constructed of welded Al 6061-T6, with dimensions of approximately 0.8 × 0.7 × 0.3 m, and wall thicknesses varying between approximately 15 and 20 mm. During observations, the interior of the box is exposed directly to the pressure in the telescope cavity, approximately 200 torr at 12 km altitude. The box is the pressure boundary between the aircraft cabin and this exterior air pressure. The baseplates of the two cryostats also form part of this pressure boundary. The telescope beam enters from the right of this figure, approximately 150 mm below the bases of the cryostat. It is then reflected through 90° and directed through windows in the cryostat baseplates. This is the only pressure boundary in the entire astronomical signal beam path, i. e., between the aircraft exterior pressure and the high vacuum within the cryostat.

CONCLUSIONS

CASIMIR is a FIR/Submm, heterodyne spectrometer for SOFIA, well suited for the studies of the warm ($T \sim 100$ K) interstellar medium. Particularly suited to detect water, it will also measure many other significant lines unobservable from the ground. Initially, the instrument will cover 500 to 1400 GHz. Eventually the frequency coverage may be extended up to 2000 GHz. CASIMIR will provide unprecedented sensitivity in this frequency region, due to recent advancements in SIS mixer design and local oscillator development. There will be up to 4 channels available per flight of the observatory. Any one of these channels can be selected at any time during the flight. All observing bands will have an IF bandwidth of 4 GHz. A FFT digital spectrometer will provide continuous coverage of this band with very high resolution, up to greater than 10^6. The instrument design is extremely modular and will allow the continuous incorporation of new hardware, accommodating future improvements in mixer, LO and microwave spectrometer technologies, throughout the lifetime of the SOFIA observatory.

ACKNOWLEDGMENT

Various subsystems of the CASIMIR instrument have been or continue to be developed by a number of people at several institutions: H. G. Le Duc, Micro Devices Lab, JPL (mixer fabrication), N. R., M. R. Haas, NASA Ames (optics), the Kosma I/O Team, U. of Köln and S. W. Colgan, NASA Ames (software). The development of CASIMIR is supported by NASA/USRA SOFIA Instrument Development Fund.

REFERENCES

[1] Casey, S. C., "The SOFIA program: astronomers return to the stratosphere," *Proc. SPIE* 6267, 2006.

[2] Becklin, E. E, Tielens, A. G. G. M., and Callis, H. H. S., "Stratospheric Observatory for Infrared Astronomy (SOFIA)," *Mod. Phys. Lett. A* 21, 2551-2560, 2006.

[3] Neufeld, D. A., and Kaufan, M. J. "Radiative Cooling of Warm Molecular Gas," *Ap. J.* 418, 263, 1993.

[4] Vastel, C., Caselli, P., Ceccarelli, C., Phillips, T., Wiedner, C., Peng, R., Houde, M., and Dominik, C., "The distribution of ortho- $H2D^+$ ($1_{1,0}$–$1_{1,1}$) in L1544: tracing the deuterization factory in prestellar cores," *Ap. J.* 645, 1198-1211, 2006.

[5] Harju, J., Haikala, L. K., Lehtinen, K., Juvela, M., Matilla, K., Miettinen, O., Dumke, M., Gusten, R., and Nyman, L.-A., "Detection of $H2D^+$ in a massive prestellar core in Orion B*," *A&A* 454, L55-58, 2006.

[6] Boreiko, R. T., and Betz, A. L., "A search for the rotational transitions $H2D^+$ at 1370 GHz and $H3O^+$ at 985 GHz," *Ap. J. (Letters)* 405, L39-L42, 1993.

[7] Karpov, A., Miller, D., Rice, F., Stern, J.A., Bumble, B., LeDuc, H.G., & Zmuidzinas, J., "Low Noise 1 THz–1.4 THz Mixers Using Nb/Al-AlN/NbTiN SIS Junctions," *IEEE Trans. Applied Superconductivity* 17, 343, 2007.

[8] Wadefalk, N., Mellberg, A., Angelov, I., Barsky, M. E., Bui, S., Choumas, E., Grundbacher, R. W., Kollberg, E. L., Lai, R., Rorsman, N., Starski, P., Stenarson, J., Streit, D. C., and Zirath, H., "Cryogenic wide-band ultra-low-noise IF amplifiers operating at ultra-low DC power," *IEEE Trans. Microwave Theory Tech.* 51, 1705-1711, 2003.

[9] Pamtech, Passive Microwave Technology Inc., 4053 Calle Tesoro, Suite A, Camarillo, CA. 93012.

[10] CTT Inc., 3005 Democracy Way, Santa Clara, CA 95054, USA. [Online]. Available: http://www.cttinc.com/

[11] Virginia Diodes Inc., 979 Second St. S.E., Suite 309, Charlottesville, VA 22902-6172, USA. [Online]. Available: http://www.virginiadiodes.com/

[12] Mehdi, I., Schlect, E., Chattopadhyay, G., and Siegel, P. H., "THz local oscillator sources: performance and capabilities," *Proc. SPIE* 4855**,** 435-446, 2003.

[13] Emrich, A., Krus, M., and Reisbeck, J., "FFT spectrometer for (sub)mm radiometer applications," *Proc. 18th Int. Symp. Space Terahertz Tech.*, 140, 2007.

[14] Omnisys Instruments AB, Gruvgatan 8, 421 30 Goteborg, Sweden, [Online]. Available: http://www.omnisys.se/

Upgrade of the SMART Focal Plane Array Receiver for NANTEN2

U.U. Graf, C.E. Honingh, K. Jacobs, M. Justen, P. Pütz, M. Schultz, S. Wulff, J. Stutzki
KOSMA, 1. Physikalisches Institut der Universität zu Köln, Germany

We present the recent upgrade to the KOSMA SMART 2x 8-pixel dual-color focal plane array receiver. The 460–490 GHz channel has been upgraded from 4 to 8 pixels. We use standard tunerless waveguide mixers with corrugated horns and all-Niobium single junction SIS devices. The measured noise temperatures are around 70 K over the RF band for an IF of 3.5–4.5 GHz for all pixels. At the IF the receiver is enhanced with new bias-tees and low noise MMIC amplifiers developed at Caltech.

In the 800–880 GHz channel, devices with NbTiN-SiO_2-Al tuning structures replace older SIS devices with Al-SiO_2-Al tuning microstrip circuits. Their fabrication at KOSMA's nanofabrication facilities utilizes electron beam lithography and chemical-mechanical planarization processing steps developed for the HIFI Band 2 devices. These devices need less local oscillator power, which facilitates the upgrade from 4 to 8 pixels. Measured noise temperatures per pixel are between 250 K and 300 K over the RF band for an IF of 4–8 GHz. In SMART the IF band is 1–2 GHz in order to simultaneously cover the CO 7-6 and the $^3P_2$-$^3P_1$ Carbon lines at 807 GHz and 809 GHz in the lower and upper sidebands. All noise temperatures are measured with a 13 μm thick Mylar beam splitter, are uncorrected and calculated according to the Callen-Welton formalism.

The receiver is currently being installed at the KOSMA Gornergrat observatory. After a two- month test run, it will be shipped to the NANTEN2 telescope in Chile to be installed as a facility instrument in time for the southern hemisphere winter.

New Challenge for 0.1 - 0.3 THz Technology: Development of Apparatus for Radio Telescope RT-70

V. Vdovin[1], I. Zinchenko[1]
Yu. Artemenko[2], V. Dubrovich[3]
A. Baryshev[4]

[1] Institute of Applied Physics of Russian Academy of Sciences, Nizhniy Novgorod, Russia (IAP RAS)
[2] Astro Space Center of Lebedev Physical Institute of Russian Academy of Sciences, Moscow, Russia (LPI RAS)
[3] Special Astrophysical Observatory of Russian Academy of Sciences, St. Petersburg, Russia (SAO RAS).
[4] Institute of Radio-engineering and Electronics of Russian Academy of Sciences, Moscow, Russia (IRE RAS)

The 70-m radio telescope is now under construction on plateau Suffa in Uzbekistan at an altitude of 2500 m. It will have an actively controlled main mirror with the goal to achieve the shortest operational wavelength 1 mm. The project started many years ago but was frozen after USSR disintegration. The telescope support and the basic parts of the antenna were manufactured (Fig. 1). During the last few years the project has restarted and plans are being made to complete it in collaboration with Russia and Uzbekistan. The organization which is responsible for the project as a whole in Russia is the Astro Space Center of the Lebedev Physical Institute.

The telescope should operate both in single-dish mode and as a part of VLBI networks, in particular in combination with planned radio telescopes in space such as Millimetron. The collecting area of the antenna greatly exceeds that of existing mm-wave facilities and is comparable to the total area of the ALMA antennas. This provides unprecedented capabilities for studies of compact faint objects which will be the primary targets for this instrument. The scientific program includes a wide range of astrophysical problems from studies of Solar system objects to the most distant radio galaxies and quasars. One of the most important tasks will be investigations of small scale primordial and secondary fluctuations of the CMB. For this task RT-70 will be significantly more efficient than a system of smaller telescopes like ALMA.

In this report we mainly discuss the project status and development of the scientific instruments for this antenna which is still at a preliminary stage. They should incorporate the latest technological achievements and provide a superior performance over the operational frequency range. Both single-pixel and large format array (direct detection and heterodyne) receivers are considered. The receiver design is performed in the framework of a wide cooperation of Russian and Ukrainian organizations but is also open for the international community.

The work is supported by the Program of Fundamental Researches of the Russian Academy of Sciences #5.2. “Electromagnetic THz- waves” and a special program Suffa project of ASC LPI RAS.

Fig 1. The Suffa observatory with the radio telescope RT-70 now and after 2012.

Development of a Two-Pixel Integrated Heterodyne Schottky Diode Receiver at 183GHz

Hui Wang [1, *], Alain Maestrini [1], Bertrand Thomas [2], Byron Alderman [2] and Gérard Beaudin [1]

[1]*Observatoire de Paris, LERMA, 61 Avenue de l'Observatoire, 75014 Paris, France*

[2]*Rutherford Appleton Laboratory, STFC, Chilton Didcot, OX11 0QX, Oxfordshire, UK.*

* Contact: hui.wang@obspm.fr, phone +33-1-40512079

***Abstract*— This paper describes the design of a two-pixel Schottky diode-based heterodyne receiver working at 183GHz. The receiver is the integration of two 183GHz subharmonic mixers and a frequency tripler into the same mechanical block. A Y junction divider is used to split the power produced by the frequency multiplier. The chips have been fabricated using the standard BES process of United Monolithic Semiconductors (UMS) in the frame of a contract with the Centre National d'Etudes Spatiales (CNES) and the European Space Agency (ESA). The integrated two-pixel receiver is expected to work in the band 170-195 GHz with a double side band (DSB) conversion gain greater than -5.5dB when pumped with less than 50mW of input power at 30GHz. A minimum DSB conversion gain of -4.5dB at 183 GHz is expected.**

I. Introduction

In planetary and atmospheric sciences large arrays of millimeter wave heterodyne Schottky diode-based receivers can offer higher mapping speed and mapping consistency while avoiding the use of cryogenic receivers. To reduce the size, the weight and the power consumption of a multi-pixel receiver it is necessary to optimize the interface between the mixers and the local oscillator unit. One solution consists in integrating in the same mechanical block a frequency multiplier and one or several mixers to create a compact sub-array.

II. Two-pixel integrated receiver at 183GHz

A novel approach to design multi-pixel heterodyne receiver is described below. Based on this idea, we could extend the number of beams after changing the LO distribution network. This concept could be applied to higher frequencies.

A. Design Approach and Model

Large heterodyne arrays are possible only by higher levels of component integration with associated package and power dissipation issues [1]. The challenges in developing large arrays of heterodyne detectors relate to the mixer configuration, local oscillator (LO) power coupling, the intermediate frequency (IF) layout, and the back-end processing. In our configuration, one single solid state LO source pump two mixers simultaneously by using a power divider. In addition, the mixers and the frequency multiplier are integrated in a same waveguide block. Figure 1 shows the topology of this two-pixel integrated receiver. Two IF signals are collected vertically with standard SMA connector. The mixer and the tripler chips were both optimized independently for two stand-alone circuits. The design of this mixer and this tripler are detailed respectively in section III and section IV.

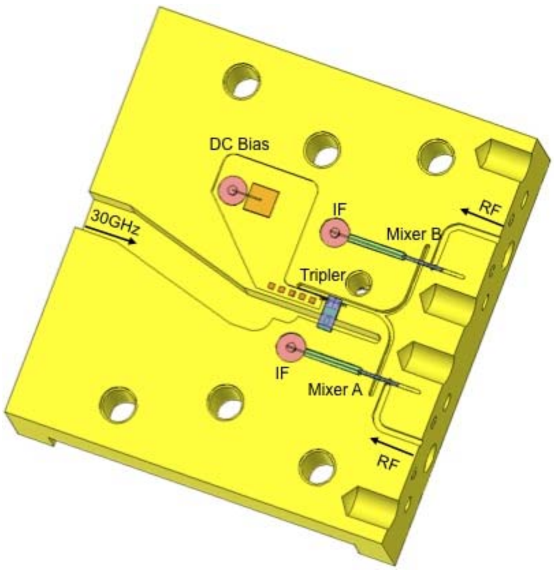

Fig. 26 Schematic of the bottom block of the two-pixel integrated receiver with the IF connector and DC bias.

B. Optimization and Simulation Result

We used the same mixer and tripler chips for the two-pixel integrated receiver as for the stand-alone 183 GHz mixer and 90 GHz tripler circuits. The optimization of the two-pixel receiver was performed by several steps. Firstly, the input waveguide back short, the input waveguide steps and the output waveguide back short of the tripler were re-optimized as a novel stand-alone tripler. Actually, to reduce the size of the integrated receiver, the height of the output waveguide of the tripler and the height of the LO waveguide of the mixers were reduced contrary to the stand-alone versions that had full height waveguides. Secondly, a reduced-height waveguide Y junction was optimized for splitting evenly the output power of the 90 GHz tripler. Thirdly, the RF waveguide back short, RF waveguide steps and the OL waveguide back short of the 183GHz mixers were re-optimized. Finally, the optimization of the complete receiver was performed by tuning both the distance between the output probe of the tripler and the Y junction, and the distance between the LO waveguide of the mixer and the Y junction in order to get an optimum LO coupling. All the simulations and optimizations were performed by using Ansoft HFSS and Agilent ADS.

The predicted performance of the integrated receiver is presented in Figure 2. The two mixers have almost identical noise temperature. By tuning the input power of the receiver from 30mW to 100mW, the optimum performance of the receiver can be reached. A minimum DSB mixer noise temperature of 500K at 183GHz is expected for the two mixers with an input power of 50mW at 30GHz.

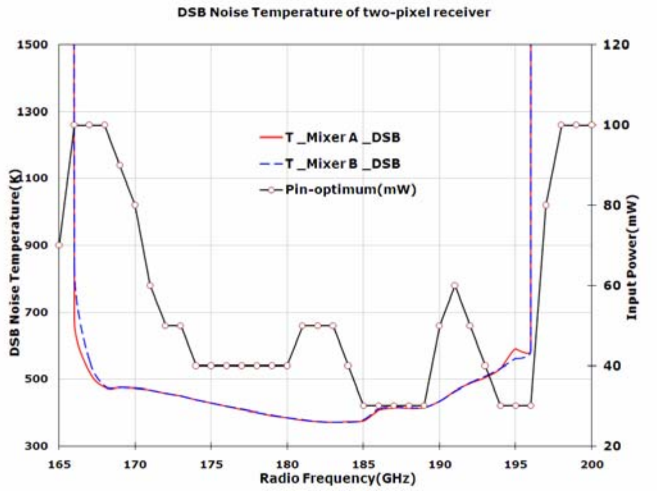

Fig. 27 The bottom solid line and the dashed line show respectively the simulated DSB mixer noise temperature for two pixels with optimum input power; the plain curves with open marker show the optimum input power to the receiver.

III. 183GHZ MMIC SHP2 MIXER

The 183GHz MMIC subharmonic mixer was optimized independently for a stand-alone circuit.

A. *Mixer Layout*

This is a broadband fixed-tuned 183 GHz sub-harmonically pumped mixer featuring an anti-par -8allel pair of planar Schottky diodes monolithically integrated on a 50 µm-thick GaAs substrate. The circuit was fabricated using the standard BES process of United Monolithic Semiconductors (UMS). The circuit is about 4 mm long, 0.28 mm wide and is mounted in a waveguide split block that includes waveguide matching elements at the Local Oscillator (LO) and RF frequencies (Figure 3). Design details are described in [2].

The mixer is expected to work efficiently in the band 160-190 GHz using only 2mW of LO pump power, with a Double Side Band (DSB) conversion gain greater than -5.5 dB. The best performance obtained in simulations is a DSB gain of -5.1 dB at 183 GHz.

Unfortunately, due to misalignments during the steps processing, the mixer chip presents unbalanced diodes with series resistances of 21Ω and 12.5Ω.

B. *Measurements*

For the experiments, the LO fundamental source was provided by a 8-18GHz Yig oscillator from an AB Millimetre Network Vector Analyzer, which as used to drive a commercial sextupler followed by a power amplifier both from Radiometer Physics GmbH; this LO source chain could provide about 10mW from 75GHz to 100GHz. This source chain was calibrated with an Erickson power meter [3]. A W band waveguide attenuator was used to adjust the pump power for the mixer. A directional coupler inserted before the mixer measured the pump power coupled into the mixer.

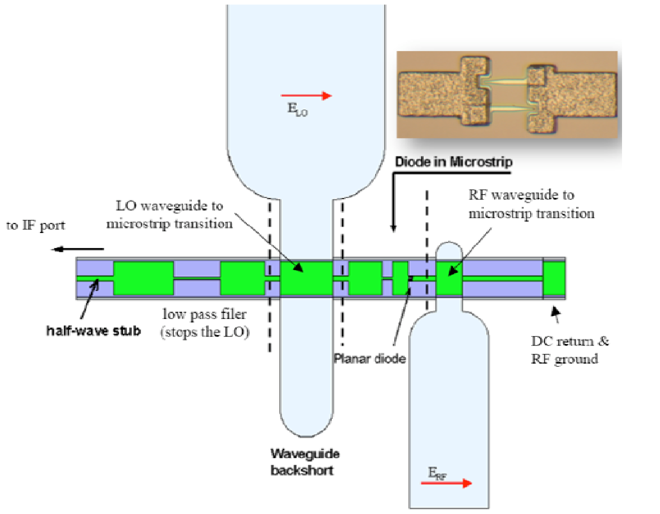

Fig. 28 Schematic of the MMIC mixer circuit and waveguide matching elements, an anti-parallel pair of diodes is shown on the top right.

We use a 2-4GHz IF chain that includes a low-loss isolator at its input and an internal noise source that can be switched ON and OFF to modify the noise factor of the IF chain. The noise temperature of the IF chain is 194.4K when the internal noise source is ON, and 81.2K when the noise source is OFF.

The equivalent noise temperature of the receiver was measured by presenting alternatively a room temperature and a liquid nitrogen-cooled blackbody in front of the mixer feed-horn. Two independent receiver equivalent noise temperature measurements are performed: one with the internal noise source ON the other with the internal noise source OFF. We use the classic Y-factor method to calculate the receiver noise temperature. The Y factor was measured with an Agilent E9325A (0.05-18GHz) power sensor corrected from its non-linearity in a separate calibration procedure. This test bench can achieve an accuracy of 0.001dB for the Y factor measurement.

All the measurements were performed at room temperature. Mixer DSB noise temperatures, mixer conversion losses and the LO pump powers as a function of RF frequency are presented below in Figure 4&5. The measured noise temperatures and conversion losses are significantly higher than the predicted values. This could be partly due to the unbalance of the diodes. Preliminary simulations have been performed with unbalanced diodes, showing that the difference on the mixer noise temperature is only of about 100K. The optimum pump power in the band 160-190GHz is however in very good agreement with simulation results.

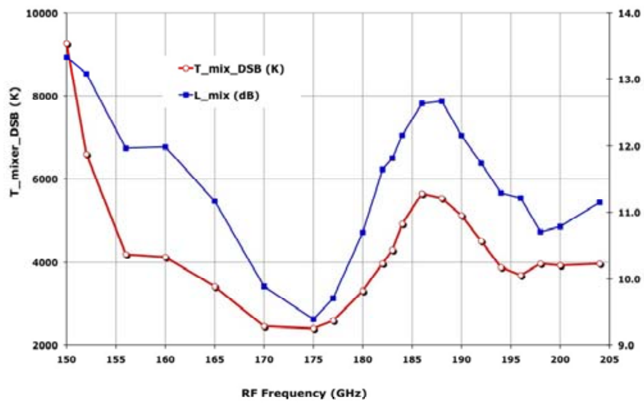

Fig. 29 The top plain curve with filled square markers and the bottom plain curve with open circles show respectively the measured DSB mixer noise temperature and the measure DSB mixer conversion losses.

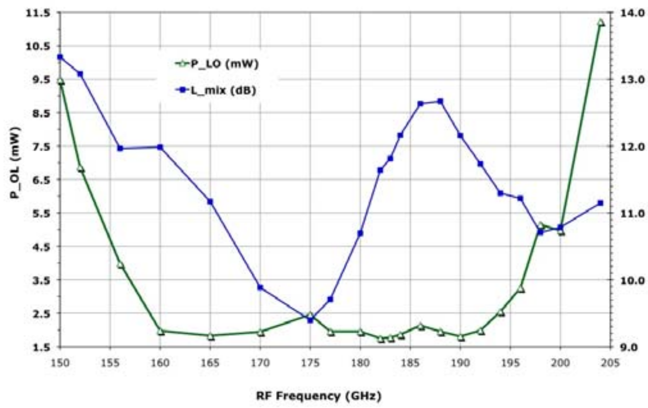

Fig. 30 The top plain curve with filled square markets shows the measure DSB mixer conversion losses, the bottom plain curve with open circles show the LO pump power.

IV. 90GHZ MMIC FREQUENCY TRIPLER

A. Design

A 6-anode balanced tripler was designed based on the same topology shown in [4]. The tripler uses the so-called open-loop configuration that allows more than two diodes to be easily implanted on chip dramatically increasing the power handling capabilities of the multiplier.

1) Topology and optimization

In our design, this loop is created by 6 diodes that are in series at DC but appear to be in an anti-parallel configuration at the RF, due to the symmetry of the excitation and the symmetry of the circuit. This virtual loop can only work if the suspended microstrip line that the diodes are connected to cannot propagate the parasitic (TE) mode at the second harmonic.

The matching of the diode is performed both by a succession of high and low impedance sections printed on chip and by the input and the output probes with their respective back-shorts. To widen the bandwidth, the circuit features additional matching elements in the input and output waveguides, made with a succession of waveguide sections of different heights and lengths.

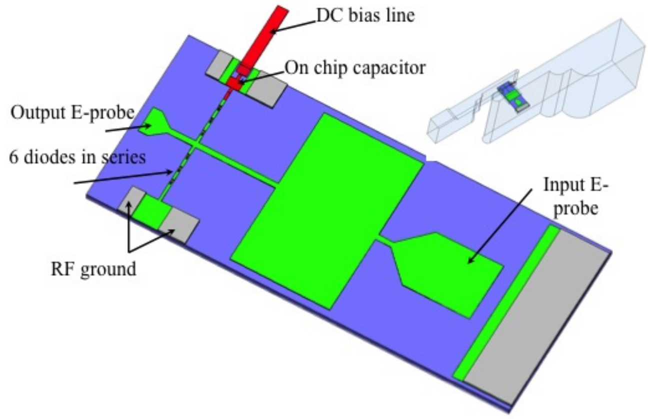

Fig. 31 Schematic of tripler chip on GaAs substrate without channel and waveguides and the top right corner shows the hip inside waveguide.

Special attention was put on the biasing scheme, which is usually tricky for high frequency circuits. UMS BES process provides on-chip capacitors: that can be small enough to fit on the multiplier chip. The RF grounding to the block will be made by silver epoxy glue; the DC line will be connected to the on-chip-capacitor via a wire-bond.

The optimization is performed using Ansoft HFSS and Agilent ADS. The optimization method was presented in [5].

2) Tripler architecture and fabrication

The chip features six Schottky diodes using UMS BES process with wide gate width (>10µm), each anode has the following characteristics: an ideality factor η =1.2, saturation current I_{SAT}=4.10-15A, series resistance Rs=5 Ω, the optimum junction capacitance Cj = 36 fF (optimized) and the length of anode 22 um (gate width). The 6 diodes are connected in series and integrated on a 1360 um wide substrate, suspended in a channel with the width of channel of 1400 um and the height of channel of 550 um (Figure 6). Figure 7 shows a wafer photograph of the tripler chip.

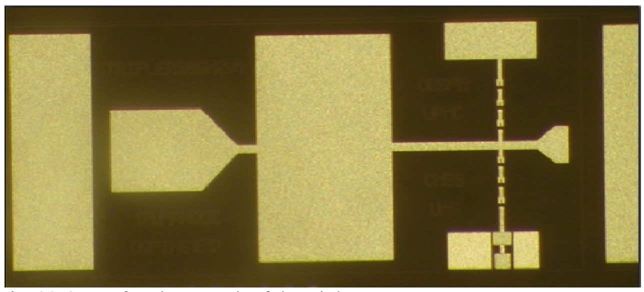

Fig. 32 On wafer photograph of the tripler.

B. Simulation Result

The predicted performance of the tripler is presented in Figure 8. The average efficiency from 29- 32GHz is about

13% and corresponds to the output powers of about 6.5mW, which is sufficient to pump the subharmonic mixer. These estimated efficiencies are for 50mW of input power.

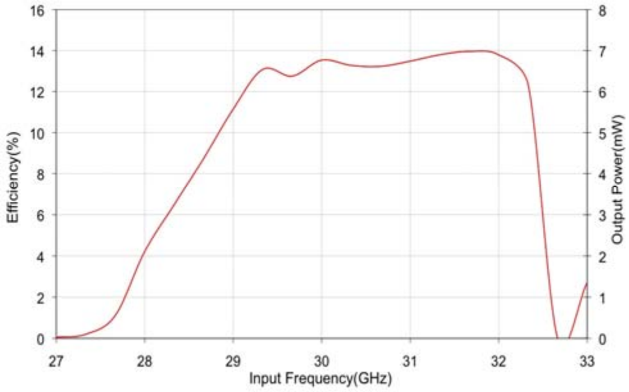

Fig. 33 Predicted efficiency and output power VS input frequency for an input power of 50 mW.

CONCLUSIONS

A novel topology of integrated heterodyne detector working at room temperature has been proposed. It is believed that this design is suitable to create larger arrays of heterodyne detectors and apply for higher frequencies. The circuits have been fabricated using the standard BES process of United Monolithic Semiconductors (UMS). The measurement of the 90GHz tripler and the machining of the two-pixel receiver will be accomplished during the summer of 2008. The test of the complete receiver would be performed later this year.

ACKNOWLEDGMENT

The authors wish to thank the Precision Development Facility at RAL for the machining of the mixer and tripler block and the support from CNES, the Centre National Recherche Scientifique (CNRS), AB Millimetre in France, ESA and the Rutherford Appleton Laboratory in the United Kingdom.

REFERENCES

[1] G. Chattopadhyay, I.Mehdi, J. S. Ward, E.Schlecht, A. Skalare, and P. H. Siegel, “Development of Multi-pixel Heterodyne Array Instruments at Submillimeter Wavelengths,” *Proceedings of the Asia Pacific Microwave Conference*, New Delhi, India, December2004.

[2] H. Wang, J.-M. Rollin, B. Thomas, S. Davies, B. Alderman and A. Maestrini, “Design of a low noise integrated sub-harmonic mixer at 183 GHz using European Schottky diode technology,” in *Proceedings of the 4th ESA workshop on Millimetre-Wave Technology and Applications*, Espoo, Finland, February 2006, pp.249-252, .

[3] N. R. Erickson, “A fast and sensitive submillimeter waveguide power sensor,” in *Proc. 10th Int. Symp. Space Terahertz Technology*, Charlottesville, VA, 1999, pp. 501–507.

[4] A. Maestrini, Charlotte Tripon-Canseliet, John S. Ward, John J. Gill, Hamid H. S. Javadi, Erich Schlecht, Goutam Chattopadhyay, and Imran Mehdi, “Multiple-Anode Broadband Frequency Triplers at Submillimeter Wavelengths,” in *Proc. 16th Int. Symp. Space Terahertz Technology*, Göteborg, Sweden, May 2005.

[5] A. Maestrini, John S. Ward, John J. Gill, Hamid H. S. Javadi, Erich Schlecht, Charlotte Tripon-Canseliet, Goutam Chattopadhyay, and Imran Mehdi, “A 540-640 GHz High Efficiency Four Anode Frequency Tripler,” *IEEE Transactions on Microwave Theory and Techniques*, vol. 53, no. 9, pp. 2835-2843, Sep. 2005.

UTC-PD Integration for Submillimetre-wave Generation

Biddut Banik, Josip Vukusic, Hans Hjelmgren, Henrik Sunnerud, Andreas Wiberg and Jan Stake

Department of Microtechnology and Nanoscience, Chalmers University of Technology; SE-41296 Göteborg, Sweden (e-mail: biddut.banik@chalmers.se).

Abstract: Because of the inherent difficulty to generate power in the frequency range 0.l-10 THz, the term 'THz-gap' has been coined. Among a number of MW/THz generation techniques, the photomixer based sources hold high potential offering wide tunability and decent amounts of output power. The photomixing technique relies on the nonlinear mixing of two closely spaced laser wavelengths generating a beat oscillation at the difference frequency. In recent years, there has been an increasing interest in the Uni-Travelling-Carrier PhotoDiode (UTC-PD) [1] for photomixing, photo receivers, MW/THz-wave generation, fibre-optic communication systems, and wireless communications. UTC-PDs have become very promising by demonstrating output powers of 20 mW at 100 GHz [1] and 25 μW at 0.9 THz [2].

Our ongoing research work concentrates on extending the previously accomplished UTC-PD fabrication and modelling techniques to ~300 GHz and above. We have already fabricated and characterised UTC-PDs intended for millimetre-wave generation. Several integrated antenna-detector circuits have been designed and characterised. Fig.1 (a) shows the SEM of a fabricated UTC-PD. Furthermore, in order to understand the device behaviour and its dependence on various factors, we have developed an accurate device model [3] implementing hydrodynamic transport model. The model has also enabled us to design and optimise the device for any specific application and target frequency [4].

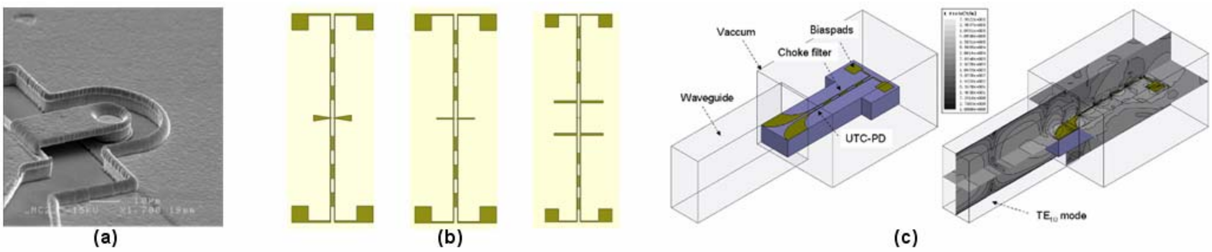

Fig. 1. (a) SEM of a fabricated UTC-PD (b) antenna integrated UTC-PDs, and (c) waveguide integrated UTC-PDs.

The current research-focus encompasses different integration approaches, and the construction of various antenna-integrated circuits and waveguide blocks that can be used as millimetre-wave (300 GHz and above) generator for local-oscillator and free-space applications. Fig. 1 (b-c) shows several antenna integrated UTC-PDs and an example of the waveguide integrated UTC-PD. The designs of those blocks and integrated circuits, their fabrication and characterisation results will be presented.

REFERENCES

[1] H. Ito, T. Nagatsuma, A. Hirata, T. Minotani, A. Sasaki, Y. Hirota, and T. Ishibashi, "High-power photonic millimetre wave generation at 100 GHz using matching-circuit-integrated uni-travelling-carrier photodiodes," *Optoelectronics, IEE Proceedings*, vol. 150, pp. 138-142, 2003.

[2] C. C. Renaud, M. Robertson, D. Rogers, R. Firth, P. J. Cannard, R. Moore, and A. J. Seeds, "A high responsivity, broadband waveguide uni-travelling carrier photodiode," *Proceedings of the SPIE*, vol. 6194, pp. 61940C, 2006.

[3] S. M. M. Rahman, H. Hjelmgren, J. Vukusic, J. Stake, P. Andrekson, and H. Zirath, "Hydrodynamic simulations of uni-traveling-carrier photodiodes," *IEEE J. Quantum Electron.*, vol. 43, pp. 1088-1094, 2007.

[4] Biddut Banik, Josip Vukusic, Hans Hjelmgren, and Jan Stake, "Optimization of the UTC-PD Epitaxy for Photomixing at 340 GHz", submitted to *IEEE Electron Dvice Letters*

Development of superconductive parallel junction arrays for Submm-wave local oscillator applications

F. Boussaha[1*], A. Féret[1], B. Lecomte[1], M. Salez[1,2], L. Loukitch[3], C. Chaumont[4], J-M. Krieg[1], M. Chaubet[5]

[1]LERMA - Observatoire de Paris, 77 avenue Denfert-Rochereau, 75014 PARIS – France
[2]Laboratoire des solides irradiés –Ecole Polytechnique, route du plateau de Saclay, 91128 PALAISEAU – France
[3] Laboratoire de Mathématique, INSA de Rouen, B.P.8, 76131 Mont-Saint-Aignan cedex – France
[4]GEPI – Pôle instrumental - Observatoire de Paris, 77 avenue Denfert-Rochereau, 75014 PARIS – France
[5]CNES - BP 2220, 18 avenue Edward Belin, 31401 Toulouse Cedex 4 – France
*Contact: faouzi.boussaha@obspm.fr, Tel: +33-1-40 51 20 69

***Abstract*—In order to develop Submillimiter-wave fully Integrated Superconducting Receivers (SIRs) based on parallel small SIS junction arrays (multijunction) operating as local oscillator, we investigate their performance through measurement and simulation. Multijunction may be an interesting alternative to LJJ because it allows wide LO tunability, wide impedance matching bandwidths and increase design flexibility and control of technological parameters.**

I. Introduction

Because of its low size, mass and power consumption the complete compact ultra-sensitive submm receiver system is very attractive for multi-spacecraft applications using interferometry technique for post-Herschel submm-wave spaceborne instruments or for distant monitoring of the Earth atmosphere from space. They also open the way to on-chip integration of heterodyne receivers with the digital processing unit. Khoshelets & al [1-2] developed an efficient SIR system using a Long Josephson Junction (LLJ) operated in the Flux-Flow Oscillator (FFO) regime. In this study, we propose to use SIS parallel junction arrays as local oscillators instead of a LJJ. Indeed, the latter has an impedance often < 1Ω while the multijunction can present several tens of ohms making it suitable to deliver higher output power with larger bandwidth. Moreover, non-uniform arrays can be designed to provide very wide coupling bandwidths, a property which has already been employed to optimize multijunction quasiparticle mixers [3]. The resonance shapes observed in multijunction I-V curve and their behavior versus external applied magnetic field remind strongly Zero Field Steps (ZFS) and Fiske Steps (FS) usually seen in LLJ suggesting travelling fluxons [4]. A fundamental issue to use this kind of circuit as local oscillator is their ability to produce usable submillimeter signals. In this paper, we report the first measurement results of multijunction-generated radiation in the submm-wave range by using the heterodyne technique. We will also briefly present the modelling work of this kind of circuits.

II. Circuits

The non-uniform parallel junction arrays investigated here were initially designed for broadband submillimeter-wave heterodyne quasiparticle SIS mixers [3] (see figure 1). The circuits are made up of 5 identical junctions of l_jxw_j=1x1 µm² embedded in superconductive Nb/SiO/Nb stripline of width w=5 µm and length l=80 µm. The spacings between junctions, allowing to tune out the tunnel barrier capacitance at desired frequencies, were optimized for best RF coupling in 480-640 GHz frequency range, and are summarized in the following table:

TABLE XI
DIMENSIONS OF THE SIS JUNCTION ARRAYS (µM)

N x junction	l_1	l_2	l_3	l_4
5	20	42	12	6

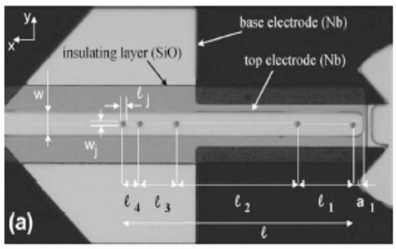

Fig. 1 Photograph of multijunction circuit. The 1 µm² junctions are made out of Nb/Al-AlO$_x$/Nb.

The multijunction is integrated with a bowtie antenna and RF choke filters, on a 50 µm thickness quartz substrate, mounted across a 100×400 µm half-height rectangular waveguide followed by a corrugated horn. In this particular configuration, the source impedance at the bowtie is real (~50 Ω) over 480-640 GHz [5] [7], allowing an optimized detection, but potentially also emission, of submillimeter-wave signals in that range. The multijunction circuits were made at Paris Observatory facility using standard Selective Niobium Etching Process [6] [12].

III. Experiment

The aim is to study the radiation generated by a 5-junction array circuit with current density of ~ 10 kA/cm², in a Josephson resonant mode, by using the heterodyne technique as shown in figure 2. Two identical mixers blocks optimized for the 480-640 GHz band were employed, each in its own liquid helium cryostat, respectively hosting the multijunction used as a submm-wave source, and a twin-junction fabricated by the KOSMA group as the SIS mixer [13]. The mixer output signal at intermediate frequency (IF) is fed through an isolator and a cryogenic HEMT preamplifier at 4-8 GHz, then measured using a power-meter and spectrum analyzer. The Josephson currents are entirely suppressed in the twin-junction and must be finely controlled in the multijunction by a magnetic field generated by NbTi superconductive wire coiled around a cryoperm core. On its quasioptical path, the RF signals from the multijunction must pass through a 13-µm mylar beam splitter, and twice across a 25-µm mylar window at room temperature, a 250-µm Zitex infrared filter at 77K, and a pair of cold elliptical mirrors at 4.2K. A 385-550 GHz solid-state local oscillator (LO), combining a Gunn source and a Schottky frequency-multiplier, was used to pump the SIS mixer's twin-junction.

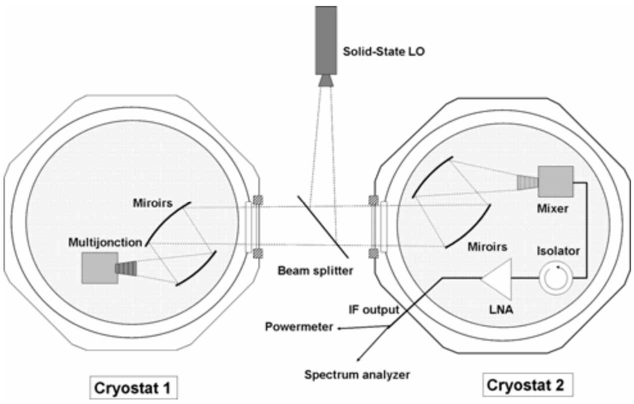

Fig. 2 Schematic diagram of the setup bench to characterize resonances observed in multijunction IV curve. Cryostat 1 and cryostat 2 contain respectively multijunction operating as LO and twin-junction as mixer.

A. Preliminary measurements

Figure 3 shows typical resonances appearing in the I-V curve of the multijunction. Three resonances emerged at V_{Res} ~ 0.5 mV, 0.84 mV and 1.02 mV for different values of the magnetic field. The corresponding fundamental frequencies (f_{Res}= $2eV_{Res}$ / h) are ~ 242, 406.5 and 493.6 GHz.

To determine which Josephson resonances in the multijunction, i.e which frequencies, could be observed with our setup, we measured the RF coupling bandwidths of both the emitter (multijunction) and the detector (twin-junction), by Fourier Transform Spectrometry technique (FTS), as shown in figure 4.

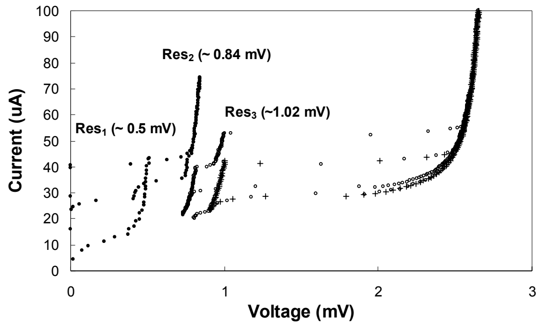

Fig. 3 I-V curve of multijunction. Resonances obtained for different values of applied magnetic field.

Note that in this characterization we operate the multijunction as a detector, and assume the equation between input and output coupling responses. We find a low-frequency cutoff at 400 GHz for the twin-junction and at 435 GHz for the multijunction. We conclude that the first two resonances at 242 and 406 GHz are out-of-band and that consequently their associated fundamental Josephson frequencies cannot be detected. The heterodyne measurement was therefore carried out mainly with the third resonance (f_{Res3} = 493.6 GHz).

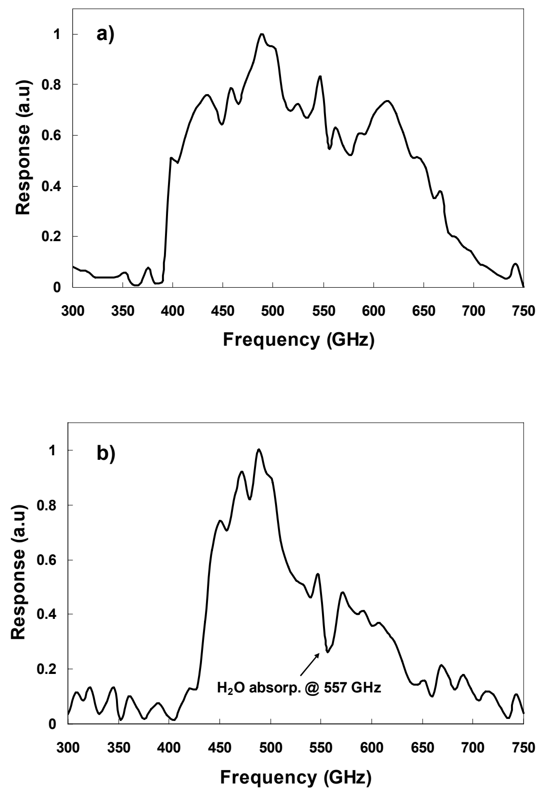

Fig. 4 Instantaneous frequency response measured by Fourier Transform Spectroscopy (FTS) of a) the twin-junction (mixer) and b) the multijunction circuit (emitter).

Figure 5 shows the I-V curve of the SIS mixer pumped by a LO at 494 GHz and the corresponding output IF power, integrated over the 4 GHz bandwidth, obtained at two bias voltages, respectively in the presence (ON) and in the absence (OFF) of the resonance. Absence of resonance means that the multijunction is biased either at V=0, V_{res}< V< V_{gap} or V> V_{gap} for each measurement. Those three bias voltages give the same IF output response at the mixer. However, when the multijunction is biased at V_{Res3} = 1.02 ± 0.01 mV, the mixer IF power increases over the quasi-particle step as is shown in figure 5. From the curve, the mixer twin-junction is expected to be most sensitive in the 1.6-2.3 mV bias voltage range.

B. Heterodyne measurement

In the ON position the multijunction was biased on the resonance at 1.02 ± 0.01 mV (493 ± 4.84 GHz), whereas the solid-state LO was tuned at 495 GHz. The twin-junction mixer is biased at 1.9 mV (for maximum sensitivity). The IF power spectrum measured across the 4-8 GHz frequency range is shown in figure 6. Several reproducible spectral structures probably corresponding to the beat signal were observed, *only* in the presence of the resonance (ON).

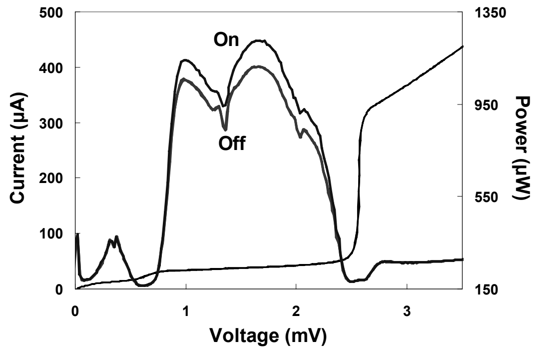

Fig. 5 Twin-junction mixer Pumped IV curve at 495 GHz and the output power FI obtained in the presence (On) and absence (Off) of the resonance Res_3.

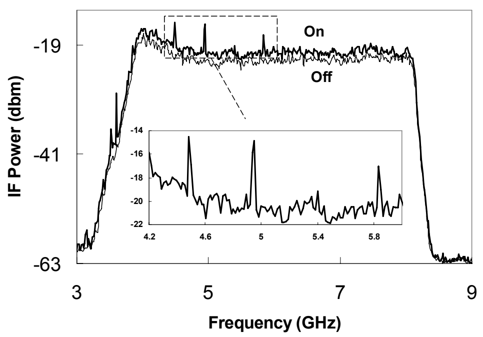

Fig. 6 IF power spectrum measured across the IF band of 4-8 GHz.

The measured linewidth is $\Delta f \approx 50$ MHz for all spectral lines. Nevertheless, we have not yet clearly identified the source of noise in these structures even though we strongly suspect the instability due to the multijunction bias voltage, since the Josephson resonance was not phase-locked. More measurements with very stable bias are needed to confirm these results.

IV. Simulations

To understand the complex Josephson behaviour of non-evenly distributed, parallel junctions, we developed a new model based on sine-Gordon equation, suitable for any small junction arrays embedded in superconductive stripline. The mean difficulty to model this kind of circuits lies in the inhomogeneous distribution of the junctions, unlike the cases treated by [8-9]. In our case, the junctions are considered as a sum of Dirac distribution δ [10-11] within the stripline. This original approach allowed us to analyze finely the Josephson static regime of any non-uniform arrays, which is also a non-uniform SQUID array or grating (SQUIG). Figure 7 shows the experimental and theoretical curves of critical current I_{max} at V=0 versus an externally applied magnetic field H_{ext}. The excellent agreement between simulations and measurements confirms the validity of this model. The shape of the curves indicates that the static magnetic field penetrates in the multijunction as flux quanta. Further details are given by [12].

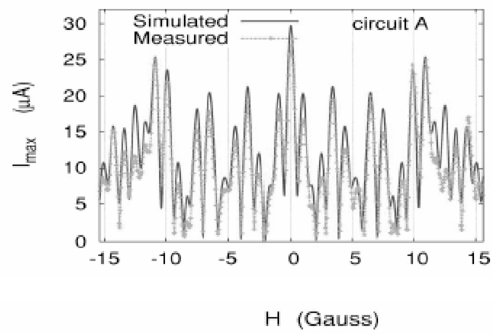

Fig. 7 Measured and simulated $I_{max}(H_{ext})$ at V=0 of our multijunction circuit.

This static model constitutes the first step toward the global electrodynamic model to describe the exact operating mechanism and to determine the performance when the multijunction operates as a source in order to design new circuits at desired frequencies. Preliminary simulations on similar arrays using this model indicate that depending on geometry, current density, SIS junctions and superconductive stripline electrodes intrinsic parameters, solitons (fluxons), can be generated in the multijunction circuit in Flux Flow Oscillator (FFO) regime [10].

Conclusions

We investigate a non-uniform arrays of small Nb/AlO_x/Nb junctions with ~ 10 kA/cm² of current density operating as submm signals generator. Using the heterodyne technique and a second SIS junction circuit used as a mixer, we made preliminary measurements indicating with no ambiguity that resonances can generate submm-wave signals. However, to confirm these results, more measurements are needed. Based on a sine-Gordon equation, an accurate model for the non-uniform junction arrays has been developed, giving excellent fits to experiments in the static regime, and on the verge of explaining the fluxon-based resonances observed in the dynamic regime.

ACKNOWLEDGMENT

The authors would like to thanks G. Beaudin and J-M. Lamarre for their continued support. The circuits and the mixer blocks were optimized by Y. Delorme and F. Dauplay. The parallel junction arrays is sponsored by the Centre National d'Etudes Spatiales (CNES) and the Institut National des Sciences de l'Univers (INSU).

REFERENCES

[1] V. Koshelets and J. Mygind, "Flux Flow Oscillators for Superconducting Integrated Submm Wave Receivers," *Studies of High Temperature Superconductors 39 (2001)*, 213–244,. Ed. A.V. Narlikar, NOVA Science Publishers, New York.

[2] V.P. Koshelets, S.V. Shitov, A.B. Ermakov, O.V. Koryukin, L.V. Filippenko, A. V. Khudchenko, M. Yu. Torgashin,P. Yagoubov, R. Hoogeveen, O.M. Pylypenko, "Superconducting Integrated Receiver for TELIS", *Report 2ET06 at the Applied Superconductivity Conference ASC'2004*, USA, October 2004.

[3] M. Salez, Y. delorme, M.-H. Chung, F. Dauplay, "Simulated Performance of multi-junction parallel array SIS mixers for ultra broadland submillimeter-wave applications ", *Proc. 11th International Symposium on Space Terahertz Technology*, Ann Arbor, MI, May 1-3, 2000.

[4] M. Salez, F. Boussaha, Y. Delorme, F. Dauplay, B. Lecomte "Observation of terahertz fluxons in superconducting junction non-uniform arrays" (to be published).

[5] F. Boussaha, M. Salez, Y. Delorme, B. Lecomte, F. Dauplay, A. Feret, J. M. Kreig, J. Spatazza, C. Chaumont, M. Chaubet. "Broadband submillimeter receivers using same mechanical block" *Proc. 16th International Symposium on Space Terahertz Technology*, Goteborg, 2005.

[6] Boussaha F.; Salez M.; Delorme Y.; Féret A.; Lecomte B.; Westerberg K.; Chaubet M. "Submillimeter mixers based on superconductive parallel junction arrays" SPIE; *1st Int.Symp. Microtechnologies for the New Millennium 2003*; Maspalomas; Canary Islands; Spain ; 19-20 mai 2003.

[7] M. Salez, Y. Delorme, I. Peron, B. Lecomte, F. Dauplay, F. Boussaha, J. Spatazza, A. Feret, J. M. Krieg and K. -F. Schuster, "A 30% bandwidth tunerless SIS mixer of quantum-limited sensitivity for Herschel/HIFI band 1" *Proc. of the SPIE conference on Telescopes and Astronomical Instrumentation, Hawaii,* Vol. 4855, pp. 402-404, 2002.

[8] A. Ustinov, M. Cirillo, B. H. Larsen, V. A. Oboznov, P. Carelli, and G. Rotoli, Phys. Rev. B 51, 3081 1995.

[9] J. H. Miller, G. H. Gunaratne, J. Huang, and T. D. Golding Appl. Phys. Rev. Lett. 59, 3330 1991.

[10] L. Loukitch, Ph. D. thesis, Institut National des sciences applisquées, Rouen, France.

[11] J. G. Caputo and L. Loukitch, SIAM J. Appl. Math 67 810 2007

[12] M. Salez, F. Boussaha, L. Loukitch, J-G. Caputo "Interference filter properties of non-uniform Josephson junction arrays" *J. Appl. Phys*, Octobre 2007.

[13] KOSMA : Physics Institute of the University Cologne – Germany

Sideband Noise Screening of Multiplier-Based Sub-Millimeter LO Chains using a WR-10 Schottky Mixer

Eric W. Bryerton[1,*] and Jeffrey Hesler[2]

[1]National Radio Astronomy Observatory, Charlottesville, VA 22903, USA

[2]Virginia Diodes, Inc., Charlottesville, VA, 22902, USA

* Contact: ebryerto@nrao.edu, phone +1-434-296-0336

***Abstract*— A method is presented for measuring the AM noise of signal sources as a function of frequency offset from the carrier. This method is particularly helpful for local oscillator sources for sub-millimeter wave single-ended mixers with wide IF bandwidths. Measurements on ALMA LO sources are presented using the described tests. The measurements are compared to receiver noise measurements using a SIS mixer. Close agreement is seen, indicating that these measurements can be used to predict added noise of sub-millimeter wave local oscillators for SIS mixers with room temperature millimeter-wave measurements.**

I. Introduction

Due to the difficulty in fabricating precision submillimeter hybrids, mixers at these wavelengths are typically single-ended. This is the case, for example, for the SIS mixers used for ALMA. In a single-ended mixer, there is no suppression of noise on the local oscillator (LO). Therefore in a sub-millimeter low-noise heterodyne receiver, the LO is required to have a very high signal-to-noise ratio (SNR).

The LO power required by a SIS mixer is proportional to the frequency squared and can be calculated from Tucker's formula [1]. Typical LO power values, at the SIS junction, for the ALMA receiver bands range from 0.03 uW to over 1.0 uW for the highest frequency bands. Therefore, an appropriate unit to quantify noise on the LO signal is to express the noise as a noise-to-signal ratio (NSR) in K/uW. A LO signal with 10 K/uW NSR used to pump a mixer which requires 0.5 uW of LO power would contribute 5 K to the overall receiver noise. For the ALMA project it was determined that AM noise on the LO should not contribute more than a few percent to overall receiver noise for any receiver band. To achieve this, the ALMA LO systems were required to have a NSR of 10 K/uW, or alternatively, a SNR of 158.6 dB.

In order to verify that the ALMA LOs are meeting this specification, it has been necessary to use the LO under test to pump the actual SIS mixer in a receiver. This test requires the full sub-milllimeter cryogenic SIS receiver. Since this is a time and cost intensive task, and since the LO and SIS mixer development in ALMA are at different institutions around the world, it is highly desirable to have a simpler screening measurement which can be performed with room temperature test equipment at a lower frequency.

The final LO multiplication in ALMA is on the 77K temperature stage inside the cryostat. The warm LO components outside the dewar are housed in an assembly called the Warm Cartridge Assembly (WCA). Fig. 1 shows a block diagram of the typical ALMA LO. The output frequency of the WCAs range from 65 to 122 GHz, depending on the particular receiver band. It is at this frequency where it would be most convenient to measure AM noise. If the final cryogenic multipliers are properly pumped, then this is an accurate representation of the signal-to-noise ratio at the SIS mixer. However, in many cases the final multiplier is underpumped. If this is the case, the measured power characteristics of the multiplier can be used to estimate the degradation in SNR in the underpumped multiplier [2]. It has been seen that the AM noise from the LO is a strong function of the IF. Therefore, the AM noise measurement should also measure the noise versus IF.

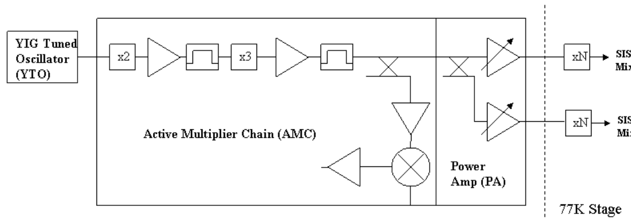

Fig. 9 Block diagram of typical ALMA first local oscillator chain.

II. Description of AM Noise Measurement

The goal of the measurements described here is to determine the level of AM noise present on a carrier signal. The measurement system must be capable of measuring sources with different output power levels and provide a fair comparison between these. The experimental setup used is the one presented in [3] and consists of a device under test (DUT), a level-set attenuator, and a radiometer. The radiometer is a single-ended mixer with a bias tee and subsequent IF amplifier to increase the signal level prior to detection (typically by a Spectrum Analyzer). The LO power induces a current in the mixer, which is used as a measure of the power delivered to the mixer by the DUT. By keeping the rectified current fixed, the power delivered to the mixer is kept constant, thus allowing for a comparison between DUTs possessing different output powers.

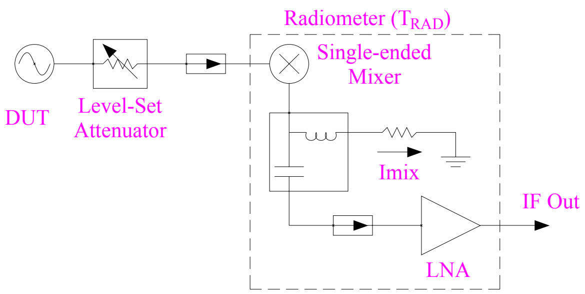

Fig. 10 Block diagram of AM noise measurement system.

One key decision is how to set a reference level for the radiometer. If an isolator is used between the mixer and the LNA, then a measurement of the radiometer output power with no LO power can be used as the reference. With no LO power, the mixer has a high impedance, and the isolator then provides a matched termination at the input to the IF amplifier. By this method we assume that the output noise for a mixer driven by a noiseless LO (with 290 K at its RF input) is the same as that produced by a matched load. By measuring an LO source that is believed to be clean we can gauge the accuracy of this assumption, as described below.

However, it is often desirable to measure the output noise over an IF bandwidth that is wider than can be obtained with an isolator (which is typically not much more than an octave of bandwidth). Without an isolator the input noise to the IF amplifier with no LO power is not well determined, and so this is not necessarily a useful reference. Instead, we can use a matched termination at the IF amplifier input to set the reference level. A mechanical coaxial switch at the LNA input can be used to easily switch from the mixer to the reference termination. The reference level in this case is the same at that described above for the isolator.

Once we have decided upon our reference level, T_{REF}, the noise of the DUT can be determined by using a Y-factor method, and is found to be

$$T_{DUT} = T_{RAD}(Y-1) + YT_{REF}$$

Alternately, we can measure the excess noise above T_{REF}, which is given by

$$T_{DUT,excess} = (T_{RAD} + T_{REF})(Y-1)$$

The DUT NSR can then be calculated by dividing this by the DUT output power.

III. Measurements

In order to verify that a room temperature Schottky mixer is sensitive enough to detect AM noise sidebands at the levels of concern to the ALMA LO, a prototype testset was assembled from a VDI WR-10 single-ended Schottky mixer, two Miteq 0.1-12 GHz low-noise amplifiers (AFS3-00101200-42-LN), and a spectrum analyzer.

The mixer conversion loss is relatively flat over a 6dB range of LO drive. At 8dBm of LO drive, the dc voltage across the 50 ohm bias resistor of the mixer is 100 mV. Therefore, to ensure constant LO power across the LO frequency band, a variable attenuator is used to keep the bias voltage constant at 100 mV. In the production testset, a directional coupler will be used to monitor the actual LO power going into the mixer.

The noise temperature of the IF amplifiers is specified by Miteq to be 475K. An isolator was not used between the mixer and IF amplifier for these measurements. For this particular broadband amplifier, it seemed that its effective input noise temperature was independent of the source impedance. In general, this will not be the case, and an isolator (or alternatively a switched termination) should be used as the reference.

Multiplying the IF amplifier noise temperature by the conversion loss of the mixer gives a 7500K noise temperature estimate for T_{RAD}. Dividing this by the 8dBm LO power gives a 1.2K/uW NSR referenced to the front of the mixer. T_{REF} is assumed to be ambient temperature, 297K. Measurement of an ON/OFF Y-factor (where the ON and OFF refer to the LO DUT being turned on or off) is then used to calculate the NSR of the DUT.

For example, a 10 dB ON/OFF ratio gives a [(7500K+300K)*(10-1)] / 8dBm = 11.1K/uW NSR for the LO under test. For verification, a Gunn oscillator, which should have minimal AM noise content at 4-12 GHz IF was measured at 77 GHz, see Fig. 3. The photograph of the prototype AM noise test set is shown in Fig. 4.

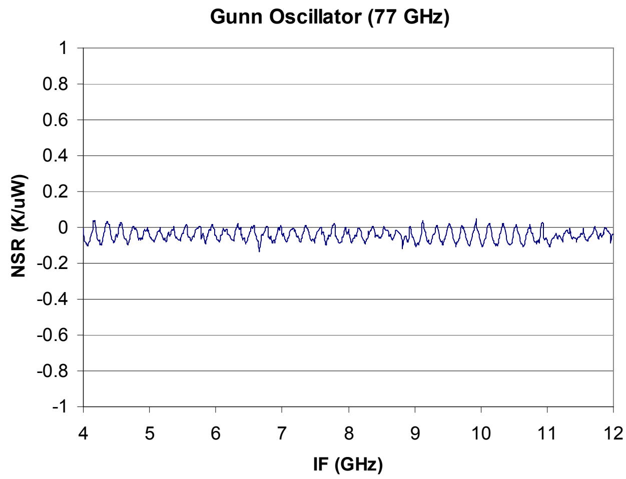

Fig. 11 Measured NSR of a Gunn oscillator output at 77 GHz.

Fig. 12 Photograph of prototype AM noise test set.

A. ALMA Band 8

The ALMA band 8 receiver uses a single-ended SIS mixer to cover 385-500 GHz with a 4-8 GHz IF, therefore the LO needs to tune from 393-492 GHz. The warm portion of the LO, the WCA, generates 65.5-82.0 GHz and is followed by a cryogenic sextupler from VDI.

Fig. 5 shows AM noise measured at the warm power amplifier output from 65.5-82.0 GHz, with the legend showing the scaled LO frequency at the SIS mixer.

Fig. 6 shows the measured receiver noise of the band 8 cartridge using a WCA of the same design as that used for the measurements in Fig. 5. These measurements were performed by the band 8 cartridge group at NAOJ (National Astronomy Observatory of Japan). The measured noise is shown for a LO frequency of 450 GHz. Similar levels of noise are seen at other LO frequencies across the band and correspond fairly closely to the AM noise measurements seen in Fig, 5 at the WCA output.

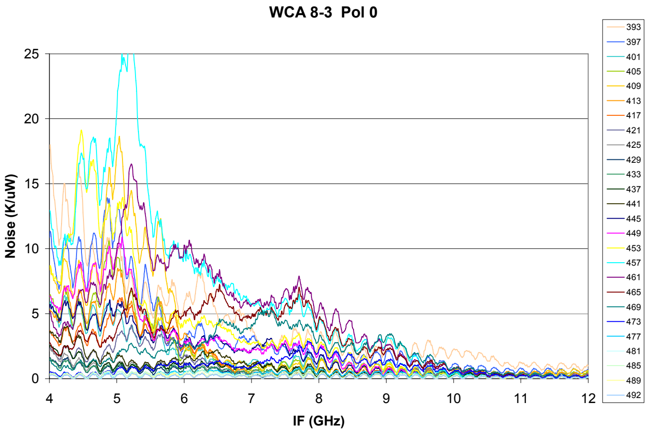

Fig. 13 Measured NSR of an ALMA Band 8 WCA.

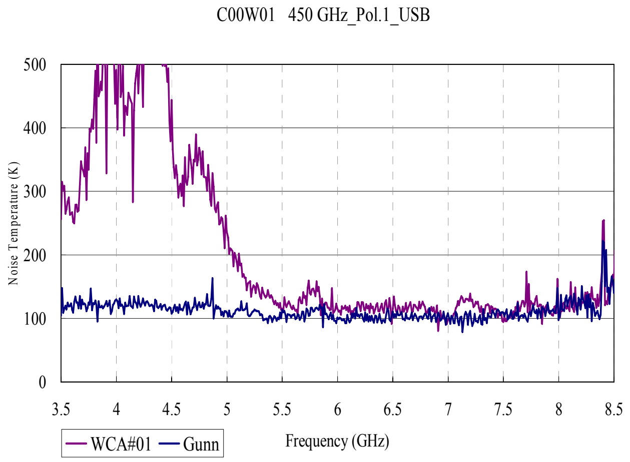

Fig. 14 Measured receiver noise termperature at 450 GHz LO for an ALMA Band 8 receiver with a Gunn LO and with a WCA LO.

B. ALMA Band 9

The ALMA band 9 receiver uses a single-ended SIS mixer to cover 602-720 GHz with a 4-8 GHz IF, therefore the LO needs to tune from 610-712 GHz. The warm portion of the LO, the WCA, generates 67.8-79.1 GHz and is followed by a cryogenic nonupler from VDI.

Fig. 7 shows the measured receiver noise of a band 9 receiver as a function of LO frequency and IF, indicating excess noise from the LO at LO frequencies between 670-700 GHz at IFs below 6 GHz. These measurements were performed by the band 9 cartridge group at SRON (Netherlands Institute for Space Research).

The WCA used in these measurement was then returned to the LO group and was measured using the prototype AM noise measurement test set described in this work. The results at a frequency corresponding to a LO frequency of 678 GHz are shown in Fig. 8. A narrower bandpass filter was then installed in the warm LO and the LO source was remeasured, showing less noise. The modified warm LO was sent back to SRON where it was reconnected to the band 9 SIS receiver and remeasured. The new measurements are shown in Fig. 9 and show that the excess LO noise has been significantly reduced, as predicted by the warm AM noise measurements.

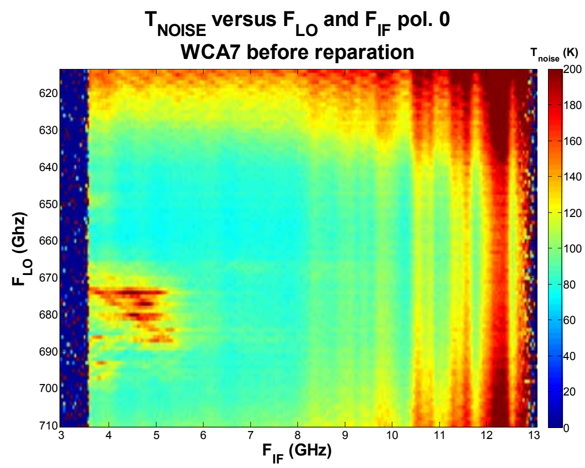

Fig. 15 Measured receiver noise of an ALMA Band 9 receiver using a noisy band 9 LO.

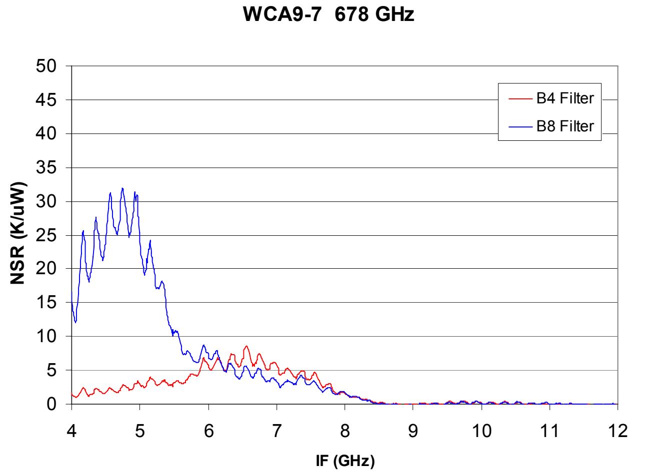

Fig. 16 Measured NSR of an ALMA band 9 WCA at a frequency scaled to a LO frequency of 678 GHz before (blue line) and after (red line) installing a narrower bandpass filter.

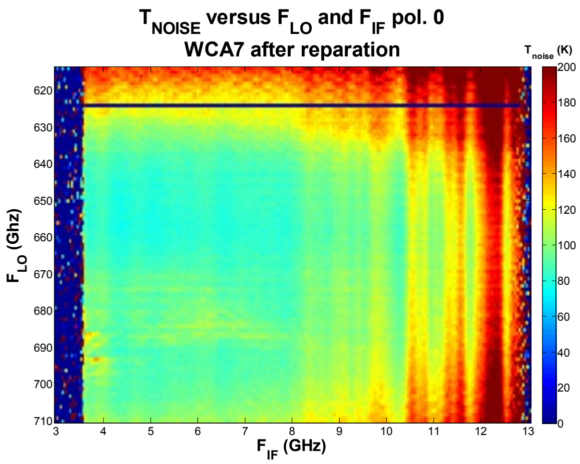

Fig. 17 Measured receiver noise of an ALMA Band 9 receiver after installing a narrower bandpass filter in the LO.

CONCLUSIONS

AM noise measurements using the method described in this paper were presented for ALMA band 8 and 9 local oscillators. Comparisons with receiver noise measurements using the sources under test as local oscillators for SIS mixers show high correlation. This indicates that these AM noise measurements can be used as a screening test to show sources that will add excess noise to the overall receiver without the delay and expense of measuring every LO source with a SIS receiver. Measurements of other ALMA bands have also been performed. We have yet to see an instance where LO noise seen with a SIS receiver was not also seen using the AM noise measurements before the final multiplier presented here.

We are currently in the process of automating these AM noise measurements and integrating them with the suite of acceptance tests for the ALMA LOs. Instead of a spectrum analyzer, a YIG tuned filter and power meter will be used. Output power leveling in the ALMA LOs is performed by adjusting the drain bias of the final power amplifier. A directional coupler will be used to monitor the LO power while the noise measurements are performed, eliminating the need for a manual variable waveguide attenuator.

ACKNOWLEDGMENT

We wish to acknowledge all the ALMA cartridge groups for measurements and helpful discussion. In particular, we thank NAOJ and SRON for providing the band 8 and 9 receiver noise measurements presented in this paper.

REFERENCES

[1] J. R. Tucker and M. J. Feldman, "Quantum detection at millimeter wavelengths," Rev. of Modern Phys., vol. 4, pp. 1055-1113, 1985.

[2] E. Bryerton, M. Morgan, D. Thacker, and K. Saini., "Maximizing SNR in LO chains for ALMA single-ended mixers," *Proc. of the 18th Intl. Symp. on Space THz Tech*., pp. 68-73, Apr 2007.

[3] N. Erickson, "AM noise in drivers for frequency multiplied local oscillators," *Proc. of the 15th Intl. Symp. on Space THz Tech*., pp. 135-142, Apr 2004.

Frequency tunability and mode switching of quantum cascade lasers operating at 2.5 THz

S. G. Pavlov[1], H.-W. Hübers[1], H. Richter[1], A. D. Semenov[1], A. Tredicucci[2], R. Green[2], L. Mahler[2], H. E. Beere[3] and D. A. Ritchie[3]

[1]*German Aerospace Center (DLR), Berlin, Germany*
[2]*NEST CNR-INFM and Scuola Normale Superiore, Pisa, Italy*
[3]*Cavendish Laboratory, University of Cambridge, Cambridge, UK*

Quantum cascade lasers (QCLs) are promising devices for local oscillators in terahertz heterodyne receivers. The lasing mechanism is based on intersubband transitions in the conduction band of heterostructures, most commonly made from GaAs/AlGaAs. A key issue for application in a heterodyne receiver is the frequency stability and tunability. Linear continuous frequency tuning is not straightforwardly obtained. We have investigated two QCLs. They are designed for an operation frequency at about 2.5 THz. One of the lasers has a Fabry-Perot resonator while the other laser is a distributed feedback (DFB) laser. The active medium of both lasers is based on a GaAs/AlGaAs superlattice. The design follows the so-called bound-to-continuum approach with a rather uniformly chirped superlattice and no marked distinction between the injection and lasing regions. Detailed high-resolution spectra of the laser emission as a function of temperature and current have been obtained by self-beating of the laser modes (only laser with Fabry-Perot resonator) as well as by mixing with the emission of a THz gas laser. We report on some spectral features, such as nonlinear dependences of the laser emission frequency on the current and singularities due to mode switching. The analysis shows frequency- and current-dependent nonlinearities of the frequency tuning for both lasers. The multi-mode QCL shows larger variations of the output power of a particular mode as well as larger frequency instabilities at the current values related to the mode switching. Less-expressed power variations have been found for the single mode DFB QCL. The results of the homodyne mixing indicate large variations of the effective refractive index in the active medium caused by the drive current. The implications for the use of the QCL as local oscillator in a heterodyne receiver will be discussed.

Capabilities of GaN Schottky Multipliers for LO Power Generation at Millimeter-Wave Bands

José V. Siles and Jesús Grajal

Universidad Politécnica de Madrid, Dept. Señales, Sistemas y Radiocomunicaciones, Madrid, Spain

* Contact: jovi@gmr.ssr.upm.es, phone +34 91-336-73-58

***Abstract*— Gallium Nitride (GaN) is a very promising material for either electronic and optoelectronic devices because of its high breakdown field, and peak and saturated electron drift velocity. Hence, despite of its lower electron mobility, GaN Schottky diodes might represent a good alternative to GaAs Schottky diodes for LO power generation at millimetre-wave bands due to a much better power handling capabilities. Results from numerical simulations for a 200 GHz doubler predict a ~25 % lower conversion efficiency for GaN Schottky multipliers when compared to GaAs Schottky multipliers. However, higher power handling capabilities, an order of magnitude higher than GaAs with same anode sizes, are predicted for GaN diodes.**

I. Introduction

In the recent years, GaN has emerged as a very promising material for either electronic and optoelectronic devices mainly due to its wide direct bandgap (3.4 eV), which results in a high breakdown field, and its high peak and saturated electron drift velocity [1]. High breakdown voltage materials increase the power handling capabilities of the devices. Hence, GaN Schottky diodes might represent a good alternative to GaAs Schottky diodes for LO power generation at millimeter-wave bands in a near future, when solid-states sources can provide larger amounts of LO power at frequencies around 100-150 GHz. The potential capabilities of GaN Schottky diodes are not in the frame of the design of high frequency multiplier circuits, well within the submillimeter-wave region, but in the early stages of high-frequency multiplier chains where the excellent power handling capabilities of GaN can be exploited. However, GaN has the inconvenient of a lower electron mobility than GaAs, which results in an increase in the series resistance, and thereby, in lower efficiencies.

The objective of this paper is to investigate the capabilities of GaN Schottky diodes for LO power generation at millimeter-wave and submillimeter-wave bands as an alternative to the widely used GaAs Schottky diodes. For this task, we have included the GaN material in an already available in-house CAD tool for Schottky diode-based circuits design. This simulator incorporates an accurate physics-based Drift-Diffusion model for Schottky diodes and has demonstrated very good results for the analysis of GaAs Schottky diodes at millimetre and submillimeter-wave bands [2]. Firstly, the electrical properties of both GaN and GaAs diodes are compared, paying special attention to those with a major impact on the frequency multiplying process, such as the breakdown voltage, the electron mobilities and the nonlinear capacitance. Nevertheless, the key point of the comparison lies in the much higher power handling capabilities of GaN diodes. This is due to the excellent characteristics of GaN in terms of breakdown voltage, which represents the real advantage of this material over GaAs. Moreover, the enhanced power handling capabilities of GaN diodes will lead to simplified designs at the early multiplication stages of THz LO chains, allowing the use of either single-diode configurations or 2-diodes balanced configurations. Current designs with GaAs Schottky diodes employ at least 4-6 anodes balanced configurations for the low frequency multiplication stages [3].

II. Description of the Simulation Tool

The simulation environment couples a Schottky diode physical model with a circuit simulator using appropriate harmonic-balance techniques (see Fig. 1). This allows the concurrent design of circuits taking into account both the device structure (doping and length of the epitaxial layer, and area of the device) and the embedding circuit (bias, available power, and loads at different harmonics).

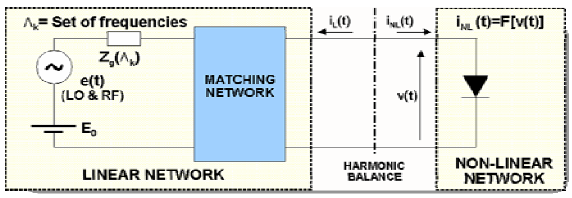

Fig. 34 General scheme of the numerical Harmonic Balance simulator for the design and optimization of Schottky- diode-based circuits at millimeter and submillimeter-wave bands.

The Schottky diode model consists of a physics-based drift-diffusion numerical device simulator [4], which incorporates accurate boundary and interface conditions for self-consistent treatment of tunnelling transport, image-force effects, impact ionization, and non-constant recombination velocity. This physics-based simulator accounts for limiting mechanisms such as avalanche breakdown, velocity saturation, and increase in the series resistance with the input power [4].

This CAD tool has already been validated in previous works [2,4-5], and very good agreements between simulation results and measurements have been obtained not only for GaAs Schottky multipliers [2], but also for GaAs Schottky mixers [5].

III. Electrical Properties of GaN vs. GaAs

In order to evaluate the potential capabilities of GaN Schottky diodes for millimeter and submillimeter-wave applications, a comparative study for GaN and GaAs Schottky diodes has been carried out from DD simulation results in DC at room temperature. The characteristics of the Schottky diode taken as a reference for this study are: An ideal barrier height of 0.99 V for GaAs and 1.2 V for GaN, an anode area of 36 μm^2, an epilayer thickness of 350 nm, an epilayer doping in the range 0.3 to $5 \cdot 10^{17}$ cm^{-3}, and a substrate doping (n^{++} layer) of $2 \cdot 10^{18}$ cm^{-3}.

The major disadvantage of GaN in comparison to GaAs lies in its lower electron mobility. As can be appreciated in Fig. 2, for typical epilayer doping employed for GaAs Schottky multipliers (N_D = 1 to $5 \cdot 10^{17}$ cm^{-3}), GaAs mobility is in the order of 6-8 times higher than GaN mobility. This has a high impact on the series resistance of GaN Schottky diodes since it is inversely proportional to the mobility. It can be derived from Fig. 2 that GaN resistivity will experience a higher increase with the doping than GaAs resistivity due to the faster decrease of GaN mobility with the doping level. Note that GaN resistivity is 6 times higher than GaAs resistivity for a $1 \cdot 10^{17}$ cm^{-3} doping level, and 11 times higher when the doping is increased up to $2 \cdot 10^{18}$ cm^{-3}. Hence, once the doping levels of the Schottky diode are fixed, worse relative performances for GaN diodes with respect to GaAs diodes will be obtained for high dopings.

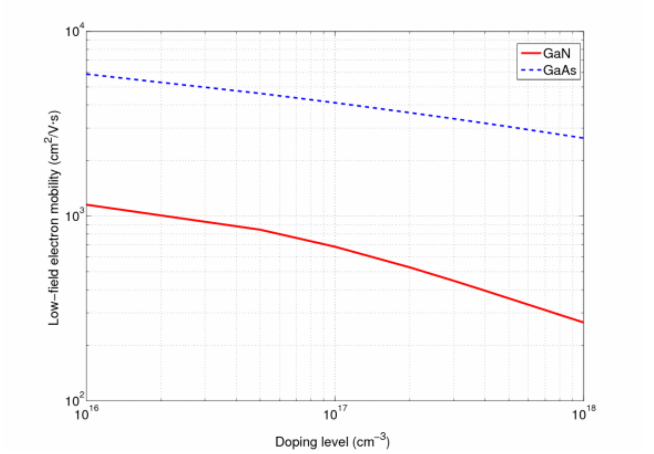

Fig. 35 Low-field electron mobility for GaAs and GaN as a function of the epilayer doping.

The higher series resistance of GaN does not necessary imply a proportional degradation of the conversion efficiency in GaN multipliers in comparison to GaAs multipliers. It is shown in Fig. 3 that the zero junction capacitance (C_{j0}) corresponding to the GaN diode is around a factor of 1.3 lower than the one for the GaAs diode. It can be demonstrated that the effective voltage in the junction nonlinear capacitance (responsible for the frequency multiplication in the varactor mode of operation of the Schottky diode) is inversely proportional to the junction capacitance. Higher multiplication efficiencies are obtained when this effective voltage is maximized as a result of the higher modulation of the nonlinear capacitance. It is obvious that a high series resistance will negatively affect the capacitance sweep. However, the already discussed inconvenience of the increase in the series resistance of GaN can be somewhat compensated by its lower capacitance, as can be seen in Eq. 1. Thus, the joint effect of the series resistance and the capacitance might not result in dramatically lower efficiencies in GaN Schottky multipliers.

$$V_C = -j \cdot \sqrt{\frac{2P_{av}}{R_S}} \cdot \frac{1}{\omega \cdot C_J} \quad (1)$$

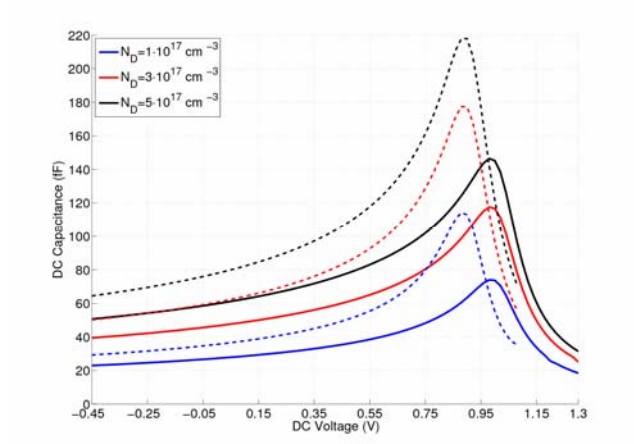

Fig. 36 DC capacitance curves for GaAs (dashed lines) and GaN (solid lines) as a function of the epilayer doping.

However, the real advantage of GaN Schottky diodes comes from its higher critical electric field. This leads to much higher breakdown voltages in GaN diodes than in GaAs diodes, and therefore, to much better power handling capabilities in GaN. Figs. 4 and 5 show the comparison of the breakdown voltages for both materials as a function of the doping level and thickness of the epitaxial layer.

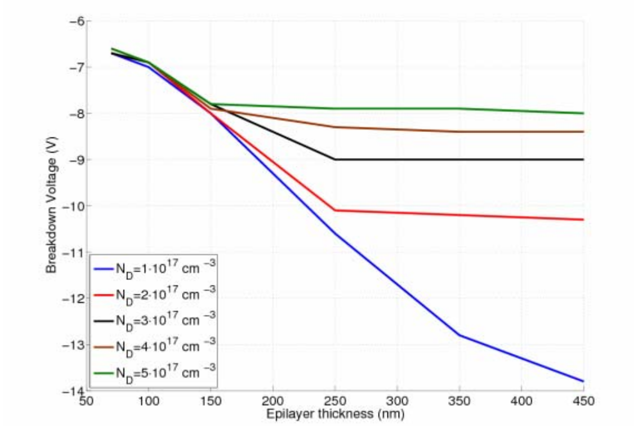

Fig. 37 DC breakdown voltage as a function of the epilayer length and doping for GaAs Schottky diodes.

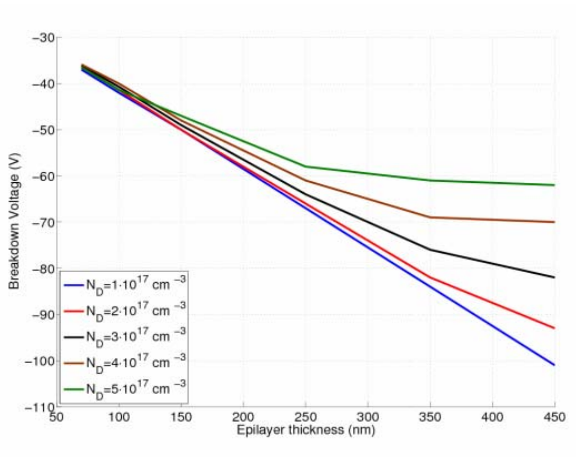

Fig. 38 DC breakdown voltage as a function of the epilayer length and doping for GaN Schottky diodes.

IV. Optimization of a 200 GHz GaN Schottky Doubler

In order to establish a performance comparison between both GaN and GaAs Schottky multipliers, the design of a 200 GHz Schottky doubler is presented in this section, assuming a nominal input power of 150 mW at 100 GHz and a unique anode. This value for the input power is typically considered in practice for the first stages of LO sources at THz frequencies [3].

The optimization of the 200 GHz GaN Schottky doubler was performed by means of our physics-based in-house CAD tool. The results are presented in Figs. 6 and 7. It can be seen that the optimum doping level for the epilayer is 3-5·10^{16} cm^{-3}. For higher dopings, the important decrease of the mobility leads to lower conversion efficiencies.

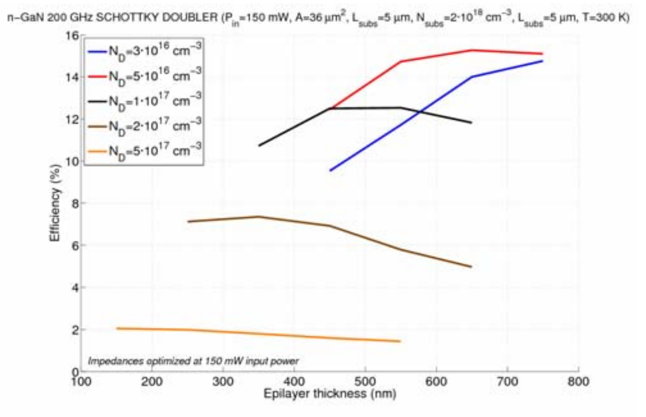

Fig. 39 Simulated performance of a 200 GHz GaN Schottky doubler as a function of the epilayer thickness and the doping level (anode area is 36 μm^2).

Regarding the epitaxial layer, thicknesses between 500-800 nm are necessary for the selected doping levels in order to support the 150 mW input power, as shown in Fig. 6. Reverse bias voltages between -15 and -20 V are also necessary to maximize the voltage swing in the capacitance, and thereby, the efficiency. It can be derived from Fig. 5 that the breakdown voltage will be below -100 V. Hence, the doubler will operate in safe conditions, with no risk of reaching the breakdown regime.

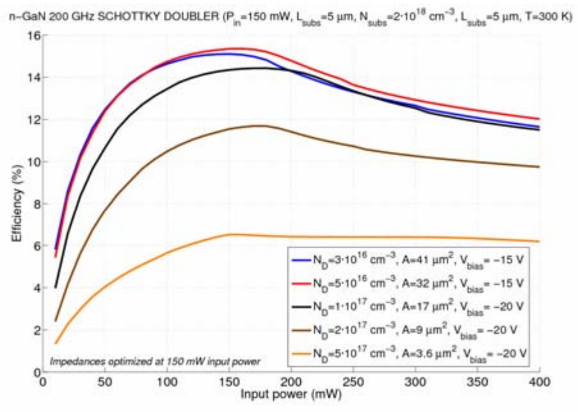

Fig. 40 Simulated performance of a 200 GHz GaN Schottky doubler as a function of the input power and the epilayer doping level. Bias and anode areas have been optimized for a 150 mW input power.

The last step of the optimization process consists in selecting the adequate value for the anode area so that the maximum efficiency is achieved at the available input power. For a 5·10^{16} cm^{-3} doping level in the epilayer, a 15 % peak efficiency is achieved for a 150 mW input power when a 32 μm^2 anode area is selected (see Fig. 7).

It is important to address that for all the simulations in this section, a mobility-field characteristic according to the representative fit in Fig. 8 has been considered for GaN. This fit was proposed by F. Schwierz in 2005, and is based on a large amount of experimental data on low-field electron mobilities for GaN [1].

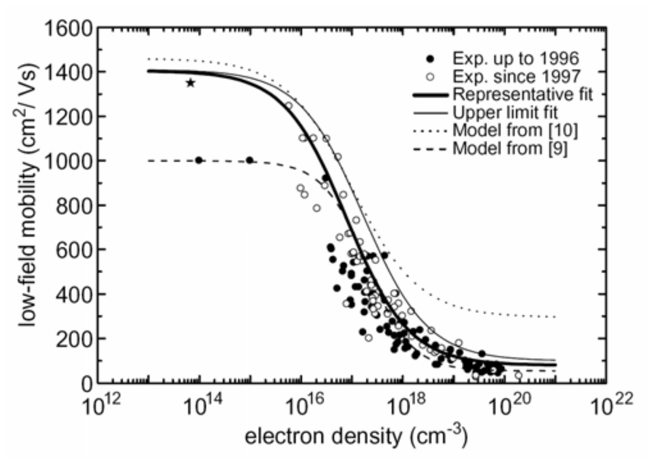

Fig. 41 Measured low-field mobility for wurtzite n-GaN as a function of doping density (reprinted from [1]).

V. GaN vs. GaAs Schottky Multipliers

Fig. 9 shows a comparison between the 200 GHz GaN Schottky doubler optimized in the previous section (featuring a single anode), and a 200 GHz GaAs Schottky doubler with similar anode areas to that considered for the GaN doubler. For the GaAs doubler, 8 anodes are necessary for a 150 mW available input power as a consequence of the lower power handling capabilities of GaAs diodes with respect to GaN diodes.

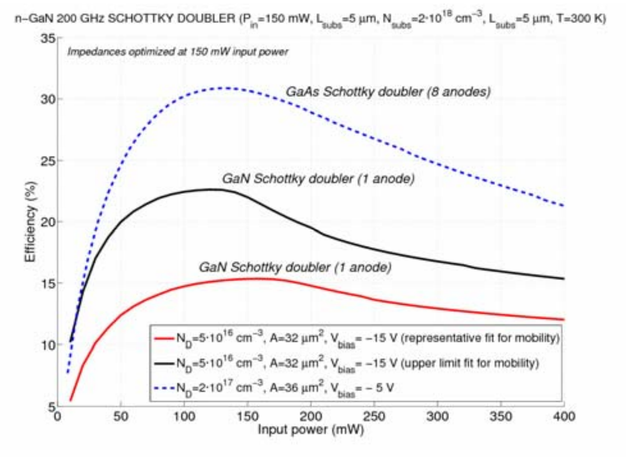

Fig. 9 Performance comparison between a 200 GHz GaAs Schottky doubler (featuring 8 anodes with a 350 nm epilayer) and a 200 GHz GaN Schottky doubler (featuring 1 anode with a 650 nm epilayer).

On the one hand, if the representative fit for the low-field mobility is considered (see Fig. 8), the conversion efficiency of the GaN Schottky doubler is approximately half the obtained with the GaAs doubler. On the other hand, if the upper limit fit in Fig. 8 is used, which is based in the most recent results regarding measured low-field GaN mobilities, a 23 % efficiency is predicted, which is just a 25 % lower than that obtained with the GaAs Schottky doubler. However, the most remarkable result comes from the fact that only one diode has been considered for the GaN doubler.

Typical balanced configurations employed in low frequency multiplication stages (around 200 GHz) include up to 6-8 diodes pumped with around 150-200 mW at 100 GHz. The effective input power per anode yields around 25-30 mW, which is an adequate value for GaAs Schottky diodes in order not to require excessively high anode areas and to prevent the diode from entering the breakdown regime. Balanced configurations are therefore necessary in order to reduce the input power per diode. But great advances are being made in solid-state sources so the available input power at frequencies around 100 GHz is rapidly increasing. This will result in a need for employing more GaAs Schottky diodes in the first multiplication stages or in an increase of the anode areas in order to raise the power handling capabilities of the GaAs diodes. In both cases, it will represent an increase in the length of the chips containing the Schottky diodes. However, the maximum length is limited by the dimensions of the transmission wave-guide, fixing an upper limit to the maximum diode dimensions or number of supported diodes. In addition, the higher the number of diodes, the more difficult it is to achieve a good and equitable power coupling among all the diodes, as there is a major risk for the presence of asymmetries in the circuit due to the fabrication process. This can be catastrophic for the resultant performance. GaN Schottky multipliers might solve part of these problems in the near future when the available input power at frequencies around 100 GHz is high enough to guarantee good output power levels in spite of the lower efficiencies of GaN multipliers. Moreover, the possibility of employing single-diode or 2-diode configurations, with the subsequent reduction in the technological complexity of the circuitry, may represent an extra motivation that encourages the use of GaN Schottky multipliers.

CONCLUSIONS

The potential capabilities of GaN Schottky diodes, according to the results presented in this work, are not in the frame of high frequency multipliers (well within the submillimeter-wave region), but in the first stages of high-frequency multiplier chains where the excellent power handling capabilities of GaN can be exploited, i.e. in the upper part of the millimeter-wave region (100-300 GHz).

The simulation results presented in this work showed that excellent power handling capabilities can be achieved with GaN Schottky diodes at these. Moreover, GaN multipliers can provide good efficiencies (just a 25 % lower than those obtained with GaAs multipliers) at 200 GHz. The efficiency of GaN multipliers might be even closer to that obtained with GaAs multipliers if GaN mobility were slightly improved, which can be possible as new advances on fabrication technologies are constantly going on.

ACKNOWLEDGMENT

This work was supported by the Spanish National Research and Development Program under project number TEC2005-07010-C02-01/TCM.

REFERENCES

[1] F. Schwierz, “An electron mobility model for wurtzite GaN”, *Solid-State Electronics*, vol. 48, no. 6, pp. 889-895, June 2005.

[2] J. Grajal, J.V. Siles, V. Krozer, E. Sbarra and B. Leone, “Performance Evaluation of Multiplication Chains up to THz Frequencies”, *in Proc. 29th Int. Conf. on Infrarred and Millimeter-waves & 12th Int. Conf. on THz Electronics*, September, 2004.

[3] J. Ward, E. Schlecht, G. Chattopadhyay, A. Maestrini, J. Gill, F. Maiwald, H. Javadi and I. Mehdi, “ Capability of THz sources based on Schottky diode frequency multiplier chains”, *IEEE MTT-S International Microwave Symposium Digest,* pp.1587-1590, June 2004.

[4] J. Grajal, V. Krozer, E. González, F. Maldonado, and J. Gismero, “Modelling and design aspects of millimeter-wave and submillimetre-wave Schottky diode varactor frequency multipliers,” *IEEE Transactions on Microwave Theory and Techniques*, vol. 48, pp. 700-711, April 2000.

[5] J.V. Siles, J. Grajal and V. Krozer, “Design of subharmonically pumped Schottky mixers for submillimetre-wave applications,” *1st European Microwave Integrated Circuits Conference (EuMIC 2006),* September 2006

High Power Heterostructure Barrier Varactor Quintupler Sources for G-Band Operation

Josip Vukusic[1,2*], Tomas Bryllert[2,3], and Jan Stake[1,2]

[1]Department of Microtechnology and Nanoscience, Chalmers University of Technology, SE-41296 Göteborg, Sweden

[2]Wasa Millimeter Wave AB, SE-41296 Göteborg, Sweden

[3]California Institute of Technology, Pasadena, CA 91125, USA

* Contact: vukusic@chalmers.se, phone +46-31-772 5866

***Abstract*— We have designed a frequency multiplier based on Heterostructure Barrier Varactors (HBVs) at 202 GHz. The InGaAs/InAlAs/InP HBV diodes were flip-chip mounted onto an aluminium-nitride (AlN) substrate with the microstrip pattern. The AlN-circuit was then mounted in an ultra compact 30x9 mm waveguide block. A quintupler (x5) operating at 202 GHz produced an output power of 23 mW.**

I. Introduction

The mm-wave and THz frequency spectra is rich on possible applications. But the difficulty to supply room-temperature, compact, high power sources at these frequencies has hampered an otherwise booming technology development. As an example, imaging applications such as a heterodyne receiver array requires local oscillator power of several tens of mW's.

The THz spectral window (~ 0.1-3 THz) , also nicknamed 'THz-gap', is difficult to reach from the electrical side. This is exemplified by the sharp decline of efficiency at higher frequencies for fundamental sources such as IMPATT and Gunn oscillators [1]. Other methods to produce THz output power such as the quantum cascade laser (QCL) is promising but is yet to operate at frequencies well below < 1.4 THz [2].

Because of the inherent difficulty to generate power at these frequencies, the output power from a lower frequency source can be multiplied [3-5] to higher frequencies using a nonlinear device such as the Heterostructure Barrier Varactor (HBV) diode [6]. The HBV has a symmetric capacitance-voltage (C-V) characteristic, operates unbiased and only generates odd harmonics of the pump signal. These specific properties simplify the design of high order multipliers (×3, ×5, ×7, etc.) [7-8]. Moreover, since cascading the epitaxial growth scales the voltage handling capability of the HBV, this device is well suited for high power generation [9-10].

The progress on HBV multiplier includes multi diode quasi-optical circuits [11-12], NLTLs [13] and highly efficient single diode waveguide circuits [14]. For instance, an HBV quintupler (×5) with a state-of-the-art conversion efficiency of 11% has been demonstrated at 100 GHz [15-16], HBV triplers (×3) have been shown to provide 0.2 W at 113 GHz [9], 10 mW and at least 10% efficiency has been demonstrated at short millimeter wavelengths [17-19], and 1 mW has been reported for a HBV tripler up to 450 GHz [20]. In terms of output power, the best results have been achieved using a filter circuit on AlN instead of quartz due to a better heat sink for the flip-chip mounted diode.

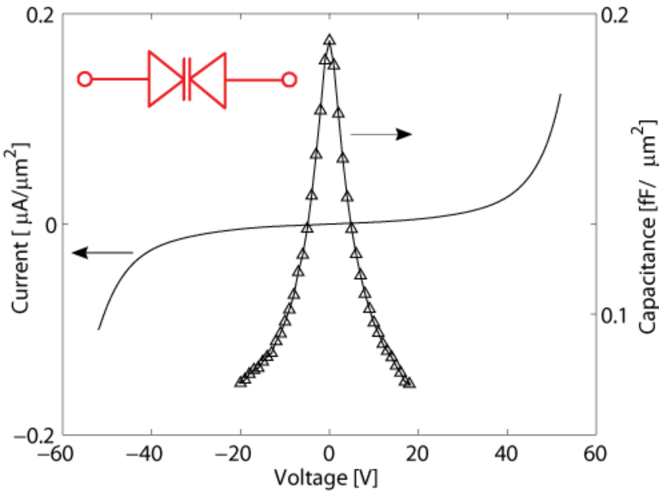

Fig. 1 Graph showing the I-V and C-V curves measured on a 12-barrier 700 μm^2 HBV. The inset shows the circuit symbol of the HBV as two anti-serially connected diodes.

In this paper we present the design, fabrication and measurement results of state-of-the-art G-band (140-220 GHz) HBV quintuplers. Initially, a brief description of the underlying HBV multiplier technology is presented together with an account of the design and fabrication process. The measurement setup and the results at 202 GHz follow with concluding remarks.

II. HBV Multiplication

The physical property for achieving unbiased multiplication (i.e creation of higher harmonics) in this work is the nonlinearity provided by the HBV diode. This type of diode is realized by epitaxially growing a heterostructure sequence of low-high-low bandgap material. When a voltage is applied across such a semiconductor material, the high bandgap material acts as a barrier for the carriers causing accumulation and depletion of carriers in the respective low bandgap layers. This has the effect of changing the capacitance as a function of the applied voltage C = C(V) as shown in figure 1.

The HBV heterostructure epi-material within this work consists of periodically stacked InAlAs/InGaAs/InP layers[21] repeated three times, in order to withstand high voltages and therefore operate at high power. For this structure, the modulation layer is 250 nm with a doping concentration of 1×10^{17} cm^{-3} and a 13-nm barrier thickness. The epitaxial material was grown by molecular beam epitaxy (EPI930) at the Chalmers Nanofabrication Laboratory.

We chose the symmetric planar topology [9] for the HBV diode. This discrete device is shown in figure 2. It actually consists of four mesas of the aforementioned epi-material that are series connected. This amounts to a total of 12 barriers in series. As shown in figure 1 by the I-V curve, this type of 12 barrier device can operate at voltage amplitudes in excess of 50 V.

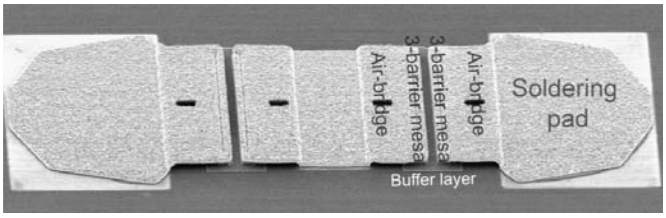

Fig. 2 SEM micrograph of a 500 μm² HBV. This 4-mesa device has a total of 12-barriers.

Standard III–V processing techniques were used to fabricate the HBV devices. These techniques include photolithography, e-beam contact evaporation, plasma-enhanced chemical vapor deposition (PECVD), inductively coupled plasma (ICP) dry etching.

III. QUINTUPLER CIRCUIT DESIGN

In order to facilitate efficient multiplication the HBV has to be properly matched at the input frequency and higher harmonics. This was realized using a microstrip circuit incorporating filters and impedance matching elements embedding the diode. The microstrip circuit was fabricated on an AlN substrate (thermal conductivity ~ 170 W/mK) to improve the power handling capability. No DC connection between the waveguide block and the circuit was used since simplicity was one of the design objectives. This also means that open waveguide probes were used both at the input and at the output side. Figure 3 shows the CAD layout for the 3-D electromagnetic solver used to design the quintupler microstrip circuit and waveguide. We can see that the input/output waveguides are connected by probes at each end of the circuit .

The optimum embedding impedances were extracted from harmonic balance simulations using the Chalmers HBV device model [22]. This model self-consistently calculates the interdependent electrical and thermal properties of the device. Three-dimensional FEM modeling was applied to calculate the thermal resistance and electrical series resistance used in the model.

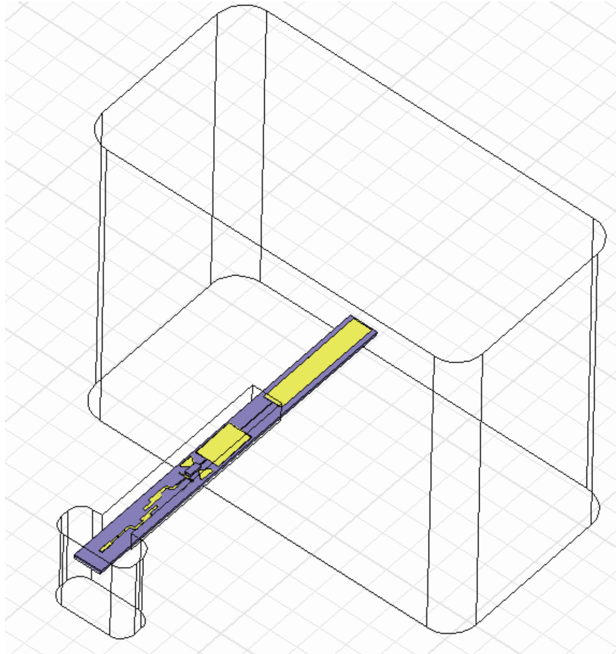

Fig. 3 CAD layout of the quintupler microstrip circuit and waveguide attachments for a G-band quintupler. A 3-D electromagnetic solver was used for the detailed design.

The diced HBV devices from figure 2 were flip-chip soldered onto the microstrip. This hybrid circuit was then mounted in the waveguide block with a WR22/WR5 input and output, respectively. The two-piece compact waveguide block, with dimensions Ø 30 mm × 9 mm, was milled out of brass and gold electroplated. Figure 4 shows a photograph of the two waveguide block halves with the AlN microstrip circuit mounted in the left. The waveguide block has no movable tuners.

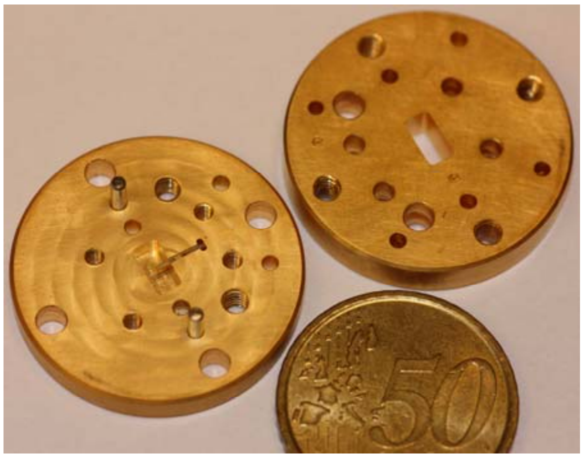

Fig. 4 Two-piece waveguide block halves for the 202 GHz quintupler. The AlN microstrip circuit is mounted in the waveguide channel of the block half on the left. A 50€ cent is included for size comparison.

IV. RESULTS

The input signal to the multiplier was provided by a HP83650B frequency synthesizer followed by a Spacek power amplifier. A waveguide isolator was used between the power amplifier and the HBV multiplier (DUT). The output power was measured using an Erickson PM2 power meter. In figure 5 the output power is plotted as a function of input power showing a maximum output power of more than 20 mW for the 202 GHz quintupler. This result was achieved with a 500 μm^2 HBV diode from the same batch as used for the high power W-band tripler in [9]. The test was limited by available input (pump) power at 40 GHz and even higher efficiency and output is expected at higher input power levels.

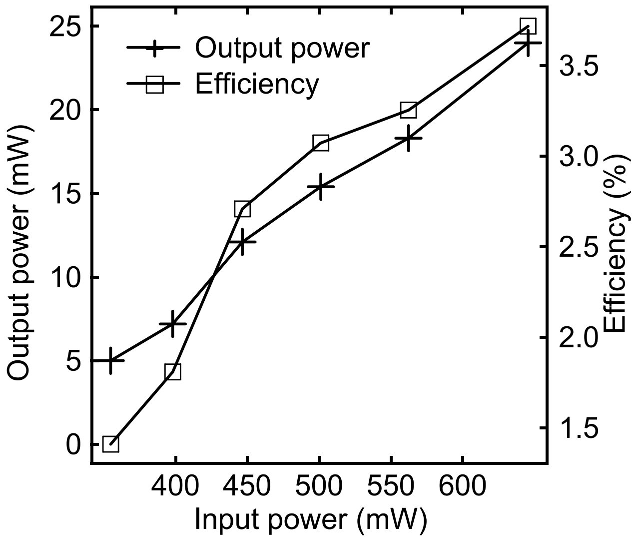

Fig. 5 Graph showing the quintupler output power and efficiency at 202 GHz versus the input power

Figure 6 shows a frequency sweep at a constant input power of 560 mW into the quintupler.

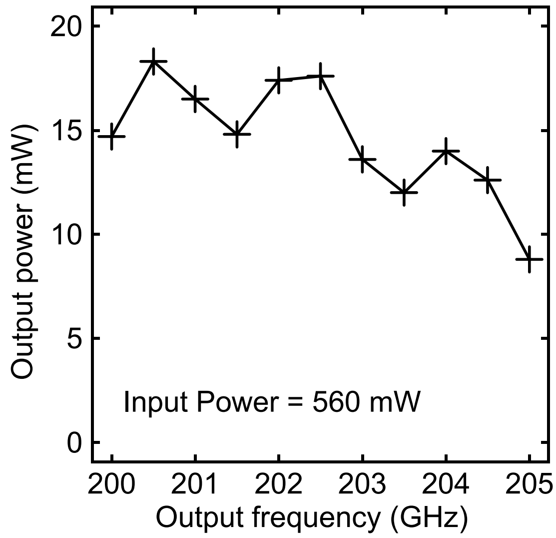

Fig. 6 Graph showing the quintupler output power versus frequency at a fixed input power of 560 mW.

The output spectrum was measured with a Fourier Transform Spectrometer (FTS), which confirmed that the output signal only contains the fifth harmonic.

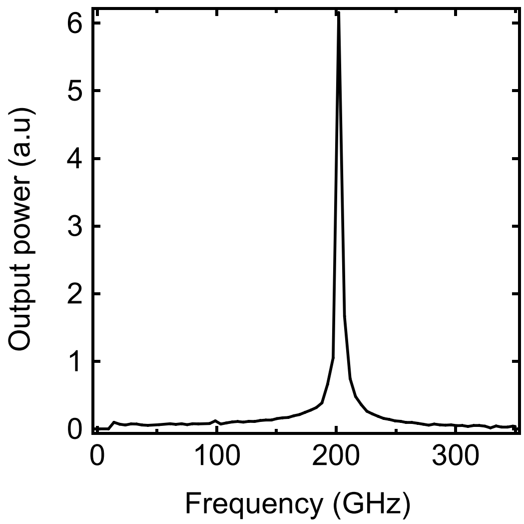

Fig. 7 FTS spectra confirming that the output power measured is all contained in the fifth harmonic at 202 GHz.

CONCLUSIONS

World-record output power performance of more than 20 mW at 202 GHz for an HBV quintupler has been demonstrated. The output power was limited by the available input power so additional improvements of output power and efficiency is expected with increased pump power.

A new and novel design of the waveguide block has been presented that makes the machining of the block simple and repeatable.

Today, the output power for HBV multipliers are comparable to state-of-the-art Schottky doublers at short millimeter wave frequencies. Finally, the HBV multiplier performance can be further enhanced by optimizing circuits, devices and using monolithic integration techniques (MMICs).

ACKNOWLEDGMENT

The authors would like to thank Carl-Magnus Kihlman, Chalmers, for fabricating the waveguide blocks and Mahdad Sadeghi, Nanofabrication laboratory, Chalmers, for the growth of epi-material.

This work was supported in part by the European Space Agency, in part by the Swedish Foundation for Strategic Research (SSF), in part by the Swedish National Space Board, and in part by the Swedish Defence Material Administration (FMV), the Swedish Emergency Management Agency (KBM) and the Swedish Agency for Innovation Systems (VINNOVA) through the FOI projects NanoComp and Radar eyes.

REFERENCES

[1] G. I. Haddad, J. R. East, H. Eisele, "Two-terminal active devices for terahertz sources," *International Journal of high Speed Electronics and Systems,* vol. 13, pp. 395-427, June 2003.

[2] M. Tonouchi, "Cutting-edge THz technology," *Nature Photonics,* vol. 1, pp. 97-105, Feb 2007.

[3] P. Penfield and R. P. Rafuse, *Varactor applications*. Cambridge: The MIT Press, 1962.

[4] A. Räisänen, "Frequency multipliers for millimeter and submillimeter wavelengths," *Proc. IEEE,* vol. 80, pp. 1842-1852, Apr 26 1992.

[5] G. Chattopadhyay, E. Schlecht, J. Ward, J. Gill, H. Javadi, F. Maiwald, and I. Mehdi, "An All-Solid-State Broad-band Frequency Multiplier Chain at 1500 GHz," *IEEE Transactions on Microwave Theory and Techniques,* vol. 52, pp. 1538-1547, 2004.

[6] E. L. Kollberg and A. Rydberg, "Quantum-barrier-varactor diode for high-efficiency millimetre-wave multipliers," *Electronics Letters,* vol. 25, pp. 1696-1698, 1989.

[7] L. Dillner, J. Stake, and E. L. Kollberg, "Analysis of symmetric varactor frequency multipliers," *Microwave and Optical Technology Letters,* vol. 15, pp. 26-29, May 1997.

[8] J. Stake, S. H. Jones, L. Dillner, S. Hollung, and E. L. Kollberg, "Heterostructure-barrier-varactor design," *IEEE Transactions on Microwave Theory and Techniques,* vol. 48, pp. 677-682, 2000.

[9] J. Vukusic, T. Bryllert, T. A. Emadi, M. Sadeghi, and J. Stake, "A 0.2-W heterostructure barrier varactor frequency tripler at 113 GHz," *IEEE Electron Device Letters,* vol. 28, pp. 340-342, May 2007.

[10] A. Rahal, R. G. Bosisio, C. Rogers, J. Ovey, M. Sawan, and M. Missous, "A W-Band Medium Power Multi-Stack Quantum Barrier Varactor Frequency Tripler," *IEEE Microwave Guided Wave Lett.,* vol. 5, pp. 368-370, 1995.

[11] J. B. Hacker et al.. "A high-power W-band quasi-optical frequency tripler," in *IEEE International Microwave Symposium*, vol. 3 pp. 1859-1862, 2003.

[12] S. Hollung, J. Stake, L. Dillner, and E. L. Kollberg, "A 141-GHz Integrated Quasi-Optical Slot Antenna Tripler," in *IEEE AP-S International Symposium and USNC/URSI National Radio Science Meeting*, Orlando, FL, USA, 1999, pp. 2394-2397.

[13] S. Hollung, J. Stake, L. Dillner, M. Ingvarson, and E. L. Kollberg, "A Distributed Heterostructure Barrier Varactor Frequency Tripler," *IEEE Microwave and Guided Wave Letters,* vol. 10, pp. 24-26, 2000.

[14] J. Vukusic, B. Alderman, T. A. Emadi, M. Sadeghi, A. Ø. Olsen, T. Bryllert, and J. Stake, "HBV tripler with 21% efficiency at 102 GHz " *Electronics Letters,* vol. 42, pp. 355-356, 2006.

[15] T. Bryllert, A. Ø. Olsen, J. Vukusic, T. A. Emadi, M. Ingvarson, J. Stake, and D. Lippens, "11% efficiency 100 GHz InP-based heterostructure barrier varactor quintupler," *Electronics Letters,* vol. 41, p. 30, 2005.

[16] A. Ø. Olsen, M. Ingvarson, B. Alderman, and J. Stake, "A 100-GHz HBV Frequency Quintupler Using Microstrip Elements," *IEEE Microwave and Wireless Components Letters,* vol. 14, pp. 493-495, 2004.

[17] T. David, S. Arscott, J.-M. Munier, T. Akalin, P. Mounaix, G. Beaudin, and D. Lippens, "Monolithic integrated circuits incorporating InP-based heterostructure barrier varactors," *IEEE Microwave and Wireless Components Letters,* vol. 12, pp. 281-283, 2002.

[18] Q. Xiao, J. L. Hesler, T. W. Crowe, I. Robert M. Weikle, and Y. Duan, "High Efficiency Heterostructure-Barrier-Varactor Frequency Triplers Using AlN Substrates," in *IMS 2005*, Long Beach, CA, 2005.

[19] R. Meola, J. Freyer, and M. Claassen, "Improved frequency tripler with integrated single-barrier varactor," *Electronics Letters,* vol. 36, pp. 803-804, 2000.

[20] M. Saglam, B. Schumann, K. Duwe, C. Domoto, A. Megej, M. Rodriguez-Gironés, J. Müller, R. Judaschke, and H. L. Hartnagel, "High-performance 450-GHz GaAs-based heterostructure barrier varactor tripler," *IEEE Electron Device Letters,* vol. 24, pp. 138- 140, 2003.

[21] L. Dillner, W. Strupinski, S. Hollung, C. Mann, J. Stake, M. Beardsley, and E. L. Kollberg, "Frequency Multiplier Measurements on Heterostructure Barrier Varactors on a Copper Substrate," *IEEE Electron Device Letters,* vol. 21, pp. 206-208, 2000.

[22] M. Ingvarson, J. Vukusic, A. Ø. Olsen, T. A. Emadi, and J. Stake, "An electro-thermal HBV model," in *IMS 2005*, Long Beach, CA, 2005, pp. 1151-1153.

Cryogenic Phase Locking Loop System for Flux-Flow Oscillator

A.V. Khudchenko[1,2], V.P. Koshelets[1,2], P.N. Dmitriev[1], A.B. Ermakov[1,2], O.M. Pylypenko[3] and P.A. Yagoubov[2]

[1]Institute of Radio Engineering and Electronics, Moscow, Russia

[2] SRON Netherlands Institute for Space Research, Groningen, the Netherlands

[3] State Research Center of Superconducting Electronics "Iceberg", Kyiv, Ukraine

* Contact: Khudchenko@hitech.cplire.ru, phone +7-495-629 3418

Abstract— Recently a cryogenic phase detector (CPD) based on a superconductor-insulator-superconductor junction has been proposed and preliminary tested. The CPD is initially intended for phase locking of a Flux-Flow Oscillator (FFO) in a Superconducting Integrated Receiver (SIR). A model to describe coupling between the CPD and the FFO has been developed and experimentally verified. We present a design of the Cryogenic Phase Locking Loop (CPLL) system implemented for the SIR and discuss the results of the CPLL experimental tests. The effective bandwidth of the CPLL system exceeds 25 MHz at the reference oscillator frequency of 400 MHz. The CPLL bandwidth considerably surpasses that of the room-temperature PLL system, for which it is limited to 12 MHz by inevitable delays in the long cables and semiconductor devices. The novel CPLL system can phase-lock more than 50% of the emitted by FFO power even if the free-running FFO linewidth is about 10 MHz. This fraction of phase-locked power is twice as much as the result of the conventional room-temperature PLL. Such an improvement allows to reduce the FFO phase noise and extend the SIR operation range.

I. Introduction

A Cryogenic Phase Locking Loop system (CPLL) described in this report is primarily designed for phase stabilization of a Local Oscillator (LO) of a Superconducting Integrated Receiver (SIR) [1], [2]. The SIR circuit comprises on a single chip (size of 4 mm by 4 mm) a planar antenna integrated with an SIS (superconductor – insulator - superconductor) mixer, a superconducting flux flow oscillator (FFO) acting as a LO in the frequency range 400 - 700 GHz and the second SIS harmonic mixer (HM) to phase-lock the FFO.

The shape of the FFO radiation spectral line was found to be Lorentian [3], [4] at the frequencies up to 750 GHz. It indicates that the free-running (“natural”) FFO linewidth is determined by the wideband noise, i.e. thermal fluctuations and the shot noise. It differs from many traditional microwave oscillators (for example, backward-wave and Gunn oscillators) where the “natural” linewidth is rather small and is broadened mainly by external fluctuations. For stabilization of the FFO frequency a specially designed wide-band phase locking loop (PLL) has been developed [4]. The effective bandwidth (BW) of the existing room temperature PLL (RT PLL) is about 10 - 12 MHz, while the FFO linewidth may exceed 10 MHz. The so-called “spectral ratio” (SR) is the ratio between the phase-locked and the totally emitted by oscillator power. The RT PLL provides SR value around 50% for the 5 MHz wide FFO radiation line. For the Terahertz Limb Sounder (TELIS) balloon project intended to measure a variety of stratosphere trace gases [5] the SR value better than 50% was desired.

The wider PLL BW is the more power of the FFO can be phase-locked (resulting in higher SR). The BW is determined by the group delay τ in the PLL loop. In our experiments the dependence of the SR on the length of the PLL cables was found to be linear in the wide range of parameters. [6]. The existing RT PLL has τ about 15 ns, which contains 5 ns contribution from the PLL filtering part and semiconductor electronics and 10 ns from the 2 m long cables connecting the RT PLL electronics with the HM and the FFO. The minimal length of the cabling is restricted by the geometric size of a cryostat and can not be essentially reduced without increasing the heat flux into the cryogen space. From the other hand the traditional PLL can not be placed directly into the cryogenic volume inside the cryostat, as it is a semiconductor-based device designed for room temperature.

There are several motives to extend the BW of the PLL systems for FFO phase-locking to values much higher than present 10 MHz. The FFO linewidth exceeds 10 MHz at the voltages above the one third of the FFO gap voltage, where the Josephson self-coupling effect drastically modifies FFO IVCs increasing differential resistance and internal damping [7], [8]. In case of such a wide line an essential part of the emitted FFO power can not be phase-locked with the RT PLL and contributes directly into the receiver phase noise.

An FFO based NbN or NbTiN films is the most attractive for future SIR applications at the frequencies around 1 THz. The linewidth of this type of the FFO can considerably exceed 10 MHz due to higher surface losses. In this situation the PLL has to have the bandwidth as large as 30 MHz (to reach the SR value desirable for most radio-astronomy projects), which can not be provided by the RT PLL.

Using an SIR for interferometry applications requires an LO with high phase stability. For example, for ALMA project (interferometer in Chile with the up to 15 km base line) the LO rms phase noise should be considerably less than 75 fs (the value of rms atmospheric fluctuation in location of the interferometer) [9]. The rms phase noise and SR of the phase-locked LO are related by:

$$\tau = \frac{1}{\omega_{LO}}\sqrt{\frac{100\% - SR}{SR}},$$

where ω_{LO} is the operation frequency of typical value about 600 GHz. From this dependence (see Fig. 1) one can estimate that the SR > 95 % is required for ALMA applications. To provide such a large SR value for the FFO with linewidth of 2 MHz the PLL should have BW about 50 MHz.

To improve spectral characteristics of the FFO and to overcome the limitation of RT PLL we propose the Cryogenic Phase Locking Loop system (CPLL). The key element of the CPLL is a cryogenic phase detector (CPD) [6] based on a well-developed tunnel SIS junction. The CPD can be placed very close to the FFO to minimize the loop length, since both devices operate at the same temperature; all other elements of the loop can be placed inside a cryostat as well. Negligible delay in the CPD and small time delays in the short loop lead to ultra wide BW.

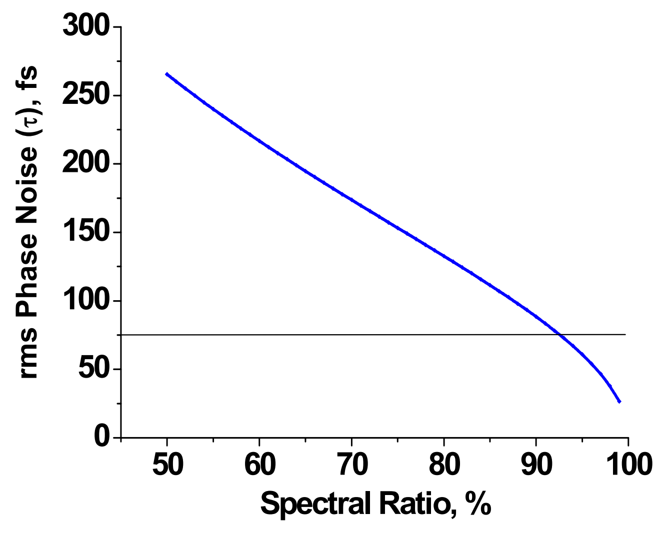

Fig. 1. Dependence of the rms phase noise value vs SR at ω_{LO} = 600 GHz.

A. Cryogenic Phase Detector

SIS junction is a well known mixer element due to its nonlinear properties; see [10] for example. Any mixer can operate as a phase detector, so a micron size Nb-AlOx-Nb tunnel junction with R_nS product (the product of the area and the normal state resistance) about 30 $\Omega*\mu^2$ was chosen to be a cryogenic phase detector (CPD) for the CPLL.

B. I-V curves of the CPD

First successful results of the CPD implementation were presented very recently in [6]. A principle of the CPD operation can be demonstrated by IVCs of the SIS tunnel junction. A typical autonomous IVC of the SIS junction is shown in Fig. 2 (curve 1); curve 2 corresponds to the IVC of the SIS pumped by a microwave signal. Although the frequency of the synthesizer is a few GHz, and rather low compare to the smearing of the superconducting gap, the shape of the CPD IV-curve pumped by the synthesizer looks very much like a result of irradiation by a high frequency signal rather than a low frequency one. Moreover, this shape is qualitatively the same at the synthesizer frequency in range 0.4 – 10 GHz. Apparently, a certain number of higher order harmonics of the applied signal are excited in the SIS junction due to its non-linearity; these harmonics effectively pump the tunnel junction.

Curves 3 and 4 are measured in situation when the two microwave signals are fed to the junction in phase and with 180 degree shift correspondingly. The phase response, which is the difference between curve 3 and curve 4 is also presented in Fig. 2. A very important point here is that the phase response is almost independent on the CPD bias voltage above 1 mV. Looking forward we can say that the best bias voltage for CPD operation is in region 2...2.5 mV.

It was shown [6] that dependence of the phase response versus the phase difference between the two signals can be sinusoidal for the CPD under proper experimental circumstances (see inset in Fig. 2).

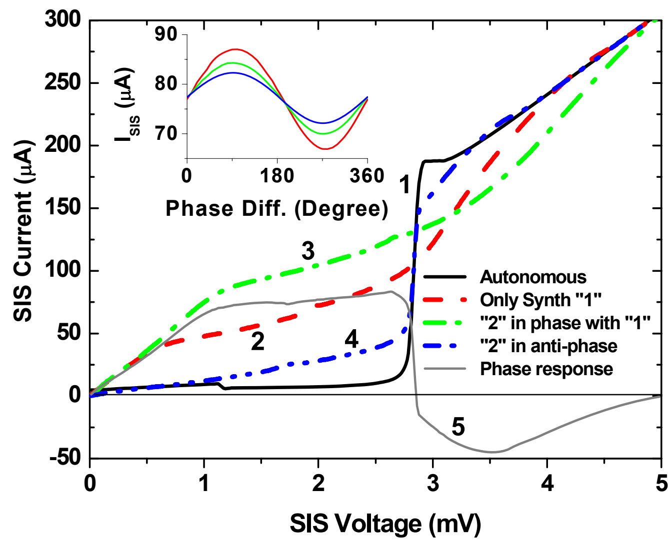

Fig. 2. IVCs of the SIS junction measured at different settings of the microwave signals (frequency 5 GHz): curve "1" – autonomous; "2" – pumped by one microwave signal; "3"- pumped by two microwave signals in phase; "4" – pumped by 2 microwave signal in anti-phase; PSynth1 = 0.3 μW, PSynt2 = 0.1 μW; "5" – phase response of the CPD – difference between curves "3" (in phase) and "4" (anti-phase). Inset shows a sinusoidal dependence of the SIS current on the phase difference between the signals.

C. CPD – FFO coupling

The phase response shown in Fig. 2 was measured at DC by voltage biased source. However, the CPD of the CPLL is supposed to be connected to the FFO control line channel (CL FFO) to tune the FFO frequency [8]. The frequency of the FFO is controlled by the two currents and the one, producing the magnetic field at the FFO ends (the so-called control line current I_{CL}) is employed as a FFO-CPD interface. The simplified equivalent diagram shown in Fig. 3 effectively describes this connection at frequencies of interest 0 – 100 MHz. The current source generates current I_0 and a part of it I split to the CPD. The CPD voltage V_0 can be expressed in terms of load R and current I from simple formula:

$$I_0 = I + V_0/R \, .$$

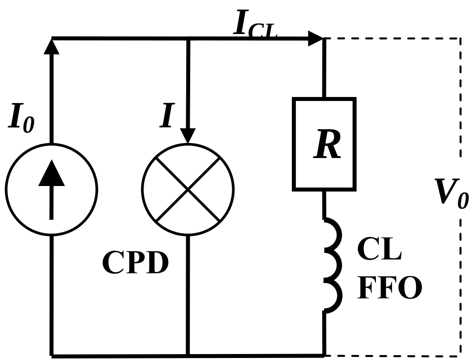

Fig.3 Simplified equivalent diagram of the CPD - FFO coupling. Connection that provides constant FFO CL current is not shown.

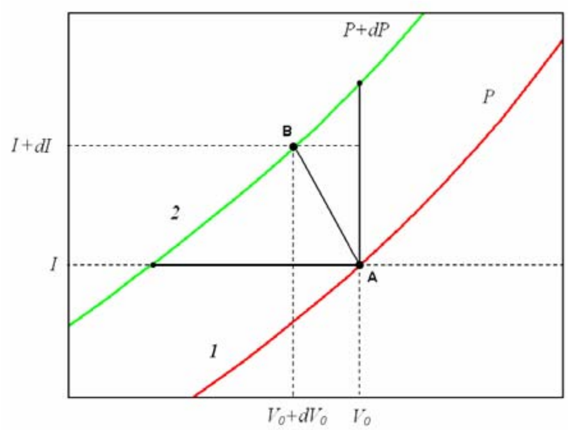

Fig. 4. Demonstration of the CPD operation with load R. Two IVCs of the CPD pumped at slightly diriment powers are presented.

Let's consider the microwave power P applied to the CPD and introduce it's variation dP to estimate the coupling between the FFO and the CPD. The current of the pumped junction depends on the power P (see Fig. 4 curves 1 and 2). The CPD biasing point goes along the load line ($1/R$) from point A to point B at changing of the microwave power. The variation of the CPD voltage dV_0 is given by the relation:

$$dV_0 = -\frac{r_d R}{r_d + R}\frac{\partial I}{\partial P}dP \, ,$$

where r_d is a CPD differential resistance, $\partial I/\partial P$ is a partial derivative (can be calculated from the dependence *I(P)* measured at the fixed CPD voltage). The contribution to the current I_{CL} from the CPD is the ratio dV_0/R. From these considerations the variation of the FFO frequency df_{FFO} is equal to:

$$df_{\mathrm{FFO}} = kdV_{\mathrm{FFO}} = k\frac{dV_0}{R}Rd_{\mathrm{CL\,FFO}} = -kRd_{\mathrm{CL\,FFO}}\frac{r_d}{r_d + R}\frac{\partial I}{\partial P}dP$$

Here $k = 483.6$ MHz/μV is the Josephson constant and $Rd_{\mathrm{CL\,FFO}}$ is the FFO differential resistance by I_{CL} (typically, about 0.02 Ω).

In case of the two microwave input signals of the power $P1$ and $P2$ with the phase difference φ the expression $\partial I/\partial P*dP$ should be replaced with $\partial I/\partial P*(P_1P_2)^{1/2}*d\varphi$ (here $P = (\sqrt{P_1} + \sqrt{P_2})^2$). So, for the two coherent signals:

$$df_{\mathrm{FFO}} = kdV_{\mathrm{FFO}} = -kRd_{\mathrm{CL\_FFO}}\frac{r_d}{r_d + R}\frac{\partial I}{\partial P}\sqrt{P_1P_2}\,d\varphi \quad (1)$$

This formula gives the efficiency of the CPD - FFO coupling and has been experimentally verified with a good accuracy [11]. An important result is the value of df_{FFO} is found to be linearly proportional to the derivative $\partial I/\partial P$. The CPD parameters r_d and $\partial I/\partial P$ can be preliminary measured to choose the best sample for the CPD operation. Detailed analysis of this formula is presented in the next chapter, where the CPLL optimization is considered.

Frequency parameters of the CPD are also an important issue briefly studied in [6]. The results of additional experiments demonstrate that the CPD is applicable for the FFO phase locking [11]. The operation frequency of the CPLL can be ranged from 200 MHz to 20 GHz and the response amplitude remains flat at least up to 750 MHz, that considerable exceeds 100 MHz required for the CPLL.

D. Cryogenic Phase Locking Loop System

Experimental Details

A block diagram of the CPLL is shown in Fig. 5. The FFO radiation of the frequency around 600 GHz is down converted by the harmonic mixer (HM) to the frequency 400 MHz and amplified by the two HEMT-amplifiers HEMT #1 and HEMT #2. This signal is compared by the CPD with the external reference signal and the resulting output error signal is proportional to the phase difference φ and fed to the FFO via the channel of the I_{CL} current. Some part of the microwave power after HEMT #1 is spitted to the spectrum analyzer by the directional coupler and can be also used as the input of the RT PLL and Frequency Detector, FD (the RT PLL and FD can operate together with the CPLL). It makes possible to stabilize the FFO frequency by the RT system mounted outside the cryostat.

The HEMT #2 varies the overall loop gain, it also is used to prevent a leak of the reference signal to the HM and spectrum analyzer. The total gain of the amplifiers is about 30 dB. The loop gain can be also controlled by the CPD gain factor, which depends on the CPD biasing voltage and the power of the reference signal.

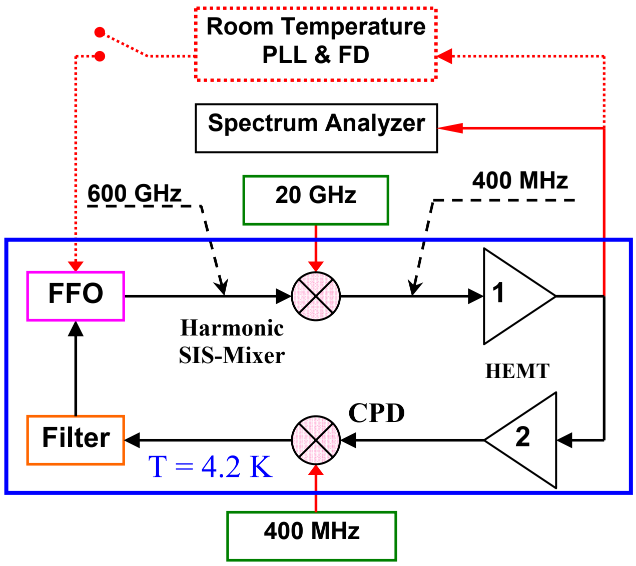

Fig. 5. Block diagram of CPLL for FFO.

The filter (see Fig. 5) blocks the signals around 400 MHz. There is very important requirement on the group delay introduced by the fitter - this delay should be as small as possible. So there are two main parameters of the filter: the group delay and a reflective characteristic (or transparency) at operation frequency. For better filter reflection a bigger value of reactive elements or higher number of them is necessary, but it leads to an increasing of the delay, so for these two parameters a trade off should be found. Two types of filters can be used: a low pass filter and a rejecter or a band-stop filter (the bandwidth of the stop-band should be no less than PLL BW to avoid a distortion of signal going to CPD from HEMT #2). The band-stop filter has smaller group delay than the low pass filter with the same reflective characteristic in the required frequency range, so a band-stop filter with a transparency -20 dB and the group delay 2 ns have been chosen for the presented CPLL. For the CPD output signal (frequencies up to 100 MHz) filter is transparent and only a resistance R (Fig. 3) is placed between the CPD and the FFO. It should be mentioned that such a filter will have significantly smaller delay for the CPLL with higher operation frequencies.

For optimization of the CPLL with the fixed loop length the effective CPD - FFO coupling and the minimal group delay in the filter of the loop must be achieved. The parameters for tuning are the load R and differential resistance r_d of the CPD (by varying the area of the SIS junction S). We assume that the R_nS product and filter parameters are fixed. Analyze is based on formula (1) and gives the following results:

1) value of R should be smaller then r_d (optimal value is R *of* about $0.2r_d$);

2) the larger area S the better is the CPD - FFO coupling. At realization of these conditions some problems can be foreseen: a) large required power of the microwave signal for the CPD pumping (larger SIS needs more power, while small r_d causes a bad coupling of the CPD with 50 Ohm source of microwave signal), b) larger power of the microwave signals will require a modification of the filter for better reflection, that leads to increasing of the group delay, c) increasing of the filter group delay because of its input and output impedances (r_d and R) decreasing. Taking into account all these conditions the CPLL have been realized with area of the CPD S ≈ 1 um^2 (r_d ~ 50 Ohm) and R = 10 Ohm.

The results presented for the CPD are obtained with suppressed critical current (CC) of the SIS junction. There is no significant influence of the CC on phase response, but for the CPD implementation in real CPLL system the CC can results in instability of the FFO line, high noise level and excitations in the loop. The way to minimize CC influence is to work at the CPD voltages about 2.5 mV (almost near the gap voltage). However, it is better to suppress the CC.

E. Experimental Results

The presented realization of CPLL has the length of the loop about 1 m (group delay 5 ns). The delay in filter is 2 ns. So the total group delay is 7 ns (compare to 15 ns for the RT PLL). This reduction of the loop delay results in increasing of the BW from 12 MHz to 25 MHz (see Fig. 6). For the FFO linewidth of 2 MHz this CPLL is able to phase-lock 91% against 82% for the RT PLL. For the FFO linewidth as large as 10 MHz the CPLL gives SR = 50% instead of 20-25% for the RT PLL. A summary of these results is presented in Fig. 7.

The dependences of the SR vs FFO linewidth demonstrates the efficiency of the FFO phase locking by different systems. The stars show the experimental data for the RT PLL with the BW of 12 MHz. Dashed line is a result of simulations approximating the experiment [12]. The “regulation BW” of 10 MHz in simulations corresponds to “BW” = 12 MHz in experiment. The measurements for the CPLL (squares) approximated theoretically by a solid line for regulation BW 20 MHz show the advantage of BW widening and prospects for future improvement. We can say roughly that a twice wider FFO line can be phase locked by the PLL with two times wider BW resulting in the same SR.

Phase noise of the FFO locked by the two systems is shown in Fig. 8. This figure demonstrates an advantage of the CPLL on the RT PLL in the range of offsets from the carrier higher 10 kHz, whereas there is a strong increasing of phase noise level for the CPLL at small offsets from the carrier frequency. This noise increasing is because the CPLL is a first-order PLL system without additional amplifier and any integration filter in the loop. An amplifier and integration filter will give an improvement of a phase noise performance and CPLL stability (wider holding range).

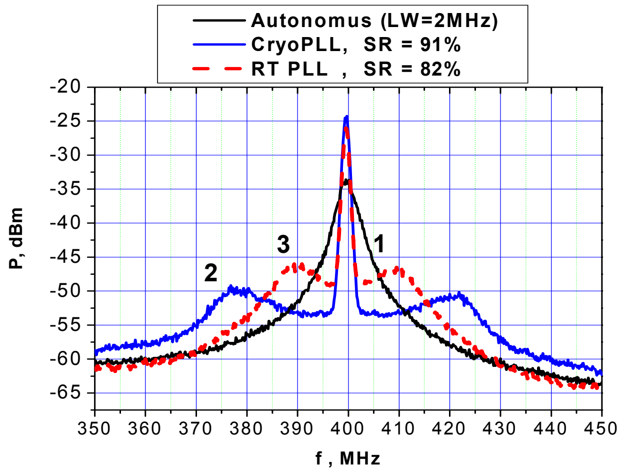

Fig.6. . Down-converted spectra of the FFO operating at 600 GHz: curve “1” – autonomous, “2” – phase locked by CPLL; “3” – phase locked by RT PLL.

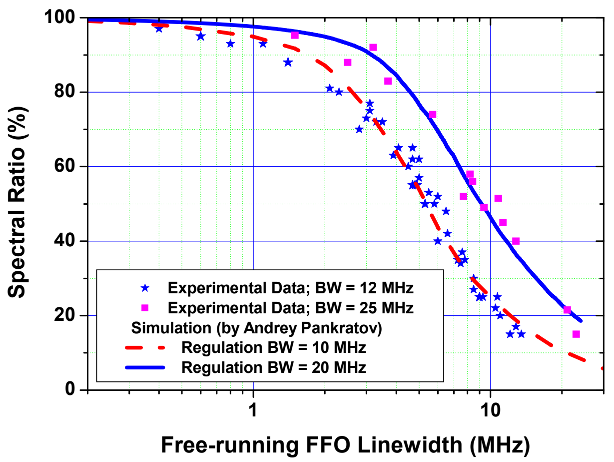

Fig.7. Dependence of the SR vs FFO linewidth for different PLL bandwidths.

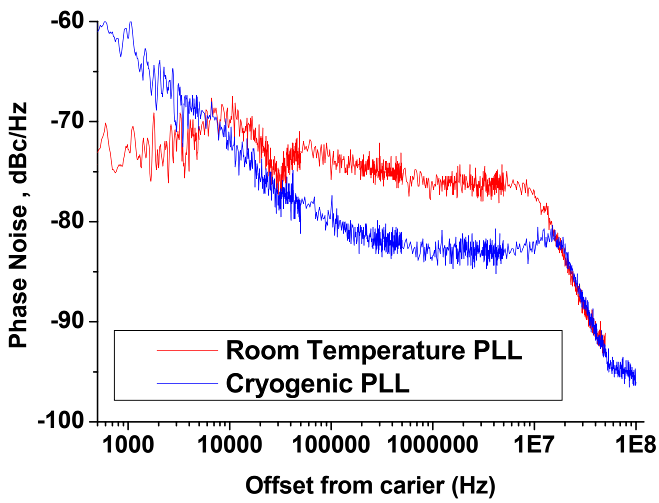

Fig. 8. Phase noise diagram of the phase-locked FFO (linewidth is 4.3MHz).

CONCLUSIONS

Ultra wideband Cryogenic Phase Locking Loop system has been developed and tested. The CPLL has a bandwidth wider than 25 MHz and demonstrate an evident advantage on the RT PLL. The novel CPLL system can phase-lock more than 50% of the FFO spectral line if the free-running FFO is about 10 MHz. Practical implementation of CPLL looks especially promising for the development of the SIR arrays.

ACKNOWLEDGMENT

Authors thank Hans Golstein, Andrey Pankratov, Sergey Pripolzin, Alexander Sobolev, Vladimir Vaks and Wolfgang Wild for fruitful and stimulating discussions.

The work was supported in parts by the RFBR projects 06-02-17206, the ISTC project # 3174, NATO SfP Grant 981415, and the Grant for the Leading Scientific School 5408.2008.2

REFERENCES

[1] V. P. Koshelets and S. V. Shitov, “Integrated Superconducting Receivers,” *Superconductor Science and Technology*, vol. 13, pp. R53-R69, 2000.
[2] V.P. Koshelets, S.V. Shitov, A.B. Ermakov, O.V. Koryukin, L.V. Filippenko, A. V. Khudchenko, M. Yu. Torgashin,P. Yagoubov, R. Hoogeveen, O.M. Pylypenko, “Superconducting Integrated Receiver for TELIS”, “*IEEE Trans. on Appl. Supercond.”,* vol. 15, pp. 960-963, 2005.
[3] V.P. Koshelets, A.B. Ermakov, P.N. Dmitriev, A.S. Sobolev, A.M. Baryshev, P.R. Wesselius, J. Mygind, “Radiation linewidth of flux flow oscillators”, *Superconductor Science and Technology,* **v. 14,** pp. 1040 - 1043, 2001.
[4] V.P. Koshelets, S.V. Shitov, P.N. Dmitriev, A.B. Ermakov, L.V. Filippenko, V.V. Khodos, V.L. Vaks, A.M. Baryshev, P.R. Wesselius, J. Mygind, “Towards a Phase-Locked Superconducting Integrated Receiver: Prospects and Limitations”, *Physica C*, **367,** pp. 249 - 255, 2002.
[5] V.P. Koshelets, A.B. Ermakov, L.V. Filippenko, A.V. Khudchenko, O.S. Kiselev, A.S. Sobolev, M.Yu. Torgashin, P.A. Yagoubov, R.W.M. Hoogeveen, and W. Wild, “Integrated Submillimeter Receiver for TELIS”, “*IEEE Trans. on Appl. Supercond.”,* vol. 17, pp 336-342, 2007.
[6] A.V. Khudchenko, V.P. Koshelets, P.N. Dmitriev, A.B. Ermakov, P.A. Yagoubov, and O.M. Pylypenko, “Cryogenic Phase Detector for Superconducting Integrated Receiver“ “*IEEE Trans. on Appl. Supercond.”,* vol. 17, pp. 606-608, 2007.
[7] V. P. Koshelets, S. V. Shitov, A. V. Shchukin, L. V. Filippenko, J. Mygind, and A. V. Ustinov, ”Self-Pumping Effects and Radiation Linewidth of Josephson Flux Flow Oscillators”, *Phys Rev B*, vol. 56, p. 5572-5577, 1997.
[8] V.P. Koshelets, P.N. Dmitriev, A.B. Ermakov, A.S. Sobolev, M.Yu. Torgashin, V.V. Kurin, A.L. Pankratov, J. Mygind, “Optimization of the Phase-Locked Flux-Flow Oscillator for the Submm Integrated Receiver”, “*IEEE Trans. on Appl. Supercond.”,* vol. 15, pp. 964-967, 2005.
[9] S. AlBanna, R. Brito, B. Shillue “ALMA 1st LO Photonic Reference: Status of Phase Drift Measurements” 2008, NRAO website. Available: http://www.tuc.nrao.edu/~bshillue/E2E_Phase_Drift_Status_RevB.doc.
[10] J. R. Tucker, M. J. Feldman, ”Quantum detection at millimeter wavelengths”, Rev. Mod. Phys., vol. 57 .No. 4. p. 1055, 1985.
[11] A.V. Khudchenko, V.P. Koshelets,, A.B. Ermakov and P.N. Dmitriev “A cryogenic phase detector for a cooled wideband phase-lock loop system”, Journal of Communications Technology and Electronics, vol. 53, No. 5, pp. 594-599, 2008.
[12] A.L. Pankratov, V.L. Vaks, and V.P. Koshelets, “Spectral properties of phase locked Flux Flow Oscillator”, *Journal of Applied Physics,* vol. 102, pp. 0629, (1-5), 2007..

Fabrication of GaAs Schottky Nano-diodes with T-Anodes for Submillimeter Wave Mixers

Cécile Jung, Hui Wang, Alain Maestrini, Yong Jin

Abstract **- We report on the design and fabrication of a T-anode Schottky structure for millimeter and submillimeter wave mixers. The process for anti-parallel pairs of diodes with submicronic anode areas on 10µm thick GaAs substrate is presented and these diodes will be used in a 330GHz sub-harmonic mixer block. I(V) measurements have been performed and values of the ideality factor and the reverse saturation current have been determined.**

Index Terms **– Nano Schottky diodes, GaAs substrates, T-Anodes, Air-bridges, Submillimeter wavelengths, Frequency mixer**

I. Introduction

Millimeter and submillimeter heterodyne observations at THz frequencies will improve our understanding of the universe and the submillimeter-wave spectrum band 300GHz-400GHz continues to be of much interest for the exploration of the earth's and planets' atmospheres. A GaAs Schottky diode is one of the key elements for multipliers and mixers at these frequencies since the diode can be extremely fast by reducing its size and also very efficient thanks to the low forward voltage drop [1].

A. Fabrication technology

The fabrication process presented below makes use of the electron beam lithography and conventional epitaxial layer designs. The starting material is a semi-insulating 500µm thick GaAs substrate with epitaxial layers grown by Molecular Beam Epitaxy (MBE).

The layer structure consists of a 50nm $Al_{0,8}Ga_{0,2}As$ etch-stop layer, an 800nm heavily doped $5x10^{18}$ cm^{-3} n^+ GaAs layer and a 100nm thick n type GaAs layer doped $1\text{-}5x10^{17}cm^{-3}$.

C. Jung is with Laboratoire de Photonique et Nanostructures (LPN) – Centre National de la Recherche Scientifique (CNRS), route de Nozay, 91460 Marcoussis, France, and is associated with Laboratoire d'Etude du Rayonnement et de la Matière en Astrophysique (LERMA) - Observatoire de Paris, 77 avenue Denfert-Rochereau, 75014 Paris, France.
Email: cecile.jung@lpn.cnrs.fr
H. Wang and A. Maestrini are with Laboratoire d'Etude du Rayonnement et de la Matière en Astrophysique (LERMA) – Observatoire de Paris.
Y. Jin is with Laboratoire de Photonique et Nanostructures (LPN) – Centre National de la Recherche Scientifque (CNRS).

B. Device Processing

A selective AlGaAs/GaAs wet etching is used to define the device mesas (a), the etch rate slows down sufficiently when the etch-stop layer is reached.
The ohmic contacts are first recessed into the n+ GaAs layer, Ni/Ge/Au/Ni/Au metal films are successively evaporated and a rapid thermal annealing is performed (a).
An air-bridge process is used to define the T-anodes and the connection pads at the same step. A first square of resist is exposed and reflowed to form the support for the air-bridges.

The T-anodes are fabricated using multi layer of resists and the required profile is obtained by the combination of resist layer thicknesses, sensitivities and exposure dose.
A Ti/Au Schottky and connection pads metal film is evaporated (b).

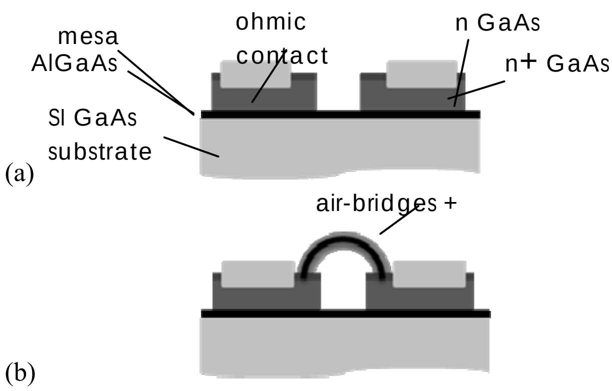

Fig.1 Fabrication process. (a) Ohmic and mesas definition. (b) T-anodes / air-bridge Schottky and connection pads deposition followed by passivation.

The diodes are finally passivated using Si_3N_4 deposited by Plasma Enhanced Chemical Vapor Deposition (PECVD). To allow a circuit integration, each circuit is separated from the others by a deep dry etching with an Inductive Coupled Plasma (ICP).

The wafer is then mounted topside-down onto a carrier wafer by using wax. The Semi-insulating GaAs substrate is thinned to the desired thickness (12-10µm) using the process exposed in [2].

Some scanning electron microscopy (SEM) pictures of the circuit and the diodes are shown in Fig 2.

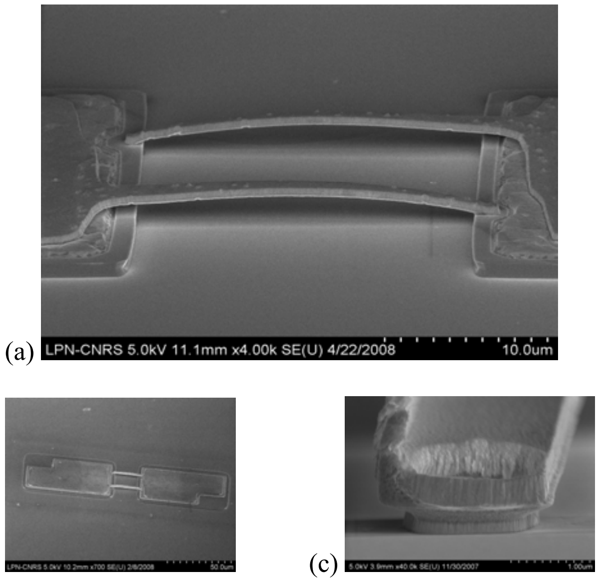

Fig.2 SEM pictures before passivation. (a) Air-bridges and the pair of anodes. (b) The 330GHz circuit. (c) Close-up of the T-Anode.

C. DEVICE DC CHARACTERISTICS

Table I represents diode parameters fabricated at the LPN in term of doping density and anode area. All the diodes have the same finger length of 20µm. Electrical characteristics for each diode are deduced by standard I(V) measurements and reported in Table II.

Diode	Doping (cm^{-3})	Anode Area (µm²)
A-517-Sok	$5x10^{17}$	0.8
B-217-Sok	$2x10^{17}$	0.8
C-117-Sok	$1x10^{17}$	0.8
D-117-Ssup	$1x10^{17}$	1
E-217-Ssup	$2x10^{17}$	1

Table I. Fabricated diodes parameters.

Diode Pair	n	R_s (Ω)	I_s (A)
A	1.41	11	$1.6x10^{-13}$
B	1.20	11	$1.3x10^{-14}$
	1.24	12	$1.2x10^{-14}$
C	1.19	9	$6.8x10^{-16}$
	1.25	8	$2x10^{-15}$
D	1.28	13	$5.3x10^{-15}$
E	1.25	16	$8.3x10^{-15}$

Table II. Measured DC parameters for pairs of anti-parallel diodes.

It should be pointed that the process has not been fully optimized yet, and it is expected that the diode performances will be improved in the future.

D. Circuit Integration

The completed testing structure consists of a pair of antiparallel diodes transfered topside down onto a 50µm thick quartz filter circuit substrate using epoxy, a second quartz circuit and a subharmonically pumped mixer block at 330GHz [3]. RF measurements will be performed at the Observatoire de Paris.

CONCLUSION

Schottky diodes with T-anodes have been fabricated and their electrical parameters have been characterized. Since all fabrication steps are performed using e-beam lithography, our process allows futher shrinking of the anode surface for higher frequencies mixers and multipliers.

ACKNOWLEDGEMENT

The authors wish to thank the MBE team of the LPN who grew the substrates and all the clean room staff involves in this project. This work was supported by the Centre National d'Etudes Spatiales (CNES), the Centre National de la Recherche Scientifique (CNRS) and Astrium in Toulouse.

REFERENCES

[1] I. Mehdi, S. C. Martin, R. J. Dengler, R. P. Smith and P. H. Siegel, “Fabrication and Performance of Planar Schottky Diodes with T-Gate-Like Anodes in 200-GHz Subharmonically Pumped Waveguide Mixers”, IEEE Microwave and Guided wave letters, Vol. 6, No. 1, January 1996.

[2] S. Martin, B. Nakamura, A. Fung, P. Smith, J. Bruston, A. Maestrini, F. Maiwald, P. Siegel, E. Schlecht & I. Mehdi, “Fabrication of 200GHz to 2700GHz multipliers devices using GaAs and metal membranes”, proceedings of the IEEE MTT-S, Vol.3, pp. 1641-1644, Phoenix, Arizona, May 20-25, 2001.

[3] B. Thomas, A. Maestrini, and G. Beaudin, ”A Low-Noise Fixed-Tuned 300-360 GHz Sub-Harmonic Mixer using Planar Schottky Diodes”, IEEE Microwave and Wireless Component Letters, Vol. 15, Issue 12, pp. 865 - 867, December 2005.

Towards a THz Sideband Separating Subharmonic Schottky Mixer

Peter Sobis [1,2], Jan Stake[1] and Anders Emrich[2]

[1]Chalmers University of Technology Department of Microtechnology and Nanoscience, Göteborg, Sweden
[2]Omnisys Instruments AB, Västra Frölunda, Sweden

Today GaAs Schottky mixers with state of the art planar submicron diodes are used for THz-detection up to 3 THz [1]. GaAs Schottky diodes can operate in room temperature which makes them good candidates for space applications and an interesting low cost alternative to low noise cryogenic SIS and HEB technologies.
To our knowledge this is the first time a sideband separation mixer [2] using subharmonic Schottky mixers is presented. We will present the current status of the development of a novel sideband separating subharmonic reciever topology operating at 340 GHz, see Fig1. The design of a subharmonic mixer and the LO and RF waveguide hybrids will be presented followed by an account of measured S-parameters and mixer noise temperature.

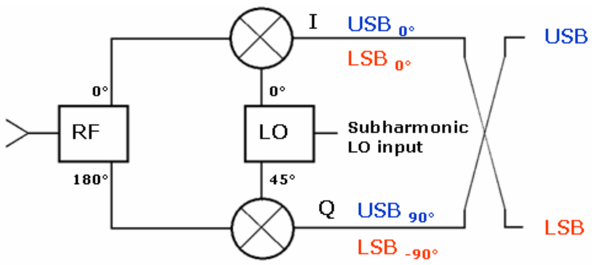

Fig1. Schematic of the sideband separation mixer (left) and modular assembly (right).

[1] L. Hesler, T.W. Crowe, W.L. Bishop, R.M . Weikle, R.F. Bradley and Pan Shing-Kuo, “The development of planar Schottky diode waveguide mixers at submillimeter wavelengths”, IEEE MTT-
S International Microwave Symposium Digest, vol 2, pp. 953-6, 1997.

[2] Risacher, V. Vassilev, V. Belitsky, A. Pavolotsky, “Design of a 345 GHz Sideband Separation SIS Mixer”, Proceedings of 3rd ESA Workshop on Millimeter Wave Technology and Applications: Circuits, Systems and Measurement Techniques, 21-23 May 2003, Espoo, Finland

Ultrawideband THz detector based on a zero-bias Schottky diode

C. Sydlo[1], O. Cojocari[1], D. Schoenherr[2], T. Goebel[2], S. Jatta[2],
H.L. Hartnagel[2] and P. Meissner[2]

C. Sydlo[1], O. Cojocari[1], D. Schoenherr[1], T. Goebel[2], S. Jatta[2], H.L. Hartnagel[2] and P. Meissner[2]

The work in the field of THz technology includes the emitters as well as the detectors. While a large number of approaches for THz emitters with increased power levels are evolving the detectors have show less progress in the last years. But essential for all THz work is the signal to noise ratio which also benefits from improved detectors.
Nowadays, pyroelectric detectors and Golay cells are the most common room-temperature THz detectors available. They feature NEPs (noise-equivalent powers) down to 100 pW/Hz^{½}, but their response time is quite large limiting the modulation to few tens Hertz. These detectors are quite bulky which inhibits flexible use.

ACST has recently established a Schottky process for zero-bias detector diodes aiming at frequencies up to one THz and possibly higher. A specialised process allows forming of Schottky contacts with a very low barrier. This in turn provides low video resistances without the need for biasing. Due to the absence of bias, the noise of the detectors reduces to the Johnson limit of the video resistance and is free of 1/f noise. The presented devices exhibit a video resistance less than 10 kΩ at zero-bias and voltage noise of less than 15 nV/Hz^{½} (measurements in full paper). Also the devices responsitivity shows values of more than 15 A/W or 2500 V/W. This results in a NEP of less than 6 pW/Hz^{½} combined with arbitrarily high modulation frequencies. The size of this detector with appendant amplifier is smaller than a matchbox (picture in full paper) allowing it to be placed and moved freely in any THz setup. However, it should be mentioned here, that this detector cannot compete yet with pyroelectric detectors or Golay cells at frequencies far beyond 1 THz.
The main frequency limiting factors for the Schottky detectors are the RC time constant and the size of the diode. The diodes size should be small compared to the effective wavelength to diminish effects of the geometry. The RC time constant is formed by the total capacitance of the diode and the RF impedance of the antenna. In this work a planar logarithmic-spiral antenna has been deployed with circular polarisation to be independent of the polarisation angle in case of linear polarised THz radiation. Hence, the responsitivity of the detector reduces to half of its value due to the coupling of linear to circular polarisation. ´The impedance of the antenna is around 50 Ω and the total capacitance of the diode is around 3 fF resulting in a roll-off frequency of about 1 THz. First measurements up to 700 GHz have revealed no sign of a roll-off (measurements >1 THz in full paper). Further measurements will be carried out for the full paper.

This work presents a very compact, highly sensitive and fast THz detector based on RF rectification by a Schottky diode. It suits ideally the needs for fast spectroscopy due to the very fast response time and high sensitivity. The developed process allows for larger integration into arrays for imaging applications.

[1] C. Sydlo and O. Cojocari are with the ACST GmbH, Darmstadt, Germany (sydlo@acst.de)
[2] D. Schoenherr , T. Goebel, S. Jatta, H.L. Hartnagel and P. Meissner are with the TU Darmstadt, Darmstadt, Germany

ALMA band 10 optics tolerance analysis

M. Candotti[1], Y. Uzawa[1], S. V. Shitov[1], Y. Fujii[1], K. Kaneko[1].

[1]National Astronomical Observatory of Japan
2-21-1, Osawa, Mitaka, Tokyo
181-8588,
JAPAN
* Contact: m.candotti@nao.ac.jp, phone +81-422-34-3780

Abstract — **The effects of mechanical tolerances for the cryostat and antenna interface levels and cold optics mechanical structure have been studied in relation to the loss of aperture efficiency and separation angle between the two orthogonal main beams of the ALMA band 10 front-end. Simple ABCD ray tracing method and full electromagnetic physical optics simulations were used to assess the optics performance under misalignment assumptions. As expected, tight tolerances of the cold optics are required for the fulfilment of the ALMA front-end specifications.**

I. Introduction

The ALMA band 10 Front-End (FE) optical configuration has been designed and theoretically assessed by means of accurate Physical Optics (PO) electromagnetic analysis [1], [2]. The optical design goal was to maximise the overall antenna efficiency and at the same time maintaining the optics structure as simple as possible. In designing the mechanical structure, holding the optical system parts, efforts had to be made to minimise possible deviations from the nominal design. Uncertainties in the mechanical fabrication and assembly process can lead to degradation of the optical front-end performances such as illumination efficiency and orthogonal polarisation beam co-alignment on the sky.

In order to correlate mechanical uncertainties with optical parameter deviations, tolerance analysis techniques can be used. There are different techniques of analysis, each of it combines various uncertainties to get an estimate of the expected optical performance. The worst case analysis consists of simply adding up all of the individual absolute uncertainties to get the worst expected level of performance. This is the most conservative approach, giving the largest possible expected uncertainty values. The root-sum-of-squares (RSS) is based on the fact that the uncertainties are considered normally distributed and independent. Under these assumptions the standard deviation of the resulting distribution is equal to the square root of the sum of the squares of the standards deviations of the initial distributions.

Another popular method of error analysis is the Monte Carlo analysis. With this technique, all uncertainties are characterised by a probability distribution which gives the probability of a certain variable to assume a value within a defined range. For instance a mathematical model is evaluated several times each of it with a new random definition of the uncertainty variables. Each case is a simulation of a possible real case of misalignment. By collecting several simulations (order of 10^3-10^4) allows one to create a statistical distribution of certain output variables. In the contest of this study, the beam separation and the beam tilt at the Focal Plane (FP) can be related to the misalignments characteristic of the system. The assessment of the beam field distribution at the FP by fundamental Gaussian beam analysis gives insights for the allocation of tolerances leading to system performance optimisation and achievement of front-end related ALMA specifications.

In this paper the ALMA specifications closely affected by the tolerance problem are presented. Subsequently, a tolerance study is conducted on the base of simple ray tracing of the optical design and then by PO simulations with the Monte Carlo method. In this analysis, the mechanical assembly error budget assumptions are made and used to statistically describe the errors affecting each of the optical components.

II. ALMA Front-End Specifications and Optical Performance Requirements

Deviations of the optical system assembly from its nominal configuration arise degradation of the power coupling at the antenna aperture between the illuminating beam and the plane wave representing the incoming radiation from the observed astronomical source. In double orthogonally polarised detector systems, it is also desirable to have the pair of orthogonally polarised main beam simultaneously pointing to the same direction in the sky. Again relative misalignments of optical elements in the FE optical system can induce a beam squint between the two beams when quasi-optical polarisation filtering is applied such as in ALMA band 10. The requirements to be fulfilled in relation the previously described issues are hereby listed:

1) Illumination efficiency

The degradation of the power coupling at the antenna aperture can be due to loss of illumination efficiency that directly relates to an offset illumination of the secondary (truncation at the edge) and/or presence of extra aberrations caused by off-axis mirrors operating at misaligned positions with respect to the nominal optical configuration. Off-axis illumination of the antenna aperture plane also causes non-uniform phase distribution across the primary aperture, that is, loss of power coupling efficiency [3]. Therefore within a first degree of generalisation, a radial shift at the aperture plane of the illuminating beam can be considered as cause of efficiency degradation. This can also be seen at the focal plane as a tilt of the illuminating beam [3].

Following [3] a maximum drop of efficiency of *1%* is taken into account as a limit of tolerable illumination efficiency loss. In [2], it has been shown that the beam illuminating the sub-reflector has an edge taper of *-12.4dB*. With this illumination distribution at a distance of *5909mm* from the secondary [2], the maximum lateral shift that causes *1%* power coupling efficiency drop with a top-hat field distribution is *41.25mm* (or $0.11R_{sec}$, with R_{sec}*=375mm* [5]). This corresponds to an angular offset from the nominal illumination angle at the focal plane of *0.4°* (*7 mrad*). The effect of on-axis shift of the illuminating beam is not taken into account in this study, since the sub-reflector position can be re-adjusted in order to refocus the whole optical system to optimal antenna focusing configuration [3].

2) *Beam separation between the two orthogonally polarised main beams*

The on sky co-alignment of the beams of the orthogonally polarised channels shall be less than *10%* of the Full Width Half Maximum (*FWHM*) of the primary beam [4].

A first approximation analysis of the far-field of the main beam *FWHM* can be given by the far-field of a uniform circular field distribution, i.e. the Airy disk *FWHM*:

$$FWHM = 1.02\frac{\lambda}{D_p},$$

where D_p is the primary mirror diameter and λ is the wavelength. The beam squint between the two main beams on the sky can be related to the focal plane through the telescope image scale relation, given by:

$$d_{FP} = \frac{f_e}{206265}\delta\theta_{Bdev} = 0.256mm \div 0.311mm$$

where f_e = *96000mm* is the equivalent focal length for the ALMA Cassegrain antenna [5] and $\delta\theta_{Bdev} = 0.54''\div 0.65''$ are the *10%* of the *FWHM* of the primary beam at *950* and *787GHz* respectively. Therefore, in order to achieve the on sky alignment of the two main beams according to specifications, the beam separation at focal plane should not be more than *0.256mm* and *0.311mm* for the frequencies of *950* and *878GHz* respectively. However this analysis should be considered as guide line. Extra beam squint contributions can arise from the presence of beam aberrations introduced by the telescope system, which can alter the previous results valid for a non diffracted beam.

In the ALMA band 10 optics designs, the cause of beam deviation angle of the two main beams is strictly connected to the two polarisation horns and the grid sub-system alignment accuracy. The two beams following a common optical path after the wire grid element, might however also show extra pointing deviation due to variation on the higher order mode content in their beam pattern field distribution at the focal plane. The use of PO throughout the whole optical system will take into account these extra contributions.

III. Front-end global alignment

The deviation of the FE global alignment (mechanical and optical between antenna and cold optics) from the nominal design is expressed by combination of uncertainties. Uncertainties occur in the manufacturing and assembling of various parts constituting the mechanical structure. Operation factors such as evacuation of the cryostat, cooling down and structural tilts in observational mode also cause deflection of the optical system.

All these uncertainty contributions can be grouped together in order to define a global misalignment error budget. The alignment budget is described by linear and angular factors. The error budget can be separated in two groups: the cryostat and antenna budget and the cold optics budget. Each degree of freedom is thought as a random Gaussian variable which 3σ equals the absolute tolerance parameters listed in table I and II.

A. *Antenna and cryostat alignment budget*

Table I list the FE interface levels as reported in [6]. For ALMA band 10 the interface levels of concern are:

1. L-a - Antenna flange to FESS (Front-End Support Structure).
2. L-b - FESS to Cryostat.
3. L-c - Cryostat to 4K plate.
4. L-d - Cryostat window angular alignment.
5. L-e - 4K plate to Cold Optics.

The alignment budget (linear and angular) for each interface level is reported in [6, 7], where the system stability due to elevation motion of the antenna and receiver cabin is also taken into account. Table I summarises the FE interface levels, where L-e has been taken from [3].

TABLE I
LINEAR AND ANGULAR ABSOLUTE TOLERANCES FOR CRYOSTAT AND ANTENNA INTERFACE LEVELS [6, 7].

Interface level	Linear [mm]	Angular [°]	Note
L –a	-	0.036	Antenna flange to FSS
L-b	-	0.014	FESS alignment
	-	0.007	FESS to cryostat
L-c	0.689	0.023	Cryostat to 4K plate
L-d	-	0.009	Cryostat window angular alignment
L-e	0.020	0.006	4K plate to cold optics

B. *Cold optics alignment budget*

The deviation of the cold optics mechanical structure from its nominal design is in principle related to machining precision and mechanical parts assembling. Therefore alignment issues arise in relation to fabrication process and to the adopted mechanical structure design. The fabrication process is characterised by absolute accuracy, meaning that actual measured numbers are expected to be well within the nominal design length plus/minus a specified range (tolerance τ). Computer numerical controlled milling

TABLE II
LINEAR AND ANGULAR ABSOLUTE TOLERANCES FOR THE COLD OPTICS ELEMENTS

L,	[mm]	τ, [μm]			θτ, [°]
		Milling	Assembling	Total	
Horn	20	20	40	60	0.057
Grid	40	20	40	60	0.057
M1	47	20	40	60	0.045
M2	57	20	40	60	0.040

machines can achieve standard tolerances of ±20μm. Higher level of accuracy can also be achieved, but with an increase of production time. A simple model of defining linear and angular accuracy can result as direct consequence of assuming machining tolerance as absolute uncertainties. That is to say, mechanical parts are characterised by the machining linear accuracy τ, and angular accuracy related to the length of the mechanical part *L*, as shown in Fig. 1. The accuracy of milling an oblique line is related to the linear absolute milling accuracy position within the nominal design. The absolute angle accuracy is then given by θτ.

In the analysis of the mechanical accuracy of the optical system studied in this paper, extra linear inaccuracies are added to the milling ones. This takes into account inaccuracies that arise when the optical parts are assembled together on the Mirror Block (MB). The MB is the mechanical structure where horns, wire grid, mirrors M1 and M2 will be mounted. Table II lists the absolute linear and angular deviations for the model of Fig. 1, where *L* is the length of the optical element along the tangent at the chief ray incident point. The linear tolerances represent a conjunction of milling machine precision and further assembling error of the optical parts. Each degree of freedom is thought as a random Gaussian variable which 3σ equals the absolute tolerance parameters listed in table I and II.

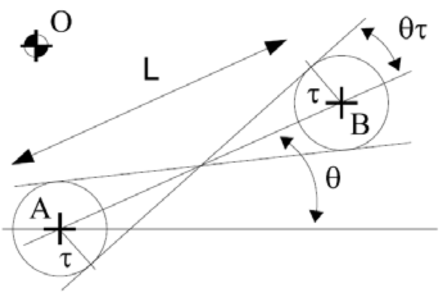

Fig. 1. Simplified model for the absolute angular accuracy of optical elements.

IV. RAY TRACING METHOD

For small linear and angular deviations of the optical elements from the nominal design configuration, the position and tilt of the beam through the optical path can be tracked

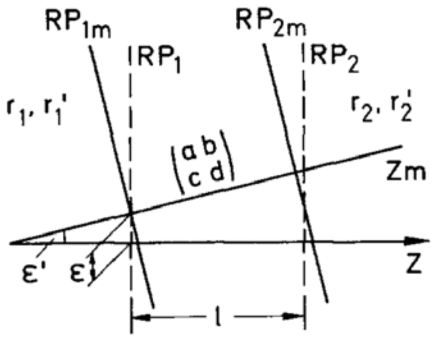

Fig. 2. Misalignment diagram for a forward going system, [REF7].

by ray tracing methods for paraxial beams, as in the case of sub-mm optical systems.

In general linear and/or angular displacements of a single part in the optical system rises a combination of linear and angular displacements in a different location of the system, for example at the focus location of a lens. Therefore when seeking for the total amount of linear displacement at a certain point of the optical path, both contributions coming from linear-to-linear and angular-to-linear relations, are considered. The same concept applies for angular displacements which can be originated from linear and angular displacements of parts in the mechanical system. The ray transfer method used to describe the propagation of a fundamental Gaussian beam for a perfect centred optical system, can be applied to describe misalignments that occur in a optical sub-system where all linear and angular displacements take place on the same plane. Fig. 2 depicts the case of a misaligned forward going system, where r_1, r'_1, r_2 and r'_2 are ray parameters for the incoming and outgoing rays [8]; RP_1 and RP_2 are the aligned reference planes, l is the geometrical distance from RP_1 to RP_2 and *a*, *b*, *c*, and *d* denote the ray transfer matrix elements of this optical system. RP_{1m} and RP_{2m} mean the misaligned reference planes. ε and ε' express the misalignment parameters of this optical system, i.e. distance and slope between the misaligned axis and the ideal axis of this optical system at the input plane [8]. In the paraxial approximation, from geometrical consideration it can be seen that:

$$\begin{bmatrix} r_2 \\ r'_2 \end{bmatrix} = \begin{bmatrix} a & b \\ c & d \end{bmatrix} \cdot \begin{bmatrix} r_1 \\ r'_1 \end{bmatrix} + \begin{bmatrix} \alpha & \beta \\ \gamma & \delta \end{bmatrix} \cdot \begin{bmatrix} \varepsilon \\ \varepsilon' \end{bmatrix}.$$

Where α, β, γ and δ are called misalignment matrix elements determined by:

$$\alpha = 1 - a \quad \beta = 1 - b$$
$$\gamma = -c \quad \delta = 1 - d.$$

If the system depicted in Fig. 2 is a backward going system, then $\delta = 1 - d$ [8]. This is the case of a mirror for example. The linear shift, in the direction of the nominal incident chief ray (Z direction), can also be taken into account. This has been shown in [3]. Misalignments in the Z direction of an optical part introduce further linear and angular deviations of the propagating ray. This is described by the following matrix notation:

$$\begin{bmatrix} r_2 \\ r'_2 \end{bmatrix} = \begin{bmatrix} a & b & e \\ c & d & f \end{bmatrix} \cdot \begin{bmatrix} r_{1x} \\ r'_1 \\ r_{1z} \end{bmatrix}$$

From geometrical considerations, the misaligned matrices for a plane mirror and a concave mirror (for small ray deviations from the nominal chief ray direction) can be obtained as reported in table III. The wire grid in the ALMA band 10 optics design is modelled as a flat mirror.

TABLE III
MISALIGNED MATRICES FOR RAY TRACING INCLUDING THE Z DIRECTION [3].

Misaligned matrix	Note
$E_{fm} = \begin{bmatrix} 1 & 0 & \sin(2\theta_i) \\ 0 & -2 & 0 \end{bmatrix}$	Flat mirror incident angle θi
$E_{em} = \begin{bmatrix} 1-\cos(2\theta_i) & 0 & \sin(2\theta_i) \\ 1/f & -2 & 0 \end{bmatrix}$	Ellipsoidal mirror incident angle θi and focal length f

V. RAY TRACING MODEL FOR THE ALMA BAND 10 OPTICS

According [1, 2], the optics design make use of a pair of corrugated horns which linearly polarised beams are coupled to the Cassegrain focal plane by means of a wire grid and a pair of ellipsoidal mirrors. Fig. 3 depicts the ALMA band 10 optics scheme for the ray tracing analysis. Details of the design can be found in [2]. The ALMA band 10 optical system is designed in such a way that the P1 polarisation optical path lies on a plane. On the other hand the P0 optical path is divided in to two planes at the level of the wire grid. Therefore the model adopted for the ray tracing analysis, is in somehow different from the original system. In the former model, depicted in Fig. 3, lateral and angular misalignments in the plane normal to the paper are also not considered. In Fig. 3 angular displacements and linear displacements in X and Z are depicted for each optical element. In the ray tracing model each element is subjected to displacement error. Therefore the chief ray is deviated from the nominal path according to the ABCD matrix theory.

Each optical element introduces an error $\boldsymbol{\varepsilon} = [\varepsilon_x \quad \varepsilon \quad \varepsilon_z]^T$ which can be combined into an ABCD matrix expression that keeps trace of the chief ray deviation at the FP. The P0 chief ray deviation at the FP due to the optical displacement errors is described by the following equation:

$$\boldsymbol{r}_{FPP0} = \boldsymbol{M}_{tot}\boldsymbol{r}_{HP0} + \boldsymbol{M}_{tot}\boldsymbol{E}_{HP0}\boldsymbol{\varepsilon}_{HP0} + \boldsymbol{M}_{L4}\boldsymbol{M}_{M2}\boldsymbol{M}_{L3}\boldsymbol{M}_{M1}\boldsymbol{M}_{L2}\boldsymbol{E}_{G}\boldsymbol{\varepsilon}_{G} + \boldsymbol{M}_{L4}\boldsymbol{M}_{M2}\boldsymbol{M}_{L3}\boldsymbol{E}_{M1}\boldsymbol{\varepsilon}_{M1} + \boldsymbol{M}_{L4}\boldsymbol{E}_{M2}\boldsymbol{\varepsilon}_{M2}$$

where **M**i are the usual ABCD matrices for a propagation in a uniform medium or focusing elements and $\mathbf{M}_{\mathrm{tot}} = \boldsymbol{M}_{L4}\boldsymbol{M}_{M2}\boldsymbol{M}_{L3}\boldsymbol{M}_{M1}\boldsymbol{M}_{L2}\boldsymbol{M}_{L1}$.

For the P1 polarisation signal:

$$\boldsymbol{r}_{FPP1} = \boldsymbol{M}_{tot}\boldsymbol{r}_{HP1} + \boldsymbol{M}_{tot}\boldsymbol{E}_{HP1}\boldsymbol{\varepsilon}_{HP1} + \boldsymbol{M}_{L4}\boldsymbol{M}_{M2}\boldsymbol{M}_{L3}\boldsymbol{E}_{M1}\boldsymbol{\varepsilon}_{M1} + \boldsymbol{M}_{L4}\boldsymbol{E}_{M2}\boldsymbol{\varepsilon}_{M2},$$

where the contribution of the grid has been left out, since it does not introduce ray deviations for the P1 signal. The previous relations are used to calculate the linear and angular deviations at the focal plane with the statistical methods described in the introduction for the ray tracing method.

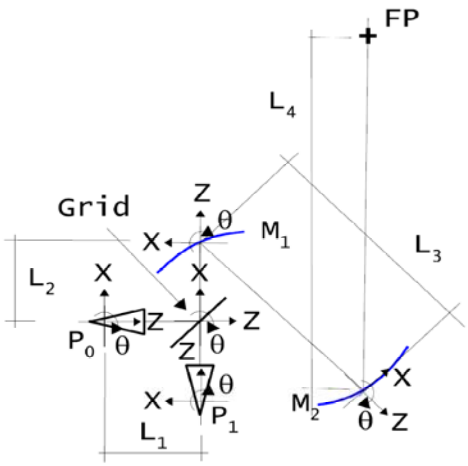

Fig. 3. ALMA band 10 optics schematic describing the ray tracing model.

VI. RAY TRACING ANALYSIS

C. Worst case and RSS

For the Worst Case and RSS error analysis each optical element misalignment parameter is changed at once in the ABCD matrix expressions introduced in the previous section. The resulting linear and angular standard deviations from the nominal chief ray position are then observed at the FP. For the study of the ray tilt due to misalignments, the contributions of all interfaces between the 4K plate and the antenna flange are also considered. The ray tilt analysis at FP is reported in table IV. For the ray separation at the FP the only study of the two horns and wire grid is necessary, since the two rays after the grid are exposed to the same deviation contributions of M1 and M2. Thus keeping the ray separation unchanged from the wire grid to the FP. The separation at the FP for the worst case is then computed by adding the two polarisation's ray linear deviation from the nominal chief ray. The RSS ray separation is computed as the square root of the sum of squares of the P0 and P1 RSS separations from the nominal case, since the separation variable is a result of linear independent normal distribution random variables. Table IV shows these results.

TABLE IV
WORST CASE AND RSS TILT AND RAY SEPARATION AT FP FOR THE RAY TRACING ANALYSIS OF THE ALMA BAND 10 OPTICS.

	Ray til, [°]		Ray separation, [mm]	
	Worst Case	RSS	Worst Case	RSS
P0	0.436	0.143	0.356	0.150
P1	0.373	0.136		

D. Monte Carlo

By using the same equations for the ray tracing previously described, the displacement errors are now considered simultaneously. The displacement errors are described by random variables with a Gaussian probability distribution function of zero mean and standard deviation such as 3σ equals to the absolute tolerance value listed in table I and II. The 3σ rule ensures 99.73% chances to select a Gaussian random variable within $\pm 3\sigma$ range.

Table V lists the standard deviation for the ray separation and ray tilt of the two polarisation rays at the FP. The results for the ray separation at the focal plane out of $30 \cdot 10^3$ simulations, each of them with a different error misalignment set, are shown in Fig. 4. The output histograms for the ray tilt (not shown here) and rays separation (Fig. 4) are fitted with a Gaussian distribution and a Chi probability distribution respectively. The distribution parameters (i.e. standard deviation and probability of a random variable of falling inside a determined range) are then used to compare with the ALMA specifications introduced in the beginning of this work. For instance the probability of having a ray separation at the FP smaller than *0.257mm* is *0.9477*.

TABLE V
STANDARD DEVIATION OF THE RAY TILT AND RAY SEPARATION BETWEEN THE TWO POLARISATION SIGNAL PATHS OBTAINED FROM MONTE CARLO SIMULATIONS.

Ray tilt, [°]		Ray separation, [mm]
P0	P1	
0.136	0.129	0.077

VII. MONTE CARLO ANALYSIS BY MEANS OF PHYSICAL OPTICS ELECTROMAGNETIC SIMULATIONS

The concept of Monte Carlo analysis can be applied to the full 3D geometrical model built with the GRASP software. The optical parts can be displaced relatively to their local Co-ordinate System (CS) that has been carefully chosen in order to represent the final alignment error that occurs in the assembling procedure. The model in GRASP, as depicted in Fig. 5, allows linear displacements along the 3 axis of the local CS and rotation around the principal axis of the single optical parts. For the mirrors and the grid this translates into rotations around the minor and major axis of the surface rim.

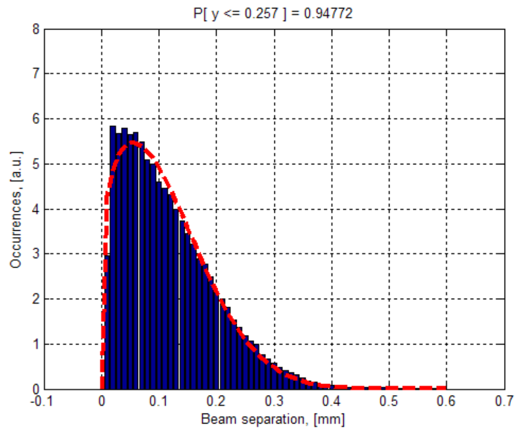

Fig. 4. Ray separation distribution at the focal plane, as a result of ray tracing Monte Carlo simulations over $30 \cdot 10^3$ cases.

The horns are modelled in such a way that they can assume a tilt respect to the cone axis (elevation) in any azimuth direction. All displacements, linear and angular are described as Gaussian random variable according to table II, except for the horn azimuth being described as a random variable of uniform distribution between *-180°* and *180°*. A total of *2000* simulations have been performed for the mirror optical coupling system, each of them characterised by linear and angular displacements at each single optical part. The beam at the focal plane (180mm from M2, [2]) was computed on a grid normal to the chief ray, for each simulation at the lower frequency of Band 10 (*787GHz*), where aberrations are more likely to influence the beam pattern. The two beam polarisation patterns where therefore analysed by means of fundamental Gaussian beam mode fitting procedure. The fundamental Gaussian waist location parameters are used to evaluate the distance between the two polarisation beams at the focal plane. The beam tilt in X and Y gives the beam directions.

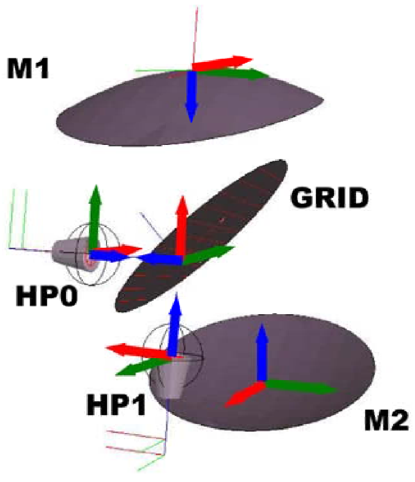

Fig. 5. Local co-ordinate systems of the optics parts for the GRASP Monte Carlo simulation. Red arrow indicates X axis, green arrow stands for Y axis and blue for Z axis. Θ rotation is around Y axis for M1, M2 and grid.

The distance between the fitted Gaussian for the P0 and the P1 beams gives the beam separation at FP. In this work only misalignments of the optics parts are taken into account, no cryostat and other external tilts are hereby considered. The X tilt is on the plane of M1 and M2 and Y tilt is in the plane normal to this. The standard deviation of the beam separation retrievable from the Chi distribution function fitting the beam separation histogram of Fig. 6 is *0.061mm*. From the same histogram the probability of having a beam separation less than *0.31mm* at the focal plane is *0.9954*, over a population distribution of 2000 cases. The standard deviation for the tilt angle of the P0 and P1 beams at the focal plane in the X and Y directions are reported in table VI. Fig. 7 depicts the statistical linear correlation between the beam deviation at the focal plane and each single linear or angular displacement introduced in the 2000 simulated cases for each of the optical elements. The highest correlations are for linear displacements of the two horns and grid along the direction belonging to the plane containing the two horns and the grid, see Fig. 5. Positive displacement of the grid toward the x direction causes deterioration of the beam separation at FP. Similarly, negative displacement in y direction for the P0 horn and x direction for the P1 horn increases the beam separation at FP. If the grid gets closer to the P0 horn, it also causes beam separation at FP. As expected the beams separation is also sensitive to tilt of the grid around its y axis.

TABLE VI

STANDARD DEVIATION OF THE BEAM TILT AND SEPARATION BETWEEN THE TWO POLARISATION SIGNAL OBTAINED FROM PO MONTE CARLO SIMULATIONS.

Beam tilt, [°]				Beam separation [mm]
P0 P1				
θ_x	θ_y	θ_x	θ_y	
0.081	0.087	0.078	0.070	0.061

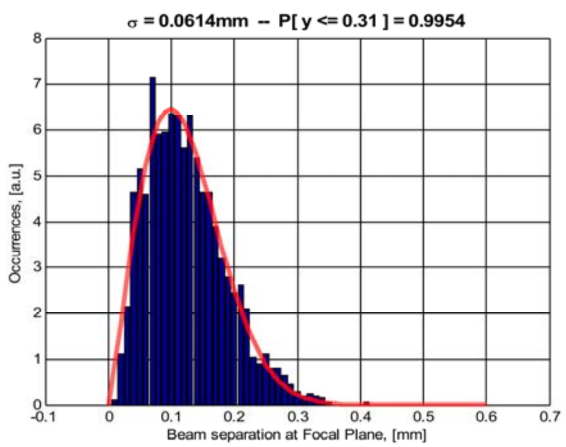

Fig. 6. Beam separation distance at focal plane for 2000 PO simulations.

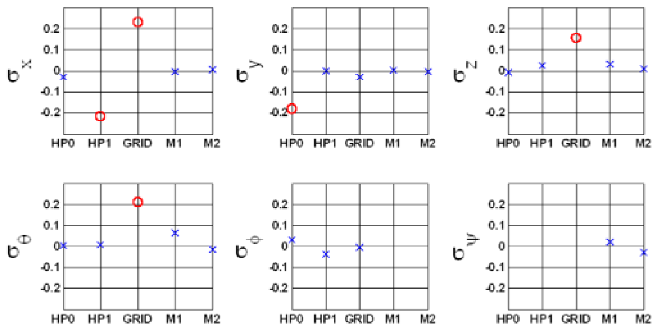

Fig. 7. Linear correlation between the beam separation at FP and error displacement of single optical element. HP0 and HP1 stand for horn P0 and P1, then GRID and mirrors M1 and M2.

VIII. ILLUMINATION EFFICIENCY DEGRADATION

Previously it has been shown that concurrent misalignments of the optical parts translate into beam pointing deviations from the nominal design configuration. In this section selected cases from the PO Monte Carlo simulation are chosen and the beam propagated toward the secondary. The illumination efficiency is then computed with a top hat field distribution of the size of the secondary reflector. The selected cases are those which the fundamental Gaussian fitting analysis gave absolute angular tilts bigger than *0.25°*. For these cases, the illumination efficiency loss with respect to the efficiency evaluated for the nominal optical configuration (i.e. without introducing misalignments) is shown in Fig. 8. The correlation results show that the tilts angle derived from the fundamental Gaussian fitting procedure is not always directly related to the loss of illumination efficiency. The presence of amplitude distortions in the beam patter also causes variations in the illumination efficiency. The drop of illumination efficiency gets to values up to 1% for some of the listed cases, by just considering only optical parts misalignments. Further degradation might be expected if also the operational cryostat tilts will contribute to the total tilt of the receiver system.

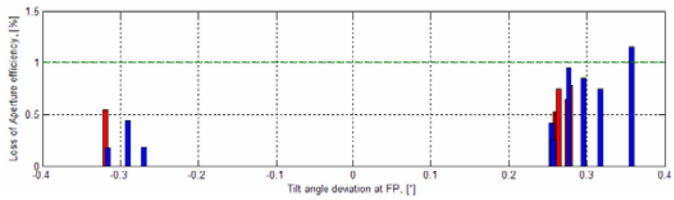

Fig. 8. Drop of illumination efficiency for selected cases where the fundamental Gaussian fitting analysis gave absolute beam tilts in X and Y bigger than 0.25°. The loss of efficiency is this case is only due to the optical part misalignments; the cryostat tilt contributions are not considered here.

IX. CONCLUSIONS

In this paper the effect of alignment displacements of the ALMA band 10 front-end optical parts, has been studied for the purpose of fulfilling particular optical specifications such as: deviation angle between the two orthogonal polarisation main beams and loss of illumination efficiency at the secondary. These specifications have been addressed and translated to the focal plane interface. The analysis has been carried out by means of different techniques: Worst Case, RSS, and Monte Carlo. A first order study of the beam misalignment at the focal plane followed ray tracing techniques. Monte Carlo statistical analysis was applied to the ray tracing model and also to a more sophisticated model involving 3D full electromagnetic analysis by means of GRASP PO predictions. The general assumption for linear and angular displacements of the optical parts reported in table II, showed that ray tracing RSS analysis gives more pessimistic results compared to the Monte Carlo counterpart.

On the other hand full electromagnetic analysis gave results which show that the beam separation at focal plane can be within the specification of *10%HFBW* for *99%* of the *2000* simulated cases.

However the angular displacement derived by fundamental Gaussian beam mode analysis of the beam pattern at the focal plane, shown to be not fully correlated with the loss of efficiency at the secondary. Aberrations of the amplitude beam pattern at the secondary can also cause drop of illumination efficiency.

It has been shown that loss of efficiency is already reaching values around *1%* for the assumed tolerances in this study. In summary, it seems that as far as concerning the beam separation at focal plane the specifications can be achieved within a *1%* margin in terms of statistical probability. However once the beams propagate through the Cassegrain system they could get further separated due to amplitude distortions at the aperture plane. Illumination efficiency loss is occurring at tilts angles that are less than the upper limit defined by the ray tracing analysis. This result suggests that tighter tolerances should be applied compared to the ones assumed in this work in order to fully meet the specifications.

FUTURE WORK

Further improvements can be considered for the next study of the ALMA band 10 optics. The misalignment errors of the cryostat and antenna levels will be also introduced in the PO calculations. Selected cases might be used to characterise the main beam out of entire PO calculation of the entire optical system including the 12m Cassegrain antenna, therefore validating the study conducted at the focal plane level. Deviation of the cold optics mirror surface parameters due to fabrication process might also be introduced into the statistical description of the optics alignment error budget.

ACKNOWLEDGMENT

The authors would like to acknowledge Y. Sekimoto, A.M. Baryshev and P. T. Peacocke for valuable comments and suggestions.

REFERENCES

[1] K. Murata, *Design of the optics for ALMA 900 GHz band and VSOP-2 40GHz band*, Master thesis, University of Osaka, Japan, 2006.

[2] M. Candotti, Software analysis of the ALMA band 10 optical front-end, Part 1. NAOJ band 10 receiver group internal report, Japan, 2007.

[3] B. Lazareff, Alignment tolerances for ALMA optics, ALMA memo 395, 2007.

[4] C. T. Cunningham, G. H. Tan, H. Rudolf, K. Saini, “Front-end sub-system for the 12m antenna array – Technical specifications,” [ALMA-40.00.00.00-001-A-SPE], March 21st, 2007.

[5] V. Gasho, S. Stanghellini, “Technical Specification for the Design, Manufacturing, Transport and Integrationon Site of the 64 ALMA Antennas”, ALMA-34.00.00.00-006-A-SPE Version: A, December 15th, 2003.

[6] V. Heinz, “ALMA Mechanical Tolerance Budget”, ALMA-80.00.00.00-006-A-REP Version: A, February 28th, 2006.

[7] A. Orlowska, M. Harman, “ALMA Cryostat Tolerance Budget”, ALMA-40.03.00.00-033-C-GEN Version: C, January 11th, 2005.

[8] W. Shaomin, *Matrix methods in treating decentered optical systems*, Optical and Quantum electronics, November 29th, 1999.

ALMA 183 GHz Water Vapor Radiometer

A. Emrich, S.Andersson, Mats Wannerbratt
Omnisys Instruments AB, Gruvgatan 8, 421 30 Göteborg, Sweden

ABSTRACT

The ALMA project hardware development is a challenge for many research groups and commercial companies. It is not common that state-of art performance must be combined with reliability and low cost in high frequency radiometer hardware.

The ALMA Water Vapor Radiometer is a complete radiometer system consisting of quasi optics, calibration system, 183 GHz mixers and LNA's, local oscillator system and filter-bank back-end. This is supported by an embedded computer, a high performance power system and an advanced thermal control of the complete system as well as key components.

Omnisys is responsible for the design, implementation, verification and production of 60 WVR's. The development part of the project is 12 months from kick-off to delivery of the first unit, including verification. The design will not be based on the demonstration models in any sense, not on component level, not on subsystem level and not on system level. The only common parts are that it is a switched system and a schottky mixer is used in the Front-End.

The preliminary design indicates a mass of less than 25 kg and a power consumption of 25-30 W for the complete instrument, including features and functions such thermal stabilization, a chopper wheel and extensive monitoring and control.

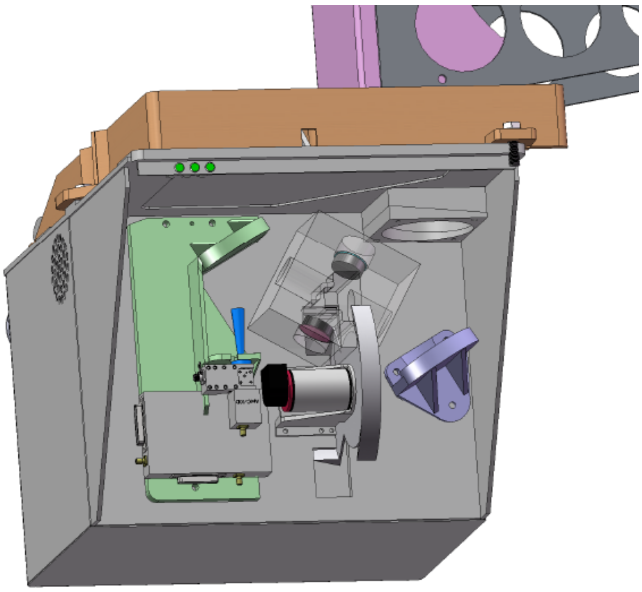

The radiometer system optimization as such will be presented.

The design for production and design for reliability aspects will be presented.

The signal chain from mixer to filter-bank design will be presented, including test results.

The quasi optical design will be presented, including test results.

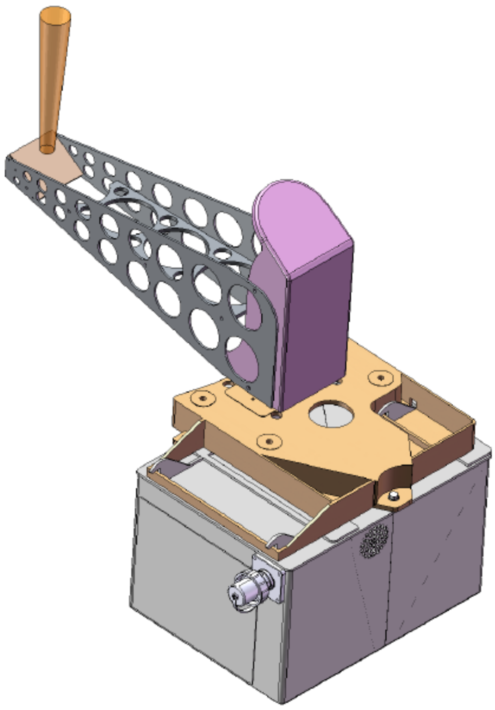

Characterization of waveguide components for the ALMA band 10

T. Kojima[1), 2)], Y. Uzawa[1)], W.-L. Shan[3)], Y. Fujii[1)], M. Takeda[4)], M. Kroug[1)], S. Shitov[1)], and H. Ogawa[2)]

1) National Astronomical Observatory of Japan, 2-21-1 Osawa, Mitaka, Tokyo 181-8588, Japan
2) Osaka Prefecture University, 1-1 Gakuen-cho, Naka-ku, Sakai, Osaka 599-8531, Japan
3) Purple Mountain Observatory, 2 West Beijing Road, Nanjing,210008,China
4) National Institute of Information and Communications Technology, 588-2 Iwaoka, Iwaoka-cho, Nishi-ku, Kobe 651-2492, Japan

The Atacama Large Millimeter and Submillimeter Array (ALMA) band 10 cartridges are being designed based on use of waveguide components such as couplers, because of their mechanical ruggedness and reliability. Although recent machining technology makes it possible to fabricate such small waveguide components with sizes of down to several tens of microns, it is important to characterize their electrical performance experimentally at room and cryogenic temperatures. For the room temperature measurements, we have developed a vector network analyzer, which consists of a W-band Gunn oscillator followed by a nonupler as a transmitter and a subharmonic Schottky diode mixer pumped by another W-band Gunn oscillator as a receiver. Both Gunn oscillators are phase-locked to a single microwave reference, but on different sidebands. The device under test (DUT) is put between the transmitter and the receiver and the insertion loss and phase difference is measured. For the cryogenic temperature measurements, we used SIS mixers consisted of a corrugated horn and a mixer block. These are connected by a common waveguide flange. The DUT is inserted between them. By measuring the mixer gains or noise temperatures with and without the DUT, the insertion loss is simply estimated from the change of the gains or noise temperatures due to the input loss.

Figure 1 shows a photograph of a 10-dB directional coupler with WR-1.2 (0.305×0.152 mm) gold-plated waveguide made by machining. The total length of the waveguides is 30 mm. Figure 2 shows the measured insertion losses at room temperature. This result is reasonable if we assume an electrical conductivity of the gold at room temperature, which suggests that the part of the 10-dB coupler with two slits works well as expected. However, the insertion loss at cryogenic temperature showed a large loss of about 1.8 dB/30 mm. To confirm this unexpected waveguide loss, we measured the loss in a 25-mm-length straight waveguide as well. The result showed the waveguide losses of about 1.3 dB/25 mm, which is similar to the result of the 10-dB coupler. This implies that the length of the waveguide components should be designed as short as possible to reduce the waveguide loss in more than this frequency band.

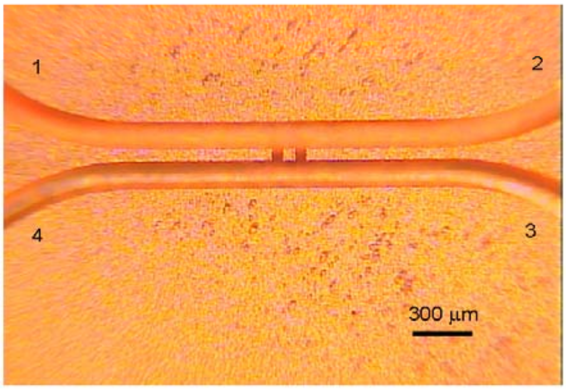

Fig. 1 A photograph of a 10-dB directional coupler at the Band 10 frequencies.

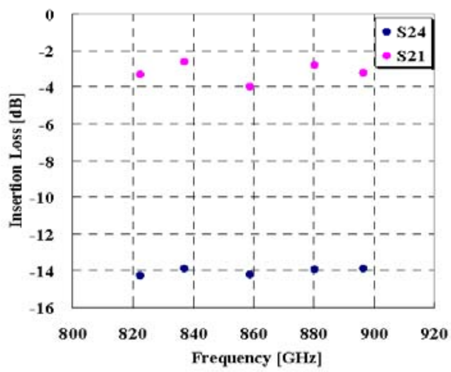

Fig. 2 Measured S-parameters as a function of frequency.

Characterization of ALMA Calibration Targets

A. Murk*, A. Duric*, and F. Patt†
*Institute of Applied Physics, University of Bern, Switzerland
† ESO, ALMA Front End Division, Garching, Germany
Contact: axel.murk@iap.unibe.ch

***Abstract*— This paper describes active and radiometric reflection measurements of blackbody calibration targets for ALMA.**

I. Introduction

The Atacama Large Millimeter Array (ALMA) has the challenging goal to achieve an absolute radiometric accuracy better than 5% at frequencies between 30 - 950 GHz. For the calibration of the receivers ambient and hot blackbody calibration target will be used, which can be inserted in the optical path using a robotic arm (Fig. 1). These targets need to have a high emissivity, which is equivalent to a low value of integrated scattering into all possible directions. Even more critical is the coherent backscatter of the target, since it will lead to frequency dependent standing waves between the target and the receiver. In addition the targets have to be held at a uniform temperature to ensure that the surface brightness temperature corresponds to the reading of the thermometers in their body.

The ALMA specifications for the calibration targets [1] require an emissivity >99.8% and temperature gradients below ±0.5K (ambient) and ±1K (hot target at 70°C). The required accuracy for the effective brightness temperature of the targets is specified with ±0.3K and ±0.5K for ambient and hot, respectively.

In this paper we present detailed active backscatter measurements between 30-700GHz of different target prototypes, passive radiometric measurements of their integrated scattering, and thermal IR images of the temperature gradients of a prototype of the hot target. The complete test series is described in more details in [2].

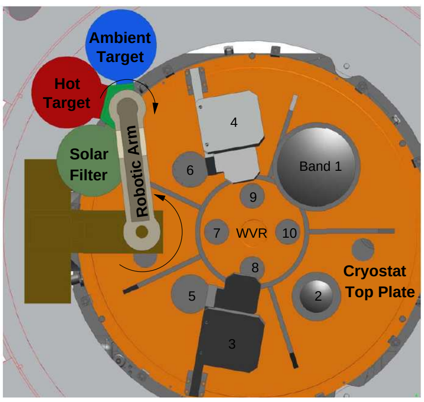

Fig. 1. Schematic design of the ALMA calibration unit.

TABLE I
Target prototypes.

Pyramids (RAL)	Array of Aluminum pyramids (10×10×40mm) covered with 0.7mm casted Eccosorb MF114 absorber.
Tiles (TK)	Carbon loaded polypropylene absorber with 10mm thickness and pyramidal surface (4×4×6mm).
Cone (TK)	Conical target with 0.14m aperture, 0.5m length and 10mm thickness made of carbon loaded polypropylene absorber.

Table I shows the target prototypes that were used for the comparison. Only the pyramidal design with a relative thin layer of epoxy based absorber on a metal backing is suitable for the hot target. The other two are made of a thermoplastic absorber with a low thermal conductivity, which makes it more difficult to heat them uniformly to an elevated temperature. Their main advantage is that they can be mass produced by injection molding, which could make them a cost efficient solution for the ambient target.

II. Active Backscatter Measurements

The coherent backscatter at the target results in a standing wave to the receiver, which should be as small as possible for spectroscopic observations. We measured this backscatter performance of the prototypes using an AB-Millimetre vector network analyzer and a quasi-optical reflectometer (Fig. 2). Since the results depend also on the beam parameters of the test setup we used similar beam waists and target distances as in the ALMA optics. For Band 1 and 2 prototypes of the ALMA feeds and lenses were used together with directional waveguide couplers (Fig. 3).

The targets under test were mounted on a translation and rotation stage to allow a sliding load calibration and measurements at different angles of incidence. The axial translation of the target under test leads to a phase change of the reflected signal, whereas the phase of the spurious signals, e.g. from the crosstalk in the directional coupler, remains constant. As a result the data points move on a circle in the complex measurement plane (Fig 4). Fitting the radius and the offset of this circle allows to determine the target reflectivity and the directivity of the setup, respectively.

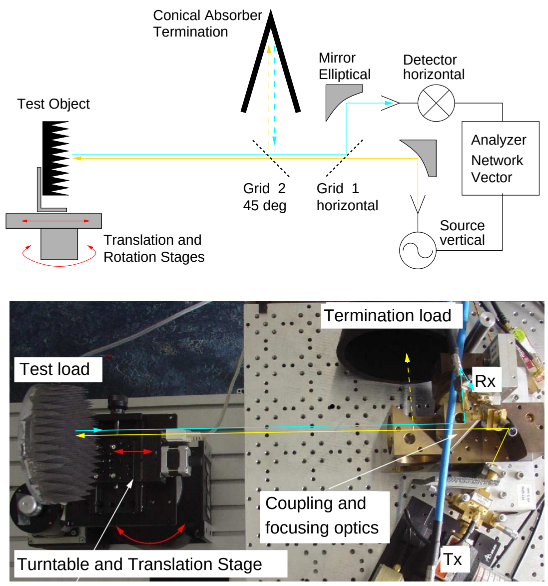

Fig. 2. S11 test setup for Band 6 (211–275GHz) using a quasi-optical reflectometer setup.

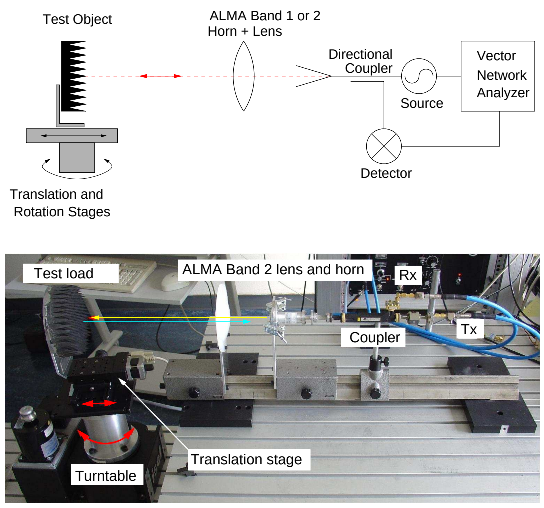

Fig. 3. S11 test setup for Band 2 (67–90GHz) using a wwaveguidecoupler and the actual ALMA lens antenna.

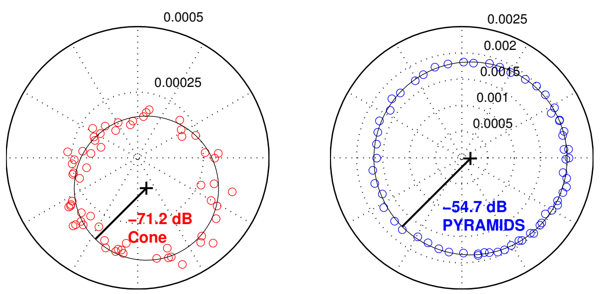

Fig. 4. Measurement examples of the conical (left) and the pyramidal target (right) in polar coordinates recorded during an axial $\lambda/2$ shift.

The periodic surface of the pyramidal targets acts as a diffraction grating and causes an angular dependence of the backscatter signal. For that reason the measurements were repeated with varying angles of incidence. Figure 5 gives examples for such angular resolved measurements for a few spot frequencies. The worst case values over the complete frequency range of the test series are shown in figure 6.

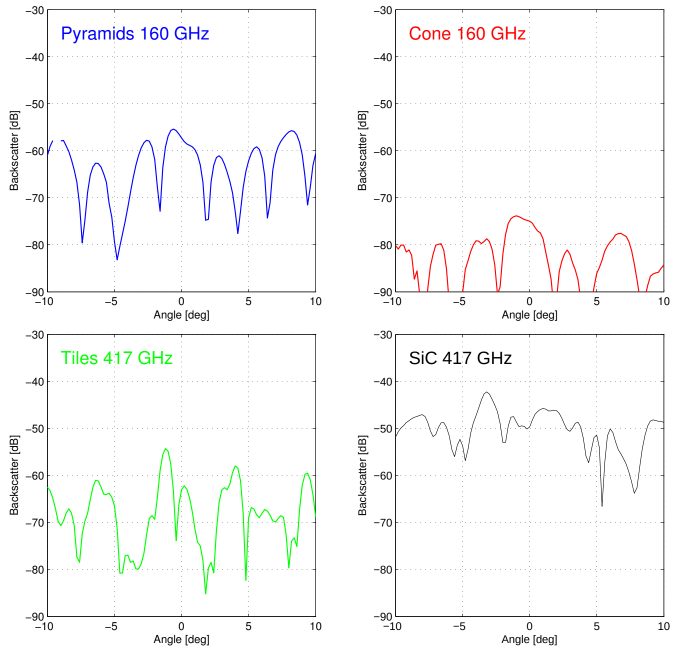

Fig. 5. Calibrated S11 results for different incidence angles with distinct Bragg reflections for the pyramidal and TK-RAM targets. The plot labeled SiC is a sample with the Stycast/SiC absorber coating used in ttheHIFI instrument, which acts as an almost isotropic scatterer.

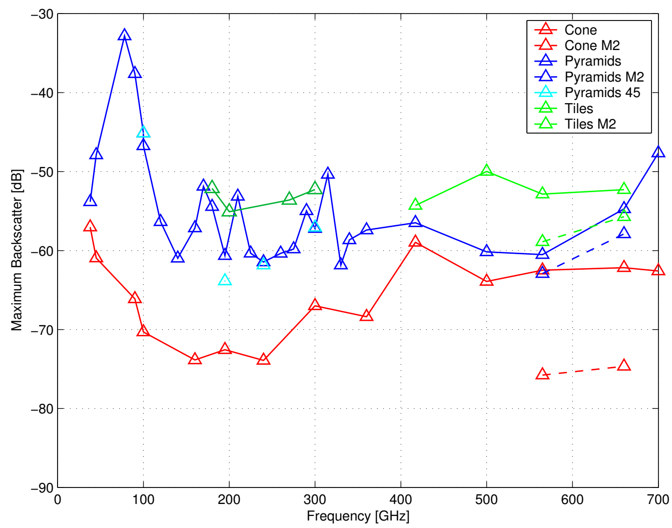

Fig. 6. Summary of the active backscatter measurements between 30 and 700GHz.

III. Radiometric Tests

The integrated scattering of the targets is always significantly higher than their coherent backscatter, but this parameter cannot be measured easily with active reflection measurements. For that reason we performed radiometric tests with a 90GHz and a 323 GHz SIS receiver which were available at IRAM. In our test setup a chopper wheel switches at about 80Hz between two ambient temperature targets, and the modulation on the IF signal is analyzed with a power detector and a Lock-In amplifier. The target under test is mounted in a metal enclosure above an extended LN2 background target, which can be covered by a another ambient temperature absorber (Fig. 7). When this ambient background is removed, almost the complete field of view of the target under tests becomes exposed to the cold background signal. The background signal reflected at the reference target remains unchanged. For that reason any change of the Lock-In signal corresponds to the integrated scattering of the target under test. To normalize the results an additional measurement has been made in the same setup where the target under test is replaced by a 45 degree reflector pointing to the cold background.

The normalized results in Fig. 8 indicate at 90GHz emissivities of the different targets between 0.997 and 0.999. At 323GHz the pyramidal and the tile target show an emissivity of about 0.9994, whereas the conical target is better than 0.9999.

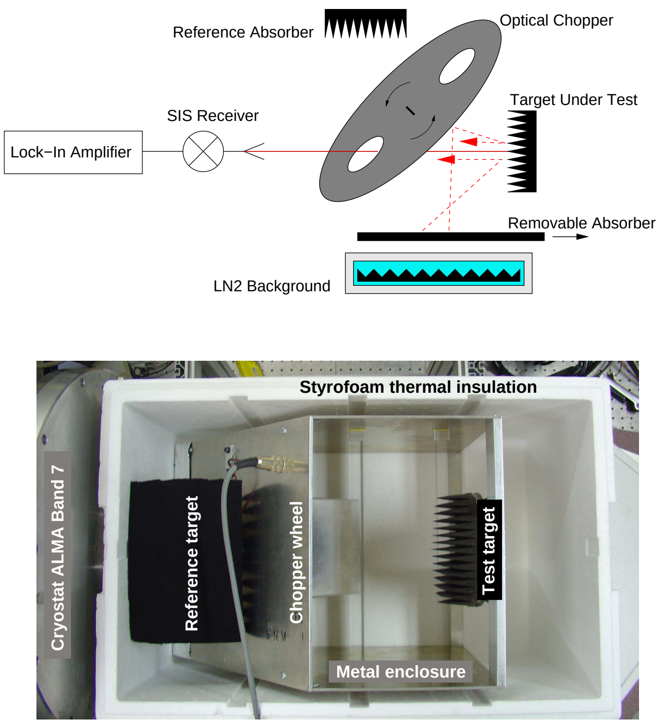

Fig. 7. Measurement setup for the radiometric tests with an ALMA Band 6 receiver at IRAM.

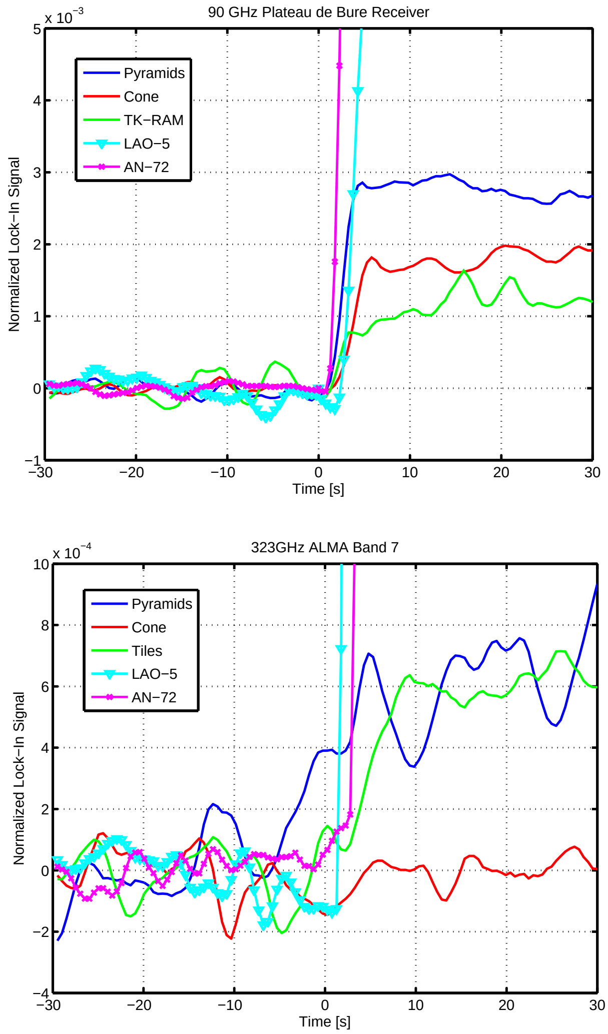

Fig. 8. Normalized results or the radiometric tests. LAO-5 and AN-72 are flat foam absorbers, which resulted in reflections between 0.5 and 4%, respectively.

IV. Thermal Gradients

Thermal gradients within the target lead to a difference between its effective brightness temperature and the readout of the temperature sensors. This effect is difficult correct because it depends on the changing environmental conditions and the orientation of target. We used an IR camera to measure the gradients of the surface temperature of the hot pyramidal target. Figure 9 shows that the tips of the pyramids are significantly colder than their base. These gradients depend on the orientation of the target, which has a significant influence on the convective cooling rate. This becomes evident in the linear temperature profiles of IR images with different target orientations in Fig. 10.

The polymer absorbers TK-RAM and Cone are not suited for the hot target because of their low thermal conductivity. Thermal simulations for this material showed that even for the ambient target an air temperature change in the receiver cabin can result in unacceptable gradients over their surface area.

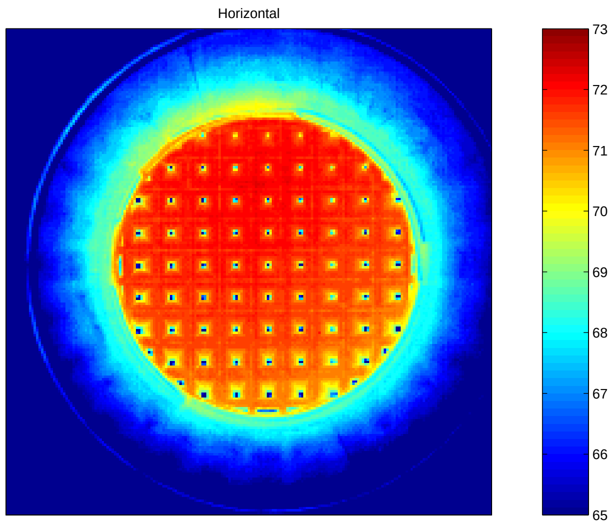

Fig. 9. Thermal images with an IR camera of the hot calibration target in horizontal orientation.

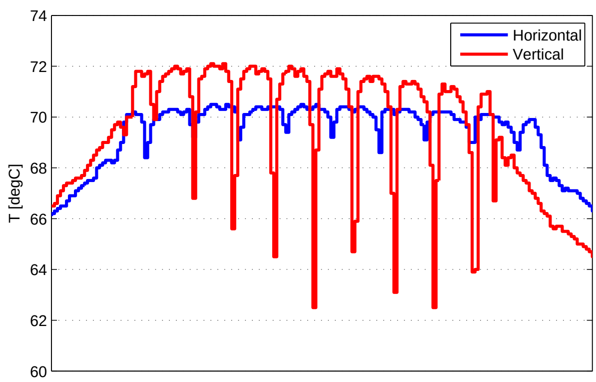

Fig. 10. Temperature profile from different IR images where the hot pyramidal target was mounted in horizontal and vertical orientation.

V. Conclusions

The pyramidal prototype showed a coherent backscatter between -50 to -60dB for most frequencies. Below 100GHz it is up to -35dB, which would result in significant standing waves. The backscatter of the TK-RAM tiles was below -50dB. They could not be used for the elevated temperatures, but for the ambient target they would be the most economical option. The total reflectivity of both targets was about 0.6E-3 at 323GHz. At 90GHz the pyramids were with 3E-3 three times worse than the tiles. The best electrical performance was achieved with the conical design. The polymer absorber of the tested version would be well suited for economic mass production, but it has severe disadvantages because of its bad thermal conductivity. None of the tested targets would be fully cocompliantith the ALMA requirements.

The best RF and thermal performance could be achieved with a conical target made of a thin layer of thermally conducting absorber on a metal backing. We have already tested similar targets for various other projects, and they achieved routinely a coherent backscatter below -60dB [3]. In order to improve the thermal accuracy we have now started to investigate different shroud geometries, which will help to decouple the target from the thermal environment and to make it a better approximation to an ideal blackbody.

References

[1] "ALMA Calibration Device: Technical Specifications," Tech. Rep. FEND-40.06.00.00-009-C-SPE, European Southern Observatory, Munich, Germany, Dec. 2007.

[2] A. Murk and A. Duric, "ALMA Calibration Device: Prototype Calibration Load Test Report," FEND-40.06.04.00-005-A-REP, IAP Research Report 2007-10-MW, Institut für Angewandte Physik, Universität Bern, Bern, Switzerland, July 2007.

[3] A. Murk, R. Wylde, R. Spurrett, P. Fürholz, and N. Kämpfer, "Blackbody Calibration Targets with Ultralow Reflectivity at Submillimeter Wavelengths," in *4th ESA Workshop on Millimetre-Wave Technology and Applications*, vol. WPP-258, pp. 359–364, Feb. 2006.

Near-field Beam and Cross-polarization Pattern Measurement of ALMA Band 8 Cartridges

Masato Naruse[1,2,*], Mamoru Kamikura[1,2], Yutaro Sekimoto[1,2], Tetsuya Ito[2], Masahiro Sugimoto[2], Yoshizo Iizuka[2],

[1]*Department of Astronomy, University of Tokyo, Japan*

[2]*National astronomical Observatory of Japan*

* Contact: masato.narsue@nao.ac.jp, phone +81-422-34-3981

***Abstract*—We meas ured corrugated h orns, O MTs [1] (Orthomode T ransducer), op tics b locks at room temp erature with a vecto r near fi eld m easurement s ystem. Th e amp litude and phase me asured at ne ar-field a re transformed to far-f ield pattern, and compared to calculations with Gr asp 9 and CORRUG . The c o-polar beams were found to be c onsistent with the simulations at 385 , 442, 500 GHz , and the calcula ted taper efficiency at the sub-reflector of ALMA 12-m antenna was greater than 92 % . Side lobe was less than -30 dB. The peak of cross-polar relative to co-polar found to be less than -20.5 dB. In addition, to evaluate accuracy of m easurements, we stu died both effects of standing w ave and stability of t he amplitude and phase. The error of the far-field was found to be less than 0.2dB between 0 and -20 dB range.**

I. INTRODUCTION

The Atacama Large Millimeter/submillimeter Array (ALMA) [2] is an interferometer for radio astronomical observations. The development of this facility is the result of an international effort between Europe, North America, and Japan in cooperation with the Republic of Chile. ALMA consisting of 64 12-meter diameter antennas and 16 ACA (Atacama Compact Array) antennas is located in Chile at an elevation of 5000 meters. At this elevation the atmosphere has a maximum transparency at mm and sub-mm wavelength. ALMA will cover the radio sepctrum from 30 to 950 GHz using 10 frequency distinctive bands with relatively wide bandwidth of around 25 %. Each frequency band is observed with a cartridge-type receiver with orthogonal polarization-receiving capabilities. The cartridge-type receiver contains optics, mixers, amplifiers and local oscillators to achieve a modular concept. The cartridges are installed in a cryostat at the Cassegrain focus with an offset for the telescope axis. Each cartridge has receiver optics in itself or outside of the cryostat toward the sub-reflector. The receiver optics of ALMA has been described by [3]. It does not use a mechanical tuner in the receiver because of operational reliability.

A physical optics calculation of the ALMA receiver optics was made by [4], [5]. It uses a commercial software, GRASP9 (TICRA Co.).We have repeated their calculation with the same software. The beam pattern of corrugated horns is simulated with a commercial software, CORRUG (Antenna Software Co.).

For astronomical receivers, it is essential to understand the beam pattern on the sky. Since ALMA receivers are installed on the Cassegrain focus of the antenna, the beam pattern of the receiver directly determines that of the telescope. Since ALMA makes polarization observations of astronomical sources, it is also critical to know its cross-polarization pattern. On the symmetrical Cassegrain system, cross-polarization components are mainly generated at the receiver. It is important to measure beam pattern at the same or a similar condition of operational 4 K temperature for SIS receivers. In addition, room temperature measurements are useful for a selection of corrugated horns. Because corrugated horns are fabricated by electroforming, it is not possible to know their performance using easy mechanical measurements.

We designed and developed a near-field measurements system according to the experience maturated in the field of beam pattern measurements at sub-mm wavelength in the past 20 years. A near-field measurement, and probe compensation concept have been established ([6], [7], [8]), ([9], [10]), respectively. Sub-mm beam pattern measurements were reported in [11], [12], [13] and vector measurements in [14], [15]. Other examples of room temperature measurements of sub-mm receiver optics and corrugated horns are documented in [16], [17]. We established the beam pattern measurements of both receiver components at room temperature and the receiver itself as both detector and antenna under test (AUT). Owing to its wide dynamic range, the cross-polarization pattern of the receiver is also reported.

II. ALMA BNAD 8 CARTRIRGE

The ALMA band 8 cartridge receives [18] frequency from 385 GHz to 500 GHz, which is 26 % bandwidth to the center frequency of 442.5 GHz. We have developed a pre-production model (PPM) of the ALMA band 8 cartridge. The ALMA band 8 PPM receiver [19] is a dual polarization receiver, which uses a OMT as a polarization splitter. The receiver optics block adopts a single mirror to couple the feed horn in front of the mixer and the sub-reflector. One of the advantage of adopting a single mirror system is the relative easiness at the optical alignment. It leaves, however, less freedom for the mechanical designs. The incident angle at the mirrors is as small as 25 ° (Figure 1), which aim is to keep the cross-polarization as low as possible [20]. The optical parameters were chosen as frequency independent at both the feed horn and the sub-reflector in the frequencies of between 385 and 500 GHz as listed in Table 1. The proof of this is shown in Figure 2, where the symmetric and asymmetric electric field distribution cuts are reported for the lowest, middle and highest frequencies. The receiver optics is tilted 1.2 degrees toward the sub-reflector.

The optics block was carefully designed to realize the optical parameters at 4 K [21]. The shrinkage of all components from 300 K to 4 K was taken into consideration. The block was designed to be easily measured with a coordinate machine. Optical block and mirrors were made of pure aluminum. The optics block and mirrors were measured mechanically with a coordinate measuring machine, resulting in consistency with designed values within typically 20 μm.

The corrugated horn, which design is reported in [22,23], has a diameter of 8 mm and a slant length of 24.43 mm. Due to the fine structure of the corrugations, the horn and the transformer waveguide, which connects the horn to the rectangular waveguide, were made in one piece using electroforming machining technique.

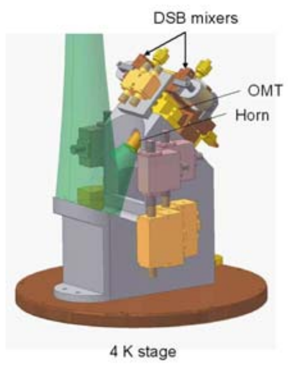

Fig. 1 The 4K Optics of Band8 Cartridge Receiver

TABLE I
OPTICAL PARAMETER OF ALMA BAND 8 CARTCIDGE

		Band 8	385	442	500
horn diameter	d_h	7.99			
horn axial length	L_h	24.10			
horn slant length	R_h	24.43			
horn waist	w_0		1.736	1.603	1.482
horn waist offset	$dz_{(w_0)}$		-13.291	-14.933	-16.319
waist at horn aperture	w_{ha}		2.572	2.572	2.572
distance from mirror to horn	d_1	50			
radius of curvature	R_{s1}		66.133	67.529	68.637
focal length of mirror	f_1	49.59			
radius of curvature	R_{il}		198.227	186.663	178.690
beam radius at mirror			9.200	8.890	8.671
reflection angle of mirror	θ_1	45			
waist at focal plane	w_{fp}		4.7018	4.0955	3.6205
distance from mirror to subref	$d_{mirror-subref}$	6150			
beam radius at subref	w_{subref}		316.27	316.27	316.27
radius of subref	R_{subref}	375			
Edge taper		12	12.21	12.21	12.21

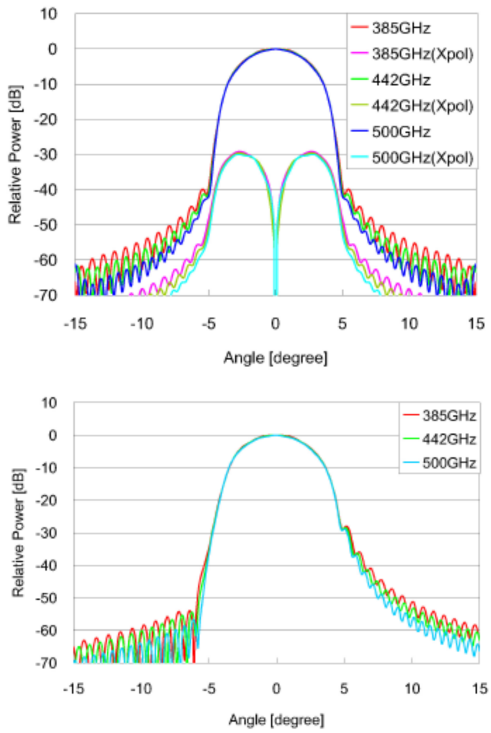

Fig. 2 Physical Optics calculation of the 4K optics with Grasp9. Upper and lower panels show beam pattern of a symmetric and asymmetric plane.

III. INSTRUMENT

A. Submillimeter Vector Network Analyzer

In order to measure amplitude and phase of electromagnetic field distribution, a submillimeter network analyzer, (Figure 3) a XYZθ planar scanner, and probe horns have been developed [24]. The band 8 RF signal is obtained with a Gunn oscillator source tuned at 77-110 GHz, followed by a x5 multiplier. The transmitter chain is located on the XYZθ planar scanner as shown in figure 3, while the receiver which has the optics under test connected at the harmonic mixer is located on a test bench. The whole system uses a common reference signal at the frequency of 10 MHz. This reference signal is used to phase lock the Gunn diode and as reference for the generation of the LO signal. The LO signal is used to generate the higher harmonics of the Gunn oscillator signal through a harmonic mixer. The LO signal frequency is chosen such as the 6th harmonic equals the 10 MHz reference signal for phase locking. On the receiver side the LO signal is mixed with the RF signal in order to obtain the 30th harmonic which is giving the 50 MHz signal. Amplitude and phase information of the RF signal are then measured by the vector voltmeter which compares the 30th harmonic with the reference signal multiplied.

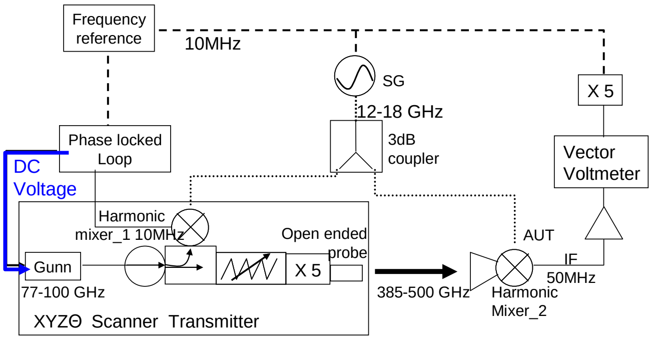

Fig. 3 Block diagram of near-field beam measurement system of receiver components with a room-temperature mixer. PLL controls the frequency of Gunn varying the DC Voltage.

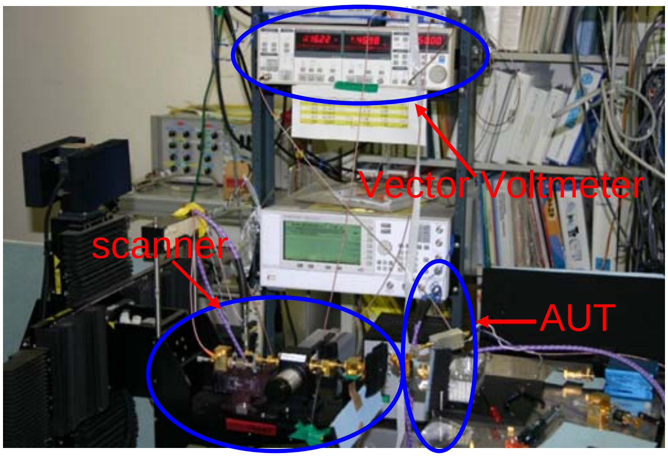

Fig. 4 A picture of beam pattern measurement system configuration

B. Planar XYZθ Scanner

A planar XYZθ scanner for submillimeter-wave measurement is highly necessary for flatness [25, 26]. A XYZθ scanner has been employed to accommodate a cartridge test cryostat (Figure 5), which was developed for testing cartridge type receivers [27]. The XYZθ scan area is 300 mm × 300 mm × 600 mm and -180 degrees to 180 degrees, which is driven with 10 μm and 0.1 degree step by stepping motors. The motors are controlled via GPIB interface by LabView software. The Z stage of this scanner was used to investigate VSWR of the measurement configuration. The absorber was appropriately installed to reduce VSWR. The θ stage of this scanner was used to measure the cross-polarization pattern and the alignment of the polarization. The flatness of this scanner has been measured as follows:

1. A flat aluminum mirror with a diameter of 300 mm was fabricated for reference with a high precision lathe (Toshiba Co. ULG-300C H3).
2. The reference mirror was measured with 0.1 μm accuracy by a coordinated machine (Mitsutoyo LEGEX910). The flatness of the reference mirror was 2 μm peak to peak.
3. The flatness of the XYZθ scanner relative to the reference mirror was measured with a laser sensor of Kyence LK-500, which has a resolution of 10 μm at 690 nm wavelength. After removing the linear component, the flatness was 4.3 μm r.m.s. and 17.2 μm peak-to-peak for horizontal axis and 3.3 μm r.m.s. and 13.5 μm peak-to-peak for vertical axis.

C. System Stability and Standing Wave Characterization

Reproducibility and accuracy of the beam pattern measurements is directly related by intrinsic system stability over the time of measurement. The issue of standing wave phenomena is also affecting the quality of the beam pattern structure. Amplitude and phase stability over a time of one hour is shown in Figure 5. It can be seen that 0.2 dB amplitude and 2 degree phase stability are obtained in 5 minutes span. Since a typical 2D scan takes 4 hours, the long term amplitude and phase drift are corrected by periodically referencing at the main beam peak at every 5 minutes.

In Figure 6 the effect of standing wave in relation to the measurement plane is reported. The plot shows the superposition of 9 far-field cuts of consecutive near-field line scans taken at a distance of $\lambda/4$ from each other. TK-RAM (Thomas-Keating Co.) was installed at the transmitter and receiver sides. The effects of the standing wave at 385, 442 and 500 GHz were measured at the same level and to be at typical minimum level of 0.5 dB peak-to-peak. The effects of the standing wave at 385, 442 and 500 GHz were at the same level. The measurement repeatability was evaluated by measuring the band 8 corrugated horn 9 times at the same location. The difference between these measurements gave a 0.1 dB and 1 dB amplitude variation respectively at the level of -25 and -40 dB.

The return loss of submillimeter components such as a corrugated horn was derived from standing wave ratio (SWR). For example, the lower panel of Figure 6 shows the SWR of a corrugated horn radial offsets from beam center. These SWR are averaged to convert the return loss. At large offsets, the SWR has a tendency to increase. It may be caused by reflection from metal components of measurement support structure.

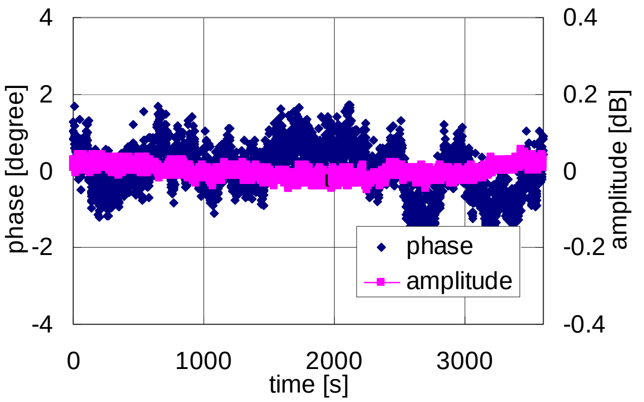

Fig. 5 Amplitude and phase stabilities of this system at room temperature, and RF frequency of 442 GHz and IF frequency of 50 MHz.

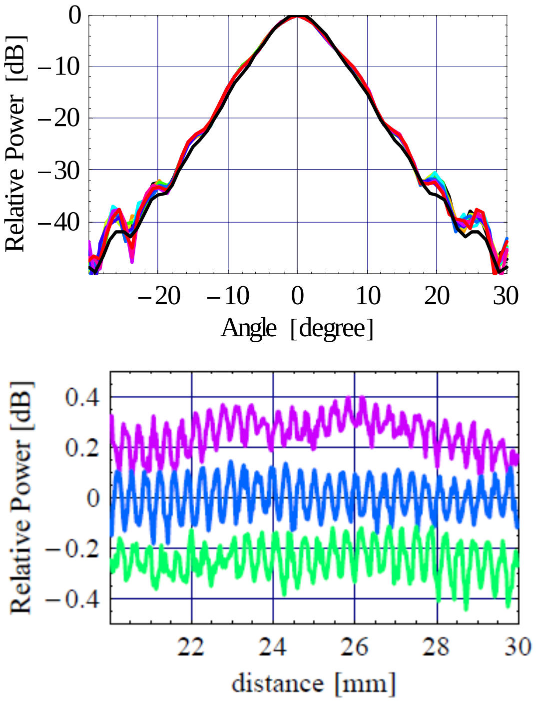

Fig. 6 Upper:Standing measurement at 442 GHz with the corrugated horn. The 9 lines with every 1/4 λ moving and simulation with CORRUG (black line) are superimposed. Lower:The standing wave of a corrugaterd horn at center and offset position of X-direction at 442GHz. The purple, blue, and green lines respectively show at -4, 0, 4 mm offsets.Power scale of each lines has been offset by 0.25 dB. Rreturn loss of the corrugated horn was derived around -40 dB using the average of three SWR.

D. Submillimeter Probe Horn

When measuring beam pattern with a planar near-field measurement system, it is very important to understand the effects of the probe with on the measured electric field distribution. In [28] it is reported that open-ended waveguides introduce less effects on the measured electric field distribution. Nevertheless we performed probe compensation of the measured near-field beam patterns, by dividing the far-field distribution of the measured field by the far-field distribution of the measured open-ended waveguide probe, [10]. Characterization of the open-ended WR2.0 waveguide was performed by independent measurements of two out of three " identical " probes. Figure 7 shows the electroformed open-ended waveguide surrounded by electromagnetic absorber tiles such as TK-RAM (Thomas-Keating Co.). The improvement achieved in reduction of standing waves is depicted in figure 9, where the electric field has been sampled along the Z direction, 26 mm far away from the probe aperture with and without absorbers. Return loss of the configuration was improved from -20.1 dB to 34.2 dB by adding the absorber. The co-polar and cross-polar far-field pattern of were measured with two probe horns as shown in Figure 10. In Figure 11, the co-polar patterns are compared with an approximate formula for an open-ended waveguide [29] and are consistent with the calculation. The peak of the cross-polar pattern was around -20 dB less than that of the co-polar pattern.

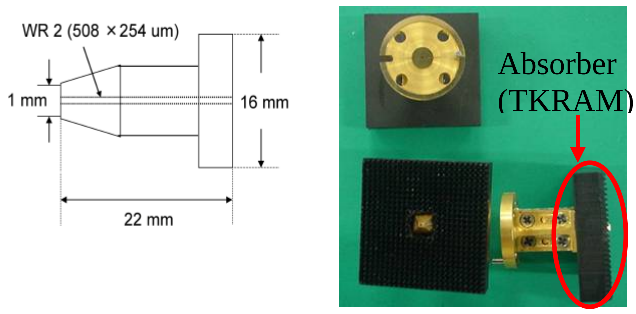

Fig. 7 The design (left) and picture (right) of WR2.0 open-ended waveguide horn

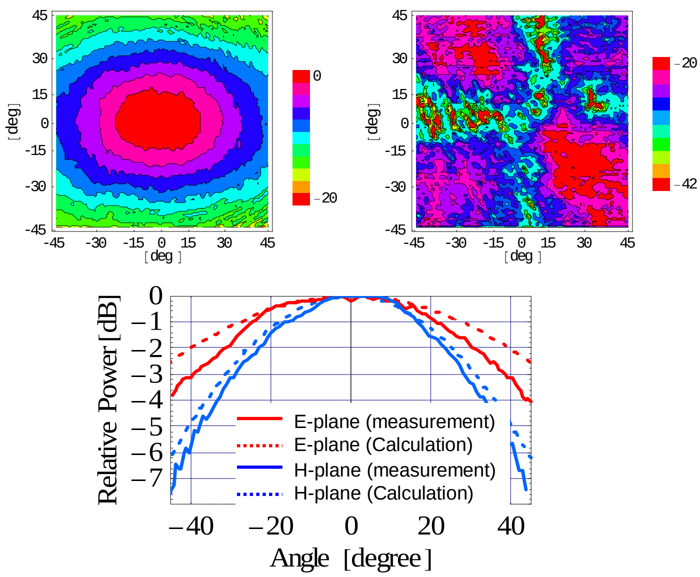

Fig. 8 The far-field pattern of WR2.0 open-ended waveguide horn. Co-(upper left) and Cross-polarization (upper right) pattern at 442GHz. The measured far-field pattern compared with the calculation.

IV. Results

The 0.5 mm steps of X and Y stages satisfy the requirement of spatial sampling theorem [30]. Every 5 minutes, phase reference was checked at the center position.

A typical 2-dimensional scan took around 4 hours. Distance between AUT and the probe horn was around 50 mm at the room temperature measurement.

A. Corrugated Horns at Room Temperature

Vector near-field measurements of two corrugated horns at room temperature were taken at 385, 442, 500 GHz. Far-field patterns transformed from near-field measurements of two horns are compared to simulations with CORRUG (Figure 9). The far-field patterns of corrugated horns were found to be identical with each other, very symmetric, low side-lobe, consistent with simulation within a dynamic range of greater than 40 dB, and the peaks of cross-polarization level were -30 dB lower than that of co-polar.

Far-field patterns of the corrugated horn with OMT, which has h-polarization and v-polarization, at 385, 442, and 500 GHz transformed from near-field are shown in Figure 10. The far-field patterns of OMT were also found to be identical with two polarizations, very symmetric and low side-lobe, but the cross-polarization level were slightly higher than corrugated horn only.

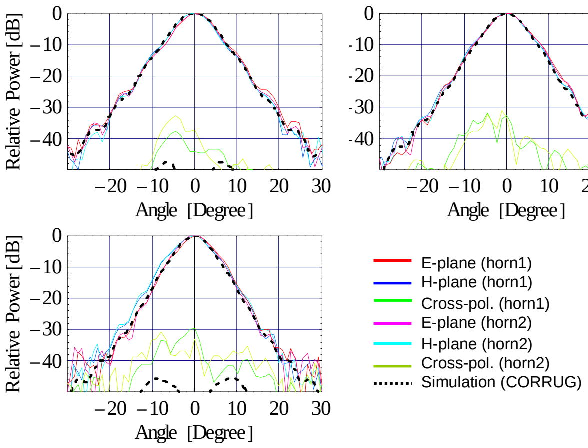

Fig. 9 The far-field pattern of two corrugated horns at 385(upper left), 442(upper right) and 500 GHz(lower).

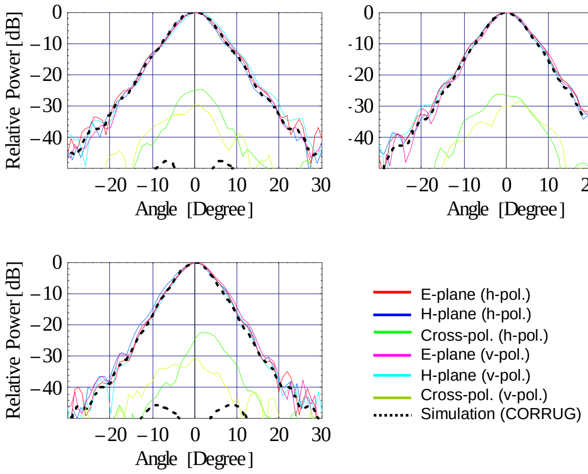

Fig. 10 The far-field pattern of the corrugated horn with OMT at 385(upper left), 442(upper right) and 500 GHz(lower).

B. The Optics block with the Corrugated horn and OMT at Room Temperature

The far-field beam pattern of an optics block of the band 8 cartridge fed by a corrugated horn was measured at room temperature Figure 11, 12. This optics block includes the OMT, an ellipsoidal mirror and the corrugated horn as well as their holding structure. The WR2.0 flange of the corrugated horn was connected to a harmonic mixer and its IF output was fed to the vector voltmeter.

The far-field patterns of optics block were found to be very symmetric, low side-lobe, and consistent with simulation with range from -3.5 to 3.5 degree, with which the beam from mirror of optics block illuminates the sub-reflector of ALMA 12-m. The peaks of Cross-polar were -21.4, -23.3, -20.5 dB lower than that of co-polar at 385, 442, 500 GHz, respectively.

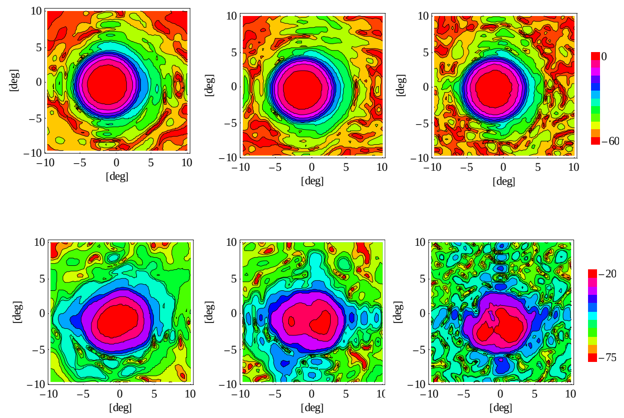

Fig. 11 The far-field pattern of optics block at 385(left), 442(middle) and 500 GHz(right). Upper panels show co-polarization, and lower panels show cross-polarization.

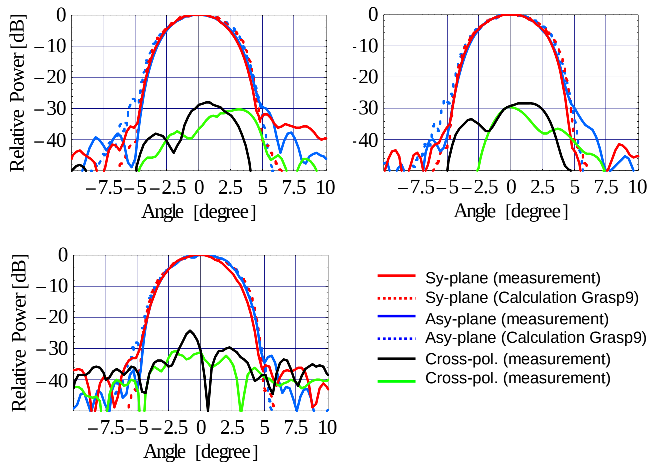

Fig. 11 The far-field pattern of the optics block with the OMT and corrugated horn at 385(upper left), 442(upper right) and 500 GHz(lower).

V. Conclusions

1. We have developed a beam measurement system covering from 385 to 500 GHz, which can measure vector near-fields with wide dynamic range of amplitude (> 50 dB) and stable phase with a high precision XYZθ planar scanner.

2. Beam patterns of corrugated horns for ALMA band 8 cartridge receiver have been measured and compared with simulations at far-field. They are consistent within a dynamic range of greater than 40 dB at three frequencies of 385, 442 and 500 GHz.
3. Beam patterns of the optical block of ALMA band 8 PPM cartridge which includes the ellipsoidal mirrors, the OMT and the corrugated horn have been measured at room temperature and compared with simulations at far-field. They are consistent within a dynamic range 30 dB at the three frequencies of 385, 442 and 500 GHz.
4. The side lobe levels at 385, 442 and 500 GHz of ALMA band 8 receiver were less than −30 dB at far-field. The measured beam patterns correspond to taper efficiency of greater than 92 % at the sub-reflector of the ALMA 12 m antenna.

ACKNOWLEDGMENT

The authors thank Massimo Candotti, Junji Inatani, Mayumi Matsunaga of Ehime University, Mattew Carter of IRAM, Tham Choy Yoong of Universiti Tunku Abdul Rahman, Sheng-Cai Shi of Purple Mountain Observatory, Charles Cunninham of Herzberg Institute for Astrophysics, Masato Ishiguro, Takashi Noguchi, Shinichiro Asayama, Ryo Kandori, Ken'ichi Tatematsu, Akitoshi Ueda of NAOJ for advice. This work was partially supported by Grant-in-Aid of JSPS No. 17340058.

REFERENCES

[1] Kamikura M. et al. "Development of a 385-500 GHz Orthomode Transducer (OMT).", This conference.
[2] Brown, R. L. et al., "Alma - the atacama large millimeter array." Advances in Space Res. 24, 555 - 559 (2004)
[3] Carter, M. C.et al., "ALMA front-end optics." SPIE, 5489, 1074 - 1084 (2004).
[4] Tham, C. Y., Withington, S.,"Receiver optics design electromagnetic analysis, second report (Bands 3, 6,7 and 9)." Tech. rep., Chambridge University (2003).
[5] Tham, C. Y., Withington, S.,"Receiver optics design electromagnetic analysis, third report (Bands 4, 8and 10)." Tech. rep., Chambridge University (2003).
[6] Johnson, R. C. et al., "Determination of far-field antenna patterns from near-field measurements." Proc. ofthe IEEE, 61, 1668 - 1694 (1973) M. Shell. (2002)
[7] Slater, D."Near-Field Antenna Measurements." Artech House Publishers (1991)
[8] Yaghjian, A. D. "An overview of near-field antenna measurements." IEEE Trans. of Antennas and Propagation, 34 (1986)
[9] Joy, E. B. et al. "Applications of probe-compensated near-field measurements." IEEE Trans. on Antennas and Propagation, 26, 379 - 389 (1978).
[10] Paris, D. T., Leach, W.M.Jr., Joy, E. B. "Basic theory of probe-compensated near-field measurements." IEEE Trans. on Antennas and Propagation, 26, 373 - 379 (1978).
[11] Chen, M.T. et al. "Receiver beam characterization for the SMA." Part of the SPIE Conf. on Advanced Technology MMW, Radio, and THz Telescopes Kona, Hawaii. 106 -113 (1998).
[12] Slater, D. "A 550 GHz near-field antenna measurement system for the NASA submillimeter wave astronomy." Antenna Measurement Techniques Association Conf. (1991).
[13] Tong, C-Y. E. et al. "Near-field characterization of 2-D beam patterns of submillimeter superconducting receivers." Proc. 5th Int. Symp. Space THz Tech., Ann Arbor, MI, 660 - 672 (1994)
[14] Goy, P. et al. "Vector measurements at millimeter and submillimeter wavelength: Fasibility and Applications." Proc. of 2nd ESA Workshop on Millim. Wave Technology and Appl. Antennas, Circuits and Systems, Millilab Espoo, Finland, 89 - 94, (1998)
[15] Tong, C. Y. E. et al."Near field vector beam measurements at 1 THz." IEEE Microwave and Wireless Components Lett. 13, 235 - 237 (2003)
[16] Murk, A., Magun, A. "Characterization of corrugated horn antennas for HIFI." 25th ESA Antenna Workshop on Satellite Antenna Technology, 159 (2002)
[17] Murk, A. et al."Beam pattern measurements of the submillimeter limb-sounder SMILES Ambient Temperature Optics." 3rd ESA Workshop Millim. Wave Technology (2003)
[18] Y. Sekimoto et al. "Development of ALMA Band8 Cartridge and its Measurement System." This conference.
[19] Lamb, J.W. et al. "ALMA receiver optics design." ALMA memo 362(2001)
[20] Murphy, J.A. "Distortion of a single Gaussian beam on reflection from off-axis ellipsoidal mirrors." International J. of Infrared and Millim. Waves 8, 1165-1187 (1987)
[21] Satou, N. et al. "A submillimeter cartridge-type receiver for ALMA Band 8 (385 - 500 GHz) " PASJ in press(2008)
[22] Matsunaga, M. et al. "An experimental study of submillimeter-save horn antennae for a submillimeter-wave astronomy. "PASJ 55, 1051 - 1057 (2003)
[23] Matsunaga, M. et al. "Analysis of submillimeter-wave horn antennas for submillimeter-wave telescopes." Proc. of SPIE, 5445, 446 - 449 (2004)
[24] Naruse M., "Near-field Beam and Cross-polarization Pattern Measurement of ALMA Band 8 Cartridges", to be submitted.
[25] Slater, D. "A 550 GHz near-field antenna measurement system for the NASA submillimeter wave astronomy." Antenna Measurement Techniques Association Conf. (1991)
[26] Slater, D."A large aperture 650 GHz near-field measurement system for the Earth Observing System Microwave Limb Sounder." Antenna Measurement Techniques Association Conf.(2001)
[27] Sekimoto, Y. et al. "Cartridge test cryostats for ALMA front end." ALMA memo 455 (2003)
[28] Richond, J.H.et al. "Probes for microwave near-field measurements." IEEE Trans. on microwave theory and techniques, 3, 32 - 34 (1955)
[29] Yaghjian, A.D. "Approximate formulas for the far field and gain of open-ended rectangular waveguide." IEEE Trans. of Antennas and Propagation, 32, 378 - 384 (1984)
[30] Joy, E.B., Paris, D.T. "Spatial sampling and filtering in near-field measurements." IEEE Trans. on Antennas and Propagation, 20, 253 - 261 (1972)

SIS Mixers for ALMA Band-10: Comparison of Epitaxial and Hybrid Circuits

M. A. Bukovski[2], S. Shitov[1,2], T. Kojima[1], W.-L. Shan[3], M. Kroug[1], T. Noguchi[1], M. Takeda[4], Z. Wang[4], A. V. Uvarov[2], O. V. Koryukin[2], A. N. Vystavkin[2] and Y. Uzawa[1]

[1] *National Astronomical Observatory of Japan, Mitaka, Japan*

[2] *Institute of Radio Engineering and Electronics, Russian Academy of Sciences, Moscow, Russia*

[3] *Purple Mountain Observatory, Nanjing, China*

[4] *National Institute of Information and Communication Technology, Kobe Advanced ICT Research Center, Japan*

***Abstract*— To provide a basis for optimum choice of a SIS mixer for ALMA Band-10 (787-950 GHz), numerical simulations on performance of receiver are made using properties of both SIS junction and possible design of its tuning/coupling circuit. "Traditional" Nb-AlO$_X$-Nb and epitaxial NbN-AlN-NbN junctions are studied being integrated with either NbN(NbTiN)/Al or all-epitaxial NbN circuit. Calculations are based on Tucker's theory using 3-port approximation. The extra noise associated with MAR effect in NbN junctions is taken into account. Numerical simulations are finally fitted to best experimental data demonstrating good agreement.**

I. Introduction

The Band-10 (787-950 GHz) is the most difficult band of the whole ALMA project. This is not only due to small mechanical tolerances allowed at these high frequencies. The essential part of difficulties is originated from limited choice of conductors to be used in the tuning circuit of the Band-10 SIS mixer along with lacking of well-established processing for a number of available materials. For example, such popular material as Nb is good for producing suitable SIS junctions, but it cannot be used efficiently as a part of their tuning circuit for Band-10. This situation suggests more difficult process of implementation of Nb-based SIS trilayer into a waveguiding sandwich made from low-loss normal metals or from higher-T$_c$ superconductors (NbN, NbTiN). However, the use of mentioned higher-T$_c$ superconductors for wiring of Nb trilayer was not successful since now; the wiring has to be made from relatively lossy normal metals (Al, Au). The epitaxial NbN structures fabricated at NiCT (Japan) are a good exception [1].

The NbN epitaxial films can be treated as perfect conductors with magnetic penetration depth that is quite similar to performance of Nb films below 700 GHz. The fully epitaxial SIS junction (ex. NbN/AlN/NbN) has advantages of higher gap energy and lower RF loss in electrodes. The higher gap voltage allows for higher frequency limit (up to 2 THz) yet for better response, dI_{IF}/dV_{RF}, of the mixer at about 1 THz, if compare with all-Nb devices. However, two serious drawbacks are known for epitaxial NbN SIS junctions: i) lower than for Nb quality of IV-curve and ii) extra noise associated with multiple Andreev reflection (MAR) [2, 3].

The primary goal of this paper is to analyze numerically a few most promising configuration of terahertz-band SIS mixers in respect to available experimental data. The calculations are based on Tucker's theory, which simplest 3-port approximation, according to M. Feldman, fits the terahertz-range SIS mixers [4, 5]. Authors hope that this work can facilitate the hard choice of a mixer for ALMA Band-10.

II. Modeling of IV-curves and Tuning Circuit

To calculate performance of a real SIS mixer, an appropriate model of its IV-curves is necessary. This model will be then input in most of equations of Tucker's theory on quantum mixing with SIS junctions [4]. We have synthesized IV-curves of Nb junctions using a sum of exponential functions with adjustable parameters. All functions are smooth and can be treated as a *basic functions*.

$$I(V) = I_{LEAK}(V) + I_{KNEE}(V) + I_N(V) \tag{1}$$

$$I_{LEAK}(V) = \frac{V}{R2} \cdot \left(1 + \exp\left(\frac{V - Vg}{\Delta Vg \cdot 10}\right)\right) + I0 \cdot \frac{V}{V + Vexcess \cdot 0.5} \tag{2}$$

$$I_{KNEE}(V) = I_{MAX\_KNEE} \cdot \exp\left(-\left(V - V_{KNEE}\right)^2 \cdot Q_{KNEE}\right) \tag{3}$$

$$IN(V) = \frac{\exp\left[\frac{V - Vg}{\Delta Vg}\right]}{\exp\left[\frac{V - Vg}{\Delta Vg}\right] + 1} \cdot \left(\frac{V - V_e}{Rn} - I_{LEAK}(V)\right) \tag{4}$$

IV-curves for epitaxial NbN junctions are also synthesized in fine details using its *generalized expansion* with (1)-(4). The results of modeling are presented in Fig. 1 and Fig. 2. To analyze the effect of quality of SIS junction on the final performance of a whole receiver, the IV-curves with different Q-factor from Fig. 3 are used. The Q-factor is controlled by parameter *R2*. Since the leakage current of a perfect SIS junction is fundamentally depends on the physical temperature only, the model leak current, I_{LEAK}, is presenting both the voltage independent thermal current, *I0* , and current of micro-shorts as the shunting resistor *R2* (see eq.2).

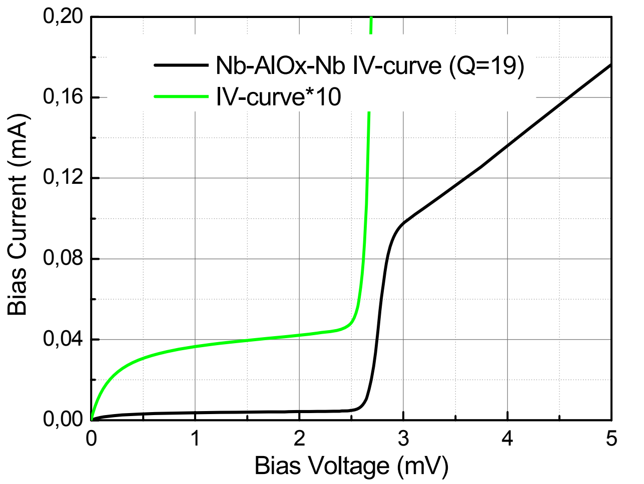

Fig. 1 Model IV-curve for high-quality high current density (J_c = 12 kA/cm^2) micron-size all-Nb SIS junction.

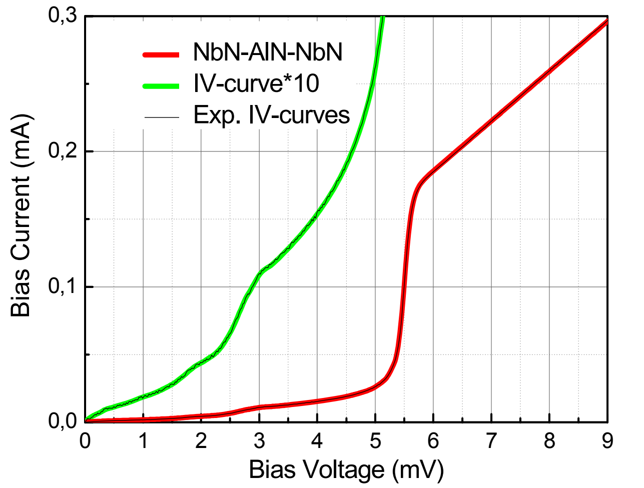

Fig. 2 Model IV-curve for epitaxial all-NbN SIS junction. Four curves are presented. Note that experimental IV-curves are almost indistinguishable from modeled IV-curves. Parameter R_NA = 34 of experimental mixer is equivalent to J_c = 6 kA/cm^2 of a "traditional" all-Nb SIS junction.

To develop a practicable model of a SIS mixer tuning circuit, the specific materials are used. Table 1 summarizes parameters used in our calculations. Since it is known of extremely good RF properties of epitaxial NbN films, they are assumed being perfect RF conductors with the magnetic field penetration depth λ = 250 nm. Note that NbN epitaxial tuning circuit is employing also epitaxial insulation of MgO (ε≈9.6) while NbTiN is usually covered with SiO_X (ε≈4.2).

TABLE I
MATERIAL PARAMETERS.

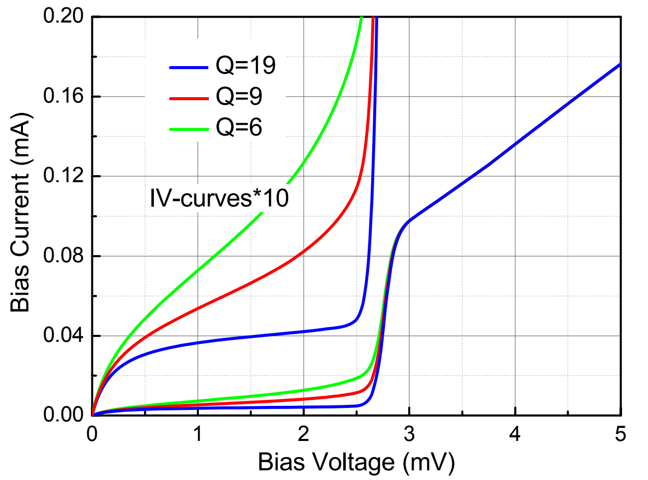

Fig. 3 Model IV-curves for Nb/AlO_X/Nb junctions of different quality, Q, which is defined by parameter *R2* of eq.(2).

The polycrystalline films of NbTiN are known for varying their properties dependent on condition of deposition. Since they are assumed for use in combination with relatively resistive aluminum wiring, the RF conductivity of NbTiN film is (voluntary) assumed to be about twice better than one of aluminum. This assumption makes aluminum wiring dominating with RF loss in the tuning circuit.

We modeled only the twin-SIS tuning circuit [6, 7]. The twin-type of tuning arrangement consists of two lumped SIS junctions and two sections of microstrips: one connecting them in parallel and second one – to the feed point. The GTM-method of calculating superconducting microstrips is used; the method is described elsewhere [8]. The feed-point impedance of the tuning structure is assumed to be 50 Ω. The IF chain following the mixer is estimated to have noise temperature about 10 K that includes noise of coolable amplifier and effects of loss in IF cables and wide-band (4-12 GHz) isolator.

III. RESULTS OF CALCULATIONS

The effect of quality of all-Nb SIS junction on performance of the whole receiver is presented in Fig. 4. It seems that the sensitivity of receiver is almost proportional to the quality factor of the mixing junction. This effect is possible to explain qualitatively with the experimental fact that the best noise temperature of the receiver observed at condition close to the infinite mixer gain (at extremely large R_d). Under this condition all output current is driven into the IF chain. Thus the upper limit of R_d defines the efficiency of the transfer of IF current towards the output. The maximum R_d is defined by the leakage resistance of the particular sample of SIS junction, i.e. by its Q-value.

Structure	**R_NA**	**A (μm^2)**	**C0 (fF)**	**Total (Ω/sq)**	**Ground plane (Ω*m)$^{-1}$ / λ(nm)**	**Wiring (Ω*m)$^{-1}$ / λ(nm)**	**Insulation t(nm) / ε**
NbTiN-Nb/AlO_X/Nb-Al	17	0.64	85	0.239	2.3e8 / 250	1.16e8 / 0	300 / 4.2
NbN-NbN/AlN/NbN-Al	17	0.64	120	0.165	perfect cond. / 250	1.16e8 / 0	300 / 4.2
NbN-NbN/AlN/NbN-NbN	17	0.64	120	0	perfect cond. / 250	perfect cond. / 250	300 / 9.6
Al-Nb/ AlO_X /Nb-Al	10	0.64	85	0.28	1.16e8 / 0	1.16e8 / 0	300 / 4.2

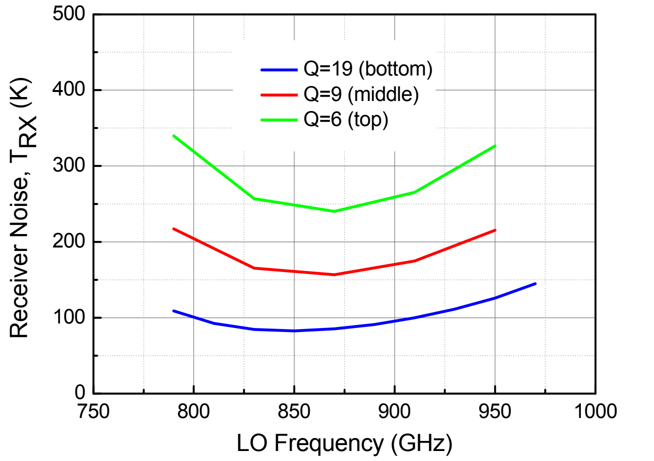

Fig. 4 Effect of quality of Nb/AlO_X/Nb junction on performance of the receiver using twin-type mixer. Noise temperature is referenced to the feed-point of the tuning structure, also for all graphs below.

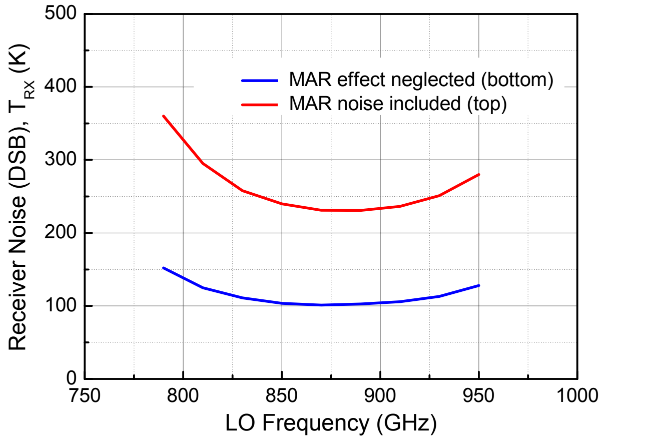

Fig. 5 Result of excessive noise in the NbN SIS mixer due to effect of multiple Andreev reflection (MAR effect) [2, 3]. IV-curve from Fig. 2 is used in calculation of twin-type mixer.

The best experimental epitaxial NbN junctions usually have Q-value about 10. According to Fig. 4 this Q-value can result in performance essentially better than 200 K, since higher responsivity, dI_{IF}/dV_{RF}, and lower loss in electrodes are that essential advantages of a NbN junction.

TABLE II
EVALUATION OF EXPERIMENTAL DATA.

Mixer type	Experimental T_{RX} (beam splitter noise excluded)	Loss preceding SIS junction	T_{RX} at the mixer
Quasi optical mixer with epitaxial NbN/AlN/NbN (twin-SIS with Al wiring)	660 K @ 890 GHz	spillover 1 dB = 60 K lens loss 2 dB (no AR-coating) tuning circuit loss 3dB	300 K @ feed-point 150K @ SIS
Waveguide mixer with epitaxial NbN/AlN/NbN (resonant half-wavelength)	300 K @ 840 GHz	spillover 1 dB = 60 K mixer block loss 1 dB tuning circuit loss 0.5 dB	165 K @ feed-point 150 K @ SIS
Waveguide mixer with hybrid twin NbTiN/Nb/AlO_X/Nb/Al	180 K @ 875 GHz	spillover 1 dB = 60 K mixer block loss 1 dB tuning circuit loss 2.5 dB	80 K @ feed-point 45 K @ SIS

However, the presence of excessive noise due to MAR effect [2, 3 makes these expectations less encouraging as presented in Fig. 5.

IV. COMPARISON TO EXPERIMENTAL DATA

Recently we got a series of quite encouraging experiments with ALMA Band-10 mixers that allow for some preliminary comparison. Our best experimental data (at the moment of the Conference) are presents in Fig. 6 as three thick dots along with calculated performance for variety of SIS mixers presented as solid curves. (The details on the experimental study will be presented elsewhere.) The dots of experimental data are evaluated according to Table 2, which presents the break-down for known noise components of our receiver system. Estimate of optical noise is the important part of the noise breakdown as shown in Fig. 7.

Since the relatively large value of the optical noise (≈150 K) can be hardly explained with parameters of the RF and IF circuits, the effect of beam spillover is suggested. This effect has been both detected and predicted from presence of two non-compensated elliptical mirrors used for guiding the beam towards the cold load. The estimate shows that 1 dB spillover is that realistic value to characterize the experimental discxrepancy. In the near future we are going to improve the beam quality and report the resulting effect.

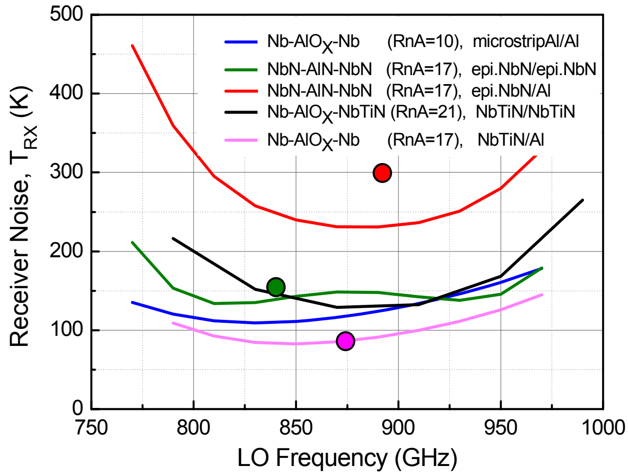

Fig. 6 Calculated performance of SIS mixers along with our best experimental data: red dot (top at 300 K) is measured for $J_c = 6$ kA/cm^2 that is reason for discrepancy from calculated red curve $J_c = 12$ kA/cm^2; green dot (middle) is for resonant λ/2 junction, while the green curve is calculated for twin-SIS mixer; magenta (lowest dot at 80 K) is calculated and measured for hybrid twin-SIS mixer.

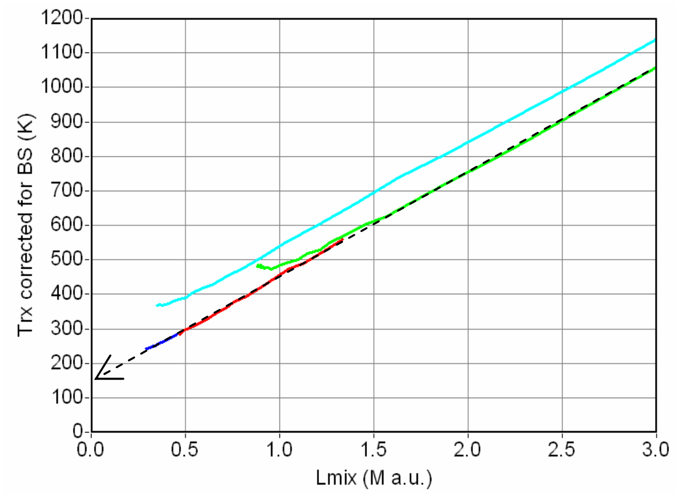

Fig. 7 Estimate for optical noise via extrapolation of measured mixer's conversion loss toward zero. The relatively high value of about 150 K is found that can be explained with presence of excessive noise (beam spillover).

Conclusions

We conclude that, in spite the relatively leaky IV-curve, the performance of an epitaxial NbN junction embedded into a low-loss epitaxial NbN tuning circuit can be close to a high-quality Nb/AlO_X/Nb junction embedded into a aluminum-based tuning circuit. This conclusion is now supported by our own experimental data.

- T_{RX} below 700 K (DSB) is demonstrated with epitaxial NbN/AlN/NbN twin-type mixer with Al wiring.
- T_{RX} about 300 K (DSB) is demonstrated with epitaxial NbN/AlN/NbN mixer employing resonant SIS junction.
- T_{RX} below 200 K (DSB) is demonstrated with hybrid SIS mixer NbTiN/Nb/AlO_X/Nb/Al cooled down to 2 K.
- Assuming presence of spillover of input beam ≈20% (1 dB of spillover loss at 300 K), the experimental results, including the optics noise of about 150 K, are in good agreement with the simulated data.

Acknowledgements

This work is supported in parts by ALMA-J Office and Program for Scientific Instrumentation of Russian Academy of Sciences.

References

[1] Y. Uzawa, Z. Wang, A. Kawakami, "Terahertz NbN/AlN/NbN mixers with Al/SiO/NbN microstrip tuning circuits," Appl. Phys. Lett., vol. 73, no. 5, pp. 680–682, 1998.
[2] Y. Uzawa, Z. Wang, "Coherent multiple charge transfer in a superconducting NbN tunnel junction," Phys. Rev. Lett. 95, 017002 (2005).
[3] P. Dieleman et al., Phys. Rev. Lett. 79, 3486 (1997).
[4] Tucker J. R., Feldman M. J. "Quantum detection at millimeter wavelengths," Rev. Mod. Phys., vol. 4. pp. 1055-1113 (1985).
[5] M. J. Feldman, Private communication (2005).
[6] T. Noguchi, K. Sunada, J. Inatani, "An SIS mixer with integrated tuning circuit (II) - A proposal of SQUID-type mixer," Proc.39th Spring Meeting of the Japanese Society Appl. Physics, Tokyo, Japan, p. 76, March 1992.
[7] J. Zmuidzinas, H. G. LeDuc, J. A. Stern, and S. R. Cypher, "Two junction tuning circuits for submillimeter SIS mixers," IEEE Trans. Microwave Theory Tech., vol. 42, pp. 698–706, Apr. 1994.
[8] S. V. Shitov, O. V. Koryukin, Y. Uzawa, T. Noguchi, A. V. Uvarov, M. A. Bukovski, I. A. Cohn, "Design of Balanced Mixers for ALMA Band-10," IEEE Trans. Appl. Supercond., 17(2), 347-350 (2007).

A semiconductor quantum dot for spectral sensitive detection of THz radiation

R Davis[1], S Pelling[1], A. Tzalenchuk[2] and V. Antonov[1]

[1] *Physics Department, Royal Holloway University of London, Egham, Surrey TW20 0EX, UK*
[2] *National Physical Laboratory, Hampton Road, Teddington, Middlesex TW11 0LW, United Kingdom*

Spectral sensitive detection of THz radiation can be performed using a quantum dot formed in a two dimensional electron gas of GaAs/AlGaAs heterostructure. Different types of quantum dot sensors have been fabricated and studied. The most sensitive sensor, which is able to detect individual terahertz photons, consists of a quantum dot coupled to a metallic single electron transistor. This sensor however requires state of the art nanofabrication, delicate operation and temperatures below 1K. A more robust but less sensitive sensor is a quantum dot coupled to the point contact. It has reasonable nanofabrication demands and relaxed operation at T~1.5K. We compare two types of detectors, and suggest optimisation of the design aiming at improvement of quantum efficiency.

Epitaxial ultra-thin NbN films grown on sapphire dedicated for superconducting mixers

B. Guillet[1], R. Espiau de Lamaestre[2], P. Odier[3], M.P. Chauvat[4], P. Ruterana[4], L. Méchin[1], J.C. Villégier[5]

[1] GREYC, CNRS, ENSICAEN & Université Caen Basse Normandie, 6 Bd Maréchal Juin, 14050 Caen, France
[2] CEA-LETI, MINATEC, 17 Avenue des Martyrs, 38054 Grenoble Cedex 9, France
[3] Institut Néel, CNRS-Grenoble, 38042 Grenoble, France
[4] SIFCOM, CNRS, ENSICAEN & Université Caen Basse Normandie, 6 Bd Maréchal Juin, 14050 Caen, France
[5] CEA-DRFMC, MINATEC, Superconducting Device Group, 17 Avenue des Martyrs, 38054 Grenoble Cedex 9, France

Sputtered niobium nitride (NbN) films have been considered as a good candidate for rapid single flux quantum electronics based on Josephson Junctions, for THz mixers based on Hot Electron Bolometric effect or for single photon detection applications (SSPD). Applications would benefit from higher quality films (epitaxial growth) with low concentration of defects, such as grain boundaries or twins, whose nature and concentration depend on the deposition conditions and the substrate.

Efforts devoted to grow NbN aim at improving their critical temperature and critical current density, while keeping their thickness in the 3 to 5 nm range and Tc above 10 K, which insure a large bandwidth and large SNR detection at 4K. Choice of substrate is critical: for applications, MgO wafers and R-plane sapphire are usually considered as best choice. However, growing NbN on either M-plane or A-plane orientations of sapphire wafers, 3 inch in diameter, can help improving the film quality and fabrication yield. NbN thin films were grown by reactive DC magnetron sputtering at about 600°C and passivated by an AlN layer 1.5 nm thick deposited in-situ at room temperature. Growth on M-plane is shown to be better than on other sapphire orientations, including R-plane. NbN layer critical temperature reaches 13.3 K. Their properties are uniform on the 3 inch wafer, for a film thickness of 4.4 nm measured by X-ray reflectivity. We also obtained promising results on NbN growth on silicon wafers by using either an epitaxial YSZ/CeO_2 buffer layer grown ex-situ by PLD or a thin NbMgO buffer sputtered in-situ. Transport properties of NbN grown on those various substrates have been correlated to their crystallographic microstructure, examined by both symmetric and asymmetric X ray diffraction, high resolution transmission electron microscopy (HRTEM), spectroscopical ellipsometry, atomic force microscopy (AFM). These results will be presented in the framework of HEB and SSPD applications. Epitaxial multilayers NbN/MgO/NbN on M-plane sapphire have been also studied. Applications of these tunnel junctions as superconductor-insulator-superconductor (SIS) mixers have been considered.

Terahertz emission from ZnSe nano-dot surface

Shan He[a,b], Xiaoshu Chen[a], Xiaojun Wu[a], Fuli Zhao[a], Reng Wang[c], Weizheng Fang[c], Shuhong Hu[c], Ning Dai[c] and *Gang Wang[a]

[a] *State Key Laboratory of Optoelectronic Materials and Technologies, Sun Yat-Sen University, Guangzhou 510275, P. R. China*
[b] *School of Chemistry and Chemical Engineering,, Sun Yat-Sen University, Guangzhou 510275, P. R. China*
[c] *National Laboratory for Infrared Physics, Shanghai Institute of Technical Physics, Chinese Academy of Sciences, Shanghai, P. R. China, 200083*
*email: stswangg@mail.sysu.edu.cn

ABSTRACT

As shown in Figure 1 (Fig. 1) ZnSe nano dots are fabricated on the surface of <111> orientation ZnSe using femtosecond laser ablation technique. In this work, we studied the THz generation properties of the ZnSe nano-dots by electro-optic detection configuration. Three THz radiation mechanisms are observed in experiments: current surge effect (drift current), Photo Dember effect (diffusion current) and optical rectification. Compared with bulk ZnSe, the ZnSe nano dots generated much higher THz radiation power at the same experimental condition. When the ZnSe nano-dots covered 10% of total radiation surface, the radiation power is about two times stronger than that from the bulk bare sample (Fig. 2).

Basicly, there are two kinds of mechanisms occur predominantly for the THz radiation of ZnSe nano dots: the first is lighting-rod effect that fields tend to concentrate at the tips of protrusions on surface; the second is local-plasmon effect that collective oscillation of electrons occurs in these protrusions. These two effects make the total surface electric field largely enhanced. In this study, we attribute the THz radiation enhancement phenomenon of ZnSe nano dots to the surface field enhancement effect. Using a simple hemispheriod model, we also obtained the enhancement factor of ZnSe nano dots.

Keywords: THz radiation, surface field enhancement, surface nano-dot, ZnSe.

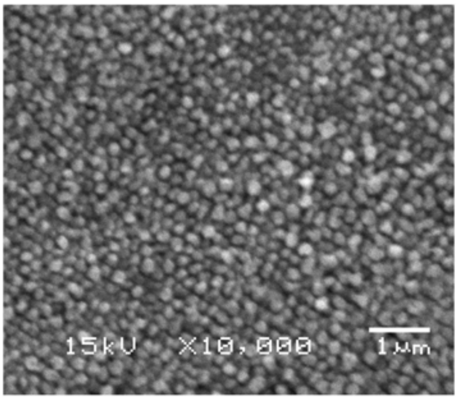

Fig. 1. SEM micrograph of ZnSe nano-dots.

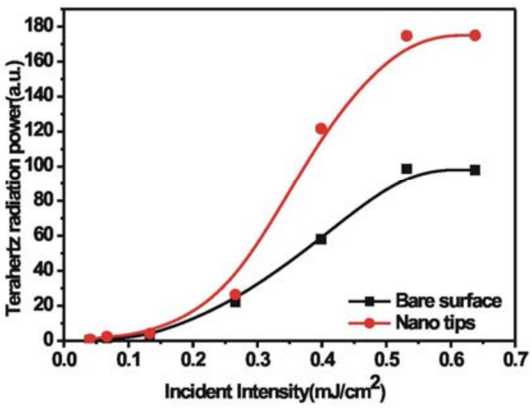

Fig. 2. THz fluence as a function of pump fluence for nano-dot and bulk ZnSe samples.

The response rate of a room temperature terahertz InGaAs-based bow-tie detector with broken symmetry

I. Kašalynas[1,2,*], D. Seliuta[1], R. Simniškis[1], V. Tamošiūnas[1], V. Vaičikauskas[2], and G. Valušis[1]

[1] Semiconductor Physics Institute, A. Goštauto 11, LT-01108 Vilnius, Lithuania
[2] Institute of Physics, Savanoriu ave. 231, LT-02300 Vilnius, Lithuania
* Contact: irmantak@ktl.mii.lt, phone +370-5-231 24 18

***Abstract* — Transients of an InGaAs-based bow-tie diode with broken symmetry are experimentally investigated. The 100 MHz bandwidth low-noise preamplifier is designed and successfully adapted. The main peculiarities of the terahertz detector are detection in passive scheme, flat frequency response up to 1 THz, the voltage sensitivity of about 5 V/W, and the rise time less than 40 ns.**

***Index Terms* — infrared, submillimeter wave, microwave, and radiowave detectors; terahertz detectors; hot carriers; semiconductor asymmetrically shaped diodes.**

I. Introduction

Rapid evolution of terahertz (THz) electronics and its implementation in many areas require new concepts in developing compact broad-band THz sensors operating at room temperature [1]. In addition, rapid response of the detectors would be an advantage indicating their versatility in recording circuits.

In this work, we report an experimental study of transient properties of the InGaAs-based bow-tie diode with broken symmetry. The principle of operation is based on a non-uniform carrier heating in a high-mobility electron gas layer [2-3]. Electromagnetic waves detection on mobile carriers heating promises much faster detector transients in comparison to bulk detectors of thermal action, for example thermopile, bolometers etc. Here we show the potential of the InGaAs-based bow-tie detector connected in a passive detection scheme and in common with the fast low-noise current preamplifier.

II. Detector

The detector design is shown in Fig. 1. Its active part is an $In_{0.54}Ga_{0.46}As$ layer grown by molecular beam epitaxy on a semi-insulating substrate of InP (001). The thickness of the InGaAs layer is of about 534 nm. The concentration of free electrons is of about 2×10^{15} cm^{-3} and the low-field mobility is of about 13300 cm^2/Vs at room temperature. The Ohmic contacts are made of Ti/Au/Pt compound evaporated and annealed on top of the InGaAs layer. One of the structure's leafs is also metallised in order to concentrate an incident radiation into the neck. The mesas of the height of a few micrometers are created by wet etching. After cleaving of the wafer, the sample is wired and attached to a hemispherical silicon lens of 6 mm diameter from the substrate side. All elements are then mounted in the cylindrical metal case with 29 mm diameter and 32 mm length.

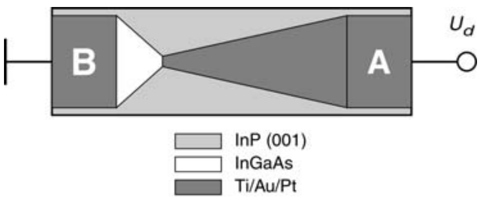

Fig. 1 Top view of the detector made of bow-tied InGaAs with broken symmetry formed on the InP substrate. The size of the detector: total length is 500 µm, width – 100 µm, apex size – 12 µm, lengths of the InGaAs leaf – 50 µm, and metallized 'right' leaf – 250 µm. The contacts are labelled as A and B to clarify the polarity of applied voltage. The electric field of incident THz radiation is oriented along the diode.

The principal of operation relays on non-uniform carrier heating in high-mobility electron gas. The metallized leaf acts as a coupler of the incident THz radiation, while the second leaf is active where electrons are heated non-uniformly. Consequently, the voltage signal with a polarity corresponding to the hot-carrier effect is induced over the leaves without any application of the dc-bias.

An internal electric field distribution along the neck for different polarity of the external dc-voltage is shown in Fig. 2. The forward bias connection is for electron flow from 'A' contact towards 'B' contact (see Fig. 1). In-plane geometrical asymmetry induces a different gradient of the internal electric field depending on the polarity of the voltage applied. It is seen that this difference is appreciable only within several microns from the neck for this particular design which parameters is indicated in the caption of Fig. 1. The electric field distribution dependence on the polarity of an external voltage causes the different spatial accumulation of hot-carriers in the vicinity of the neck resulting in asymmetry of the current.

The measured I/V characteristic of the asymmetrically shaped diode is shown in the inset of Fig. 2. At low electric field the current magnitude does not depend on the polarity of the applied voltage. But, when the sample is turned to a strong field regime, the temperature of electrons increases and they accumulate differently in the vicinity of the detector neck. This affects on the symmetry of the I/V characteristic and can be successfully used for the detection of the THz radiation

The asymmetrically shaped diode is sensitive to the polarization of the incident electromagnetic wave. The strongest signal is obtained when diode is oriented along the direction of the electric field. The difference found experimentally is up to 10 times between the signals for perpendicular and parallel detector orientations.

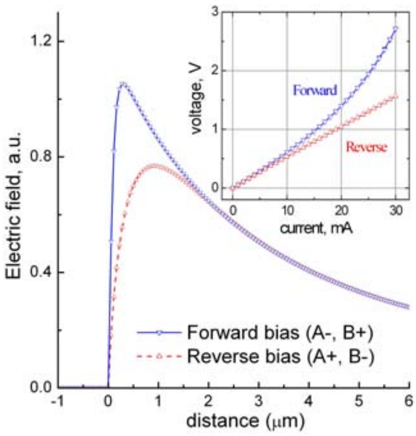

Fig. 2 Calculated internal electric field distribution along bow-tie diode neck. The X-axis denotes the distance from the apex of the sample. The InGaAs leaf is placed from position 0 to the direction of positive numbers. The insert shows I/V curve of the diode. The reverse bias curve corresponds to polarity: contact A is positive, contact B is negative.

III. Detector with preamplifier

Additionally, a low-noise preamplifier is designed to make easier signals readout. The InGaAs asymmetrically shaped diode is connected to the preamplifier in the photovoltaic mode as it is depicted in the inset to Fig. 3. Advantages of such connection are absence of dark current flow through the diode, low noise and signal linearity. We managed to design the preamplifier with performances: the impedance of signal conversion is of 100 000 V/A, the bandwidth is up to 100 MHz, the output noise voltage is below 250 nV/Hz$^{1/2}$. Calculated and measured preamplifier parameters are shown in Fig. 3. The signal at the output can swing up to ± 1.5 V corresponding to maximum input currents of 150 μA. The preamplifier low power consumption (voltage and current is ± 3 V and 25 mA, respectively) allows simple batteries to source an electrical scheme avoiding an additional noise introduction.

The view of the THz detector with internal low noise preamplifier is shown in Fig. 4. The InGaAs asymmetrically shaped diode and preamplifier are shielded from external noise pick-up inside the metal cylinder. The silicon lens is mounted in the centre of the cap. The dimensions of the THz detector with preamplifier are 46 mm diameter and 40 mm length.

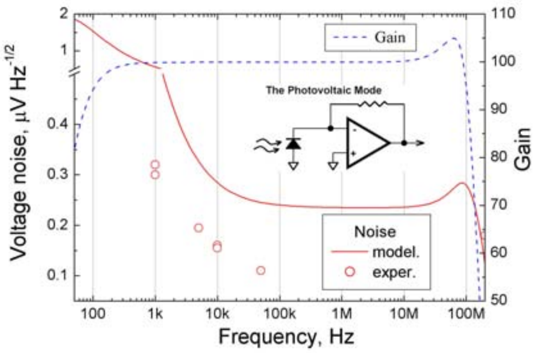

Fig. 3 Preamplifier gain-frequency (dashed line – modelling) and voltage noise-frequency (solid line – modelling, dots – experiment) characteristics.

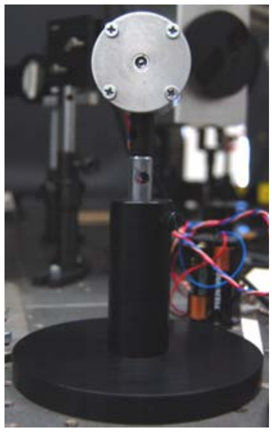

Fig. 4 Picture of the THz detector composed of the silicon lens, InGaAs asymmetrically shaped diode, and low-noise preamplifier. The detector is suited for free space experiment. The preamplifier is sourced from four AA-size alkaline batteries.

IV. Results in THz range

The THz radiation source is an optically-pumped molecular laser generating 0.1 ms duration and 30 Hz repetition rate pulses. The gas of HCOOH is pumped and the laser is set to operate at the wavelength of 433 μm (0.69 THz frequency). The 25 cm focal length lens is used to focus THz laser beam to the spot size of roughly 2 mm a full width at half maximum. No other optical elements are used between the laser and the THz detector placed at the focal distance.

The detector response to the THz excitation at room temperature is shown in Fig. 5. The results were recorded turning the length of the laser resonator. In this manner different longitudinal modes in the THz resonator are selected for the lasing. It is seen that the parameters of the THz pulse (rise time, duration, and shape) can be recorded. To estimate transient characteristics, the microwave radiation source with a fast rise time was involved.

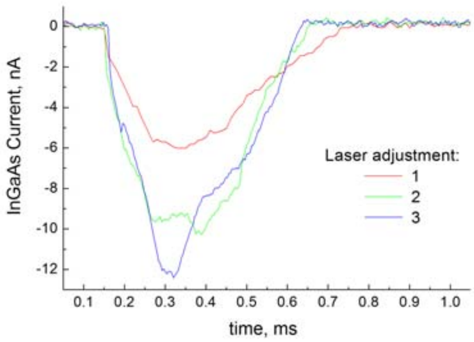

Fig. 5 The pulse shape of the THz laser for different mode structure of the output beam.

V. Results in GHz range

The signal synthesizer (model HP 8673C) and the TWT amplifier was used as another source delivering the pulse power up to 100 W. This source was set to generate 10 GHz frequency with 10 Hz repetition rate, 40 ns rise time, and up to a few milliseconds duration pulses. The parameters of the pulse were controlled with the Schottky diode and the resistive sensor specially designed for X-band [4].

The time response of the asymmetrically shaped diode excited with a rectangular pulse is shown in Fig. 6. It is seen that the pulse shape is well preserved. Note that the differentiating RC circuit is used to separate an offset voltage.

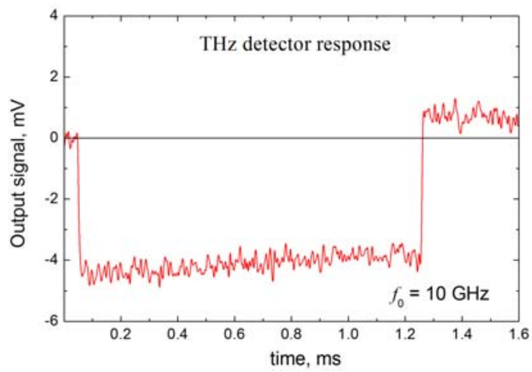

Fig. 6 An oscilloscope trace of the THz detector with preamplifier. The pulse duration is about 1.1 ms, the frequency – 10 GHz.

An expanded oscilloscope trace of the THz detector with and without preamplifier is shown in Fig. 7. One can see that the rise time of the detector response is equal to 40 ns at both experimental setups. The last and the pulse shape confirm that the applied low-noise preamplifier does not slow down the response of detector or distort the signals. Attentive investigations of the synthesizer pulses revealed that InGaAs-based bow-tie detector exactly replicates the excitation pulse. Therefore, one can conclude that the response time of the THz detector is not worse than 40 ns, as the rise time of the microwave source.

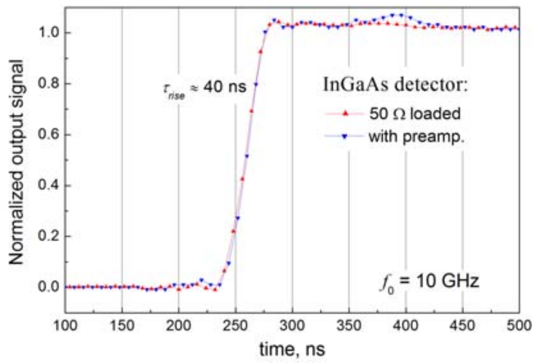

Fig. 7 An oscilloscope trace of the THz detector loaded with 50 Ohm resistor or connected to the fast current-preamplifier.

Conclusions

The response rate of a room temperature terahertz InGaAs-based bow-tie detector with broken symmetry has been experimentally investigated. The 100 MHz low-noise preamplifier connecting THz detector in the photovoltaic scheme has been developed and tested. The response time of the THz detector has been found to less than 40 ns. The real value is hidden by limited possibilities of the pulse source used. It has been demonstrated that the room temperature THz detector is fast enough to record longitudinal modes beating in the optically-pumped molecular laser cavity.

Acknowledgment

We are very grateful to Klaus Köhler for excellent quality wafer and Saulius Balakauskas for help in preparing samples for measurements.

The research at the Semiconductor Physics Institute at Vilnius was performed under topic "Terahertz photonics and spectroscopy".

References

[1] R. Tauk, F. Teppe, S. Boubanga, D. Coquillat, W. Knap, Y. M. Meziani, C. Gallon, F. Boeuf, T. Skotnicki, C. Fenouillet-Beranger, D. K. Maude, S. Rumyantsev and M. S. Shur, *Appl. Phys. Lett.*, vol. 89, p. 253511 (2006).

[2] D. Seliuta, E. Širmulis, V. Tamošiūnas, S. Balakauskas, S. Ašmontas, A. Sužiedėlis, J. Gradauskas, G. Valušis, A. Lisauskas, H. G. Roskos, and K. Köhler, *Electron. Lett.*, vol. 40, pp. 631-633 (2004).

[3] D. Seliuta, I. Kašalynas, V. Tamošiūnas, S. Balakauskas, Z. Martūnas, S. Ašmontas, G. Valušis, A. Lisauskas, H.G. Roskos, and K. Köhler, *Electron. Lett.*, vol. 42, pp. 825-827 (2006).

[4] (2008) The Microwave Laboratory website. [Online]. Available: http://www.pfi.lt/index_e

A 585 GHz Quasi-Optical HEB Six-Port Reflectometer Based on an Annular Slot Antenna

R. Percy, L. Liu, H. Xu, J. Schultz, A.W. Lichtenberger, R.M. Weikle, II

Charles L. Brown Department of Electrical and Computer Engineering

University of Virginia, Charlottesville, VA 22904, U.S.A.

* Contact: rrp4d@virginia.edu, phone +1-434-924-6575

Abstract **— Six-port reflectometers have become a topic of interest due to the scarcity of instrumentation for measuring scattering parameters (s-parameters) at terahertz frequencies. This paper presents a quasi-optical six-port reflectometer designed for 585 GHz using hot-electron bolometers (HEB's). In this design, a ring slot antenna couples a signal into the reflectometer creating a standing wave along a microstrip transmission line. The standing wave is sampled by three evenly spaced HEB's. A polarization rotation resulting from the feed of the transmission line allows the antenna to act as both the input and measurement ports (horizontally polarized energy is coupled into the device and re-radiated with vertical polarization). The reflectometer is expected to be sensitive to nanowatt power levels from 570 GHz to 640 GHz. The annular slot antenna and microstrip portion of the device have been independently fabricated and tested. This proof-of-concept test verifies that the polarization is rotated and provides an estimate of the power available for sampling. It was found that approximately 30 μW of power is available, as measured with an Erickson power meter. Simulations in conjunction with these data indicate that the HEB's should be capable of detecting 100's of nanowatts. This requires each HEB to have approximate dimensions of 100nm by 200nm. This paper presents the six-port design and preliminary measurements.**

I. INTRODUCTION

A six-port reflectometer is a compact and relatively inexpensive method for measuring scattering parameters that has outstanding potential for characterizing terahertz components and materials. The realization of such a device at terahertz frequencies would permit diagnostic and measurement capabilities not currently available. Potential uses include characterizing materials such as absorbers, windows, lenses, and other components used in terahertz systems. The six-port reflectometer presented in this work will be realized using three diffusion cooled niobium hot-electron bolometers operating as direct detectors. The input and measurement ports will utilize the antenna using a rotation in the polarization of the signal.

II. SIX-PORT REFLECTOMETERS

A six-port reflectometer measures the reflection coefficient of a material using four evenly spaced power detectors [1]. If the device under test is known to be passive, then only three detectors are necessary, resulting in a five-port reflectometer [2]. These detectors sample a standing wave that results from the reflection of a signal on a device under test (DUT). A general representation of a six-port is illustrated in fig. 1. Using various calibration schemes and the ratios of the measured powers, the reflection coefficient for the device can be determined [3].

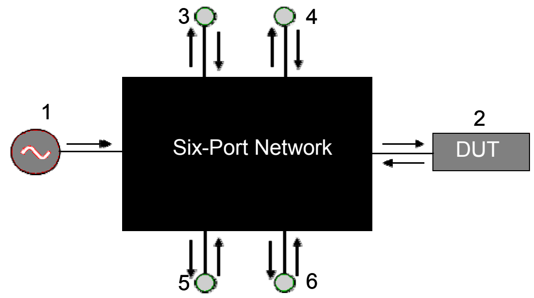

Fig. 1: Representation of a six-port reflectometer. Port 1 is the signal input port, port 2 is the measurement port, and ports 3-6 couple to the power detectors.

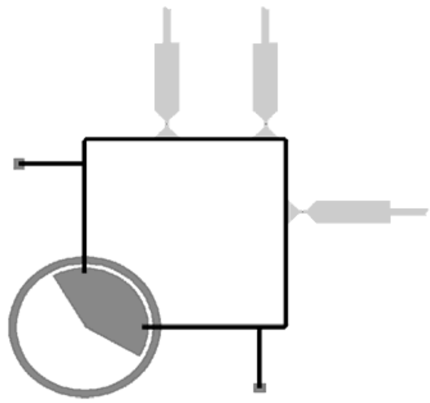

Fig. 2: Prototype submillimeter six-port reflectometer. The ring slow antenna acts as ports 1 and 2 from fig. 1. The detectors at ports 3, 4, and 5, are connected to low pass filters (truncated in this figure). There is a ground pad in the center of the antenna and at the end of each stub.

III. DEVICE DESIGN

A. Polarization

This prototype submillimeter six-port reflectometer utilizes a ring slot antenna to couple both source (port 1) and measurement (port 2) ports (FIGURE # 2). Three hot-electron bolometers (HEB) are used as direct power detectors and are located at ports 3, 4, and 5. A low pass filter follows each HEB to block the RF signal and allow the DC detected response to pass. A fourth detector (port 6) is not necessary for the measurement of passive devices and has not been included. The port numbers in the device schematic (fig. 2) correspond with the port numbers in the general six-port representation (fig. 1).

The use of the antenna as two different ports is achieved by exploiting a change in polarization. An experimental setup (fig. 3) illustrates this idea. The input signal is passed through a polarization grid allowing only one polarization (e.g. – horizontal) to reach the antenna and be coupled into the device as illustrated by the solid arrows. This signal passes through a transmission line with a 90º bend and is re-radiated with the opposite polarization (e.g. – vertical). When this re-radiated signal reaches the polarization grid, it is completely reflected and is directed toward the DUT as shown by dotted arrows. The reflected portion of the signal follows its path back into the six-port (dashed) and creates a standing wave along the transmission line. Three probes along the line allow the HEB's to detect the power at each point.

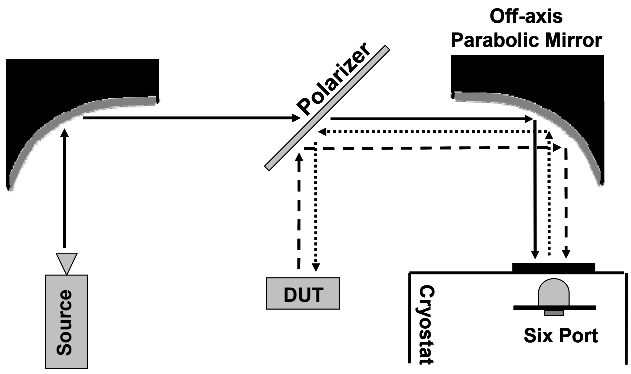

Fig. 3: The experimental setup. The input signal (solid line) is vertically polarized. The output signal (dotted line) is horizontally polarized from the six-port. The signal (dashed line) is the reflection from the DUT.

B. *Power Detector Coupling*

An important design consideration is the location and size of the probes. Ideally, they are λ/6 apart so that the standing wave is sampled within a half-wavelength over an octave bandwidth [2]. Another consideration is balancing the power available to each individual HEB and to the output. Two designs have been considered: the first employs a shorted stub tuning network to match the antenna impendence to the microstrip impedance and to provide a ground for the HEB's as (fig. 2); a second uses an open circuited stub matching network and includes separate quarter-wave stubs to ground. The coupling data for the first design is shown in fig. 4 and is similar to that of the second design. These ADS Momentum simulations are used to calculate the amount of power available to each HEB and the size required for the HEB.

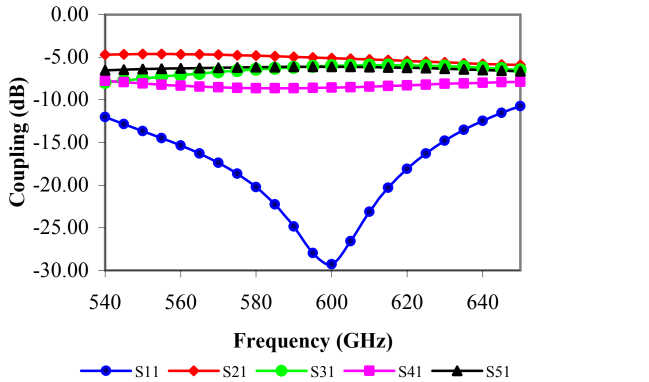

Fig. 4: ADS Momentum simulation of the power in dB coupled into each port for scheme 1. S11 is the input reflection, S21 is the output signal, and S31, S41, and S51 are the ports. Each port is identical with the exception of position showing they are not independent.

C. *Power Detectors*

The power detectors to be used in this six-port reflectometer are niobium hot-electron bolometers (HEB's). The slope of the R-T curve (fig. 5a) near the superconducting transition for these devices is very sharp, allowing a small change in temperature to change the resistance of the device significantly. Monitoring the I-V curve (fig. 5b) of the bolometer allows the power absorbed to be determined [4]. The sensitivity of an HEB depends on its volume. The devices designed for this application will be 10 nm thick and have area of 100nm x 200nm [5].

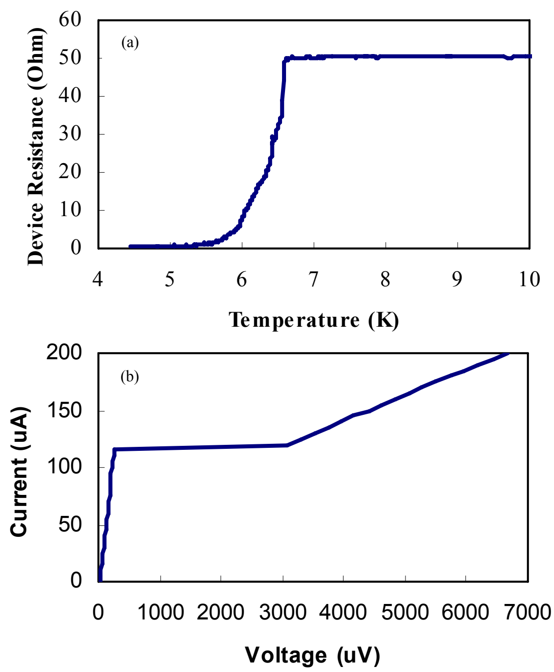

Fig. 5: Typical (a) R-T and (b) I-V curves for a Niobium HEB fabricated at the University of Virginia. *Courtesy of Lei Lui [4].*

IV. Fabrication

The size of the HEB's requires nanoscale fabrication techniques. The options available in the University of Virginia Microfabrication Laboratory (UVML) include electron-beam lithography and a recently developed procedure known as "Ti-line processing" [6]. The later approach is attractive in that it does not require direct-write processing, allows all devices to be made in parallel, and exploits 2 µm conventional lithography to yield nanoscale devices.

The Ti-line technique (fig. 7) is based on forming a thin strip of titanium suspended above a substrate to form a shadow mask. The width of the titanium line is controlled by the sputter conditions (rate and angle) under which the material is deposited. The line is formed by creating a step profile in a polyimide coating the substrate (fig. 7a). Titanium is sputtered onto the substrate, including the step sidewalls. Resist "anchors" are put on either side of the Ti-line (fig. 7b). Reactive Ion Etching (RIE) removes the flat surfaces of Ti and the underlying resist, leaving a titanium bridge suspended over the substrate. The suspended Ti-line is used as either an evaporation or an etch mask. In fabricating the HEB's for the six-port, two different Ti-lines are employed to form the length and width of the bolometer. A 200 nm wide line is used as an evaporation mask for the gold that comprises the microstrip circuit (fig. 7c). This determines the length of the HEB. All unnecessary gold is lifted off using traditional lithography. The HEB length is now defined and the Ti-line removed. A second Ti-line, perpendicular to the first, is used to define the HEB width of 100 nm (fig. 7d). This Ti-line is used as an etch mask to form the niobium bridge (fig. 7e). This etch mask is employed to remove all underlying niobium except that needed for the HEB's. Once these Ti-lines are removed, the six-port reflectometer is complete (fig. 7f).

V. Proof of Concept

The microstrip feed and antenna portion of the instrument have been independently fabricated to test the polarization concept and provide estimates for the power available to each HEB. The power available at the theoretical DUT location is measured using an Erickson Power Meter. The losses between the DUT and HEB's can be calculated and combined with the measured data to estimate the power available to each HEB. The polarization dependence is tested by rotating the annular slot structure and measuring the resulting change in power.

A. Design and Test Setup

Two different microstrip designs have been fabricated and tested (fig. 8). The first design (fig. 8a) is simply a loop of microstrip line with impedance that matches as closely as possible to the antenna impedance (110Ω). The microstrip impedance (28Ω) is determined by the fabrication tolerances and practical limits on the dielectric thickness (4000Å) and microstrip line width (2µm). The second design (fig. 8b) includes a stub tuning network to more closely match the

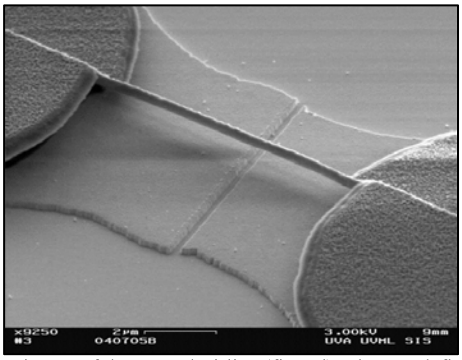

Fig. 6: SEM image of the second Ti-line (fig. 7d). The gap defines the HEB length and the Ti-line will define the HEB width. *Courtesy of J. Schultz [4]*.

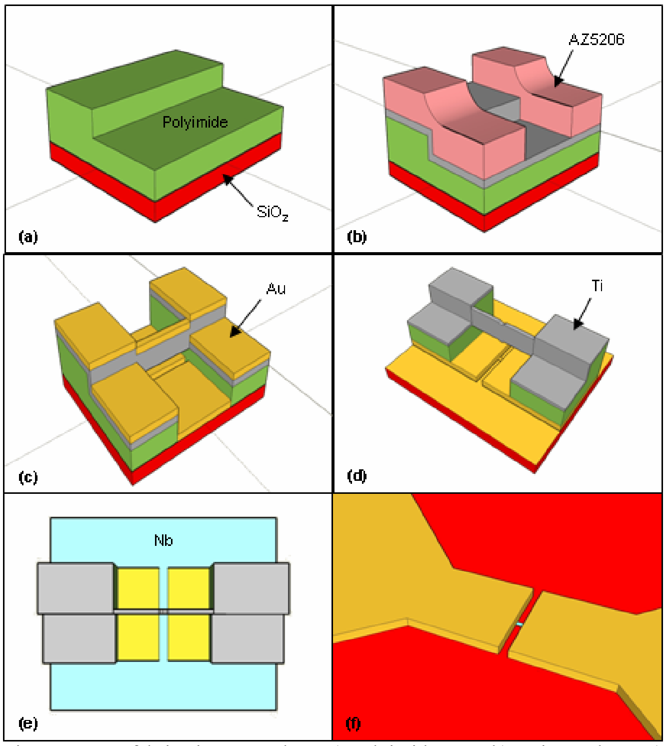

Fig. 7: HEB fabrication procedure; a) polyimide step; b) resist anchors; c) Ti-line after gold evaporation – HEB length is now defined; d) Ti-line defining HEB width; e) Ti-line as an etch mask (top view); f) final HEB. Materials are color coded as labeled.

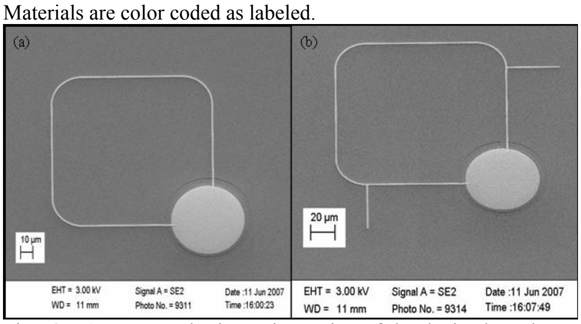

Fig. 8: Antenna and microstrip portion of the device have been fabricated independently to measure available power, validate loss calculations, and prove the polarization concept. Two designs were fabricated – (a) contains a large mismatch between the antenna and microstrip impedance; (b) utilizes a stub tuning network to address the mismatch.

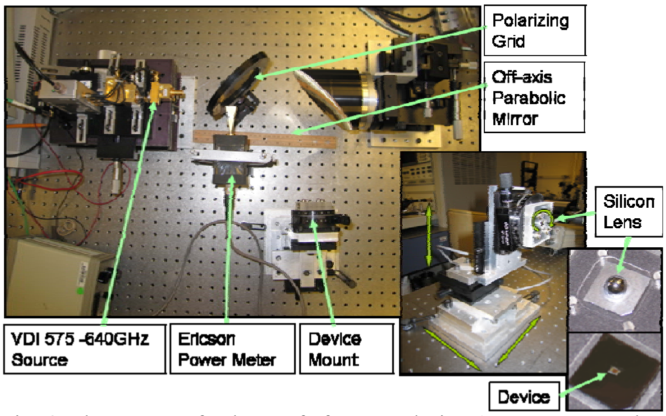

Fig. 9: The test setup for the proof-of-concept device. A VDI source sends a signal through a polarizer, off from an off-axis polarization mirror, and into the device. The device is given four axis of freedom (x, y, z, rotation) for alignment. It re-radiates the signal which now is reflected by the polarization grid and into a power meter.

antenna and microstrip impedances. Upon testing the designs, no detectable signal was measured using the network with no matching.

The test setup (fig. 9) for these measurements is a portion of the overall setup shown in fig. 3. Using this configuration helps fine tune the overall setup design. A power meter is put in place of the DUT and the "return trip" does not occur. A cryostat is unnecessary as there are no HEB's on the test chip. Lastly, to help with alignment, a mount has been improvised allowing four axis of freedom, one of which is necessary for the polarization measurements.

B. *Polarization measurements*

The polarization change is demonstrated by rotating the device and measuring the resulting power at the Erickson power meter. It is seen in fig. 10 that the power nulls occur when the orientation of the device is at odd multiples of 45º and peaks at even multiples of 45º. The variations are likely caused by stray reflections in the laboratory. The expected rotational dependence can be calculated and the data is shown to follow the expected dependence:

$$\frac{P}{P_{\max}} = \cos^2(2(\theta_{\deg} - 10)),$$

where the 10° is added to account for a misalignment between the device and the 0° point.

C. *Power and loss measurements*

The power measured with the Erickson meter varies from 3 µW at 605 GHz to 34 µW at 585 GHz. The variations at different frequencies across the bandwidth are largely accounted for by the frequency response of the source (fig. 11).

The system losses can be determined through a combination of measurement and simulation. The primary source of loss is the silicon lens used to focus the signal onto the device antenna. There is a 1.5dB reflection loss on each pass, totaling 3dB. Additionally, there are smaller losses

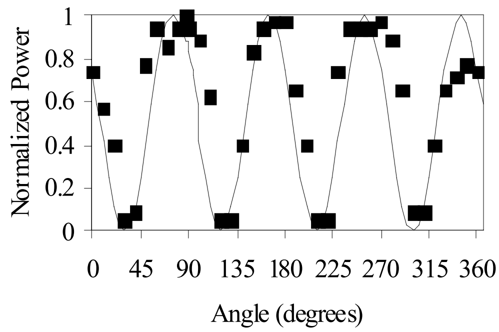

Fig. 10: The change in normalized power as the device is rotated. This shows that the polarization is being changed as expected with nulls occurring at an angle of 45°.

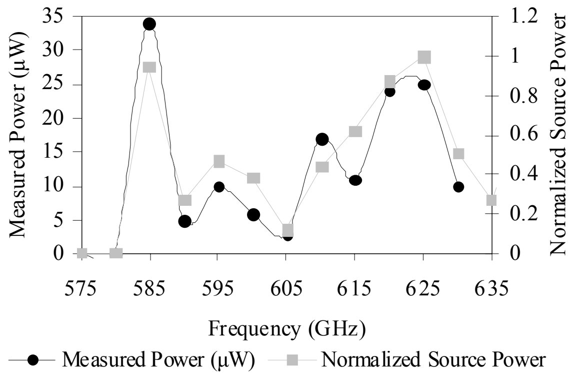

Fig. 11: The power measured in microwatts by the Erickson power meter compared to the normalized source power. The variations in measured power are a result of variations in the source.

TABLE I

POWER AVAILABLE FOR MEASUREMENT AT EACH HEB WHEN USING THE SIMULATIONS TO DETERMINE S31, S41, AND S51, AND A DUT REFLECTION COEFFICIENT OF 6DB.

	Loss (dB)	Power available (µW)
Avail. to DUT	10.8	25.2
Total losses	19.5	3.3
Coupling S31	6.3	0.79
Coupling S41	8.6	0.46
Coupling S51	6.2	0.81

predominantly from attenuation within various materials. The overall loss within this test setup is just under 9dB. Using a power available from the source of 300 µW at 585GHz gives a power available at the DUT of about 40 µW. The measured power of 34 µW agrees reasonably with these calculations.

The strong correlation between theory and measurement implies that the calculations can be applied to the final test set-up from fig. 3. Using the calculated losses through the system and assuming a DUT reflection of 6dB, the total loss is just under 20dB thus yielding an available power for coupling to the HEB's of 3.3 µW. This number can then be combined with the coupling simulation results (fig. 4) predicting values available at each HEB to be on the order of hundred's of nanowatts (table 1). These considerations determine the HEB size to be approximately 100x200nm.

CONCLUSIONS

A method for building a six-port reflectometer at submillimeter frequencies has been outlined and the design has been laid out, simulated, and is currently being fabricated. A newly developed lithography technique known as "Ti-line processing" is being employed to fabricate the nanoscale HEB's using conventional two micron lithography. A change in polarization allows a ring slot antenna to be used for both an input and measurement port. This concept has been demonstrated to agree with theory. The system losses and available power have been calculated and provide groundwork for determining the HEB size. The realization of this device will be an exciting demonstration of the ideas presented in this paper.

ACKNOWLEDGMENT

The authors thank their colleagues in the Far-Infrared Laboratory and the Microfabrication Laboratory at the University of Virginia for their advice, insight, and patience. This work is funded by the Army National Ground Intelligence Center (contract W911W5-06-C-0001) and the National Science Foundation (grant ECS-0524284).

REFERENCES

[1] G. F. Engen, "The six port reflectometer: An alternative network analyzer," *IEEE Trans. Microwave Theory Tech.*, vol. MTT-25, pp. 1075-1080, Dec. 1977.

[2] Weikle, R. M., II; Liu, Z.; Liu, H.; Liu, L.; Ulker, S.; Lichtenberger, A. W. "Six port reflectometers for terahertz scattering parameter measurements using submillimeter-wavelength detectors," *Nanofabrication: Technologies, Devices, and Applications*," vol. 5592, pp. 328-340, January 2005.

[3] G. F. Engen, "Calibrating the Six-Port Reflectometer by Means of Sliding Terminations," *IEEE Trans. Microwave Theory Tech.*, vol. MTT-26, pp. 951-957, Dec. 1978.

[4] L. Liu, "Integrated 585 GHz hot-electron bolometer mixers and focal-plane arrays for imaging applications," Ph.D. dissertation, University of Virginia, Charlottesville, VA, 2008.

[5] J. Schultz, "Superconducting hot electron bolometer terahertz mixers and related technologies," Ph.D. dissertation, University of Virginia, Charlottesville, VA, 2007.

[6] J. Schultz and A. Lichtenberger, "Investigation of Novel Superconducting Hot Electron Bolometer Geometries Fabricated with Ultraviolet Lithography," *IEEE Trans. Applied Superconductivity*, vol. 17, pp.645-648, June 2007.

Solid-state non-stationary spectroscopy of 1-2.5 THz frequency range

V.L.Vaks[1], A.V.Illyuk[1], A.N.Panin[1], S.I.Pripolsin[1],
D.G. Paveliev[2], Yu.I Koshurinov[2]
[1] *Institute for physics of microsructures RAS, Nizhny Novgorod, Russia*
[2] *N.I.Lobachevsky Nizhny Novgorod State University, Nizhny Novgorod, Russia*

The THz frequency range is attractive for spectroscopic investigations, since many strong molecule lines lie in this range. Absorption lines of light hydrides and vibration motions of many molecules lie here. It gives possibility of studying molecules (for example metalloorganic molecules) which absorption lines in other frequency ranges are very weak.

The high precision, time-domain spectroscopy is unique method of analysis of multicomponent gas mixtures. This method has the sensitivity at level of 0,2 ppb, has high selectivity and possibility of measuring the investigated substances concentration. Besides, this method is simple to using.

Nowadays there exist two approaches for THz pulse generation for tabletop devices. These are photoconductive switches illuminated by femtosecond laser pulses, and optical rectification using ultrashort laser pulses in nonlinear crystals. However the problem of frequency stability and bad resolution provides a fundamental limitation for these methods in high precision spectroscopy. This method is not suitable for high resolution spectroscopy. The second way is the classic approach to transfer the microwave methods to THz frequency range which is elaborated in IPM RAS.

The spectrometer of 1-2.5 THz frequency range (with registration of a signal in time area) based on solid-state radiation sources is considered in this report. The necessity of development the new THz sources is concerned with the fact, that the present emission sources (such as back-wave oscillator (BWO)) are extremely expensive and have large sizes and quite short time of exploitation. They operate in the frequency range from 100 up to 1250 GHz and are base for creation of the synthesizers for precision measurements.

Our approach consists of the application of the solid-state synthesizers of millimeter wavelength range based on e.g. Gunn generator (97.5-117 GHz) with PLL of reference generator and frequency multipliers on quantum semiconductor structures. Over the last several years, the superlattice structures are more effective for frequency transformation and detection, since the lower values of inertness and parasitic capacitances and presence of negative differential conductivity (till 1 THz) on the volt-ampere characteristic. The results of measurements of spectral distribution up to 4.9 THz after multiplier by using the Furie spectrometer on silicic helium bolometer are shown on Fig 1. The measurements of spectral line of methanol at 1062 GHz were carried out.

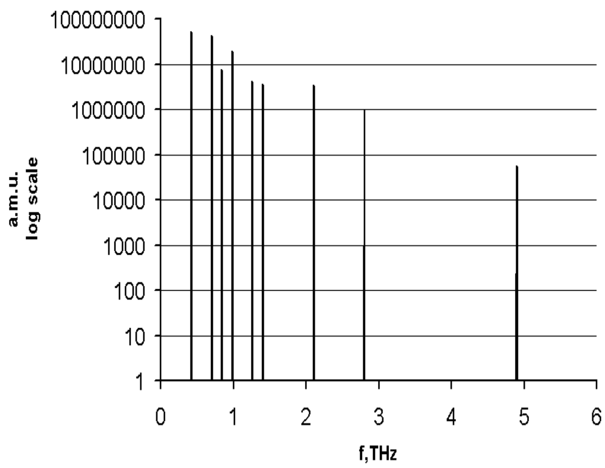

Fig.1. The measurements of spectral distribution after multiplier

This work was supported by RFBR (grants 07-03-91143, 06-08-01332-a, 03-02-17088), ISTC (project 3174 «Development and study of integrated receivers for operation frequencies 0.5 – 1 THz»), SCIENCE FOR PEACE PROGRAMME (CBP.NR.SfPP 981415, "Integrated Spectrometers for Chemical Agents Detection and Atmosphere Monitoring").

Design and Simulation of a Corrugated Polarizer and Waveguide-based OMT for a 129 GHz VLBI Receiver of KVN

Moon-Hee Chung, Do-Heung Je, Seog-Tae Han, Changhoon Lee, and Duk-Gyoo Roh

Radio Astronomy Division, Korea Astronomy & Space Science Institute

In millimeter-wave VLBI systems, dual-circular polarization observations are generally performed. As the highest frequency band of KVN(Korean VLBI Network), a 129 GHz band receiver is being designed for prototype. To reduce the receiver noise temperature, it is necessary that passive components including polarizer and OMT are inserted into the cryogenically cooled dewar. Traditionally septum polarizers are used at lower frequencies like 22 and 43 GHz bands because of its simplicity. But this type polarizer has relatively narrow bandwidth and is difficult to be fabricated and assembled at higher frequencies. To overcome these drawbacks, corrugated phase shifter or polarizer integrated into waveguide-based OMT is expected to be employed for the 129 GHz VLBI receiver of KVN. Intensive simulations using commercially available tool like CST MWS are being carried out to optimize and predict the performance of the proposed polarizer and OMT. In this paper, the design and theoretically calculated performance of our prototype polarizer and OMT for the 129 GHz band receiver will be presented.

Development of a 385-500 GHz Orthomode Transducer (OMT)

Mamoru Kamikura[1,2,3], Masato Naruse[1,2], Shin'ichiro Asayama[2], Naohisa Satou[2], Wenlei Shan[4], and Yutaro Sekimoto[1,2]

[1]Department of Astronomy, School of Science, University of Tokyo, Japan
[2]Advanced Technology Center and ALMA-J project office
National Astronomical Observatory of Japan, National Institutes of Natural Sciences
[3]JSPS Research Fellowship for Young Scientists
[4]Purple Mountain Observatory, Chinese Academy of Sciences
* Contact: kamikura.mamoru@nao.ac.jp, phone +81-424-34 3981

***Abstract*—We report on the development of an orthomode transducer (OMT) for ALMA Band 8 (385-500 GHz). The OMT is a scaled model of that of ALMA Band 4 (125-163 GHz), which has a Bϕifot junction and a double ridge. The transmission loss of the OMT at 4 K was derived to be 0.4-0.5 dB from noise measurements with an SIS mixer. The polarization isolation was measured to be larger than 20 dB from quasioptical measurements. For electromagnetic design, effects of mechanical errors have been studied and then a robust design with allowable mechanical errors of 10 μm has been obtained.**

I. Introduction

An orthomode transducer (OMT) is a passive waveguide device that separates a received signal by a feed horn into its two orthogonal linearly polarized components. For submillimeter receivers, the conventional way to separate orthogonal polarizations is to use a wire grid, which is a quasioptical device that consists of free-standing wires.

Optical systems of a dual polarization receiver with a wire grid or an OMT are shown in Fig.1. The merits and demerits of an OMT compared with a wire grid are the following:

Merits

1) Optical system of a receiver can be quite simple and compact. An ellipsoidal mirror, a corrugated horn, and a wire grid can be removed from that with a wire grid.
2) There is no beam squint between two polarizations.
3) A problem of the life time of a wire grid can be solved.

Demerits

1) A Fabrication is relatively difficult.
2) The Joule loss of the waveguide is added, although an ideal wire grid has almost no loss.

These demerits can be solved if we can design mechanical robust OMT, and if waveguide is gold-plated. The transmission loss at 4 K is calculated as 0.5 dB/ 25 mm at 385 GHz when the OMT is cooled down to 4 K. We assume the conductivity of gold film at 4 K is 1.0×10^8 S/m [1].

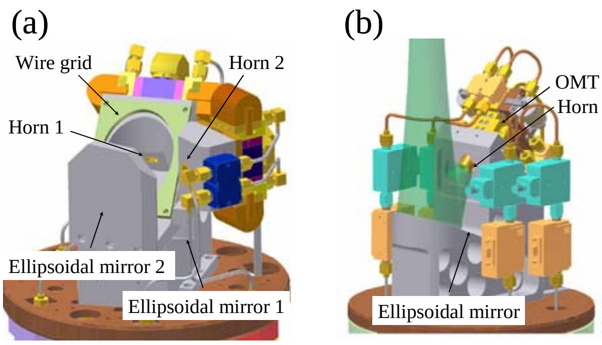

Fig. 1 Optical systems of a dual polarization receiver with (a) a wire grid, (b) an OMT.

Three types of OMTs have been developed for broadband (fractional bandwidth ≥ 26 %) applications at millimeter and submillimeter wavelengths. This classification is similar to that in [2], which is based on the symmetry of the junction.

1) Bϕifot junction with a septum [3-5]
2) Bϕifot junction with a double ridge [6-7]
3) Turnstile junction [8-9]

So far an OMT with a Bϕifot junction and a septum for the 211-320 GHz band [3] was the one demonstrated at the highest frequency range.

We adopted an OMT with a Bϕifot junction with a double ridge. This design has no additional component like septa, and can be realized in a two-split block with conventional CNC milling techniques and partly with electroforming ones. On the other hand, turnstile junction is made in (1) a four-split block with CNC milling techniques, or (2) one block with electroforming techniques. Since Bϕifot junction with a double ridge is simple, it is the most promising for a submillimeter OMT among these designs.

We have developed a 385-500 GHz OMT for ALMA [10]. To meet the ALMA specification, following requirements were set for an ALMA Band 8 (385-500 GHz) [11] OMT from a prototype study of the performance of a receiver [12] with a 2SB mixer [13].

Input Reflection: < - 20 dB
Insertion loss at 4 K: < 0.5 dB
Polarization isolation: > 25 dB

II. Design

A wire-flame model of a 385-500 GHz OMT is shown in Fig. 2. The OMT is basically scaled from that of ALMA Band 4 (125-163 GHz) developed by Asayama *et al.* [7]. The concept of the double ridged OMT is to concentrate the vertical polarization (V-pol.) between two ridges in the center of a square waveguide and to lower the impedance of it. Therefore the polarization can go though the junction. However, the horizontal polarization (H-pol.), which is to a large extent unaffected by the ridges, is divided at the Bϕifot junction because of impedance mismatch at the junction, and then output after recombined at the power combiner.

To optimize dimensions, the OMT was decomposed into five parts as shown in Fig. 3: (1) double ridge, (2) Bϕifot junction, (3) transformer, (4) right angle bend, and (5) side-arm. Each part was optimized with a commercial 3D EM simulator (CST MW Studio). Another commercial simulator (Ansoft HFSS) was also used to cross-check the results. First dimensions of the Bϕifot junction were optimized, then those of the other components were independently optimized based on parameters of the junction.

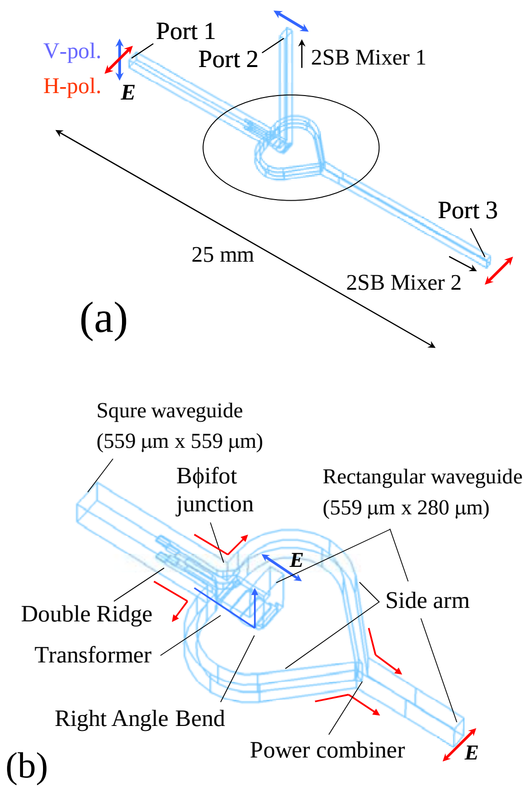

Fig. 2 a) Overview, b) Close-up view of a wire-flame model of a 385-500 GHz OMT.

Mechanical tolerance of waveguide dimensions was investigated in detail, since it becomes crucial in submillimeter-wave range. Fig. 4 shows the mechanical tolerance of the optimized Bϕifot junction. The optimized design is so robust that mechanical errors of 10 μm have little effect on the S-parameters. The double ridge waveguide and the transformer consist of a 3-step Chebyshev transformer, and 2-step one, respectively. The right angle bend is a 2-step type. The numbers of steps are optimized from a point of view of mechanical tolerance. All components of the OMT were confirmed to have mechanical tolerance of 10 μm. The results with two simulators, CST and HFSS, were almost consistent.

Detail dimensions and simulated S-parameters of the whole OMT are shown in Fig. 5. The conductivity of gold films at 4 K is assumed to be 1.0 x 10^8 S/m [2]. For the initial value of the dimensions of the double ridge, the equivalent impedances of each ridge section were calculated based on the theory described in [14] and [15].

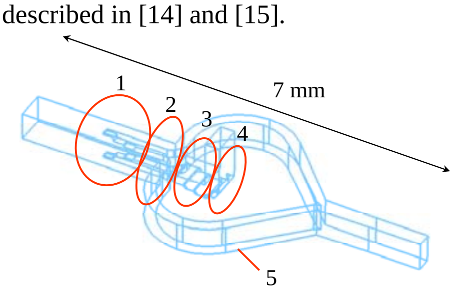

Fig. 3 Decomposed OMT model. (1) Double ridge, (2) Bϕifot junction, (3) transformer, (4) right angle bend, (5) side-arm.

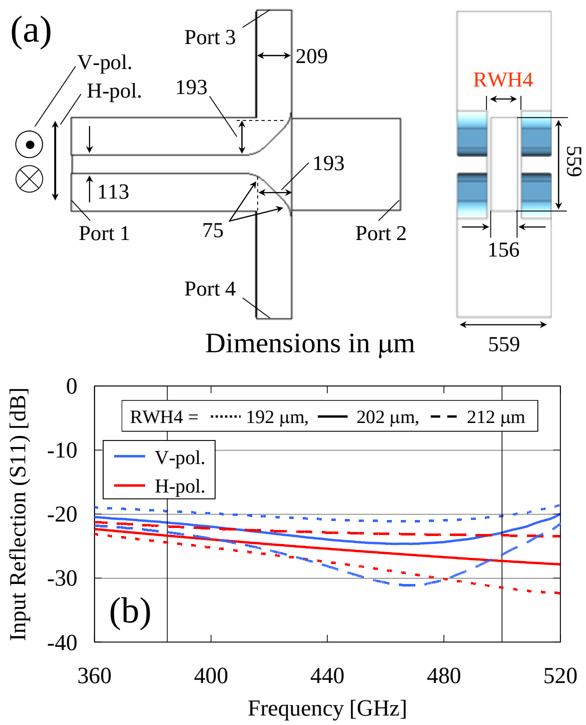

Fig. 4 Mechanical tolerance of the optimized Bϕifot junction (see Fig. 3). a) Dimensions of waveguide, and b) simulated input reflection of the junction with mechanical error of 10 μm at the section named RWH4.

Mechanically, the OMT consists of a two-split block at the center of the E-plane of the horizontal polarization as shown in Fig. 6. It can be made in (a) a three-split block with CNC milling techniques only, or (b) a two-split block with combinations of CNC milling and electroforming techniques. For the section at the vertical branch of the OMT, electroforming fabrication was valid to achieve designed performance. Three-split block scheme looked easier to be fabricated, however, it was not easy to obtain good mechanical contact among three blocks.

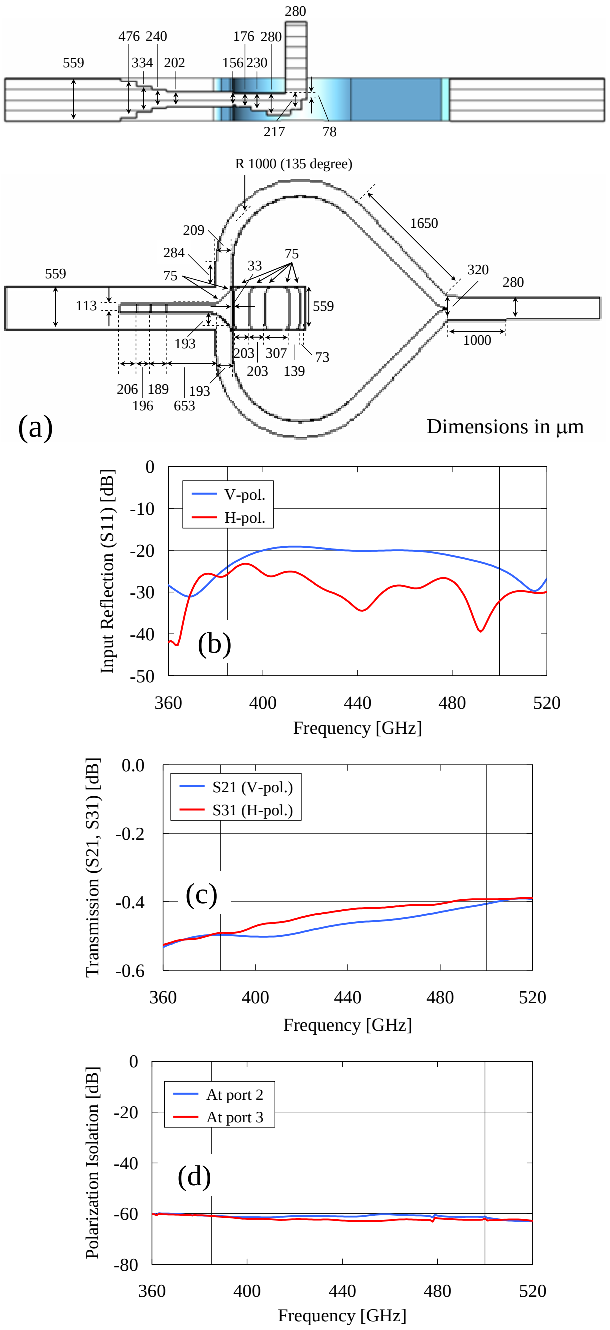

Fig. 5 (a) Dimensions and simulated (b) input reflection, (c) transmission at 4 K, and (d) polarization isolation of the 385-500 GHz OMT. Port definition is shown in Fig. 2 (a).

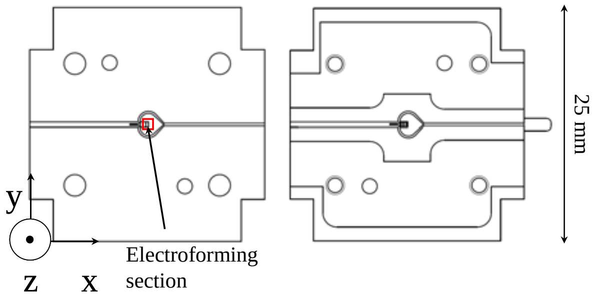

Fig. 6 Mechanical design of the 385-500 GHz OMT. The OMT is a two-split block at the center of the E-plane of the horizontal polarization. For the vertical branch, the electroforming technique was used.

III. EVALUATIONS

The OMT was fabricated by Oshima Prototype Engineering and made of TeCu with gold-plated. Results of the mechanical measurements are shown in Fig. 7. Measurements of xy- and xz-plane are done with a digital microscope, with a non-contact coordinate measuring machine (NH-3SP, Mitaka Kohki Co.,Ltd.), respectively. Dimensions are calibrated with a high precision scale (HL-250, Mitsutoyo Corporation). Typical mechanical error was ~ 5 μm from the measurements.

The polarization isolation of the OMT was measured with a quasioptical method [16]. We measured beam patterns of a corrugated horn [17] with and without an OMT as shown in Fig. 8. The increase in the amplitude of the cross-polarization due to the OMT at the center (0 degree) represents the

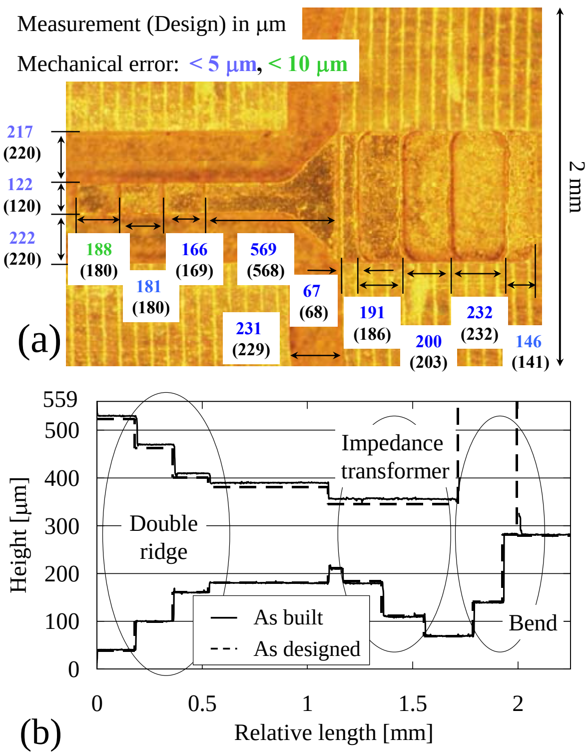

Fig. 7 Mechanical measurements over the area around the Bϕifot junction at a) xy-plane, b) xz-plane. Coordinate system is defined as in Fig. 6.

polarization isolation of the OMT. Polarization isolation of the OMT was measured to be larger than 20 dB over the 385-500 GHz band.

Fig. 9 shows the measured and simulated transmission loss at 300 K of the OMT. The measurements were done with a submillimeter VNA shown in Fig. 10. The conductivity of gold at 300 K is assumed to be 1.1 x 10^7 S/m [18], which is derived from a curve-fitted formula when ~ 1 μm of surface roughness is taken into account.

The additional noise due to the loss of the OMT was measured with an SIS mixer [19] as shown in Fig. 11. We measured the DSB noise temperature of an SIS mixer with and without an OMT. From these measurements, transmission loss of the OMT at 4 K was derived to be as low as 0.4-0.5 dB as shown in Table I. It is reasonably expected from the waveguide length of 25 mm and is consistent with simulated transmission loss in Fig. 5.

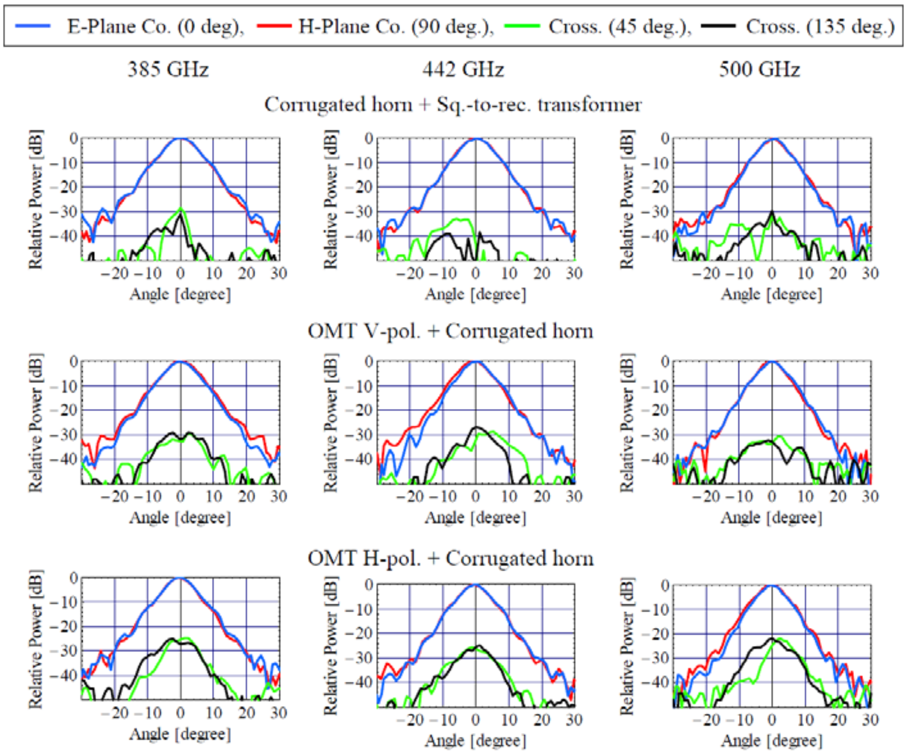

Fig. 8 Measured polarization isolation [16] of the OMT. These panels show beam patterns of the co- and cross- polarization of a corrugated horn [17] and the OMT. The upper, the middle, the lower panels show those of (1) the corrugated horn and a square-to-rectangular transformer, (2) the vertical branch of the OMT and the corrugated horn, (3) the horizontal branch of the OMT and the corrugated horn, respectively.

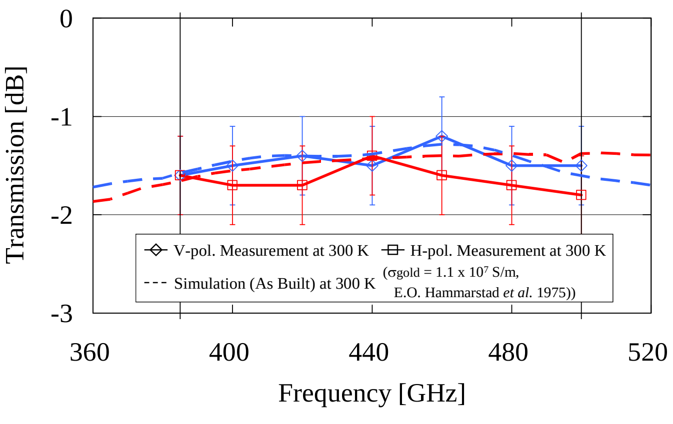

Fig. 9 Measured transmission loss and as built simulation of the OMT and a square-to-rectangular transformer (transmission is ~ 0.1 dB) at 300 K. The error bars are derived from reproducibility.

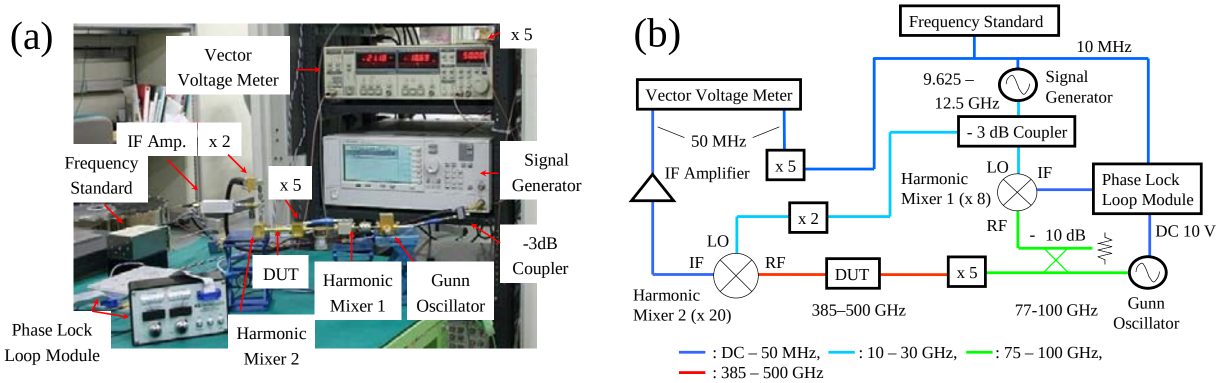

Fig. 10 (a) Photo and (b) block diagram of a 385-500 GHz vector network analyzer.

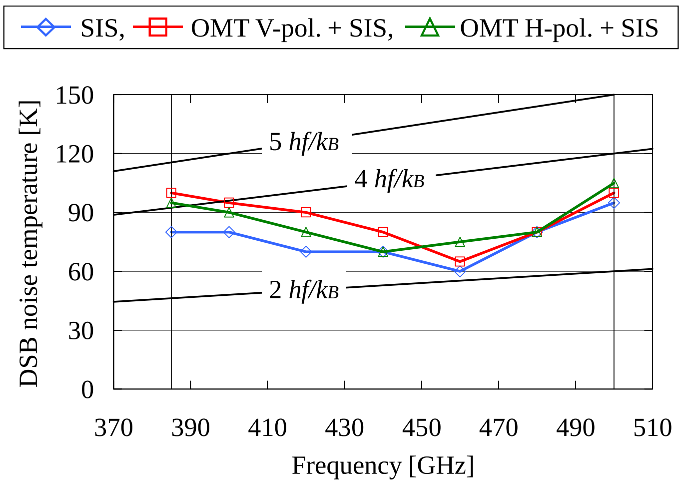

Fig. 11 The DSB noise temperature of an SIS mixer with and without the OMT. The noise increase was ~ 5-10 K around the band edges, and less than typical error of ~ 5 K at the band center.

TABLE I.

MEASURED CONTRIBUTIONS OF EACH COMPONENT TO THE RECEIVER NOISE.

Component	385 GHz				440 GHz				500 GHz			
	Gain [dB]		Te [K]		Gain [dB]		Te [K]		Gain [dB]		Te [K]	
	DSB	OMT + DSB	DSB	OMT + DSB	DSB	OMT + DSB	DSB	OMT + DSB	DSB	OMT + DSB	DSB	OMT + DSB
Window, Filter	-0.7		33	33	-0.5		25	25	-0.6		30	30
OMT	0	-0.5	0.0	0.6	0	-0.4	0.0	0.4	0	-0.4	0.0	0.4
LO coupler	-0.5		0.6	0.6	-0.4		0.4	0.5	-0.5		0.6	0.6
DSB mixer	-0.8		31	35	0.0		29	32	-2.6		35	39
Cooled IF chain	25		23	28	25		18	21	25		35	41
Warm IF chain	30		0.6	0.6	30		0.4	0.4	30		0.9	1.0
Sum	--	--	88	98	--	--	74	79	--	--	102	112

IV. CONCLUSIONS

We have developed a 385-500 GHz OMT for ALMA Band 8. The OMT is based on a Bøifot junction with a double ridge. Mechanical tolerance of the waveguide structures was studied in detail. The transmission loss at 4 K was derived to be as low as 0.4-0.5 dB with an SIS mixer. The polarization isolation was measured to be larger than 25 dB over the 385-500 GHz band with a quasioptical method.

ACKNOWLEDGMENT

The authors would like to thank Sheng-Cai Shi, Junji Inatani, Genshiro Fujii, Yoshizou Iizuka, Kazuyoshi Kumagai, Mutsumi Yokota. MK was supported by Grant-in-Aid for JSPS Research Fellowships for Young Scientists.

References

[1] J.R. Sambles, K.C. Elsom, D.J. Jarvis, "The Electrical Resistivity of Gold Films," *Phil. Trans R. Soc. Lond. A*, vol. 304, no. 1486, pp. 365–396, 1982.

[2] A.M. Bϕifot, "Classification of Ortho-Mode Transducers," *European Transactions on Telecommunications and Related Technologies*, vol. 2, no. 5, pp. 503–510, 1991.

[3] E.J. Wollack and W. Grammer, "Symmetric Waveguide Orthomode Junctions," *Proc. of the 14th Int. Symp. on Space Terahertz Tech.*, pp. 169–176, 2003.

[4] R. Banham, G. Valsecchi, L. Lucci, G. Pelosi, S. Selleri, V. Natele, R. Nesti, and G. Tofani, "Electroformed front-end at 100 GHz for radio-astronomical applications," *Microwave journal*, vol. 48, no. 8, pp. 112–122, 2005.

[5] G. Narayanan and N. Erickson, "Full-Waveguide Band Orthomode Transducer for the 3 mm and 1 mm Bands," *Proc. of the 14th Int. Symp. on Space Terahertz Tech.*, pp. 508–512, 2003.

[6] G. Moorey, R. Bolton, A. Dunning, R. Gough, H. Kanoniuk, and L. Reilly, "A 77-117 GHz Cryogenically Cooled Receiver for Radio Astronomy," *Proc. of the Workshop on the Applications of Radio Science*, 2006.

[7] S. Asayama, S. Kawashima, H. Iwashita, M. Inata, Y. Obuchi, T. Suzuki, and T. Wada, "Design and Development of ALMA Band 4 Cartridge Receiver," *Proc. of the 19th Int. Symp. on Space Terahertz Tech.*, 2008.

[8] A. Navarrini and R.L. Plambeck, "A Turnstile Junction Waveguide Orthomode Transducer," *IEEE Microwave Theory and Tech.*, vol. 54, no. 1, pp. 272–277, 2006.

[9] G. Pisano, L. Pietranera, K. Isaak, L. Piccirillo, B. Johnson, B. Maffei, and S. Melhuish, "A Broadband WR10 Turnstile Junction Orthomode Transducer," *IEEE Microwave and Wireless Components Letters*, vol. 17, no. 4, pp. 286–288, 2007.

[10] A. Wootten, "The Atacama Large Millimeter Array (ALMA)," *Arxiv preprint astro-ph/0209630*, 2002.

[11] Y. Sekimoto, Y. Iizuka, N. Satou, T. Ito, K. Kumagai, M. Kamikura, Y. Serizawa, M. Naruse, and W.L. Shan, "Development of ALMA Band 8 (385-500 GHz) Cartridge and its Measurement System," *Proc. of the 19th Int. Symp. on Space Terahertz Tech.*, 2008.

[12] N. Satou, Y. Sekimoto, Y. Iizuka, T. Ito, W.L. Shan, T. Kamba, K. Kumagai, M. Kamikura, Y. Tomimura, Y. Serizawa, S. Asayama, M. Sugimoto, "A Submillimeter Cartridge-Type Receiver: ALMA Band 8 (385 - 500 GHz) qualification model," PASJ, in press.

[13] M. Kamikura, Y. Tomimura, Y. Sekimoto, S. Asayama, W.L. Shan, N. Satou, Y. Iizuka, T. Ito, T. Kamba, Y. Serizawa, and T. Noguchi, "A 385-500 GHz Sideband-Separating (2SB) SIS Mixer Based on a Waveguide Split-Block Coupler," *Int. J. Infrared and Millimeter Waves*, vol. 27, no. 1, pp. 37-53, 2006.

[14] W.J.R. Hoefer and M.N. Burton, "Closed form expressions for parameters of finned and ridge waveguide," *IEEE Microwave Theory Tech.*, vol. 82, no. 12, pp. 2190–2194, 1982.

[15] N. Marcuvitz, Waveguide Handbook: Peter Peregrinus Ltd., 1993.

[16] M. Naruse, T. Ito, Y. Sekimoto, H. Toba, N. Satou M. Sugimoto, W. Shan, Y. Iizuka, T. Kamba M. Kamikura, Y. Serizawa, "Near-Field Beam Pattern Measurement of Qualification Model of ALMA Band 8 (385 – 500 GHz) Cartridge Receiver," submitted.

[17] M. Matsunaga, Y. Sekimoto, T. Matsunaga, and T. Sakai, "An Experimental Study of Submillimeter-Wave Horn Antennae for a Submillimeter-Wave Array," *PASJ*, vol. 55, no. 5, pp. 1051–1057, 2003.

[18] E.O. Hammerstad and F. Bekkadal, Microstrip Handbook, *ELAB Report*, 1975.

[19] W.L. Shan, T. Noguchi, S.C. Shi, and Y. Sekimoto, "Design and Development of SIS Mixers for ALMA Band 8," *IEEE Appl. Superconductivity*, vol. 15, issue 2, pp. 503–506, 2005.

Investigation of a 600-GHz Membrane-Based Twin Slot Antenna for HEB Mixers

W. Miao[1, 2,*], Y. Delorme[1], F. Dauplay[1], R. Lefevre[1], B. Lecomte[1], A. Feret[1], G. Beaudin[1], J. M. Krieg[1], W. Zhang[2], S. H. Cheng[2], and S. C. Shi[2].

[1]LERMA, Observatoire de Pairs, France
[2]Purple Mountain Observatory, NAOC, CAS, China
* Contact: wei.miao@obspm.fr, phone: 33-1-40-51-20-60

***Abstract*—In this paper, a 600-GHz membrane-based twin slot antenna for superconducting HEB (hot-electron-bolometer) mixers was investigated. The simulation on the radiation pattern and return loss (refer to the feed point) of the twin slot antenna including an RF choker filter was performed with Microwave Studio CST, Ansoft HFSS, and EMSS FEKO. An additional parabolic mirror is taken into account as focusing element in the membrane-based design and analyzed by using physical optics ray tracing approximation. We also fabricated a 200-times scale model of the designed twin slot antenna to validate the simulated results. For the scale model measurement, a de-embedding measurement technique was adopted to extract the input impedance of the twin slot antenna. The measured results are found in good agreement with the simulation.**

I. INTRODUCTION

FOR development of a closely packed multi-pixel superconducting HEB receiver, a new integrated quasi-optical design was proposed [1] to achieve efficient RF radiation coupling. The planar quasi-optical antenna in this design is integrated on an electrically thin substrate (membrane) and it couples the RF radiation via a metallic back reflector and a parabolic mirror (as shown in Fig. 1). Normally, the thickness of the membrane is less than $0.04\ \lambda_0$ (for slot antenna) [2] to avoid excitation of substrate modes. In contrast with the conventional substrate-lens integrated configuration, the absence of a thick substrate reduces the dielectric loss and enlarges the antenna structure. The usage of an antenna with a large dimension makes the device fabrication process much easier, especially for very high frequencies like terahertz. In this paper, we thoroughly investigate the quasi-optical properties of this new design incorporating with a planar twin slot antenna. At 600-GHz the radiation pattern and return loss of a membrane-based twin slot antenna were simulated with the aid of three different full wave electromagnetic solvers. The simulated input impedance (i.e. feed point impedance) of the twin slot antenna is validated by a 200-times scale model measurement employing a de-embedding technique.

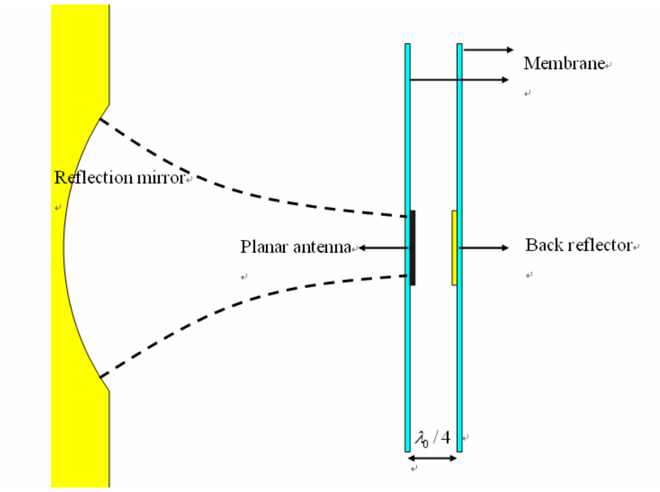

Fig. 1. Configuration of a membrane based quasi optical antenna.

II. NUMERICAL SIMULATION

A. *Design of a Membrane-Based Twin Slot Antenna*

Planar twin slot antennas have been widely used in quasi-optical receivers to achieve highly symmetric Gaussian beams and low cross polarization levels. The conventional design rule for twin slot antennas based on a scale model [3], is no longer valid for membrane-based twin slot antennas since the membrane is extremely thin and the substrate's influence is no longer same [1]. Therefore we defined the membrane-based twin slot antenna with the aid of a full wave electromagnetic solver Microwave Studio CST [4], which is based on the method of finite integration technique. Fig. 2 illustrates the simulated structure by Microwave Studio CST. The twin slot antenna is integrated on the membrane and a metallic back reflector is placed at a quarter-wavelength (in vacuum) behind the antenna for increasing the antenna's gain. The membrane is made of a silicon-on-insulator (SOI) wafer with a thickness of 3 μm and a dielectric constant of 11.7. An RF choker filter consisting of three consecutive low and high impedance quarter wavelength CPW stages is included to prevent the leakage of the RF signal into the IF port without stopping the IF and DC signal.

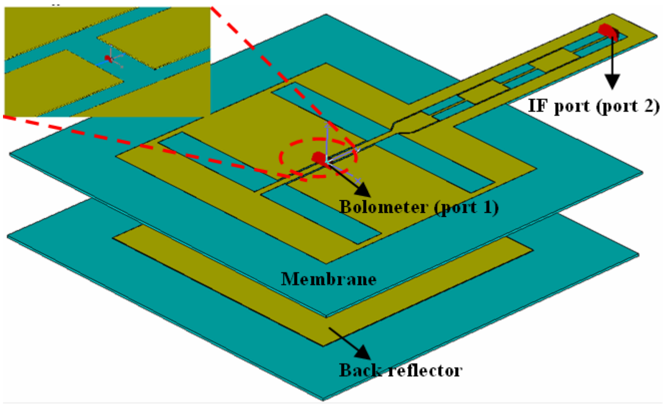

Fig. 2. CST simulated structure of the twin slot antenna. The bolometer (discrete port) is located on the center and coupled with the twin slot antenna via CPW lines.

In the simulation, the bolometer (i.e. HEB) is taken as a discrete port, designated as port 1, with a reference impedance of 100 Ω and coupled with the twin slot antenna via coplanar waveguide (CPW) transmission lines. The IF port, at the end of the RF choker filter, is defined as the other discrete port (port 2) with a reference impedance of 50 Ω. The reference impedance of port 1 was chosen to be analogous to the normal-state impedance (normally around 100 Ω) of our superconducting HEB devices. Fig. 3 shows the simulated reflection and transmission coefficients of this two-port network after optimizing the antenna's parameters for the minimum return loss at the antenna's feed point at 600 GHz. The optimized length and width of the slot is 350 μm (0.7 λ_0) and 43.5 μm (0.087 λ_0) respectively. According to Fig. 3, we can find that the twin slot antenna is well matched (to 100 Ω) at the design frequency of 600 GHz with a 10% relative bandwidth at a return-loss ($|S_{11}|^2$) level below -20 dB. The reflection coefficient at IF port is nearly equal to 0 dB, indicating that the field transmission between the two ports is efficiently prevented by the RF choker filter in the design frequency range. The superposition of the transmission coefficients (S_{12} and S_{21}) indicates the reciprocity of this two-port network and makes possible the application of the de-embedding technique between two ports. Fig. 4 shows the simulated radiation patterns of the twin slot antenna. Nearly perfectly symmetric radiation patterns are obtained in both E- and H-plane within a large angle range (100 degree). Notice that the effect of the parabolic mirror is not taken into account for the moment due to its extremely large size.

B. Comparison with HFSS and FEKO

In order to validate the optimized results, we simulated the same structure of the membrane-based twin slot antenna with two other full wave electromagnetic solvers Ansoft HFSS [5] and EMSS FEKO [6] based respectively on finite element method (FEM) and on method of moment (MoM). Fig. 3 and Fig. 4 show the simulated results with respect to return loss and radiation pattern. Clearly these three electromagnetic solvers have given nearly identical results over the whole frequency

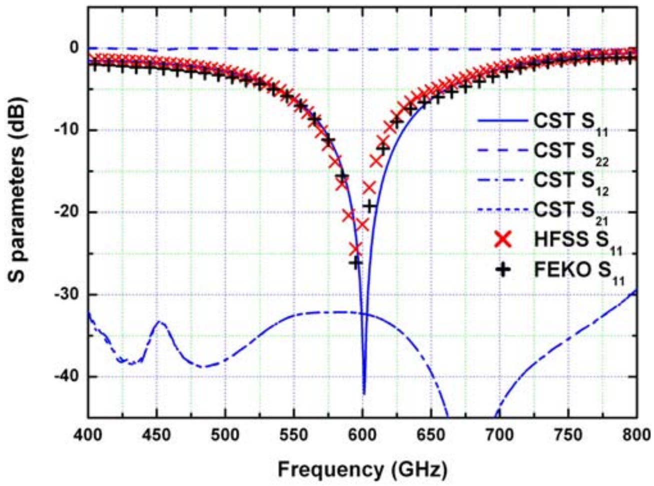

Fig. 3. Simulated S parameters seen from bolometer and IF port as a function of frequency.

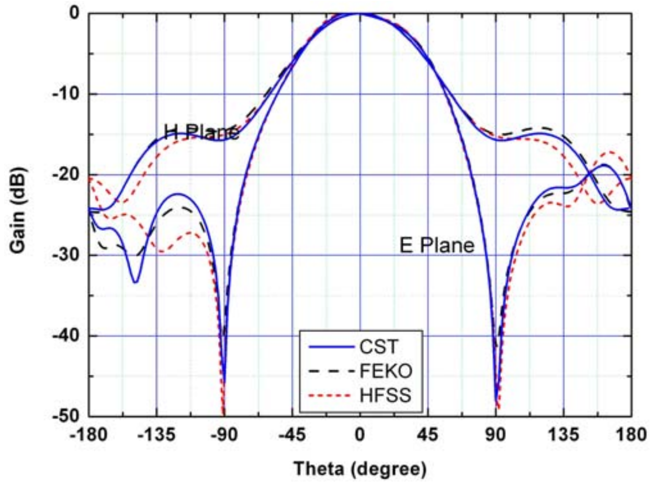

Fig. 4. Radiation patterns of the membrane-based twin slot antenna.

range. The insignificant frequency shift (Fig. 3) may be caused by the different mesh definition around the feed port

(port 1) which is extremely small in comparison to the twin slot antenna.

C. Effect of a parabolic mirror

We evaluated the effect of a parabolic mirror to the integrated antenna by means of an asymptotic high frequency technique employing physical optics (PO) ray tracing approximation. This technique has been hybridized by EMSS FEKO to solve electromagnetic problems when the object under consideration is too large (in terms of wavelength) to be dealt with by MoM.

The parabolic mirror adopted in our analysis has a diameter of 5 mm and a focal length of 2.5 mm. The membrane-based twin slot antenna is placed on the focal plane of the mirror and firstly simulated by using MoM. The results are then used as an input for the physical optics (PO) ray tracing approximation to simulate the whole mirror-membrane-based antenna

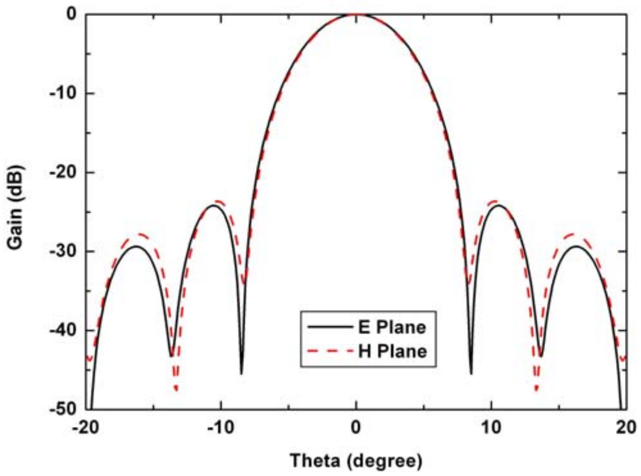

Fig. 5. Radiation patterns in E- and H-Plane of the membrane-based twin slot antenna including a 5 mm parabolic mirror.

structure. The calculated radiation patterns in E- and H-Plane at 600 GHz are illustrated in Fig. 5. The first side lobe level in two planes drops to -24 dB and the HPBW (Half Power Beam Width) of main lobe is around 6.4°, while 5.9° was given by diffraction limited beam pattern calculated [7] by the expression $(2J_1(\nu)/\nu)^2$, where $\nu = (\pi \tan(\theta)D)/\lambda_0$, J_1 is the first-order Bessel function of the first kind and D is the diameter of the mirror. It suggests that a diffraction-limited beam pattern can be achieved with the proposed quasi-optical design combining membrane-based twin slot antenna with parabolic mirror.

III. Scale Model Measurement

We also fabricated a 200 times scale model, as shown in Fig. 6, for the membrane-based twin slot antenna to validate the simulated results. In this model, the SOI membrane was replaced by a 0.635 mm thick high frequency laminate RT/Duroid 6006/6010 (ε_r = 10.8±0.25) [8]. As superconducting HEB devices can be equivalent to a resistance, we adopted a three-standard de-embedding measurement technique [9], [10] to characterize the input impedance of the twin slot antenna. Notice that in order to avoid too small (e.g. smaller than -20 dB) reflection coefficients measured at the IF port for the three standards, which may affect the accuracy of the de-embedding measurement technique, here we removed the RF choke filter and preserved only the tapered section used to connect the RF choke filter and the CPW.

This de-embedding measurement technique extracts the scattering parameters of the twin slot antenna from the reflection coefficients measured at the IF port when the feed point of the twin slot antenna is terminated with three different impedance standards. In terms of the extracted scattering parameter S_{11}, the input impedance of the twin slot antenna can

Fig. 6. Left: photo of a 200 times scale model fabricated for the membrane-based twin slot antenna and Right: experimental setup used to measure the impedance of a chip resistor.

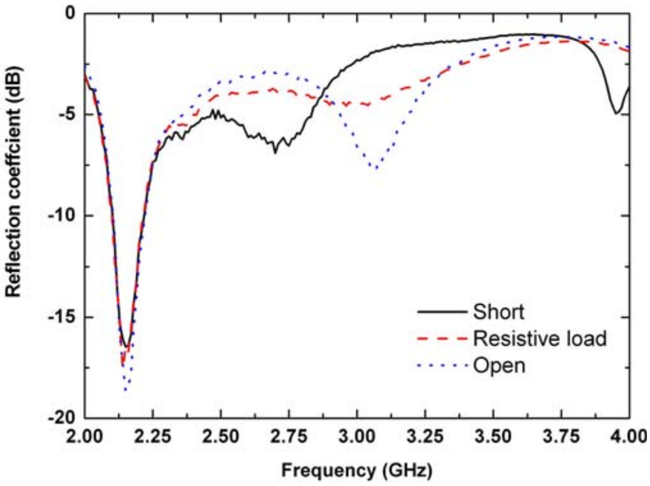

Fig. 7. Reflection coefficients measured at the IF port for three respective standards (open, short, resistive load) terminated at the feed point of the twin slot antenna.

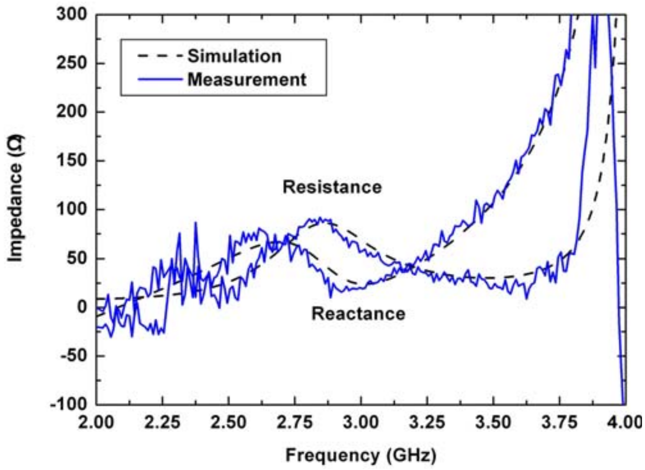

Fig. 8. Input impedances calculated by Microwave Studio CST and extracted from the scale model measurement.

be calculated by

$$Z_{input} = Z_0 \frac{1+S_{11}}{1-S_{11}} = \frac{\Gamma_1 Z_{L1}(Z_{L3}-Z_{L2}) + \Gamma_2 Z_{L2}(Z_{L1}-Z_{L3}) + \Gamma_3 Z_{L3}(Z_{L2}-Z_{L1})}{\Gamma_1(Z_{L2}-Z_{L3}) + \Gamma_2(Z_{L3}-Z_{L1}) + \Gamma_3(Z_{L1}-Z_{L2})} \quad (1)$$

where Z_0 is an arbitrarily specified reference impedance at port 1. Z_{Li} (i=1, 2, 3) and Γ_i (i=1, 2, 3) denote the impedance standards at the feed point of the twin slot antenna and the corresponding complex reflection coefficients measured at the IF port, respectively. For our scale model measurement, we chose open, short and resistive load as the three impedance standards. The input impedance can be therefore simplified as

$$Z_{input} = Z_r(\Gamma_o - \Gamma_r)/(\Gamma_r - \Gamma_s) \quad (2)$$

Where Γ_i (i=o, s, r) denote the reflection coefficients measured at the IF port when the feed point of the twin slot antenna is terminated by open, short and resistive load, and Z_r is the impedance of the resistive load.

According to Eq. (2), we know that having an accurate value of the resistive load is crucial to the de-embedding measurement technique. An additional experimental set, as shown in Fig. 6, was employed to determine the impedance of the chip resistor, which has a nominal resistance of 47.5 Ω. We soldered the chip resistor at the center of a microstrip line (DUT) with a width of 0.5 mm. The microstrip lines have the same substrate as that of the scale model. In order to remove the discontinuity effect between the SMA connector and the microstrip line as well as the loss and phase shift of the microstrip line, we also fabricated a corresponding microstrip calibration kit including Thru, Reflect and Line (shown in Fig. 6). After performing the standard TRL calibration, the impedance of the chip resistor was extracted from the measured *S* parameters of the DUT. It has a real part (from 48 to 56 Ω) close to its nominal value and a small imaginary component around 10 Ω.

Fig. 7 shows the reflection coefficients measured at the IF port when the feed point of the twin-slot antenna is terminated with three different standards (open, short, resistive load). Using these results and the measured load impedance Z_r, we calculated the input impedance of the twin slot antenna in terms of Eq. (2). Fig. 8 shows the calculated results. Clearly, the measured impedance agrees well with the one simulated by Microwave Studio CST in the frequency range of 2.5 to 4 GHz. A small discrepancy at low frequencies (from 2.0 to 2.4 GHz) might be caused by extremely low transmission between the two ports since the reflection coefficient measured at the IF port in this frequency range is indeed almost independent of the load terminated at the feed point of the twin-slot antenna (refer to Fig. 7).

Conclusion

A 600-GHz membrane-based twin slot antenna for superconducting HEB mixers has been investigated by numerical simulation and scale model measurement. The twin slot antenna is well resonant at the design frequency with a 10% relative bandwidth at return-loss level below -20 dB. A nearly diffraction-limited radiation pattern with a HPBW of 6.4° and a side lobe level of -24 dB is obtained after considering the effect of a 5 mm parabolic mirror. The validation of the simulated results of the membrane-based twin slot antenna is performed by a 200-times scale model incorporating with a three-standard de-embedding measurement technique. The measured results agree well with the numerical simulation.

ACKNOWLEDGMENT

W. M. would like to thank French Embassy in China for the funding of the joint French-Chinese PhD program. This work is supported by CNES (Centre National d'Etudes Spatiales) under contract No. RS06/SU-0002-041 and the NSFC under contracts No. 10673033 and No. 10621303.

REFERENCES

[1] J. Baubert, P. Khosropanah, V. Desmaris, V. Drakinskiy, P. Pons, P. Calmon, H. Merkel, M. Salez, "FTS measurement of a 2.5 THz double slot antenna on SiO_2/Si_3N_4 membrane with a NbN HEB mixer," in *Proc. 16th Int. Symp. Space Terahertz Technology,* 2005, pp. 260–264.

[2] D. F. Filipovic, S. S. Gearhart, and G. M. Rebeiz, "Double slot antennas on extended hemispherical and elliptical silicon dielectric lenses," *IEEE Trans. Microwave Theory Tech.,* vol. 41, pp. 1738-1749, 1993.

[3] G. V. Eleftheriades *et al.*, "Self and mutual admittance of slot antennas on a dielectric half space," *Int. J. Infrared Millimeter Waves,* vol. 14, pp. 1925–1946, 1993.

[4] *Computer Simulation Technology,* http://www.cst.com/

[5] *High Frequency Structure Simulator*, http://www.ansoft.com/.

[6] *Feldberechnung bei Korpern mit beliebieger Oberflache: Field computations involving bodies of arbitrary shape*, http://www.feko.info/.

[7] A. D. Semenov *et al.*, "Design and performance of the lattice-cooled hot-electron terahertz mixer," *Int. J. Applied Physics,* vol. 88, pp. 6758–6767, 2000.

[8] *RT/Duroid 6006/6010 LM High Frequency Laminates*, http://www.rogerscorporation.com/.

[9] W. Zhang, C. Y. Edward Tong, and S. C. Shi, "Scale model measurement of the embedding impedance of a 660-GHz waveguide SIS mixer with a 3-stardard de-embedding method," *IEEE Microwave and Wireless Component Letters,* vol. 13, no. 9, pp. 376–378, 2003.

[10] S. Ramo, J. R. Whinnery, and T. Van Duzer, *Fields and Waves in Communication Electronics*, 2nd ed. New York: Wiley, 1984, pp. 538.

Terahertz Attenuator Based on the Sub-wavelength Metal Structures

Guozhong Zhao*, Jie Bai, Yang Wang and Cunlin Zhang

Department of Physics, Capital Normal University, Beijing 10037, P. R. China
Beijing Key Lab for Terahertz Spectroscopy and Imaging, P. R. China
Key Lab of Terahertz Optoelectronics, Education Committee, P. R. China
*Contact: guozhong-zhao@mail.cnu.edu.cn, phone: +86-10-6898 0838

Abstract — **In this paper, we present a THz attenuator based on the sub-wavelength metal s tructures. The T Hz attenuator is designed and fabricated on a copper foil. We measured TH z transmission of the at tenuator by means of terahertz time domain spectroscopy. The experimental results s how th at the attenuator ca n h ave a good frequency selectivity which depends on the polarization of THz radiati on. T Hz power can be atten uated continuously into any level at a certain THz frequency without changing the polariz ation and c oherence of T Hz beam. Its attenuated frequency is designable by ch anging the size and shape of metal s tructures. The frequency selective transmission of th e attenuator is determined experimentally. We belie ve that our r esults suggest a valuable T Hz component fo r THz a pplication, in particular, for THz space instruments.**

Keywords: Terahertz, Attenuator, Metal, Structure

Introduction

In recent years, terahertz (THz) optical components have been paid more and more attention. This is due to two reasons. One is from the technological needs of THz applications. Another is from the physics of THz devices. The surface plasma polaritons of metal have attracted much attention of scientists and engineers over the world. THz photonic components based on the sub-wavelength metal structures have been regarded as a potential candidate of THz devices.

Ever since 1998 Ebbesen *et al* [1] discovered the extraordinary optical transmission through sub-wavelength periodic of thin metal film, the physical origin of enhanced transmission has been investigated by huge experimental and theoretical work. The enhanced transmission exceed the limit of conventional electromagnetic wave theory [2], the numeric value exceed several magnitude relative to conventional aperture theory [3]. Such extraordinary enhanced transmission is often explained by two representative views: one regarded that it is induced by the resonant interaction between incident light and Surface Plasmon Polarizations (SPPs) on the metal surface [4-7], but it can not explained the wavelength of enhanced transmission occurs red shift with the increase of the thickness of metal film [1]. The other hold that it is caused by like F-P cavity effect [8, 9]. Such high enhanced transmission is very attractive for several potentials applications in nanometre scale and high efficiency electrical-optical device and large density numeral store, such as electrical-optical modulator, near-field microscope, photolithography technology and new type of optical integrated component. Therefore, the research of physical origin of the enhanced transmission has got more and more attentions.

As for optical device, manipulating and controlling light by photonic crystals is very attractive. In certain cases, metals tend to play an important role in photonic crystals. Particularly, a two-dimensional metallic photonic crystal (2D-MPC), which is perforated periodically with circular holes, has been known as a band-pass filter in the millimetre and far-infrared regions [10, 11]. At 2003, Fumiaki Miyamaru *et al*. [12] studied the interesting polarization characteristics of two-dimensional metallic photonic crystal (2D-MPC) through THz time-domain spectroscopic system, their studies indicates that in sub-terahertz region, 2D-MPC not only as band-pass filter, but also as a wave plate, the linear polarization of the THz wave transmitted through 2D-MPC becomes elliptical with a slight tilting of the incident angle from the normal incidence. At 2004, Fumiaki Miyamaru *et al.* [13] also found that the frequency range at which the polarization rotation occurs is related to the lattice constant of a photonic crystal, indicating the importance of photonic band modes of the 2-D MPC in the mechanism of the phenomenon. At 2004, R.Gordon *et al.* [14] investigated the strong polarization dependence of optical transmission through elliptical nanometre ring. Their results show that the degree of polarization is determined by the ellipticity and orientation of the holes, the polarization axis lies perpendicular to the broad edge of the ellipse. At 2006, Jean-Baptiste Masson *et al.* [15] investigated two overlapping arrays of orthogonally oriented sub-wavelength elliptical holes over 0.1-1THz range. Their experimental result shows that the enhanced transmission exhibits polarization sensitive frequency shift. At 2004, Cao Hua and Ajay Nahata [16] also refer to the polarization property of rectangular holes with different aspect ratio, but they mainly describe the effect of hole's shape to the transmission and do not consider the polarization property profoundly. In this paper, we investigate the polarization dependence of enhanced transmission through the period array of rectangular holes with different aspect ratio of length to width. The polarization dependence of sub-wavelength metal structures has the potential for many applications, such as band-pass filter and wave plate in the THz frequency region.

I. EXPERIMENT SETUP AND SAMPLE PREPARATION

Our experiment setup used in this research is a type of THz Time-Domain Spectroscopy (THz-TDS) system. The schematic diagram of THz-TDS setup is shown in Figure 1. A repetition rate of 82 MHz, diode-pump mode-locked Ti:Sapphire laser (Mai Tai, Spectra-Physics) provided the femtosecond pulses with a pulse duration of 100 fs and the centre wavelength of 810 nm. The femtosecond beam is divided into two beams: one is used as a pump beam, another as a probe beam. A p-type InAs wafer with <100> orientation is used as the THz emitter. A 1mm-thick of <110> ZnTe crystal is employed as the sensor. The pump beam is used to generate THz radiation and the probe beam acted as a gated detector to monitor the temporal waveform of THz field. A silicon lens and four parabolic mirrors are used to collimate and focus the THz beam through the free space onto the detector. A balanced photodiode detector detected the probe beam. The measured signal is amplified by a lock-in amplifier and sent to the computer for the data processing and analysis. The THz beam path as the dashed line frame in Fig. 1 is purged with the dry nitrogen to minimize the absorption of water vapour and enhance the SNR. The spectral resolution is better than 50 GHz. The effective range of frequency is 0.2-2.5THz. The temperature is keep around 21.2^{o}C. The relative humidity is keep at 3.6% in this experiment.

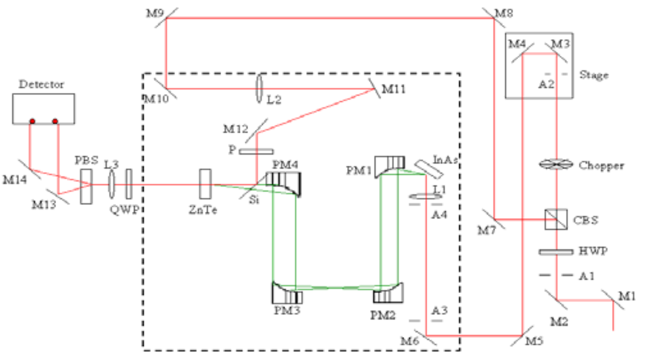

Fig.1 Schematic Diagram of THz-TDS System
M1~M14: mirrors; CBS: cubic beam splitter; L: convex lens; PM1~PM4: parabolic mirrors; PBS: polarized beam splitter; HWP: 1/2 wave plate; QWP: 1/4 wave plate.

We design a set of periodic array of rectangular holes with different aspect ratio of length-to-width. Our design principle is to change the aspect ratio of rectangular holes while keeping their area (~22500 μm^2) and the period of their lattice as a constant. We design totally five periodic arrays of rectangular holes. The aspect ratio of length-to-width for single rectangular hole are 1:1, 1.5:1, 2:1, 2.5:1, 3:1, respectively. The array patterns of rectangular holes are fabricated by the cut of YAG laser on a 100um thickness of copper film. The specification of the five rectangular holes array with different aspect ratio is designed as in table 1.

TABLE 1
SAMPLE PARAMETER OF STRUCTURES

Sample	**Parameters of Structure (μm)**		
	a:b	**a (μm) b**	**(μm)**
1	1:1	150	150
2	1.5:1	184	122
3	2:1	212	106
4	2.5:1	236	95
5	3:1	260	86

In Table 1, *a* represents the length of a single rectangular hole, and *b* as the width of a single rectangular hole. The *a:b* is the aspect ratio of a single rectangular hole. We designs the period of rectangular holes array *T* as 425 μm, which is the spacing between the centres of two adjacent rectangular holes. The thickness of copper foil used is 100 μm.

II. DATA EXTRACTING OF THZ TRANSMISSION SPECTRUM

Terahertz time-domain spectroscopy (THz-TDS) can provide the information of THz electric field of incident and transmitted THz wave including amplitude and phase. By means of Fast Fourier Transform (FFT), we can obtain the frequency-domain transmission spectra $E_{reference}$ (f) and $E_{transmitted}$ (f) as, respectively, the incident and transmitted THz field. Therefore, the transmission coefficient of sample can be extracted as follows

$$T(f) = \frac{E_{transmitted}(f)}{E_{reference}(f)}, \qquad (1)$$

Here *T(f)* is the transmission spectrum. The transmission coefficient as a function of frequency indicates the amplitude and phase of transmission ability of THz radiation through the periodic array of rectangular holes on the copper foil. So we obtain THz transmission spectrum by means of FFT and from the THz-TDS measurement.

III. EXPERIMENT RESULTS AND DISCUSSIONS

Using a THz time domain spectroscopic system (THz-TDS), we can measure directly the temporal waveform of reference signal and sample signal. After Fast Fourier Transformation (FFT), we can obtain the corresponding frequency spectrum. After that we can extract out the transmission spectrum of samples by keeping the incidence angle as a constant ϕ =0^{o}, that is the case of normal incidence, and varying the azimuth angle θ, where θ is the angle between THz polarization and the long side of rectangular holes. Through measuring the signal of the sample every 15^{o} of azimuth angle, we can get transmission spectrum at different azimuth angle. Figure 2 presents the transmission spectrum of rectangular holes array with the aspect ratio of 2:1, that is the sample 3 at different azimuth angle θ =0°, 15°, 30°, 45°, 60°, 75°, and 90°. Other samples show the similar properties of THz transmission except for the sample 1 with the structure of square hole shown as figure 3.

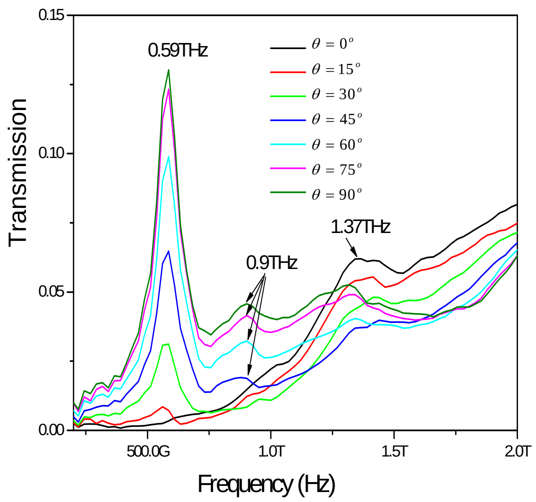

Fig. 2 THz transmission of rectangular hole array with the 2:1 of length-to-width ratio at different polarization

Fig. 3 shows that the THz transmission through the array of square holes is less obviously than those through the rectangular holes, and its polarization dependence of THz transmission is not so distinguished. It is clear that the polarization dependence of THz transmission results mainly from the unsymmetrical metal structures.

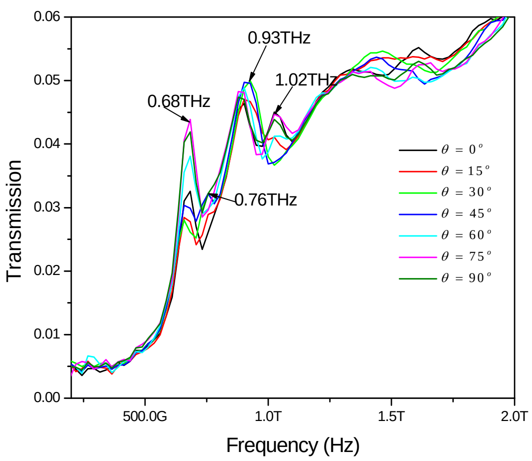

Fig. 3 THz transmission of square hole array with the 1:1 of length-to-width ratio at different polarization

By comparing THz transmission spectrum of the five samples at different azimuth angle, we found that the five period arrays of rectangular holes with different aspect ratio have obvious resonant transmission peak at 0.68THz, 0.63THz, 0.59THz, 0.54THz, 0.49THz, respectively. This indicates that the transmission of sub-wavelength periodic array of rectangular holes has obvious frequency selectivity in THz frequency region. This is significant for the band-pass filter of THz wave.

More importantly, due to the strong polarization dependence of THz transmission through the metal structures, it is possible to develop the sub-wavelength THz attenuator. From Fig. 2 and Fig. 3, we can see that the frequency position of resonant transmission peak do not change with the increase of azimuth angle, that is, the angle between the THz polarization and the long side of rectangular hole. However, THz transmission of four samples 2-5 with the rectangular holes at their resonant frequencies increases with increasing of azimuth angle. Figure 4 shows that the THz transmission peak of four samples 2-5 of rectangular holes as a function of azimute angle between the THz polarization and

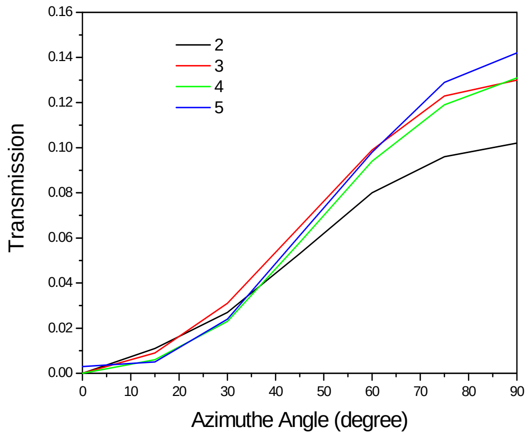

the long side of rectangular holes.

Fig. 4 THz transmission peak of four arrays of rectangular holes for the sample structures 2-5 as a function of azimuth angle.

From Fig. 4, it is clear that THz transmission peak of the periodic array of rectangular holes depends nonlinearly on the polarization of incident THz wave. By rotating the metal structures on the copper foil, one can change the THz transmission at the resonant frequency. Based on this kind of THz transmission, it is helpful to serve as an attenuator of THz wave. It is significant to attenuate THz wave for the application of high power of THz radiation. We believe that the sub-wavelength metal structures will play an important role on the application of the THz photonic devices in the future.

IV. Conclusions

THz Transmissions of sub-wavelength metal structures show the obvious frequency selectivity and polarization dependence. The frequency position of transmission peak does not change with changing of the direction of THz polarization, but its transmission peak depends strongly on the THz polarization. Therefore, it is easy to utilize the metal structures as an attenuator of THz wave. By rotating the metal structure, one can change the THz transmission intensity through the metal plate. The THz attenuator can be fabricated based on the metal structures.

ACKNOWLEDGMENT

This work has been supported by National Keystone Basic Research Program (973 Program) under Grant No. 2007CB310408 , National Natural Science Foundation of China under Grant No. 10474067, Natural Science Foundation of Beijing under Grant No. 4073030, and Funding Project for Academic Human Resources Development in Institutions of Higher Learning Under the Jurisdiction of Beijing Municipality.

REFERENCES

[1] T. W. Ebbesen, H. J. Lezec, H. F. Ghaemi, T. Thio, Nature, 391, pp. 667-669, 1998.
[2] H. A. Bethe, Phys. Rev. 66, pp.163-167, 1944.
[3] R. H. Ritchie, Phys. Rev. 106, pp.874-881, 1957.
[4] T. Thio, H. F. Ghaemi, H. J. Lezec, P. A. Wolff and T. W. Ebbesen, J. Opt. Soc. Am. B, 16, pp.1743-1749, 1999.
[5] D. E. Grupp, H. J. Lezec, T. W. Ebbesen, K. M. Pellerin and T. Thio, Appl. Phys. Lett. 77, pp.1569-1573, 2000.
[6] H. F. Ghaemi, T. Thio, and D. E. Grupp, Phys. Rev. B 58, pp.6779-6782, 1998.
[7] L. Martín-Moreno, F. J. García-Vidal, H. J. Lezec, K. M. Pellerin, T. Thio and T. W. Ebbesen, Phys. Rev. Lett. 86, pp.1114-1117, 2001.
[8] S. Astilean, Ph. Lalanne and M. Palamaru, Opt. Commun. 175, pp.265-269, 2000.
[9] Y. Takakura, Phys. Rev. Lett. 86, pp.5602-5605, 2001.
[10] T. K. Wu, Frequency Selective Surface and Grid Array, Wiley Interscience, 1995.
[11] C. C. Chen, IEEE Trans. Microwave Theory and Technology, MTT-21, pp.1-6, 1973.
[12] Fumiaki Miyamaru, Takashi Kondo, Takeshi Nagashima, and Masanori Hangyo, Appl. Phys. Lett. 82**,** pp. 2568-2571, 2003.
[13] Fumiaki Miyamaru, Masanori Hangyo, Appl. Optics, 43, pp.1412-1416, 2004.
[14] R. Gordon, A. G. Brolo, A. Mckinnon, A. Rajora, Phys. Rev. Lett. 92. pp.037401, 2004.
[15] Jean-Baptiste Masson and Guilhem Gallot, Phys. Rev. B, 73, pp.121401(R), 2006.
[16] Cao Hua and Ajay Nahata, Optics Express, 12, pp.3664-3667, 2004.

Registered participants

First name	Last name	Institution	Country	Email
Shin'ichiro	Asayama	NAOJ	Japan	shinichiro.asayama@nao.ac.jp
Damian	Audley	University of Cambridge	UK	audley@mrao.cam.ac.uk
Biddut	Banik	Chalmers University of Technology	Sweden	biddut.banik@chalmers.se
Tarun	Bansal	SRON	Netherlands	t.bansal@tudelft.nl
Rami	Barends	Delft University of Technology	Netherlands	r.barends@tudelft.nl
Jan	Barkhof	SRON	Netherlands	J.Barkhof@sron.nl
Andrey	Baryshev	NOVA/SRON/RuG	Netherlands	a.m.baryshev@sron.nl
Jochem	Baselmans	SRON	Netherlands	J.Baselmans@sron.nl
Eric	Becklin	UCLA/USRA-SOFIA	USA	ebecklin@sofia.usra.edu
Victor	Belitsky	Chalmers University of Technology, GARD	Sweden	victor.belitsky@chalmers.se
Dominic	Benford	NASA / GSFC	USA	dominic.benford@gsfc.nasa.gov
Bhushan	Billade	Chalmers University of Technology	Sweden	bhushan.billade@chalmers.se
Raymond	Blundell	SAO	USA	rblundell@cfa.harvard.edu
Albert	Bos	Astron	Netherlands	bos@astron.nl
Faouzi	Boussaha	LERMA - Obesrvatoire de Paris	France	faouzi.boussaha@obspm.fr
Jeffrey	Bout	University of Groningen	Netherlands	bout@astro.rug.nl
Eric	Bryerton	NRAO	USA	ebryerto@nrao.edu
Massimo	Candotti	NAOJ	Japan	m.candotti@nao.ac.jp
Thomas	Cecil	University of Virginia	USA	twc7c@virginia.edu
Goutam	Chattopadhyay	JPL/Caltech	USA	Goutam.Chattopadhyay@jpl.nasa.gov
Xiaoshu	Chen	State Key Laboratory of Optoelectronic Materials and Technologie	China	chenxshu@hotmail.com
Jean Yves	Chenu	IRAM	France	chenu@iram.fr
Sergey	Cherednichenko	Chalmers University of Technology	Sweden	serguei@chalmers.se
Moon-Hee	Chung	Korea Astronomy & Space Science Institute	South Korea	mhchung@kasi.re.kr
Oleg	Cojocari	ACST GmbH	Germany	cojocari@acst.de
Gerard	Cornet	SRON	Netherlands	g.cornet@sron.nl
Ray	Davis	Royal Holloway Physics Dept	UK	r.p.davis@rhul.ac.uk
Thijs	de Graauw	Leiden Univ./SRON	Netherlands	thijsdg@sron.rug.nl
Leo	de Jong	SRON	Netherlands	L.de.jong@sron.nl
Gert	de Lange	SRON	Netherlands	gert@sron.nl
Vincent	Desmaris	GARD, Chalmers University	Sweden	Vincent.Desmaris@chalmers.se
Pieter	Dieleman	SRON	Netherlands	P.Dieleman@sron.rug.nl
Simon	Doyle	Cardiff University	Wales, UK	Simon.doyle@astro.cf.ac.uk
Vladimir	Drakinskiy	Chalmers University of Technology	Sweden	vladimir.drakinskiy@chalmers.se

First name	Last name	Institution	Country	Email
Michael	Edgar	California Institute of Technology	USA	rena@submm.caltech.edu
Iraj	Ehtezazi Alamdari	University of Waterloo	Canada	iraj@maxwell.uwaterloo.ca
Anders	Emrich	Omnisys	Sweden	ae@omnisys.se
Akira	Endo	NAOJ / Univ. of Tokyo	Japan	akira.endo@nao.ac.jp
Neal	Erickson	University of Massachusetts	USA	neal@astro.umass.edu
Corinne	Evesque	IAS - CNRS	France	corinne.evesque@ias.fr
Timothy	Finn	CAY	Spain	t.finn@oan.es
Jian-Rong	Gao	SRON-TU Delft	Netherlands	j.r.gao@tudelft.nl
Hans	Golstein	SRON	Netherlands	J.F.Golstein@sron.nl
Gregory	Goltsman	Moscow State Pedagogical University	Russia	goltsman@mspu-phys.ru
Paul	Grimes	Oxford University	UK	pxg@astro.ox.ac.uk
Christopher	Groppi	University of Arizona	USA	cgroppi@as.arizona.edu
Bruno	Guillet	GREYC CNRS	France	bguillet@greyc.ensicaen.fr
Andre	Gunst	ASTRON	Netherlands	gunst@astron.nl
Shan	He	State Key Laboratory of Optoelectronic Materials and Technologie	China	hs99zdy@163.com
Abigail	Hedden	Harvard-Smithsonian Center for Astrophysics	USA	ahedden@cfa.harvard.edu
Panu	Helistö	VTT	Finland	panu.helisto@vtt.fi
Doug	Henke	Chalmers University of Technology, GARD	Sweden	doug.henke@chalmers.se
Jeffrey	Hesler	VDI/UVA	USA	hesler@vadiodes.com
Ronald	Hesper	University of Groningen / SRON	Netherlands	r.hesper@sron.nl
Stefan	Heyminck	Max-Planck-Institut für Radioastronomie	Germany	heyminck@mpifr-bonn.mpg.de
Richard	Hills	ALMA	Chile	rhills@alma.cl
Rik	Hortensius	TU Delft	Netherlands	rikhortensius@hotmail.com
Niels	Hovenier	TU Delft	NL	j.n.hovenier@tudelft.nl
Heinz-Wilhelm	Hübers	German Aerospace Center	Germany	heinz-wilhelm.huebers@dlr.de
Konstantin	Ilin	University of Karlsruhe	Germany	k.ilin@ims.uni-karlsruhe.de
Hirofumi	Inoue	University of Tokyo	Japan	h-inoue@ioa.s.u-tokyo.ac.jp
Herman	Jacobs	SRON	Netherlands	H.M.Jacobs@sron.nl
Willem	Jellema	SRON	Netherlands	W.Jellema@sron.nl
Ling	Jiang	University of Tokyo	Japan	ljiang@taurus.phys.s.u-tokyo.ac.jp
Cécile	Jung	Observatoire de Paris	France	cecile.jung@obspm.fr
Mamoru	Kamikura	NAOJ	Japan	kamikura.mamoru@nao.ac.jp
Lin	Kang	Nanjing University	China	kanglin@nju.edu.cn
Alexandre	Karpov	California Institute of Technology	USA	karpov@submm.caltech.edu
Irmantas	Kašalynas	Semiconductor Physics Institute	Lithuania	irmantak@ktl.mii.lt
Pourya	Khosropanah	SRON	Netherlands	p.khosropanah@sron.nl
Andrey	Khudchenko	Institute of Radio-engineering and Electronics	Russia	Khudchenko@hitech.cplire.ru

First name	**Last name**	**Institution**	**Country**	**Email**
Reece	Kind	Glenair UK	UK	rkind@glenair.co.uk
Phichet	Kittara	Mahidol University	Thailand	tepcy@mahidol.ac.th
Teun	Klapwijk	Delft University of Technology	Netherlands	T.M.Klapwijk@tudelft.nl
Bernd	Klein	Max-Planck-Institut for Radioastronomy	Germany	bklein@MPIfR-Bonn.MPG.de
Takafumi	Kojima	Osaka Prefecture University/NAOJ	Japan	s_kojima@p.s.osakafu-u.ac.jp
Jacob	Kooi	Caltech	USA	kooi@caltech.edu
Valery	Koshelets	Institute of Radio Engineering and Electronics	Russia	valery@hitech.cplire.ru
Craig	Kulesa	University of Arizona	USA	ckulesa@as.arizona.edu
Leonid	Kuzmin	Chalmers University	Sweden	leonid.kuzmin@mc2.chalmers.se
Wouter	Laauwen	SRON	Netherlands	W.M.Laauwen@SRON.NL
Igor	Lapkin	Chalmers University of Technology, GARD	Sweden	lapkin@chalmer.se
Mark	Lee	Sandia National Laboratories	United States	mlee1@sandia.gov
Roland	Lefèvre	LERMA	France	roland.lefevre@obspm.fr
Mikko	Leivo	VTT - Finland	Finland	mikko.leivo@vtt.fi
Jing	Li	Purple Mountain Observatory,CAS	China	lijing@mail.pmo.ac.cn
Chris	Lodewijk	Delft University of Technology	Netherlands	c.f.j.lodewijk@tudelft.nl
Arttu	Luukanen	Millimetre-wave Laboratory of Finland - MilliLab	Finland	arttu.luukanen@vtt.fi
Guohong	Ma	Shanghai University	P. R. China	ghma@staff.shu.edu.cn
Alain	Maestrini	Observatoire de Paris, LERMA	France	alain.maestrini@obspm.fr
Sylvain	Mahieu	IRAM	France	mahieu@iram.fr
Doris	Maier	IRAM	France	maier@iram.fr
Chris	Martin	Oberlin College	US	Chris.Martin@oberlin.edu
Hiroshi	Matsuo	NAOJ	Japan	h.matsuo@nao.ac.jp
Francois	Mattiocco	IRAM	France	mattiocc@iram.fr
Imran	Mehdi	JPL	USA	imran.mehdi@jpl.nasa.gov
Denis	Meledin	Chalmers University of Technology, GARD	Sweden	denis.meledin@chalmers.se
Patricio	Mena	SRON	Netherlands	mena@rug.nl
Wei	Miao	LERMA, Observatoire de Paris	France	wei.miao@obspm.fr
David	Miller	Caltech	USA	davem@submm.caltech.edu
Raquel	Monje	Chalmers University of Technology, GARD	Sweden	raquel.monje@chalmers.se
Tetsuo	Mori	INFRARED LIMITED	Japan	tmori@infrared.co.jp
Pat	Morris	Caltech/NHSC	USA	pmorris@ipac.caltech.edu
Axel	Murk	University of Bern	Switzerland	murk@iap.unibe.ch
Takao	Nakagawa	ISAS/JAXA	Japan	nakagawa@ir.isas.jaxa.jp
Taku	Nakajima	Osaka Prefecture University	Japan	s_tac@p.s.osakafu-u.ac.jp
Masato	Naruse	University of Tokyo, NAOJ	Japan	masato.naruse@nao.ac.jp
Alessandro	Navarrini	INAF-Cagliari Astronomy Observatory	Italy	navarrin@ca.astro.it

First name	Last name	Institution	Country	Email
Omid	Noroozian	California Institute of Technology	USA	omid@caltech.edu
Olle	Nyström	Chalmers University of Technology	Sweden	olle.nystrom@chalmers.se
Vladimir	Parshin	Institute of Applied Physics of RAS	Russia	parsh@appl.sci-nnov.ru
Dmitry	Pavelyev	Nyzny Novgorod State University	Russia	pavelev@rf.unn.ru
Sergey	Pavlov	German Aerospace Center	Germany	sergeij.pavlov@dlr.de
Becca	Percy	University of Virginia	USA	rrp4d@virginia.edu
Thomas G.	Phillips	Caltech	USA	rena@submm.caltech.edu
Göran	Pilbratt	European Space Agency	Netherlands	gpilbratt@rssd.esa.int
Patrick	Pütz	Universität zu Köln	Germany	puetz@ph1.uni-koeln.de
Pekka	Rantakari	Millimetre Wave Laboratory of Finland - MilliLab	Finland	pekka.rantakari@vtt.fi
Paul	Richards	University of California, Berkeley	USA	richards@cosmology.berkeley.edu
Heiko	Richter	German Aerospace Center	Germany	heiko.richter@dlr.de
Erich	Schlecht	Jet Propulsion Laboratory	USA	Erich.Schlecht@jpl.nasa.gov
Yutaro	Sekimoto	NAOJ	Japan	sekimoto.yutaro@nao.ac.jp
José Manuel	Serna	Centro Astronómico de Yebes	Spain	jm.serna@oan.es
Masumichi	Seta	University of Tsukuba	Japan	seta@physics.px.tsukuba.ac.jp
Wenlei	Shan	Purple Mountain Observatory, CAS	China	shawn@mwlab.pmo.ac.cn
Sheng-Cai	Shi	Purple Mountain Observatory, CAS	China	scshi@mail.pmo.ac.cn
Shoichi	Shiba	The University of Tokyo	Japan	shiba@taurus.phys.s.u-tokyo.ac.jp
Sergey	Shitov	NAOJ / IREE	Russia	sergey@hitech.cplire.ru
Jose V.	Siles	Universidad Politecnica de Madrid	Spain	jovi@gmr.ssr.upm.es
Andrey	Smirnov	Moscow State Pedagogical University	Russia	s_andrey1981@yahoo.com
Peter	Sobis	Omnisys Instruments AB	Sweden	peter.sobis@chalmers.se
Gordon	Stacey	Cornell University	USA	gjs12@cornell.edu
Johannes	Staguhn	NASA/GSFC & Univ. of Maryland	USA	johannes.g.staguhn@nasa.gov
Jan	Stake	Chalmers	Sweden	jan.stake@chalmers.se
Nopporn	Suttiwong	German Aerospace Center	Germany	nopporn.suttiwong@dlr.de
Cezary	Sydlo	ACST GmbH	Germany	sydlo@acst.de
Gie Han	Tan	ESO	Germany	ghtan@eso.org
David	Teyssier	ESAC	Spain	dteyssier@sciops.esa.int
Bertrand	Thomas	Rutherford Appleton Laboratory	UK	b.thomas@rl.ac.uk
Christopher	Thomas	University of Cambridge	UK	cnt22@cam.ac.uk
Ross	Thomson	Glenair	UK	rthomson@glenair.co.uk
Edward	Tong	Harvard-Smithsonian Center for Astrophysics	USA	etong@cfa.harvard.edu

First name	Last name	Institution	Country	Email
Jeanne	Treuttel	Observatory of Paris LERMA	France	jeanne.treuttel@obspm.fr
John	Tucker	University of Illinois	USA	jrtucker@uiuc.edu
Vladimir	Vaks	Institute for Physics of Microstructures RAS	Russia	elena@ipm.sci-nnov.ru
Henk	van der Linden	SRON	Netherlands	H.H.van.der.Linden@sron.nl
Elfi	van Zeijl	TU Delft	Netherlands	e.vanzeijl@student.tudelft.nl
Anastasios	Vayonakis	Caltech	USA	avayona@submm.caltech.edu
Vyacheslav	Vdovin	IAP RAS	Russia	vdovin@appl.sci-nnov.ru
Jean-Claude	Villégier	CEA-Grenoble, DRFMC	France	jean-claude.villegier@cea.fr
Josip	Vukusic	Chalmers University of Technology	Sweden	vukusic@chalmers.se
Christopher	Walker	University of Arizona	USA	cwalker@as.arizona.edu
Hui	Wang	Observatoire de Paris	France	hui.wang@obspm.fr
Ming-Jye Wang	Wang	ASIAA	Taiwan	mingjye@asiaa.sinica.edu.tw
Michael	Wanke	Sandia National Labs	USA	mcwanke@sandia.gov
Mark	Whale	NUI Maynooth	Ireland	mark.r.whale@nuim.ie
Wolfgang	Wild	SRON	Netherlands	w.wild@sron.rug.nl
Satoshi	Yamamoto	University of Tokyo	Japan	yamamoto@phys.s.u-tokyo.ac.jp
Stephen	Yates	SRON	Netherlands	s.yates@sron.nl
Sigfrid	Yngvesson	University of Massachusetts	USA	yngvesson@ecs.umass.edu
Atik	Youssef	CNRS-IAS	France	youssef.atik@ias.u-psud.fr
Wen	Zhang	SRON	Netherlands	W.Zhang@sron.nl
Cunlin	Zhang	Capital Normal University	P. R. China	cunlin_zhang@mail.cnu.edu.cn
Guozhong	Zhao	Capital Normal University	P. R. China	guozhong-zhao@126.com